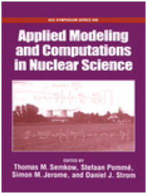

ACS SYMPOSIUM SERIES [illegible]

Applied Modeling and Computations in Nuclear Science

EDITED BY

Thomas M. Semkow, Stefaan Pommé,
Simon M. Jerome, and Daniel J. Strom

Downloaded by 89.163.34.136 on August 6, 2012 | http://pubs.acs.org
Publication Date: November 16, 2006 | doi: 10.1021/bk-2007-0945.fw001

Applied Modeling and Computations in Nuclear Science

In Applied Modeling and Computations in Nuclear Science; Semkow, T., et al.;
ACS Symposium Series; American Chemical Society: Washington, DC, 2006.

Downloaded by 89.163.34.136 on August 6, 2012 | http://pubs.acs.org
Publication Date: November 16, 2006 | doi: 10.1021/bk-2007-0945.fw001

ACS SYMPOSIUM SERIES **945**

Applied Modeling and Computations in Nuclear Science

Thomas M. Semkow, Editor
New York State Department of Health

Stefaan Pommé, Editor
Institute for Reference Materials and Measurements

Simon Jerome, Editor
National Physical Laboratory

Daniel J. Strom, Editor
Pacific Northwest National Laboratory

Sponsored by the
ACS Divisions of Nuclear Chemistry and Technology and Computers in Chemistry

American Chemical Society, Washington, DC

Downloaded by 89.163.34.136 on August 6, 2012 | http://pubs.acs.org
Publication Date: November 16, 2006 | doi: 10.1021/bk-2007-0945.fw001

Library of Congress Cataloging-in-Publication Data

Applied modeling and computations in nuclear science / Thomas M. Semkow, editor ... [et al.] ; sponsored by the ACS Divisions of Nuclear Chemistry and Technology and Computers in Chemistry.

p. cm.—(ACS symposium series ; 945)

ISBN 13: 978-0-8412-3982-1 (alk. paper)

ISBN 10: 0-8412-3982-7 (alk. paper)

1. Radiation—Congresses. 2. Radiochemistry—Mathematical models—Congresses. 3. Radiation—Measurements—Congresses. 4. Nuclear chemistry—Congresses.

I. Semkow, Thomas M. II. American Chemical Society. Division of Nuclear Chemistry and Technology. III. American Chemical Society. Division of Computers in Chemistry. IV. Series.

QD601.A1A67 2006
539.7—dc22 2006042988

The paper used in this publication meets the minimum requirements of American National Standard for Information Sciences—Permanence of Paper for Printed Library Materials, ANSI Z39.48-1984.

Copyright © 2007 American Chemical Society

Distributed by Oxford University Press

All Rights Reserved. Reprographic copying beyond that permitted by Sections 107 or 108 of the U.S. Copyright Act is allowed for internal use only, provided that a per-chapter fee of $33.00 plus $0.75 per page is paid to the Copyright Clearance Center, Inc., 222 Rosewood Drive, Danvers, MA 01923, USA. Republication or reproduction for sale of pages in this book is permitted only under license from ACS. Direct these and other permission requests to ACS Copyright Office, Publications Division, 1155 16th Street, N.W., Washington, DC 20036.

The citation of trade names and/or names of manufacturers in this publication is not to be construed as an endorsement or as approval by ACS of the commercial products or services referenced herein; nor should the mere reference herein to any drawing, specification, chemical process, or other data be regarded as a license or as a conveyance of any right or permission to the holder, reader, or any other person or corporation, to manufacture, reproduce, use, or sell any patented invention or copyrighted work that may in any way be related thereto. Registered names, trademarks, etc., used in this publication, even without specific indication thereof, are not to be considered unprotected by law.

PRINTED IN THE UNITED STATES OF AMERICA

Downloaded by 89.163.34.136 on August 6, 2012 | http://pubs.acs.org
Publication Date: November 16, 2006 | doi: 10.1021/bk-2007-0945.fw001

Downloaded by 89.163.34.136 on August 6, 2012 | http://pubs.acs.org
Publication Date: November 16, 2006 | doi: 10.1021/bk-2007-0945.fw001

Foreword

The ACS Symposium Series was first published in 1974 to provide a mechanism for publishing symposia quickly in book form. The purpose of the series is to publish timely, comprehensive books developed from ACS sponsored symposia based on current scientific research. Occasionally, books are developed from symposia sponsored by other organizations when the topic is of keen interest to the chemistry audience.

Before agreeing to publish a book, the proposed table of contents is reviewed for appropriate and comprehensive coverage and for interest to the audience. Some papers may be excluded to better focus the book; others may be added to provide comprehensiveness. When appropriate, overview or introductory chapters are added. Drafts of chapters are peer-reviewed prior to final acceptance or rejection, and manuscripts are prepared in camera-ready format.

As a rule, only original research papers and original review papers are included in the volumes. Verbatim reproductions of previously published papers are not accepted.

ACS Books Department

Downloaded by 89.163.34.136 on August 6, 2012 | http://pubs.acs.org
Publication Date: November 16, 2006 | doi: 10.1021/bk-2007-0945.pr001

Preface

In each area of applied nuclear science in general, and nuclear chemistry in particular, there is usually a modeling or computational component. Typically one finds several modelers presenting their work in the course of almost every conference. Computational aspects of applied nuclear science have been subjects of topical conferences under auspices of the organizations such as American Nuclear Society or Health Physics Society: They usually focus on specific topics. However, there has been a lack of forum devoted to cross-disciplinary facets of computations in applied nuclear science. To fill this void, a Symposium entitled *Applied Modeling and Computations in Nuclear Science* was held at the 230th American Chemical Society (ACS) National Meeting on August 28–September 1, 2005, in Washington, D.C. Nuclear chemists and radiochemists have been traditionally interested in modeling and significantly contributed to its development. Let us recall Proceedings of the Symposium *Applications of Computers to Nuclear and Radiochemistry* held in Gatlinburg, Tennessee, in 1962 (Report NAS-NS-3107, US AEC, 1962). Since then, significant improvements have been made in computer hardware and their widespread use. In addition, sophisticated mathematical/software tools in areas such as transport, statistics, or simulations have been developed and have gained wide acceptance among researchers in nuclear science. It was, therefore, a ripe time to bring all such theoretical and computational work in applied nuclear science under one umbrella, so that the nuclear scientists, who are interested in modeling could have a broader forum for their research, as well as to enable those who are learning related techniques.

The Symposium *Applied Modeling and Computations in Nuclear Science* was organized by a Committee with the following membership:

- Cynthia Atkins-Duffin, Lawrence Livermore National Laboratory

- Carl V. Gogolak, US Department of Homeland Security
- Ralph B. James, Brookhaven National Laboratory
- Simon M. Jerome, National Physical Laboratory, United Kingdom
- Stefaan Pommé, Institute for Reference Materials and Measurements, Belgium
- Thomas M. Semkow, New York State Department of Health and State University of New York
- Daniel J. Strom, Pacific Northwest National Laboratory
- X. George Xu, Rensselaer Polytechnic Institute

This ACS Symposium Series book contains Proceedings of the Symposium under the same title. The book combines twenty four chapters selected from the papers presented at the Symposium and includes several invited review articles written by recognized experts in the field. The book is divided into five parts, each comprising several chapters: Introduction and General Topics (four chapters), Radiation Risk (seven chapters), Radiation Transport (four chapters), Radiation Detection (four chapters), and Radiation Quantification (five chapters). This collection of research topics has not been compiled in one publication before and it represents the state-of-the-art modeling and computations as performed today in applied nuclear science. The book has applications in areas such as radiation dosimetry, homeland security, medicine, environmental radioactivity, designing of detectors/experiments, as well as data reduction. Recently developed sophisticated mathematical tools are described in areas such as transport, statistics, or simulations, performed in some cases on computer clusters or supercomputers. Accessing of nuclear data compilations from the National Nuclear Data Center is described. Modeling and computations are important tools in a mature field. Applied nuclear science is a wide cross-disciplinary field. Therefore, this book can be of interest to nuclear chemists, health physicists, nuclear engineers, nuclear and radiation physicists, as well as environmental and analytical chemists who are working with radioactivity. The book or parts of it can serve as a textbook in advanced courses as well as a reference.

We are taking this opportunity to acknowledge our sponsors for supporting the Symposium. They included: ACS Division of Nuclear Chemistry and Technology (NUCL), ACS Division of Computers in

Downloaded by 89.163.34.136 on August 6, 2012 | http://pubs.acs.org
Publication Date: November 16, 2006 | doi: 10.1021/bk-2007-0945.pr001

Chemistry, American Nuclear Society, and Health Physics Society. Special thanks are due to Kimberly W. Thomas, the 2005 NUCL Program Chair, for encouragement and support of this Symposium from its conception to a successful completion.

Thomas M. Semkow
Wadsworth Center
New York State Department of Health and
University at Albany
State University of New York
P.O. Box 509
Albany, NY 12201

Stefaan Pommé
EC-JRC-IRMM
Institute for Reference Materials and Measurements
Retieseweg 111
B–2440 Geel
Belgium

Simon M. Jerome
Radioactivity Metrology Group
National Physical Laboratory
Hampton Road
TW11 0LW Teddington
United Kingdom

Daniel J. Strom
Environmental Technology Directorate
Pacific Northwest National Laboratory
Mail Stop K3–56
P.O. Box 999
Richland, WA 99352–0999

Downloaded by 89.163.34.136 on August 6, 2012 | http://pubs.acs.org
Publication Date: November 16, 2006 | doi: 10.1021/bk-2007-0945.pr001

In Applied Modeling and Computations in Nuclear Science; Semkow, T., et al.;
ACS Symposium Series; American Chemical Society: Washington, DC, 2006.

Downloaded by 89.163.34.136 on August 6, 2012 | http://pubs.acs.org
Publication Date: November 16, 2006 | doi: 10.1021/bk-2007-0945.ch001

Chapter 1

Applied Modeling and Computations in Nuclear Science: The Foundation for Risk Assessment and Decision Making

John E. Till[1] and Helen A. Grogan[2]

[1]Risk Assessment Corporation, 417 Till Road, Neeses, SC 29107
[2]Cascade Scientific, Inc., 1678 NW Albany Avenue, Bend, OR 97701

Most of the chapters in this book and the symposium from which they are taken help support a key objective of nuclear science today - developing a thorough understanding of the risks to people exposed to nuclear radiation so that better decisions can be made to manage those risks. This introductory chapter describes how basic research in applied modeling and nuclear science discussed in this book inherently supports the objectives of risk assessment. The chapter also examines the importance of focusing research on areas that most effectively reduce uncertainty in quantifying risk. Finally, the chapter suggests specific areas in the field of applied modeling and computations in nuclear science that need further work to support risk assessment in the future.

In Applied Modeling and Computations in Nuclear Science; Semkow, T., et al.;
ACS Symposium Series; American Chemical Society: Washington, DC, 2006.

Introduction

In this brief introductory chapter, we emphasize the importance of basic research in applied modeling and computations in nuclear science, demonstrate how these topics are inherently linked together, and examine how they support a key objective of making better decisions based on understanding risk.

Although the connection between nuclear science and risk may appear tenuous, most of the chapters presented here provide input and support to the estimation of risk from radioactive materials released to the environment. This field is known as *environmental risk assessment* or *environmental risk analysis* and involves the merging of a number of scientific disciplines to provide quantitative estimates of risk. Risk assessment is a contemporary form of mathematical modeling and computations in nuclear science, which is the topic of this book.

Risk assessments consider both humans and the environment as the target of risk. Too frequently, however, they focus on human health alone, with the result that large areas of the environment and entire ecological systems are destroyed in the interests of reducing what are often inconsequential human health risks. Ultimately, a sound decision requires a holistic approach to assessing these risks.

Why study risk? Risk is a universal common denominator that allows scientists and decision makers to address the impact of a source. Risk is also a concept that can be readily understood and compared with other activities in life.

We define risk to humans as a chance of harm. The chance of harm is generally expressed as the health risk, specifically increased risk of cancer from radionuclides released into the environment from a source.

Estimates of risk to people and the environment are used extensively to help guide decision makers in their efforts to invest resources most effectively. This introduction uses examples of our work to emphasize how basic research in applied modeling and computations in nuclear science, as illustrated so profoundly in this symposium, remains the solid foundation for risk science. The chapter also describes several key areas where additional future research needs to be undertaken.

Risk Assessment and Nuclear Science: The Connection

Risk assessment and nuclear science are inherently connected. Modern-day risk assessment began with the testing of nuclear weapons as scientists tried to predict the path of radioactive fallout and the dose to people who lived downwind. Early research in this area, more than any other, laid the foundation for the methods we still use today to estimate risk to people from radioactive materials in the environment. More recently, research to reconstruct historical

Downloaded by 89.163.34.136 on August 6, 2012 | http://pubs.acs.org
Publication Date: November 16, 2006 | doi: 10.1021/bk-2007-0945.ch001

releases of radionuclides to the environment from atmospheric nuclear weapons testing and from nuclear weapons facilities resulted in significant improvements in methods to estimate risk. This research included many new areas of investigation, such as estimation of source terms, transport of radioactive materials in the environment, uptake of radionuclides by humans and biota, and the development of dose and risk coefficients. Each of these scientific disciplines has its foundation in nuclear science.

The components that comprise risk assessment today evolved from individual sciences that have been merged gradually (and lately, more frequently) to form the computational methods we now use to estimate risk. Risk can be estimated for present-day releases of materials, and for potential future releases of materials at existing or planned facilities. Such assessments are typically designed to demonstrate compliance with standards. Risk can also be estimated for releases that occurred in the past to help understand the impact of those releases. Although the methods used for the two types of risk assessment differ, there are many similarities in the techniques applied to each.

In explaining the process of risk assessment to our colleagues and to the public, we often use the following illustrative equation to express the interdisciplinary nature of this research:

$$Risk = (S \bullet T \bullet E \bullet D \bullet R)_{uvcp}\,, \qquad (1)$$

where

S = source term (characterization of the quantity and type of material released)
T = environmental transport (estimation of concentrations in the environment)
E = exposure factors (characteristics of individuals exposed)
D = conversion of intake rate or exposure rate to dose
R = conversion of dose to risk
u = uncertainty analysis
v = validation
c = communication of results
p = public participation.

We will briefly explain each component needed to estimate risk and note how some of the research described in this book contributes to our knowledge of risk science.

The source term (*S*) in the risk equation is the characterization and quantification of the material released to the environment. It is the heart of a risk assessment and has deservedly received significant attention. Our ability to

Downloaded by 89.163.34.136 on August 6, 2012 | http://pubs.acs.org
Publication Date: November 16, 2006 | doi: 10.1021/bk-2007-0945.ch001

reconstruct or predict a source term directly affects the estimates of risk and thus the credibility of the assessment.

Two chapters in this book pertain to a better quantification of the source term. The chapters by Viggato *et al.* (**Thermohydraulic and Nuclear Modeling of Natural Fission Reactors**) and Semkow *et al.* (**Modeling the Effects of the Trinity Test**) help increase our understanding of materials present in sources that could ultimately be released to the environment.

A number of other chapters indirectly describe how to better define a source. Examples of these chapters include those that focus on improving detection of radioactivity, as described by Pommé (**Dead Time, Pile-up, and Counting Statistics**), Keightley (**DCC_SIM: A Simulation Routine for the Validation of 4π β-γ Digital Coincidence Counting Software**), Jenkins *et al.* (**Corrections for Overdispersion Due to Correlated Counts in Radon Measurements Using Grab Scintillation Cells, Activated Charcoal Devices and Liquid Scintillation Charcoal Devices**), as well as by Brüchle (**Simulation of Elution Curves for Chromatography Columns with a Low Number of Theoretical Plates**).

The next term in the equation is environmental transport (*T*). In this step, we estimate the concentrations of a radionuclide in environmental media such as air, soil, sediment, surface water, or groundwater. In some cases, these concentrations can be estimated from direct measurements; in other cases, they must be inferred using mathematical models. Although our understanding of radionuclide transport in the environment has improved greatly over the past several decades, we continue to refine our modeling methods as demonstrated by several chapters in this book. Only one chapter directly addressed environmental transport, by Yu (**Modeling Radionuclide Transport in the Environment and Assessing Risks to Humans, Flora, and Fauna - The RESRAD Family of Codes**).

In addition to environmental transport, we can have radiation transport which is also related to the source term. Two chapters addressed the principles of radiation transport, by Haghighat and Sjoden (**Three-Dimensional Particle Transport Methods and Their Applications**), as well as by Berlizov (**MCNP-CP: A Correlated Particle Radiation Source Extension of a General Purpose Monte Carlo N-Particle Transport Code**). The next two chapters describe important applications, by Robinson *et al.* (**Creation of Realistic Radiation Transport Models of Radiation Portal Monitors for Homeland Security Purposes**) and by O'Brien (**A Random-Walk Solution to the Heliospheric Transport Equation**).

There are no chapters in the symposium related to the next step of the calculation of risk, exposure factors (*E*), which is understandable since this component of risk assessment is primarily derived from physiological, dietary, and habit data. However, considerable progress continues to be made in this

Downloaded by 89.163.34.136 on August 6, 2012 | http://pubs.acs.org
Publication Date: November 16, 2006 | doi: 10.1021/bk-2007-0945.ch001

area, particularly with regard to how individuals are characterized for the purpose of determining compliance with regulations.

Once exposure is determined, coefficients are used to convert it to a dose (*D*), which may be internal, external, or an effective dose, or to risk directly. Several of the chapters in the symposium help to improve our understanding of these dose coefficients. The chapters by Miller *et al.* (**Markov Chain Monte Carlo for Internal Dosimetry on a Supercomputer Cluster**), Vojtyla (**Calculation of the External Effective Dose from a Radioactive Plume by Using Monte Carlo Dose Kernel Integration**), and Xu (**Modeling of Human Anatomy for Radiation Dosimetry: An Example of the VIP-Man Model**) provide us with new insight into the dosimetry part of the risk calculation.

None of the chapters addresses risk coefficients (*R*), although this field is of major interest today as evidenced by the extensive research being placed on the effects of low-dose radiation.

A number of chapters help improve our understanding of uncertainty (*u*). Three chapters address issues related to uncertainty of radiation quantification: by Pommé (**Problems with the Uncertainty Budget of Half-Life Measurements**), Berlizov *et al.* (**Evaluating Detection Limits for Environmental Monitoring Techniques in the Areas of Potential Impact from Nuclear Installations**), and Potter (**New Approach for the Decision Level and the Detection Limit in Paired Counting When There is Uncertainty Concerning the Expected Blank Count**). Two other chapters: by Pommé and Keightley (**Count Rate Estimation of a Poisson Process: Unbiased Fit versus Central Moment Analysis of Time Interval Spectra**), as well as by Semkow (**Bayesian Inference from Binomial and Poisson Processes for Multiple Sampling**), discuss inference from the Poisson data encountered in nuclear science. Analysis of uncertainty continues to make important advances in nuclear science and is an area that will continue to require emphasis in the future.

Validation (*v*), communication of results (*c*), and public participation (*p*) are not addressed in the symposium but are topics of key importance in risk assessment that are too frequently overlooked by scientists. In our work at *Risk Assessment Corporation*, we believe that if the public is the target of risk, then the public should be involved in the risk assessment process. We believe a better product results if members of the public are encouraged to provide input and if they become engaged in the process as it occurs rather than waiting until the work is completed. Involving citizens, who are typically not scientists, significantly complicates the process but inevitably strengthens the work, especially in terms of its credibility. Furthermore, communication of the work and its results is best performed by the scientists who conducted the work.

It is important to note that several chapters focus on the entire risk equation. The abovementioned chapter by Yu as well as the chapter by Grogan *et al.*

Downloaded by 89.163.34.136 on August 6, 2012 | http://pubs.acs.org
Publication Date: November 16, 2006 | doi: 10.1021/bk-2007-0945.ch001

(Modeling of the Cerro Grande Fire at Los Alamos: An Independent Analysis of Exposure, Health Risk, and Communication with the Public) look at risk assessment objectives in a comprehensive sense and are examples of the computational methods currently used to estimate dose and risk.

Finally, the book contains several review chapters of general interest to applied nuclear-science modeling. These include chapters by Obložinský **(Nuclear Data Analysis and the National Nuclear Data Center)**, Currie **(Some Perspectives on Nuclear Detection and the Blank)**, and Semkow **(Exponential Decay Law and Nuclear Statistics)**.

Obviously, not every chapter in this book can be directly linked to the risk assessment process, but each author presents results that help improve our knowledge and understanding of risk assessment. This continuing evolution and improvement of nuclear science helps us in merging the different scientific disciplines and is critical to decision makers who are the ultimate end users of our work.

Downloaded by 89.163.34.136 on August 6, 2012 | http://pubs.acs.org
Publication Date: November 16, 2006 | doi: 10.1021/bk-2007-0945.ch001

Risk Assessment as a Guide to Research in Nuclear Science

Risk assessment can provide valuable insight to guide future research in nuclear science because of the "big picture" view it provides of the different sciences that it represents. This holistic approach allows us to identify the largest contributors to uncertainty. As we continue to improve our capability to quantify risk, we are always looking for ways to strengthen the weakest link in the calculation and to reduce the overall uncertainty. This information can be used to help focus our efforts on areas of nuclear science that most effectively reduce uncertainty or provide a better understanding of the results. Listed below are several areas of risk assessment and nuclear science that need more emphasis in the future, based on lessons from our recent work.

Background Radiation

Dealing with background concentrations of naturally occurring radionuclides in risk assessment has always been problematic. In most cases, the concentrations in the environment are poorly characterized on a site-specific basis forcing scientists to use data imported from a variety of sources to quantify background for a specific area. This approach does not work well in risk assessment since background concentrations of radionuclides vary widely from one facility to another and between locations for a given facility. As a result, it is difficult to adequately account for background concentrations in a meaningful way in the risk assessment process. Several authors in this book propose new methods for detecting background concentrations of radionuclides that could ultimately lead to better estimates of background in the future.

Uncertainty

Improving estimates of uncertainty continues to be one of the most important fields of nuclear science. Although major improvements have been made in methods for uncertainty analysis in risk assessment, much more work is needed in this area. In particular, we need a better understanding of uncertainties associated with dose and risk coefficients, source terms, and environmental transport models. These three areas seem to dominate uncertainties in the overall estimation of risk when uncertainties are involved.

Validation

Validation and testing of mathematical models used in nuclear science must continue to be a key focus of work in the future. Although it is impractical to validate estimates of risk to individuals, it is possible to validate and test different components of the risk calculation equation. Validation is particularly important for environmental transport models because, in most cases, it is not possible to measure concentrations at all locations. Therefore, mathematical modeling is the only way to reconstruct or predict concentrations.

Simplification of Risk Estimation Methods

Another key area that requires further study is the development of readily available tools that allow a quick determination of radionuclides, pathways, and estimates of risk. These tools are especially needed to support emergency response to a nuclear accident or terrorist event. Although there are a number of computational methods available that could provide this information to decision makers, these computer codes are not easily applied to emergency response. It is crucial that we develop computer software that can quickly convey information about radionuclide behavior in the environment and the relative importance of pathways and radionuclides in terms of risk.

Downloaded by 89.163.34.136 on August 6, 2012 | http://pubs.acs.org
Publication Date: November 16, 2006 | doi: 10.1021/bk-2007-0945.ch001

Conclusions

The chapters presented in this book contribute significantly to our knowledge and understanding of applied modeling and computations in nuclear science. The continuation and expansion of this fundamental research is vital to our future. Risk assessment is a form of applied modeling that combines the knowledge of many aspects of nuclear science in estimating risk to humans and the environment. The results of risk assessment can then be used to guide decision makers and help people understand the significance of radioactive materials present in their environment. Risk assessment can also be used to help researchers in nuclear science identify gaps in our knowledge and focus on issues that most effectively reduce uncertainty. This chapter explains the need for continued collaboration in these fundamental sciences and emphasizes the importance of efforts to bring scientists together to share and discuss the results of recent advances. All of the authors are commended for taking the time to document their research and share them with the editors of this book so that a lasting record of this knowledge now exists.

Downloaded by 89.163.34.136 on August 6, 2012 | http://pubs.acs.org
Publication Date: November 16, 2006 | doi: 10.1021/bk-2007-0945.ch001

Downloaded by CORNELL UNIV on August 6, 2012 | http://pubs.acs.org
Publication Date: November 16, 2006 | doi: 10.1021/bk-2007-0945.ch002

Chapter 2

Nuclear Data Analysis and the National Nuclear Data Center

P. Obložinský

National Nuclear Data Center, Brookhaven National Laboratory, P.O. Box 5000, Upton, NY 11973

An overview is presented of the nuclear reaction and nuclear structure data, available at the National Nuclear Data Center, that are of importance as input for applied modeling and computations in nuclear science. These applications include radiation transport calculations, detector response, dosimetry, γ spectroscopy analysis, and homeland security. Several relevant databases and products along with their Web retrieval are described. These include nuclear reaction database ENDF, code EMPIRE, nuclear structure database NuDat and Nuclear Wallet Cards.

The mission of the National Nuclear Data Center (NNDC) is to collect, evaluate and disseminate nuclear physics data for basic science and nuclear technology communities in the United States. The NNDC is a worldwide resource of nuclear data.

Nuclear data are of importance, often of critical importance, for modeling and simulations in nuclear science since they provide input to simulation codes. For example, neutron cross sections are used as input to the Monte Carlo simulation code MCNP. Also, nuclear data serve as input to codes analyzing experimental results, such as γ-ray energies and intensities to analyze complex spectra measured by Ge detectors.

In Applied Modeling and Computations in Nuclear Science; Semkow, T., et al.;
ACS Symposium Series; American Chemical Society: Washington, DC, 2006.

The present chapter focuses on the most important databases and tools maintained by the NNDC. First, the chapter describes evaluated nuclear reaction database ENDF along with advanced nuclear reaction model code EMPIRE. Then, it proceeds by describing nuclear structure database NuDat and Nuclear Wallet Cards.

Nuclear Reactions

It is convenient to start the present discussion by displaying the front page of the web service of the National Nuclear Data Center (NNDC) in Fig. 1. Eight databases seen at the top left portion of the figure include both nuclear reaction and nuclear structure databases (*1*).

CINDA, CSISRS and ENDF are pure nuclear reaction databases, while XUNDL, ENSDF and MIRD are pure nuclear structure databases. NSR contains both reaction and structure data, while NuDat contains mostly structure data.

CINDA (Computer Index to Nuclear Reaction Data) is the oldest nuclear database, containing references to 275,000 neutron-induced reactions from 55,000 works. The database was traditionally dedicated to neutron data and in this area it is considered to be comprehensive. In 2005, the database was extended to cover charged-particle reactions (in general, light incident charged-particles with mass $A < 12$ and energy $E < 1$ GeV) and photonuclear reactions.

NSR (Nuclear Science References) database contains references describing contents of 180,000 articles from more than 80 journals. The database, initially known as Nuclear Structure References, evolved into a broad bibliography database for nuclear science. The strength of the database is in keywording that allows efficient search over research topics, nucleus, reaction, author, etc.

Evaluated Nuclear Data File, ENDF

ENDF database contains evaluated (recommended) nuclear reaction cross-section data for all nuclei relevant for applied technology. It currently covers 328 target materials (nuclides) interacting mostly with neutrons, however, protons and other charged particles are also partly covered. Incident energies up to 20 MeV are mainly covered, but important cases up to 150 MeV are also included.

The last release, ENDF/B-VI.8, was issued in 2001. The database provides input to neutronics calculations such as the design of nuclear reactors and design of other nuclear systems, accelerators, radiation shielding and protection, etc. The database is maintained by the Cross Section Evaluation Working Group (CSEWG); it is archived and distributed by the NNDC.

Downloaded by CORNELL UNIV on August 6, 2012 | http://pubs.acs.org
Publication Date: November 16, 2006 | doi: 10.1021/bk-2007-0945.ch002

Downloaded by CORNELL UNIV on August 6, 2012 | http://pubs.acs.org
Publication Date: November 16, 2006 | doi: 10.1021/bk-2007-0945.ch002

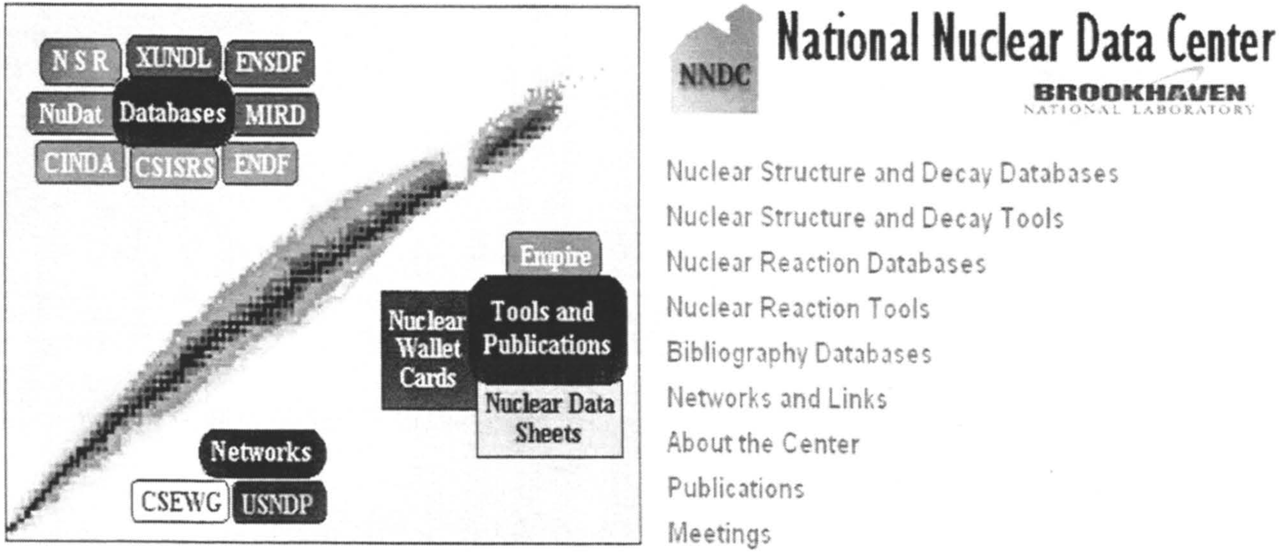
N S R
XUNDL
ENSDF
NuDat
Databases
MIRD
CINDA
CSISRS
ENDF
Empire
Nuclear Wallet Cards
Tools and Publications
Nuclear Data Sheets
Networks
CSEWG
USNDP
NNDC
National Nuclear Data Center
BROOKHAVEN NATIONAL LABORATORY
Nuclear Structure and Decay Databases
Nuclear Structure and Decay Tools
Nuclear Reaction Databases
Nuclear Reaction Tools
Bibliography Databases
Networks and Links
About the Center
Publications
Meetings

Figure 1. Front page of the web service of the National Nuclear Data Center (NNDC), www.nndc.bnl.gov, offers nuclear databases at top left. (See page 1 of color inserts.)

Currently, ENDF/B-VII is under development. It should contain better and more extensive data for actinides, new version of neutron cross-section standards, vastly improved cross sections for fission products, an entirely new photonuclear library and other improvements. The number of materials will be close to 400 and its release is scheduled for the middle of 2006.

The web retrieval interface for ENDF as shown in Fig. 2 provides an easy access to this important resource of recommended cross section data. The data are used heavily in many neutronics simulation codes such as MCNP.

Nuclear Reaction Model Code EMPIRE

This code represents an advanced tool for nuclear reaction cross-section calculations. EMPIRE uses a broad set of nuclear reaction models at low incident energies, combined with extensive international library of Reference Input Model Parameters as well as easy access to experimental cross-section database CSISRS along with powerful graphics and a host of utility codes. Thus, EMPIRE is of considerable interest to applied users, to nuclear reaction theory developers as well as to nuclear data evaluators (*2*). Arguably it is currently one of three most powerful low energy nuclear reaction codes worldwide, the others being McGnash (Los Alamos) and Talys (Europe).

The code is freely available, see www.nndc.bnl.gov/empire. It is easy to use thanks to the powerful graphic user interface that allows performing complex calculations with a couple of mouse clicks.

To illustrate its capabilities, we show in Fig. 3 recent results obtained by EMPIRE. Photon production for Ge(n,xγ) reactions was calculated to meet the needs of the homeland security community for detector simulations with the code MCNP. Other examples would include complex fission cross sections for ^{232}Th(n,f), and photoabsorption ^{235}U(γ,abs) that is of interest for detection simulation calculations of nuclear materials with small electron accelerators.

Downloaded by CORNELL UNIV on August 6, 2012 | http://pubs.acs.org
Publication Date: November 16, 2006 | doi: 10.1021/bk-2007-0945.ch002

Nuclear Structure and Decay

The basic nuclear structure database maintained by the NNDC is the Evaluated Nuclear Structure Data File, ENSDF. This database is the worldwide resource for nuclear structure and radioactive decay data. ENSDF is produced by the US Nuclear Data Program with contributions from the Network of Nuclear Structure and Decay Data Evaluators. The database contains information on virtually all known nuclei (currently 2,932) that is updated regularly.

Downloaded by CORNELL UNIV on August 6, 2012 | http://pubs.acs.org
Publication Date: November 16, 2006 | doi: 10.1021/bk-2007-0945.ch002

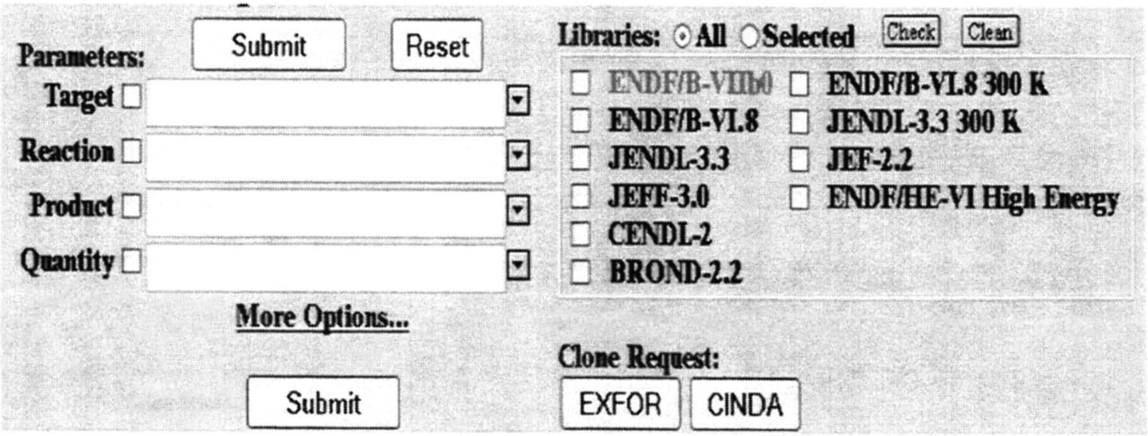
Parameters:
Submit
Reset
Target ☐
Reaction ☐
Product ☐
Quantity ☐
More Options...
Submit
Libraries: ● All ○ Selected
Check
Clean
☐ ENDF/B-VIIb0
☐ ENDF/B-VI.8
☐ JENDL-3.3
☐ JEFF-3.0
☐ CENDL-2
☐ BROND-2.2
☐ ENDF/B-VI.8 300 K
☐ JENDL-3.3 300 K
☐ JEF-2.2
☐ ENDF/HE-VI High Energy
Clone Request:
EXFOR
CINDA

Figure 2. Web interface for the Evaluated Nuclear Data File operated by the NNDC, www.nndc.bnl.gov/endf. The latest ENDF/B-VI.8 along with preliminary ENDF/B-VII and databases from Japan, EU, China and Russia are available. (See page 2 of color inserts.)

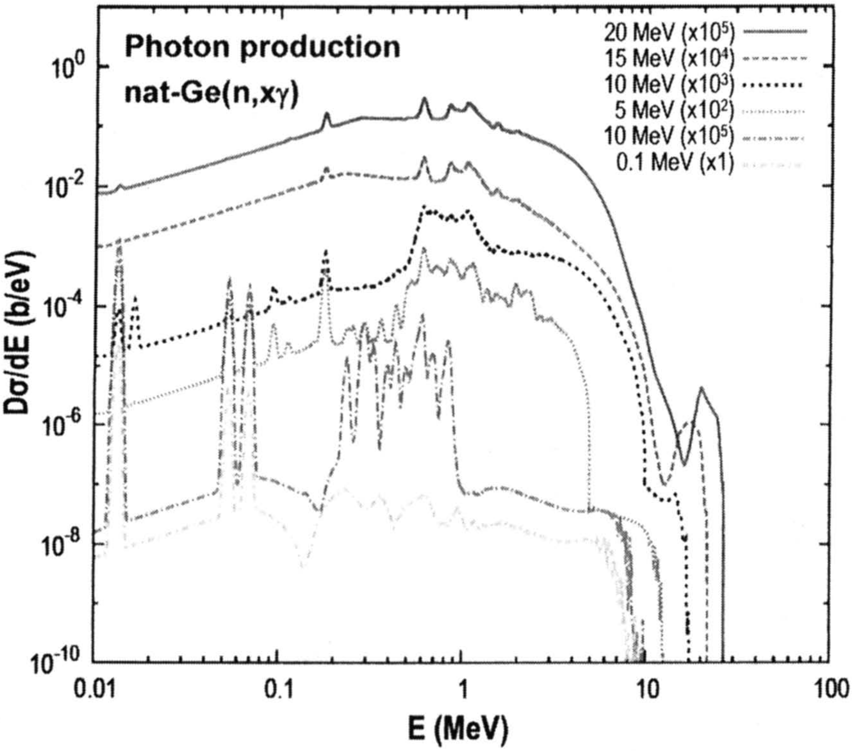

Figure 3. Photon production spectra from Ge(n,xγ) reactions for neutrons of several incident energies in the range of 0.1- 20 MeV. (See page 3 of color inserts.)

Downloaded by CORNELL UNIV on August 6, 2012 | http://pubs.acs.org
Publication Date: November 16, 2006 | doi: 10.1021/bk-2007-0945.ch002

NuDat Database

The most popular product that offers ENSDF data is NuDat (*3*). It combines advantages of the chart of nuclides with the table of isotopes. It is interactive and searchable (see Fig. 4) with numerous options for data retrieval.

The NuDat interface, developed in 2004 and based on modern programming techniques, achieved several recognitions. One of them is shown in Fig. 5.

Downloaded by CORNELL UNIV on August 6, 2012 | http://pubs.acs.org
Publication Date: November 16, 2006 | doi: 10.1021/bk-2007-0945.ch002

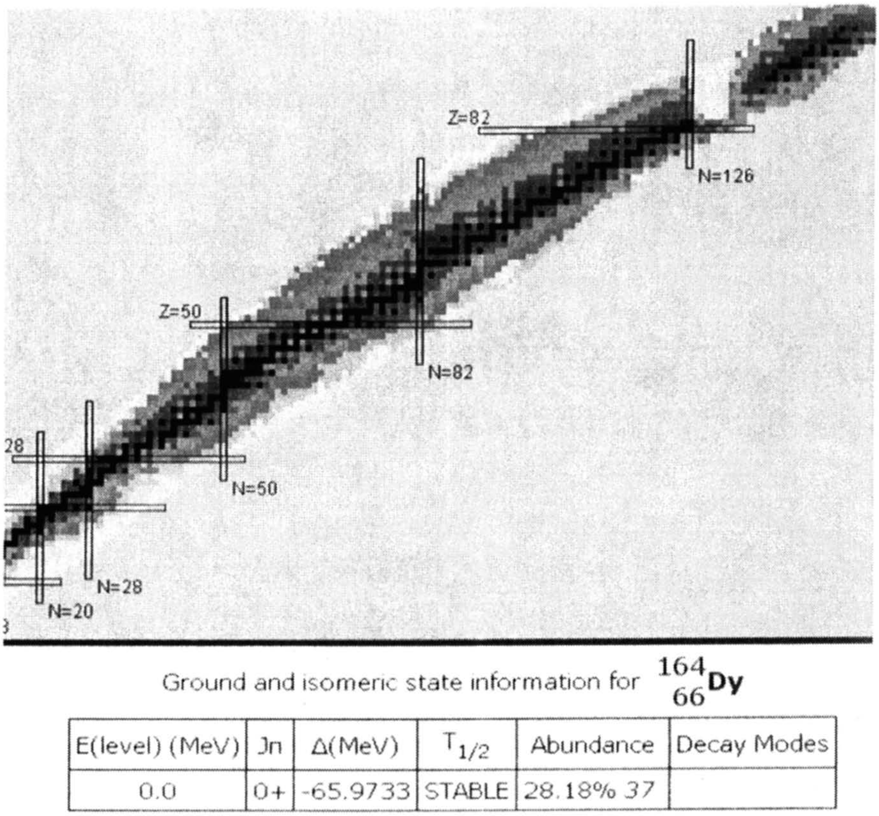

Ground and isomeric state information for $^{164}_{66}\mathrm{Dy}$

E(level) (MeV)	Jπ	Δ(MeV)	$T_{1/2}$	Abundance	Decay Modes
0.0	0+	-65.9733	STABLE	28.18% 37	

Figure 4. NuDat web interface operated by the National Nuclear Data Center, www.nndc.bnl.gov/nudat. Shown is the front page with the chart of nuclei (20, 28,..., 128 are magic numbers) and basic information retrieved for Dy-164. (See page 4 of color inserts.)

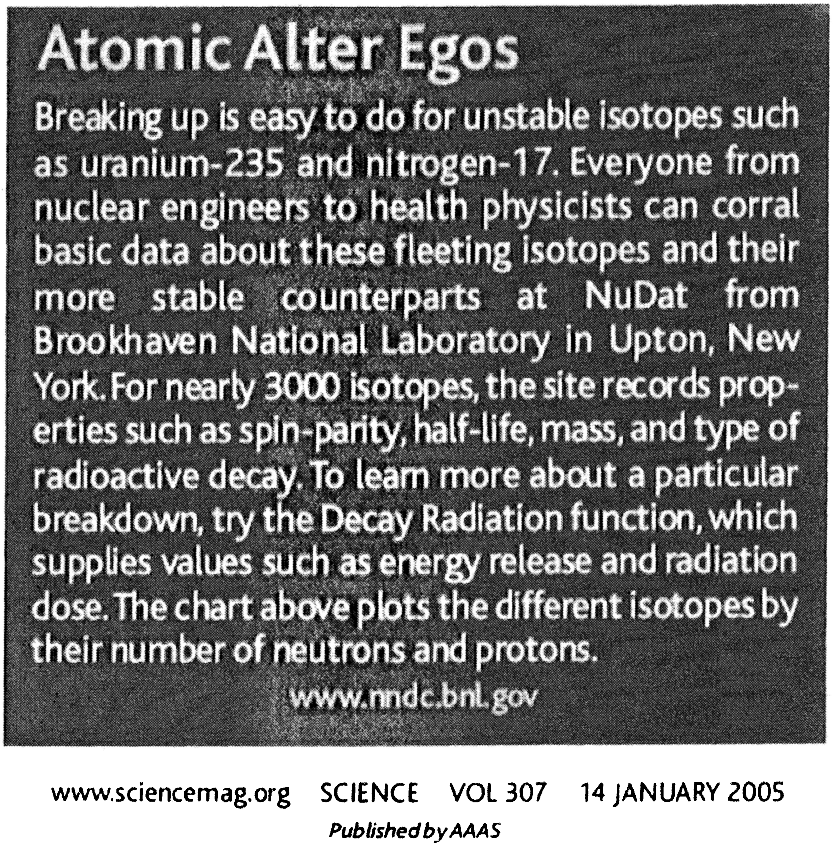

Atomic Alter Egos

Breaking up is easy to do for unstable isotopes such as uranium-235 and nitrogen-17. Everyone from nuclear engineers to health physicists can corral basic data about these fleeting isotopes and their more stable counterparts at NuDat from Brookhaven National Laboratory in Upton, New York. For nearly 3000 isotopes, the site records properties such as spin-parity, half-life, mass, and type of radioactive decay. To learn more about a particular breakdown, try the Decay Radiation function, which supplies values such as energy release and radiation dose. The chart above plots the different isotopes by their number of neutrons and protons.

www.nndc.bnl.gov

www.sciencemag.org SCIENCE VOL 307 14 JANUARY 2005

Published by AAAS

Figure 5. Recognition to NuDat interface published in Science, Vol. 307, 2005, 187. (See page 5 of color inserts.)

Downloaded by CORNELL UNIV on August 6, 2012 | http://pubs.acs.org
Publication Date: November 16, 2006 | doi: 10.1021/bk-2007-0945.ch002

Nuclear Wallet Cards

Nuclear Wallet Cards provides information on basic properties of 3,841 ground and isomeric states for all known nuclei. It is available as handy booklet, on the web and in Palm Pilot format, at www.nndc.bnl.gov/wallet/. The NNDC offers 3 versions of Nuclear Wallet Cards:

- Version 2000, adopted by DOE Safeguards as the U.S. standards of decay data used to determine absolute amounts of nuclear materials.
- Version 2004, a special version to meet needs of the homeland security community, entitled Nuclear Wallet Cards for Radioactive Nuclides.

- Version 2005, the latest standard version produced in 10,000 hardcopies, most of them already distributed.

Acknowledgements

This work was supported by the Office of Nuclear Physics, Office of Science of the U.S. Department of Energy, under contract no. DE-AC02-98CH10886 with the Brookhaven Science Associates, L.L.C.

References

1. Pritychenko, B.; Arcilla, A.; Burrows, T. W.; Dunford, C. L.; Herman, M. W.; McLane, V.; Obložinský, P.; Sonzogni, A. A.; Tuli, J. K.; Winchell, D.F. *International Conference on Nuclear Data for Science and Technology 2004*; Haight, R. C.; Chadwick, M. B.; Kawano, T.; Talou, P., Eds.; American Institute of Physics **2005**, 769, p. 132.
2. Herman, M. W.; Obložinský, P.; Capote, R.; Sin, M.; Trkov, A.; Ventura, A.; and Zerkin, V. *International Conference on Nuclear Data for Science and Technology 2004*; Haight, R. C.; Chadwick, M. B.; Kawano, T.; Talou, P., Eds.; American Institute of Physics **2005**, 769, p. 1184.
3. Sonzogni, A. *International Conference on Nuclear Data for Science and Technology 2004*, Haight, R. C.; Chadwick, M. B.; Kawano, T.; Talou, P., Eds.; American Institute of Physics **2005**, 769, p. 574.

Downloaded by CORNELL UNIV on August 6, 2012 | http://pubs.acs.org
Publication Date: November 16, 2006 | doi: 10.1021/bk-2007-0945.ch002

Chapter 3

Some Perspectives on Nuclear Detection and the Blank

L. A. Currie

National Institute of Standards and Technology, 100 Bureau Drive, Gaithersburg, MD 20899–8370 (Retired)

Downloaded by COLUMBIA UNIV on August 9, 2012 | http://pubs.acs.org
Publication Date: November 16, 2006 | doi: 10.1021/bk-2007-0945.ch003

The blank (background, baseline) is generally the central factor limiting low-level measurement capabilities. In this chapter, we consider briefly the nature and distribution of the blank in the "real world" as manifest in environmental baseline radioactivity (atmospheric ^{85}Kr) and low-level counting background, and in the ideal world of Poisson counting statistics. Tests of distributional assumptions for the actual baseline radioactivity and counter background demonstrated the presence of significant non-random components, which (1) carry important environmental /physical information about the nature of the blank, and (2) must be controlled for meaningful detection decisions. For the ideal case where the blank can be treated as a Poisson process, some limitations and modes of application of the Poisson-normal approximation were first explored, followed by an historical look at the exact solution for the detection of differences between two Poisson variables.

In Applied Modeling and Computations in Nuclear Science; Semkow, T., et al.;
ACS Symposium Series; American Chemical Society: Washington, DC, 2006.

1. Introduction

The variability of the blank (B) constitutes an ultimate limiting factor for detection, and to some extent, quantification capabilities. It is recognized, also, that B may have several manifestations, *e.g.*, detector background, baseline (environmental, spectroscopic, chromatographic), or procedural (chemical, isotopic) blank. Some interesting questions arise, however, concerning the assumed nature and distribution of the blank, and its impact on the validity of detection decisions and estimated detection limits. In this brief essay we begin and end with a look at the 'real world' - actual B-distributions in the atmospheric environment, and in the low-level counting laboratory, respectively. In each case, ***things are not necessarily what they seem to be***, leading to questions about assumption validity. The 'ideal world' of Poisson counting statistics lies in between, where we review some ancient history and consider questions about ultimate detection capabilities.

To set the stage, we present in Figure 1 two empirical B distributions, without further comment until they are revisited in Sections 3 and 6.

Downloaded by COLUMBIA UNIV on August 9, 2012 | http://pubs.acs.org
Publication Date: November 16, 2006 | doi: 10.1021/bk-2007-0945.ch003

2. Detection Capabilities: Concepts and International Standards

Building on early work by Feigl (*1*), Przyborowski and Wilenski (*2*), Roos (*3*), Nicholson (*4*,*5*), Altshuler and Pasternack (*6*), Kaiser (*7*), and Currie (*8*,*9*), among others, the International Union of Pure and Applied Chemistry (IUPAC) and the International Organization for Standardization (ISO) have prepared, during the past decade or so, a series of international standards and recommendations on concepts and expression for detection and quantification capabilities. IUPAC recommendations (*10*) address measurement capabilities in Chemistry; the ISO 11843 series (*11*) addresses metrology in general, and the ISO 11929 series (*12*) addressed ionizing radiation. Among recent national documents, are the American Society for Testing and Materials (ASTM) interlaboratory standards (*13*,*14*), and the Multi-Agency Radiological Laboratory Analytical Protocols Manual (MARLAP) (*15*). An excellent source for low-background metrology and applications is the proceedings volume of the International Committee for Radionuclide Metrology (ICRM) Conference on Low-level Radioactivity Measurement Techniques (*16*).

Hypothesis testing, with the errors of the first (β) and second (β) kinds, serves as the conceptual framework for detection decisions and capabilities. The basic concepts are given algebraic expression below (Eqs. 2). Each case requires parameter specification: α and β, for the probabilities of the errors of the first and second kinds (false positives and false negatives); and RSD_Q, for the relative standard deviation at the Quantification Limit. Mandatory values of these

Downloaded by COLUMBIA UNIV on August 9, 2012 | http://pubs.acs.org
Publication Date: November 16, 2006 | doi: 10.1021/bk-2007-0945.ch003

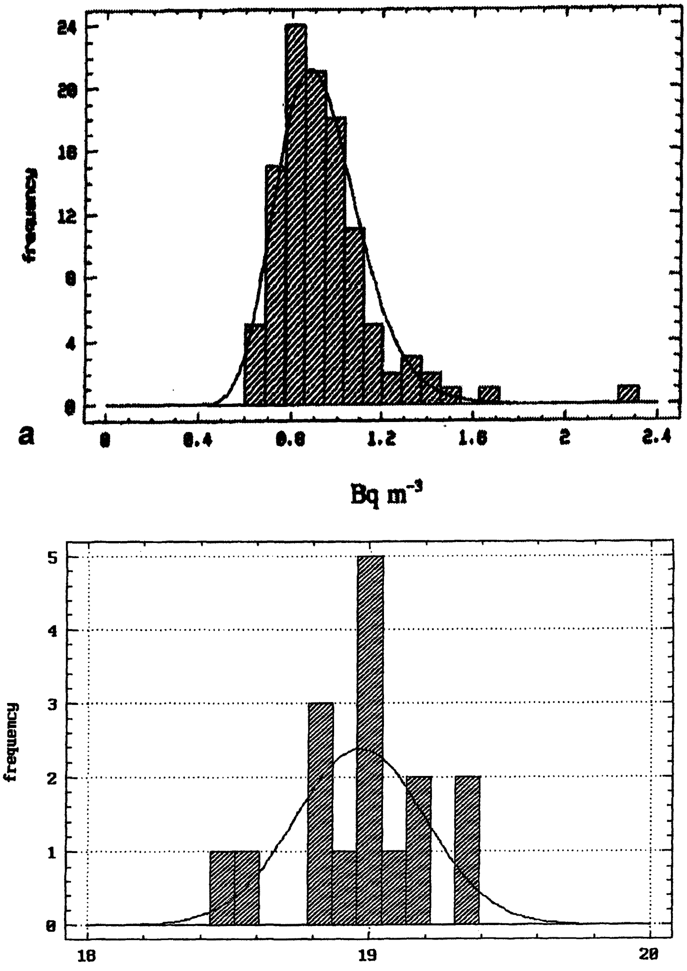

Figure 1. a) Frequency histogram of atmospheric background (baseline) data for ^{85}Kr in central Europe. b) Frequency histogram of low-level GM background data at National Institute of Standards and Technology (NIST) (x-axis, bkg rate, cpm.)

parameters are *not* incorporated in the defining expressions; recommended default values are shown in parentheses.

Detection Decision (Critical Value) (L_C, $\alpha = 0.05$)

$$\Pr(\hat{L} > L_C \mid L = 0) \le \alpha\,, \tag{2.1}$$

Detection Limit (Minimum Detectable Value) (L_D, $\beta = 0.05$)

$$\Pr(\hat{L} \le L_C \mid L = L_D) = \beta\,, \tag{2.2}$$

Quantification Limit (Minimum Quantifiable Value) (L_Q, $RSD_Q = 0.10$)

$$L_Q = k_Q \sigma_Q, \qquad \text{where } k_Q = 1/RSD_Q. \qquad (2.3)$$

Note that the generic symbols L_D, L_Q, and σ_Q denote "true" characteristic values for the measurement process, referring to net signals (S) or concentrations (x) above the background or blank. In practice the L's may be derived from estimates (or assumptions), such that calculated values themselves will be characterized by uncertainties. Also, for L_D and β to be meaningful, $L_C(\alpha)$ must be employed for detection decision making. The relation, β vs. L_D is known as the "Operating Characteristic" (OC) of the (detection) significance test performed at significance level α; and $1 - \beta$ is the "power" of the test. Equation 2.1 is given as an inequality, because not all values of α are possible for discrete distributions, such as the Poisson. The IUPAC recommended default values for α, β, and k_Q serve as a common basis for measurement process assessment, but they may be adjusted appropriately in particular applications where detection or quantification needs are more or less stringent.

Downloaded by COLUMBIA UNIV on August 9, 2012 | http://pubs.acs.org
Publication Date: November 16, 2006 | doi: 10.1021/bk-2007-0945.ch003

3. B as an Environmental Baseline: ^{85}Kr Case Study

In the best of cases, empirical B distributions may be used directly to estimate critical levels and detection limits, especially when there are many observations, such as for the frequency histogram of atmospheric ^{85}Kr shown in Figure 1a, where number of measurements was 109. Simplistic application of the apparent distributional parameters for estimating capabilities to detect or quantify departures from environmental baselines can be seriously misleading, however, unless assumptions about stationarity and randomness are valid. Apart from careful testing of such assumptions, it can be quite illuminating to understand the underlying causes for such departures. The B (as baseline) data for ^{85}Kr are offered in this spirit.

The histogram of the complete dataset can be fit to a lognormal distribution (p = 0.12), whereas a normal fit is unacceptable ($p \approx 0.0002$). Omitting the "unusual" point at 2.23 Bq m^{-3} brings about an improved lognormal fit (p = 0.59), which is the one shown in Figure 1a. The fitted parameters ($\bar{x}$, s) are (0.930, 0.185) Bq m^{-3}, equivalent to a relative standard deviation of 19.9 % - well beyond the 10 % required for single-sample quantification. Although the frequency distribution is still noticeably skew, a normal distribution cannot be rejected.

3.1. Unfolding the Structure of the Data

Looking beyond summary statistics and the empirical frequency histogram can be quite revealing. In particular, the added dimension of time (or space) can provide vital insight regarding the stability of the mean and variance of a laboratory or environmental baseline. Beyond that, visual examination of the time series can often reveal important structure, the removal of which may result in significant improvement in detection and quantification capabilities.

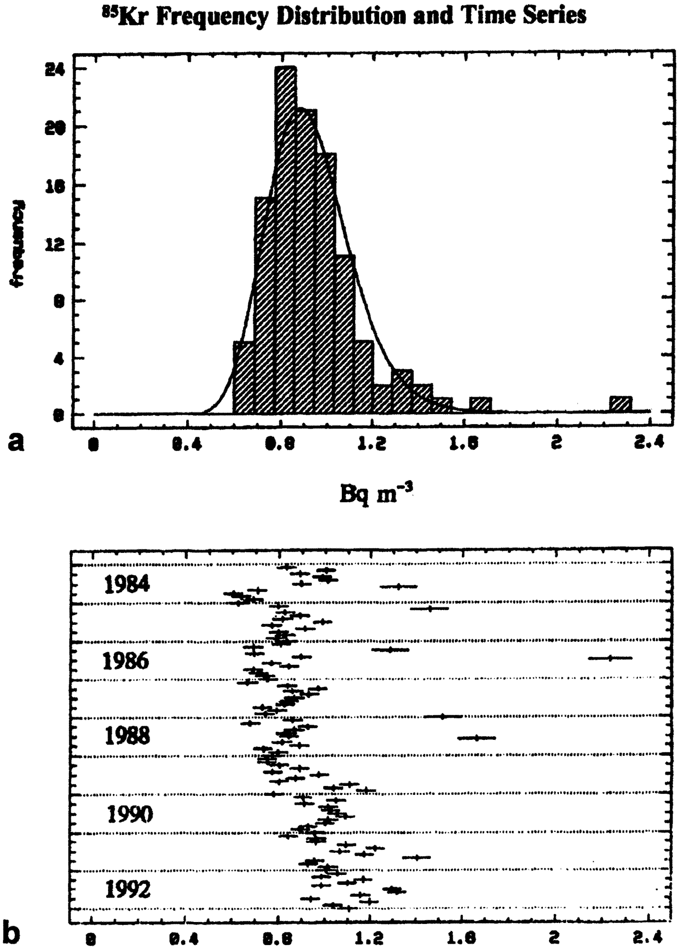

Figure 2. a) Empirical frequency histogram of ^{85}Kr in the central European atmosphere. b) Time series of background ^{85}Kr in Prague: 1984-1992.

To illustrate, the actual time series for the ^{85}Kr atmospheric baseline data is shown in Figure 2. It represents a record of atmospheric (^{85}Kr) background radioactivity in central Europe (Prague), collected by Wilhelmova and

Downloaded by COLUMBIA UNIV on August 9, 2012 | http://pubs.acs.org
Publication Date: November 16, 2006 | doi: 10.1021/bk-2007-0945.ch003

coworkers (*17*) during the period 1984-1992. As such, it is interesting to explore the data structure in the context of events in European history at the time. Space limitations prevent further discussion here, but the rest of the story can be found in Ref. (*18*), where robust techniques of exploratory data analysis are employed to partition the complex data structure into systematic and random components. The systematic structure was striking: a dramatic shift in the ^{85}Kr baseline was found to coincide with the year of profound sociopolitical change in eastern Europe (1989). The residual random component was reasonably normal, with an excess (non-Poisson) relative standard deviation of about 10 %. A final, noteworthy point: the sharp peak at 2.23 Bq m^{-3} resulted from sampling during the spring of 1986, shortly after the fateful event of 26 April 1986 at Chernobyl.

Downloaded by COLUMBIA UNIV on August 9, 2012 | http://pubs.acs.org
Publication Date: November 16, 2006 | doi: 10.1021/bk-2007-0945.ch003

3.2. Non-Counting Variance

Once the systematic structure in a spectral or environmental baseline has been accounted for, attention must be turned to non-Poisson error components, namely "excess" random error (*19*), overdispersion in counting statistics (*20,21*), and "total propagated uncertainty" (*22*). Such error components are crucial in the setting of critical (decision) levels and the estimation of detection, quantification capabilities of a specified measurement process. For the case in point (environmental ^{85}Kr baseline), detailed analysis of the impact of the mean environmental baseline and its excess variance showed that the ideal low-level laboratory instrumental detection and quantification limits for ^{85}Kr were increased by factors of 3.5 and 2.3, respectively, once the environmental background and its variability were taken into account (*23*).

4. Counting Statistics: How Far Can We Stretch the Poisson-Normal Approximation?

It is well known that for large numbers of counts the Poisson distribution of counts is asymptotically normal, with the mean (expectation, μ) equal to the variance (σ^2). In this case the basic expressions for S_C, S_D, and S_Q, using default values for α, β, and k_Q, (Section 2; and Ref. (*8*)) are

$$S_C = z_{1-\alpha}\,\sigma_0 = 1.645\,\sigma_0\,, \tag{4.1}$$

$$S_D = z_{1-\alpha}^2 + 2z_{1-\alpha}\,\sigma_0 = 2.71 + 3.29\,\sigma_0\,, \tag{4.2}$$

$$S_Q = (k_Q^2/2)(1 + \sqrt{(1 + 4\sigma_0^2/k_Q^2)}) = 50(1 + \sqrt{(1 + \sigma_0^2/25)})\,. \tag{4.3}$$

When σ_0^2 is estimated as s_0^2, by replication, $S_C = t_{\nu,1-\alpha}\,s_0$, where ν represents the number of degrees of freedom. Here, the variance of the estimated net signal ($\hat{S}$) when its expectation (S) equals 0, is $\sigma_0^2 = \eta\sigma_B^2 = \eta\mu_B$, where μ_B is expectation (true mean) of the blank, and $\eta = (1 + r^{-1}) = 1$ for the "well-known blank, and $\eta = 2$ for paired measurements. For counting data, r equals the ratio of background to gross count measurement times (t_B/t_S). (Note that μ_B, and the three S's have units of counts.) As shown in Ref. (*8*), for the default values of α, β, and k_Q, the asymptotic expressions for S_D ($3.29\ \sigma_0$) and S_Q ($10\ \sigma_0$) lie within 10 % of the complete expressions (Eqs. 4.2, 4.3) when σ_0^2, *i.e.*, $\eta\mu_B$, exceeds 67 counts and 2500 counts, respectively.

In the following subsections we consider two important questions (and three issues) concerning the applicability of the Poisson-normal approximation for low-level counting: (1) minimum μ_B for a satisfactory approach of the Poisson distribution to normality; and (2) minimum acceptable values for the observed number of background counts (n_B) to serve as a satisfactory estimate for μ_B. The basic question is, "How low can we go, before the great simplicity and convenience of the Poisson-normal approximation must be discarded?"

Downloaded by COLUMBIA UNIV on August 9, 2012 | http://pubs.acs.org
Publication Date: November 16, 2006 | doi: 10.1021/bk-2007-0945.ch003

4.1. Issue-1: Approach to Normality vs. μ_B

The transition region, below which the Poisson-normal approximation must give way to an exact Poisson treatment, has been explored by many authors, particularly in statistical disciplines, and found to be of the order of several counts. In our 1972 study (*9*) we found that the width of the normal (90 %, 2-sided) confidence interval fell within about 10 % of the Poisson confidence interval, once the number of observed background counts (n_B) was of the order of 9.[1] In Ref. (*24*), it was stated the Poisson normal approximation may be adequate, provided that the expected value of the background was at least several counts (≥ 5), (not an integer).[2] The judgment may be made also by comparing upper and lower critical values for the exact Poisson and approximate Poisson-normal distributions. For example, one finds for $\mu_B = 5.00$, that the exact (Poisson) probability that $n_B \leq 9$ equals 0.968, whereas the continuity-corrected normal approximation gives 0.978. At the same time, the two distributions can never be taken to be rigorously equivalent, because of certain immutable differences - such as non-negativity for the Poisson, and continuity for the normal.

---

[1] 90 % *Poisson* confidence limits for μ_B, given n_B, are: μ_L (0.05) equals $\chi^2_{0.05}/2$ with $2n_B$ degrees of freedom, and μ_U (0.95) equals $\chi^2_{0.95}/2$ with $2n_B + 2$ degrees of freedom. 90 % *Poisson-normal* confidence limits are given by the solution of: $\mu_L + 1.645\sqrt{\mu_L} = n_B = \mu_U - 1.645\sqrt{\mu_U}$.

[2] This statement (p. 49 of Ref. (*24*)), has on occasion been misinterpreted as referring to the *estimated* (observed) number of background counts, as opposed to the *expected* (true mean) value, for use as σ_B^2. The difference is profound, given the uncertainty of μ_B, for $n_B = 5$ counts. (90 % confidence limits for ($\mu_B|n_B = 5$) are 1.97, 10.51 - Table III, in Ref. (*9*)).

4.2. Issue-2: Observed Background Counts (n_B) Required to Serve as an Acceptable Estimate of μ_B

This question arises in connection with the approximation in Eq. 4.4,

$$S_C = z_{1-\alpha}\sigma_0 = z_{1-\alpha}\sqrt{(\eta\mu_B)} \approx z_{1-\alpha}\sqrt{(\eta n_B)}\,. \qquad (4.4)$$

Unfortunately, "≈" is generally omitted from the above expression, such that, for paired measurements ($\alpha = 0.05$, $\eta = 2$), the equation is written as $S_C = 2.33\sqrt{n_B}$. MARLAP (*15*) has been more cautious distinguishing between $S_C = z_{1-\alpha}\sqrt{(2\mu_B)} = 2.33\sqrt{\mu_B}$ as "Currie's equation" and $S_C = 2.33\sqrt{n_B}$ as one that "resembles" it - equivalent in a sense to MARLAP Eqs. 20.8 and 20.9, respectively. To control the error from substituting n_B for μ_B, in forming a *fixed* estimate for the critical value, a relatively large number of background counts are recommended. Alternative criteria led Currie to recommend background counts in excess of 70 (*9*) and 87 (using a conservative criterion (*24*), pp. 83f). At stake is control of the systematic error in estimating $S_C(\alpha)$ when that estimate is used repeatedly for making detection decisions.

4.3. Issue-3: S_C as a Random Variable

When σ_B^2 is estimated by replication (r-replicates), as s_B^2, S_C becomes a random variable, equal to $t_{\nu,1-\alpha}s_B\sqrt{\eta}$. More conventionally, for paired comparisons, the test is cast as $d/(s_B\sqrt{2}) > t_{\nu,1-\alpha}$, where the degrees of freedom equal $r - 1$, and net counts $d = y - n_B$, where y = gross (sample) counts, and n_B = background counts. An analogous expression might be expected where the s_B^2 estimate is taken as n_B, where in this case the degrees of freedom are taken as approximately twice the number of background counts.[3] Since, apart from its discrete character, the Poisson distribution appears to resemble the normal down to relatively few counts (μ_B), one might expect that the approximate t-test would be reasonably successful. That seems not bore out, however, by the excessive false positives reported in the literature, using a seemingly similar test, with $S_C = 2.33\sqrt{n_B} = z_{0.95}\sqrt{(2n_B)}$. Converted to standardized form, this test becomes:

---

[3] The t-distribution is clearly only an approximation for small numbers of counts, but certainly better than the z-(normal) distribution, when μ_B is replaced with a random estimate n_B. The approximate number of degrees of freedom is based on the relation between χ^2 and μ_B bounds, given n_B, plus the fact that the asymptotic relative standard uncertainty of $\hat{\sigma}$ is $1/\sqrt{(2\nu)}$, while that of $\sqrt{\hat{\mu}}$ is $0.5/\sqrt{\mu}$.

Downloaded by COLUMBIA UNIV on August 9, 2012 | http://pubs.acs.org
Publication Date: November 16, 2006 | doi: 10.1021/bk-2007-0945.ch003

$$\text{“Detected”, if } (y - n_B)/\sqrt{(2\,n'_B)} > z_{1-\alpha}\,. \tag{4.5}$$

For relatively small numbers of counts, however, this equation presents some problems. First, since s_0 represents only an estimate of σ_0, z is the inappropriate statistic; Student's-*t* would be better, using $2n_B$ for the number of degrees of freedom. Second, there is the zero catastrophe. If n_B should be zero, the (approximate) Studentized ratio on the left side of Eq. 4.5 is either unbounded or indeterminate. Third, there is the matter of independence. In the conventional expression for the *t*-test, the numerator and denominator are independent. In the "usual formulation" for low-level counting decisions, however (Ref. (*15*), p. 20-15), they are correlated with the same $n_B = n'_B$ appearing in both numerator and denominator.

The first difficulty is approached by substituting $t_{\nu,1-\alpha}$ for $z_{1-\alpha}$. For $\mu_B = 5.00$ counts, for example, the approximate test would use $t_{10,0.95} = 1.813$. The zero catastrophe can be minimized by limiting the use of the approximate *t*-test to μ_B's for which $\Pr(n_B = 0)$ is negligible. For $\mu_B = 5.00$, this is already small, namely exp(−5.0), or 0.0067. To achieve a probability < 0.001, μ_B should exceed 6.91. A supplementary fix is to add a small constant to the observed n_B. We chose this route, also to help compensate for the inherent asymmetry in the Poisson-normal approximation. Specifically, s_B^2 was taken equal to $n_B + 0.6$. Such an adjustment places the corrected n_B quite close to the mid-point of the "central" (68 %) confidence interval for μ_B, given n_B. Actually, 0.6 is the closest single decimal digit adjustment for n_B in the range $n_B = 3$ to 20. Above $n_B = 20$, the asymptotic Poisson-normal correction, + 0.50, rapidly obtains. The resulting, approximate Poisson-normal *t*-test procedure would be

$$\text{“Detected,” if } (y - n_B)/\sqrt{(2\,(n'_B + 0.6))} > t_{\nu,1-\alpha}\,, \tag{4.6}$$

where n_B, n'_B are independent background observations - thus overcoming the most serious deficiency of Eq. 4.5, as usually applied.

A miniature Monte-Carlo experiment, repeated five times for each formulation for the null case ($S = 0$), with $\mu_B = 5.00$, was performed as an exploratory study. The results show a dramatic difference between the usual practice (Eq. 4.5) and the application of Eq. 4.6 as an approximate *t*-test (Figure 3). For the independent, *approximate* *t*-test, using $t_C = 1.813$ (Figure 3a), $\hat{\alpha}(u) = 0.038\ (0.002)$; for the dependent *z*-test, using $z_C = 1.645$ (Figure 3b), $\hat{\alpha}(u) = 0.100\ (0.002)$, where u = standard uncertainty.

The empirical distribution in Figure 3a is clearly not normal, especially in the tails. Except for Poisson granularity, most apparent at $T_{ghi} = 0$, however, it does resemble a longer tailed *t*-distribution (with nominal df = 10). The distribution in Figure 3b, labeled T_{jkk}, shows the impact of the correlated background estimates. It resembles neither *z*- nor *t*-distributions, and the negative curvature implies false positives.

Downloaded by COLUMBIA UNIV on August 9, 2012 | http://pubs.acs.org
Publication Date: November 16, 2006 | doi: 10.1021/bk-2007-0945.ch003

Downloaded by COLUMBIA UNIV on August 9, 2012 | http://pubs.acs.org
Publication Date: November 16, 2006 | doi: 10.1021/bk-2007-0945.ch003

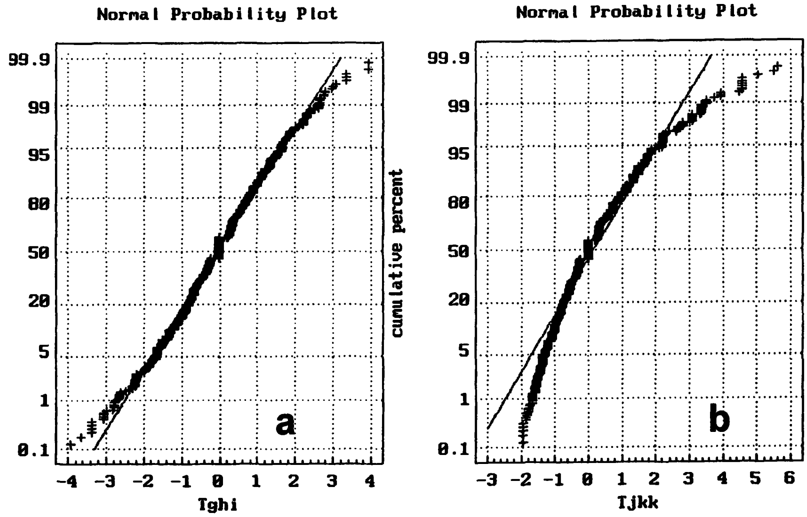

Figure 3. Empirical distributions of independent (a) and dependent (b) S_C ratios, for $S = 0$, $\eta = 2$ (paired measurements), and Poisson parameter $\mu_B = 5.00$.

The latter result, linked with the decidedly non-normal empirical distribution is consistent with the "formula A" Type-I error rates (false positives) depicted in Fig. 20.4 of Ref. (*15*) and a reference therein. The bottom line is that the independence requirement, which is automatically met in the conventional application of the *t*-test ($\bar{x}$, s^2), should not be ignored. Doing so in the present context guarantees an excessive number of false positives.[4] The problem is not in the formulation of S_C, but in the way in which it is applied.[5]

The effects of Poisson granularity and degrees of freedom on the approximate *t*-test for moderately small background counts are being further explored. One resulting observation is that inclusion of an asymmetry constant (+ 0.6 in Eq. 4.6) tends to increase the effective number of degrees of freedom, bringing α closer to the target value (0.05).

---

[4] This may be seen qualitatively from Eq. 4.5, if $n_B = n'_B$: on average, when n_B is relatively small, the numerator tends to be larger, while the denominator is smaller - leading to an excessive increase in the ratio.

[5] Certain alternative Poisson-normal tests are more robust to the non-independence problem (*26*). One that performs quite well, even for rather small values of μ_B, utilizes the well-known Poisson variance stabilization (square root) transformation (Hald, Ref. (*27*); Stapleton, in Ref. (*15*)).

When μ_B is quite small, one should consider abandoning the Poisson-normal approximation for the exact Poisson treatment. Application of exact Poisson significance tests is straightforward, and it was solved long ago. Recent treatments of the exact Poisson detection tests and detection limits abound (*e.g.*, Potter (*25*), MARLAP (*15*)). In the next section, therefore, we simply present a glimpse of the "ancient history."

5. Exact Poisson Treatment: Some Comparative Ancient History

When the Poisson-normal approximation is no longer adequate, one has recourse to the exact Poisson treatment. Although this approach has been well documented in a number of recent publications, it seemed appropriate to include this section as a brief historical footnote regarding treatments in the literature of more than 30 to 60 years ago. Detection decisions and detection limits are considered in Sections 5.1 and 5.2 for the two asymptotic cases: $\eta = 1$ (well-known background) and $\eta = 2$ (paired observations), respectively.

5.1. Poisson Detection Decisions and Detection Limits for the Well-Known Background Asymptote ($\eta = 1$) *(9)*

The ($\eta = 1$) case is particularly straightforward. Given the expectation for the background counts (μ_B), we can apply the exact cumulative Poisson distribution to calculate the critical number of counts n_C, considering the error of the first kind (α), and then the detection limit for the expectation of the gross sample counts μ_D (or y_D), considering the error of the second kind (β). These values follow from the defining Eqs. 2.1 and 2.2, adapted to this special case.

$$\text{Critical value:} \quad \Pr(n > n_C \mid \mu_B) \leq \alpha\,, \qquad (5.1)$$

$$\text{Detection limit:} \quad \Pr(n \leq n_C \mid \mu_D) = \beta\,. \qquad (5.2)$$

Derived relations for the net signal are then: $S_C = n_C - \mu_B$, and $S_D = \mu_D - \mu_B$.

The solutions to Eqs. 5.1 and 5.2, for any particular choice of μ_B, can be calculated directly from the Poisson cumulative distribution, or simply from a table of the confidence limits for the Poisson parameter (μ) vs. the integer values of n. The confidence limits are conveniently derived also from the chi-square table.[6] Table I links μ_B, n_C, and μ_D, extracted from Currie (*24*) (Table 7).

---

[6] Confidence limits for the Poisson parameter (μ), as a function of the observed number of counts (n) are: $\mu = \pm\chi_P^2/2$ ($\nu_- = 2n$, $\nu_+ = 2n + 2$). For $n = 4$, for example, the 90 % confidence limits are (2.72/2), (18.31/2).

Downloaded by COLUMBIA UNIV on August 9, 2012 | http://pubs.acs.org
Publication Date: November 16, 2006 | doi: 10.1021/bk-2007-0945.ch003

Table I. Poisson Critical Values and Detection Limits ($\eta = 1$; $t_B >> t_{S+B}$)

α (minimum)[a]	μ_B (range)	$n_C = S_C + \mu_B$ ($\alpha \leq 0.05$)	$\mu_D = S_D + \mu_B$ ($\beta = 0.05$)
-	0 - 0.051	0	3.00
0.0013	0.052 - 0.35	1	4.74
0.0060	0.36 - 0.81	2	6.30
0.0089	0.82 - 1.36	3	7.75
0.013	1.37 - 1.96	4	9.15
0.016	1.97 - 2.60	5	10.51
0.018	2.61 - 3.28	6	11.84
0.020	3.29 - 3.97	7	13.15
0.021	3.98 - 4.69	8	14.44
0.022	4.70 - 5.42	9	15.70

[a] For each μ_B range, α varies monotonically from α_{min} to 0.05.

Downloaded by COLUMBIA UNIV on August 9, 2012 | http://pubs.acs.org
Publication Date: November 16, 2006 | doi: 10.1021/bk-2007-0945.ch003

To illustrate, let us take μ_B to be 2.30 counts (expectation). Referring to Table I, we find that n_C = 5 counts (integer), and μ_D = 10.51 counts (expectation). Thus, $S_C = 5 - 2.30 = 2.70$ counts; and $S_D = 10.51 - 2.30 = 8.21$ counts. The net count detection limit, expressed in units of background equivalent activity (BEA) is 8.21/2.30 = 3.57. The first column of Table I shows us that the actual value of α falls in the range of 0.016 to 0.050. The expression for the cumulative Poisson distribution, with $\mu_B = 2.30$ and $n = n_C = 5$, gives the result, $\alpha = 0.030$. For $n = 4$, $\alpha = 0.084$. (Results given by the Poisson-normal approximation, Eqs. 4.1, 4.2, are not so different: $S_C \approx 2.49$, $S_D \approx 7.70$.)

5.2 Extreme Low-Level (Poisson) Detection Decisions and Limits for Paired Counting ($\eta = 2$)

The solution for the other asymptotic case, where detection decisions and limits must be evaluated for pairs of Poisson variables, was published more than 65 years ago, by Przyborowski and Wilenski (*2*). The stimulus for the work of these authors was the practical problem of detecting small numbers of dodder seeds in clover. This was of some practical import, because the contaminating seeds belong to the class of twining herbs that are parasitic to plants. In the context of this chapter, the detection of the rarely occurring dodder seeds is the analog of the detection of rarely occurring nuclear particles or decays.

Unlike the previous section, where the challenge was to detect a significant signal above a well-known background, we now address the problem of detecting a significant (1-sided) difference between two extreme low-level Poisson variables. The relative simplicity of the previous section is gone, since the distribution of the difference between two Poisson variables is no longer Poisson-distributed. In fact, the solution space is now 2-dimensional, with a critical region replacing the critical level of the single Poisson variable. Przyborowski and Wilenski formulated the problem by first expressing the joint probability law for observations x, y as

$$\Pr(x,y \mid \mu_x,\mu_y) = (\mu_x^{\,x}\, \mu_y^{\,y} / x!y!)\, \exp[-(\mu_x + \mu_y)]\,, \tag{5.3}$$

where, in the context of low-level counting, x represents counts observed from the background having expectation (mean) μ_x, and y represents counts observed from the gross count (signal + background) variable having expectation μ_y. The density function follows from the fact that the distribution of the sum of Poisson variables is itself Poissonian.[7]

Equation 5.3 can be transformed into a more interesting form (Eq. 5.4) using the following substitutions: $n = x + y$, $\mu = \mu_x + \mu_y$, $\rho = \mu_y/(\mu_x + \mu_y)$,

$$\Pr(x, y \mid \rho, \mu) = \frac{\mu^n e^{-\mu}}{n!} \frac{n!}{y!(n-y)!} \rho^y (1-\rho)^{n-y}\,. \tag{5.4}$$

Critical Region

The sample space is necessarily a 2-dimensional (integer) grid, with the possible sample points (E) defined by the discrete observable values of x (background counts) and y (gross sample counts). For a given n, the partition into y and $x = n - y$ is governed only by the second factor in Eq. 5.4, which is a term in the binomial expansion of $[\rho + (1-\rho)]^n$. For the null hypothesis $\mu_y = \mu_x$, so $\rho = 1/2$; thus, for each n, the critical value for y is given by $\Pr(y > y_C|n,\rho = 0.5) \leq 0.05$, independent of μ. The y_C are simply the 1-sided critical values for proportions, which may be determined from the binomial (cumulative) distribution (n, ρ). To give a specific illustration, consider an observation pair for which $x + y = n = 12$ counts. Then the integer y_C derives from the ≥ 95 percentile of the binomial distribution (12, 0.5), which equals 9 counts. (The probability that $y > 9$ counts, for the given (n, ρ), is 0.019.)

---

[7] For more convenient application to the low-level counting problem, slight changes have been made from the original formulation (in notation, only).

Downloaded by COLUMBIA UNIV on August 9, 2012 | http://pubs.acs.org
Publication Date: November 16, 2006 | doi: 10.1021/bk-2007-0945.ch003

Detection Limit

Evaluation of the detection limit for the exact paired count Poisson problem is not so simple, in that the full probability Eq. 5.4 must be considered. Przyborowski and Wilenski calculate the power function $1-\beta$, given α, from the expression,

$$\Pr(E \in w \mid \rho, \mu) = \sum_{n=0}^{\infty} \frac{\mu^{n} e^{-\mu}}{n!} \sum_{w} \frac{n!}{y!(n-y)!} \rho^{y} (1-\rho)^{n-y}, \qquad (5.5)$$

where ($E \in w$) refers to all observable pairs of observations (x, y) that lie within the critical region w.

Numerical data given for power $1-\beta = 0.95$, for $\alpha \leq 0.05$, were combined with critical values y_C to construct plots showing the critical values (y_C, discrete; dashed curve) and detection limits (y_D, continuous; solid curve) as a function of μ_x (which is μ_B). This information is given in Figure 4a. Note that, although the detection test is based strictly on the observed count pair (x, y), the detection limit necessarily depends on μ_B. Figure 4b gives similar information for the well-known blank case, based on the derivations of Section 5.1.

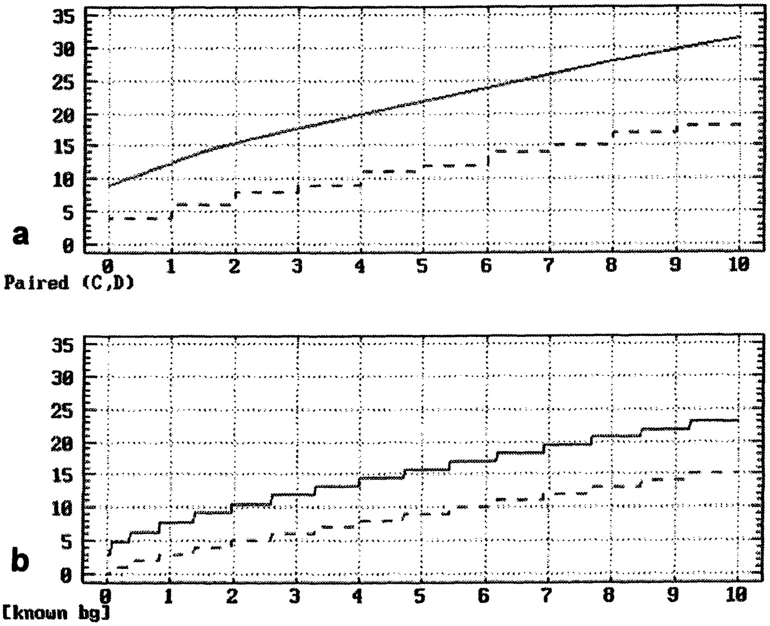

Figure 4. Critical regions (dashed curves) and detection limits (solid curves) for a) $\eta = 2$, paired counting, and b) $\eta = 1$, well-known blank. (x-axes: background counts, y-axes: gross counts, default α, β.)

Downloaded by COLUMBIA UNIV on August 9, 2012 | http://pubs.acs.org
Publication Date: November 16, 2006 | doi: 10.1021/bk-2007-0945.ch003

Downloaded by COLUMBIA UNIV on August 9, 2012 | http://pubs.acs.org
Publication Date: November 16, 2006 | doi: 10.1021/bk-2007-0945.ch003

Some summary observations can be drawn from the two sets of y_C critical boundaries and two sets of y_D detection limit curves in Figure 4. For the paired case (Figure 4a), the minimum value for y_C (4 counts) occurs when $x = 0$; thus, the smallest integer pair that would indicate "detection" would be $(x, y) = (0,5)$. Similarly, for $x = 4$ counts, the smallest significant value for y would be 12 counts ($y_C = 11$). Looking at the detection limit curve, we see that for a truly zero background, the minimum detectable gross count (y_D) is approximately 9.0 counts, which here also equals S_D. For $\mu_B = 4.0$ counts, the minimum detectable $y_D \approx 20.0$ counts ($S_D \approx 16.0$ counts). To detect a net signal (S) equal to 4 times the background, the intersection of line of slope 5 (μ_y/μ_x) with the (gross signal) detection limit curve is needed. That occurs at $\mu_B = 4.0$ counts. (Note that uncertainty in μ_B translates into uncertainty in y_D and S_D.)

Considering the same background values ($\mu_B = 0$, $\mu_B = 4.0$ counts) for the well-known background case (Figure 4b), the minimum detectable gross counts are $y_D = 3.00$ counts and $y_D = 14.44$ counts, respectively. The corresponding values for the minimum detectable net signal are $S_D = 3.00$ counts and $S_D = 10.44$ counts, respectively. So, for this small count range, excellent knowledge of the background expectation carries a benefit (reduction in S_D) of a factor of 1.5 to three. (The Poisson-normal approximation, Eq. 4.2, applied to $\mu_B = 4.0$, gives $S_D = 9.29$ counts ($\eta = 1$) and $S_D = 12.02$ counts ($\eta = 2$).) Although the critical value boundary curve allows rigorous testing for significant signal, background differences in the two asymptotic ($\eta = 1,2$) extreme Poisson cases, the corresponding detection limit curves are essential for planning for successful extreme low-level studies. For an approximate, but excellent analytic expression for the $\eta = 2$ detection limit curve, see Shiue and Bain (*28*).

There has been a resurgence of interest in recent years in the low-level counting communities in the problem addressed by Przyborowski and Wilenski so long ago, in part because of major advances in, and needs for, low-level radiation measurement, and in part because of then un-dreamed of advances in computing power. For a recent review and bibliography, see Ref. (*15*); for an exact treatment of paired counting with known background, see Refs. (*27,29*); for reviews of ultra-low-level counting capabilities and applications, see Ref. (*16*).

6. On the Validity of the Poisson Hypothesis for Background Counts

At this point we return to the "real world," and the second empirical B-distribution, shown in Figure 1b - namely the frequency histogram of (gross) low-level background counts, in the NIST low-level, small counter, gas counting system. Use of this system alternately in the Geiger or proportional regions has seen practical service in the measurement of ^{14}C, ^{37}Ar, and ^{85}Kr in the natural environment.

It seems to be conventional wisdom, at least for low to moderate counting rates, that the counting background can be described as a Poisson process. Such an assumption, of course, affects uncertainty estimates, as well as computed critical levels and detection limits, where the variance of the background is dominant. For those background components from long-lived radioactivity, the assumption for the decay process is doubtless valid, but the assumption for the counting process deserves rigorous testing for possible environmental and/or measurement process artifacts. The following summary is drawn from a comprehensive study of time series of some 1.4×10^6 individual low-level GM background events (coincidence and anticoincidence) spanning a period of nearly one month, where the amplitude and time of occurrence of each pulse was recorded to the nearest 100 μs. Additionally, the system provided pulse-pair resolution to the nearest 1 μs, and full waveform analysis (*30*).

Downloaded by COLUMBIA UNIV on August 9, 2012 | http://pubs.acs.org
Publication Date: November 16, 2006 | doi: 10.1021/bk-2007-0945.ch003

6.1. Background as a Poisson Process; Expected Characteristics

If the counter background can be described as a Poisson process, it would be expected to be consistent with: (1) the Poisson distribution of counts, which is asymptotically normal, but discrete and increasingly positively skewed for small numbers of counts, and for which the expectation of the index of dispersion I_d (variance/mean) is unity (*26*); (2) the uniform distribution of arrival times; and (3) the exponential distribution of inter-arrival times, also positively skewed. These expected characteristics served as the basis for our investigation of the validity of the Poisson assumption for low-level counting background. For this purpose, measurements were performed with the NIST individual pulse analysis system, with 40 cm^3 cylindrical gas counters operated in the Geiger mode. Essential characteristics of the system are: (1) ca. 80 % of the gross background was eliminated by surrounding the counting tube with 25 cm of pre-nuclear era steel (World War I naval gun barrel); (2) the bulk (98 %) of the residual background (ca. 20 counts per minute, cpm), due to penetrating cosmic ray muons, was "canceled" by anticoincidence counting.

The fundamental assumption to be tested was whether the muon (coincidence) background and the net (anticoincidence) background could be treated as independent Poisson processes.

6.2. Empirical Distributions and Tests of the Poisson (Background) Hypothesis

Distributional highlights from the NIST study are given in Figs. 6.1-6.3. The basic information is generated from the individual pulse arrival and inter-arrival times, as shown in Figure 5, which represents a 150 s glimpse of the pulse data stream (arrival times) for coincident (C) and anticoincident (A) events from a 980 min background counting experiment. (*DT* and *dt* represent A-A and C-A inter-arrival times, respectively; and event-G represents a rare giant pulse, atypical of the ordinary GM process.)

Considering first the Poisson distribution of counts and the corresponding count rates, we examined results for C (muon) and A (net background) events spanning a period about sixteen thousand times as long as that shown in Figure 5 (nearly a month). At the beginning of this period, the GM counting tube was filled with purified counting gas; following that, background (C- and A-) counts were aggregated for 21 individual counting periods, 16 of which had relatively uniform counting times of about 1600 min. The Poisson hypothesis was tested with χ^2, considering the ratio of the observed variance to the theoretical variance based on the number of counts accumulated in each counting period. The A-events passed the test ($I_d = 1.36, p = 0.16$) but the C-events failed ($I_d = 4.92, p < 0.000001$).

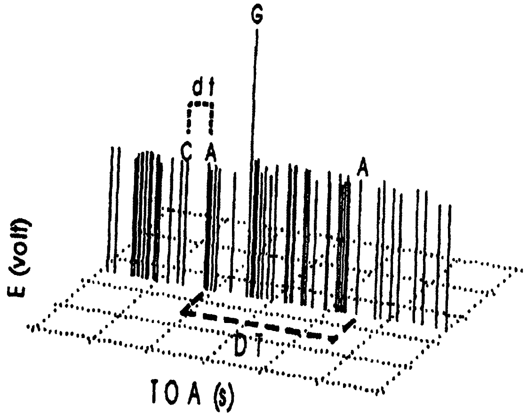

Figure 5. A 150 s snapshot of the background pulse data stream from a NIST low-level GM counting tube, showing times of arrival (TOA, x-axis) and pulse amplitudes (E, z-axis). Two anticoincidence pulses (A) occurred during this interval, the remainder (excluding G) being coincidence pulses (C).

Downloaded by COLUMBIA UNIV on August 9, 2012 | http://pubs.acs.org
Publication Date: November 16, 2006 | doi: 10.1021/bk-2007-0945.ch003

Insight is gained by looking beyond the summary statistics. The presumably random, symmetric distribution of the 1600 min aggregated C-background counts, shown in Figure 1b, is repeated in Figure 6a, together with further exploration in two additional dimensions: time (Figure 6b) and barometric pressure (not shown). The time series shows immediately that the extra C-background variance (above Poisson) is not due simply to an added component of normal, random error. Rather, a distinctive quasi-periodic pattern is evident, well in excess of the Poisson-normal standard uncertainty bars. In fact, the source of the non-Poisson, non-random C-background variance represents an interesting blend of meteorology and physics, with time as surrogate: increased barometric pressure leads to increased attenuation of mesons in the atmosphere. This is supported by the data. When the "hidden dimension" (barometric pressure) is viewed, one sees a strong negative correlation (– 0.91) between muon count rate and pressure; and the pressure coefficient (– 2.5 %/cm Hg) is consistent with the mean free path of muons in the atmosphere. Once the data are corrected for the pressure effect, I_d drops to 2.19.

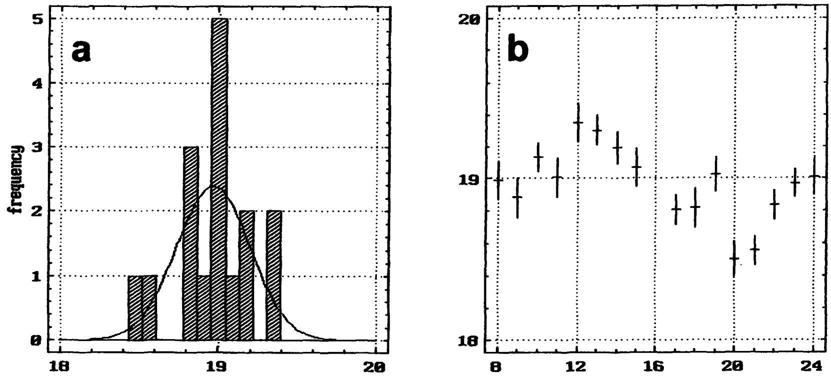

Figure 6. NIST background counts. a) frequency histogram of aggregated gross background counts (x-axis, bkg rate, cpm). Although the histogram appears somewhat symmetric that does not guarantee that the background events are normally distributed. b) time series of background counts reveals a non-random, quasi-periodic structure (x-axis, order; y-axis, bkg rate, cpm). Hidden dimension of major consequence: barometric pressure (see text).

Arrival time distributions for the C- and A- pulses (not shown) from the 980 min experiment referenced in Figure 5 showed no significant difference from a Poisson process (uniform distribution), but inter-arrival times were a different matter. The inter-arrival times (*DT*) for the low-level anticoincidence

Downloaded by COLUMBIA UNIV on August 9, 2012 | http://pubs.acs.org
Publication Date: November 16, 2006 | doi: 10.1021/bk-2007-0945.ch003

background (AC-AC) did show a good fit (p = 0.40) to the exponential distribution as shown in Figure 7a, but the AC vs. Coincidence (muon) inter-arrival times (*dt*) did not. As seen in Figure 7b, there were an excessive number of very short intervals falling within the first (1 s) histogram bin. Upon expansion of the time scale, it was found that the excess was concentrated almost entirely between 150 and 350 μs.

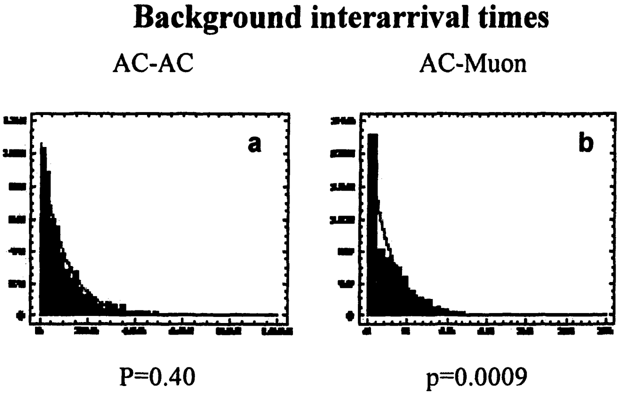

Relative frequencies:

- muons: 1.00 (reference)
- net background (AC): 0.015
- afterpulses: 0.0012 [*Artifacts;* deadtime effect]
- giant pulses: 0.000042

Figure 7. Empirical background inter-arrival time distributions: y-axes, frequencies; x-axes, times. a) DT, summarizes anticoincidence (AC-AC) inter-arrival times between zero and 1000 s with a mean of 100.7 s (for 2 counters). The fit is good (p = 0.40). b) dt, summarizes anticoincidence-coincidence (AC-muon) inter-arrival times between zero and 30 s with a mean of 2.72 s. The fit is not good (p = 0.0009), showing excessive counts in the first 1 s bin.

The physics of this phenomenon is well known. It relates to a counting process artifact whereby a secondary event ("afterpulse"), which occurs within a

Downloaded by COLUMBIA UNIV on August 9, 2012 | http://pubs.acs.org
Publication Date: November 16, 2006 | doi: 10.1021/bk-2007-0945.ch003

few hundred microseconds of the primary event, is occasionally generated by a complex photo-electric process within the counting tube. For the NIST system the afterpulse probability is ca. 0.1 %. Because of their absolute abundance and time constant, the spurious pulses are scarcely detectable in the *DT* distribution. They have a good chance of escaping cancellation during the C-pulse time gate, however, and appearing in the *dt* distribution where intervals may be as short as the intrinsic deadtime of the GM tube (≈ 140 μs). Since the primary coincidence pulse rate (≈ 20 min^{-1}) exceeds the single counter rate (≈ 0.30 min^{-1}) by about a factor of 70, the contamination probability is raised to ca. 7 % for the anticoincidence background. A further, interlaboratory complication is that the afterpulse contamination of the A-background depends on the electronic deadtime of the specific low-level counting system.

Because of the enormous excess of C-events over A-events in low-level anticoincidence counting, it is essential to provide extremely effective muon (anticoincidence) shielding and afterpulse control via special timing and pulse shape circuitry. The non-random character of the muon background, together with its effect on afterpulse amplification, makes it clear that strict validity of the Poisson assumption for counting background requires systems where "meson leakage" (*31*) can be controlled by extremely efficient anticoincidence shielding, or better, by largely eliminating the cosmic ray meson background by going deep underground (*16*).

Downloaded by COLUMBIA UNIV on August 9, 2012 | http://pubs.acs.org
Publication Date: November 16, 2006 | doi: 10.1021/bk-2007-0945.ch003

7. Summary and Conclusions

The impact of the blank B (background, baseline), the distribution of which ultimately determines nuclear detection capabilities, has been examined briefly from three broad perspectives: (1) from the point of view of observed variability in laboratory or environmental measurements, (2) for the ideal limiting case, where the blank can be treated strictly as a Poisson process, and (3) for the actual low-level counting background. The first instance, illustrated with an environmental baseline for atmospheric ^{85}Kr, indicated that the radioactivity monitoring series had significant systematic variations (both short-term and long-term) suggestive of specific socio-scientific events, as well as Poisson and non-Poisson (sampling, measurement) random error. Successful partition of the total "noise" and the systematic structure in such circumstances, is an essential goal for making valid detection decisions and realistic estimates of detection and quantification capabilities.

The ideal, and ultimately limiting situation, where the variability of the blank derives strictly from Poisson counting statistics, was next considered. Following a presentation of the fundamental hypothesis testing expressions for the critical level L_C or S_C (decision level), detection limit L_D , and quantification limit L_Q, discussion focused on the moderate to large count case (Poisson-normal approximation), and the extreme low-level (exact Poisson) case. An exploratory extension of the conventional *t*-test to moderate counts (a few to say, 70) showed that inappropriate use of the *same* observed B-value in numerator and denominator of the common approximate (Poisson-normal) detection test ratio ($\hat{S}/\hat{\sigma}_0$) can be disastrous - yielding decidedly non-normal, non-*t* frequency distributions, with a propensity for excessive false positives. For extreme low-level counting, the exact Poisson distribution must be employed. Expressions developed in historical research on the topic were presented, together with tabular and graphical results for L_C and L_D as a function of background counts.

While the distribution of the counting background is absolutely central to meaningful detection tests and estimated detection limits, this background does not necessarily constitute a pure Poisson process. Extensive tests of individual background pulses in a NIST low-level counting laboratory showed significant deviations from such a process - related to non-ideal counter behavior and the cosmic ray (muon) background component, which includes systematic variations.

Downloaded by COLUMBIA UNIV on August 9, 2012 | http://pubs.acs.org
Publication Date: November 16, 2006 | doi: 10.1021/bk-2007-0945.ch003

Acknowledgment

Special thanks to R. Hanlen for important suggestions that grew out of his review of this chapter.

References

1. Feigl, F. Tüpfel- und Farbreaktionen als mikrochemische Arbeitsmethoden. *Mikrochemie* **1923**, *1*, 4.
2. Przyborowski, J.; Wilenski, H. Homogeneity of results in testing samples from Poisson series. *Biometrika* **1939**, *31*, 313-323.
3. Roos, J. B. The limit of detection of analytical methods. *Analyst* **1962**, *87*, 832.
4. Nicholson, W. L. Fixed time estimation of counting rates with background corrections; AEC Research and Development Report HW-76279; Hanford Atomic Products Operations: Richland, WA, 1963.
5. Nicholson, W. L. Statistics of net counting rate estimation with dominant background corrections. *Nucleonics* **1966**, *24(8)*, 118-121.
6. Altshuler, B.; Pasternack, B. Statistical measures of the lower limit of detection of a radioactivity counter. *Health Phys.* **1963**, *9*, 293-298.
7. Kaiser, H. Zum Problem der Nachweisgrenze. *Z. Anal. Chim.* **1965**, *209*, 1-18.
8. Currie, L. A. Limits for qualitative detection and quantitative determination, application to radiochemistry. *Anal. Chem.* **1968**, *40*, 586-593.

9. Currie, L. A. The measurement of environmental levels of rare gas nuclides and the treatment of very low-level counting data. *IEEE Trans. Nucl. Sci.* **1972,** *NS-19,* 119-126.
10. International Union of Pure and Applied Chemistry. Nomenclature in evaluation of analytical methods, including detection and quantification capabilities. *Pure and Applied Chemistry* **1995,** *67,* 1699-1723.
11. *Capability of Detection*; Standard ISO 11843-1,2; International Organization for Standardization: Geneva, 1997.
12. *Determination of the Detection Limit and Decision Threshold for Ionizing Radiation Measurements*; Standard ISO 11929-1,2,3,4; International Organization for Standardization: Geneva, 2000-2001.
13. *Standard Practice for 99 %/95 % Interlaboratory Detection Estimate (IDE) for Analytical Methods with Negligible Calibration Error*; Standard ASTM D 6091-97; American Society for Testing and Materials: West Conshohocken, PA, 1997.
14. *Standard Practice for Interlaboratory Quantitation Estimate*; Standard ASTM D 6512-00; American Society for Testing and Materials: West Conshohocken, PA, 2000.
15. *Multi-Agency Radiological Laboratory Analytical Protocols Manual*; Chapter 20, Detection and Quantification Capabilities; Report NUREG-1576, EPA 402-B-04-001A, NTIS PB2004-105421, 2004, www.epa.gov/radiation/marlap/manual.htm.
16. *Proceedings of the Conference on Low-Level Radionuclide Measurement Techniques*; International Committee for Radionuclide Metrology; *Appl. Rad. Isot.* **2004,** *61,* 83-421.
17. Wilhelmova, L.; Tomasek, M.; Stukheil, K. *Biol. Trace El. Res.* **1994,** *43,* 725-736.
18. Currie, L. A. Some case studies of skewed (and other ab-normal) data distributions arising in low-level environmental research. *Fresenius J. Anal. Chem.* **2001,** *370,* 705-718.
19. Currie, L. A. The limit of precision in nuclear and analytical chemistry. *Nucl. Instr. Meth.* **1972,** *100,* 387-395.
20. Semkow, T. M. Theory of overdispersion in counting statistics caused by fluctuating probabilities. *Appl. Rad. Isot.* **1999,** *51,* 565-579.
21. Semkow, T. M. Experimental verification of overdispersion in radioassay data. *Health Phys.* **2002,** *83,* 485-496.
22. Rucker, T. Calculation of decision levels and minimum detectable concentrations from method blank and sample uncertainty data - utopian statistics. *J. Radioanal. Nucl. Chem.* **2001,** *248,* 191-196.

Downloaded by COLUMBIA UNIV on August 9, 2012 | http://pubs.acs.org
Publication Date: November 16, 2006 | doi: 10.1021/bk-2007-0945.ch003

23. Currie, L. A.; Klouda, G. A. Detection and quantification capabilities for ^{85}Kr with the NIST low-level gas counting system: impacts of instrumental and environmental backgrounds. *J. Radioanal. Nucl. Chem.* **2001**, *248*, 239-246.
24. Currie, L. A. Lower limit of detection: definition and elaboration of a proposed position for radiological effluent and environmental measurements; Report NUREG/CR-4007; Nuclear Regulatory Commission: Washington, DC, 1984.
25. Potter, W. E. Neyman-Pearson confidence intervals for extreme low-level, paired counting. *Health Phys.* **1999**, *76*, 186-190.
26. Cox, D.; Lewis, P. *The Statistical Analysis of Series of Events*; Methuen & Co.: London, 1966.
27. Hald, A. *Statistical Theory with Engineering Applications*; Chapman & Hall: London, 1952.
28. Shuie, W. K.; Bain, L. J. Experiment size and power comparisons for 2-sample Poisson tests. *Appl. Stat. C* **1982**, *31*, 130-134.
29. Irwin, J. O. The frequency distribution of the difference between two independent variates following the same Poisson distribution. *J. Royal Stat. Soc.* **1937**, *100*, 415-416.
30. Currie, L. A.; Eijgenhuijsen, E. M.; Klouda, G. A. On the validity of the Poisson hypothesis for low-level counting; investigation of the distributional characteristics of background radiation with the NIST Individual Pulse Counting System. *Radiocarbon* **1998**, *40*, 113-127.
31. Theodórsson, P. Quantifying background components of low-level gas proportional counters. *Radiocarbon* **1992**, *34*, 420-427.

Downloaded by COLUMBIA UNIV on August 9, 2012 | http://pubs.acs.org
Publication Date: November 16, 2006 | doi: 10.1021/bk-2007-0945.ch003

Downloaded by PENNSYLVANIA STATE UNIV on August 8, 2012 | http://pubs.acs.org
Publication Date: November 16, 2006 | doi: 10.1021/bk-2007-0945.ch004

Chapter 4

Exponential Decay Law and Nuclear Statistics

Thomas M. Semkow

Wadsworth Center, New York State Department of Health and State University of New York, P.O. Box 509, Albany, NY 12201

The exponential decay of radionuclides is a cornerstone of applied modeling in nuclear science. This chapter reviews different facets of the exponential decay. The theory of exponential decay is outlined from probabilistic and quantum-mechanical points of view. Experimental verifications of the exponential decay and possible deviations from it are discussed. Relationship between the exponential decay and statistics is reviewed and fully derived using stochastic Markov process. Complete decay of radionuclides and its implications are discussed.

1. Introduction

The exponential decay (radioactive decay) law was discovered by Rutherford and Soddy in 1902-1903, which culminated in a summary paper (*1*). They observed that the ionization current in a chamber containing radioactive substance decreased exponentially with time, from which they concluded that the rate of decay, *i.e.*, activity $\rho(t)$, also decreased exponentially in time, $\rho(t) = \rho(0)\,\mathrm{e}^{-\lambda t}$, where λ is a rate coefficient which they named radioactive constant (see Fig. 1). Therefore, the number of radioactive atoms $N(t)$, which survived the decay in time t is given by

$$N(t) = \int_t^{\infty} \rho(t)dt = \frac{\rho(0)}{\lambda}\mathrm{e}^{-\lambda t}. \qquad (1)$$

In Applied Modeling and Computations in Nuclear Science; Semkow, T., et al.;
ACS Symposium Series; American Chemical Society: Washington, DC, 2006.

Downloaded by PENNSYLVANIA STATE UNIV on August 8, 2012 | http://pubs.acs.org
Publication Date: November 16, 2006 | doi: 10.1021/bk-2007-0945.ch004

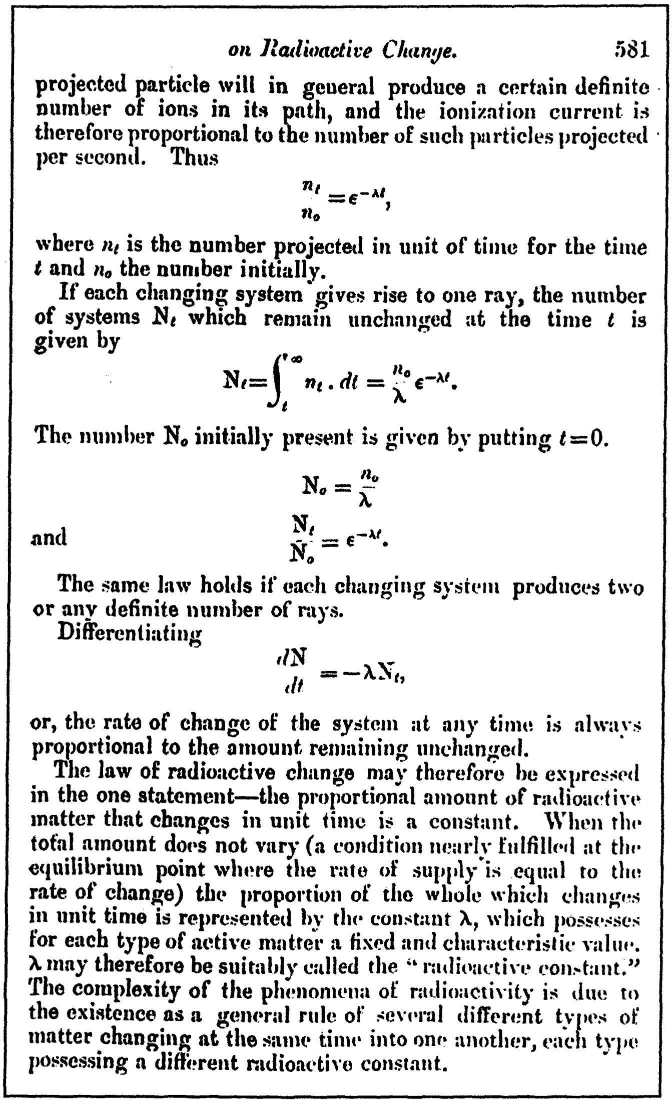

on Radioactive Change. 581

projected particle will in general produce a certain definite number of ions in its path, and the ionization current is therefore proportional to the number of such particles projected per second. Thus

$$\frac{n_t}{n_0} = \epsilon^{-\lambda t},$$

where n_t is the number projected in unit of time for the time t and n_0 the number initially.

If each changing system gives rise to one ray, the number of systems N_t which remain unchanged at the time t is given by

$$N_t = \int_t^{\infty} n_t \,.\, dt = \frac{n_0}{\lambda}\epsilon^{-\lambda t}.$$

The number N_0 initially present is given by putting $t=0$.

$$N_0 = \frac{n_0}{\lambda}$$

and

$$\frac{N_t}{N_0} = \epsilon^{-\lambda t}.$$

The same law holds if each changing system produces two or any definite number of rays.

Differentiating

$$\frac{dN}{dt} = -\lambda N_t,$$

or, the rate of change of the system at any time is always proportional to the amount remaining unchanged.

The law of radioactive change may therefore be expressed in the one statement—the proportional amount of radioactive matter that changes in unit time is a constant. When the total amount does not vary (a condition nearly fulfilled at the equilibrium point where the rate of supply is equal to the rate of change) the proportion of the whole which changes in unit time is represented by the constant λ, which possesses for each type of active matter a fixed and characteristic value. λ may therefore be suitably called the "radioactive constant." The complexity of the phenomena of radioactivity is due to the existence as a general rule of several different types of matter changing at the same time into one another, each type possessing a different radioactive constant.

Figure 1. Discovery of exponential decay by Rutherford and Soddy (Reproduced from reference (1), with the permission of Taylor & Francis, www.tandf.co.uk).

Two fundamental relations follow from Eq. 1: the exponential decay law,

$$N(t) = N(0)\,e^{-\lambda t}, \tag{2}$$

and the rate equation,

$$\rho(N,t) = \lambda N(t). \tag{3}$$

Both are fundamentally associated with each other. By differentiating Eq. 2 with respect to time, one obtains a 1st order kinetic equation

$$\frac{dN(t)}{dt} = -\lambda N(t).$$

The kinetic equation is a consequence of the exponential decay law, and not vice versa, as it is sometimes assumed.

2. Theory of Exponential Decay

The theory of exponential decay is described in terms of a probabilistic approach, quantum approach, and the deviations from it.

A. Probabilistic Approach

Early theoretical treatments of exponential decay used probabilistic arguments. In 1905, Schweidler (*2*) assumed that the probability of an atom decaying in time dt is λdt (see Fig. 2), whence its probability of survival is equal to $1 - \lambda dt$. Furthermore, the probability of survival in one time interval is independent of survival in any other time interval. Therefore, by subdividing time t into n intervals dt, the probability $S(t)$ of survival in time t is given by (*3*)

$$S(t) = (1 - \lambda t/n)^n = \exp\{n\ln(1 - \lambda t/n)\} = \exp\{-\lambda t - (\lambda t)^2/2n + \ldots\}$$

$$\xrightarrow[n \to \infty]{} e^{-\lambda t}. \tag{4}$$

In 1913, Bortkiewicz (*4*) also considered statistical independence of survival probability S in any time interval (see also Ref. (*5*)). Thus, for a time $t + t_l$,

$$S(t + t_1) = S(t)S(t_1). \tag{5}$$

By differentiating Eq. 5 with respect to t, and subsequent dividing by Eq. 5, one obtains $S'(t+t_1)/S(t+t_1) = S'(t)/S(t)$, from which $S'(t)/S(t)$ is constant in time. Also $S'(t) < 0$, since $S(t)$ diminishes in time. Therefore, by equating $dS(t)/S(t)dt = -\lambda$, and solving with a boundary condition $S(0) = 1$, one also obtains Eq. 4. Equation 4 does not represent just any exponential function, but a probability of survival of a single atom in time t, given a constant rate coefficient of decay λ. This is the interpretation of the exponential decay law.

Downloaded by PENNSYLVANIA STATE UNIV on August 8, 2012 | http://pubs.acs.org
Publication Date: November 16, 2006 | doi: 10.1021/bk-2007-0945.ch004

Several useful probabilistic identities follow from Eq. 4. If the probability of survival of a single atom is $e^{-\lambda t}$, then the average number of atoms which survived the decay in time t, $\bar{N}(t)$, is given by

$$\bar{N}(t) = N(0)\,e^{-\lambda t}. \tag{6}$$

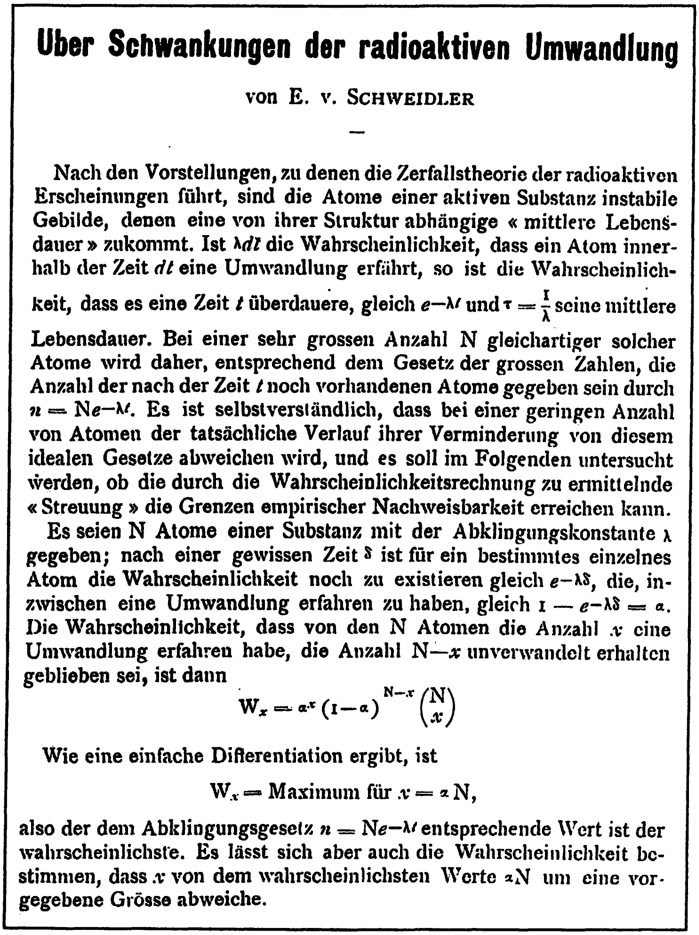

Uber Schwankungen der radioaktiven Umwandlung

von E. v. SCHWEIDLER

—

Nach den Vorstellungen, zu denen die Zerfallstheorie der radioaktiven Erscheinungen führt, sind die Atome einer aktiven Substanz instabile Gebilde, denen eine von ihrer Struktur abhängige « mittlere Lebensdauer » zukommt. Ist λdt die Wahrscheinlichkeit, dass ein Atom innerhalb der Zeit dt eine Umwandlung erfährt, so ist die Wahrscheinlichkeit, dass es eine Zeit t überdauere, gleich $e^{-\lambda t}$ und $\tau = \frac{1}{\lambda}$ seine mittlere Lebensdauer. Bei einer sehr grossen Anzahl N gleichartiger solcher Atome wird daher, entsprechend dem Gesetz der grossen Zahlen, die Anzahl der nach der Zeit t noch vorhandenen Atome gegeben sein durch $n = Ne^{-\lambda t}$. Es ist selbstverständlich, dass bei einer geringen Anzahl von Atomen der tatsächliche Verlauf ihrer Verminderung von diesem idealen Gesetze abweichen wird, und es soll im Folgenden untersucht werden, ob die durch die Wahrscheinlichkeitsrechnung zu ermittelnde « Streuung » die Grenzen empirischer Nachweisbarkeit erreichen kann.

Es seien N Atome einer Substanz mit der Abklingungskonstante λ gegeben; nach einer gewissen Zeit ϑ ist für ein bestimmtes einzelnes Atom die Wahrscheinlichkeit noch zu existieren gleich $e^{-\lambda\vartheta}$, die, inzwischen eine Umwandlung erfahren zu haben, gleich $1 - e^{-\lambda\vartheta} = \alpha$. Die Wahrscheinlichkeit, dass von den N Atomen die Anzahl x eine Umwandlung erfahren habe, die Anzahl $N-x$ unverwandelt erhalten geblieben sei, ist dann

$$W_x = \alpha^x (1-\alpha)^{N-x} \binom{N}{x}$$

Wie eine einfache Differentiation ergibt, ist

$$W_x = \text{Maximum für } x = \alpha N,$$

also der dem Abklingungsgesetz $n = Ne^{-\lambda t}$ entsprechende Wert ist der wahrscheinlichste. Es lässt sich aber auch die Wahrscheinlichkeit bestimmen, dass x von dem wahrscheinlichsten Werte αN um eine vorgegebene Grösse abweiche.

Figure 2. First theory of exponential decay by Schweidler (Reproduced from reference (2), with the permission of Dunod, www.dunod.com).

Downloaded by PENNSYLVANIA STATE UNIV on August 8, 2012 | http://pubs.acs.org
Publication Date: November 16, 2006 | doi: 10.1021/bk-2007-0945.ch004

Note a subtle difference between Eqs. 2 and 6. $\overline{N}(t)$ is an average number of atoms, not necessarily integral, whereas $N(0)$ is the initial, integral number of atoms. Other probabilistic identities are:

$$e^{-\rho(0)t}, \tag{7a}$$

$$1-e^{-\lambda t}, \tag{7b}$$

$$(1-e^{-\lambda t})^{N(0)}. \tag{7c}$$

Equation 7a gives the probability of survival of $N(0)$ atoms in time t (using Eq. 3). Equation 7b is a probability of decay of a single atom in time t. If $\lambda t \ll 1$, one obtains $1-e^{-\lambda t} \approx \lambda t$ from Eq. 7b. However, λt is not, in general, the probability of decay in time t, only if $\lambda t \ll 1$. Equation 7c is a probability of decay of $N(0)$ atoms in time t.

Ruark has pointed out (*6*) that, in derivation such as by Schweidler, constant rate coefficient λ is a necessary condition for the exponential decay. He subsequently proved mathematically that the exponential decay implies constant rate coefficient. Therefore, constant rate coefficient is the necessary as well as sufficient condition for the exponential decay.

Another statistical derivation of the exponential decay law follows from the information theory by adopting a treatment by Hamburger *et al.* (*7*). Let us consider an atom which survived the decay in time interval $(0, t)$ and decayed in time interval $(t, t + dt)$. Since such decay is random, there will be a distribution of intervals t with the probability density function $T(t)$. We require only two constraints on T: constant average lifetime τ (related to a constant λ), as well as normalization:

$$\int_0^\infty tT(t)\,dt = \tau, \tag{8a}$$

$$\int_0^\infty T(t)\,dt = 1. \tag{8b}$$

The statistical entropy E of the system is given by

$$E = -\int_0^\infty T(t)\ln T(t)\,dt. \tag{9}$$

In order to derive $T(t)$, we maximize the entropy using Lagrange multipliers μ and λ. To achieve this goal, we define a functional F, using Eqs. 8a, 8b, 9,

$$F[T] = -\int_0^\infty \{T\ln T + \mu T + \lambda t T\}dt,$$

whose variational derivative is

$$\delta F = -\int_0^\infty \{\ln T + 1 + \mu + \lambda t\}dt\delta T.$$

The derivative $\delta F = 0$, if $\ln T + 1 + \mu + \lambda t = 0$, from which

Downloaded by PENNSYLVANIA STATE UNIV on August 8, 2012 | http://pubs.acs.org
Publication Date: November 16, 2006 | doi: 10.1021/bk-2007-0945.ch004

$$T(t) = \mathrm{e}^{-1-\mu}\mathrm{e}^{-\lambda t}. \tag{10}$$

By inserting Eq. 10 into the constraint Equations 8a, 8b, one obtains the probability $T(t)dt$ of decay in $(t,t + dt)$:

$$T(t)dt = \mathrm{e}^{-\lambda t}\lambda dt, \tag{11}$$

where $\lambda = 1/\tau$ is the rate coefficient. The probability in Eq. 11 is a product of two probabilities: survival in time t, $\mathrm{e}^{-\lambda t}$ (*i.e.*, the exponential decay law), and an immediate decay in time dt, λdt.

Downloaded by PENNSYLVANIA STATE UNIV on August 8, 2012 | http://pubs.acs.org
Publication Date: November 16, 2006 | doi: 10.1021/bk-2007-0945.ch004

B. Quantum Mechanics of Decaying State

Quantum mechanics treats the decay of any quantum state, including radioactive decay. The precursors of the ideas of quantum-state decay are found in the 1917 Einstein's paper on radiation (see Kleppner (*8*)). Einstein proposed that an excited atom in empty space will spontaneously decay into a lower state with the emission of radiation and with a constant rate coefficient. The quantum theory of decaying state was created by Weisskopf and Wigner in 1930 (*9,10*), Krylov and Fock (*11*), and others as outlined below. A modern outline of the decay theory is given in the textbook by Merzbacher (*5*).

The time evolution of a quantum state, described by a time-dependent wave function $\Psi(t)$, is given by the time-dependent Schrödinger equation

$$i\hbar\frac{\partial\Psi(t)}{\partial t} = H\Psi(t), \tag{12}$$

where $H = H_0 + V$ is the Hamiltonian operator. It can be split into two terms: H_0, describing unperturbed system, and a perturbation V which generates time evolution of $\Psi(t)$ understood as a spontaneous decay of quantum state. Equation 12 has an operator solution

$$\Psi(t) = \mathrm{e}^{-iHt/\hbar}\,\Psi(0).$$

The survival amplitude $A(t)$, that the state did not decay in time, is given by

$$A(t) = \langle\Psi(0)\,|\,\Psi(t)\rangle = \langle\Psi(0)\,|\,\mathrm{e}^{-iHt/\hbar}\,|\,\Psi(0)\rangle, \tag{13}$$

where angle brackets indicate integration over the spacial coordinates in the Dirac notation.

Evaluating Eq. 13 is complicated (*5*), and it requires several simplifying assumptions, which include: a constant perturbation V, the use of the 2nd-order perturbation theory, a transition from the initial discrete, unperturbed state of energy E_0 to a quasi-continuum of final states with the energy distribution $Q(E)$, and a time of observing the system not too short compared to its lifetime τ. The derived $Q(E)$ is then given by a Lorentzian (or Cauchy) distribution:

$$Q(E) = \frac{1}{2\pi} \frac{\Gamma}{(E - E_0)^2 + (\Gamma/2)^2}, \tag{14}$$

where Γ is an energy uncertainty (width) of the state, related to its lifetime by the Heisenberg uncertainty principle, $\Gamma\tau = \hbar$.

The survival amplitude is a Fourier transform of Eq. 14,

$$A(t) = \int_{-\infty}^{+\infty} Q(E)\,\mathrm{e}^{-iEt/\hbar} dE = \frac{1}{2\pi i} \oint \frac{dE}{E - (E_0 - i\Gamma/2)} \left\{ \frac{-i\Gamma\,\mathrm{e}^{-iEt/\hbar}}{E - (E_0 + i\Gamma/2)} \right\}$$

$$= \mathrm{e}^{-iE_0 t/\hbar}\,\mathrm{e}^{-\Gamma t/2\hbar}, \tag{15}$$

by a Cauchy contour integration. The survival probability of quantum state is a square modulus of the survival amplitude, Eq. 15,

$$S(t) = |A(t)|^2 = \mathrm{e}^{-iE_0 t/\hbar}\,\mathrm{e}^{-\Gamma t/2\hbar}\,\mathrm{e}^{+iE_0 t/\hbar}\,\mathrm{e}^{-\Gamma t/2\hbar} = \mathrm{e}^{-\Gamma t/\hbar}, \tag{16}$$

which is the exponential decay law. The quantum-mechanical result confirms the probabilistic arguments of Section 2A. Quantum mechanics does not predict which atom will decay or when it decays.

The transition rate coefficient, $w \equiv \lambda = \Gamma/\hbar = 1/\tau$, can be derived under similar assumptions (*5*), and is given by

$$w = \frac{2\pi}{\hbar} |\langle \psi_k | V | \psi_0 \rangle|^2 \rho_f(E_0), \tag{17}$$

where the wave functions ψ are time independent, k is any final state with the density ρ_f evaluated at unperturbed energy E_0; w is, therefore, constant in time. Equation 17 is called the Fermi Golden Rule No. 2, although Fermi (*12*) gave actually credit to Schiff (*13*) for its derivation.

C. Theoretical Deviations from the Exponential Decay

The quantum-mechanical exponential decay law (Eq. 16) has been derived under several assumptions mentioned in Section 2B, and is valid only for intermediate values of t/τ. For t/τ either « 1 or » 1, it is predicted not to be valid as demonstrated computationally in a simple barrier penetration problem (*14*). Frequent interrogation of the quantum system at $t \ll \tau$, to determine if it is decaying, interferes with it and causes the decay to slow down or even stop, $S(t) \approx 1$. This is called quantum Zeno paradox (*15-19*).

Long-term behavior is related to the integration limit in Eq. 15, where unphysical time of $-\infty$ was used. Evaluating this integral in the physical time interval $(0, +\infty)$ leads to the terms which predict a survival probability $S(t) \propto t^{-n}$, for $t/\tau \gg 1$, where n depends on the model assumptions (*20-23*).

Downloaded by PENNSYLVANIA STATE UNIV on August 8, 2012 | http://pubs.acs.org
Publication Date: November 16, 2006 | doi: 10.1021/bk-2007-0945.ch004

The estimates of the onsets of deviations from the exponential decay depend on a model, and typical values are $t/\tau < 10^{-14}$ *(17)* and $t/\tau > 71$ *(21)* or > 190 *(17)*.

3. Experimental Verifications of the Exponential Decay Law

The verifications will be discussed for nuclear and atomic systems separately. It is possible to change radioactive decay constant in the processes where atomic environment couples to the nuclear decay. For instance, a half-life of ^{7}Be electron capture decay was increased by 0.83%, by encapsulating beryllium atoms inside fullerene (*24*). The half-life of K-shell internal conversion from the 1st excited state of highly ionized ^{57}Fe depends on the extent of ionization (*25*). The observed neutral atom $T_{1/2}$ was 98.1 nsec, the 2-electron ion 100 nsec, and the 1-electron ion 79 nsec (with the total nuclear plus electron spin $F = 1$).

Any deviation of the energy distribution from the Lorentzian shape in Eq. 14 would result in a nonexponential decay, according to Eq. 15. Such effect has been claimed in the x-ray spectrum of ^{235}U from the α decay of ^{239}Pu (*26*). The 116.24-keV γ transition from the decay is internally converted, and its energy is only 0.63 keV about the binding energy of the K electron. This situation sets an upper cutoff on the Lorentzian energy distribution of the resulting $K_{\alpha1}$ and $K_{\alpha2}$ x rays. This is visible as small deviations in the fit to the x-ray spectrum approximately 0.6 keV above the x-ray energies of 94.65 and 98.43 keV. However, it is not clear if this is a real quantum effect or the deficiency of a fit, since the effect is very small and the 0.6 keV is still much larger than the natural width of the U K x rays equal to 0.1 keV (*27*).

Putting the above controversy aside, however, the half-life is fixed for a particular nuclear system and no deviations from the exponential decay have ever been observed. Norman *et al.* (*28*) established the validity of the exponential decay of ^{56}Mn ($T_{1/2}$ = 2.579 hr) over the time range from $0.3T_{1/2}$ to $45T_{1/2}$. This is one of the best satisfied laws in nature. Reference (*28*) also summarized earlier works by other researchers. In the experiment by Norman *et al.*, radioactivity was generated in several samples separately and measured after different delay times to match the response of the detection system. The exponential curves were fitted separately, and then matched. Any long-term correlations which could possibly be present in a single sample, and could have possibly led to a nonexponential decay, were lost. Any extension of the exponential decay beyond $45T_{1/2}$ is difficult, as it would require an enormous amount of radioactivity to begin with. For instance, in order to have 1 pCi at $t = 100T_{1/2}$, one would have to start with $2^{100}\cdot 10^{-12} \approx 10^{18}$ Ci of radioactivity.

Downloaded by PENNSYLVANIA STATE UNIV on August 8, 2012 | http://pubs.acs.org
Publication Date: November 16, 2006 | doi: 10.1021/bk-2007-0945.ch004

Concerning the short-time scales, the validity of the exponential decay in ^{40}K ($T_{1/2}$ = 1.28·10^{9} yr) has been established down to ~ 10^{-10} $T_{1/2}$ with 11% uncertainty (*29*). The validity of the exponential decay of the τ lepton was established down to ~ 10^{-13} sec, with upper limit of any deviations of 8.5% (*30*). Such extensive verifications of exponential decay in nuclear systems were possible, because they satisfy quantum conditions for spontaneous decay very well, and it is difficult to disturb them. As an example, the much sought after x-ray induced acceleration of the decay of ^{178m}Hf ($T_{1/2}$ = 31 yr) was unsuccessful (*31*).

It is not so for the atomic systems, where more experimental opportunities exist to disturb exponential decay. Observation of quantum Zeno effect has been claimed in an rf transition between hyperfine levels in ^{9}Be^{+}, confined in a Penning trap (*32*), although the interpretation of this results was questioned (*19*). Nonexponential decay was observed of an autoionizing shock wave packet in Ca (*33*). Experimental evidence exists for the nonexponential decay in quantum tunneling of Na atoms trapped in a potential created by a standing wave of light (*34*). A decay scaling as $1/t$, rather than exponentially, was observed for cluster anions in an electrostatic storage ring (*35*).

4. Stochastic Markov Approach

Equation 6 gives an average number of atoms that survived decay in time t. Upon repeating such experiment, always starting with $N \equiv N(0)$ atoms, a different number of survived atoms would be found in each trial due to statistical fluctuations. At any time during the decay, we must have $N = x + y$, where x, y are the numbers of decayed and survived atoms, respectively. We are seeking the dispersions of x and y. This subject has been considered by Schweidler (*2*), Ruark and Devol (*36*), and Jorgensen (*37*). None of these authors presented full derivations, which will be given here using modern formalism of stochastic processes such as described in Ref. (*38*). We begin with deriving the dispersion of y.

Radioactive decay is a completely random process: we do not know which atom or when will it decay. The decay process is discrete in a space of the number of atoms and continuous in time. It can be modeled with a stochastic Markov process, where the outcome depends only on the immediately preceding step and has no memory of anything happening earlier than that. It is therefore of the order o(dt). Such process is also called "pure death," since the number of surviving atoms y decreases in time. Markov process is also linear, *i.e.*, it depends linearly on the rate $\rho(y) \equiv \rho(y, t)$ (compare Eq. 3).

We consider a Markov step in time interval between (t, $t + dt$), as depicted in Fig. 3. To have y atoms survived at time $t + dt$, we must have two possibilities:

Downloaded by PENNSYLVANIA STATE UNIV on August 8, 2012 | http://pubs.acs.org
Publication Date: November 16, 2006 | doi: 10.1021/bk-2007-0945.ch004

$y + 1$ atoms present at time t and 1 decayed, or y atoms present at time t and 0 decayed. The probability distribution function $P(y, t + dt)$ of finding y atoms at time $t + dt$ is thus the sum of these two independent outcomes,

$$P(y,t+dt) = P(y+1,t)\,\rho(y+1)dt + P(y,t)\left[1-\rho(y)dt\right], \tag{18}$$

where $\rho(y+1)dt$ is a probability of 1 atom decay out of $y + 1$, and $1 - \rho(y)dt$ is a probability of 0 decay out of y. Equation 18 is essentially a conservation of probability and is called a Kolmogorov-Chapman equation.

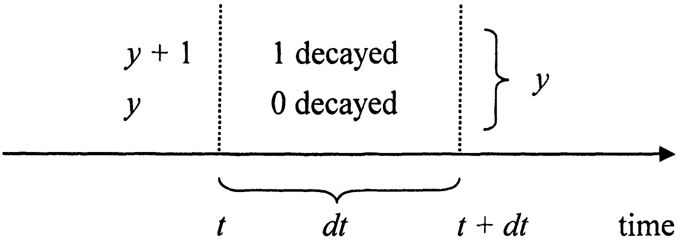

Figure 3. Definition of Markov step, discrete in number of surviving atoms y and continuous in time t.

The left-hand side of Eq. 18 is expanded in a Taylor series,

$$P(y,t+dt) = P(y,t) + \frac{dP(y,t)}{dt}dt + \ldots \tag{19}$$

Since the Markov process is o(dt), we take only the 1st derivative and neglect higher order terms. Taking the second derivative, for example, would make the process of the order o$(dt)^2$, and would require considering of what happened before time t in Fig. 3. The process would, therefore, have a memory and would violate the assumptions of the Markov process. By plugging Eq. 19, as well as the definitions of $\rho(y) = \lambda\, y$ and $\rho(y + 1) = \lambda\,(y + 1)$ (Eq. 3) to Eq. 18, and rearranging the terms, we obtain a set of the stochastic differential equations:

$$\frac{dP(y,t)}{\lambda dt} = (y+1)P(y+1,t) - yP(y,t), \qquad y = N,\ldots,0 \tag{20}$$

The set of Eqs. 20 is solved by the generating function method. The generating function $G \equiv G(z,t)$ is defined as

$$G(z,t) = \sum_{y=0}^{N} z^y P(y,t).$$

We multiply Eqs. 20 by z^y and sum over allowed y, which results in

$$\frac{\partial G}{\lambda \partial t} = \sum_y (y+1)z^y P(y+1) - \sum_y yz^y P(y). \tag{21}$$

Downloaded by PENNSYLVANIA STATE UNIV on August 8, 2012 | http://pubs.acs.org
Publication Date: November 16, 2006 | doi: 10.1021/bk-2007-0945.ch004

By changing variable $y \rightarrow y - 1$ in the 1st sum on the right-hand side of Eq. 21, one obtains $\sum yz^{y-1}P(y) = \partial G/\partial z$. The second sum on the right is equal to $z\partial G/\partial z$. Finally, Eq. 21 is transformed to

$$\frac{\partial G}{\lambda \partial t} + (z-1)\frac{\partial G}{\partial z} = 0. \tag{22}$$

As a result, we converted the set of Eqs. 20 to one Eq. 22 for the generating function.

Equation 22 is called a linear Lagrange differential equation and can be solved by a method by Forsyth (*39*). By dividing both sides of Eq. 22 by ∂G, one obtains

$$\frac{1}{\lambda dt} + \frac{z-1}{dz} = \frac{0}{dG}. \tag{23}$$

By equating any two of the three terms from Eq. 23, one can obtain two independent auxiliary equations which, when solved, will provide two integration constants: c_1 and c_2. The general solution is then $c_1 = \Phi(c_2)$, where function Φ is to be determined from the boundary conditions. By equating the 2nd and the 3rd terms, one obtains $\partial G/\partial z = 0$, from which $G = c_1$. By equating the 1st and the 2nd terms, one obtains a linear equation $dz/(z-1) = \lambda dt$, which yields upon integration $c_2 = (z-1)\,\mathrm{e}^{-\lambda t}$. The general solution of Eq. 22 is then

$$G(z,t) = \Phi\,[(z-1)\,\mathrm{e}^{-\lambda t}].$$

The boundary conditions for the generating function are: $G(1,t) = 1$, $G(z,\infty) = 1$, $G(z,0) = z^N$. From the 1st and the 2nd boundary conditions, the solution must be proportional to $1 + (z-1)\,\mathrm{e}^{-\lambda t}$. The 3rd boundary condition fixes the solution at

$$G(z,t) = [1 + (z-1)\,\mathrm{e}^{-\lambda t}]^N. \tag{24}$$

Using the property of the generating function (*40*), the average number of surviving atoms $\bar{y}$ is given by

$$\bar{y} = \left(\frac{\partial G}{\partial z}\right)_{z=1} = N\,\mathrm{e}^{-\lambda t},$$

which confirms the radioactive decay law from Eq. 6. Equation 24 is a generating function of the binomial distribution (*40*). Therefore,

$$P(y,t) = \binom{N}{y}\left(\mathrm{e}^{-\lambda t}\right)^y \left(1 - \mathrm{e}^{-\lambda t}\right)^{N-y} \tag{25}$$

describes the fluctuations of y. Equation 7a is equal to $P(N, t)$ from Eq. 25. The fluctuations of the number of decayed atom x can be solved similarly, or obtained from Eq. 25 by substituting $y = N - x$, to arrive at

Downloaded by PENNSYLVANIA STATE UNIV on August 8, 2012 | http://pubs.acs.org
Publication Date: November 16, 2006 | doi: 10.1021/bk-2007-0945.ch004

$$P(x,t) = \binom{N}{x}\left(1 - e^{-\lambda t}\right)^{x}\left(e^{-\lambda t}\right)^{N-x}. \tag{26}$$

This is the binomial distribution postulated by Schweidler in 1905 (*2*) as depicted in Fig. 2. Equation 7c is equal to $P(N, t)$ from Eq. 26.

The generating function of $P(x, t)$ from Eq. 26 is

$$G(z,t) = [1 + (z-1)(1 - e^{-\lambda t})]^{N}. \tag{27}$$

If $N \gg 1$ and the decay is slow, $\lambda t \ll 1$, one obtains from Eq. 27 (compare Eq. 4)

$$G(z,t) = [1 + (z-1)N\lambda t/N]^{N} \xrightarrow[N\to\infty]{} e^{(z-1)N\lambda t}. \tag{28}$$

However, Eq. 28 is a generating function of the Poisson distribution (*40*) with a parameter $\mu = N\lambda t$,

$$P(x,\mu) = \frac{\mu^{x}\, e^{-\mu}}{x!}. \tag{29}$$

The Poisson distribution, Eq. 29, has also been derived from the stochastic processes by Bateman in 1910 (*41*), which was historically the second derivation (*40*) (see also Ref. (*42*)).

5. Complete Decay of Radionuclides

This subject has been described by Jackson (*43*), Meck (*44*), and O'Brien (*45*). Owing to the probabilistic character of the radioactive decay law, one cannot ascertain that the radionuclide has decayed completely in a given time t. One can only calculate probability p of that happening, given by Eq. 7c. Conversely, one can calculate time for a complete decay with a given probability p. By rearranging Eq. 7c and abbreviating $N \equiv N(0)$, we obtain

$$t = \frac{1}{\lambda}\ln\frac{1}{1 - p^{1/N}}. \tag{30}$$

Since we are interested in a long-time decay, $\lambda t \gg 1$, with high probability, $p \approx 1$, Eq. 30 can be approximated with

$$t = \frac{1}{\lambda}\ln N + \frac{1}{\lambda}\ln\frac{1}{1-p}. \tag{31}$$

The first term on the right-hand side of Eq. 31 is the time to decay from N atoms to 1. The second term is the time for the last atom to decay with a probability p. Eq. 31 can be rearranged to

$$t/\tau = \ln\frac{\rho\tau}{1-p}, \tag{32}$$

where $\tau \ln 2 = T_{1/2}$.

Downloaded by PENNSYLVANIA STATE UNIV on August 8, 2012 | http://pubs.acs.org
Publication Date: November 16, 2006 | doi: 10.1021/bk-2007-0945.ch004

As an example, one can calculate from Eq. 32 the time for a complete decay of 1 Ci of ^{24}Na ($T_{1/2}$ = 15 hr) and ^{90}Sr ($T_{1/2}$ = 28 yr) with probability 0.99. We obtain $t = 58T_{1/2}$ for sodium and $t = 72T_{1/2}$ for strontium. The reason for that is that is that strontium contains many more atoms than sodium, for the same initial radioactivity, according to Eq. 3. This has obvious implications to the radioactive waste disposal. It is favorable to wait for decay of a short-lived radionuclide and then dispose it as a non-radioactive waste. Long-lived radionuclides must be stored as radioactive waste.

Acknowledgements

Thanks are due to A. N. Berlizov for fruitful discussion, E. B. Norman for critical reviewing the manuscript, as well as to D. Koreman for typing the manuscript.

References

1. Rutherford, E.; Soddy, F. Radioactive change. *Phil. Mag. S. 6* **1903**, *5*, 576-591.
2. Schweidler, von E. v. Uber schwankungen der radioaktiven umwandlung. *Comptes Rendus du Premier Congrès International pour L'Étude de la Radiologie et de l'Ionisation,* Liége, Sep. 12-14, 1905; H. Dunod & E. Pinat: Paris, 1906, Section de physique, Langue allemande, 1-3.
3. *Handbook of Mathematical Functions*; Abramowitz, M.; Stegun, I. E., Eds.; Dover: New York, NY, 1964.
4. Bortkiewicz, L. v. *Die Radioaktive Strahlung als Gegenstand Wahrscheinlichkeits-theoretischer Untersuchungen*; Verlag von Julius Springer: Berlin, 1913.
5. Merzbacher, E. *Quantum Mechanics*; J. Wiley & Sons: New York, NY, 1998.
6. Ruark, A.E. The exponential law of radioactive disintegration. *Phys. Rev.* **1933**, *44*, 654-656.
7. Hamburger, D.; Biham, O.; Avnir, D. Apparent fractality emerging from models of random distributions. *Phys. Rev. E* **1996**, *53*, 3342-3358.
8. Kleppner, D. Rereading Einstein on radiation. *Physics Today* **2005**, *58(2)*, 30-33.
9. Weisskopf, von V.; Wigner, E. Berechnung der natürlichen linienbreite auf grund der Diracschen lichttheorie. *Z. Phys.* **1930**, *63*, 54-73.
10. Weisskopf, von V.; Wigner, E. Über die natürliche linienbreite in der strahlung des harmonischen oszillators. *Z. Phys.* **1930**, *65*, 18-29.

Downloaded by PENNSYLVANIA STATE UNIV on August 8, 2012 | http://pubs.acs.org
Publication Date: November 16, 2006 | doi: 10.1021/bk-2007-0945.ch004

11. Krylov, N. S.; Fock, V. A. On the two main interpretations of the energy-time uncertainty relation. *Zh. Eksp. Teor. Fiz.* **1947**, *17*, 93-107.
12. Fermi, E. *Nuclear Physics*. Course notes compiled by Orear, J.; Rosenfeld, A. H.; Schluter, R. A.; The University of Chicago Press: Chicago, IL, 1950.
13. Schiff, L. I. *Quantum Mechanics*; McGraw-Hill: New York, NY, 1968.
14. Winter, R. G. Evolution of quasi-stationary state. *Phys. Rev.* **1961**, *123*, 1503-1507.
15. Khalfin, L. A. Phenomenological theory of K° mesons and the non-exponential character of the decay. *JETP Lett.* **1968**, *8*, 65-68.
16. Misra, B.; Sudarshan, E. C. G. The Zeno's paradox in quantum theory. *J. Math. Phys.* **1977**, *18*, 756-763.
17. Chiu, C. B.; Sudarshan, E. C. G.; Misra, B. The evolution of unstable quantum states and a resolution of Zeno's paradox. *Phys. Rev. D* **1977**, *16*, 520-529.
18. Peres, A. Zeno paradox in quantum theory. *Am. J. Phys.* **1980**, *48*, 931-932.
19. Home, D.; Whitaker, M. A. B. A conceptual analysis of quantum Zeno; paradox, measurement, and experiment. *Ann. Phys.* **1997**, *258*, 237-285.
20. Khalfin, L. A. Contribution to the decay theory of a quasi-stationary state. *Sov. Phys. JETP* **1958**, *6*, 1053-1063.
21. Arthur, M. D.; Brysk, H.; Paveri-Fontana, S. L.; Zweifel, P. F. The law of radioactive decay. *Il Nuovo Cimento* **1981**, *63*, 565-587.
22. Brysk, H.; Slawny, J.; Zweifel, P. F. The law of radioactive decay - II. *Il Nuovo Cimento* **1983**, *73*, 213-225.
23. Jakobovits, H.; Rothschild, Y.; Levitan, J. The approximation to the exponential decay law. *Am. J. Phys.* **1995**, *63*, 439-443.
24. Ohtsuki, T.; Yuki, H.; Muto, M.; Kasagi, J.; Ohno, K. Enhanced electron-capture decay rate of ^{7}Be encapsulated in C_{60} cages. *Phys. Rev. Lett.* **2004**, *93*, 112501.
25. Phillips, W. R.; Ahmad, I.; Banes, D. W.; Glagola, B. G.; Henning, W.; Kutschera, W.; Rehm, K. E.; Schiffer, J. P.; Wang, T. F. Charge-state dependence of nuclear lifetimes. *Phys. Rev. Lett.* **1989**, *62*, 1025-1028.
26. Gunnink, R. *MGA: a Gamma-Ray Spectrum Analysis Code for Determining Plutonium Isotopic Abundances*. Lawrence Livermore National Laboratory Report UCRL-LR-103220, Vol. 1: Livermore, CA, 1990, pp. 39-41.
27. Salem, S. I.; Lee, P. L. Experimental widths of K and L x-ray lines. *Atomic Data Nucl. Data Tables* **1976**, *18*, 233-241.
28. Norman, E. B.; Gazes, S. B.; Crane, S. G.; Bennett, D. A. Tests of the exponential decay law at short and long times. *Phys. Rev. Lett.* **1988**, *60*, 2246-2249.
29. Norman, E. B.; Sur, B.; Lesko, K. T.; Larimer, R. M.; DePaolo, D. J.; Owens, T. L. An improved test of the exponential decay law. *Phys. Lett. B* **1995**, *357*, 521-525.

Downloaded by PENNSYLVANIA STATE UNIV on August 8, 2012 | http://pubs.acs.org
Publication Date: November 16, 2006 | doi: 10.1021/bk-2007-0945.ch004

30. Alexander, G.; *et al.* Test of the exponential decay law at short decay times using tau leptons. *Phys. Lett. B* **1996**, *368*, 244-250.
31. Ahmad, I.; *et al.* Search for x-ray induced acceleration of the decay of the 31-yr isomer of ^{178}Hf using synchrotron radiation. *Phys. Rev. Lett.* **2001**, *87*, 072503.
32. Itano, W. M.; Heinzen, D. J.; Bollinger, J. J.; Wineland, D. J. Quantum Zeno effect. *Phys. Rev. A* **1990**, *41*, 2295-2300.
33. Thoma, J. E.; Jones, R. R. Nonexponential decay of autoionizing shock wave packets. *Phys. Rev. Lett.* **1999**, *83*, 516-519.
34. Wilkinson, S. R.; Bharucha, C. F.; Fischer, M. C.; Madison, K. W.; Morrow, P. R.; Niu, Q.; Sundaram, B.; Raizen, M. G. Experimental evidence for non-exponential decay in quantum tunneling. *Nature* **1997**, *387*, 575-577.
35. Hansen, K.; Andersen, J. U.; Hvelplund, P.; Møller, S. P.; Pedersen, U. V.; Petrunin, V. V. Observation of 1/*t* decay law for hot clusters and molecules in a storage ring. *Phys. Rev. Lett.* **2001**, *87*, 123401.
36. Ruark, A.; Devol, L. The general theory of fluctuations in radioactive disintegration. *Phys. Rev.* **1936**, *49*, 355-367.
37. Jorgensen, T., Jr. On probability generating functions. *Am. J. Phys.* **1948**, *16*, 285-289.
38. Bailey, N. T. J. *The elements of stochastic processes*; J. Wiley & Sons: New York, NY, 1990.
39. Forsyth, A. R. *A treatise on differential equations*; Dover: Mineola, NY, 1996.
40. Johnson, N. L.; Kotz, S.; Kemp, A. W. *Univariate discrete distributions*; J. Wiley & Sons: New York, NY, 1993.
41. Bateman, H. On the probability distribution of α particles. *Phil. Mag. S. 6* **1910**, *20*, 704-707.
42. Semkow, T. M. Comment on ''Algebraic approach to the radioactive decay equations,'' by L. Moral and A. F. Pacheco [Am. J. Phys. 71 (7), 684–686 (2003)]. *Am. J. Phys.* **2004**, *72*, 410-411.
43. Jackson, H. L. A discussion of the approximate nature of the exponential decay law as applied to radioactive nuclides and gamma ray absorption. *Health Phys.* **1965**, *11*, 179-183.
44. Meck, R. A. Complete decay of radionuclides: implications for low-level waste disposal in municipal landfills. *Health Phys.* **1996**, *70*, 706-711.
45. O'Brien, K. Complete decay of radionuclides: a "last-flight" approximation. *Health Phys.* **1996**, *71*, 795.

Downloaded by PENNSYLVANIA STATE UNIV on August 8, 2012 | http://pubs.acs.org
Publication Date: November 16, 2006 | doi: 10.1021/bk-2007-0945.ch004

Downloaded by UNIV OF GUELPH LIBRARY on August 9, 2012 | http://pubs.acs.org
Publication Date: November 16, 2006 | doi: 10.1021/bk-2007-0945.ch005

Chapter 5

Modeling Radionuclide Transport in the Environment and Assessing Risks to Humans, Flora, and Fauna: The RESRAD Family of Codes

Charley Yu

**Environmental Science Division, Argonne National Laboratory,
9700 South Cass Avenue, Argonne, IL 60439**

Potential risks to humans and the environment (flora and fauna) are a primary consideration in federal agencies' efforts to formulate key environmental decisions and policies. Specific questions such as "How clean is clean?" cannot be answered without a scientific basis. Studying the possible impacts resulting from exposure to radioactive and chemical contaminants often requires the modeling of contaminant transport in the environment. The RESRAD family of codes was developed to assess human health and environmental risk at sites contaminated with radioactive materials and hazardous chemicals. All RESRAD codes have user-friendly interfaces and provide on-line help. They can be used for various applications, ranging from cleanup of contaminated sites, to assessments of waste disposal facility performance, to dose assessments for animals and plants.

In Applied Modeling and Computations in Nuclear Science; Semkow, T., et al.;
ACS Symposium Series; American Chemical Society: Washington, DC, 2006.

Introduction

The RESRAD family of computer codes was developed by Argonne National Laboratory to provide a scientifically defensible answer to the question "How clean is clean?" and to provide useful tools for evaluating human health risks and nonhuman biota (flora and fauna) doses at sites contaminated with radioactive materials and hazardous chemicals (*1*,*2*). These codes model the transport of radionuclides and hazardous chemicals in the environment and calculate the intake by human and biota. Then the doses and risks from both internal and external exposure are estimated.

The transport of radionuclides in the environment is a complex process. The method used to model this transport in the RESRAD codes is pathway analysis. Although pathway analysis requires the use of many models and equations, the detailed equations are not presented here because of page limitations. The mathematical models and equations can be found in the references cited.

Downloaded by UNIV OF GUELPH LIBRARY on August 9, 2012 | http://pubs.acs.org
Publication Date: November 16, 2006 | doi: 10.1021/bk-2007-0945.ch005

RESRAD Family of Codes

The RESRAD code was initially developed in the early 1980s. As a result of the different conditions, needs, and sponsor requirements, a suite of codes was developed over the past 20 years. This suite of risk assessment codes is referred to as the RESRAD family of codes.

The RESRAD family of codes includes (1) RESRAD (onsite) for assessing soil contaminated with radionuclides; (2) RESRAD-BUILD for assessing buildings contaminated with radionuclides; (3) RESRAD-CHEM for assessing soil contaminated with hazardous chemicals; (4) RESRAD-BASELINE for making baseline risk assessments with measured concentrations of both radionuclides and chemicals; (5) RESRAD-ECORISK for assessing ecological risks from exposure to hazardous chemicals; (6) RESRAD-BIOTA for assessing doses to nonhuman biota from exposure to radionuclides; (7) RESRAD-RECYCLE for assessing the recycling and reuse of radiologically contaminated metals and equipment; and (8) RESRAD-OFFSITE for assessing radiological doses to off-site human receptors. Four of the codes — RESRAD (onsite) and RESRAD-BUILD, -RECYCLE, and -OFFSITE — also have probabilistic analysis capabilities that allow the user to input distributions of parameters. Five — RESRAD (onsite) and RESRAD-BUILD, -RECYCLE, -OFFSITE, and -BIOTA — are being regularly maintained and updated. The other three — RESRAD-CHEM, -BASELINE, and -ECORISK — are beta versions for test and evaluation and receive less maintenance.

Pathway Analysis

The RESRAD family of codes uses the pathway analysis method to model contaminant transport in the environment. The method used in the RESRAD (onsite) code is presented as an example. The methods used in other codes are similar, and special models have been developed for each code under various conditions. For example, the RESRAD-OFFSITE code has a three-dimensional (3-D) groundwater dispersion model and an atmospheric Gaussian plume model; RESRAD-BUILD has an indoor air quality model (*3*); RESRAD-RECYCLE has a mass and radionuclide partition model (*4*); and RESRAD-BIOTA considers water and soil submersion doses (*5*).

In general, there are three major pathways by which radionuclides or radiation can enter the body. In the first pathway, exposure is by external radiation from radionuclides outside the body. In the second and third pathways, exposure is by internal radiation from radionuclides that are inhaled or ingested. For each exposure pathway, radionuclides can migrate from a source to a receptor (human, animal, or plant) exposure location by many environmental pathways. The major categories of environmental pathways are illustrated in Figure 1. The radionuclide contamination in soil (the first column in Figure 1 — the source term) is transported through the environmental pathways and contributes to external, inhalation, and ingestion doses and risks to a receptor (the last column in Figure 1). The calculation from source to dose is referred as a forward calculation. RESRAD can also do a backward calculation that allows the user to input a dose limit or dose constraint, and the code can then back-calculate a corresponding soil concentration known as a cleanup criterion or soil guideline or derived concentration guideline level (DCGL). Each pathway is discussed in the following sections.

Downloaded by UNIV OF GUELPH LIBRARY on August 9, 2012 | http://pubs.acs.org
Publication Date: November 16, 2006 | doi: 10.1021/bk-2007-0945.ch005

External Radiation Pathways

Gamma and beta radiations from radionuclides distributed throughout the contaminated soil are the dominant external radiation pathways that are taken into account in calculating soil guidelines. The dose due to external radiation is first calculated for an individual exposed continuously to radiation from an infinite contaminated zone at a distance of 1 m from the ground surface. Correction factors are then applied for the finite area and thickness of the contaminated zone, shielding by a cover of uncontaminated soil, irregular shape, shielding by the floors and walls of a house, and less-than-continuous occupancy (*2*,*3*).

Inhalation Pathways

Inhalation exposure results from inhalation of contaminated dust and radon decay products. An inhalation pathway consists of two segments: (1) an airborne exposure segment linking the source (contaminated zone) with the airborne radionuclides at an exposure location and (2) an inhalation segment linking the airborne radionuclides with the exposed individual. The inhalation segment is characterized by an occupancy factor (*i.e.*, an equivalent fraction of time during which an individual inhales contaminated air) and a factor for the inhalation

Downloaded by UNIV OF GUELPH LIBRARY on August 9, 2012 | http://pubs.acs.org
Publication Date: November 16, 2006 | doi: 10.1021/bk-2007-0945.ch005

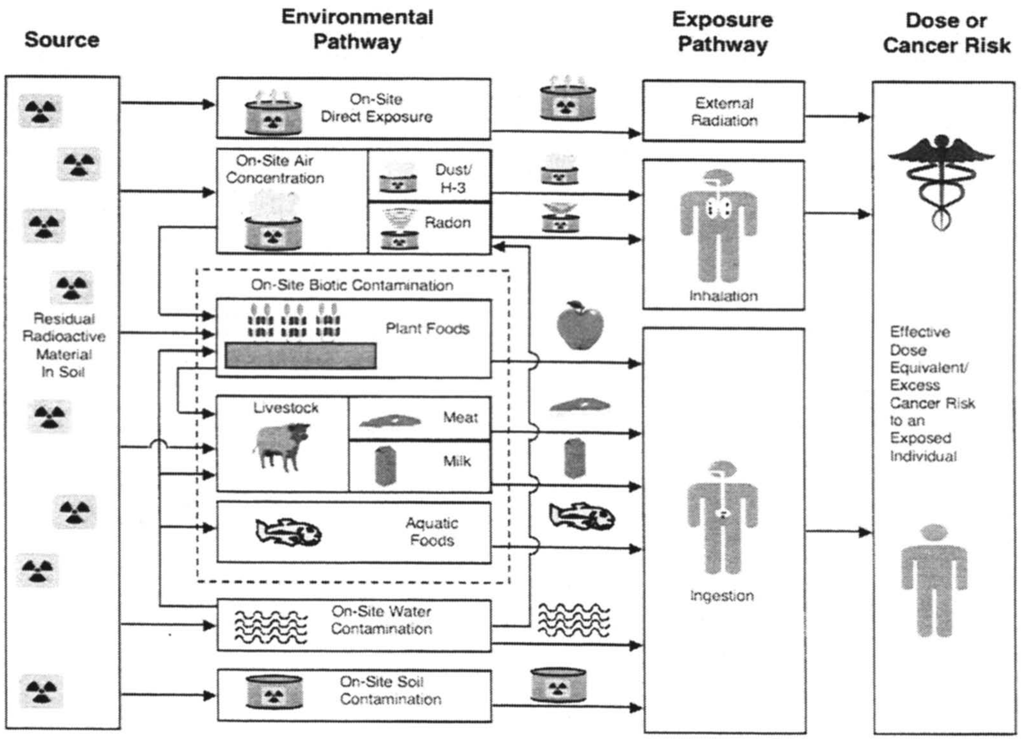
Source
Environmental Pathway
Exposure Pathway
Dose or Cancer Risk
Residual Radioactive Material In Soil
On-Site Direct Exposure
On-Site Air Concentration
Dust/ H-3
Radon
On-Site Biotic Contamination
Plant Foods
Livestock
Meat
Milk
Aquatic Foods
On-Site Water Contamination
On-Site Soil Contamination
External Radiation
Inhalation
Ingestion
Effective Dose Equivalent/ Excess Cancer Risk to an Exposed Individual

Figure 1. Major categories of environmental pathways.

rate. Numerical values for these factors can be obtained by using well-established procedures (*6,7*). The airborne exposure pathway segment is the critical segment. In the RESRAD (onsite) code, a simple mass loading model is used. It is characterized by the air/soil concentration ratio, which is defined as the ratio of the airborne concentration of a radionuclide at a human exposure location to the concentration in the soil. The air/soil concentration ratio for contaminated dust depends on the complex processes by which soil particles become airborne by resuspension and are transported to an exposure location. This ratio is also used in the food chain pathways (for the foliar deposition subpathways). In the RESRAD-OFFSITE code, a Gaussian plume model is used for estimating the air concentration at off-site locations. For the radon pathway, the air/soil concentration ratio is calculated by solving radon diffusion equations for the soil and for the atmosphere.

Downloaded by UNIV OF GUELPH LIBRARY on August 9, 2012 | http://pubs.acs.org
Publication Date: November 16, 2006 | doi: 10.1021/bk-2007-0945.ch005

Ingestion Pathways

The ingestion pathways include ingestion of food, water, and soil. The soil ingestion pathway corresponds to direct ingestion of soil. This pathway is especially significant for a child afflicted with pica (a compulsive craving for nonfood objects). The dose due to ingestion of soil depends on the amount of soil ingested and the concentration of soil. For water ingestion, RESRAD and RESRAD-OFFSITE have specific models to analyze the transport of contaminants in the groundwater system (*2,8*). The radionuclide transport models take into account advection, dispersion, radioactive decay and progeny ingrowth, and soil adsorption/desorption. The models have been benchmarked (*9–11*) and verified/validated by using real world data (*8*). Both well water and surface water can be used for drinking. The fraction of well water blended with or supplemented by surface water is used to calculate the total contribution from groundwater and surface water.

For food ingestion, four food categories are considered: plant foods, meat, milk, and aquatic foods. The plant food pathway category is further divided into four subcategories corresponding to (1) root uptake from crops grown in the contaminated soil, (2) foliar uptake from contaminated dust deposited on the foliage, (3) root uptake from contaminated irrigation water, and (4) foliar uptake from contaminated irrigation water. The plant food pathway subcategories are applicable to livestock fodder; hence, they are applicable to the pathways through which meat and milk become contaminated by ingestion of contaminated fodder. A fifth subcategory for the meat and milk pathways corresponds to ingestion of contaminated water (either groundwater or surface water) by livestock. A sixth subcategory corresponds to ingestion of contaminated soil by livestock. The aquatic food pathway is for ingestion of fish, crustacea, and mollusks from a nearby pond that has been contaminated.

The food pathways may be classified as water-independent or water-dependent. The direct root uptake and foliar dust deposition pathways for plant foods, meat, and milk are water-independent, as is the soil intake by livestock (here water refers to the water that has been contaminated by radionuclides that have been leached from the contaminated zone). Water-dependent pathways are the irrigation water pathway for plant foods, meat, and milk; the livestock water pathway for meat and milk; and the aquatic food pathway. In regions where natural rainfall is the only source of water used in raising crops, the only water-dependent pathways are the livestock water branch of the meat and milk pathways and the aquatic food pathway. The contribution from water-dependent pathways will be delayed until the radionuclides transported by groundwater reach a point of water withdrawal (*i.e.*, well or pond). The time dependence of these pathways is determined by the time dependence of the radionuclide concentrations in the contaminated water, as determined by the hydrological model used for the groundwater pathway segment. A fraction of a radionuclide will have been leached from the root zone before the radionuclide first reaches a point of water withdrawal in concentrations above background (the breakthrough time); hence, the contributions to the dose from the water-independent and water-dependent pathways will occur at different times. After the breakthrough time, the contaminated irrigation water will create a new contaminated zone as it percolates down through the soil. The contribution of this secondary contaminated zone to pathways other than the food pathway is not taken into account in the current version of the RESRAD (onsite) code because it is assumed to be small when compared with the contributions of the food pathway. This secondary pathway is considered, however, in the RESRAD-OFFSITE model.

Radionuclide transport through the food pathways is determined by the quantities of different foods consumed (dietary factors), the fraction of the diet that is from foods that are contaminated by radionuclides from the contaminated zone (which is determined by the fraction raised locally and the area of the contaminated zone), the cover depth and contaminated zone thickness relative to the root zone of the plants, the various transfer factors from root or foliage to plants and from fodder or water to meat or milk, and the concentrations of radionuclides in water that have percolated through the contaminated zone. The transfer factors for plants, meat, and milk and the soil-water distribution coefficients are radionuclide dependent, and the dose estimates are usually very sensitive to them. These transfer factors and distribution coefficients are available in many reports (*12–14*). However, if site-specific values are available (*e.g.*, for a specific soil and plant type), it is strongly recommended that site-specific data be used in dose calculations.

Dose Assessment for Humans

The distribution of dose within the body depends on the type of radiation and radionuclides involved and the location of the radionuclides emitting the radiation (*i.e.*, whether they are within or external to the body). The International Commission on Radiological Protection (ICRP) has provided a useful quantity that, on a risk scale, can be applied to any radiation type (*15–17*). This quantity, either the effective dose (ED) based on ICRP Publication 60 or the effective dose equivalent (EDE) based on ICRP Publication 30, is the weighted sum of the

Downloaded by UNIV OF GUELPH LIBRARY on August 9, 2012 | http://pubs.acs.org
Publication Date: November 16, 2006 | doi: 10.1021/bk-2007-0945.ch005

dose equivalent in various organs. The major difference between the ED and EDE is the organ weighting factors used. In the United States, the "official" dose factors used are those published in Federal Guidance Report Number 11 (FGR-11) and Number 12 (FGR-12) (*18*,*19*). FGR-11 and FGR-12 use dose conversion factors (DCFs) based on ICRP Publication 30. A newer FGR — FGR-13 — contains cancer risk coefficients for exposure to radionuclides (*20*). FGR-13's companion compact disk (CD) also lists the DCFs based on ICRP Publication 60. These ICRP-60-based DCFs are being incorporated in the RESRAD family of codes. For example, the age-specific DCFs published in ICRP Publication 72 (*21*) have already been added to the RESRAD-OFFSITE database. The weighting factors for the organs are proportional to the potential risk associated with the irradiation of those organs. Internal radiation doses to organs and tissues of the body are frequently estimated by using factors that represent the 50-year committed dose equivalent for a unit intake of a radionuclide via inhalation or ingestion. In the case of external radiation, the dose rate in organs depends on the concentration of the radionuclide in the environment. For internal exposure, a DCF is the ratio of the committed effective dose equivalent (CEDE) to the activity of a radionuclide that is inhaled or ingested. For external exposure, a DCF is the ratio of the effective dose equivalent (EDE) rate to the concentration of a radionuclide in the air, water, or ground.

Downloaded by UNIV OF GUELPH LIBRARY on August 9, 2012 | http://pubs.acs.org
Publication Date: November 16, 2006 | doi: 10.1021/bk-2007-0945.ch005

Dose from Ingestion and Inhalation

The radiation dose from inhalation and ingestion of radionuclides has been systematically evaluated in ICRP Publication 30 and publications after that. Dose equivalents in organs or tissues of the body are calculated with models that describe the entrance of materials into the body (respiratory and gastrointestinal [GI] tract) and the deposition and subsequent retention of the radionuclides in body organs (referred to as metabolic and biokinetic models) and models that estimate the energy deposition in tissues of the body. In applying the results of these calculations, some insight into the details of the models used for the lung and GI tract is required, because these models serve as the interface between humans and the environment.

In calculating the dose from intake of radionuclides into the body, the occurrence of radioactive decay products must be considered. When an atom undergoes radioactive decay, the new atom formed may also be radioactive and thus contribute to the dose. Although these decay products may be treated as independent radionuclides in external exposures, they must be considered in conjunction with the parent in the evaluation of radionuclides inhaled or ingested, because their distribution among the organs of the body depends on the metabolism of the parent. Thus, the contributions to dose from decay products formed within the body are included in the DCF for any radionuclide with radioactive decay products.

Factors representing the CEDE per unit intake of radionuclides are given in FGR-11 (*18*). In many instances, several chemical forms have been considered;

that is, more than one clearance class (inhalation) or f1 (ingestion) value is given for the radionuclide. DCFs identified with "+D" in the RESRAD family of codes are the sum of DCFs for a principal radionuclide (*i.e.*, one with a half-life greater than a selected cutoff time like 6 months) and its associated decay chain (*i.e.*, all its short-lived decay products down to, but not including, the next principal radionuclide or the final nonradioactive nuclide in the chain). These aggregated DCFs correspond to ingestion or inhalation of the principal radionuclide together with its associated decay product radionuclides, which are assumed to be in secular equilibrium at the time of intake. In the latest versions of the RESRAD code (Version 6.3) and RESRAD-BUILD code (Version 3.3) released in September 2005, users can select (input) any cut-off half-life, and the code will automatically generate the associated decay chain and add the appropriate (+D) radionuclide DCFs to the parent radionuclide.

Dose from External Exposure

Organs of the body may be irradiated by radiation emitted from radionuclides present in the environment. Both gamma and beta radiation are taken into account in calculating soil guidelines. Gamma radiation is of particular concern because it is sufficiently penetrating that the dose at a given location depends on the spatial distribution of the source over considerable distances. In addition, the dose distribution pattern within the body is rather uniform. The actual distribution of dose in the body depends somewhat on the distribution pattern of the radionuclide in the environment. An idealized distribution pattern that is often assumed is a uniform distribution of the radionuclide within an infinite or semi-infinite region. By considering such idealized distributions, DCFs relating the EDE rate to the radionuclide concentration can be tabulated. For other situations, the details of radionuclide distribution must be included in the numerical calculation of dose. Eckerman and Ryman (*19*) published the dose-rate factors for soil volume contamination and surface contamination in FGR-12. The model used in the RESRAD family of codes for external dose calculation extended the FGR-12 external dose-rate factors to any shape and thickness of contamination, with or without a cover, and to contaminated materials other than soil (*2*).

Dose Assessment for Flora and Fauna

Stakeholders and regulators are increasingly interested in having it demonstrated that the environment is protected from the potential effects of ionizing radiation. For the past three decades, most such efforts have been indirectly based on established radiological dose limits that are considered protective of human health. The use of human radiation protection to infer ecological protection has been based on the assumption made by ICRP that "if man is adequately protected then other living things are also likely to be sufficiently protected" (*15*). This assumption is now being revisited, and its

Downloaded by UNIV OF GUELPH LIBRARY on August 9, 2012 | http://pubs.acs.org
Publication Date: November 16, 2006 | doi: 10.1021/bk-2007-0945.ch005

scientific basis is being questioned. A recent ICRP publication states that "ICRP therefore needs to revise its current system of protection, and particularly, develop a comprehensive approach to the study of the effects on, and protection of, all living matter with respect to the effects of ionising radiation" (*22*). Dose rate guidelines and approaches for evaluating doses to biota are under development by, or becoming available from, several countries and international organizations (*23*). Unlike the case for human dose calculations, however, there are no standard dose conversion factors available yet. The dose to flora and fauna must be calculated from the first principle (*i.e.*, by calculating the energy absorbed by using a Monte Carlo radiation transport code, such as the MCNP code). To distinguish the dose factors for biota from the DCFs used for humans, the dose factors for biota are called dose conversion coefficients (DCCs).

The first step in biota dose calculation is to estimate the radionuclide concentration in the tissue of biota (animals or plants). In the RESRAD-BIOTA code, users can choose one of two methods to estimate biota concentrations. The first method is to use a simple lumped parameter to relate the radionuclide concentration in the media external to the organism to its internal tissues. The second is to use empirical allometric equations based on the body weight of the organism (*23*). Once the tissue concentration is estimated, the internal dose can be calculated by using the DCCs, which are discussed in the following section.

Downloaded by UNIV OF GUELPH LIBRARY on August 9, 2012 | http://pubs.acs.org
Publication Date: November 16, 2006 | doi: 10.1021/bk-2007-0945.ch005

Internal Biota Dose Calculation

For internal dose calculation, it is assumed that the organism is uniformly contaminated and that its geometry is defined as ellipsoid. Table I shows the organism geometries and masses assumed in the RESRAD-BIOTA code. ICRP is proposing a set of reference animals and plants in its draft publication for comment. The animals and plants are similar to the ones used in RESRAD-BIOTA but the number of geometries is greater (more than 12). It is expected that the geometries will eventually be standardized so that the doses to flora and fauna can be compared on the same geometric basis. The electron and gamma energy absorbed by the organism geometry is then calculated by using the MCNP code. It is assumed that for alpha particles emitted from radionuclides in the organism, all the energy is absorbed. Currently, IAEA's Environmental Modeling for Radiation Safety (EMRAS) Program has a Biota Dosimetry Working Group that is comparing the biota doses calculated by different modelers from different countries. The RESRAD-BIOTA code is one of the models being compared in this exercise. Additional information on the EMRAS Biota Dosimetry Working Group can be found at its Web site, http://www-ns.iaea.org/projects/emras/emras-biota-wg.htm.

External Biota Dose Calculation

For external dose calculation, the medium is assumed to be uniformly contaminated. The energy absorbed in the organism for electrons and photons

Downloaded by UNIV OF GUELPH LIBRARY on August 9, 2012 | http://pubs.acs.org
Publication Date: November 16, 2006 | doi: 10.1021/bk-2007-0945.ch005

Table I. Organism Geometries Used in RESRAD-BIOTA

Model Geometry No.	*Mass Category (kg)*	*Example Receptors*	*Specific Geometric Dimensions (cm)*	*Specific Mass (kg)*
1	1E–5	Fish egg,* plant seed, plant shoot (meristem)	0.2 × 0.2 × 0.2	4.2E–6
2	1E–3	Fish (young-of-year), mollusk,* tadpole	2.5 × 1.2 × 0.62	1E–3
3	1E–2	Frog, shrew, vole, white-footed mouse*	10 × 2 × 2	2.1E–2
4	1	Black bass, large fish*	45 × 8.7 × 4.9	1
5	1E1	Beaver, carp, coyote, raccoon*	50 × 26 × 13	8.8
6	1E2	Mule deer, white-tailed deer*	100 × 42 × 33	72.6
7	5E2	Elk*	270 × 66 × 48	447.9
8	1E3	Grizzly bear*	220 × 100 × 100	1150

NOTE: Asterisks indicate default organism.

emitted from the contaminated media is calculated by using the MCNP code foreach radionuclide. It is assumed that the energy absorbed from external alpha particles is negligible. For beta and gamma radiation, the total energy absorbed is converted to a dose rate in units of rad/h or Gy/h. Figure 2 shows the DCCs calculated for ducks.

The DCCs for eight geometries for about 30 radionuclides have been calculated and incorporated in the RESRAD-BIOTA code. RESRAD-BIOTA is based on the U.S. Department of Energy's (DOE's) graded approach to biota dose evaluation and on associated biota concentration guides (BCGs). It includes advanced features and additional analysis capabilities that range from conservatively derived screening methods to realistic organism-specific dose and risk assessments.

Discussion and Conclusions

The RESRAD family of codes has been used by health physicists and radiological engineers as a tool for radiological risk assessment. RESRAD has been widely used in the United States and abroad and has been approved by many federal and state agencies including DOE and the U.S. Nuclear Regulatory Commission. The U.S. Environmental Protection Agency has used the RESRAD family of codes in many generic studies, including the proposed rule-making on the cleanup of radiologically contaminated sites and the assessment of

Downloaded by UNIV OF GUELPH LIBRARY on August 9, 2012 | http://pubs.acs.org
Publication Date: November 16, 2006 | doi: 10.1021/bk-2007-0945.ch005

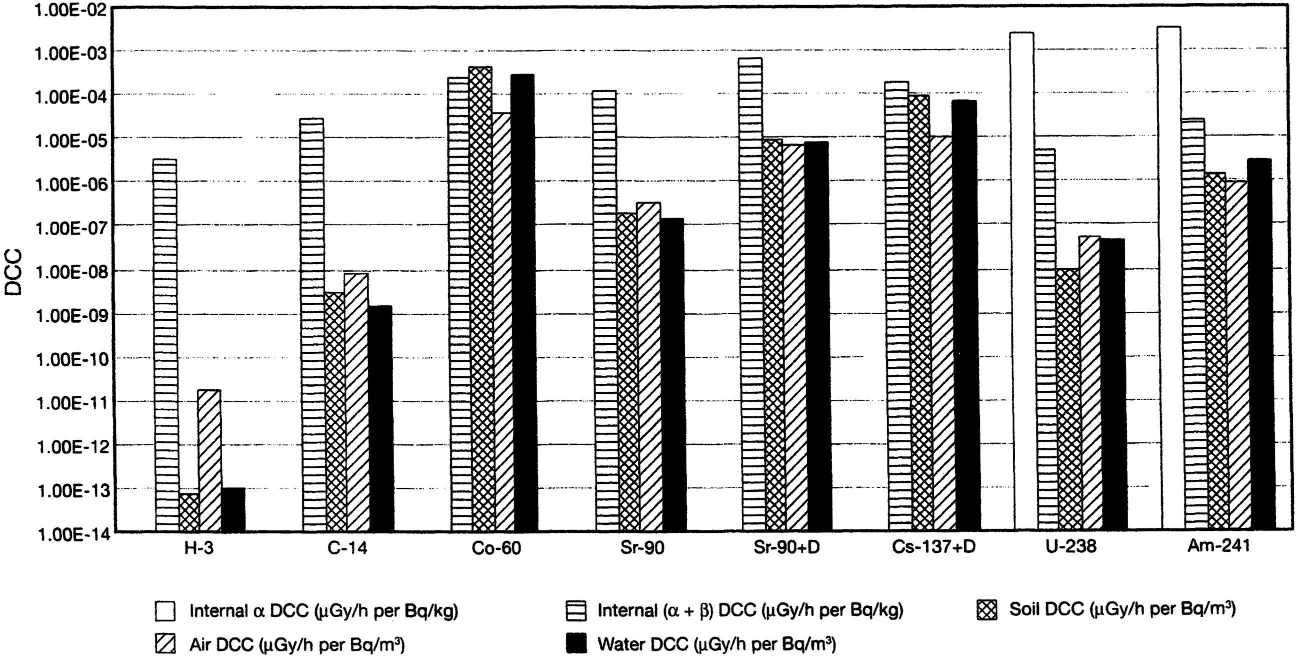

Figure 2. Internal and external DCCs for ducks.

municipal sewage sludge and ash. The U.S. Army Corps of Engineers and DOD have used RESRAD codes at many FUSRAP (formerly utilized sites remedial action program) sites and other sites. Many new features have recently been added to the RESRAD family of codes. These new features include the incorporation of the ICRP-38 radionuclide database of more than 830 radionuclides, an enhanced probabilistic analysis feature (in RESRAD and RESRAD-BUILD), and a significantly improved user interface (in RESRAD-OFFSITE and RESRAD-BIOTA). Most of the RESRAD codes are regularly updated, and many supporting documents have been prepared to facilitate their applications. All RESRAD codes and supporting documents can be downloaded free of charge from the RESRAD Web site at http://www.evs.anl.gov/resrad.

Downloaded by UNIV OF GUELPH LIBRARY on August 9, 2012 | http://pubs.acs.org
Publication Date: November 16, 2006 | doi: 10.1021/bk-2007-0945.ch005

References

1. Yu, C. RESRAD family of codes and comparison with other codes for decontamination and restoration of nuclear facilities. In *Decommissioning and Restoration of Nuclear Facilities*; Slobodien, M. J., Ed.; Health Physics Society 1999 Summer School Textbook 1999, Chapter 11, pp. 207-231.
2. Yu, C.; *et al. User's Manual for RESRAD Version 6*; Report ANL/EAD-4; Argonne National Laboratory: Argonne, IL, 2001.
3. Yu, C.; *et al. User's Manual for RESRAD-BUILD Version 3*; Report ANL/EAD/03-1; Argonne National Laboratory: Argonne, IL, 2003.
4. Cheng, J. J.; *et al. RESRAD-RECYCLE: A Computer Model for Analyzing the Radiological Doses and Risks Resulting from the Recycling of Radioactive Scrap Metal and Reuse of Surface-contaminated Material and Equipment*; Report ANL/EAD-3; Argonne National Laboratory: Argonne, IL, 2000.
5. *RESRAD-BIOTA: A Tool for Implementing a Graded Approach to Biota Dose Evaluation, User's Guide, Version 1*; Report DOE/EH-0676, ISCORS Technical Report 2004–02; U.S. Department of Energy, Interagency Steering Committee on Radiation Standards: Washington, DC, 2004.
6. Yu, C., *et al. Data Collection Handbook to Support Modeling the Impacts of Radioactive Material in Soil*; Report ANL/EAIS-8; Argonne National Laboratory: Argonne, IL, 1993.
7. *Exposure Factors Handbook*; Report EPA/600/8-89/043; U.S. Environmental Protection Agency, Office of Health and Environmental Assessment: Washington, DC, 1989.
8. Gnanapragasam, E.; Yu, C. Application of RESRAD-OFFSITE to two probabilistic test scenarios. *Practice Periodical of Hazardous, Toxic, and Radioactive Waste Management* **2002,** *6*, 112-119.
9. Whelan, G.; *et al.* Benchmarking of the saturated-zone module associated with three risk assessment models: RESRAD, MMSOILS, and MEPAS. *Environ. Eng. Sci.* **1999,** *16*, 67-80.
10. Gnanapragasam, E.; Yu, C.; Whelan, G.; Mills, W. B.; McDonald, J. P.; Lew, C. S.; Hung, C. Y.; Hoffmeyer, D. Comparison of multimedia model predictions for a contaminant plume migration scenario. *J. Contam. Hydrol.* **2000,** *46*, 17–38

11. Mills, W. B.; *et al.* Multimedia benchmarking analysis for three risk assessment models: RESRAD, MMSOILS, and MEPAS. *Risk Analysis* **1997,** *17,* 187–201.
12. Wang, Y.-Y.; Biwer, B. M.; Yu, C. *A Compilation of Radionuclides Transfer Factors for the Plant, Meat, Milk, and Aquatic Food Pathways and the Suggested Default Values for the RESRAD Code*; Report ANL/EAIS/TM-103; Argonne National Laboratory: Argonne, IL, 1993.
13. Yu, C.; *et al. Development of Probabilistic RESRAD 6.0 and RESRAD-BUILD 3.0 Computer Codes*; Report NUREG/CR-6697, ANL/EAD/TM-98; Argonne National Laboratory: Argonne, IL, 2000.
14. *Handbook of Parameter Values for the Prediction of Radionuclide Transfer in Temperate Environments*; Technical Reports Series No. 364; International Atomic Energy Agency: Vienna, 1994.
15. *Recommendations of the International Commission on Radiological Protection*; ICRP Publication 26; Annals of the ICRP 1(2), International Commission on Radiological Protection; Pergamon Press: Oxford, 1977.
16. *Limits for Intakes of Radionuclides by Workers*; ICRP Publication 30; Parts 1, 2, 3 and Index; Annals of the ICRP; International Commission on Radiological Protection; Pergamon Press: Oxford, 1979-1982.
17. *1990 Recommendations of the International Commission on Radiological Protection*; ICRP Publication 60; Annals of the ICRP 21(1–3), International Commission on Radiological Protection; Pergamon Press: Oxford, 1991.
18. Eckerman, K. F.; *et al. Limiting Values of Radionuclide Intake and Air Concentration and Dose Conversion Factors for Inhalation, Submersion, and Ingestion*; Report EPA-520/1-88-020, Federal Guidance Report No. 11; U.S. Environmental Protection Agency: Washington, DC, 1988.
19. Eckerman, K. F.; Ryman, J. C. *External Exposure to Radionuclides in Air, Water, and Soil, Exposure to Dose Coefficients for General Application, Based on the Federal Radiation Protection Guidance*; Report EPA 402-R-93-081, Federal Guidance Report No. 12; U.S. Environmental Protection Agency: Washington, DC, 1993.
20. Eckerman, K. F.; et al. *Cancer Risk Coefficients for Environmental Exposure to Radionuclides;* EPA 402-R-99-001; Federal Guidance Report No. 13; U.S. Environmental Protection Agency: Washington, DC, 1999.
21. *Age-Dependent Doses to Members of the Public from Intake of Radionuclides: Part 5, Compilation of Ingestion and Inhalation Dose Coefficients*; ICRP Publication 72; Annals of the ICRP 26(1), International Commission on Radiological Protection; Pergamon Press: New York, NY, 1996.
22. *A Framework for Assessing the Impact of Ionizing Radiation on Non-human Species*; ICRP Publication 91; Annals of the ICRP 33(3), International Commission on Radiological Protection; Pergamon Press: New York, NY, 2003.
23. A Graded Approach for Evaluating Radiation Doses to Aquatic and Terrestrial Biota; Report DOE-STD-1153-2002; U.S. Department of Energy: Washington, DC, 2002.

Downloaded by UNIV OF GUELPH LIBRARY on August 9, 2012 | http://pubs.acs.org
Publication Date: November 16, 2006 | doi: 10.1021/bk-2007-0945.ch005

Downloaded by STANFORD UNIV GREEN LIBR on August 8, 2012 | http://pubs.acs.org
Publication Date: November 16, 2006 | doi: 10.1021/bk-2007-0945.ch006

Chapter 6

Modeling of the Cerro Grande Fire at Los Alamos: An Independent Analysis of Exposure, Health Risk, and Communication with the Public

Helen A. Grogan[1], Jill W. Aanenson[2], Patricia D. McGavran[3], Kathleen R. Meyer[4], H. Justin Mohler[5], S. Shawn Mohler[6], James R. Rocco[7], Arthur S. Rood[8], John E. Till[9], and Lesley H. Wilson[7]

[1]Cascade Scientific, Inc., 1678 NW Albany Avenue, Bend, OR 97701
[2]Scientific Consulting, Inc., 1103 East 4th Street, Freeman, SD 57029
[3]Environmental Risk Assessment, Inc., 795 River Heights Drive, Meridian, ID 83642
[4]Keystone Scientific, Inc., 5009 Alder Court, Fort Collins, CO 80525
[5]Bridger Scientific, Inc., 125 Jackpot Lane, Belgrade, MT 59714
[6]Independent Consultant, 340 Meyers Street, Oak Creek, CO 80467
[7]Sage Risk Solutions, LLC, 3267 Bee Caves Road, Suite 107, Austin, TX 78746
[8]K-spar, Inc., 4835 West Foxtrail Lane, Idaho Falls, ID 83402
[9]Risk Assessment Corporation, 417 Till Road, Neeses, SC 29107

In May 2000, the Cerro Grande Fire burned across the lands of Los Alamos National Laboratory, a nuclear research facility. This chapter summarizes a study to evaluate the impacts in terms of increased public health risks from radioactive materials and chemicals that were potentially released into the atmosphere and surface water, and recommendations for improving communication of risks to the public.

In Applied Modeling and Computations in Nuclear Science; Semkow, T., et al.;
ACS Symposium Series; American Chemical Society: Washington, DC, 2006.

Introduction

The Cerro Grande Fire burned about 45,000 acres (~ 180 km^2) in northern New Mexico in May 2000. It began as a controlled burn on May 4, 2000 that soon became out of control and spread east-northeast over the next 16 days, consuming parts of Bandelier National Monument, the Santa Fe National Forest, the Los Alamos National Laboratory (LANL), the Santa Clara Pueblo, and residential land and structures within the County of Los Alamos (Fig. 1). The fire burned approximately 7,500 acres (~ 30 km^2) within the LANL boundary, causing significant damage to structures and property. During the fire, high winds carried huge smoke clouds in a north-northeasterly direction over Los Alamos, Española, and the many small communities north to Taos. The smoke clouds could be seen from southern Colorado and western Oklahoma. Ash deposits blanketed cars and the ground surface in these areas.

When the Cerro Grande Fire no longer threatened to consume nuclear facilities at LANL, public attention quickly turned to the health risks associated with the burning of contaminated sites at LANL. Two main sources of risk were identified: the release of hazardous materials into the atmosphere when the fire was burning and smoldering; and the increased potential for transport of hazardous materials into surface water from the hillsides denuded by the fire. As the fire burned, the Department of Energy (DOE) and LANL reassured the public with statements about the lack of risk. However, these statements did not allay public fear. DOE and LANL were faced with the dilemma of making a credible assessment of these risks from the fire. The solution presented itself through the State of New Mexico Environment Department (NMED), which contracted *Risk Assessment Corporation* (*RAC*), a team of scientists independent of LANL, to evaluate the risks to the public from the Cerro Grande Fire, and to recommend steps that could be taken to improve communication of risks to the public in future emergencies. The study did not address the health risks associated with the burning of buildings and home sites in Los Alamos, or the future impact of the fire on groundwater. This chapter summarizes the results of the study, which were documented in a series of reports (*1*,*2*,*3*).

Study Focus and Approach

The primary focus for the study was the analysis of radionuclides and chemicals derived from LANL operations that may have been released from the Cerro Grande Fire burning on LANL property. For releases into the atmosphere, the study area covered 815,000 acres (3300 km^2) (see Fig. 1) and included the cities of Santa Fe and Española. For releases into surface water, the study area was smaller, covering approximately 182,000 acres (738 km^2), and extended to

Downloaded by STANFORD UNIV GREEN LIBR on August 8, 2012 | http://pubs.acs.org
Publication Date: November 16, 2006 | doi: 10.1021/bk-2007-0945.ch006

the west of LANL to include the watersheds for the canyons that cross the LANL facility.

Environmental data were collected by four organizations (LANL, NMED, U.S. Environmental Protection Agency (EPA), and DOE) during and after the fire, and were made available to the *RAC* team for analysis.

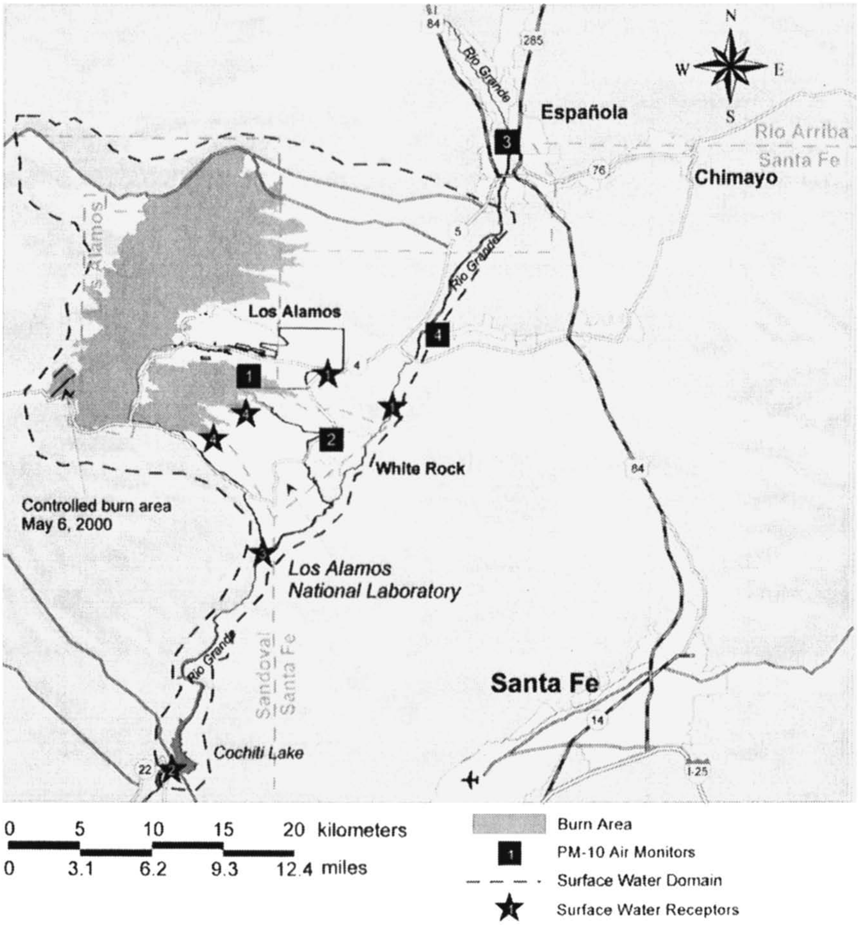
N
W
E
S
84
285
Rio Grande
Española
3
Rio Arriba
Santa Fe
76
Chimayo
Los Alamos
5
Rio Grande
Los Alamos
4
1
2
White Rock
84
Controlled burn area
May 6, 2000
Los Alamos
National Laboratory
Rio Grande
Sandoval
Santa Fe
Santa Fe
14
Cochiti Lake
22
I-25
0 5 10 15 20 kilometers
0 3.1 6.2 9.3 12.4 miles
Burn Area
PM-10 Air Monitors
Surface Water Domain
Surface Water Receptors

Figure 1. Study areas for analysis of releases to air and surface water from the Cerro Grande Fire.

For releases to the atmosphere, the team expected that these data would be sufficient to estimate the amount of radionuclides and chemicals released. The team anticipated developing this source term estimate by relating concentrations

Downloaded by STANFORD UNIV GREEN LIBR on August 8, 2012 | http://pubs.acs.org
Publication Date: November 16, 2006 | doi: 10.1021/bk-2007-0945.ch006

Downloaded by STANFORD UNIV GREEN LIBR on August 8, 2012 | http://pubs.acs.org
Publication Date: November 16, 2006 | doi: 10.1021/bk-2007-0945.ch006

of chemicals and radionuclides in soil and biota from areas of known contamination to the temporal progression of the fire on a daily basis, the prevailing meteorological conditions, and the radionuclide and chemical concentration measurements in air at specific locations. Such information, coupled with an air dispersion model, would allow an effective release rate from an area of known contamination to be "back-calculated." These release rate estimates, combined with the air dispersion model and meteorological data, could then be used to predict concentrations in air at locations that lacked direct measurements. Since measured radionuclide and chemical concentrations in air were lacking, the *RAC* team relied on measurements of particulate matter less than 10 micrometers (PM_{10}), which was monitored more extensively in the study area before, during, and after the fire. PM_{10} is a combustion product that is released in relatively large quantities during a forest fire. Measurements of PM_{10} during the fire showed a marked increase over background levels. The measured PM_{10} concentrations, coupled with models to estimate PM_{10} emissions from the fire and an air dispersion model to estimate the transport and dispersion of airborne particles, were used to estimate daily dispersion factors. The product of the dispersion factor and an estimated quantity of radionuclides and chemicals released from contaminated soil during the fire allowed the *RAC* team to estimate radionuclide and chemical concentrations in air within the study area. Since gasses tend to have deposition properties that differ from particulates, carbon monoxide, a gaseous forest fire combustion product, was used instead of PM_{10} to calculate dispersion factors for chemicals that volatilize during a fire.

For releases to surface water, the team needed to estimate the concentrations of chemicals and radionuclides in surface water and sediments because of increased storm water runoff and erosion in the canyons that cross the LANL facility. The volumes of storm water passing through the canyons during storm events of varying magnitude were estimated considering conditions prior to and after the fire because the fire caused the loss of vegetation and trees in the canyons above and below the LANL facility. Based on these storm water volumes, the volume of suspended solids resulting from erosion of soils was estimated.

The study tasks were complicated because radionuclides and chemicals released into the air or transported into surface water because of the fire do not originate from contaminated areas at LANL alone. Other sources include (1) naturally occurring radionuclides and chemicals, (2) anthropogenic (human-made) radionuclides that have deposited on vegetation and ground (such as $^{239/240}Pu$ and ^{137}Cs from global weapons testing fallout), (3) more than 50 years of LANL operations that have deposited chemicals and radionuclides on the surrounding lands, (4) radionuclides and chemicals that may have been suspended from contaminated areas that were not affected by the Cerro Grande Fire, and (5) combustion products from the burning of LANL structures.

To fill data gaps not covered by available monitoring data and to allow for a prediction of potential future risks, soil characterization data were used to estimate source terms for contaminated sites at LANL that burned during the fire or were susceptible to erosion following the fire. Because of uncertainties surrounding the development of the source terms, conservative assumptions were made to help ensure that releases were not underestimated. These source terms provided the basis for calculating the risks from the fire using computer models that predict transport of materials in the environment. To the extent possible, the model-predicted concentrations were compared with environmental monitoring data to assess the legitimacy of the predictions.

The soil monitoring data available to characterize burned source areas suggested that a large number of radionuclides and chemicals were potentially released during or after the fire. A screening process was established to focus on those chemicals and radionuclides most likely to contribute to the health risk of people exposed directly or indirectly to air or surface water impacted by LANL. Two categories of health risk were considered: the risk of cancer incidence from exposure to radionuclides or carcinogenic chemicals, and the risk of non-cancer health effects from exposure to noncarcinogenic chemicals. The latter was calculated using a hazard quotient (HQ). The HQ is the ratio of the level of exposure to a chemical of concern over a specified time period to a reference dose (RfD) for that chemical derived for a similar exposure period. The HQ assumes that there is an exposure level (defined by the RfD) that can be tolerated with no adverse effects even for sensitive populations. If the exposure level exceeds this threshold ($HQ > 1$), there may be concern for potential health effects.

The methodology used to obtain the screened list of potential contaminants of concern (PCOCs) for releases to air is shown in Fig. 2. The concentrations of chemicals and radionuclides measured in soil at individual contaminated areas, referred to as potential release sites (PRS), were used to estimate an inventory across the entire PRS area. An atmospheric dispersion coefficient was then applied to the inventory value to estimate an air concentration, assuming the entire inventory was released during the fire (*1*). These air concentrations were used to calculate a screening risk index or HQ. A similar approach was used to obtain a screened list of PCOCs for releases to surface water (*2*). The concentrations of chemicals and radionuclides measured in surface water after the fire were used to calculate a screening risk index or HQ based on the ingestion of water containing these measured concentrations of chemicals and radionuclides. For the air and surface water releases, contaminants with a cancer incidence screening risk estimate of less than 10^{-5} (1 chance in 100,000) or a screening HQ of less than 1 were removed from further consideration.

Source terms were calculated for the most important radionuclides and chemicals, using available information on the quantities present at the

Downloaded by STANFORD UNIV GREEN LIBR on August 8, 2012 | http://pubs.acs.org
Publication Date: November 16, 2006 | doi: 10.1021/bk-2007-0945.ch006

Downloaded by STANFORD UNIV GREEN LIBR on August 8, 2012 | http://pubs.acs.org
Publication Date: November 16, 2006 | doi: 10.1021/bk-2007-0945.ch006

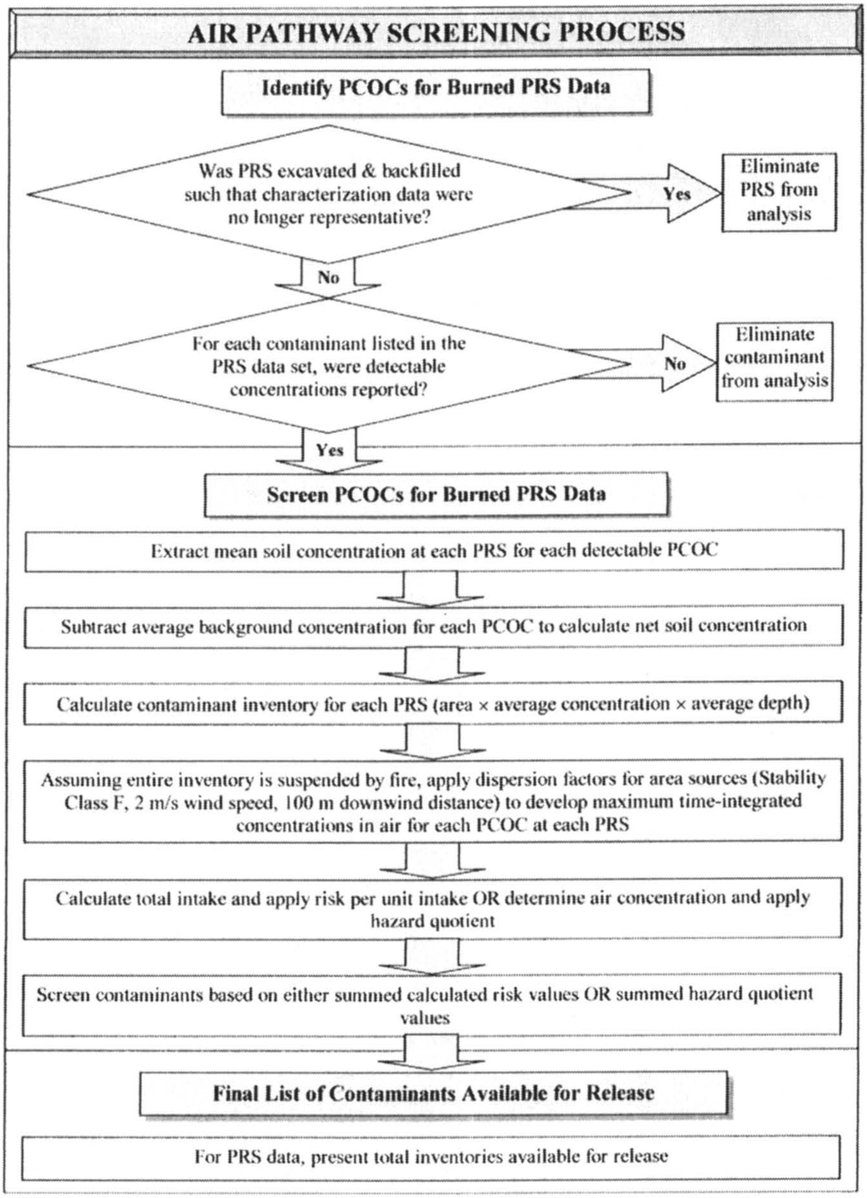
AIR PATHWAY SCREENING PROCESS
Identify PCOCs for Burned PRS Data
Was PRS excavated & backfilled such that characterization data were no longer representative?
Yes
Eliminate PRS from analysis
No
For each contaminant listed in the PRS data set, were detectable concentrations reported?
No
Eliminate contaminant from analysis
Yes
Screen PCOCs for Burned PRS Data
Extract mean soil concentration at each PRS for each detectable PCOC
Subtract average background concentration for each PCOC to calculate net soil concentration
Calculate contaminant inventory for each PRS (area × average concentration × average depth)
Assuming entire inventory is suspended by fire, apply dispersion factors for area sources (Stability Class F, 2 m/s wind speed, 100 m downwind distance) to develop maximum time-integrated concentrations in air for each PCOC at each PRS
Calculate total intake and apply risk per unit intake OR determine air concentration and apply hazard quotient
Screen contaminants based on either summed calculated risk values OR summed hazard quotient values
Final List of Contaminants Available for Release
For PRS data, present total inventories available for release

Figure 2. Flow chart of the screening process for the air pathway.

contaminated sites and how they may have been released to the air and storm water during the Cerro Grande Fire. The source terms were used to estimate air and surface water concentrations for the risk estimates. The following sections address the specifics of the air and surface water exposure pathways and risk estimates.

Air Transport Pathway

Downloaded by STANFORD UNIV GREEN LIBR on August 8, 2012 | http://pubs.acs.org
Publication Date: November 16, 2006 | doi: 10.1021/bk-2007-0945.ch006

The primary focus for the air pathway was the analysis of radionuclides and chemicals derived from LANL operations that may have been released during the Cerro Grande Fire while the fire burned and subsequently smoldered on LANL property. A secondary objective was to estimate the release of radionuclides and chemicals from the burning of natural vegetation both on and off LANL property. The sources of radionuclides and chemicals on or in natural vegetation included naturally occurring radionuclides and metals and worldwide fallout of radionuclides from atmospheric testing of nuclear weapons. Some radionuclides on or in natural vegetation were also attributed to the presence of LANL. The process of calculating the potential risks associated with these releases included:

- Evaluating the available air monitoring data and procedures
- Identifying sources and estimated amounts of LANL-derived chemicals and radionuclides on LANL lands that burned during the fire
- Estimating amounts of radionuclides and chemicals on or in all vegetation that burned during the Cerro Grande Fire
- Using computer modeling to predict the release and transport of chemicals and radionuclides carried in the fire plume
- Developing exposure scenarios based on hypothetical representative individuals
- Estimating the resulting health risks and the associated uncertainties.

Calculating the transport of radionuclides and chemicals released into the air during burning of the PRS first required an understanding of the behavior of the fire itself. During forest fires, combustion products in the form of particulate matter are emitted in large quantities and provide a measurable material that can be used to estimate the concentration of other fire-related products as the smoke plume travels downwind.

The three-dimensional complex terrain model system CALPUFF (*4*) was used to estimate PM_{10} concentrations in the model domain. The CALPUFF modeling system consists of a three-dimensional wind field model (CALMET), a Lagrangian puff dispersion model (CALPUFF), and a post processing program (CALPOST). Terrain and land use data were obtained from the USGS 7.5

minute and two degree digital elevation models, and digital land use maps, respectively. Terrain was averaged across a 120 × 110 node grid having a grid spacing of 500 m. Surface meteorological data consisted of 5 surface stations operated by LANL on LANL property, five community monitoring stations (Cochiti, Santa Clara Pueblo, San Juan Pueblo, Española, and Santa Fe Indian School), the NMED meteorological tower located near the Santa Fe Airport, and cloud cover and ceiling height data obtained from the Santa Fe Airport. Surface meteorological data used in CALMET consisted of hourly-averaged wind speed, wind direction, temperature, barometric pressure, relative humidity, cloud cover, and ceiling height. No precipitation was recorded during the entire event. Upper air data were obtained from the Albuquerque Airport. A separate model, the Emissions Production Model (*5*), was used to estimate the quantities of combustion products released to the air during the fire based on the type and quantity of fuel loading associated with each burn area. The computer-model-estimated concentrations of PM_{10} were then compared with the measured concentrations. Adjustments were made to fuel loading and the timing of a particular burn day to bring the computer-model-estimated PM_{10} concentrations into reasonable agreement with the measured PM_{10} concentrations (see Fig. 3). This process is termed model calibration. The process of calibrating the model to PM_{10} measurements involved (1) identifying the geographical area that was burned, (2) defining the time history of the fire, (3) estimating the amount of vegetation that burned, (4) estimating the amount of PM_{10} released by the burning vegetation and the heat generated during burning, and (5) modeling the transport in air of PM_{10} released by the fire. During this calibration process, it was necessary to account for contributions of PM_{10} from sources other than the fire. In the absence of a fire, PM_{10} concentrations are known to increase with wind speed (*6*). Pre-fire PM_{10} data coupled with 24-hour mean wind speeds provided a way to account for background PM_{10} concentrations as a function of the mean 24-hour wind speed. Figure 3 compares the model predicted PM_{10} concentrations at three offsite locations (San Ildefonso, Santa Clara, and White Rock) and one onsite location (TA-54) to the measured PM_{10} concentrations. The monitor locations are shown in Fig. 1. The TA-54 measurements represent 24-hour average concentrations, while measurements at San Ildefonso, Santa Clara, and White Rock represent average concentrations of varying time periods. Predicted-to-observed ratios of PM_{10} in the study area had a geometric mean value of 0.87 with a geometric standard deviation of 1.7.

Concentrations were calculated for the radionuclides and chemicals identified as important through the screening process. In general, most predicted air concentrations were relatively low. The maximum seven-day, time-integrated concentrations of radionuclides were generally less than 0.1 aCi-d m^{-3}, and the maximum seven-day, time-integrated concentrations of chemicals and metals were generally less than 0.01 μg-d m^{-3}.

Downloaded by STANFORD UNIV GREEN LIBR on August 8, 2012 | http://pubs.acs.org
Publication Date: November 16, 2006 | doi: 10.1021/bk-2007-0945.ch006

In contrast, the predicted air concentrations and deposition amounts for the explosive compounds RDX, HMX, DNB, and TNT were relatively high. The maximum seven-day, time-integrated concentrations for the explosive compounds were in the 10-100 μg-d m^{-3} range. The integration period of seven days represents the time over which the fire actively burned on LANL property. After the fire, a limited amount of soil sampling was performed; however, no explosive compounds were detected. The predicted deposition of these compounds would have been easily detected in soil, suggesting that the source terms for these compounds were overestimated because of the cautious assumptions made in the calculations.

Downloaded by STANFORD UNIV GREEN LIBR on August 8, 2012 | http://pubs.acs.org
Publication Date: November 16, 2006 | doi: 10.1021/bk-2007-0945.ch006

Surface Water Transport

The Cerro Grande Fire significantly altered the landscape by destroying vegetation and changing the surface soil characteristics, which allowed greater quantities of storm water to flow through the canyons. The increased storm water flow could carry greater amounts of soil, sediment, and ash from the entire burned watershed, including some areas at LANL where chemicals and radioactive materials are present in soils. The process of estimating the potential increased exposure through the surface water included:

- Evaluating the available surface and storm water monitoring data and procedures
- Identifying sources and estimated amounts of LANL-derived chemicals and radionuclides that burned during the fire
- Using computer models to predict the release and transport of radionuclides and chemicals in surface and storm water
- Developing exposure scenarios based on hypothetical representative individuals
- Estimating the resulting health risks and the associated uncertainties.

The most critical step in the risk estimation process was calculating the amounts of chemicals and radionuclides in source areas available for movement into surface water (*the source term*). The source areas included individual PRS at LANL that storm water passes over and contaminated sediment along the canyon reaches. The modeling approach used measured concentrations of chemicals and radionuclides in soil or sediment, along with water runoff and sediment erosion yields. Downstream concentrations of chemicals and radionuclides were then calculated at defined *points of exposure*, focusing on those that were identified through the screening process as most important in terms of potential health risk. Points of exposure were locations where an

Downloaded by STANFORD UNIV GREEN LIBR on August 8, 2012 | http://pubs.acs.org
Publication Date: November 16, 2006 | doi: 10.1021/bk-2007-0945.ch006

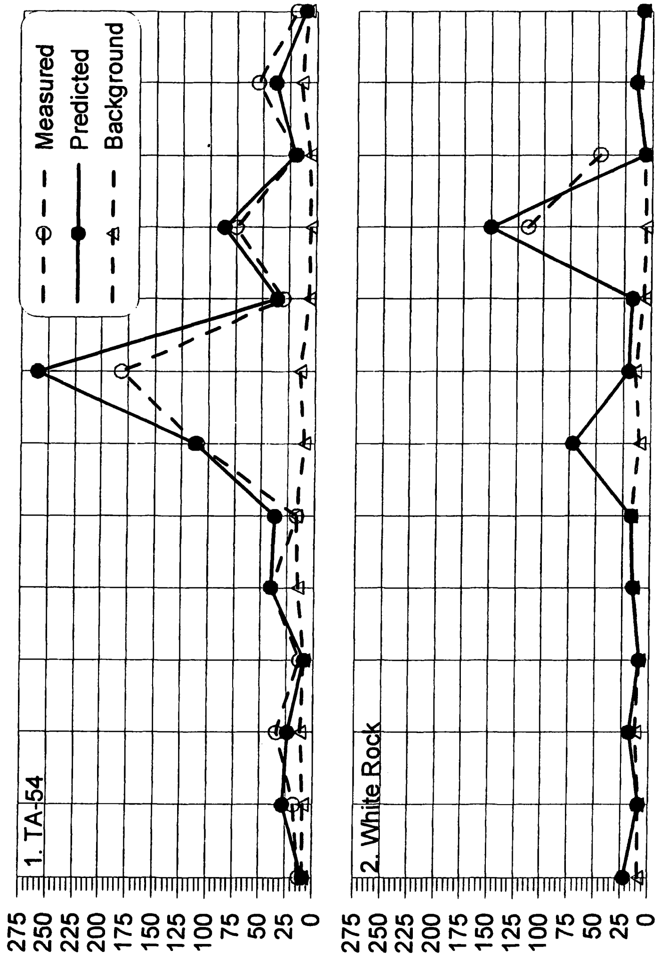

Downloaded by STANFORD UNIV GREEN LIBR on August 8, 2012 | http://pubs.acs.org
Publication Date: November 16, 2006 | doi: 10.1021/bk-2007-0945.ch006

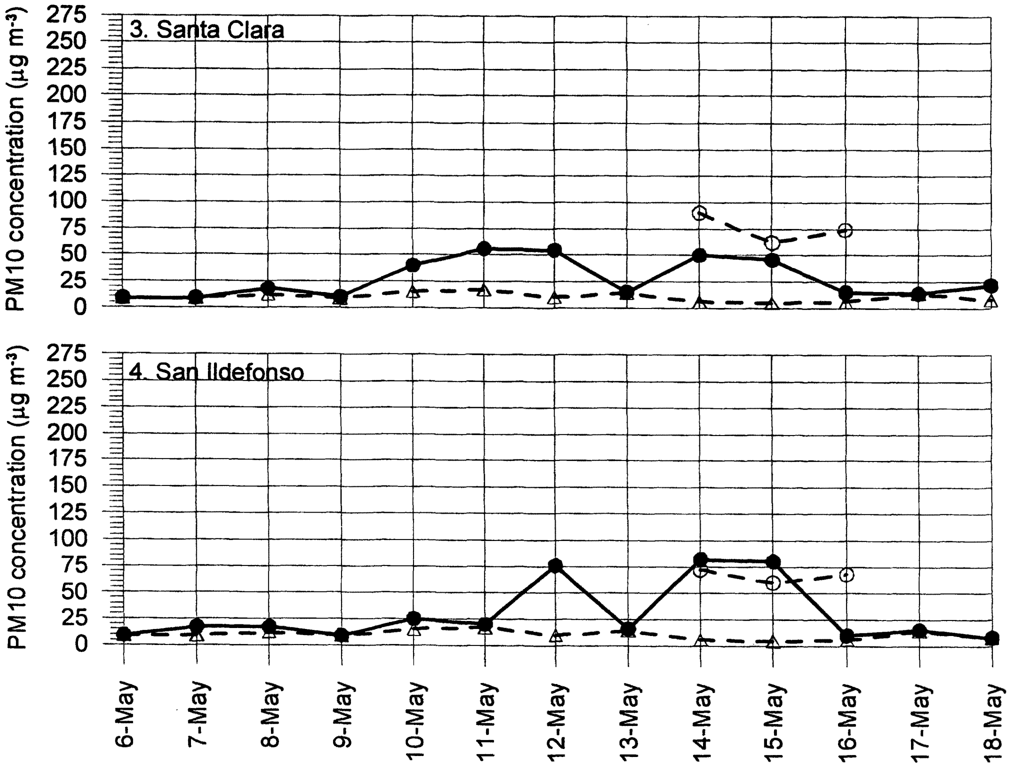

Figure 3. Predicted and measured PM_{10} concentrations at LANL Technical Area-54, White Rock, Santa Clara, and San Ildefonso. Fig. 1 shows the numbered monitor locations.

individual could potentially come in contact with surface water, suspended sediments, or deposited sediments containing chemicals or radionuclides.

Next, the concentrations at the points of exposure (surface water receptors in Fig. 1) for the 37 chemicals and radionuclides identified in the screening process were calculated in storm water, surface water, and suspended and deposited sediments. The process included:

- Estimating the surface water flow within the watersheds and at outlets to the Rio Grande for storm events of various severities, all six hours in length (ranging from a two-year to a 500-year design storm event)
- Developing estimates of suspended sediment concentrations before and after the fire based on an analysis of pre-fire and post-fire total suspended solids sampling data from the U.S. Geological Survey and LANL
- Identifying the watersheds contributing storm water flow to each point of exposure and the important source areas in the watershed
- Identifying background, or typical, storm water flow and suspended sediment concentration in the Rio Grande and in Cochiti Lake
- Estimating concentrations of chemicals and radionuclides in environmental media at each point of exposure.

Concentrations of chemicals and radionuclides measured in water after the fire differed by less than a factor of ten from concentrations measured before the fire. The results of the transport modeling suggested that while the fire impacted the potential transport of chemicals and radionuclides, there was no consistent change in the resulting concentrations from pre-fire to post-fire. Concentrations of chemicals and radionuclides decreased as the point of exposure moved further away from the source areas, resulting in higher concentrations within the canyons immediately below the LANL facility than in the Rio Grande and in Cochiti Lake.

Development of Exposure Scenarios

A variety of exposure scenarios were used to estimate a range of possible exposures to air and surface water pathways for different individuals in the area during the time period of interest. The scenarios addressed a broad range of lifestyles although the hypothetical individuals described in the scenarios did not represent known individuals at these locations. Risks estimated for the hypothetical individuals were greater than the risks estimated for other individuals in the area for less time or under less exposed conditions.

For releases to air, inhalation was the primary exposure pathway. The risk to a person from exposure during the Cerro Grande Fire depended on a number of

Downloaded by STANFORD UNIV GREEN LIBR on August 8, 2012 | http://pubs.acs.org
Publication Date: November 16, 2006 | doi: 10.1021/bk-2007-0945.ch006

factors, including location, length of time at that location, physical activity level of the individual, age, and gender. Four exposure scenarios (a firefighter, an emergency response worker (other than a firefighter), a resident adult, and a resident child) were used to determine the risks to representative individuals from the LANL-derived radionuclides and chemicals released to the air during the fire. The firefighter and emergency response worker were assumed to be active outside for extended periods of time each day and had relatively short rest and sleep periods. The firefighters were involved in physically strenuous work such as starting backfires, fighting spot fires, and building firebreaks. Emergency response workers were also situated in close proximity to the fire for extended periods of time, but generally had lower physical activity levels than the firefighters. The resident adult and child were assumed to be more active than might normally be the case. For each scenario, cancer risks for radionuclides and carcinogenic chemicals, and HQs for noncarcinogenic chemicals, were estimated. The model-estimated concentrations at eight representative exposure locations, along with the maximum predicted concentration in the study area, provided the input to the risk calculations. The risks from naturally occurring radionuclides and chemicals on vegetation that burned during the Cerro Grande Fire were calculated for the adult resident scenario only. These risks were associated with any forest fire and were not specific to LANL.

For the surface water pathway, four exposure scenarios were used to represent the different ways that individuals might be exposed to radionuclides and chemicals released as a result of increased surface water flow after the fire. The hypothetical individuals included (1) a local hunter, (2) family members (adult and child) living below Cochiti Lake, (3) an adult living below Water Canyon, and (4) a fire cleanup worker at the LANL Site. The exposure pathways for the hypothetical individuals in each surface water exposure scenario are shown in Table I.

Table I. Exposure Pathways Included in the Surface Water Risk Analysis Scenarios (see Fig. 1 for Exposure Locations)

Exposure pathways	*(1) Local hunter*	*(2) Family*	*(3) Adult resident*	*(4) Clean-up worker*
Drinking untreated water	X	X	X	
Sediment exposure	X	X	X	X
Swimming or contact with water		X		
Eating fish	X	X	X	
Eating garden produce		X	X	
Eating beef from cattle		X	X	

Downloaded by STANFORD UNIV GREEN LIBR on August 8, 2012 | http://pubs.acs.org
Publication Date: November 16, 2006 | doi: 10.1021/bk-2007-0945.ch006

Air Pathway Risks

For LANL-derived chemicals and radionuclides, the maximum risk occurred on LANL property within the active burn area. Table II summarizes the maximum estimated risks by scenario, contaminant type, and source for the air pathway.

Table II. Maximum Estimated Risks for Releases to Air by Scenario, Contaminant Type, and Source

Releases from burned contaminated areas (potential release sites)	*Lifetime cancer incidence risk (carcinogens)*		*Hazard quotient (noncarcinogens)*
Scenario	Radionuclides	Chemicals	Chemicals
Resident adult	6.7×10^{-14}	2.1×10^{-7}	2.0
Firefighter	1.0×10^{-13}	3.6×10^{-7}	3.4
Emergency response person	6.9×10^{-14}	2.2×10^{-7}	2.1
Resident child	2.6×10^{-14}	3.1×10^{-7}	2.9
Key radionuclides and chemicals	^{238,239}Pu, ^{231}Pa, ^{226}Ra	RDX [d]	RDX, HMX, TNT, DNB [d]
Releases from burned natural vegetation	*Lifetime cancer incidence risk (carcinogens)*		*Hazard quotient (noncarcinogens)*
Scenario	Radionuclides	Chemicals	Chemicals
Resident adult	4.9×10^{-7} 4.1×10^{-7} [a]	4.4×10^{-7}	142 [b] 0.78 [c]
Key radionuclides and chemicals	^{210}Pb, ^{210}Po, ^{226}Ra	Cr	Mn [b], Al [b], Ba [c], Cr [c], Fe [c]

[a] Based on release of radionuclide inventories in litter and bark only.

[b] Hazard quotient based on chronic reference dose for manganese and aluminum. Manganese and aluminum dominate the hazard quotient.

[c] Hazard quotient based on references doses derived from the eight-hour National Institute for Occupational Safety and Health standard for manganese and aluminum. Dominant metals are barium, chromium, and iron.

[d] RDX (hexahydro-1,3,5-trinitro-1,3,5-triazine), HMX, TNT (2,4,6-trinitrotoluene), and DNB (1,3-dinitrobenzene) are all explosive compounds.

The maximum total *cancer incidence risk* from breathing any LANL-derived radionuclide released to the air during the fire was less than 10^{-7} (1 chance in 10 million). By comparison, cancer incidence risks from breathing radionuclides released to the air from natural vegetation during the fire were

Downloaded by STANFORD UNIV GREEN LIBR on August 8, 2012 | http://pubs.acs.org
Publication Date: November 16, 2006 | doi: 10.1021/bk-2007-0945.ch006

estimated to be approximately 10^{-6} (1 chance in 1 million). Cancer incidence risks from LANL-derived chemicals released during the fire were generally less than 10^{-6}. The explosive compound RDX was a major contributor to this risk estimate. Cancer incidence risks from metals detected on and in natural vegetation and released during the fire were also approximately 10^{-6}.

Estimated intakes of noncarcinogenic LANL-derived chemicals throughout the study area generally resulted in a total hazard quotient less than or equal to 0.1. A hazard quotient less than 1 is defined as an acceptable intake by the EPA. Near areas where the fire burned, however, hazard quotients exceeded 1.0 and reached a maximum value of 2.0 for the resident adult scenario. This excursion above the generally accepted level of 1 was limited to a small area within the LANL site near its western boundary. Most of the non-cancer risk was associated with the explosive compounds RDX, HMX, DNB, and TNT. The deposition of radionuclides and chemicals from burned PRSs was estimated, and it was determined that these would not be detectable in soil, with the exception of the explosive compounds RDX and HMX. Furthermore, the predicted concentrations were well above the detection limits of standard laboratory equipment. However, because RDX was not detected in area soils sampled after the fire, *RAC* team members believe the amount of these explosives released during the fire, and hence the risks from these chemicals, were overestimated.

Hazard quotients for metals released during the fire from natural vegetation were less than 1.0 except for the metal manganese and, to a lesser extent, aluminum. However, the *reference doses* initially used to calculate the non-cancer health effects from these two metals were developed to evaluate chronic, or long-term, exposures, not short-term exposures such as those during the Cerro Grande Fire. The team believes that the chronic reference doses resulted in unrealistically high hazard quotients for these metals. The reference doses equated to air concentrations that were much lower than the occupational standards (eight-hour exposure) for the metals. Using reference doses based on occupational standards for these two metals resulted in a maximum hazard quotient of less than 1.

Concentrations of PM_{10} exceeded EPA air quality standards for PM_{10} averaged over 24 hours at some locations in the study area and were sufficient to cause adverse health effects. Because the dose response relationship is uncertain, however, the risk of health effects expected to result from PM_{10} exposure was not quantified.

Surface Pathway Risks

For the surface water pathway, there were 45 chemicals and radionuclides identified as most important in terms of the potential human health risk from

Downloaded by STANFORD UNIV GREEN LIBR on August 8, 2012 | http://pubs.acs.org
Publication Date: November 16, 2006 | doi: 10.1021/bk-2007-0945.ch006

more than 250 chemicals and 75 radionuclides evaluated during the screening process. The evaluation of chemicals presented a particular predicament because post-fire monitoring data were lacking for many of the chemicals. Furthermore, for other chemicals, the results were below the detection limits of the laboratory equipment used to analyze the samples so few conclusions could be drawn. As a result, the focus of the surface water risk calculations was the man-made radionuclides ^{241}Am, ^{137}Cs, ^{90}Sr, ^{238}Pu, and ^{239,240}Pu in surface water, storm water, and sediment. Trend analysis of the monitoring data was useful for identifying apparent increases in concentration for some radionuclides and chemicals following the fire, and for identifying the possibility of LANL impact on measured concentrations.

The potential health risks were estimated for hypothetical people drinking water from the Rio Grande or Cochiti Lake, contacting sediments near the edge of the water, eating fish from the Rio Grande or Cochiti Lake, eating produce irrigated with water from the lake, eating beef raised in the area, or participating in recreational activities like swimming. The results for the surface water pathway showed the potential annual cancer risk from the Cerro Grande Fire burning on the LANL site was less than 3 in one million from exposure to any LANL-derived chemical or radionuclide that may have been carried in the surface water and sediments to the Rio Grande and Cochiti Lake. If exposure to the same concentrations of LANL-derived chemicals or radioactive materials was assumed to continue for seven years (the time it may take to return to pre-fire vegetation conditions in the area), then the potential cancer risk was greater at about 20 in 1 million. Estimated intakes of noncarcinogenic LANL-derived chemicals were less than the acceptable intakes (a hazard quotient less than 1) established by the EPA. Table III shows the highest estimated impacts by scenario, individual chemical, or radionuclide, and selected pathways.

Of the different hypothetical individuals considered in the exposure scenarios, the health risks were highest for the resident living year round on the bank of the Rio Grande near the confluence of Water Canyon. The type of exposure contributing most to the potential risk was eating fish. For this type of exposure, the *RAC* team assumed that the hypothetical individuals consumed approximately 4.5 kilograms of fish per year, all from the river or Cochiti Lake. However, the risks should be viewed as upper bound, or maximum values because of the cautious assumptions made in estimating concentrations and in selecting lifestyle characteristics for the hypothetical individuals. The risks for all other types of exposure were lower than were those for eating fish.

The hunter and firefighter, who were potentially exposed to higher concentrations in water and sediments, spent less time at those locations and had fewer exposure routes. Risk estimates and hazard quotients for the child and the adult at Cochiti Lake were broadly similar. In general, risks for all pathways associated with the 500-year storm event were less than 10 times higher than the risks from the two-year storm event, and the differences are likely to be within the range of uncertainty in the estimates.

Downloaded by STANFORD UNIV GREEN LIBR on August 8, 2012 | http://pubs.acs.org
Publication Date: November 16, 2006 | doi: 10.1021/bk-2007-0945.ch006

Conservatisms and Uncertainties

Modeling radionuclide and chemical releases to air and surface water from the Cerro Grande Fire presented a number of challenges. For releases to air, there was limited information readily available about the materials present at LANL that might have been suspended into the atmosphere during the fire. Therefore, the modeling had to encompass the uncertainties associated with estimating the inventories of radionuclides and chemicals present before the fire, the amounts that were released during the fire, and their subsequent dispersion and deposition in the environment. The short time frame and limited resources available for this project required the team to make several assumptions about the data and prevented an in-depth analysis of data quality. In addition, a fair amount of uncertainty existed regarding the spatial extent of contamination at the different source areas. Because of these uncertainties and limitations, the team made conservative assumptions to avoid underestimating the quantity of contaminant available for potential release at each PRS (*e.g.*, eliminating non-detect values likely biases the calculated inventory on the high side). If risks of significant concern had been identified, further investigation into the impact of any conservative assumptions would have been required.

The goal of the surface water modeling efforts was to develop conservative estimates of the relative concentrations for pre-fire and post-fire conditions for the surface water pathways. Estimating chemical and radionuclide concentrations at selected points of exposure was central to those efforts. However, there were many uncertainties associated with environmental transport modeling, and the process of distinguishing between regional background concentrations, concentrations expected in fire-impacted areas, and concentrations related to LANL operations complicated the calculations. Because of these uncertainties, the predicted concentrations and risk estimates were intended to be conservative or cautious. Nevertheless, the results of this type of predictive modeling could be used to identify specific areas or chemicals and radionuclides contributing most to potential risk. The modeling results were also useful for understanding the relative contribution of different potential sources of chemicals and radionuclides, which is difficult to discern from environmental monitoring data alone.

Downloaded by STANFORD UNIV GREEN LIBR on August 8, 2012 | http://pubs.acs.org
Publication Date: November 16, 2006 | doi: 10.1021/bk-2007-0945.ch006

Risk Communication

A key objective following the Cerro Grande Fire was to evaluate how technical data were used to make rapid decisions about the potential health risks and the methods used to communicate that information to local residents and emergency response personnel. The *RAC* team made specific recommendations based on its experience of independently estimating the health risks to the public from the Cerro Grande Fire. The goal of these recommendations was to improve

Downloaded by STANFORD UNIV GREEN LIBR on August 8, 2012 | http://pubs.acs.org
Publication Date: November 16, 2006 | doi: 10.1021/bk-2007-0945.ch006

Table III. Highest Estimated Impacts for Releases to Surface Water by Scenario, Contaminant Type, and Exposure Pathway

Eating fish from Rio Grande or Cochiti Lake	*Lifetime cancer incidence risk*[a] *(carcinogens)*		*Hazard quotient*[a] *(noncarcinogens)*
Scenario	Radionuclides	Chemicals	Chemicals
Hunter	3.5×10^{-6}	5.5×10^{-9}	0.09
Residents near Cochiti Lake			
Adult	4.0×10^{-7}	5.1×10^{-7}	0.02
Child	1.7×10^{-7}	5.0×10^{-7}	0.02
Person near Rio Grande at Water Canyon	2.4×10^{-6}	2.7×10^{-6}	0.1
Emergency response person	na	na	na
Key radionuclides and chemicals	^{137}Cs	B(a)P[b]	chromium, lead
Drinking water from Rio Grande or Cochiti Lake	*Lifetime cancer incidence risk (carcinogens)*		*Hazard quotient (noncarcinogens)*
Scenario	Radionuclides	Chemicals	Chemicals
Hunter	4.3×10^{-8}	4.4×10^{-10}	0.0066
Residents near Cochiti Lake			
Adult	4.9×10^{-9}	3.0×10^{-7}	0.0033
Child	2.4×10^{-9}	3.5×10^{-7}	0.0039
Person near Rio Grande at Water Canyon	2.2×10^{-8}	1.4×10^{-6}	0.015
Emergency response person	na	na	na
Key radionuclides and chemicals	^{137}Cs, ^{239}Pu	RDX[b]	barium, lead
Incidental sediment ingestion	*Lifetime cancer incidence risk (carcinogens)*		*Hazard quotient (noncarcinogens)*
Scenario	Radionuclides	Chemicals	Chemicals
Hunter	6.1×10^{-9}	2.7×10^{-9}	0.00026
Residents near Cochiti Lake			
Adult	8.1×10^{-9}	3.2×10^{-7}	0.00052
Child	8.1×10^{-9}	7.4×10^{-7}	0.0012

Table III. *Continued.*

Incidental sediment ingestion	*Lifetime cancer incidence risk (carcinogens)*		*Hazard quotient (noncarcinogens)*
Scenario	Radionuclides	Chemicals	Chemicals
Person near Rio Grande at Water Canyon	3.7×10^{-9}	1.2×10^{-7}	0.00024
Emergency response person	1.8×10^{-11}	4.7×10^{-9}	0.003
Key radionuclides and chemicals	^{239}Pu, ^{226}Ra	B(a)P, RDX [b]	lead, barium

na = not applicable.

[a] The annual cancer incidence risks are presented for exposure to radionuclide or chemical concentrations after a two-year storm event; for noncarcinogens, the hazard quotient expresses the fraction of acceptable intake established by the EPA.

[b] B(a)P = benzo(a)pyrene, RDX = hexahydro-1,3,5-trinitro-1,3,5-triazine (an explosive material).

Downloaded by STANFORD UNIV GREEN LIBR on August 8, 2012 | http://pubs.acs.org
Publication Date: November 16, 2006 | doi: 10.1021/bk-2007-0945.ch006

the calculation and communication of risk in future emergencies that may be applicable to LANL and other sites. The recommendations were divided into two broad areas: (1) calculating health risks and (2) communicating those risks to the public.

Recommendations for Calculating Health Risks

The recommendations for calculating health risks included:

- Refining existing monitoring programs to establish a comprehensive program that addresses current and potential needs for both routine and emergency monitoring data collection
- Improving characterization of contaminated areas to provide defensible estimates of the quantities of chemicals and radionuclides potentially available for release
- Designing and implementing methods for monitoring and data compilation that are based on uses for the data that are collected
- Defining "background," or typical, concentrations of chemicals and radionuclides throughout the site and surrounding area more

comprehensively so that changes in contaminant concentrations in the future can be quickly identified

- Collecting data to understand typical short-term (*e.g.*, hourly or daily) changes in air concentration, which can vary significantly with time of year or season
- Developing and adopting a consistent protocol for compiling data that can be used by all data-collecting organizations to assist with evaluating and disseminating data quickly, efficiently, and comprehensively.

Downloaded by STANFORD UNIV GREEN LIBR on August 8, 2012 | http://pubs.acs.org
Publication Date: November 16, 2006 | doi: 10.1021/bk-2007-0945.ch006

Recommendations for Communicating Health Risks

The recommendations for communicating health risks included:

- Giving the primary responsibility of risk communication to an independent organization that works closely with the agencies involved in the emergency. When there is potential for public risk, the agency that the public views as responsible for the risk should not be the initial or primary source for communicating that risk to the public
- Maintaining a central point for issuing statements about health risk to avoid conflicting messages. Establish a way to reach agreement between agencies about statements that are issued
- Implementing a well-coordinated and practiced emergency response plan that clearly identifies the responsibilities and capabilities of the facility, the state and federal agencies, local communities, and other stakeholders with regard to understanding and communicating risks
- Basing statements about immediate risks and potential future risks on available data only, and identify limitations, such as data gaps or uncertainties. Clearly identify the origin of the risk and the nature of the risk
- Establishing a method to allow environmental monitoring by groups, independent of state and federal agencies, to provide additional confidence in the results obtained by the site and regulatory agencies normally involved in data collection.

In considering these recommendations, it is important to strike a balance between responding to public wishes, working efficiently to calculate and communicate potential risks, and realizing practical limitations on what can be achieved. One key to successfully implementing these recommendations is to involve all stakeholders in developing and adopting new procedures.

LANL is responding to several of the recommendations. For example, during 2005, the Los Alamos Emergency Response Organization was redefined and implemented. It is the first DOE facility to fully implement the National

Incident Management System and uses the newly completed Emergency Operations Center on W. Jemez Road in Los Alamos as its Regional Center.

Conclusions

For the air pathway, exposure to LANL-derived contaminants during the Cerro Grande Fire did not result in a significant increase in health risk over that incurred from the fire itself. The risk of cancer from exposure to radionuclides and metals in and on vegetation that burned was greater than that from radionuclides and chemicals released from contaminated sites at LANL. The vegetation that burned contained naturally occurring chemicals and radioactive materials and radioactive fallout produced during atmospheric tests of nuclear weapons. These materials and the risks they posed are present during any forest fire. The cancer risks were all below the EPA range of acceptable risks of 10^{-6} to 10^{-4}. Hazard quotients from exposure to noncarcinogenic LANL-derived chemicals exceeded the 1.0 level at some locations on LANL property. Potential exposures in the surrounding communities to LANL-derived chemicals that are not carcinogenic were about 10 times lower than generally accepted intakes established by the EPA. The monitoring data suggested that some adverse health effects resulted from breathing high concentrations of particulate matter in the smoke. Such exposures are associated with any forest fire. Deposition of LANL-derived chemicals and radioactive materials from the smoke plume to the soil was minimal based on soil samples collected after the fire.

For the surface water pathway, the potential annual cancer risk was estimated to be less than 3 in 1 million from exposure to any LANL-derived chemical or radionuclide material that may have been carried in the surface water and sediments to the Rio Grande and Cochiti Lake. If exposure to the same concentrations of LANL-derived chemicals or radionuclides materials was assumed to continue for seven years (the time it may take to return to pre-fire vegetation conditions in the area), then the potential cancer risk was greater, but still less than 20 in 1 million. Potential exposures to LANL-derived chemicals that are not carcinogenic were within acceptable intakes established by the EPA. The type of exposure contributing most to the potential risk was eating fish containing benzo(a)pyrene (BaP) and cesium-137 from the Rio Grande.

Overall, the study provided a basis for identifying specific areas at LANL, certain chemicals and radioactive materials, and the most important types of exposure that could contribute to potential risk. More focused attention can be given to refining or increasing available information about those areas, materials, and types of exposure in the future.

Downloaded by STANFORD UNIV GREEN LIBR on August 8, 2012 | http://pubs.acs.org
Publication Date: November 16, 2006 | doi: 10.1021/bk-2007-0945.ch006

References

1. Rood, A. S.; Aanenson, J. W.; Mohler, S. S; McGavran, P. D.; Mohler, H. J.; Grogan, H. A.; Till, J. E. *Analysis of Exposure and Risks to the Public from Radionuclides and Chemicals Released by the Cerro Grande Fire at Los Alamos, Estimated Risks from Releases to Air*; RAC Report No. 3-NMED-2002-FINAL (Rev.1); Risk Assessment Corporation: Neeses, SC, 2002.
2. Rocco, J. R.; Meyer, K. R.; Mohler, H. J.; Aanenson, J. W.; Wilson, L. H.; Rood, A. S.; McGavran, P. D.; Till, J. E. *Analysis of Exposure and Risks to the Public from Radionuclides and Chemicals Released by the Cerro Grande Fire at Los Alamos, Estimated Risks from Releases to Surface Water*; RAC Report No. 4-NMED-2002-FINAL (Rev.1); Risk Assessment Corporation: Neeses, SC, 2002.
3. Mohler, H. J.; Meyer, K. R.; Aanenson, J. W.; Grogan, H. A.; Rocco, J. R.; Till, J. E. *Analysis of Exposure and Risks to the Public from Radionuclides and Chemicals Released by the Cerro Grande Fire at Los Alamos, Calculating and Communicating Risks: Observations and Recommendations*; RAC Report No. 15-NMED-2001-FINAL (Rev.1); Risk Assessment Corporation: Neeses, SC, 2002.
4. Scire, J. S.; Strimaitis, D. G; and Yamartino, R. J. *A User's Guide for the CALPUFF Dispersion Model (Version 5.0)*; Earth Tech, Inc.: Concord, MA, 1999.
5. Sandberg, D. V.; Peterson, J. A. Source strength model for prescribed fires in coniferous logging slash. Presented at the Annual Meeting of the Air Pollution Control Association, Pacific Northwest Section, Portland, OR, Nov 12–14, 1984.
6. Gillette, D. A. On the production of soil wind erosion of soil: effect of wind and soil texture. Presented at the Atmospheric and Gaseous Pollutants ERDA Symposium Series 38, Oak Ridge, TN, 1974; pp. 591–609.

Downloaded by STANFORD UNIV GREEN LIBR on August 8, 2012 | http://pubs.acs.org
Publication Date: November 16, 2006 | doi: 10.1021/bk-2007-0945.ch006

Downloaded by UNIV MASSACHUSETTS AMHERST on August 9, 2012 | http://pubs.acs.org
Publication Date: November 16, 2006 | doi: 10.1021/bk-2007-0945.ch007

Chapter 7

Markov Chain Monte Carlo for Internal Dosimetry on a Supercomputer Cluster

G. Miller, L. Bertelli, T. Little, and R. Guilmette

Los Alamos National Laboratory, MS–E546, Los Alamos, NM 87545

The methods used at Los Alamos for calculating internal dose for plutonium and americium are described. The main method, the ID code, is a straightforward use of Bayes' theorem, evaluated using Markov Chain Monte Carlo. A supercomputer cluster is used to do mass calculations on many cases at once. As an alternative, a single workstation continually does calculations as new bioassay data comes in, spreading out the calculation load over the year. Both methods are being used successfully.

Introduction

Internal dosimetry is concerned with the problem of determining the radiation dose to workers caused by forms of radiation that cannot be measured directly (as with a dosimetry badge). If, for example, the α-emitting nuclide ^{239}Pu is inhaled, it will impart radiation dose to the lungs, and after dissolving will be absorbed to blood and deposited in the bone and liver, imparting dose to these organs. Monitoring for exposure to ^{239}Pu is done by measuring the ^{239}Pu content in various kinds of samples (bioassay), for example, urine, fecal, lung count, etc.

The measurements are interpreted using biokinetic models that describe how ^{239}Pu is transported through the body. The biokinetic models describe how a unit

In Applied Modeling and Computations in Nuclear Science; Semkow, T., et al.;
ACS Symposium Series; American Chemical Society: Washington, DC, 2006.

amount of material taken into the body in a certain way (for example, inhalation) will later in time appear in various bioassay compartments (for example, the lungs, urinary excretion) and how radiation dose will be accumulated in the course of time in the different body organs and tissues.

Standard biokinetic models have been proposed by the International Commission on Radiation Protection (ICRP) (*1,2*).

Given a set of agreed-upon biokinetic models, the inverse problem of internal dosimetry is to use the bioassay measurements to infer if and when intakes may have occurred and the magnitude of the resultant radiation dose to the worker. Intake-based biokinetic models are used to determine the time and amount of intakes and to calculate the 50-year effective whole body dose to the worker (the CEDE, Committed Effective Dose Equivalent) associated with each intake. The process obviously entails considerable uncertainty, so quantitatively assessing uncertainty is also of great importance. For the past decade, we have been pursuing a Bayesian statistical approach to this problem. Other approaches to internal dosimetry involve an expert assessor evaluating each case, as described, for example, in Ref. (*3*).

Downloaded by UNIV MASSACHUSETTS AMHERST on August 9, 2012 | http://pubs.acs.org
Publication Date: November 16, 2006 | doi: 10.1021/bk-2007-0945.ch007

Bayesian Approach to Internal Dosimetry (ID code)

In the problem of internal dosimetry there are M bioassay data y_j taken at times t_j for $j = 1,\ldots, M$. These data are used to determine N possible intakes with amounts ξ_i, biokinetic types l_i, times of intake t_i, for $i = 1,\ldots, N$. The intake times are ordered, so that $t_1 < t_2 < \ldots < t_N$. The domain of time t_i is the time interval Δt_i. That is, t_i is in the interval Δt_i. The intervals Δt_i cover the time domain of all possible intakes in a nonoverlapping and ordered way. The time intervals are usually chosen to be the times between successive bioassay measurements, in which case $N = M - 1$. The time intervals are chosen to be sufficiently small so that the probability of multiple intakes may be neglected in any interval.

Using the notation:

$$Y \equiv \{y_1, y_2, \ldots, y_M\}$$
$$\Xi \equiv \{\xi_1, l_1, t_1, \ldots, \xi_N, l_N, t_N\},$$

the problem is to determine the parameters Ξ from the data Y.

Using Bayes theorem, the probability distribution of Ξ given Y can be immediately written down as

$$P(\Xi \mid Y) \propto P(Y \mid \Xi) P(\Xi), \tag{1}$$

that is, the probability of particular values of the parameters given the data is proportional to the probability of the measured values of the data given the parameters (the likelihood function) times the prior probability of the parameter values.

Downloaded by UNIV MASSACHUSETTS AMHERST on August 9, 2012 | http://pubs.acs.org
Publication Date: November 16, 2006 | doi: 10.1021/bk-2007-0945.ch007

The calculational problem is then to integrate over the full detailed posterior probability distribution function, given by Eq. 1, in order to determine the marginal probability distribution of quantities of interest (for example, some dose quantity of interest). This multi-dimensional integration problem can be solved with the Markov Chain Monte Carlo Method (*4*) using the Metropolis algorithm (*5*). A Markov chain is a sequence of random variables Ξ_k such that Ξ_k depends on its predecessor Ξ_{k-1} and does not depend further on the history of the chain.

The likelihood function $P(Y|\Xi)$ is of the form

$$P(Y\mid\Xi)\propto\exp\left(\sum_{j=1}^{M}L_j(\Xi)\right),$$

because of the assumed independence of the M measurements, where $L_j(\Xi)$ is the log-likelihood function for the j^{th} measurement. Exact numerical calculation of the Poisson or Gaussian/log normal likelihood function is used (*6*).

The prior probability distribution $P(\Xi)$ is taken to be of the form

$$P(\Xi)d\Xi=\prod_{i=1}^{N}P(\xi_i)d\xi_iP(l_i)P(t_i)dt_i,$$

assuming independent probabilities for intake amount, biokinetic type, and time of intake for each intake.

The prior probability distribution of biokinetic types l is a discrete probability distribution over $\{l_1, l_2, \ldots, l_{ni}\}$, usually uniform except that the ICRP-recommended default model is given a higher probability.

The prior probability distribution for ξ_i and t_i depends on whether or not a known incident has occurred in the intake time interval Δt_i. This and other details are discussed elsewhere (*7*).

In the Markov Chain Monte Carlo method, values of the parameters Ξ are moved step-wise around in their multidimensional phase space (each chain iteration is one step) in such a way that the probability of Ξ being in a some region of phase space is proportional to the posterior probability given by Eq. 1. In effect, parameter values are randomly generated from the posterior distribution. Thus, to examine the distribution of some quantity of interest, the quantity is merely calculated for each step of the chain, and a histogram made of the results. Every quantity has a distribution, and this distribution is a direct representation of the uncertainty of the quantity.

The distributions obtained as described above depend, in principle, on the number of chain iterations, the chain starting point and the random number generator seed. The chain needs to be run long enough so these dependencies are minimal. To determine chain convergence, two separate calculations are done, with widely disparate starting points and different random number generator seeds. The results of the two calculations must be sufficiently close for the calculation result to be considered to be "converged". If this is not the case, the chain is run for more iterations.

The Lambda Cluster at Los Alamos

There are a number of computer clusters in use at Los Alamos. Lambda is an unclassified general computing resource. It consists of 328 Intel Pentium 3 processors across 164 compute servers (Compaq DL360s) running Redhat Linux operating system. The processors are 1 Ghz each and every node has 1 GB of memory. Lambda uses a Gigabit Ethernet interconnect.

Lambda uses software called LSF (Load Sharing Facility) version 4.1 to control user jobs, which are submitted using the BSUB command. This software is written by Platform Computing (platform.com). All jobs are submitted to the cluster through queues which provide access to various machine groups, user groups, or resources. LSF schedules and runs jobs, distributing them across the compute nodes using features such as queue or machine limits, queue priorities, processor reservation, and job backfilling to provide efficient utilization of the cluster.

There are three main queues on Lambda, the interactive queue, the large queue (maximum job time 2 days), and the long queue (maximum job time 7 days). The ID code calculations are run in the large queue. Under optimal conditions, about 100 processors are available. A small fraction of the jobs require more than 2 days to complete (most require much less). The long running cases involve hundreds of bioassay data points spanning up to 50 years of work history. The jobs that fail to complete in 2 days are restarted in the long queue, where at most about 30 processors are available.

It has been found that cluster computing is not 100 % reliable, and methods for checking that jobs have completed satisfactorily have been developed. The small fractions of cases with problems are identified, and the calculations rerun.

Using Lambda under optimal conditions, the plutonium and americium internal dosimetry calculations for all employees who have submitted bioassay samples in the past year (some 2000 persons) can be completed in 2 days, with a small handful of cases requiring about a week. Thus, the entire task can be accomplished within one week.

Comparisons with Single Workstation Calculations

The other approach to ID code calculations used at Los Alamos is to use a single desktop workstation that runs calculations whenever new bioassay data become available. A dual 3.6 Ghz processor with hyperthreading is used so that

Downloaded by UNIV MASSACHUSETTS AMHERST on August 9, 2012 | http://pubs.acs.org
Publication Date: November 16, 2006 | doi: 10.1021/bk-2007-0945.ch007

there are 4 effective processors, two of which are used for the ID code (convergence testing requires two runs), and two are available for other purposes. Direct speed comparisons are shown in Table I.

Table I. Processor Speeds Determined From Wall-Clock Comparisons

Processor	*Relative processor speed*
Lambda	1
3.6 Ghz Intel Xeon	2.1
3.6 Ghz Intel Xeon Hyperthread	1.2

In the single-workstation mode of operation, a single dual-processor workstation continually does calculations as new data come in, spreading out the calculational load over the year. This workstation is set up with hyperthreading so it effectively has 4 processors, and therefore allows other work to be done as well. The advantage is a simpler, privately owned computing environment. The disadvantage is that it would be impossible to recalculate all cases in a short time should this be necessary.

A comparison of local calculations with supercomputer calculations is shown in Table II.

Table II. Correlation Coefficient Between Workstation And Supercomputer ID Code Results

Quantity	*Number of cases*	*Correlation coefficient*
CEDE	22079	0.9997
total CEDE	1967	0.9998

The correlation coefficient (see, for example, matheworld.com) is 1 when the two results are exactly equal. Table II shows a comparison for 1967 person, nuclide combinations. The first row shows the year by comparison of calculated CEDE for each of these person-nuclide combinations over all the years covered by the bioassay data. The reason there is any disagreement at all is that the two calculations effectively involve different random number seeds. This is because the Markov Chain Monte Carlo calculation is preceded by another Monte Carlo calculation-of the exact likelihood functions. Since these calculations are usually not done in exactly the same sequence, the random number sequence for the Markov Chain calculation is different.

Downloaded by UNIV MASSACHUSETTS AMHERST on August 9, 2012 | http://pubs.acs.org
Publication Date: November 16, 2006 | doi: 10.1021/bk-2007-0945.ch007

Comparisons with Faster, Approximate Method (UF code)

Another code, the UF or unfolding code, uses an approximate Bayesian method (*8*). The basic calculation is of a single intake, with the bioassay tail from previous intakes subtracted. An iteration process is used to eliminate intakes with large probability of the hypothesis "no intake" or "flatline" interpretation of the data relative to the hypothesis that an intake has occurred as calculated. The UF code uses numerical integration and, because of the necessity of using Gaussian uncertainty propagation in the tail subtraction, does not use the exact likelihood calculation.

The major flaw of the UF code is in the assignment of the times of intakes. The differences between the two codes are illustrated by using the test dataset shown in Fig. 1.

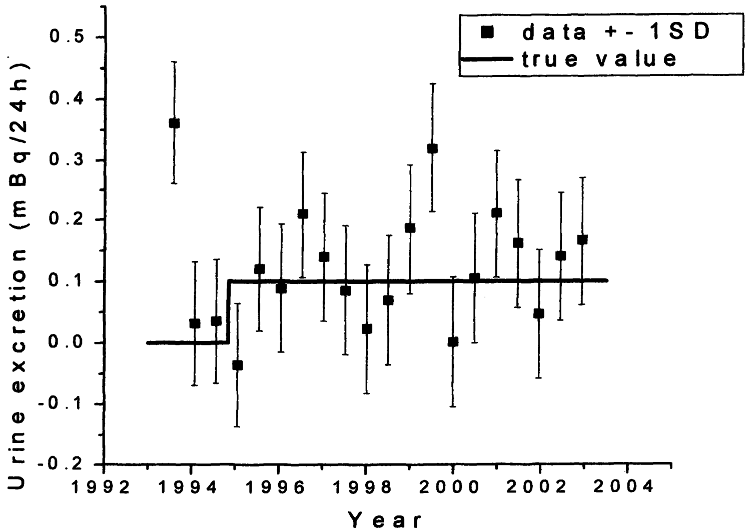

Figure 1. Numerically generated test dataset.

The data are generated from a Gaussian distribution with standard deviation 0.1 mBq/24 hr. After the 3rd data point, the data are shifted upwards by 0.1 mBq/24 hr.

The dose conversion factor from urine excretion a long time after the intake to E(50) (same as CEDE or 50-year whole body effective dose, except using a particular set of tissue weighting factors defined in ICRP publication 60) is about 50 Sv per Bq/24 hr for type S, 5 micron ^{239}Pu, so a urine excretion of 0.1 mBq/24 hr corresponds to a 5 mSv intake.

Downloaded by UNIV MASSACHUSETTS AMHERST on August 9, 2012 | http://pubs.acs.org
Publication Date: November 16, 2006 | doi: 10.1021/bk-2007-0945.ch007

The ID code result for yearly CEDE (50-year effective, whole-body dose) is shown in Fig. 2. As for all quantities, the yearly CEDE's shown in Fig. 2 are obtained from distributions. The grey bars show the 5 % and 95 % probability limits of these distributions, while the dark squares shows the average values. Note that the lower probability limit is very small in all cases, meaning that there is not certainty that an intake occurred in any particular year. In 1997 the average value exceeds the 95 % limit. This is possible for a distribution with greater than 95 % probability concentrated near zero and a small tail. The time of intake is very uncertain.

Downloaded by UNIV MASSACHUSETTS AMHERST on August 9, 2012 | http://pubs.acs.org
Publication Date: November 16, 2006 | doi: 10.1021/bk-2007-0945.ch007

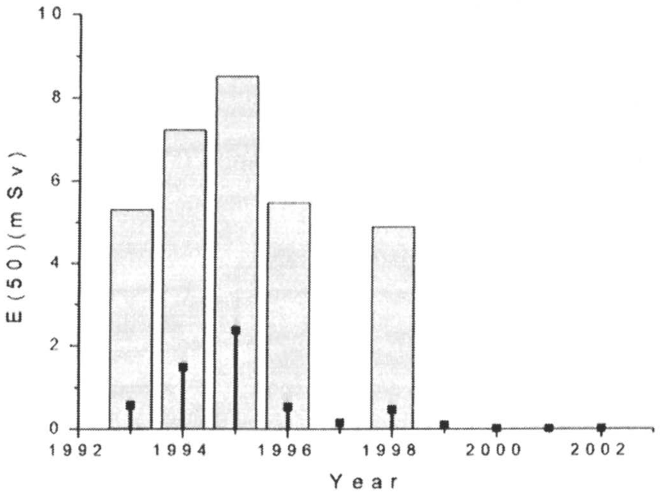

Figure 2. Yearly CEDE's calculated by ID code for test dataset.

The calculations assume an "alpha prior" for intake amount ξ

$$P(\xi) = \frac{\alpha\Delta t}{\xi}\left(\frac{\xi}{A}\right)^{\alpha\Delta t},$$

where Δt is the time interval in which the intakes occur and A is an unimportant normalizing constant, with the probability of intake per year $\alpha = 0.001/\text{yr}$ (*9*), so that the probability of more than one significant intake is small (even though 19 intakes are allowed in the calculation). The distributions of CEDE for different years shown in Fig. 2 are anticorrelated, so that they represent the uncertainty in the time of intake of a single intake rather than uncertainties of multiple intakes.

The prior probability distribution of time of intake is assumed to be uniform in each interval. The biokinetic type prior consists of the 6 biokinetic types for inhalation: dissolution type M and S, and particle size 1, 5, and 10 μm AMAD (Activity Median Aerodynamic Diameter).

The cumulative probability for the total CEDE from all intakes is shown in Fig. 3. As seen from Fig. 3, the total CEDE is calculated to be in the range from 1 to 10 mSv, with a central value near the true value of 5 mSv.

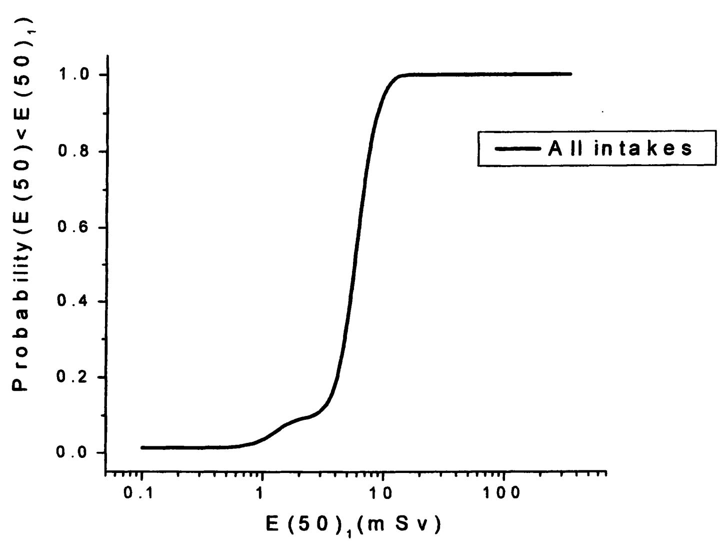

Figure 3. Cumulative distribution of total CEDE, from ID code calculation for test dataset.

The UF code result for this case is shown in Fig. 4. The curve shows the calculated average excretion. The calculated average CEDE is 2 mSv, with credible limits from 0 to 9 mSv. The main error is in the calculated time of intake, and there is no indication of the uncertainty of time of intake using the UF code.

Downloaded by UNIV MASSACHUSETTS AMHERST on August 9, 2012 | http://pubs.acs.org
Publication Date: November 16, 2006 | doi: 10.1021/bk-2007-0945.ch007

Downloaded by UNIV MASSACHUSETTS AMHERST on August 9, 2012 | http://pubs.acs.org
Publication Date: November 16, 2006 | doi: 10.1021/bk-2007-0945.ch007

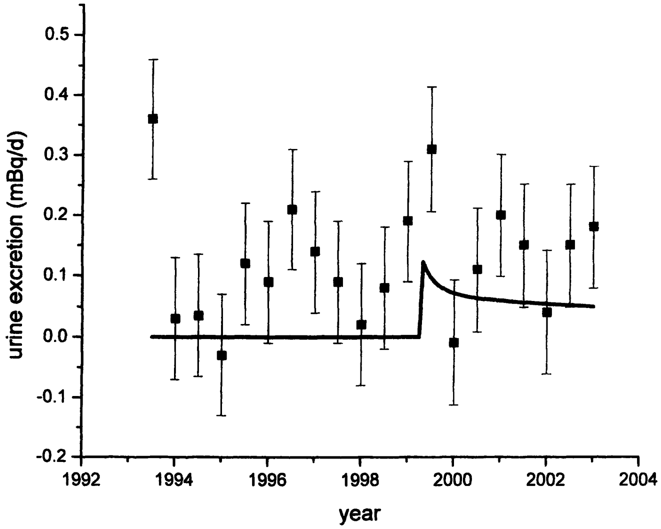

Figure 4. UF code calculation for test dataset.

Nonetheless, the correlation between ID and UF code results is rather good. Table III shows the correlation coefficients for a number of comparisons. Note that the annual dose (for the year of the last bioassay sample) and the total CEDE for all intakes are in very good agreement.

Table III. Correlation Coefficient For ID Code (Lambda) And UF Code Results

Quantity	*Number of cases*	*Correlation coefficient*
CEDE	40777	0.6964
total CEDE	3856	0.9981
annual dose	3856	0.9859

Figure 5 shows a plot of total CEDE from the UF code versus that from the ID code. The year-by-year CEDE is less well correlated. This can be understood from the test case shown in Figs. 1 and 2, where the average CEDE from the ID code is quite different from the UF code result. This agreement is really quite remarkable in that the numerical methods are completely different, and the UF code does not use the exact likelihood calculation.

Downloaded by UNIV MASSACHUSETTS AMHERST on August 9, 2012 | http://pubs.acs.org
Publication Date: November 16, 2006 | doi: 10.1021/bk-2007-0945.ch007

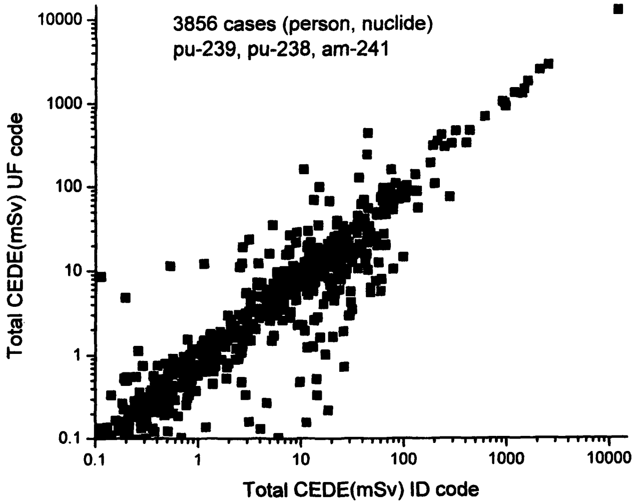

Figure 5. Comparison of total CEDE from ID and UF codes.

Discussion

The methods in use at Los Alamos for calculation of internal dose for plutonium and americium have been described. Statistical inference based on Bayes' theorem is used. Some advantages of this approach are the following:

1. It is scientifically defensible; indeed, it is definitive.
2. Professional judgment and prior knowledge are not mixed up with statistical science; they are confined to defining or specifying the prior probability distributions.
3. The full information content of the bioassay measurements is utilized; the exact likelihood calculations focus attention on the measurement science.
4. The uncertainty of yearly CEDE is often very large; this uncertainty is directly calculated.
5. Inexpensive batch processing of large numbers of cases is possible.

Straightforward parallel processing, one case to each processor, is used on a supercomputer cluster for mass calculations of large numbers of cases. As an alternative, a single workstation continually does calculations as new bioassay data comes in, spreading out the calculational load over the year. Both methods are being used successfully.

Comparisons between the ID and UF codes show excellent agreement and serve as a validation of both codes, since completely different numerical methods are used in each code.

The yearly CEDE often has a very large uncertainty. This is an unavoidable fact. It is perhaps a problem that current regulations are based on yearly CEDE rather than, say, total CEDE or annual dose, which was used before 1992. The agreement between the ID and UF codes shows that total CEDE and annual dose are easier to calculate using approximate methods; furthermore, they have much smaller uncertainties.

Downloaded by UNIV MASSACHUSETTS AMHERST on August 9, 2012 | http://pubs.acs.org
Publication Date: November 16, 2006 | doi: 10.1021/bk-2007-0945.ch007

References

1. *Individual Monitoring for Intakes of Radionuclides by Workers: Design and Interpretation*; ICRP Publication 54; Vol. 19 of Annals of the International Commission on Radiation Protection; Pergamon Press: Oxford, 1988.
2. *Individual Monitoring for Intakes of Radionuclides by Workers: Replacement of ICRP Publication 54*; ICRP Publication 78; Vol. 27 of Annals of the International Commission on Radiation Protection; Pergamon Press: Oxford, 1998.
3. Marsh, J. W.; Baily, M. R.; Birchall, A. A step-by-step procedure to aid the assessment of intake and doses from measurement data. *Radiation Protection Dosimetry* **2005**, *114*, 491-508.
4. Gilks, W. R.; Richardson, S.; Spiegelhalter, D. J. *Markov Chain Monte Carlo in Practice*; Chapman and Hall: New York, NY, 1996.
5. Metropolis, N.; Rosenbluth, A. W.; Rosenbluth, M. N.; A. H. Teller; E. Teller. Equation of state calculation by fast computing machines. *J. Chem. Phys.* **1953**, *21*, 1087-1092.
6. Miller, G.; Martz, H. F.; Little, T. T.; Guilmette, R. Using exact Poisson likelihood functions in Bayesian interpretation of counting measurements. *Health Phys.* **2002**, *83*, 512-518.
7. Miller, G.; Martz, H. F.; Little, T. T.; Guilmette, R. Bayesian internal dosimetry calculations using Markov chain Monte Carlo. *Rad. Prot. Dosimetry* **2002**, *98*, 191-198.
8. Miller, G.; Inkret, W. C.; Martz, H. F. Internal dosimetry intake estimation using Bayesian methods. *Rad. Prot. Dosimetry* **1999**, *82*, 5-17.
9. Miller, G.; Inkret, W. C.; Little, T. T.; Martz, H. F.; Schillaci, M. E. Bayesian prior probability distribution for internal dosimetry. *Rad. Prot. Dosimetry* **2001**, *94*, 347-352.

Downloaded by UNIV OF ARIZONA on August 8, 2012 | http://pubs.acs.org
Publication Date: November 16, 2006 | doi: 10.1021/bk-2007-0945.ch008

Chapter 8

Calculation of the External Effective Dose from a Radioactive Plume by Using Monte Carlo Dose Kernel Integration

P. Vojtyla

CERN, European Organization for Nuclear Research, Safety Commission, CH–1211 Geneva 23, Switzerland

The radiological impact of emissions of radioactive substances from accelerator facilities is characterized by a dominant contribution of the external exposure from short-lived radionuclides in the plume. Ventilation outlets of accelerator facilities are often at low emission heights and receptors reside very close to stacks. Simplified exposure models are not appropriate and integration of the dose kernel over the radioactive plume is required. By using Monte Carlo integration with certain biasing, the integrand can be simplified substantially and an optimum spatial resolution can be achieved. Moreover, long-term releases can be modeled by sampling real weather situations. The mathematical formulation does not depend on any particular atmospheric dispersion model and the applicable code parts can be designed separately, which is another advantage. The obtained results agree within ±10 % with results calculated for the semi-infinite cloud model by using detailed particle transport codes and human phantoms.

In Applied Modeling and Computations in Nuclear Science; Semkow, T., et al.;
ACS Symposium Series; American Chemical Society: Washington, DC, 2006.

Introduction

The effective dose to members of the public due to airborne releases of radioactive substances from accelerator facilities is dominated by the external exposure to photon radiation of several short-lived radioactive gases such as the β^+ radionuclides ^{11}C, ^{13}N, ^{14}O and ^{15}O (511 keV annihilation photons) and the β^- radionuclide ^{41}Ar (1294 keV gamma rays).

Dose conversion factors that were calculated for human phantoms submerged in a semi-infinite cloud of air containing various radionuclides can be found in the literature (see for example Reference (*1*)). They are used for situations typical around a nuclear power plant site, where members of the public reside sufficiently far away from the plant's stack so that the radionuclide concentrations in air can be considered as homogeneous. Such factors can lead to serious overestimations or even serious underestimations around a facility, where members of the public reside very close to a ventilation outlet (~100 m) that is often a short stack not exceeding much the height of an air-extraction building. The mean free path of a 511 keV photon in air of 90 m is comparable with the distance of the receptor to the source and usually longer than typical plume widths at short distances. It is clear that the semi-infinite cloud model is not appropriate in this case and that the shape of the radioactive plume must be taken into account to obtain realistic results.

The procedure to be applied in such geometry is integration of the dose kernel over the radioactive plume, which leads to a numerical calculation of a three-dimensional integral from a complicated function describing the pollutant dispersion in the atmosphere. This chapter presents a method based on a Monte Carlo approach that gives a satisfactory approximation for the integral values, provided sufficient number of Monte Carlo events is processed, and overcomes some principal difficulties of a fixed-grid integral. In addition it is faster in most cases, especially for long-term releases for which averaged radionuclide concentrations derived from weather statistics enter the integrand.

Downloaded by UNIV OF ARIZONA on August 8, 2012 | http://pubs.acs.org
Publication Date: November 16, 2006 | doi: 10.1021/bk-2007-0945.ch008

External Exposure from a Radioactive Plume

The expression for the dose kernel integral due to photon radiation from a radionuclide distributed in air around a human body is derived from basic principles and has the following form:

$$D_\gamma = Q\frac{\varepsilon}{\rho_{\mathrm{air}}}\frac{1}{4\pi}\sum_i e_{\mathrm{kerma}}(E_i)\mu_{\mathrm{a},i}E_i I_i \int \frac{B(E_i,\mu_i r)\exp(-\mu_i r)\chi(\mathbf{r})}{r^2}d^3\mathbf{r}, \quad (1)$$

where

D_γ = effective dose (Sv),

In Applied Modeling and Computations in Nuclear Science; Semkow, T., et al.;
ACS Symposium Series; American Chemical Society: Washington, DC, 2006.

Q = released activity (Bq),

ε = 1.602×10^{-13} J MeV^{-1}, conversion coefficient from MeV to J,

ρ_{air} = air density (kg m^{-3}),

$e_{\mathrm{kerma}}(E_i)$ = conversion coefficient for the isotropic external exposure (kerma-in-free-air to effective dose) for the photon energy E_i and the given age group (Sv Gy^{-1}),

$\mu_{\mathrm{a},i}$ = linear energy *absorption* coefficient in the air with the density ρ_{air} for the photon line i (m^{-1}),

E_i = energy of the photon line i (MeV),

I_i = intensity of the photon line i (absolute, i.e. 1 for 100%),

μ_i = linear *attenuation* coefficient in the air with the density ρ_{air} for the photon line i (m^{-1}),

r = distance of the volume element $d^3\mathbf{r}$ from the receptor (m),

$B(E_i, \mu_i r)$ = dose build-up factor as a function of the energy E_i of the photon line i and the number of mean free paths from the volume element $d^3\mathbf{r}$ to the receptor $\mu_i r$,

$\chi(\mathbf{r})$ = dispersion factor at a place with a radius vector $\mathbf{r}$ (s m^{-3}).

The receptor is positioned in the origin of the coordinate system. The activity concentration of the radionuclide at the point $\mathbf{r}$ is a product of the release rate $\dot{Q}$ (Bq s^{-1}) and the dispersion factor $\chi(\mathbf{r})$. The dose rate generated by the plume can be integrated in time, resulting in the dose value. Under stationary release conditions, the dose rate integration reduces to the release rate ($\dot{Q}$) integration resulting in the released activity Q. Each air volume element $d^3\mathbf{r}$ is a source of exposure into which all photon energy lines E_i contribute with the intensities I_i. The energy emitted from a volume element $d^3\mathbf{r}$ may be absorbed in the air around the receptor, giving rise to a dose absorbed in air, which is proportional to $\mu_{\mathrm{a},i}/\rho_{\mathrm{air}}$. The probability that an emitted photon will reach the receptor decreases with the distance to the volume element $d^3\mathbf{r}$ following the $1/r^2$ rule and it is proportional to the photon attenuation in air $\exp(-\mu_i r)$. The dose build-up factor B accounts for the indirect exposure, for example through multiple Compton scattering in air of the emitted photons. To estimate the *effective* dose to a human, the dose absorbed in air is multiplied by the conversion coefficient e_{kerma} that depends on the photon energy and the

Downloaded by UNIV OF ARIZONA on August 8, 2012 | http://pubs.acs.org
Publication Date: November 16, 2006 | doi: 10.1021/bk-2007-0945.ch008

receptor's age. The difference between the dose absorbed in air and the kerma-in-free-air can be neglected in this case. The linear absorption and attenuation coefficients are shown for the standard temperature and pressure (STP[1]) air in Fig. 1.

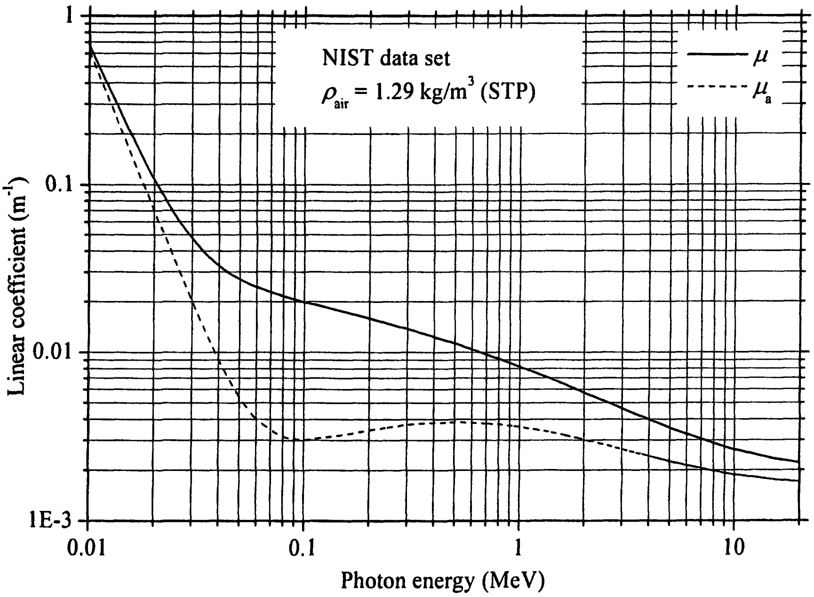

Figure 1. Linear photon attenuation and absorption coefficients for air with the standard temperature and pressure[1] (STP). Based on data from the Reference (2).

The dose build-up factors can be interpolated from values determined by Chilton et al. (*3*) in a Monte Carlo simulation. A simpler approach is to use linear build-up factors $B_{\text{lin}}(E,\mu r)=1+k\mu r$ in which the linear coefficient k depends on the photon energy through the photon attenuation and absorption coefficients, μ and μ_a, respectively: $k=(\mu-\mu_a)/\mu_a$. It can be derived from an energy equilibrium consideration (*4*). The coefficient k increases fast with the photon energy, reaches its maximum of 5.9 at 80 keV, and then it decreases rapidly to values below 1 beyond 1.6 MeV. The build-up factors from the reference (*3*) are about 20 % higher for photon energies around 100 keV but very close to the linear build-up factors for other energies.

---

[1] 273.15 K (0°C), 1.013 × 10^5 Pa.

Downloaded by UNIV OF ARIZONA on August 8, 2012 | http://pubs.acs.org
Publication Date: November 16, 2006 | doi: 10.1021/bk-2007-0945.ch008

The conversion coefficients e_{kerma} for adults can be taken from the ICRU Report 57 (*5*). Data for other age groups calculated by Yamaguchi are provided in the reference (*6*). In accordance with the recommendation of the ICRU, the isotropic irradiation geometry (ISO) shall be considered for this type of problem. Figure 2 compares the data set for adults from the reference (*5*) with the data sets for one-year old infants and adults from the reference (*6*). One can see strong photon energy dependence only for photons with energies below about 0.1 MeV.

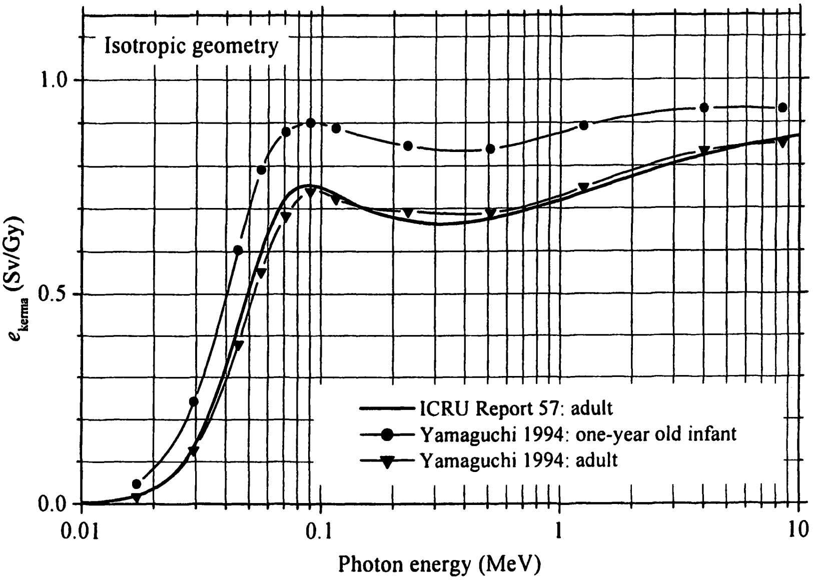

Figure 2. Conversion coefficients for the external exposure (5, 6).

Equation 1 does not take into account the bremsstrahlung radiation in air of electrons emitted during beta decay that can be neglected for strong photon emitters. However, the method shall be used with care for radionuclides emitting only rare and/or very low-energy photons such as ^{85}Kr.

The contribution of the skin dose due to electrons to the effective dose, D_β, can be obtained easily by using radionuclide-specific dose conversion factors e_{skin} from the reference (*1*) calculated for a semi-infinite cloud. The skin organ dose weighting factor of 0.01 defined in the ICRP Publication 60 (*7*) is applied:

$$D_\beta = 0.01 \times Q\chi_{\mathrm{rec}} e_{\mathrm{skin}} \,. \qquad (2)$$

The symbol χ_{rec} in Eq. 2 denotes the dispersion factor at the receptor's position. The range of beta radiation in air does not exceed several meters so that the spatial variations of the activity concentration in the plume can be neglected. For

Downloaded by UNIV OF ARIZONA on August 8, 2012 | http://pubs.acs.org
Publication Date: November 16, 2006 | doi: 10.1021/bk-2007-0945.ch008

radionuclides with strong photon radiation, D_β makes less than few per cent of D_γ.

The numerical calculation of the integral in Eq. 1 in a fixed grid of space elements poses problems concerning the required computing power and it has also some principal difficulties. A simplification was suggested by Overcamp and Fjeld (*4*) that works, however, only with dispersion factors and dose build-up factors having the specific mathematical forms: the Gaussian plume model and the linear dose build-up mentioned above, respectively. It is not straightforward to decide to what *longest* distance from the receptor the integration shall be limited (how many mean free paths) or what integration grid is most suitable. Furthermore, if a Cartesian coordinate system is used, a singularity at $r \to 0$ occurs and it is not straightforward to decide to what *shortest* distance from the receptor the integration shall be limited. The singularity can be removed by integrating in the polar coordinate system but the transformations from the Cartesian system to the polar system take computing time if the Gaussian plume model, which is formulated in the Cartesian coordinate system, is used.

A solution to these difficulties is avoiding a fixed grid by using a Monte Carlo integration method in which integration points are sampled randomly from continuous distributions. For radiation protection purposes, statistical uncertainties inherent to this method are fully acceptable if they do not exceed few per cent.

Monte Carlo integration

An integral

$$\int \frac{e^{-\mu r} f(\mathbf{r})}{r^2} d^3\mathbf{r} \tag{3}$$

can be transformed into polar coordinates:

$$\int\limits_{\Omega} \int\limits_{0}^{\infty} e^{-\mu r} f(\mathbf{r}) d\Omega dr, \tag{4}$$

where $d\Omega$ is the solid angle element, and integrated by using a Monte Carlo method with biasing the length of the radius vector length r. Assuming $\mathbf{r}$ generated isotropically so that the radius vector length r follows the probability distribution $dP/dr = \mu e^{-\mu r}$, the integral transforms to a discrete sum

$$\frac{4\pi}{\mu} \frac{1}{N} \sum_{j=1}^{N} f(\mathbf{r}_j), \tag{5}$$

Downloaded by UNIV OF ARIZONA on August 8, 2012 | http://pubs.acs.org
Publication Date: November 16, 2006 | doi: 10.1021/bk-2007-0945.ch008

where N is the total number of the Monte Carlo events and $\mathbf{r}_j$ is the j^{th} generated radius vector. The length of the radius vector r can be generated by using a simple formula: $r = -\ln[U(0,1)]/\mu$ with $U(0,1)$ being a number from a series of random numbers uniformly distributed in the interval $(0,1)$. The dose D_γ is then expressed in terms of Monte Carlo events as

$$D_\gamma = Q\frac{\varepsilon}{\rho_{\text{air}}}\sum_i\left[e_{\text{kerma}}(E_i)\frac{\mu_{\text{a},i}}{\mu_i}E_iI_i\frac{1}{N}\sum_{j=1}^{N}B(E_i,\mu_ir_j)\chi(\mathbf{r}_j)\right]. \tag{6}$$

It is assumed in Eq. 6 that the receptor can be anywhere and hence the radius vectors $\mathbf{r}_j$ are sampled from the whole space around it. In practice, the receptor is usually on the ground level and the dispersion factor χ below it is zero by definition. In this case, it is sufficient to sample the radius vector $\mathbf{r}$ only from the half-space above the ground level, saving the computing time and the random numbers, but the formula in Eq. 6 must be divided by 2.

For long-term release scenarios, the dispersion factor is sampled according to the distribution of weather situations with the probability of a given situation to occur. The Monte Carlo integration then resembles more an analog Monte Carlo simulation. Dispersion factors for very rare weather situations need not to be computed always, as it is the case of the integration with a fixed grid, when the average dispersion factor must be calculated for each volume element. This is another important advantage of the Monte Carlo integration.

At CERN we use the standard Gaussian plume model with atmospheric stability classes defined by the scheme of Pasquill and Gifford (*8*). A weather situation is characterized by the average wind speed, the average wind direction and the atmospheric stability class. We use 20 wind-speed bins, 72 wind sectors and 6 stability classes. The two former parameters are randomly sampled within their bins so that their distributions are smooth.

The convergence of the Monte Carlo integral was carefully studied for various conditions. The integral converges slower for situations with more inhomogeneous integrands, like for

- Narrow plumes,
- Receptors placed off-side the plume,
- Photon energies around 0.1 MeV, where the build-up factor changes at highest with the number of photon mean free paths,
- Radionuclides with too short half-lives ($T_{1/2} < 1\text{ min}$),
- Receptors placed very close to the source.

For short-term releases characterized by a single Gaussian plume and for receptors placed in the plume, an acceptable convergence usually occurs after

Downloaded by UNIV OF ARIZONA on August 8, 2012 | http://pubs.acs.org
Publication Date: November 16, 2006 | doi: 10.1021/bk-2007-0945.ch008

10^6 events. For long-term releases and receptors placed in a zone affected by frequent winds, at least 10^7 events are usually needed. Processing of 10^6 events lasts several seconds on presently available desktop personal computers (code written in Compaq FORTRAN for PC, double precision). The result should be handled with care if no reasonable convergence is achieved after more than 10^9 events. This may indicate unsuitable receptor position and the case should be dealt with by using a different method.

In practice we apply a simple convergence criterion to accept a result. The final value of the integral is considered to be the best estimate. The relative deviations of the integral values after ½ and ¾ of the total Monte Carlo events were processed are reported. Both the relative deviations should be smaller than few per cent and the ¾ deviation shall be smaller than the ½ one. More sophisticated criteria can be developed but the described one has proven to be satisfactory.

A considerable acceleration of the code can be reached by grouping too numerous photon lines into energy bands limited by energies E_m that are distributed uniformly on the logarithmic energy scale. Single photon energy is assigned to each band, which is an intensity-weighted average energy. The total intensity of all included photon lines is assigned to that average energy. Good results were obtained with $E_m = E_{m0}(1+a)^m$, where $E_{m0} = 0.01$ MeV and $a = 0.2$. Usually no more than 15 energy bands are needed for a single radionuclide. For example, 42 known gamma lines of ^{40}Cl ranging from 0.26 MeV to 6.5 MeV (*9*) can be reduced to 18 gamma lines. The difference between the results obtained with the exact gamma line definition and the one described above was smaller than 2 % in typical cases and could be attributed to statistical fluctuations of Monte Carlo integrals.

Verification

The correctness of the Monte Carlo integration described in this chapter was tested through comparisons of its results with results of fixed-grid integration in fine spatial grids for various situations that may occur in practice. The results of both the methods were coherent proving the mathematical correctness of Eq. 6 and the computer code.

However, the model was also verified in its radioprotection aspect by comparing its results for a semi-infinite cloud with results obtained for this exposure geometry by using dose conversion factors from the literature. To simulate a semi-infinite cloud with a constant activity concentration, the dispersion factor was forced to a constant value in the computer code. Dose conversion factors were taken from two references: (a) the US EPA Report 402-

Downloaded by UNIV OF ARIZONA on August 8, 2012 | http://pubs.acs.org
Publication Date: November 16, 2006 | doi: 10.1021/bk-2007-0945.ch008

R-93-081 (*1*), and (b) the Swiss directive HSK-R-41 (*10*). In the former reference, dose conversion factors for an adult phantom and a large number of radionuclides are computed in a very detailed way. The dosimetric quantity calculated in the US EPA report is the *effective dose equivalent* in the sense of the ICRP Publication 26 (*11*), whilst the directive HSK-R-41 provides values for the *effective dose* as defined in the ICRP Publication 60 (*7*)[2]. The two dosimetric quantities agree well for the external exposure, however (*1*).

Figure 3 shows values of the effective dose and effective dose equivalent per released activity expressed in µSv/TBq for a number of radionuclides with increasing energy of emitted photons, from ^{241}Am (14 keV X-rays, 26 keV and 60 keV gamma rays), through the positron emitters ^{11}C, ^{13}N and ^{15}O (511 keV annihilation photons), up to ^{24}Na (1.40 MeV and 2.75 MeV gamma rays). Note that ^{241}Am is an alpha emitter for which the dominating exposure pathway is inhalation. It was included in the test because it emits low-energy photons and dose conversion factors for the external exposure are available in the literature for this common radionuclide. The doses calculated by using the Monte Carlo dose kernel integration model $D_\gamma + D_\beta$ agree within ±10 % with those derived from the dose conversion factors from the literature, whilst the dose conversion factors from the literature differ by as much as 20 %. Such accuracy is sufficient for radioprotection purposes.

It seems that Eq. 1 systematically overestimates for radionuclides emitting photons with low energies (^{241}Am, ^{57}Co), probably due to the factorization of the kerma-in-free-air to effective dose conversion coefficients and the dose build-up factors in air. Note that the conversion coefficients decrease rapidly with photon energy below 0.1 MeV (Fig. 2). The dose built up from secondary processes like Compton scattering in air is due to photons with lower energies than the original photon energy, yet a greater conversion coefficient for the original photon energy is applied. Nevertheless, such behavior is acceptable because it is conservative and because the external exposure is less important for radionuclides emitting low-energy photons (Fig. 3, note the logarithmic scale).

Downloaded by UNIV OF ARIZONA on August 8, 2012 | http://pubs.acs.org
Publication Date: November 16, 2006 | doi: 10.1021/bk-2007-0945.ch008

---

[2] *Effective dose equivalent* is the weighted average of the annual dose equivalents, each weighted by a tissue or organ weighting factor. The dose equivalent is the product of the quality factor and absorbed dose in the tissue or organ. *Effective dose* is the weighted average of equivalent doses, each weighted by the appropriate tissue weighting factor. The equivalent dose is the dose absorbed in an organ or tissue multiplied by the relevant radiation weighting factor. Although the mathematical formulations of the two dosimetric quantities are similar, the classifications of organs and tissues, tissue weighting factors, quality factors and radiation weighting factors are different. To avoid confusion, the ICRP used different names for the dosimetric quantities.

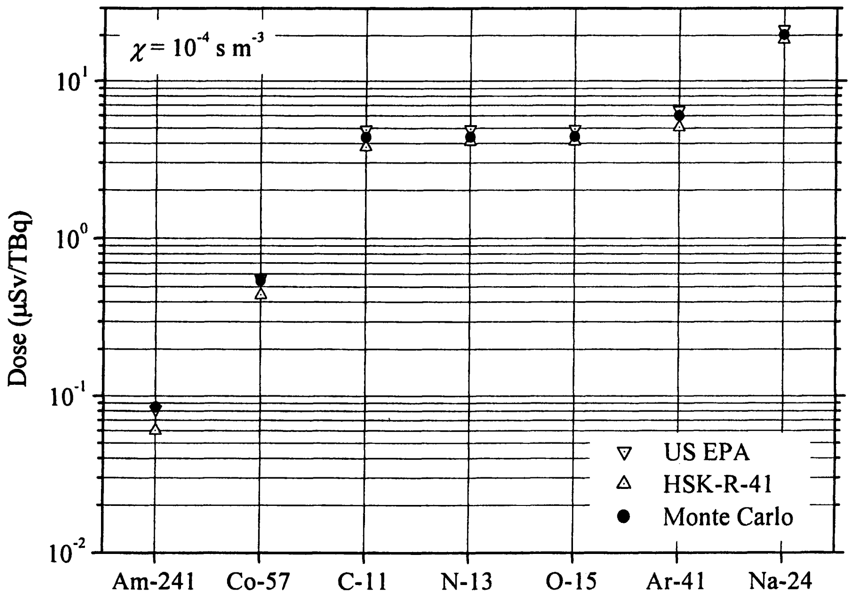

Figure 3. Comparison of results for semi-infinite cloud irradiation geometry obtained with dose conversion factors from the literature and with the Monte Carlo integration.

Conclusions

The presented Monte Carlo dose kernel integration method for calculating the external dose from a radioactive plume is fast and its uncertainties are acceptable. Its mathematical formulation does not depend on any particular atmospheric dispersion model and can be applied to more sophisticated dispersion models that could be developed in the future. The method is suitable for places downwind of ventilation outlets. Difficulties may occur at off-wind places but these are usually out of the area of concern because the exposure at such places is considerably lower then downwind. The method shall be used with care for radionuclides emitting hard beta radiation and photon radiation with too small intensity and/or energy.

The development of the method was motivated by difficulties encountered at accelerator facilities but the method can be applied to any similar problem, like ventilation outlets of a uranium mine.

Downloaded by UNIV OF ARIZONA on August 8, 2012 | http://pubs.acs.org
Publication Date: November 16, 2006 | doi: 10.1021/bk-2007-0945.ch008

Although the integrand is a complicated function of many variables, all parts can be programmed separately as functions or subroutines and tested thoroughly. The Monte Carlo loop is, however, very simple (several code lines) so that programming errors are improbable to occur. In the end, the complete program can be easily verified by running it for the semi-infinite cloud geometry so that a validated code is obtained.

Acknowledgements

Parts of the codes used in this work were written by L. Moritz and I.A. Kourotchkine. Valuable discussions with Th. Otto and H.G. Menzel are highly acknowledged as well.

Downloaded by UNIV OF ARIZONA on August 8, 2012 | http://pubs.acs.org
Publication Date: November 16, 2006 | doi: 10.1021/bk-2007-0945.ch008

References

1. Eckerman, K. F.; Ryman, J. C. *External exposure to radionuclides in air, water, and soil*; US EPA Report 402-R-93-081; U.S. Environmental Protection Agency: Oak Ridge, TN, 1993; pp. 5-7, 57-73.
2. http://physics.nist.gov/PhysRefData/.
3. Chilton, A. B.; Eisenhauser, C. M.; Simons, C. L. *Nucl. Sci. Eng.* **1980**, *73*, 97-107.
4. Overcamp, T. J.; Fjeld, R. A. *Health Phys.* **1983**, *44*, 367-372.
5. *Conversion Coefficients for use in Radiological Protection Against External Radiation*; ICRU Report 57; International Commission on Radiation Units and Measurements: Bethesda, MD, 1998; pp. 21, 109.
6. Yamaguchi, Y. *Rad. Prot. Dosimetry* **1994**, *55*, 123-129.
7. *1990 Recommendations of the International Commission on Radiological Protection*; ICRP Publication 60; International Commission on Radiological Protection; *Annals of the ICRP* **1991**, *21*, pp. 79-86.
8. *Atmospheric Dispersion in Nuclear Power Plant Siting*; IAEA Safety Guide No. 50-SG-S3; International Atomic Energy Agency: Vienna, 1980, pp. 17-56.
9. http://www.nndc.bnl.gov/nudat2/.
10. *Berechnung der Strahlenexposition in der Umgebung aufgrund von Emissionen radioaktiver Stoffe aus Kernanlagen*; HSK-R-41/d; Hauptabteilung für die Sicherheit der Kernanlagen (HSK): Villigen, 1997; pp. A5-1 - A5-2.
11. *Recommendations of the International Commission on Radiological Protection*; ICRP Publication 26; International Commission on Radiological Protection; *Annals of the ICRP* **1977**, *1*, pp. 3-13.

Downloaded by PENNSYLVANIA STATE UNIV on August 9, 2012 | http://pubs.acs.org
Publication Date: November 16, 2006 | doi: 10.1021/bk-2007-0945.ch009

Chapter 9

Modeling of Human Anatomy for Radiation Dosimetry: An Example of the VIP–Man Model

X. George Xu

Nuclear and Biomedical Engineering, Rensselaer Polytechnic Institute, Troy, NY 12180

Radiation transport calculations to determine the dose in various organs of the human body for radiation protection of workers rely on a model or models of the human anatomy. We have developed the VIsible Photographic (VIP)-Man model from segmented and labeled Visible Man cadaver image set containing about 100 radio-sensitive organs and tissues. The voxel size is 0.33 mm x 0.33 mm x 1.0 mm and the whole-body contains about 3.7 billion voxels. The VIP-Man model has been coupled with various Monte Carlo codes to simulate occupational and medical exposure scenarios. Recently, a preliminary study has developed a 4D version of the VIP-Man model to account for respiratory and cardiac motions. This chapter discusses the history of the modeling and future issues to be addressed.

1. Introduction

Modern radiation dosimetry depends increasingly on human anatomical modeling and radiation transport simulation. A worker can be routinely or accidentally exposed to an internal and/or external ionizing radiation source as a result of radiological contamination. Similarly, a cancer patient is irradiated by

In Applied Modeling and Computations in Nuclear Science; Semkow, T., et al.;
ACS Symposium Series; American Chemical Society: Washington, DC, 2006.

seeds. Assessment of radiation doses for radiation protection purposes relies largely on a few sets of basic dosimetric quantities that are derived from whole-body human models. For example, the fluence-to-dose-equivalent conversion factors for various organs are the basis for designing radiological facilities and for calculating dose to a worker/patient exposed to radiation external to the body (*1*). For assessing dose to target organs due to radionuclides internally deposited in the source organ(s) following an accidental intake or a nuclear medicine procedure, the specific absorbed fractions (SAFs) or the specific effective energies (SEEs) are used (*2-4*). The whole-body radiation cancer risk can then be assessed by using ICRP methodologies for effective dose or effective dose equivalent (*3,5*). The conversion factors and SAFs have been pre-determined using full-body human anatomical models and Monte Carlo calculations. Radiation treatment planning involving Monte Carlo simulation is performed using patient-specific images covering a portion of the body. These dosimetric tasks involve careful specification of the human body geometry and the irradiation conditions (radiation energy and direction etc). Radiation transport and energy deposition in the body are often calculated using a Monte Carlo code. It is apparent that the accuracy of these dosimetric quantities (and others derived from them) depends upon the modeling of the body, radiation environment, and Monte Carlo radiation transport. Recently, there has been a paradigm shift in the way human models are developed for radiation protection dosimetry. This chapter summarizes the latest effort in the human modeling for radiation simulations.

Computational models of the human body for radiation protection dosimetry have evolved into two types: 1) Equation-based stylized models, where organs are delineated by a combination of simple surface equations, and 2) Image-based tomographic models, in which organs are defined from segmented and labeled volume elements (voxels) from tomographic images of real individuals. An emerging third type of the models uses a hybrid method.

Stylized Models

Early models representing the human body were mostly homogeneous slabs, cylinders, and spheres. The first heterogeneous anthropomorphic model was devised at Oak Ridge National Laboratory for the Medical Internal Radiation Dose (MIRD) Committee of The Society of Nuclear Medicine (*4,6,7*). This model, known as MIRD Phantom, was based on the "Reference Man" for radiation protection purposes (*8*). Reference Man was defined as a 20-30 year old Caucasian, weighing 70 kg and 170 cm in height. The original MIRD phantom was analytically described in three principal sections: an elliptical cylinder representing the arm, torso, and hips; a truncated elliptical cone

Downloaded by PENNSYLVANIA STATE UNIV on August 9, 2012 | http://pubs.acs.org
Publication Date: November 16, 2006 | doi: 10.1021/bk-2007-0945.ch009

representing the legs and feet; and an elliptical cylinder representing the head and neck, as shown in the Fig. 1.

The stylized mathematical descriptions of the organs were formulated based on descriptive and schematic materials from general anatomy references. The goal of this approach was to make the equations simple, thus minimizing computing time. For example, the stomach wall (the football shape in Fig. 1c) is defined as the volume between two concentric ellipsoids (*9*):

$$\left(\frac{x-x_0}{a}\right)^2+\left(\frac{y-y_0}{b}\right)^2+\left(\frac{z-z_0}{c}\right)^2\le 1,\text{and}\left(\frac{x-x_0}{a-d}\right)^2+\left(\frac{y-y_0}{b-d}\right)^2+\left(\frac{z-z_0}{c-d}\right)^2\ge 1.$$

The mathematical descriptions of the organs were formulated based on descriptive and schematic materials from general anatomy references. The goal was to make the mathematical equations simple, thus minimizing computation time (*4,10,11*). More than 40 organs and tissues were specified, with basically three media of distinct densities: bone, soft tissue, and lung. Later improvements at Oak Ridge National Laboratory have led to a "family" of models having both genders at various ages (*9*). Others have developed similar models known as the "Adam" and "Eva" (*12*). One of the most recent improvements is a newly revised head and brain model (*13*). These MIRD-based models have served practically as the "standard" to radiation protection dosimetry community. For a comprehensive listing of papers and discussions on the earlier models, the readers are referred to ICRU Report 48 (*14*) and ICRP Publication 74 (*11*). For more than two decades, MIRD-based mathematical models allowed the radiation protection community to gain important insights into the distribution of organ doses that were difficult or impossible to study with physical phantoms.

It is clear, however, that the human anatomy is too complex to be realistically modeled with a limited set of equations. As such, many anatomical details in the mathematical models had to be compromised. In spite of the effort to develop more complicated mathematical models, they remain simplified and crude. For instance, the skeleton in the stylized adult male model does not resemble a human, and the radiosensitive red bone marrow is not represented. Many researchers have begun to realize that today's computers are so powerful that it is technically no longer necessary to limit the geometry representation to overly simplified shapes.

Tomographic Models

In the past decade, a new class of computational models has emerged with the advent of 3D tomographic imaging. These models contain large arrays of voxels that are identified in terms of tissue type (soft tissue, hard bone, air, etc) and unique organ identification (lungs, liver, skin, etc). 3-D medical imaging techniques, such as Computed Tomography (CT) and Magnetic Resonance Imaging (MRI), have advanced remarkably, allowing us to easily visualize the

Downloaded by PENNSYLVANIA STATE UNIV on August 9, 2012 | http://pubs.acs.org
Publication Date: November 16, 2006 | doi: 10.1021/bk-2007-0945.ch009

Downloaded by PENNSYLVANIA STATE UNIV on August 9, 2012 | http://pubs.acs.org
Publication Date: November 16, 2006 | doi: 10.1021/bk-2007-0945.ch009

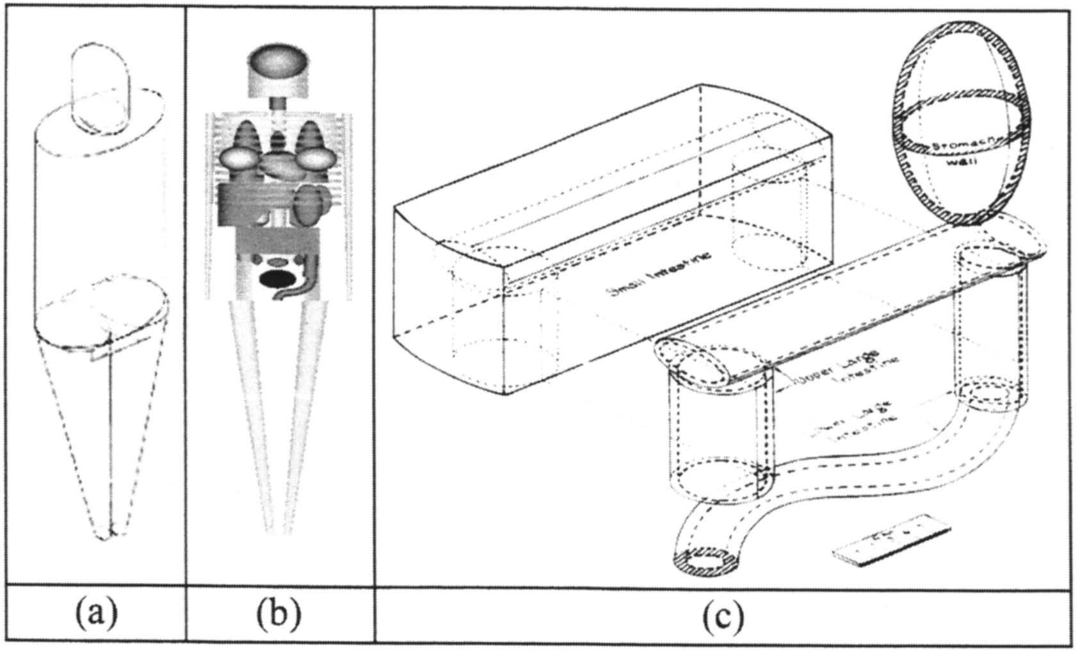
Stomach wall
Small Intestine
Upper Large Intestine
Lower Large Intestine
(a)
(b)
(c)

Figure 1. Stylized adult male models showing (a) exterior view of the adult male, (b) skeleton and internal organs of the adult male/female, (c) surface equations representing stomach and GI tract.

internal structures of the body and to store the images in versatile digital formats. In radiation treatment of cancer patients, Monte Carlo techniques are applied to patient CT images for patient-specific treatment planning (*15*). For radiation protection, one is interested in the modeling of entire body, while in the radiation treatment, only the portion of the body with a tumor is studied.

Tomographic images reveal patient internal structures accurately, but time-consuming segmentation and classification are necessary to implement the models for radiation transport calculations in a Monte Carlo code. To date, more than 20 whole-body tomographic models have been constructed (*e.g.*, *16-22*).

Downloaded by PENNSYLVANIA STATE UNIV on August 9, 2012 | http://pubs.acs.org
Publication Date: November 16, 2006 | doi: 10.1021/bk-2007-0945.ch009

Monte Carlo Methods

Analytical calculations for the transport of the radiation through media can be performed only in very simple geometries and under severe approximations. Monte Carlo methods, which are based on first principles, provide the only practical way of performing accurate calculations of 3-D dose distributions from particle interactions in a complex target such as the human body. The earliest use of a Monte Carlo simulation technique was around 1873 (*23*). The real development and application of the technique, however, stemmed from work on the atomic bomb during World War II by von Neumann, Ulam, and Fermi. Neumann coined the term "Monte Carlo" to reflect the idea that a conceptual roulette wheel could be employed to select the random nuclear processes. Today, a computer-generated random number between 0 and 1 is used for this purpose. The random number determines which interaction will occur by comparing probabilities (*i.e.*, cross sections) of each interaction to statistically sample of the probability density functions. The process is repeated and a particle is tracked in the target until it deposits all its energy or escapes. When a large number of particles (usually several millions) are studied this way, the results accurately predict the physical processes that may be experimentally determined. Validation of a code must be performed before the code may be used for calculations.

The widespread acceptance of computational models in radiation dosimetry was made possible by the availability of well-validated and maintained Monte Carlo codes and very fast personal computers since the late 1980s. Among all the Monte Carlo codes, there are four general purpose codes that have been widely used in the United States and elsewhere: 1) **EGS4**, originally developed at Stanford Linear Accelerator Center, is well known for its detailed physics treatment involving electron-gamma showers (*24*). Electron transport algorithms, such as the PRESTA, make EGS4 one of the most sophiciticated and efficient photon/electron code ever developed; 2) **MCNP**, originated from Los Alamos National Laboratory, has the capbility to transport photons, neutrons, and, since the version 4B, also the electrons (*25*). MCNP has a generalized input capability allowing a user to model a variety of source and detector conditions without having to modify the source code itself. The "lattice structure" feature facilitates the definition of repeated "cells." 3) **MCNPX**, released in 1999, is a newly merged code that combines the theoretical models of the LAHET Code System with the general features of the MCNP to provide a fully-coupled treatment of the transport problem (*26*). The **GEANT4** code, which calculates photons, electrons, neutrons and heavy charged particles such as protons, is an object-oriented toolkit of libraries based on the powerful programming language C++ (*27*). These codes represent the state-of-the-art in terms of the radiation physics, cross-section data and physical models involving photons, electrons, neutrons, and protons.

The following section of this chapter presents the development of a tomographic model, called **VIP-Man**, using images from National Library of Medicine's Visible Human Project®, and implementation of the model in various Monte Carlo codes for radiation protection and medical physics radiation dosimetry.

2. Materials and Methods

At an early stage of our project, several unique sets of whole-body CT/MR/color photographic images from the National Library of Medicine's (NLM) Visible Human Project® (VHP) became available (*28*). The ambitious goal of the VHP, which was conceived in 1988 and initiated in 1991, was to build the most detailed digital image library about the anatomy of an adult male and an adult female (*29,30*).

Cadavers that were considered "normal" and representative of a large population were evaluated. The donated body of a recently executed 38-year-old male from Texas was the first specimen to be selected for VHP. Later, a 58-year-old female was also obtained. To ensure the applicability, it was decided that the image data needed to be documented in several common formats used by radiologists and other physicians. Eventually, four modalities were used: traditional X-rays and CT scans to optimally visualize bone, MRI for soft tissue, and color photographs for definitive resolution. The photographs, which had the finest resolution, were used to provide a standard for comparison (Fig. 2). Generally, image format consists of many pixels (picture elements). The 3-D volume of the tissue is called a voxel (volume element), and it is determined by multiplying the pixel size by the thickness of an image slice (*31*).

Transversal MRI images of the head and neck and longitudinal sections of the rest of the body were obtained at 4 mm intervals. The MRI images are in 256 × 256 pixel resolution. Each pixel has 12 bits of gray tone resolution. The voxel

Downloaded by PENNSYLVANIA STATE UNIV on August 9, 2012 | http://pubs.acs.org
Publication Date: November 16, 2006 | doi: 10.1021/bk-2007-0945.ch009

Downloaded by PENNSYLVANIA STATE UNIV on August 9, 2012 | http://pubs.acs.org
Publication Date: November 16, 2006 | doi: 10.1021/bk-2007-0945.ch009

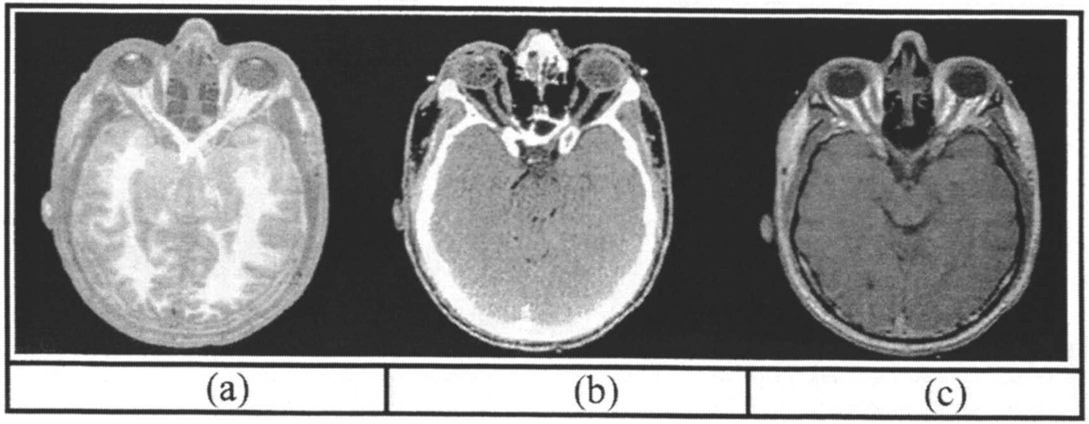

Figure 2. Images from the Visible Human Project: (a) Transversal photography at 2048 × 1216 pixel resolution showing eye lenses and optic nerves; (b) CT images at 512 × 512 pixel resolution; and (c) Magnetic Resonance Imaging at 256 x 256 pixel resolution.

size for MRI data (torso portion) set is 1.88 mm × 1.88 mm × 4 mm. The CT data consists of transversal CT scans of the entire body taken at 1-mm intervals at a resolution of 512 pixels × 512 pixels where each pixel is made up of 12 bits of gray tone. The voxel size for the CT data set (torso portion) is 0.94 mm × 0.94 mm × 1 mm. The transversal anatomical photographs for both male and female cadavers are 2048 pixels by 1216 pixels where each pixel is defined by 24 bits of color. The anatomical photographs are at 1-mm thick slices for the male cadaver and 0.33-mm for the female. There are a total of 1871 slices CT and anatomical photographs (male), respectively. The transversal anatomical images were obtained by photographing the top surface of the body block after removal of (by shaving) each successive millimeter (0.33-mm for the female) by a cryomacrotome. These color photographic data set for whole-body has a voxel size of 0.33 mm × 0.33 mm × 1 mm for the male (0.33 mm × 0.33 mm × 0.33 mm for the female). VHP images have been available in public domain (www.nlm.nih.gov/research/visible/). Since then, computer engineers and anatomists, working together, have devoted unprecedented effort to classifying and visualizing the data sets. For many years, the Visible Human Male is by far the most complete computerized database of the human body ever assembled (32). Between 1998 and 2000, we spent considerable amount of time with the Visible Human color photographic images of the male to develop and apply a radiation dosimetry model called Visible Photographic Man, or VIP-Man (28).

Downloaded by PENNSYLVANIA STATE UNIV on August 9, 2012 | http://pubs.acs.org
Publication Date: November 16, 2006 | doi: 10.1021/bk-2007-0945.ch009

Steps to Construct Whole-Body Model

In addition to adapting original VHP images, three more steps had to be completed to construct the VIP-Man model: 1) Identify and segment the organs or tissues from the original images; 2) Assign physical properties to organs or tissues; and 3) Implement the anatomical data into a Monte Carlo code. These steps are discussed in details next:

The original color photographs for the male had been identified and segmented mostly by manual procedures to yield up to 1400 structures (*32*). Figure 3 shows the segmented and labeled gastrointestinal tract.

Organs or tissues adopted to construct VIP-Man include the adrenals, bladder, esophagus, gall bladder, stomach mucosa, heart muscle, kidneys, upper and lower large intestine (ULI and LLI), liver, lungs, pancreas, prostate, skeletal components, skin, small intestine, spleen, stomach, testes, thymus, thyroid, etc. Additional automatic and manual imaging processing and segmentation were performed by this group to obtain the gray matter, white matter, teeth, skull CSF, stomach mucosa, male breast, eye lenses, and red bone marrow. Traditional image processing techniques were employed to identify tissues based on color separation (for example, redness for red bone marrow). The GI tract mucosa was

Downloaded by PENNSYLVANIA STATE UNIV on August 9, 2012 | http://pubs.acs.org
Publication Date: November 16, 2006 | doi: 10.1021/bk-2007-0945.ch009

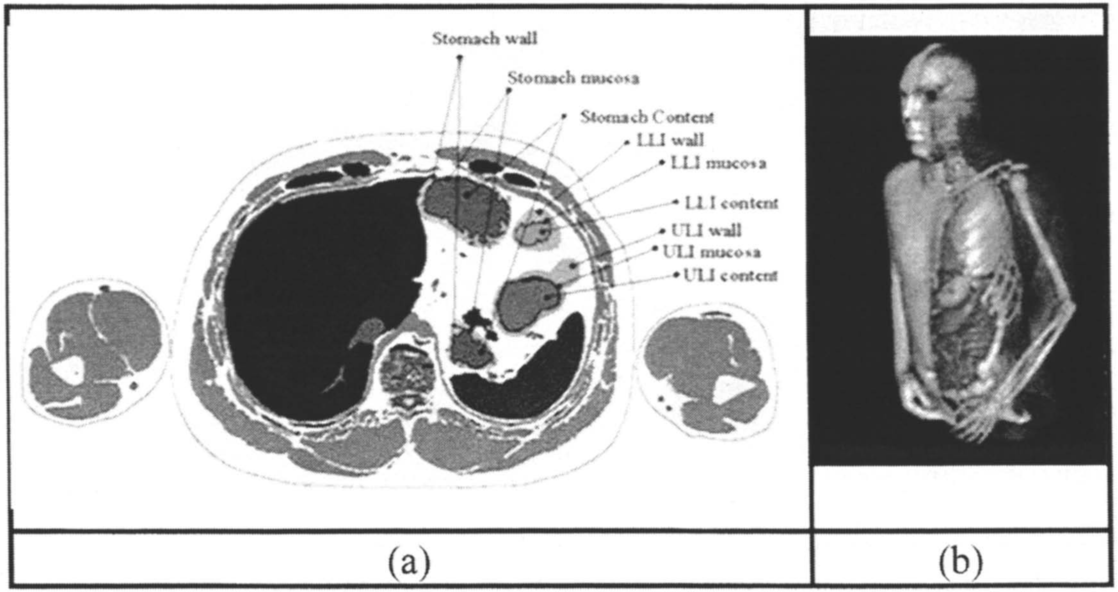
Stomach wall
Stomach mucosa
Stomach Content
LLI wall
LLI mucosa
LLI content
ULI wall
ULI mucosa
ULI content
(a)
(b)

Figure 3. The gastrointestinal tract was segmented and labeled from the Visible Human images as shown in (a). Once the entire body has been segmented, the Visualization ToolKit (49) was used to plot and view the surface rendering in 3D (b).

In Applied Modeling and Computations in Nuclear Science; Semkow, T., et al.;
ACS Symposium Series; American Chemical Society: Washington, DC, 2006.

realistically represented, except for stomach, where one voxel layer on the inner surface of the wall was used. The final list covers "critical" organs or tissues that have been assigned "tissue weighting factors" (*3,5,33*). Other organs or tissues are included because their potential roles in biomedical engineering applications. Once an organ or tissue has been segmented, the associated voxels could be arbitrarily colored for visualization.

3. Results and Discussion

Downloaded by PENNSYLVANIA STATE UNIV on August 9, 2012 | http://pubs.acs.org
Publication Date: November 16, 2006 | doi: 10.1021/bk-2007-0945.ch009

In comparison with the stylized models, the anatomical differences are strikingly obvious. As shown in Fig. 4, major organs appear to have very different geometrical shapes and locations.

VIP-Man is fatty, having nearly 20 kg more in fat than the Reference Man. The major organs seem to have much more similar masses than the Reference Man. The body had slight increase in body volume after it was frozen, causing the weight also to increase. The height of VIP-Man is 186 cm, taller than the Reference Man, which has been recently modified to be 174 cm in height and 73 kg in mass (*34*). The major organs have fairly similar masses. Technically, VIP-Man can be easily re-scaled by a user if necessary, so that the height and total weight agree even better with the Reference Man.

For bioengineering applications, organs or tissues of interest have to be related to appropriate physical properties. For radiation protection purposes, the average tissue compositions and densities recommended in ICRP 23 were used to tag each voxel in VIP-Man (*8*). This step allows the radiation interaction cross section library in a Monte Carlo code to be linked to each voxel for radiation transport simulations.

Computers have limited amount of random accessible memory (RAM). Although today's technologies are much more advanced than a few year ago, the maximum "useable" RAM for a typical PC is often less than 2 GB, seemingly less than the size of VIP-Man containing a total of about 3.7 billion voxels and additional coding. A significant amount of effort was required to reduce the memory burden by using an innovative look-up table (LUT) algorithm (*35*).

Several breakthroughs on handling the huge image data were made during this study and the VIP-Man model has been successfully used to compute organ doses for radiation protection involving photons (*36-38*), electrons (*35,39*), mixed photons/electrons (*40,41*), neutrons (*42,43*), protons (*44*) and general dose comparisons (*45*).

Currently, a Consortium of Computational Human Phantoms (www.virtualphantoms.org) has been formed to create a library of models that take into account of variation of gender and age by including representative images. These models are hoped to allow clinical applications in CT imaging, nuclear medicine and radiation beam therapy to be safer and more effective.

In the future, the Digital Human model that is centered around the VIP-Man model may be designed to serve as research testbeds covering anatomical geometry modeling, radiation treatment planning, 4D CT imaging algorithm and virtual surgical simulations. For example, a GeometryModelingBed will expand the VIP-Man model from 3D to 4D using the Non-Uniform Rational B-Splines (NURBS) to define the surfaces of the organs of the VIP-Man and clinically obtained respiratory motion data (*46*). A RadiationPLanningBed will study advanced radiation treatment method (*47*). A TomoImagingBed will be aimed at studying x-ray imaging optimization that yields good image quality and acceptable patient exposure, as shown in Fig. 5. A BiomechanicalBed will address issues related to the generation of multimodal virtual environments for surgical training (*48*). There is also a need to create a physical phantom of the VIP-Man so certain experiments can be performed to "validate" the calculated data. In addition, we are developing physical phantoms using 3D rapid prototyping and Computer Aided Design technologies. Descriptions of projects are available at RRMDG.rpi.edu.

Downloaded by PENNSYLVANIA STATE UNIV on August 9, 2012 | http://pubs.acs.org
Publication Date: November 16, 2006 | doi: 10.1021/bk-2007-0945.ch009

4. Conclusions

Human anatomical models have been used for diverse nuclear applications including workers and patients. The radiation protection community is shifting from stylized modeling to tomographic modeling that is more realistic in anatomy and physiology. An adult male whole-body model, VIP-Man, has been constructed from the color photographic images of the well-known Visible Human Project®. VIP-Man has been adopted into the state-of-the-art Monte Carlo codes, EGS4, MCNP, and MCNPX for radiation transport studies and organ dose calculations involving photons, electrons, neutron, and protons. To date, VIP-Man represents one of the world's finest and most complete human anatomical models, containing small tissues, such as skin, GI tract mucosa, eye lenses, and red bone marrow, that were not (or not as realistically) represented in the stylized models and other image-based tomographic models. The new capability in multiple particle transport and in 4D organ motion simulations not only provides needed radiation protection dosimetric data but also opens doors for applications in radiotherapy.

In the long term, an excellent opportunity seems to be within reach in establishing a centralized digital human biomedical engineering testbeds that can yield insight into exciting frontiers of research. These applications are based on radiological and mechanical properties that can be combined with the VIP-Man anatomical model. We are hoping to eventually extend the digital human platform horizontally to include additional engineering applications, such as multiphase flow (for human respiratory and circulatory systems) and biochemical engineering (for drug discovery and virtual clinical trials), and vertically to include models at the cellular and molecular levels.

Downloaded by PENNSYLVANIA STATE UNIV on August 9, 2012 | http://pubs.acs.org
Publication Date: November 16, 2006 | doi: 10.1021/bk-2007-0945.ch009

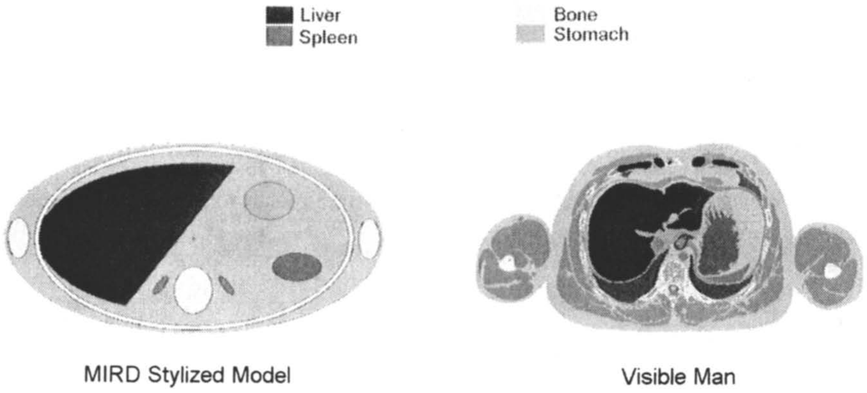
Liver
Spleen
Bone
Stomach
MIRD Stylized Model
Visible Man

Figure 4. The VIP-Man model has obviously different anatomical representation from the stylized model.

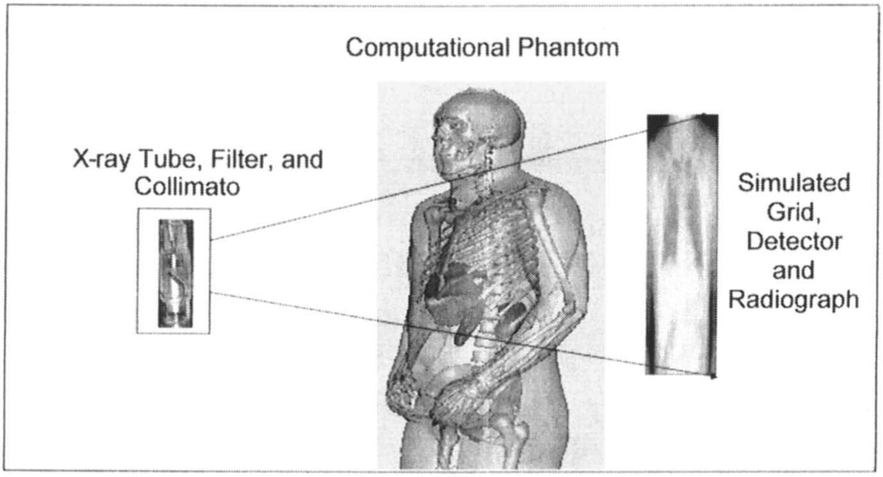
Computational Phantom
X-ray Tube, Filter, and Collimato
Simulated Grid, Detector and Radiograph

Figure 5. A TomoImagingBed will be aimed at studying x-ray imaging optimization.

Acknowledgments

This chapter is based on research projects by undergraduate and graduate students at Rensselaer: B. Bednarz, A. Bozkurt, P. Caracappa, T. C. Chao, M. Furler, J. Hanlon, M. Oakley, C. Y. Shi, H. Su, B. Wang, M. Winslow, and T. Zhang. These projects were supported by the National Science Foundation's Biomedical Engineering Program under a Faculty Early Career Development Grant Award (BES-9875532) and by the National of Institutes of Health (1 R03 LM007964-01, 1 R42 CA115122-01 and 1R01CA116743).

Downloaded by PENNSYLVANIA STATE UNIV on August 9, 2012 | http://pubs.acs.org
Publication Date: November 16, 2006 | doi: 10.1021/bk-2007-0945.ch009

References

1. *Conversion Coefficients For Use in Radiological Protection Against External Radiation*; ICRU Report 57; International Commission on Radiation Units and Measurements: Bethesda, MD, 1998.
2. *Limits for Intake of Radionuclides by Workers*; ICRP Publication 30; Pergamon Press: Oxford, 1979.
3. *Recommendations of the International Commission on Radiological Protection*; ICRP Publication 60; Pergamon Press: Oxford, 1990.
4. Snyder, W. S.; Ford, M. R.; Warner, G. G.; Fisher, H. L., Jr. Estimates of absorbed fractions for monoenergetic photon source uniformly distributed in various organs of a heterogeneous phantom. Medical Internal Radiation Dose Committee (MIRD), Pamphlet No. 5, Revised, 1978.
5. *Standards for Protection Against Radiation*; Title 10 Part 20 of the Code of Federal Regulations; U.S. Nuclear Regulatory Commission, 1991.
6. Snyder, W. S.; Ford, M. R.; Warner, G. G.; Fisher H. L., Jr. Estimates of absorbed fractions for monoenergetic photon source uniformly distributed in various organs of a heterogeneous phantom. Medical Internal Radiation Dose Committee (MIRD), Pamphlet No. 5, Supplement No. 3. *J. Nucl. Med. 10.* Society of Nuclear Medicine: New York, NY, 1969.
7. Snyder, W. S.; Ford, M. R.; Warner, G. G.; Watson, S.B. Absorbed dose per unit cumulated activity for selected radionuclides and organs. Medical Internal Radiation Dose Committee (MIRD), Pamphlet No. 11, 1975.
8. *Report of the Task Group on Reference Man*; ICRP Publication 23; Pergamon Press: Oxford, 1975.
9. Cristy, M.; Eckerman, K. F. Specific absorbed fractions of energy at various ages from internal photon sources. Report ORNL/TM-8381/V1; Oak Ridge National Laboratory: Oak Ridge, TN, 1987.
10. *Data for Use in Protection Against External Radiation*; ICRP Publication 51; Pergamon Press: Oxford, 1987.
11. *Conversion Coefficients for Use in Radiological Protection Against External Radiation*; ICRP Publication 74; Pergamon Press: Oxford, 1996.

12. Kramer, R.; Zankl, M.; Williams, G.; Drexler, G. The calculation of dose from external photon exposures using reference human phantoms and Monte-Carlo methods. Part 1: The male (ADAM) and female (EVA) adult mathematical phantoms; GSF Bericht S-885, 1982.
13. Bouchet, L. G.; Bolch, W. E.; Weber, D. A.; Atkins, H. L.; Poston, J. W., Sr. A revised dosimetric model of the adult head and brain. *J. Nucl. Med.* **1996**, *37*, 1226-1236.
14. *Phantoms and Computational Models in Therapy, Diagnosis and Protection*; ICRU Report 48; International Commission on Radiation Units and Measurements: Bethesda, MD, 1992.
15. Hartmann Siantar, C.L.; Bergstrom, P. M.; Chandler, W. P.; Chase, L.; Cox, L. J. Lawrence Livermore National Laboratory's PEREGRINE Project. Report UCRL-JC-126732; Lawrence Livermore National Laboratory: Livermore, CA, 1997.
16. Hickman, D. P.; Firpo, M. Magnetic Resonance Image Phantom. Report UCRL-MA-118455; Lawrence Livermore National Laboratory: Livermore, CA, 1997.
17. Jones, D. G. A realistic anthropomorphic phantom for calculating organ doses arising from external photon irradiation. *Rad. Prot. Dosimetry* **1997**, *72*, 21-29.
18. Petoussi-Henß, N.; Zankl, M. Voxel anthropomorphic models as a tool for internal dosimetry. *Rad. Prot. Dosimetry* **1998**, *79*, 415-418.
19. Kramer, R.; Vieira, J. W.; Khoury, H. J.; Lima, F. R. A.; Fuelle, D. All about MAX: a male adult voxel phantom for Monte Carlo calculations in radiation protection dosimetry. *Phys. Med. Biology* **2003**, *48*, 1239-1262.
20. Lee, Choonsik; Lee, Jaiki; Lee, Choonik. Korean adult male voxel model KORMAN segmented from magnetic resonance images. *Med. Phys.* **2004**, *31*, 1017-1022.
21. Nagaoka, T.; Watanabe, S.; Sakurai, K.; Kunieda, E.; Watanabe, S.; Taki, M.; Yamanaka, Y. Development of realistic high-resolution whole-body voxel models of Japanese adult males and females of average height and weight, and application of models to radio-frequency electromagnetic-field dosimetry. *Phys. Med. Biology* **2004,** *49*, 1-15.
22. Zubal, I. G.; Harrel, C. R.; Smith E. O.; Rattner, Z.; Gindi, G.; Hoffer, P. B. Computerized three-dimensional segmented human anatomy. *Med. Phys.* **1994,** *21*, 299-302.
23. Hammersley, J. M.; Handscomb, D. C. *Monte Carlo Methods*. Chapman & Hall: London, 1964.
24. Nelson, W. R.; Hirayama, H.; Rogers, D. W. O. The EGS4 code system. Report SLAC-265-UC-32; Stanford Linear Accelerator Center: Stanford, CA, 1985.
25. Brown, F. B.; et al. MCNP - A general Monte Carlo n-particle transport code, Version 5, Volume II: User's guide. Distributed by the RSICC of the Oak Ridge National Laboratory: Oak Ridge, TN, 2003.

Downloaded by PENNSYLVANIA STATE UNIV on August 9, 2012 | http://pubs.acs.org
Publication Date: November 16, 2006 | doi: 10.1021/bk-2007-0945.ch009

26. Hughes, H. G; Prael, R. E.; Little, R. C. MCNPX - the LAHET/MCNP code Merger. Report XTM-RN(U) 97-012; Los Alamos National Laboratory: Los Alamos, NM, 1997.
27. Agostinelli, S.; et al. GEANT4 - a simulation toolkit. *Nucl. Instr. Meth. Phys. Res. A* **2003,** *506*, 250-303.
28. Xu X. G.; Chao, T. C.; Bozkurt, A. VIP-Man: an image-based whole-body adult male model constructed from color photographs of the visible human project for multi-particle Monte Carlo calculations. *Health Phys.* **2000,** *78*, 476-486.
29. Ackerman, M. J. Accessing the visible human project. *D-lib Magazine: The Magazine of the Digital Library Forum.* **1995,** www.dlib.org/dlib/october95/10ackerman.html.
30. *Electronic Imaging: Report of the Board of Regents National Library of Medicine (NLM)*; U.S. Board of Regents; NIH Publication 90-2197, 1990.
31. Bushong, S.C. *Radiological Science for Technologists.* 6th Ed.; Mosby-Year Book: New York, NY, 1997.
32. Spitzer, V.M.; Whitlock, D.G. *Atlas of the Visible Human Male.* Jones and Bartlett Publishers: Boston, MA, 1998.
33. *Recommendations of the International Commission on Radiological Protection*; ICRP Publication 26; Pergamon Press: Oxford, 1977.
34. *Basic anatomical and physiological data for use in radiological protection: the skeleton*; ICRP Publication 70; Annals of the ICRP 25(2); Pergamon Press: Oxford, 1995.
35. Chao, T. C.; Xu, X. G. Specific absorbed fractions from the image-based VIP-Man body model and EGS4-VLSI Monte Carlo code: Internal electron emitters. *Phys. Med. Biology* **2001,** *46*, 901-927.
36. Chao, T. C.; Bozkurt, A.; Xu, X. G. Conversion coefficients based on VIP-Man anatomical model and EGS4-VLSI code for monoenergetic photon beams from 10 keV to 10 MeV. *Health Phys.* **2001,** *81*, 163-183.
37. Winslow, M.; Huda, W.; Xu, X. G.; Chao, T. C.; Shi, C.Y.; Ogden, K. M.; Scalzetti, E. M. Use of the VIP-Man model to calculate energy impacted and effective dose for X-ray examinations. *Health Phys.* **2004,** *86*, 174-182.
38. Winslow, M.; Xu, X. G.; Huda, W.; Ogden, K. M.; Scalzetti, E. M. Monte Carlo simulations of patient X-ray images. *Am. Nucl. Soc. Trans.* **2004,** *90*, 459-460.
39. Chao, T. C.; Bozkurt, A.; Xu, X. G. Dose conversion coefficients for 0.1-10 MeV electrons calculated for the VIP-Man tomographic model. *Health Phys.* 2001, *81*, 203-214.
40. Xu, X.G.; Chao, T.C. Calculations of specific absorbed fractions for GI-tract using a realistic whole-body tomographic model. *Cancer Biother. Radiopharm.* **2003,** *18*, 431-436.
41. Chao, T. C.; Xu, X. G. S-values calculated from a tomographic head/brain model for brain imaging. *Phys. Med. Biol.* **2004,** *49*, 4971-4984.

Downloaded by PENNSYLVANIA STATE UNIV on August 9, 2012 | http://pubs.acs.org
Publication Date: November 16, 2006 | doi: 10.1021/bk-2007-0945.ch009

42. Bozkurt A.; Chao, T. C.; Xu, X. G. Fluence-to-dose conversion coefficients from monoenergetic neutron beams below 20 MeV based on the VIP-Man anatomical model. *Phys. Med. Biology* **2000**, *45*, 3059-3079.
43. Bozkurt A.; Chao, T. C.; Xu, X. G. Fluence-to-dose conversion coefficients based on the VIP-Man anatomical model and MCNPX code for monoenergetic neutron beams above 20 MeV. *Health Phys.* **2001**, *81*, 184-202.
44. Bozkurt, A.; Xu, X. G. Fluence-to-dose conversion coefficients for monoenergetic proton beams based on the VIP-Man anatomical model. *Rad. Prot. Dosimetry*. **2004**, *112*, 219-235.
45. Xu, X. G.; Chao, T. C.; Bozkurt, A. Comparison of effective doses from various monoenergetic particles based on the stylized and the VIP-Man tomographic models. *Rad. Prot. Dosimetry*. **2005**, *115*, 530-535.
46. Xu, X. G.; Shi, C. Preliminary development of a 4d anatomical model for Monte Carlo simulations. Monte Carlo 2005 Topical Meeting; The Monte Carlo Method: Versatility Unbounded in a Dynamic Computing World; Chattanooga, TN, 2005.
47. Wang, B.; Xu, X. G.; Goldstein, M.; Sahoo, N. Adjoint Monte Carlo method for prostate external photon beam treatment planning: An application to 3-D patient anatomy. *Phys. Med. Biology* **2005**, 50, 923-935.
48. Jin, W.; Lim, Y. J.; Xu, X. G.; De, S. Image based rendering for virtual surgery. Medicine Meets Virtual Reality Conference; MMVR13; Long Beach, CA, 2005.
49. Schroeder, W.; Martin, K.; Lorensen, B. *The Visualization Toolkit - An Object-Oriented Approach to 3D Graphics*. 2nd Ed.; Prentice Hall: Upper Saddle River, NJ, 1997.

Downloaded by PENNSYLVANIA STATE UNIV on August 9, 2012 | http://pubs.acs.org
Publication Date: November 16, 2006 | doi: 10.1021/bk-2007-0945.ch009

Downloaded by STANFORD UNIV GREEN LIBR on August 6, 2012 | http://pubs.acs.org
Publication Date: November 16, 2006 | doi: 10.1021/bk-2007-0945.ch010

Chapter 10

Thermohydraulic and Nuclear Modeling of Natural Fission Reactors

Jason C. Viggato and William G. Culbreth

Department of Mechanical Engineering, University of Nevada at Las Vegas,
4505 Maryland Parkway, Las Vegas, NV 89154

A comprehensive computer code was developed to model the thermohydraulic behavior and criticality conditions that may have existed in the Oklo natural reactors. A two-dimensional finite difference numerical model that incorporates modeling of fluid flow, temperature profile, nuclear fission and subsequent heat generation was developed. The operating temperatures ranged from about 456°K to about 721°K. Critical reactions were observed for a wide range of concentrations and porosity values (9 to 30 percent UO_2 and 10 to 20 percent porosity). Periodic operation occurred in the computer model prediction with UO_2 concentrations of 30 percent in the core and 5 percent in the surrounding material. For saturated conditions and 30 percent porosity, the model predicted temperature transients with a period of about 5 hours. Kuroda predicted 3 to 4 hour durations for temperature transients. The large instantaneous jumps in temperature could be an indication of the violent ejection of water that Kuroda predicted, resulting in ongoing geyser activity. The range of temperatures simulated by the computer model within the Oklo reactors agreed with evidence from the Oklo geology.

In Applied Modeling and Computations in Nuclear Science; Semkow, T., et al.;
ACS Symposium Series; American Chemical Society: Washington, DC, 2006.

1. Introduction

Since the discovery and use of atomic energy, there has been an enormous problem with the disposal of waste products produced by radioactive material. Experimental verification of proposed nuclear waste storage schemes in geologic repositories is not possible, however, a natural analog in the form of ancient natural reactors that existed in uranium-rich ores may be used. Two billion years ago, the enrichment of natural uranium was high enough to allow a sustained chain reaction in the presence of water as a moderator. Several natural reactors occurred in Gabon, Africa and were discovered in the early 1970's. These reactors operated at low power levels for hundreds of thousands of years. Heated water generated from the reactors also leached uranium from the surrounding rock strata and deposited it in the reactor cores. This increased the concentration of uranium in the core over time and served to "refuel" the reactor. This has strong implications in the design of modern geologic repositories for spent nuclear fuel. The possibility of external criticality events in man-made repositories exists after waste package degradation and the geologic evidence from Oklo suggested how those events might progress and enhance local concentrations of uranium.

Naudet (*1*) demonstrated that spontaneous criticality could occur in high-grade sandstone ore when the uranium concentration was about 10 % for a layer two meters thick. These ores were rare, but did exist in the Oklo natural reactor zone. "Therefore, fission reactions can begin in small volumes with the resulting heat-inducing convective circulation which causes desilicification and argillization of sandstones" (*1*). The extremely hot fluid circulation may have resulted in leaching of uranium from the surrounding area as well as uranium migration, resulting in an increase of the concentration of fissionable material in the reactor zone. Areas that were depleted in uranium and that contained no fission products were discovered around the reactor zone. This is evidence that uranium migration occurred and that the result was a concentrated zone of uranium rich ore at the center of the reactor. "Thus, hydrothermal processes resulting from fission reactions produce an increase in uranium and support the on-going nuclear reactions" (*1*). Curtis and Gancarz (*2*) studied radiolysis in nature, through use of the Oklo reactor geologic data. The natural reactor operating temperatures were found to be between 450°C and 600°C. Analyses of the chemical composition in the reactor zones showed that the amounts of magnesium and uranium greatly exceeded the values in normal ore. These excessive amounts may have been increased by convective circulation during the reaction. An increase in the amount of uranium provided additional fissionable material, thus prolonging the life of the nuclear reaction. The occurrence of the nuclear reaction implied that high concentrations of uranium existed in zones prior to the convective circulation.

Downloaded by STANFORD UNIV GREEN LIBR on August 6, 2012 | http://pubs.acs.org
Publication Date: November 16, 2006 | doi: 10.1021/bk-2007-0945.ch010

Downloaded by STANFORD UNIV GREEN LIBR on August 6, 2012 | http://pubs.acs.org
Publication Date: November 16, 2006 | doi: 10.1021/bk-2007-0945.ch010

Kuroda (*3*) discussed the transient mode of operation for the natural reactor, which periodically shut down and then restarted. He suggested that the reactor operating temperature was in the range between the boiling point of iodine (183°C) and the melting point of tellurium (452°C). Xenon data was used to calculate the time interval in which the reactor operated and then shutdown. This data yielded values of the period to be between about 3 to 4 hours. Kuroda noted the similarity of these values to the duration of the eruption (181 minutes) of the Big Geyser at the Naruko Hot Springs in Japan. These results indicated the natural reactors at Oklo might have behaved in a manner similar to that of modern geysers.

Culbreth and Viggato (*4*) conducted a study to determine the depth and pressure at which the Oklo natural reactors occurred. A nuclear criticality code was developed to replicate the conditions at Oklo. From the program, the infinite neutron multiplication factor, k_∞, was computed as a function of temperature and pressure. The functions were then curve-fitted and analyzed for the conditions that would have led to the minimum and maximum temperatures suggested by Kuroda (*3*). It was observed that reactor performance was heavily dependent on water density. As the temperature inside the reactor rose above 710 °K, superheated water would expand and k_∞ would decrease. The decrease in the infinite neutron multiplication factor lead to a lower power output, and thus the cooling of the water inside the reactor. The minimum deviation occurred at values of 48.4 MPa and 44 MPa based on Kuroda's data. This corresponds to two sets of depths depending on whether hydrostatic or lithostatic pressures occurred at reactor depth during operation. Curve fits showed that in order for a geologic reactor to operate between the geologic temperature and the upper temperature range, the pressures must have been hydrostatic produced by the rock corresponding to a depth of 4.5 to 4.8 km.

Geologic records have been studied and documented in the Oklo reactor, and through use of this data, a natural analogue for geologic repositories is proposed. The results of this work and the possible implications for the design of a geologic repository are presented. The Oklo code was pursued in the interest of developing a computer model to replicate conditions and behavior found to occur in core samples at the Oklo reactor site, as well as those hypothesized by previous researchers. The focus of this investigation was to determine the reactor operating conditions such as the temperature range over time, flow patterns and the possibility of periodic fluctuations during critical operation.

2. Code Description

A transient computer model of Oklo has been developed to conduct parametric studies of the conditions that led to sustained fission. In this model, uranium concentrations, porosity, pore saturation and temperature within the core have been predicted based on the transient behavior. Transient behavior is extremely important in the operation of the reactor. After a study of the relative concentrations of radionuclides with the cores at Oklo, Kuroda indicated that the reactors operated with a periodic output. It was suggested that this might have resulted in the forceful ejection of superheated water from the reactors in the form of geysers. This water would have also contained fission products. If degradation of waste packages in a repository occurred and similar conditions existed, this could lead to the possible transport of radionuclides into the outside environment.

The theory used to compose the computer model has been taken from the areas of heat transfer and fluid flow within porous media, along with nuclear criticality. A finite difference approach was used to model flow in and around the reactor. The equations for neutron flux (1), temperature (2), and fluid flow through use of stream functions (3) within the reactor zone were solved through a Gauss-Seidel iteration with Successive Over Relaxation method.

$$\frac{\partial \Phi}{v \partial t} = D\left(\frac{\partial^2 \Phi}{\partial x^2} + \frac{\partial^2 \Phi}{\partial y^2}\right) - \Sigma_a \Phi + S \tag{1}$$

$$\frac{\partial T}{\partial t} = \frac{k_a}{\rho_f c_p}\left(\frac{\partial^2 T}{\partial x^2} + \frac{\partial^2 T}{\partial y^2} + \frac{\dot{q}'''}{k_a}\right) - \frac{\partial \psi}{\partial y}\frac{\partial T}{\partial x} + \frac{\partial \psi}{\partial x}\frac{\partial T}{\partial y} \tag{2}$$

$$\frac{\partial^2 \psi}{\partial x^2} + \frac{\partial^2 \psi}{\partial y^2} = \frac{\beta g \rho_f K}{\mu_f}\left(\frac{\partial T}{\partial y}\cos\theta - \frac{\partial T}{\partial x}\sin\theta\right) \tag{3}$$

The computer program developed consisted of one-group neutron theory, two-dimensional fluid flow and heat transfer in a porous medium, and thermodynamic properties of water. Since all fission reactions were due to thermal neutrons (slow neutrons), fast neutron groups were neglected. All of the program, subroutines and functions were written in Fortran 90 source code.

A main program called the various subroutines, and then calculated stream functions, temperatures, velocities and pressures, checked for convergence and carried out the appropriate number of iterations. During calculation of quantities that involved thermodynamic properties of water, the appropriate function for the property needed was called by passing the pressure, temperature and any other variables required. Functions computed dynamic viscosity, thermal conductivity, specific heat, density, and the compressibility factor for water. All functions were valid within a temperature range up to 1450°C and pressures up to 100 MPa, extending beyond the range of operation of the Oklo reactors. Rock

Downloaded by STANFORD UNIV GREEN LIBR on August 6, 2012 | http://pubs.acs.org
Publication Date: November 16, 2006 | doi: 10.1021/bk-2007-0945.ch010

properties were considered to be that of sandstone (SiO_2), with five percent concentrations of Al_2O_3 and Fe_2O_3 within each volume. Porosity of sandstone may be varied, while the pores at this depth were considered to be fully saturated.

Neutron flux was calculated by calculating the number densities of each element, macroscopic cross-sections corrected for temperature, factors of the four-factor equation, logarithmic energy decrement and the diffusion coefficient. Hydrogen was a moderator, and the fission process depended upon the number density of hydrogen, as well as other elements and their isotopes, present in the system. The only hydrogen found in the reactor was found in the form of water, and the density changed with temperature. As the density went down, so did the number density of hydrogen. Temperature and pressure were passed into the function for the density of water during each iteration, and for each time step until convergence was achieved. Various values of the four-factor equation along with the diffusion coefficient were then calculated. The neutron diffusion equation was then solved and checked for convergence. This cycle was repeated until the convergence criterion for the neutron flux was satisfied. A heat generation rate produced by fission was then calculated from the converged value of neutron flux. An iteration for temperature was then started and carried out until the convergence criterion was accomplished. Stream function affects the overall temperature through convective dissipation. As the temperature increased, changes in the density of water within the reactor also occurred, leading to movement of water due to natural convection. The stream function computation was carried out in the same manner as both the neutron flux and temperature iterations.

Downloaded by STANFORD UNIV GREEN LIBR on August 6, 2012 | http://pubs.acs.org
Publication Date: November 16, 2006 | doi: 10.1021/bk-2007-0945.ch010

3. Results

The Oklo reactor model was approximately 6 m long by 1 m high as shown in Fig. 1. An impermeable layer of clay below the reactor prevented the flow of water and another impermeable layer of clay capped the uranium-rich sandstone shown at the top of the figure. The two-dimensional reactor geometry represented a cross-section of a semi-infinite slab reactor extending in the *z*-direction. Three cases of UO_2 concentrations in the reactor core were investigated; 9, 15 and 30 percent. The reactor core was placed at the bottom of this model to represent the geology of a confined wall where the reactor was above a clay substrate. This type of configuration was witnessed in the geological remains of the Oklo and Cigar Lake deposits.

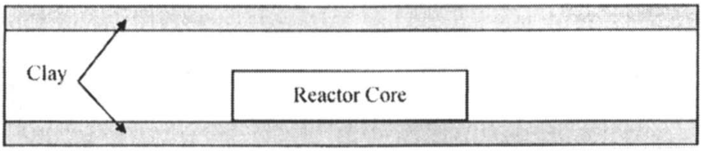

Figure 1. Oklo natural reactor geometry.

Downloaded by STANFORD UNIV GREEN LIBR on August 6, 2012 | http://pubs.acs.org
Publication Date: November 16, 2006 | doi: 10.1021/bk-2007-0945.ch010

The core of the Oklo reactor contained the highest concentration of uranium. The surrounding sandstone contained 5 percent UO_2 concentration. Core uranium concentration of 9 percent was chosen as the lower limit because it was the lowest concentration that would allow criticality to occur. This percentage also coincided with Naudet's work, which predicted minimum concentration levels of 10 percent within uranium-rich sandstone. Throughout all runs, ^{235}U enrichment values of 3.5 percent were used, as this is the approximate calculated natural abundance of ^{235}U two billion years ago. The porosity of the sandstone was also varied to investigate the effect that water content had on the behavior of the reactor. Porosity values used were 10, 20, and 30 percent for the sandstone in which the reactor resided. Limits of 1750 °K for the temperature and 1×10^{17} neutrons m^{-2} sec^{-1} for the neutron flux were applied to maintain reasonable neutron flux and temperature values during power excursions. Isothermal conditions were used at the reactor walls for temperature, pressure, stream function and neutron flux. A temperature of 400 °K was used to represent the geothermal temperature and a pressure of about 40 MPa corresponding to a depth of about 4.5 km. Stream function and neutron flux values of zero were used at the boundaries, a condition which allowed no fluid or neutron transfer across the reactor walls.

Figure 2 shows temperature profiles for 9 percent concentration in the reactor core and 5 percent for the surrounding area of UO_2 and porosity ranging from 10 to 30 percent. Temperatures in Fig. 2 show two main differences between the various values of porosity; initial peak temperature and the steady state temperature. As the porosity increased, the initial temperature and steady state temperatures increased.

Figure 3 gives the temperature plots for concentrations at the reactor core of 15 percent with varying porosity. Once again the initial peaks were higher with higher porosity, however the steady state temperature for 30 percent porosity is slightly lower than that of the 20 percent case. All the curves have similar profiles to those observed in Fig. 2.

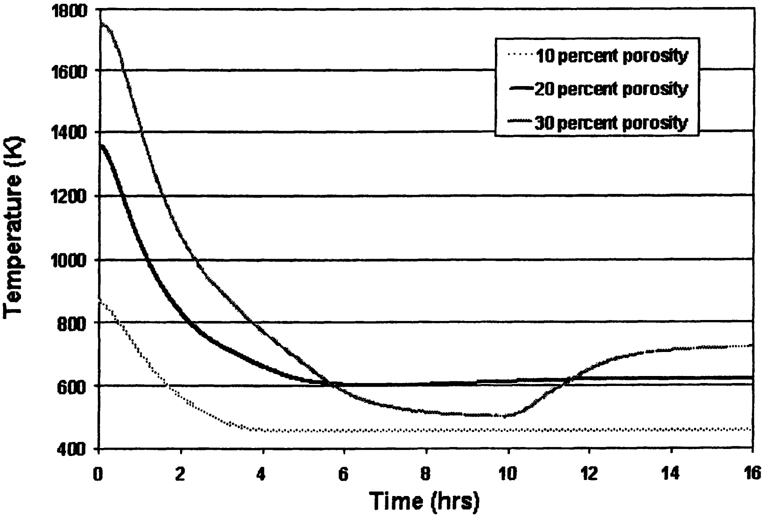

Figure 2. Temperatures for 9 percent concentration at the core and 5 percent in surrounding areas of UO_2 for varying sandstone porosity for the center of the Reactor.

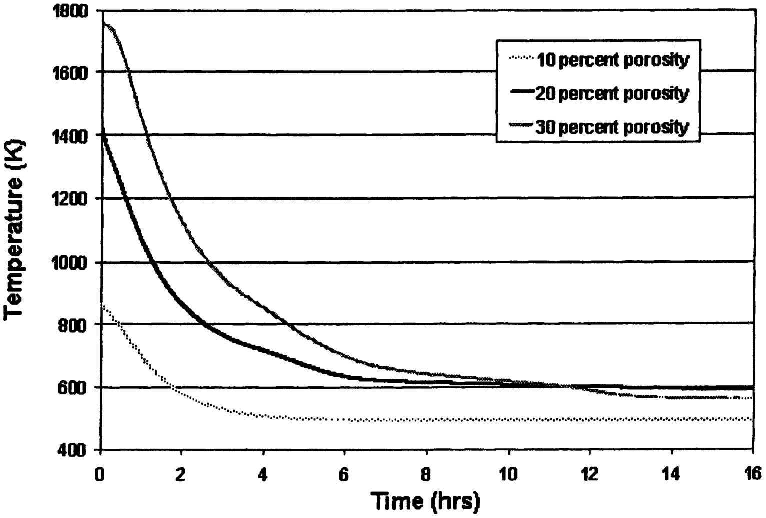

Figure 3. Temperatures for 15 Percent concentration at the core and 5 percent in surrounding areas of UO_2 for varying sandstone porosity for the center of the reactor.

Downloaded by STANFORD UNIV GREEN LIBR on August 6, 2012 | http://pubs.acs.org
Publication Date: November 16, 2006 | doi: 10.1021/bk-2007-0945.ch010

The last set of cases for 30 percent concentration for temperatures at the center of the reactor is given in Fig. 4. The temperature behavior for 10 and 20 percent behavior exhibit similar trends as those seen in the 9 and 15 percent concentration cases. A noticeable difference was observed in the 30 percent porosity case. The initial spike occurred and decayed normally. Instead of the decay to steady state temperature as seen in other runs, a second transient occurred and then decayed to a steady state temperature. The presence of a second transient indicated the possibility of periodic operation of the reactor as Kuroda states. The first and second peak to trough temperature change occurred over about 5 hours. These times are only slight greater than the 3 hour period Kuroda concluded the reactor operated in by examining xenon concentrations. The periodicity was directly affected by the thermohydraulics and thermophysical properties of water.

Downloaded by STANFORD UNIV GREEN LIBR on August 6, 2012 | http://pubs.acs.org
Publication Date: November 16, 2006 | doi: 10.1021/bk-2007-0945.ch010

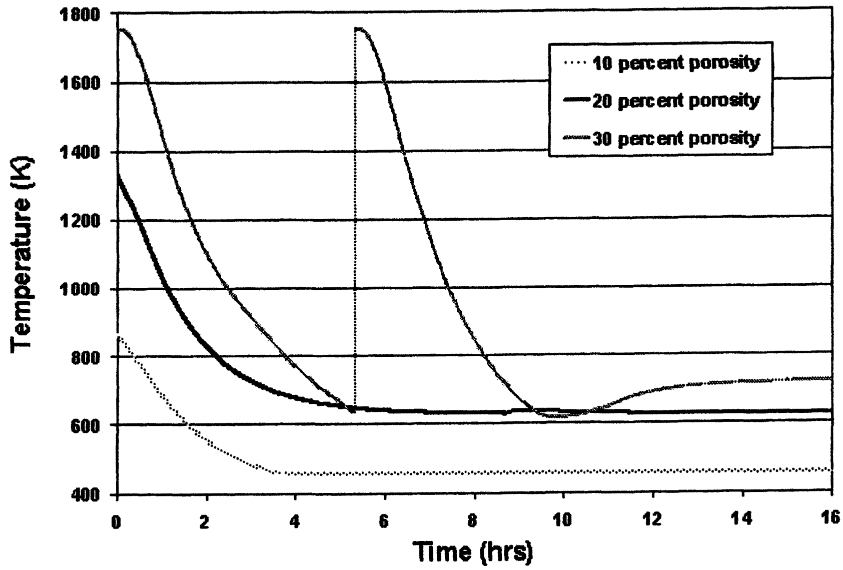

Figure 4. Temperatures for 30 percent concentration at the core and 5 percent in surrounding areas of UO_2 for varying sandstone porosity for the center of the reactor.

4. Discussion and Conclusions

A two-dimensional numerical model that incorporates modeling of fluid flow, temperatures, and nuclear fission was developed for the Oklo natural reactors. Various combinations of UO_2 in the reactor core and porosity were studied to determine the effect both have on the operating temperatures, neutron flux behavior, flow characteristics and operating modes of the reactor such as the possibility of periodic heat generation.

Temperature profiles were shown to have a large spike in the initial start up of the reactor and then decay to a steady state temperature for all cases except that of 30 percent UO_2 concentration at the reactor core with 30 percent porosity. The operating temperatures ranged from about 456 °K to about 721 °K. These temperature ranges agree exactly with Kuroda's (*3*) predicted ranges and the upper limit agrees with Curtis and Gancarz's (*2*) predicted lower limit of 723 °K as seen in Fig. 5.

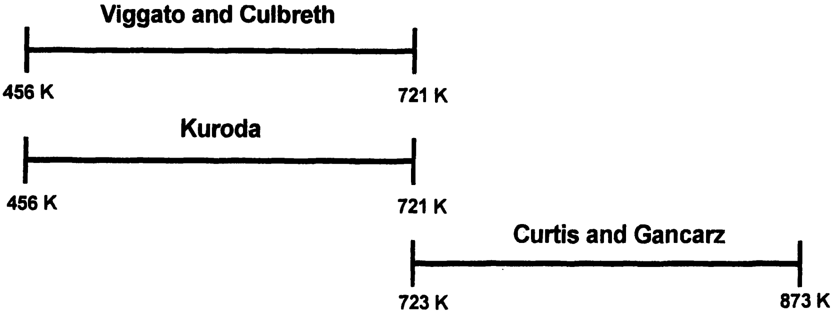

Figure 5. Operating temperature range comparison to previous studies.

Critical reactions were observed for a wide range of concentrations and porosity values (9 to 30 percent UO_2 and 10 to 20 percent porosity). The lower limit of fissionable material concentration was 9 percent for the Oklo code, which coincided with Naudet's (*1*) prediction of 10 percent concentration of highly enriched material.

The period of operation that Kuroda (*3*) predicted, occurred in the Oklo code prediction with concentrations of 30 and 5 percent UO_2 in the reactor core and surrounding material respectively, and 30 percent concentration of water (30 percent porosity) which allowed a second super-critical spike in temperature. Kuroda predicted 3 to 4 hour durations while the Oklo code produced times of

Downloaded by STANFORD UNIV GREEN LIBR on August 6, 2012 | http://pubs.acs.org
Publication Date: November 16, 2006 | doi: 10.1021/bk-2007-0945.ch010

about 5 hours. The large instantaneo-us jumps in temperature could be an indication of the violent ejection of water that Kuroda predicted, resulting in ongoing geyser activity, if uranium deposits were situated close to the surface. Naudet (*1*) indicated that the superheated hydrothermal flow of the water in the reactor could allow the leaching of uranium from the surrounding rock and transport this material back to the center, thus sustaining the reaction. The basis of this conclusion was the lack of high concentrations of uranium rich material surrounding the core. Stream function data showed bifurcating flow that could allow redistribution of uranium material back into the center of the reactor core as Naudet suggested.

The Oklo code was validated through changing the number of nodes and time step for consistency of the solution. Very little change in the temperature history at the center of the reactor was witnessed through use of these variations. The model was further validated through comparisons to known analytical solutions and behavior for temperature, stream function and neutron flux. All of these verification tests agreed nicely with the corresponding analytical solution and/or behavior for the given geometry.

Kuroda (*3*) investigated a calculation of the period of free decays of the isotopes of xenon and witnessed an upward shift of data points. "This means that here we have a powerful experimental tool with which to determine the time periods of the Oklo reactors, which have been operating intermittently nearly two billion years ago" (Kuroda, *3*). The similarity of temperatures and period shows the model developed accurately replicates the conditions under which the Oklo reactors operated.

Kuroda predicted the existence of natural fission reactors in 1956 and received criticism. In 1972, French scientists vindicated his predictions through the discovery of the Oklo Reactor Sites. In 2004, a computer model that couples thermal fluid dynamics, heat transfer and nuclear reactor physics has demonstrated Kuroda's prediction of periodicity, temperature range and the potential for violent ejection of water in the form of a geyser were all reasonable.

Further work to more accurately model the reactor operation may be conducted. The addition of neutron poisons such as xenon and samarium would be one possible modification. Concentrations of UO_2 in the reactor may have actually been as high as 90 percent. Modification of the source to allow extremely high concentrations along with the dissolution of surrounding rock to increase reactor concentrations would also be desirable. Fission products, their decay and transport and parallel implementation of source code could be integrated in to the current source. Modeling of future criticality events in geologic repositories with or without the above listed improvements could also be pursued.

Downloaded by STANFORD UNIV GREEN LIBR on August 6, 2012 | http://pubs.acs.org
Publication Date: November 16, 2006 | doi: 10.1021/bk-2007-0945.ch010

References

1. Naudet, R. Prise en Compte des Effets Thermiques Dans L'Etude du Controle et de la Propagation des Reactions Nucleaires; Report IAEA-TC-119/23, 1976, 601-618.
2. Curtis, D. B.; Gancarz, A. J. *Radiolysis in Nature: Evidence from the Oklo Natural Reactors*; New Mexico, 1983.
3. Kuroda, P. K. The pre-Fermi natural reactor: a note on the periodic mode of operation. *J. Radioanal. Nucl. Chem.* **1990**, *142*, 101-112.
4. Culbreth, W. G.; Viggato, J. C. Determination of the Depth and Pressure within the Oklo Natural Reactors; RPS: Spokane, WA, 2000.

Nomenclature

θ	angle of inclination - degrees
k_a	apparent thermal conductivity - W m^{-1} K^{-1}
ρ_f	density of water - kg m^{-3}
D	diffusion coefficient - m
μ_f	dynamic viscosity of water - N s m^{-2}
β	expansion coefficient - K^{-1}
g	gravity - m/s^2
Σ_a	macroscopic absorption - m^{-1}
Φ	neutron flux - neutrons m^{-2} s^{-1}
S	neutron source - neutrons m^{-3}
K	permeability - m^2
c_p	specific heat of water - J kg^{-1} K^{-1}
ψ	stream function - m^2 s^{-1}
T	temperature - K
v	velocity - m s^{-1}
$\dot{q}'''$	volumetric heat generation - W m^{-3}

Downloaded by STANFORD UNIV GREEN LIBR on August 6, 2012 | http://pubs.acs.org
Publication Date: November 16, 2006 | doi: 10.1021/bk-2007-0945.ch010

In Applied Modeling and Computations in Nuclear Science; Semkow, T., et al.;
ACS Symposium Series; American Chemical Society: Washington, DC, 2006.

Downloaded by NORTH CAROLINA STATE UNIV on August 9, 2012 | http://pubs.acs.org
Publication Date: November 16, 2006 | doi: 10.1021/bk-2007-0945.ch011

Chapter 11

Modeling the Effects of the Trinity Test

Thomas M. Semkow[1,2], Pravin P. Parekh[1,3], and Douglas K. Haines[1]

[1]Wadsworth Center, New York State Department of Health, P.O. Box 509, Albany, NY 12201
[2]School of Public Health, University at Albany, State University of New York, Albany, NY 12201
[3]Retired

The first nuclear explosion test, named the Trinity Test, was conducted on July 16, 1945 near Alamogordo, New Mexico. Although historical details of the Manhattan Project and the Trinity Test are well documented, some scientific characteristics of the test are not known, or are unpublished. In the tremendous heat of the explosion, the radioactive debris fused with the local soil into a glassy material named Trinitite. Radionuclides with sufficiently long half-lives survived the decay and today preserve a permanent record of the historic event. A detailed radiochemical and spectroscopic analysis of Trinitite has been recently completed by Parekh *et al.* (*1*). On the basis of those data, as well as calculations and modeling, a variety of scientific information has been unraveled about the test, and is reported here. In particular, we infer the Trinitite freeze-out time and present the following calculated test characteristics: plutonium composition in the nuclear fuel, implosion compression factor, nuclear device explosive yield, uranium contribution to the explosion, size of the nuclear eyeball, total number of prompt neutrons emitted, fast-neutron fluence, slow neutron fluence, and the debris-deposition exponent.

In Applied Modeling and Computations in Nuclear Science; Semkow, T., et al.;
ACS Symposium Series; American Chemical Society: Washington, DC, 2006.

1. Introduction

The Trinity Test was the successful culmination of the Manhattan Project and the first manmade nuclear explosion. There exists an historical and documentary account, as well as some technical information about it. On the 20th anniversary of the Trinity explosion, two detailed articles were published, one by Savage (*2*) covering construction of the first atomic device, and the other by Storms (*3*) describing the Trinity Test. Two comprehensive, scholarly treatises by Szasz (*4*) and by Rhodes (*5*) elucidate political, technical, and personnel details. The documentary movies (*6,7*), as well as the report by Mack (*8*), reveal detailed images of the explosion itself. Some information about the construction of the device has been provided by Sublette (*9*), whereas many details of the actual explosion, including several field measurements, were given by Bainbridge (*10*). The report by Hansen and Rodgers (*11*) presented radiological surveys of the Trinity Test site and fallout areas. Despite all this information, some of the scientific characteristics of the first nuclear explosion are not known or not published.

The first nuclear explosive device, named Gadget, was of the implosion type and was composed of several spherical shells, as depicted in Fig. 1. The neutron initiator consisted of a ^{210}Po/Be source placed in the center of the device. The initiator was surrounded by two hemispheres of the subcritical plutonium pit, which served as the nuclear explosive. Rhodes (*5*) presents some evidence that the device contained 11 lb or 5 kg of plutonium. Sublette (*9*) cites a memo by General Groves, who stated that it contained 13.5 lb of plutonium. In this chapter, we use the latter information, therefore, we take $m_{\mathrm{Pu}} = 6.123$ kg. That plutonium fuel was reportedly composed of $w(^{239}\mathrm{Pu}) = 99.1$ % of ^{239}Pu and $w(^{240}\mathrm{Pu}) = 0.9 - 1.0$ % of ^{240}Pu, by weight. The plutonium pit was stabilized with $w_{\mathrm{Ga}} = 0.8$ % of Ga, by weight. The pit was surrounded by $m_{\mathrm{U}} = 120$ kg of natural-uranium tamper, to prevent a premature disassembly of the pit and to provide initial confinement of neutrons. It has been reported (*9*) that about 20 % of the device's explosive yield was from uranium fission of this tamper. Surrounding the tamper was a layer containing boron, to prevent spontaneous-fission neutrons originating in the tamper, which thermalized in the outer shells, from scattering back into the pit. That was cladded by a 120-kg aluminum-pusher shell, to reduce the rapid drop in pressure occurring behind a detonation front in an implosion system. The outermost shell was the conventional-explosive implosion system, weighing at least 2500 kg. It consisted of 32 lenses: 20 hexagonal and 12 pentagonal, arranged in soccer-ball geometry. Each lens contained a combination of slow explosive (baratol: 75 % $\mathrm{Ba(NO_3)_2}$ and 25 % TNT) and a fast explosive (composition B: 60 % RDX, 39 % TNT, and 1 % wax). The combination of slow/fast explosive ensured a spherical implosion pressure wave. The whole Gadget device was encapsulated in a dural shell.

Downloaded by NORTH CAROLINA STATE UNIV on August 9, 2012 | http://pubs.acs.org
Publication Date: November 16, 2006 | doi: 10.1021/bk-2007-0945.ch011

Downloaded by NORTH CAROLINA STATE UNIV on August 9, 2012 | http://pubs.acs.org
Publication Date: November 16, 2006 | doi: 10.1021/bk-2007-0945.ch011

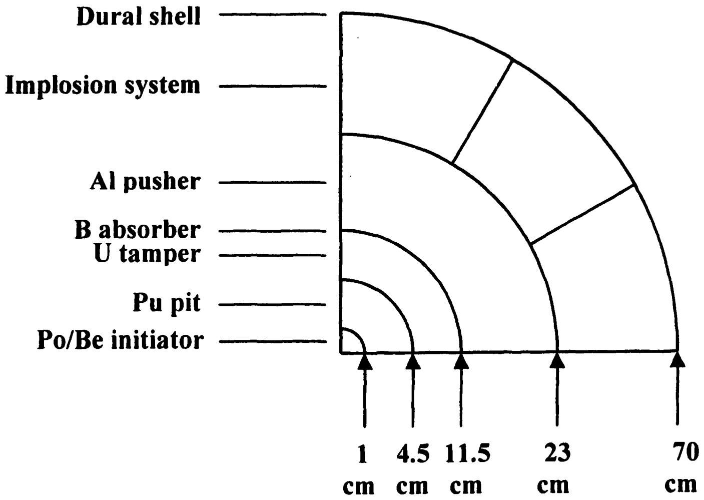

Figure 1. Schematic diagram and approximate dimensions of a quarter-section of the Gadget nuclear device (9). The diagram is not to scale.

The Gadget was raised to the top of a 100-foot steel tower positioned at ground zero (GZ) of the Trinity Test site, and was successfully exploded on July 16, 1945, at 5:29:45 am. The explosion was initiated by firing of the implosion lens system (*5*). In a matter of a few μsec, the converging shock wave generated several Mbar of pressure on the core, compressing it by a factor $\eta \sim 2 - 3$ by one estimate, and up to 2.5 times (possibly somewhat less) by another estimate (*9*). In this way, the compressed pit became a supercritical mass. Also, compression of the initiator started the ^{9}Be(α,n) reaction providing neutrons, which initiated the fission reaction of ^{239}Pu. The chain reaction grew exponentially up to ~ 56 generations, before terminating in a violent disassembly (*12*). About 99 % of the energy was released in the last four generations. The fission reaction was confined to a small nuclear eyeball and lasted for ~ 0.56 μsec.

Immediately after the termination of the chain reaction, the temperature of the nuclear eyeball reached tens of millions of °K, and the immense energy was contained in the form of thermal radiation (x-ray photons), the kinetic energy of ionized atoms and electrons, γ rays and neutrons produced in fission, as well as excitation of atoms. The subsequent radiation transport created effects of the nuclear explosion in a complicated, turbulent process, which has been described elsewhere (*5,12*). The main resultant effect was the formation of an expanding fireball, which was an isothermal sphere of hot, ionized gas. The blast wave and most of the thermal radiation separated from the fireball several msec after the explosion. Associated prompt ionizing radiation consisted of prompt γ rays, fast and thermalized prompt neutrons from fission, neutron-capture and neutron-scattering γ rays, as well as isomeric-state γ rays. Late radiations included delayed neutrons, β particles, and γ rays from the decay of short-lived fission products. The fireball rose due to buoyancy and lifted off the ground, carrying a convection stem of radioactive dust behind it, on a time scale of several tens of sec. The explosive yield Y of Gadget was determined radiochemically to be 18.6 kT (1 kT = 10^{12} cal) by Anderson, as reported by Bainbridge (*10*). The latest estimate raised the yield to 21 kT (*13*). Attempts by Atkatz and Bragg (*14*) and Schlauf *et al.* (*15*) to verify the Trinity yield, using a single radiochemical monitor, were unsuccessful.

The delayed effects of the Trinity Test consisted of the radioactive debris carried with the plume and the resultant fallout, as well as the debris remaining in the vicinity of GZ (*11*). The radioactive debris included fission products, neutron-activation products, as well as the remains of the unfissioned plutonium and the U tamper. The blast wave created a shallow depression upon striking GZ. The fireball touched the ground at 0.65 msec after the explosion (*8*) and remained as a dome on the ground, while expanding in the cooling process. The fireball reached its maximum radius of about 300 m before starting to rise at ~ 2 sec after the explosion (*10*). The immense heat of the fireball melted the desert sand, which captured a part of the radioactive debris. The melted sand created a solid layer upon cooling. Enrico Fermi described the site as "a depressed area 400 yards in radius glazed with a green, glasslike substance where the sand had melted and solidified again" (*3*). The 400-yard radius of melted sand is consistent with the 300-m maximum radius of the fireball, and can be verified from the existing photographs (*4*). The green substance was named Trinitite. In 1952, most of the Trinitite was removed from the site and buried, while the depression was filled (*16*). Only small pieces of Trinitite remained at the site.

This chapter attempts to elucidate several effects of the Trinity Test. During the past six decades, most of the radioactive debris captured in Trinitite has decayed. However, several radionuclides with sufficiently long half-lives have survived radioactive decay and preserve a permanent record of the historic event. We have recently carried out a detailed study of radioactivity in Trinitite (*1*), using radiochemical methods as well as α-/γ-spectroscopy and β-counting. We describe radioactivity in Trinitite in Section 2.1 below, where we also estimate the Trinitite freeze-out time. Using these data, we perform detailed calculations and modeling in the remainder of Section 2. In this way, a large number of the Trinity Test parameters were elucidated. Some of the parameters are new, some agree with the existing estimates, and some differ. A summary is provided in Section 3.

Downloaded by NORTH CAROLINA STATE UNIV on August 9, 2012 | http://pubs.acs.org
Publication Date: November 16, 2006 | doi: 10.1021/bk-2007-0945.ch011

Downloaded by NORTH CAROLINA STATE UNIV on August 9, 2012 | http://pubs.acs.org
Publication Date: November 16, 2006 | doi: 10.1021/bk-2007-0945.ch011

2. Evaluation of Several Trinity-Test Parameters

2.1. Radioactivity in Trinitite and Its Freeze-Out Time

Some of the results of radioactivity in Trinitite by Parekh *et al.* (*1*), pertaining to the present investigation, are given in Table I. Listed are radionuclide, half-life *T*, source of origin, and specific activity *S*.

Table I. Specific Activities *S* of Selected Radionuclides in Trinitite Normalized to the Time of the Explosion (*1*)

Radionuclide	*Half-life T [years]*	*Origin*	$S \pm 1\sigma^{\dagger}$ [Bq g^{-1}]
^{90}Sr	28.5	(n,f)	58.73 ± 1.15
^{137}Cs	30.0	(n,f)	27.33 ± 0.08
^{152}Eu	13.33	^{151}Eu(n,γ)	78.89 ± 0.61
^{238}U	4.468×10^{9}	U tamper	$1.247 \times 10^{-2} \pm 1.35 \times 10^{-3}$
^{238}Pu	87.74	^{239}Pu(n,2n)	5.965 ± 0.071
^{239}Pu	2.411×10^{4}	nuclear fuel	86.32 ± 2.68
^{240}Pu	6.563×10^{3}	^{239}Pu(n,γ)	4.102 ± 0.936

^{90}Sr and ^{137}Cs are fission products generated in the (n,f) fission reaction, induced by fast (fission-spectrum) neutrons. This fission was primarily of ^{239}Pu, but also of ^{240}Pu, as well as ^{238}U and ^{235}U contained in the natural-U tamper. These fission products will be used as monitors to determine *Y*, in Section 2.3.

^{152}Eu is an activation product of ^{151}Eu by mostly slow (thermal) and, to a lesser extent, fast neutrons in an (n,γ) reaction. ^{151}Eu was present in the GZ soil. ^{152}Eu is further used as a monitor of slow-neutron fluence, in Section 2.2.

^{238}U was present in the U tamper, and also as a natural radionuclide in the GZ soil. The reported specific activity of 1.247×10^{-2} Bq g^{-1} reflects only the contribution due to the U tamper (*1*). The latter value will be used as a monitor of *Y*, in Section 2.3.

^{239}Pu in Trinitite came from the unfissioned nuclear fuel. Plutonium used in the Gadget device was manufactured in the Hanford reactors (Washington State). ^{239}Pu was produced through neutron capture by ^{238}U and two consecutive β decays, followed by a chemical separation. In that process, small amounts of ^{240}Pu and other plutonium isotopes are also produced. ^{240}Pu is not desirable in nuclear devices due to its high spontaneous-fission rate, giving rise to neutron emission, which can pre-trigger the device. A super-grade plutonium is defined as having $w(^{240}\text{Pu}) < 3$ %. It has been reported that the Gadget plutonium fuel contained $w(^{240}\text{Pu}) = 0.9 - 1.0$ % (*9*). It was, therefore, super-grade. We have elsewhere presented detailed arguments (*1*) that the ^{240}Pu specific activity in Trinitite, listed in Table I, reflects combined contributions from Hanford as well as from the Trinity Test. These contributions will be differentiated in Section 2.4, after other necessary parameters are determined. We have also argued that other Pu isotopes were most likely produced in the Trinity Test, rather than at Hanford. Of particular interest is ^{238}Pu formed from ^{239}Pu by a (n,2n) reaction with fast neutrons, which will be used in the determination of the fast-neutron fluence, in Section 2.2.

The radionuclides of interest were fused into Trinitite, when the sand was in a molten state. It was determined by Ross (*17*), using mineralogical methods, that the temperature at GZ was at least 1470 °C. Other data suggest that it was considerably higher. Bainbridge (*10*) reported theoretical calculations, by Bethe, of the fire-ball surface brightness and temperature. The temperature dropped from extremely high, at 100 μsec after the explosion, to a minimum of 2000 °K at 40 msec. This minimum is due to opacity of the fireball surface to visible radiation after the hydrodynamic separation of the blast front, although the temperature of the fireball interior continued to be higher (*12*). After the blast-wave breakaway, the surface temperature rose to 3500 - 4000 °K, reflecting the temperature of the interior. Subsequently, the temperature continuously declined, however, it was still 2000 °K at 9 sec. These values are above the melting point of quartz equal to 1995 °K (*18*). Another possible evidence for high temperatures was the observed high porosity of the original Trinitite layer (see Fig. 1 in Ref. (*1*)), indicating a rather turbulent bubbling of melted sand. Any surface deposition after the Trinitite had solidified would have weathered away during the past six decades. It is, therefore, necessary to determine the freeze-out time after the explosion, as the time in which Trinitite solidified and stopped accommodating the radioactive debris.

We inferred the possible range of freeze-out times from the documentary films (*6,7*), as well as from the photographs reported by Mack (*8*). The fireball started to rise at ~ 2 sec after the explosion. The outermost sections of the fireball lifted off first. Since the Trinitite samples that we analyzed had originated 40 to 65 m from the position of the GZ tower, we were interested in the time when the bottom of the fireball lifted off. One photograph shows that, at 10 sec after the explosion, there was a ~ 200-m stem present under the fireball. By careful examination of the explosion sequences on the films, we concluded that the likely time of fireball separation from the ground was ~ 8 sec after the explosion. We found this consistent with the fireball velocities reported by Glasstone and Dolan (*12*). We take this time as a lower bound freeze-out time. Then came the cooling period, facilitated by a convective updraft of air and debris pulled behind by the rising fireball. For a short period of time, Trinitite may have been still in a molten state, and it could have continued absorbing the radioactive debris which fell on it (*17*). It is difficult to precisely determine the

Downloaded by NORTH CAROLINA STATE UNIV on August 9, 2012 | http://pubs.acs.org
Publication Date: November 16, 2006 | doi: 10.1021/bk-2007-0945.ch011

upper bound time, but we took it as 11 sec. Therefore, we took $t = 8 - 11$ sec as the time range of Trinitite freeze-out, which will be used for the yield determination, in Section 2.3.

2.2. Fast- and Slow-Neutron Fluences

Most of the neutrons emitted in fission are prompt, whereas the delayed neutrons, emitted by the short-lived fission products, have smaller yields: 0.60 % for ^{239}Pu, and 3.85 % for ^{238}U (*19*), two major contributors to the nuclear explosion at Trinity. Prompt neutrons are called fast or fission-spectrum neutrons, with energies ranging from 0 to > 20 MeV, and having an average energy of ~ 2 MeV (*20*). The average energy of the delayed neutrons is ~ 0.6 MeV. Both prompt and delayed neutrons slowed down in the device debris and the surrounding air, to become slow or thermal neutrons after the Trinity explosion.

The prompt fast-neutron fluence was determined with the ^{238}Pu monitor and unfissioned ^{239}Pu as a normalizer. The ^{239}Pu(n,2n)^{238}Pu nuclear reaction occurred in the eyeball, where there was a high concentration of unfissioned ^{239}Pu, as well as a high fluence of fast neutrons. This reaction has a threshold of 5.6 MeV (*21*), and an integrated cross-section for fission neutrons of $\sigma_{n2n} = 4.045$ mb (*9*). The fast neutron fluence Φ_f is given by

$$\Phi_f = \frac{S(^{238}\mathrm{Pu})T(^{238}\mathrm{Pu})}{S(^{239}\mathrm{Pu})T(^{239}\mathrm{Pu})\sigma_{n2n}}, \tag{1}$$

where S and T are the specific activities and half-lives from Table I. We obtained the value of $\Phi_f = 6.217 \times 10^{22}$ n cm$^{-2(\dagger)}$. The reason for using the ^{239}Pu normalizer is that both plutonium isotopes have the same deposition factor in Trinitite, so that term cancels out. The fast neutron fluence from Eq. 1 has not been corrected for possible neutron-induced reactions on minor components of the pit, such as nickel plating, gold foil, and beryllium initiator (*5,9*). These are believed to be secondary effects. Bainbridge (*10*) reported a measurement by Klema, who determined that a total of 6.5×10^{21} fast neutrons went through the sphere of 200-m radius from the detonation point. This gives a fluence of 1.3×10^{12} n cm^{-2}, which is smaller by a factor of 4.8×10^{10} than the fluence in the eyeball.

The slow-neutron fluence Φ_s at the location of the Trinitite sample was determined with the ^{152}Eu monitor via the (n,γ) reaction on ^{151}Eu present in the local soil at GZ. This space- and time-integrated fluence is a sum of contributions from the slowed prompt neutrons, as well as delayed neutrons. We calculated that the contribution of ^{152}Eu from fission can be neglected, since this radionuclide has a negligible independent fission yield, while its cumulative fission yield is shielded by a stable ^{152}Sm in the β-decay chain (*19*). The thermal-

Downloaded by NORTH CAROLINA STATE UNIV on August 9, 2012 | http://pubs.acs.org
Publication Date: November 16, 2006 | doi: 10.1021/bk-2007-0945.ch011

neutron activation cross-section is very high, $\sigma_{n\gamma}$ = 5300 b (*22*). Although the relative apportionment of the neutron fluence between slow and fast is not known, the contribution of fast neutrons to the activation is much smaller, and we assume that it can be approximated by the cadmium ratio for a nuclear reactor, CR = 43 (*22*). The production of ^{152}Eu via the ^{153}Eu(n,2n) reaction is neglected, due to the relatively low cross-section of this threshold reaction (in the mb range). With these assumptions, the slow-neutron fluence is given by

$$\Phi_s = \frac{STM}{N_A ac\sigma_{n\gamma} \ln 2}\left(\frac{1-e^{-x}}{x} + \frac{1}{CR-1}\right)^{-1}, \quad \text{where} \qquad (2a)$$

$$x = N_A \rho_t d_t \sum_i \left(\frac{ac\sigma_{n\gamma}}{M}\right)_i . \qquad (2b)$$

In Eq. 2a, *S* and *T* are the specific activity and half-life of ^{152}Eu, *M* is the europium atomic mass, *a* is the ^{151}Eu isotopic abundance, N_A is the Avogadro number, and c = 1.2 µg g^{-1} is the concentration of Eu in the local soil (*1*). *x* in Eq. 2b takes care of the self-shielding of slow neutrons in Trinitite. The sum was calculated over all components in the local soil deduced from Shacklette *et al.* (*23*) and Mason (*24*). The activation cross sections were taken from Friedlander *et al.* (*25*). ρ_t = 2.5 g cm^{-3} is the density of glass, and d_t = 0.8 cm is the average thickness of Trinitite. By plugging the above variables into Eq. 2a, we calculated $\Phi_s = 3.895 \times 10^{15}$ n cm^{-2}.

Bainbridge (*10*) reported slow-neutron fluence measurements of the Trinity Test, recorded by Klema at distances of 300 to 500 m from the GZ tower. Plotting them on a log-log scale in Fig. 2 (filled points), as functions of slant range *r* from the explosion center, we obtained an approximately straight line, suggesting a power-law dependence. We fitted the Bainbridge data (solid curve) and obtained the relationship

$$\Phi_s\left[\text{n cm}^{-2}\right] = \frac{5.55492 \times 10^{26}}{r^{6.25748}[\text{m}]} . \qquad (3)$$

An exponent of 2 for *r* would indicate a spherical spread of the neutrons, without attenuation. However, the exponent was greater than 6, indicating considerable attenuation and capture of the neutrons. Using Eq. 3, we extrapolated the fluence to the distances 40 to 65 m from the GZ tower, where our Trinitite sample was located, corresponding to 50.3 to 71.8 m of slant range from the nuclear explosion center (taking into consideration the height of the tower, equal to 30.5 m). We obtained the neutron fluence range between 1.349×10^{15} and 1.251×10^{16} n cm^{-2}, with the geometric mean of 4.108×10^{15}. The fluence of 3.895×10^{15} n cm^{-2}, determined from the ^{152}Eu monitor above, falls close to this mean. This is a satisfactory agreement, considering an uncertainty in the location of our sample, which could have shifted during of after site cleanup (*16*).

Downloaded by NORTH CAROLINA STATE UNIV on August 9, 2012 | http://pubs.acs.org
Publication Date: November 16, 2006 | doi: 10.1021/bk-2007-0945.ch011

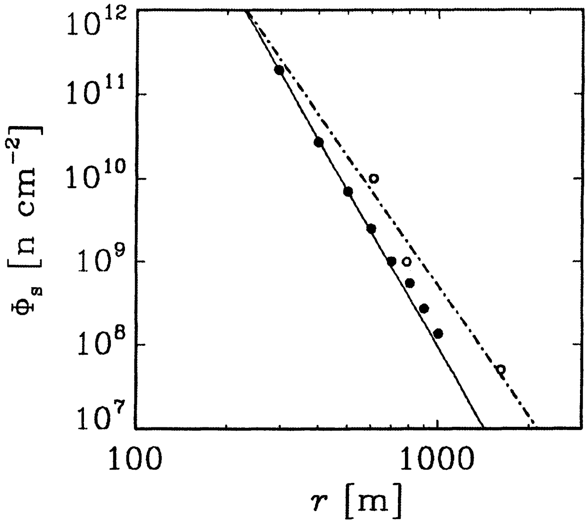

Figure 2. Filled points: slow-neutron fluence Φ_s plotted as a function of slant range r from the point of Trinity detonation (experimental data from Bainbridge (10)). Open points: rescaled concentration of ^{152}Eu [10^8 Bq mg^{-1}] plotted as a function of slant range from the point of Hiroshima detonation (experimental data by Shizuma et al. (26)). The lines represent least-squares fits.

Also plotted in Fig. 2 (open points) are rescaled concentrations of ^{152}Eu determined in the remnants of the Hiroshima explosion, by Shizuma *et al.* (*26*). The data exhibit an approximate power-law dependence, as functions of slant range, taking into account the 2000-ft explosion elevation (*27*). We fitted the data (broken curve), which resulted in an exponent of 5.15239. This exponent is smaller than the Trinity explosion exponent of 6.25748, possibly due to a contribution from fallout, however, it is still much larger than 2.

2.3. Device Explosive Yield, Participating Uranium Fraction, and the Deposition Exponent

We developed a model, based on several physical phenomena, to calculate the Gadget explosive yield Y. If all ^{239}Pu had fissioned, the maximum yield Y_m would have been

$$Y_m = \frac{m_{Pu}\, w(^{239}\mathrm{Pu})\, N_A E_f}{M(^{239}\mathrm{Pu})\, K}, \qquad (4)$$

Downloaded by NORTH CAROLINA STATE UNIV on August 9, 2012 | http://pubs.acs.org
Publication Date: November 16, 2006 | doi: 10.1021/bk-2007-0945.ch011

where $E_f = 180$ MeV is an average prompt energy released per fission event, and $K = 2.611 \times 10^{25}$ MeV kT^{-1} is the conversion factor between MeV and kT. E_f consists of the kinetic energies of fission fragments and prompt neutrons, most energy of prompt γ rays, small fraction of the decay energy of fission products, as well as energy released in neutron capture by the device debris (*12*). We obtained $Y_m = 105.4$ kT from Eq. 4. The actual yield was much lower, since the device disassembled violently, before all ^{239}Pu could have fissioned.

In the model we utilized ^{90}Sr, ^{137}Cs, and ^{238}U as monitors, as well as unfissioned ^{239}Pu as a normalizer. The model has three major components: 1) fission reactions from available Pu and U isotopes, 2) time-dependent buildup of fission products, and 3) temperature-dependent deposition of radionuclides in Trinitite. All of them are discussed below.

In addition to ^{239}Pu, we considered fission of ^{240}Pu present in the plutonium fuel. We also added fission of the U tamper, *i.e.*, of ^{238}U and ^{235}U, according to the two isotopes' natural abundances. The fraction of total fissions due to U isotopes is abbreviated as f_U, and it will be determined from the model fit. The relative contributions due to various fissioning radionuclides were scaled according to the weight fractions w, isotopic abundances a, fission-neutron-induced fission cross-sections σ_{nf}, and are given by

$$R_{Pu} = \frac{w(^{240}\mathrm{Pu})\sigma_{nf}(^{240}\mathrm{Pu})M(^{239}\mathrm{Pu})}{w(^{239}\mathrm{Pu})\sigma_{nf}(^{239}\mathrm{Pu})M(^{240}\mathrm{Pu})}, \quad (5a)$$

$$R_U = \frac{a(^{235}\mathrm{U})\sigma_{nf}(^{235}\mathrm{U})}{a(^{238}\mathrm{U})\sigma_{nf}(^{238}\mathrm{U})}, \quad (5b)$$

$$R_m = \frac{m_U\, a(^{238}\mathrm{U})M(^{239}\mathrm{Pu})}{m_{Pu} w(^{239}\mathrm{Pu})M_U}. \quad (5c)$$

The cross-section values were taken from Sublette (*9*).

We considered a time-dependent buildup of ^{90}Sr and ^{137}Cs according to β-decay chains, as depicted in Figs. 3a, b. We discuss ^{137}Cs first. All of the radionuclides in Fig. 3b can be produced independently, *i.e.*, directly in fission after prompt-neutron emission, or cumulatively, *i.e.*, when after-fission contribution from β decay is added. Accumulation of any fission product in the chain is thus a time-dependent process, which can be expressed in matrix notation (*28*,*29*). For every fission reaction of interest, we defined a vector of independent fission yields of $A = 137$ chain members at time zero (time of explosion), $\mathbf{I}(0)$, where position indices are given in the parentheses in Fig. 3b (the vector has a dimension of 6). We took the independent yields I_1 through I_6 as members of $\mathbf{I}(0)$ from the model calculations by England and Rider (*19*). The vector of cumulative fission yields after time t, $\mathbf{I}(t)$, is given by the matrix equation

$$\mathbf{I}(t) = \mathbf{P}\,\mathrm{diag}[\exp(-\lambda_i t)]\,\mathbf{P}^{-1}\,\mathbf{I}(0)\,, \quad (6)$$

Downloaded by NORTH CAROLINA STATE UNIV on August 9, 2012 | http://pubs.acs.org
Publication Date: November 16, 2006 | doi: 10.1021/bk-2007-0945.ch011

Downloaded by NORTH CAROLINA STATE UNIV on August 9, 2012 | http://pubs.acs.org
Publication Date: November 16, 2006 | doi: 10.1021/bk-2007-0945.ch011

where λ_i is the decay constant of a member i, diag denotes a diagonal matrix, whereas matrices **P** and $\mathbf{P}^{-1}$ are functions of the decay constants as well as the decay branching fractions.

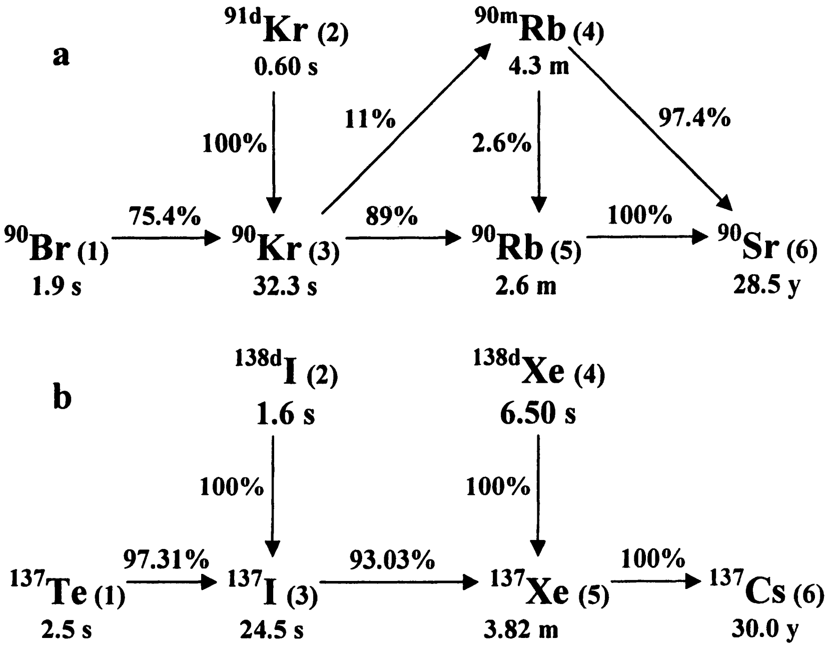

Figure 3. Beta-decay chains for the mass numbers a) $A = 90$, and b) $A = 137$. Half-lives are given below the radionuclide symbols. The metastable state is denoted by the letter m, while the delayed-neutron state from the $A + 1$ mass number is denoted by the letter d. The decay branching fractions (%) are given by the arrows. The numbers in parentheses denote position indices in the chains as well as in the vectors.

All of the fission products in Fig. 3b were initially present in the gas phase from the tremendous heat of the explosion. Tellurium decayed quickly, iodine is very volatile, and xenon is a noble gas, whereas cesium is less volatile with the boiling point B = 671 °C (*18*). Therefore, the deposition of ^{137}Cs in Trinitite was primarily as cesium, up to about the Trinitite freeze-out time t. We thus took the deposition of ^{137}Cs as proportional to $I_{Cs}(t) = I_6(t)$, the 6th member of vector $\mathbf{I}(t)$.

The situation for ^{90}Sr in Fig. 3a is more complicated. Bromine is volatile and decayed quickly, while krypton is a noble gas. However, rubidium and strontium are less volatile (B = 688 °C and 1382 °C, respectively (*18*)), and both could have deposited in Trinitite. Thus, the total ^{90}Sr in Trinitite came from the deposited strontium, proportional to $I_{\mathrm{Sr}}(t) = I_6(t)$, as well as from the deposited rubidium, proportional to $I_{\mathrm{Rb}}(t) = I_4(t) + I_5(t)$ (where we added contributions from the two isomers of rubidium in Fig. 3a), which decayed to strontium inside Trinitite after the deposition.

Subsequently, we added contributions from all fission reactions. For any product P ≡ Rb, Sr, Cs, we renamed the fission yields $I_{\mathrm{P}}(t)$ from above to $I_{\mathrm{P}}(t,\mathrm{X})$ for fission of every X ≡ ^{239}Pu, ^{240}Pu, ^{238}U, ^{235}U. The total fission yield $F_{\mathrm{P}}(t,f_{\mathrm{U}})$ of any product P of interest can be derived, using the ratios from Eqs. 5a, b, and is given below

$$F_{\mathrm{P}}(t,f_{\mathrm{U}}) = I_{\mathrm{P}}(t,{}^{239}\mathrm{Pu}) + R_{\mathrm{Pu}} I_{\mathrm{P}}(t,{}^{240}\mathrm{Pu}) + \frac{f_{\mathrm{U}}(1+R_{\mathrm{Pu}})}{(1-f_{\mathrm{U}})(1+R_{\mathrm{U}})}[I_{\mathrm{P}}(t,{}^{238}\mathrm{U}) + R_{\mathrm{U}} I_{\mathrm{P}}(t,{}^{235}\mathrm{U})]\,. \tag{7}$$

The deposition of fission products from a nuclear explosion depends on physico-chemical fractionation (*12*). Consequently, we assumed in the model that the deposition of radionuclides in Trinitite depended on their relative volatilities, expressed by the boiling points *B*, normalized to ^{239}Pu,

$$\tau_{\mathrm{P}} = \frac{B(\mathrm{P}) + 273}{B({}^{239}\mathrm{Pu}) + 273}\,, \tag{8}$$

for any P ≡ Rb, Sr, Cs, U. It is possible that using vapor pressures, rather than boiling points, would better reflect the relative volatilities. We did not consider the complicated dynamics of deposition in this simplified model. It is well-established, however, that power-law distributions are often encountered in turbulent and stochastic processes (compare Eq. 3). We, therefore, assumed that the deposition factor was proportional to $\tau_{\mathrm{P}}{}^{b}$, where deposition exponent *b* would be determined from the model fit.

Finally, we normalized measured specific activities to ^{239}Pu, where P stands for Sr, Cs, or U (*i.e.*, ^{238}U).

$$Q_{\mathrm{P}} = \frac{S({}^{239}\mathrm{Pu})\,T({}^{239}\mathrm{Pu})}{S(\mathrm{P})\,T(\mathrm{P})}\,. \tag{9}$$

By combining all the definitions, assumptions, and equations above, we derived the equations for the Gadget explosive yield

$$Y(t,f_{\mathrm{U}},b) = \begin{cases} \dfrac{Y_{\mathrm{m}}(1+R_{\mathrm{Pu}})/(1-f_{\mathrm{U}})}{1+Q_{\mathrm{Cs}}\,\tau_{\mathrm{Cs}}^{b}\,F_{\mathrm{Cs}}(t,f_{\mathrm{U}})}, & \text{Cs monitor,} \quad (10\mathrm{a}) \\[2ex] \dfrac{Y_{\mathrm{m}}(1+R_{\mathrm{Pu}})/(1-f_{\mathrm{U}})}{1+Q_{\mathrm{Sr}}[\tau_{\mathrm{Rb}}^{b}\,F_{\mathrm{Rb}}(t,f_{\mathrm{U}}) + \tau_{\mathrm{Sr}}^{b}\,F_{\mathrm{Sr}}(t,f_{\mathrm{U}})]}, & \text{Sr monitor,} \quad (10\mathrm{b}) \\[2ex] \dfrac{Y_{\mathrm{m}}(1+R_{\mathrm{Pu}})(1+R_{\mathrm{U}})(1-R_{\mathrm{m}}\,Q_{\mathrm{U}}\,\tau_{\mathrm{U}}^{b})}{(1-f_{\mathrm{U}})(1+R_{\mathrm{U}})-(1+R_{\mathrm{Pu}})Q_{\mathrm{U}}\,\tau_{\mathrm{U}}^{b}}, & \text{U monitor.} \quad (10\mathrm{c}) \end{cases}$$

Equations 10a-c were solved numerically, using the NAG software (Numerical

Downloaded by NORTH CAROLINA STATE UNIV on August 9, 2012 | http://pubs.acs.org
Publication Date: November 16, 2006 | doi: 10.1021/bk-2007-0945.ch011

Algorithms Group, Downers Grove, IL). We obtained the values of Y, f_U, and b for every given t; these are plotted in Fig. 4. By taking the Trinitite freeze-out time limits t = 8 - 11 sec (Section 2.1), we obtained Y = 21.43 ± 1.13 kT. The uncertainties of the specific activities from Table I were propagated, to arrive at Y = 21.43 ± 1.97 kT. Similarly, f_U = 30.82 ± 1.80 % and b = 0.6908 ± 0.0722. The yield agrees with the latest estimate of 21 kT (*13*). However, the fraction of fission due to U, according to our model, is higher than the "about 20 %" mentioned by Sublette (*9*). Taking a shorter Trinitite freeze-out time would result in higher values of Y and f_U, whereas taking a longer freeze-out time would lower Y and f_U (compare Fig. 4).

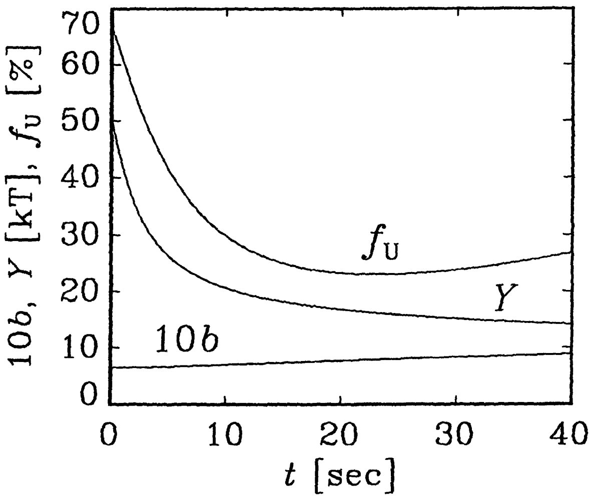

Figure 4. Plots of the model calculations for the temperature-deposition exponent b, Gadget device yield Y, and fraction of the yield due to uranium f_U, as functions of the Trinitite freeze-out time t.

2.4. Total Number of Prompt Neutrons, Size of the Nuclear Eyeball, Implosion Compression Factor, and Plutonium Composition

The total number of prompt neutrons can be calculated from

$$N_n = \frac{YK}{E_f}\left\{\begin{array}{l}\dfrac{1-f_U}{1+R_{Pu}}[\nu(^{239}\mathrm{Pu}) + R_{Pu}\,\nu(^{240}\mathrm{Pu})] \\ +\dfrac{f_U}{1+R_U}[\nu(^{238}\mathrm{U}) + R_U\,\nu(^{235}\mathrm{U})] - 1\end{array}\right\}, \qquad (11)$$

Downloaded by NORTH CAROLINA STATE UNIV on August 9, 2012 | http://pubs.acs.org
Publication Date: November 16, 2006 | doi: 10.1021/bk-2007-0945.ch011

Downloaded by NORTH CAROLINA STATE UNIV on August 9, 2012 | http://pubs.acs.org
Publication Date: November 16, 2006 | doi: 10.1021/bk-2007-0945.ch011

where $\nu(X)$ is the average number of prompt neutrons per fission event, for a particular fissioning nucleus X. We took the values of ν from England and Rider (*19*), and obtained $N_n = 5.877 \times 10^{24}$ neutrons. Comparing this with the data reported by Bainbridge (*10*), we find that only 0.1106 % of fast neutrons survived 200 m away from the detonation center.

The size of the nuclear eyeball d_e can be estimated immediately as $d_e = (N_n/\Phi_f)^{1/2} = 9.723$ cm.

The evaluated parameters allow calculation of the implosion compression factor. We assumed that the eyeball was a sphere of diameter d_e. Next, we assumed that Be, Ga, Pu, and U all experienced the same compression in the eyeball, and we took the original diameter of the initiator $d_{Be} = 2$ cm (see Fig. 1). With these assumptions, the compression factor η is given by

$$\eta = \frac{6m_{Pu}}{\pi d_e^3}\left\{\frac{1}{\rho_{Pu}} + \frac{w_{Ga}}{(1-w_{Ga})\rho} + \frac{f_U(1+R_{Pu})m_U\sigma_{nf}(^{239}Pu)}{(1-f_U)(1+R_U)R_m m_{Pu}\sigma_{nf}(^{238}U)\rho_U}\right\} + \left(\frac{d_{Be}}{d_e}\right)^3, \qquad (12)$$

where ρ_{Pu} and ρ_U are densities. $\rho = \rho_{Pu} = 15.92$ g cm^{-3}, if δ-phase Pu alloy with Ga was present; or $\rho = \rho_{Ga}$ and $\rho_{Pu} = 19.84$ g cm^{-3}, if α-phase of Pu was present separately from Ga. Using Eq. 12, we calculated the compression factors for the δ- and α-phases separately, obtaining $\eta = 2.503$ and 2.356, respectively. It has been reported that the δ-phase was present (*9*). To elucidate this point, we took the original dimensions from Fig. 1, and obtained 6.010 kg Pu if the δ-phase was present, or 7.490 kg Pu if the α-phase was present. Since the reported 6.123 kg of Pu is only slightly higher than the value that would be expected for pure δ-phase, we assumed that the excess is due to a small admixture of the α-phase. The compression factor was then averaged over both phases yielding $\eta = 2.492$, which is consistent with the "2.5 times (possibly somewhat less)" estimate reported by Sublette (*9*).

The ratio of the mass of ^{240}Pu to the mass of ^{239}Pu present in the original fuel can be derived, assuming only ^{239}Pu fission, and is given by

$$\frac{m(^{240}Pu)}{m(^{239}Pu)} = \left[\frac{S(^{240}Pu)T(^{240}Pu)}{S(^{239}Pu)T(^{239}Pu)} - \sigma_{n\gamma}\Phi_f\right]\frac{M(^{240}Pu)}{M(^{239}Pu)}, \qquad (13)$$

where $\sigma_n = 52.94$ mb (*9*) is the fission-neutron capture cross-section for the ^{239}Pu(n,γ)^{240}Pu reaction. The second term inside the brackets is the subtracted contribution from the explosion. By plugging in available values, we obtained a value of 9.685×10^{-3} for the ratio, from which, immediately, $w(^{240}Pu) = 0.9592$ %. This result can be refined by taking into account fission of all available nuclides. It leads to a quadratic equation, not reported here, from which $w(^{240}Pu) = 0.9225$ %. This result is consistent with the estimate of 0.9 - 1.0 % (*9*).

3. Discussion and Summary

Several Trinity-Test parameters were estimated, retroactively, using a combination of the experimental data by Parekh *et al.* (*1*) with the calculations and modeling. The determined parameters are listed in column 2 of Table II and they were rounded off to 1 - 3 significant digits. It is seen that most of the parameters agree with the literature values, when available (column 4), with the exception of the fraction of fission from U, which was calculated higher (30.8 %).

Table II. Comparison of Determined and Literature Values of the Trinity Test Parameters

Parameter	*Determined value*		*Literature value*	*Ref.*
	100 %^{a}	*90 %^{a}*		
^{240}Pu % weight in fuel	0.92	0.95	0.9 - 1.0	(*9*)
implosion compression factor	2.5	2.1	2.5 (possibly somewhat less)	(*9*)
size of nuclear eyeball [cm]	9.7	10.3		
% of fission from U	30.8 ± 1.8		about 20	(*9*)
number of fast neutrons	5.9×10^{24} at eyeball		6.5×10^{21} 200 m from GZ	(*10*)
fast neutron fluence [n cm^{-2}]	6.2×10^{22} at eyeball	5.6×10^{22} at eyeball	1.3×10^{13} 200 m from GZ	(*10*)
slow neutron fluence 40 - 65 m from GZ [n cm^{-2}]	3.9×10^{15}		4.1×10^{15} extrapolated	(*10*)
explosive yield [kT]	21.4 ± 2.0		21	(*13*)
Trinitite freeze-out time [sec]	8 - 11 inferred - assumed		7.6 - interpolated	(*8*, 12)
debris deposition exponent	0.691 ± 0.072			

^{a}Assumed percent of ^{238}Pu from explosion.

Our results depend on, and are limited by, any systematic errors in the experimental data given in Table I, sample location, as well as any inconsistencies in the available information about the Trinity Test and the Gadget device. Our calculations depend on the inferred Trinitite freeze-out time of 8 - 11 sec, which approximates rising of the fireball and cooling off the Trinitite. There are also several model assumption, such as the power function for the debris deposition coefficient, which depends on the boiling points only.

Downloaded by NORTH CAROLINA STATE UNIV on August 9, 2012 | http://pubs.acs.org
Publication Date: November 16, 2006 | doi: 10.1021/bk-2007-0945.ch011

Finally, the results reported here depend on the nuclear data taken from the literature, such as nuclear reaction cross-sections, fission yields, and radioactive decay data.

Several parameters depend on the percent of ^{238}Pu which was produced in the explosion as opposed to that present in the original nuclear fuel. It is likely that most of ^{238}Pu was produced in the explosion, where there was a high concentration of ^{239}Pu and a high neutron fluence, which is discussed below. The observed ratio of ^{238}Pu activity to that of ^{240}Pu in Trinitite is equal to 1.454 (Table I). If both had been produced exclusively by the fast neutrons in the explosion, the ratio of the activities should have been 5.715, according to the cross sections: σ_{n2n} = 4.045 mb and $\sigma_{n\gamma}$ = 52.94 mb (*9*). We calculated that the activation of ^{239}Pu by slow neutrons in the explosion could be neglected. The reason for the lower experimental ratio was the presence of ^{240}Pu in the nuclear fuel.

The reactors at Hanford, which produced Pu for the Trinity test, had a substantial slow-neutron component. This is supported by the observed quenching of the power by ^{135}Xe (*30*), which has enormous thermal-neutron capture cross section of 2.6×10^6 b. It follows that, if ^{238}Pu in Trinitite had originated mostly from Hanford, its activity would have been much smaller than that of ^{240}Pu due to the high ^{239}Pu(n,γ)^{240}Pu thermal-neutron cross section of 270.3 b, as compared with the σ_{n2n} above (even factoring in the shorter ^{238}Pu half-life). This is contrary to the observed activities given in Table I.

Therefore, several parameters in column 2 of Table II were calculated with an assumption that all ^{238}Pu was produced in the explosion. To determine the effect of this assumption, we recalculated the same parameters assuming that 90 % of ^{238}Pu was produced in the explosion. They are given in column 3, and can be thought as the opposite limits. These parameters could be fixed if the content of ^{238}Pu in the original plutonium fuel was known and subtracted from that measured in Trinitite.

We have also determined ^{133}Ba in Trinitite, which most likely originated from the neutron activation of barium in the baratol component of the explosive-lens system (*1*). If the quantity of barium used was known, ^{133}Ba could be employed as an additional monitor of the yield, and would enable calculation of an additional parameter from the model, such as the Trinitite freeze-out time.

Acknowledgments

R. Brodzinski, C. Brown, S. Jerome, M. Kitto, R. Rhodes, and A. Verschoor are acknowledged for very useful comments. A. Bentley and C. Harkins are acknowledged for the image processing. We are grateful to T. Flynn for library support and to D. Koreman for typing the manuscript.

Downloaded by NORTH CAROLINA STATE UNIV on August 9, 2012 | http://pubs.acs.org
Publication Date: November 16, 2006 | doi: 10.1021/bk-2007-0945.ch011

References

Disclaimer: This work uses only publicly available information, and considers Trinity test as a historical as well as scientific event.

† The numerical results in this chapter are reported to four significant digits, in order to enable their use in the following or future calculations, even if the accuracies may be lower.

1. Parekh, P. P.; Semkow, T. M.; Torres, M. A.; Haines, D. K.; Cooper, J. M.; Rosenberg, P. M.; Kitto, M. E. Radioactivity in Trinitite six decades later. *J. Environ. Radioact.* **2006**, *85*, 103-120.
2. Savage, J. Building the bomb. *The Atom* **1965**, *2*(*8*), 35-49.
3. Storms, B. Trinity. *The Atom* **1965**, *2*(*8*), 1-34.
4. Szasz, F. M. *The Day the Sun Rose Twice*; University of New Mexico Press: Albuquerque, NM, 1984.
5. Rhodes, R. *The Making of the Atomic Bomb*; Simon and Schuster: New York, NY, 1986.
6. *The Manhattan Project*; Film AAE-43497; A & E Television Networks: New York, NY, 2002.
7. *Trinity 1945*; Film 0800001; Bechtel Nevada Corporation: Las Vegas, NV, 2004.
8. Mack, J. E. Semi-popular motion-picture record of the Trinity explosion; Report MDDC-221; US Atomic Energy Commission, Technical Information Division: Oak Ridge, TN, 1946.
9. Sublette, C. http://nuclearweaponarchive.org; Nuclear weapons frequently asked questions, 2001.
10. Bainbridge, K. T. Trinity; Report LA-6300-H; Los Alamos Scientific Laboratory: Los Alamos, NM, 1976.
11. Hansen, W. R.; Rodgers, J. C. Radiological survey and evaluation of the fallout area from the Trinity Test: Chupadera Mesa and White Sands Missile Range, New Mexico; Report LA-10256-MS; Los Alamos National Laboratory: Los Alamos, NM, 1985.
12. Glasstone, S.; Dolan, P. J. *The Effects of Nuclear Weapons*; US Department of Defense and US Department of Energy; US Government Printing Office 1977 O-213-794: Washington, DC, 1977.
13. *United States Nuclear Tests July 1945 through September 1992*; Report DOE/NV-209-REV 15; US Department of Energy, Nevada Operations Office: Las Vegas, NV, 2000.
14. Atkatz, D.; Bragg, C. Determining the yield of the Trinity nuclear device via gamma-ray spectroscopy. *Am. J. Phys.* **1995**, *63*, 411-413.
15. Schlauf, D.; Siemon, K.; Weber, R.; Esterlund, R. A.; Molzahn, D.; Patzelt, P. Trinitite redux: comment on "Determining the yield of the Trinity nuclear

Downloaded by NORTH CAROLINA STATE UNIV on August 9, 2012 | http://pubs.acs.org
Publication Date: November 16, 2006 | doi: 10.1021/bk-2007-0945.ch011

device via gamma-ray spectroscopy", by D. Atkatz and C. Bragg [Am. J. Phys. 63, 411-413 (1995)]. *Am. J. Phys.* **1997**, *65*, 1110-1112.

16. *Trinity Site July 16, 1945*; US Government Printing Office 2000-844-916: Washington, DC, 2000.
17. Ross, C. S. Optical properties of glass from Alamogordo, New Mexico. *The American Mineralogist* **1948**, *33*, 360-362.
18. Lide, D. R.; Ed. *CRC Handbook of Chemistry and Physics*; 84th Ed.; CRC Press: Boca Raton, FL, 2003.
19. England, T. R.; Rider, B. F. Evaluation and compilation of fission product yields 1993; Report LA-UR-94-3106; Los Alamos National Laboratory: Los Alamos, NM 1994.
20. Ethvignot, T.; *et al.* Prompt-fission-neutron average energy for ^{238}U(n,f) from threshold to 200 MeV. *Phys. Lett. B* **2003**, *575*, 221-228.
21. Bernstein, L. A.; *et al.* ^{239}Pu(n,2n)^{238}Pu cross section deduced using a combination of experiment and theory. *Phys. Rev. C* **2002**, *65*, 021601(R).
22. Brunfelt, A. O.; Roelandts, I.; Steinnes, E. Some new methods for the determination of rare-earth elements in geological materials using thermal and epithermal neutron activation. *J. Radioanal. Chem.* **1977**, *38*, 451-459.
23. Shacklette, H. T.; Hamilton, J. C.; Boerngen, J. G.; Bowles, J. M. Elemental composition of surficial materials in the conterminous United States; Geological Survey Professional Paper 574-D; US Government Printing Office: Washington, DC, 1971.
24. Mason, B. H. *Principles of Geochemistry*; J. Wiley & Sons: New York, NY, 1966.
25. Friedlander, G.; Kennedy, J. W.; Macias, E. S.; Miller, J. M. *Nuclear and Radiochemistry*; J. Wiley & Sons: New York, NY, 1981.
26. Shizuma, K.; Fukami, K.; Iwatani, K.; Hasai, H. Low-background shielding of Ge detectors for the measurement of residual ^{152}Eu radioactivity induced by the neutrons from the Hiroshima atomic bomb. *Nucl. Instr. Meth. Phys. Res. B* **1992**, *66*, 459-464.
27. Ohba, M.; Benson, J. http://www.csi.ad.jp/abomb/; A-bomb www museum; Chugoku-Shikoku Internet Council: Japan, 2000.
28. Ford, G. P.; Wolfsberg, K.; Erdal, B. R. Independent yields of the isomers of ^{133}Xe and ^{135}Xe for neutron-induced fission of ^{233}U, ^{235}U, ^{238}U, ^{239}Pu, and ^{242}Am^{m}. *Phys. Rev. C* **1984**, *30*, 195-213.
29. Semkow, T. M. Comment on "Algebraic approach to the radioactive decay equations", by L. Moral and A. F. Pacheco [Am. J. Phys. 71(7), 684-686 (2003)]. *Am. J. Phys.* **2004**, *72*, 410-411.
30. Weinberg, A. M. Eugene Wigner, nuclear engineer. *Phys. Today* **2002**, *50(10)*, 42-46.

Downloaded by NORTH CAROLINA STATE UNIV on August 9, 2012 | http://pubs.acs.org
Publication Date: November 16, 2006 | doi: 10.1021/bk-2007-0945.ch011

Downloaded by NORTH CAROLINA STATE UNIV on August 6, 2012 | http://pubs.acs.org
Publication Date: November 16, 2006 | doi: 10.1021/bk-2007-0945.ch012

Chapter 12

Three-Dimensional Particle Transport Methods and Their Applications

Alireza Haghighat and Glenn E. Sjoden

Department of Nuclear and Radiological Engineering, University of Florida, Gainesville, FL 32611

This chapter establishes both the Monte Carlo and deterministic approaches applied to Boltzmann particle transport simulation problems; for the deterministic approach, discussion is limited to the widely used discrete ordinates (or "S_N") method. The chapter also discusses the advantages and disadvantages of each approach, and provides real-world examples of hybrid techniques developed for solving complex problems accurately and efficiently. Moreover, the chapter briefly introduces advanced particle transport methodologies and codes developed by the University of Florida Transport Theory Group (UFTTG). In particular, it discusses the Parallel Environment Neutral-particle TRANsport (PENTRAN) code system, a three-dimensional (3-D) parallel S_N transport code with pre- and post-processing software, and Automated Adjoint Accelerated MCNP (A^3MCNP), a version of the widely used Monte Carlo N-Particle (MCNP) transport code with automated variance reduction, and methodologies for multigroup cross-section generation. Finally, a comparison of the accuracy and efficiency of the Monte Carlo, S_N, and the application of hybrid combinations of each for real-world simulations is presented, with applications in homeland security, medicine, and power.

In Applied Modeling and Computations in Nuclear Science; Semkow, T., et al.;
ACS Symposium Series; American Chemical Society: Washington, DC, 2006.

1. Introduction

Simulation of neutral and charged particles is essential in the design, analysis, and optimization of "nuclear" systems to include nuclear power plants, radiation therapy and diagnostic devices, nondestructive interrogation devices, and nuclear power and propulsion systems. There are two main approaches used for particle transport simulations: deterministic (*1*,*2*), and statistical Monte Carlo (MC) (*3*,*4*). In the deterministic approach, one attempts to directly solve the Boltzmann equation to obtain the expected particle density in a phase space. Depending on particle type, problem type, and application, several different techniques have been used to solve the Boltzmann equation. In this chapter, however, we limit our discussion to neutral particles and the widely used *discrete ordinates* or "S_N" method (*2*,*5*,*6*). In the statistical Monte Carlo approach, one solves for the expected value of particle density in a phase space by averaging over a large number of particle histories or events. Both approaches are very powerful, and can lead to accurate solutions; however, depending on the problem type and overall objective, one approach can be more effective, *i.e.*, high accuracy, relatively low computational resources (memory and execution time). Moreover, often when dealing with large and complex problems, hybrid combinations of the two methods can be most effective.

This chapter is organized as follows. In Section 2, we briefly discuss the theoretical basis and formulation of both approaches. In Section 3, we discuss the advantages and disadvantages of the approaches, and introduce hybrid techniques which exploit the best of both approaches. In Section 4, we briefly review the methodologies and codes developed by the University of Florida Transport Theory Group (UFTTG). In Section 5, we compare the efficiency and accuracy of the S_N, Monte Carlo, and hybrid methods for simulation of real-world problems encountered in various applications including active interrogation (homeland security), medicine, and nuclear power.

Downloaded by NORTH CAROLINA STATE UNIV on August 6, 2012 | http://pubs.acs.org
Publication Date: November 16, 2006 | doi: 10.1021/bk-2007-0945.ch012

2. Theory – S_N and Monte Carlo Methods

In Subsection 2.1, we will briefly introduce the linear Boltzmann equation, the S_N method, and formulation in a three-dimensional (3-D) Cartesian geometry. In Subsection 2.2, we briefly discuss the Monte Carlo (history-based) methods, and provide some discussions on the "non-analog" or "biased" techniques.

2.1. Linear Boltzmann Equation and the S_N Method

The time-independent linear Boltzmann equation is given by (*1*),

$$\begin{aligned}&\hat{\Omega}\cdot\vec{\nabla}\psi(\vec{r},E,\hat{\Omega})+\sigma_t(\vec{r},E)\psi(\vec{r},E,\hat{\Omega})=\\&\int_0^{\infty}\int_{4\pi}dE'd\Omega'\sigma_s(\vec{r},E'\rightarrow E,\Omega'\rightarrow\Omega)\psi(\vec{r},E',\hat{\Omega}')+\\&\frac{\chi(E)}{4\pi}\int_0^{\infty}\int_{4\pi}dE'd\Omega'\nu\sigma_t(\vec{r},E')\psi(\vec{r},E',\hat{\Omega}')+Q(\vec{r},E,\hat{\Omega})\end{aligned}\quad, \tag{1}$$

where ψ is the expected angular flux of particles in the phase as a function of position, energy, and direction, where the angular flux spans the three-dimensional volume or *space*, particle *energy*, and particle direction or *angle* ($dVdEd\Omega$), and Q is the expected density of source particles emitted in the same phase space. The remaining terms use standard notation (see, *e.g.*, (*1*)).

2.2. S_N Method

A widely used method to solve Eq. 1 is the *discrete ordinates* "S_N" method (*2,5,6*). In the S_N method, all independent variables (space, energy, and direction) are discretized. For the angular variable, a discrete set of directions M are selected (usually symmetric about the unit sphere), and the Boltzmann equation is solved for these directions only. The selected directions (ordinates) are mathematically weighted to ensure that physical symmetries and particles are conserved. For the energy variable, energy intervals (E_{min}, E_{max}) are divided into a number of G grouped sub-intervals, where the Boltzmann equation is integrated over these intervals to obtain a set of coupled equations (*i.e.*, multigroup equations).

The original integro-differential Eq. 1 is thus replaced by a set of $M \times G$ differential equations that are coupled through the right-hand side source term:

$$\hat{\Omega}_m\cdot\vec{\nabla}\psi_{m,g}(\vec{r})+\sigma_{t,g}(\vec{r})\psi_{m,g}(\vec{r})=q_{m,g}(\vec{r})\,, \tag{2}$$

for $m = 1, \ldots, M$ and $g = 1, \ldots, G$, where, indices m and g correspond to radiation direction and energy group, respectively. For the spatial variable, the Eq. (2) is integrated over a single mesh cell to obtain an equation in terms of cell-boundary and cell-surface averaged angular fluxes. The resulting discrete ordinates form of Eq. 1, *e.g.*, in 3-D Cartesian geometry, is given by the zero-th moment balance equation:

$$\frac{|\mu_m|}{\Delta x}(\psi^m_{out,g}-\psi^m_{in,g})+\frac{|\eta_m|}{\Delta y}(\psi^m_{left,g}-\psi^m_{right,g})+\frac{|\xi_m|}{\Delta z}(\psi^m_{top,g}-\psi^m_{bottom,g})+\sigma_{ave,g}\psi^m_{ave,g}=q_{ave,g}\,. \tag{3}$$

Downloaded by NORTH CAROLINA STATE UNIV on August 6, 2012 | http://pubs.acs.org
Publication Date: November 16, 2006 | doi: 10.1021/bk-2007-0945.ch012

Downloaded by NORTH CAROLINA STATE UNIV on August 6, 2012 | http://pubs.acs.org
Publication Date: November 16, 2006 | doi: 10.1021/bk-2007-0945.ch012

The subscripts in/out, left/right, and top/bottom refer to different sides of a parallelepiped along each of the x, y, and z axes, respectively. Note that the source term q includes scattering, fission and external sources. In order to solve for the average angular flux (ψ_{ave}) for any given direction, we need to know the six boundary angular fluxes. Three of these fluxes are presumed to be known boundary values, while the remaining three are obtained from three auxiliary equations. The equations that relate the boundary and average angular fluxes are referred to as "differencing" equations.

In the past years, numerous studies have been allocated to the development of various differencing schemes to address significant issues, such as accuracy, positivity, non-physical oscillation phenomena, use of computational resources/efficiencies, convergence characteristics, and effectiveness of algorithms coupled to distinct acceleration techniques. A commonly used class of differencing schemes (*6*), *low-order*, deal with zero-th spatial moments of the Boltzmann equation which can be cast into the following form (*7*):

$$\text{Along } x\text{-axis:} \quad \psi^m_{ave,g} = a^m_{xyz,g}\psi^m_{in,g} + (1 - a^m_{xyz,g})\psi^m_{out,g} \tag{4a}$$

$$\text{Along } y\text{-axis:} \quad \psi^m_{ave,g} = b^m_{xyz,g}\psi^m_{right,g} + (1 - b^m_{xyz,g})\psi^m_{left,g} \tag{4b}$$

$$\text{Along } z\text{-axis:} \quad \psi^m_{ave,g} = c^m_{xyz,g}\psi^m_{bottom,g} + (1 - c^m_{xyz,g})\psi^m_{top,g}\,. \tag{4c}$$

A simplified form of above equations is the linear diamond-differencing (DD) scheme, where the coefficients a, b, and c are set to ½. Major shortcomings of DD are the possibility of negative solutions and non-physical oscillations. We have developed the directional theta-weighted (DTW) differencing scheme (*8*) that directly remedies both shortcomings. Recently, we extended the DTW scheme to the exponential directional weighted (EDW) scheme (*9*) for higher accuracy in thick cells; EDW uses an exponential extrapolation with exponential coefficients predicted by DTW. In spite of its very robust auxiliary equation, the EDW scheme is still classed as a *low-order scheme* as it only requires zero-th spatial transport moments. As a result, EDW is reasonably fast, well conditioned, has little overhead, and quite accurate when needed most - in pronounced streaming applications.

2.3. S$_N$ Solution Procedure

The above system of linear transport equations is commonly solved via the Gauss-Seidel iterative technique. For an initially guessed source distribution, the angular fluxes are evaluated by marching (in-out), (left-right), and (top-bottom) along a particle direction through spatial mesh cells using recursive Eqs. 3 and 4. To accelerate the solution convergence, different acceleration techniques (*10,11*) based on system rebalance and/or lower order solution methods are used.

2.4. Monte Carlo Methods

The Monte Carlo method is one of the most accurate techniques for particle transport simulation. The method is applied to both classes of nuclear problems: 1) fixed-source/shielding and 2) eigenvalue/criticality. Fixed source problems mainly involve transport of particles through thick shields that may cause a significant amount of absorption and/or scattering (isotropic/anisotropic), resulting in significant changes in particle energy and direction. This means that particle counts in small energy bins and/or localized spatial regions may be extremely small, and consequently, a large number of experiments (histories) and long computational times are needed to achieve statistically reliable results. In eigenvalue problems, since the source is not known, there is an added difficulty associated with the need for achieving global source convergence before starting tally accumulation. In recent years, some efforts have been devoted to performing Monte Carlo perturbation and depletion calculations that generally require even longer computing times. Monte Carlo perturbation for both fixed-source and eigenvalue problems has further difficulties associated with being able to distinguish between the relative statistical errors ($RE = \sigma_{\bar{x}}/\bar{x}$) and the change caused by a perturbation. Moreover, Monte Carlo depletion, because of the need for global results, generally requires impractically large amounts of computer time.

Over the past several decades, a large number of techniques have been developed to reduce the variance of Monte Carlo calculations, referred to as variance reduction and/or biasing techniques (*12*,*13*). These techniques commonly modify the natural "analog" sampling procedure/formulation (related to physical laws of particle transport) to focus computational efforts on the simulation of "important" particles. To compensate for this "non-analog" modification and to conserve the total number of particles, each particle is given a statistical weight that is adjusted based on the following equality,

$$w_{biased}\, pdf_{biased} = w_{unbiased}\, pdf_{unbiased}, \qquad (5a)$$

where *pdf* refers to the *probability distribution function* of the physical process being sampled, and *w* refers to the particle weight. It is worth noting that in special cases such as integer splitting (*i.e.*, one particle is split into *n* particles), one considers a modified form of Eq. 5a, given by

$$n \times w_{biased}\, pdf_{biased} = w_{unbiased}\, pdf_{unbiased}, \qquad (5b)$$

where $pdf_{biased} = pdf_{unbiased} = 1$. In this situation, the physical process is changed rather than the probability of its occurrence.

The main difficulty associated with using variance reduction techniques is the determination of the problem-dependent variance reduction parameters present in the biased terms (*i.e.*, pdf_{biased} or *n*). This chapter reviews the use of

Downloaded by NORTH CAROLINA STATE UNIV on August 6, 2012 | http://pubs.acs.org
Publication Date: November 16, 2006 | doi: 10.1021/bk-2007-0945.ch012

deterministic importance functions for variance reduction of Monte Carlo calculations, with emphases on fixed-source/shielding problems.

3. S_N vs. Monte Carlo (Advantages/Disadvantages)

Both the S_N and Monte Carlo methods are very powerful for solving particle transport problems; however, depending on the application and/or user needs and requirements, one method may be preferable over the other, or in some cases, a hybrid combination of both may be most effective. The inherent advantages/disadvantages of the two methods are listed in Table I.

Table I. Comparison of the S_N and Monte Carlo (MC) Methods

Method	*Advantages*	*Disadvantages*
S_N	-Detailed solution -Short execution time	-Discretized geometry representation -Large computer memory -Difficulties in preparation of mesh (space/angle) multigroup cross sections
MC	-Accurate geometry -Accurate energy treatment (continuous energy dependent cross sections) - Small computer memory	-Long execution time -Limited solution detail -Difficulty in using variance reduction techniques

Downloaded by NORTH CAROLINA STATE UNIV on August 6, 2012 | http://pubs.acs.org
Publication Date: November 16, 2006 | doi: 10.1021/bk-2007-0945.ch012

Since the inception of the atomic age, significant efforts have been dedicated to improving both techniques and/or developing hybrid techniques which benefit from the advantages of both techniques. Studies have been performed on: i) development of more efficient/accurate (clever) algorithms; ii) development and adaptation of effective algorithms for parallel processing; iii) development of acceleration or variance reduction techniques; and iv) development of hybrid techniques. The UFTTG has been involved in all the aforementioned studies, and its efforts have led to the development of two major code systems which are discussed in the following section.

4. PENTRAN and A^3MCNP Code Systems

In this section, we will briefly summarize the code systems developed by the UFTTG.

Downloaded by NORTH CAROLINA STATE UNIV on August 6, 2012 | http://pubs.acs.org
Publication Date: November 16, 2006 | doi: 10.1021/bk-2007-0945.ch012

4.1. Parallel Environment Neutral-particle TRANsport (PENTRAN) Code System

The PENTRAN code system includes pre-processing codes, PENMSH (*14*) and PENINP, the PENTRAN 3-D parallel S_N code, and post-processing codes, PENDATA and PENPRL. PENMSH prepares mesh, material, and source distributions, and PENINP prepares input file for PENTRAN. PENDATA prepares tables of flux, material, source distributions in a distributed computing environment, and PENPRL extracts flux values at specific positions corresponding to reference values (experimental/numerical). PENTRAN solves the 3-D time-independent linear Boltzmann equation using finite-volume differencing and discrete ordinates methodologies in a Cartesian geometry. The cell-balance equation of the discrete ordinates method in 3-D Cartesian geometry is given by Eq. 1.

PENTRAN is a scalable parallel code that can be distributed over a parallel cluster of processors using angular, energy, or spatial domain decomposition (or combinations of these) with parallel memory allocation. It also uses a novel differencing approach, referred to as the "adaptive differencing strategy (ADS)," (*15*) that automatically selects the appropriate differencing scheme depending on problem physics. Currently, ADS includes three differencing schemes. These are linear diamond difference (*5*), DTW (*8*), and EDW (*9*) differencing schemes.

Besides the Adaptive Differencing Strategy, PENTRAN includes the Taylor Projection Mesh Coupling (TPMC) formulation (*16*), which is essential for preserving solution accuracy when crossing regions of variable grid densities. With PENTRAN's memory partitioning, parallel I/O, hybrid spatial, angular, and energy domain decomposition algorithms, and advanced numerical formulations, the code is capable of solving complex large problems in a parallel environment.

4.2. Automated Adjoint Accelerated MCNP (A^3MCNP)

As mentioned in Section 2, two of the disadvantages of the Monte Carlo method are long running time and difficulties in using variance reduction techniques. The A^3MCNP code system (*13,17*) has been developed to overcome both difficulties for fixed source problems. A^3MCNP is an excellent example of a hybrid method, which uses the S_N method to determine the variance reduction parameters for the Monte Carlo method. It automatically prepares variance reduction parameters for the CADIS methodology, which is and effective technique for variance reduction of fixed-source/shielding problems (*13,17,18*). The Consistent Adjoint Driven Importance Sampling (CADIS) methodology includes formulations for source and transport biasing parameters, and their implementation within the weight-window technique. CADIS uses the importance function for sampling "important" particles for an objective function (or detector response). For source biasing, it utilizes the following formulation

$$\hat{q}(P) = \frac{\psi^+(P)\, q(P)}{R}, \tag{6}$$

where, $\psi^+(P)$ is the importance function, $q(P)$ is the unbiased source in phase-space P, and R is the response for the reaction of interest in s^{-1}, normally the integrated forward flux and reaction cross section over all phase space. To conserve the total number of particles, the weights of source particles are adjusted by

$$w(P) = \frac{R}{\psi^+(P)}. \tag{7}$$

And for transport biasing, CADIS alters the number of particles that are transferred from one phase space to another. This means that if the phase space P has a higher importance than the phase space P', particles are split during simulation according to the ratio of the importance function given by $\psi^+(P)/\psi^+(P')$, while if the opposite is true, the particles are rouletted. Following this split/roulette process, to preserve the expected number of particles, the particle statistical weight is modified according to

$$w(P) = w(P')\left[\frac{\psi^+(P')}{\psi^+(P)}\right]. \tag{8}$$

The major difficulty in using CADIS is determination of adjoint ("importance") function distribution. The S_N method is a more practical approach for determination of an adjoint function distribution for any general problem. However, to perform an S_N calculation, one is faced with difficulty of preparing input files for cross-section generation and deterministic adjoint transport code. To overcome this difficulty, we have developed strategies for automatically generating input files for discrete ordinates calculations, including mesh generation and material cross section preparation, directly from an MCNP code input deck. The modified version of the MCNP code that contains these features is designated as A^3MCNP.

A^3MCNP performs the following tasks (*17,19*):

1) Prepares the necessary input files for a deterministic adjoint calculation.
    - Generation of a mesh distribution for deterministic adjoint. The mesh generator utility first generates a uniform mesh distribution to extract information on material distribution, and then through a back-thinning process, prepares a variable mesh distribution.
    - Preparation of the input file for the Three-dimensional Discrete Ordinates Transport (TORT) S_N code (*19*).

Downloaded by NORTH CAROLINA STATE UNIV on August 6, 2012 | http://pubs.acs.org
Publication Date: November 16, 2006 | doi: 10.1021/bk-2007-0945.ch012

- Determination of material compositions and preparation of input files for the GIP code for generation of multigroup cross sections.

2) Reads the adjoint (importance) function from the standard TORT binary output file and prepares source biasing parameters and space- and energy-dependent weight window lower bounds via Eqs. 19 and 21.

3) Superimposes the detailed weight window values (based on the deterministic spatial-mesh distribution and energy-group structure) onto the Monte Carlo model and uses them in a transparent manner.

Downloaded by NORTH CAROLINA STATE UNIV on August 6, 2012 | http://pubs.acs.org
Publication Date: November 16, 2006 | doi: 10.1021/bk-2007-0945.ch012

5. Application of S_N, Monte Carlo, and Hybrid Techniques to Real-World Problems

In this section, we present the results of simulations of three real-world problems using S_N, Monte Carlo, or hybrid methods. The three problems are: i) Prompt Gamma Neutron Activation Analysis (PGNAA), a waste assaying device using active interrogation; ii) a Computed Tomography (CT) device for medical imaging diagnosis; and iii) a Spent Fuel (SF) Cask for storage of spent nuclear fuel.

5.1. Simulation of the PGNAA Assaying Device

This example demonstrates how one can combine the S_N and Monte Carlo methods in order to devevelop an efficient and accurate methodology.

The device is the Westinghouse PGNAA system that is used for active interrogation of a waste drum containing Resource Conservation and Recovery Act (RCRA) metals. As shown in Fig. 1, this device includes a source (deuterium-tritium (D-T) 14 MeV neutron generator), a high-purity germanium (HPGe) gamma detector, and a polyethylene interrogation chamber (for moderating neutrons), which houses the source and a waste drum.

The device functions as follows: 14-MeV neutrons are generated following a pulse, these neutrons are theremalized by scattering within the polyethylene chamber and the waste itself, thermal neutrons are captured by materials in the drum, and a fraction of resultant gamma rays are detected by HPGe following traveling through the waste. There are two transport processes: i) neutron transport which leads to the generation of gamma rays; ii) gamma transport to the HPGe gamma detector. Since the source is a pulsed source, the geometry is complex; therefore, a first approach could be full 3-D, time-dependent transport (either MC or S_N). Rather than following a brute force approach, first we studied the behavior of the thermal neutrons and the resultant gamma rays in the waste; we demonstrated that the induced gamma-ray flux reaches a quasi-static state in a rather short time. This means that the gamma transport can be performed via a time-independent transport calculation. Further, considering the adjoint methodology (*1*), the gamma detector response can be determined by

$$R = \langle S\Psi^{+} \rangle, \tag{9}$$

where, S is the gamma source distribution within the system, and Ψ^{+} is the adjoint function distribution for the detector. So, considering the above discussion, we developed a two step process: i) to obtain the gamma source from waste, we performed a time-dependent 3-D MCNP Monte Carlo calculation; ii) to obtain the detector adjoint function distribution, we performed 3-D PENTRAN S_N calculation. Besides the fact that it is more efficient to obtain a detailed adjoint function distribution via a deterministic calculation, the use of adjoint function provided significant flexibility for testing different sources and analyzing different system parameters.

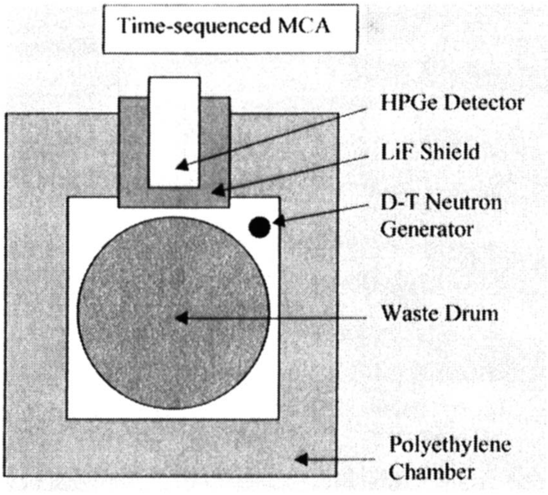

Figure 1. Schematic of the PGNAA device.

Using this hybrid methodology, we were able to optimize the PGNAA system, and determine various important parameters. As evidence of the accuracy of the methodology, Table II gives the predicted amount of contaminant by scanning different axial segments of a sample 55-gallon waste drum with a nonuniform distribution of mercury. Our results indicate that our

Downloaded by NORTH CAROLINA STATE UNIV on August 6, 2012 | http://pubs.acs.org
Publication Date: November 16, 2006 | doi: 10.1021/bk-2007-0945.ch012

hybrid methodology is not only an efficient approach, but also has accurately predicted the average amount of contaminant.

Table II. Hg Concentration Values Reported from Simulation Runs Performed with Different Numbers of Axial Locations Along the Height of a 55-gallon Drum Containing a Waste Matrix with Nonuniform Hg

Scan Height (cm)	*No. of Axial Positions*	*Average Hg Conc. Based on Detector Response (ppm)*	*Deviation from True Average Hg Conc. of 250 ppm*
5.08	12	249.8	– 0.08 %
10.16	6	250.2	0.08 %
15.24	4	247.0	– 1.2 %

5.2. Simulation of the CT Device

This example demonstrates that with a new type of angular discretization, the S_N method can be significantly more efficient for simulation of a problem which generally is modeled using the Monte Carlo method.

The process of creating a CT image is illustrated in Fig. 2. CT imaging is also known as Computed Aided Tomography (CAT) scanning. A typical CT scanner looks like a large doughnut. The patient aperture spans 60 to 70 cm (24" to 28") in diameter. Inside the CT scanner housing is a rotating frame which has an x-ray tube mounted on one side, with a the banana shaped detector mounted on the opposite side.

Medical CT scanners use a collimated x-ray source to produce a fan-beam of radiation that illuminates the entire target. Modeling of such a directional beam is highly problematic for a standard S_N transport method, which uses a standard "level-symmetric" angular quadrature set (*20-22*).

To compare PENTRAN S_N results with MCNP Monte Carlo predictions, we considered 20 tally locations on the far side of the target. The tallies are arrayed on a circle of radius 31 cm concentric to the target, equally spaced in angle around a portion of the circle. A PENTRAN model, as shown in Fig. 3, was developed with 12,500 spatial meshes (*20*). The two-group calculations performed by PENTRAN used group 16 and 17 from the 20 group BUGLE-96 gamma ray cross-section library. The source emits x-rays into the first group (between 100 and 200 keV). The second energy group effectively represents the scattered photon flux, and includes particle energies between 100 and 60 keV.

A standard level-symmetric angular quadrature set is limited to S20 (440 total directions on the unit sphere, 55 per octant). S20 does not contain enough directions for this problem, and the flux distribution calculated with S_N using this level-symmetric quadrature set is not accurate, and as shown in Figure 4, exhibits significant "ray effects" (*8,23*).

Downloaded by NORTH CAROLINA STATE UNIV on August 6, 2012 | http://pubs.acs.org
Publication Date: November 16, 2006 | doi: 10.1021/bk-2007-0945.ch012

Downloaded by NORTH CAROLINA STATE UNIV on August 6, 2012 | http://pubs.acs.org
Publication Date: November 16, 2006 | doi: 10.1021/bk-2007-0945.ch012

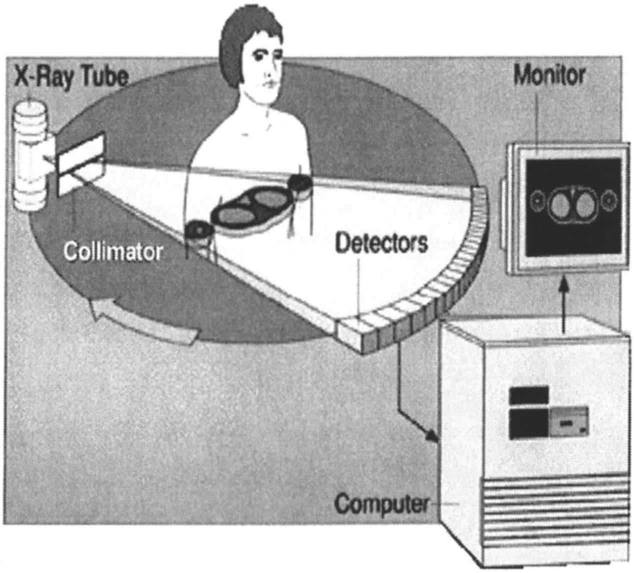
X-Ray Tube
Monitor
Collimator
Detectors
Computer

Figure 2. Schematic of CT system.

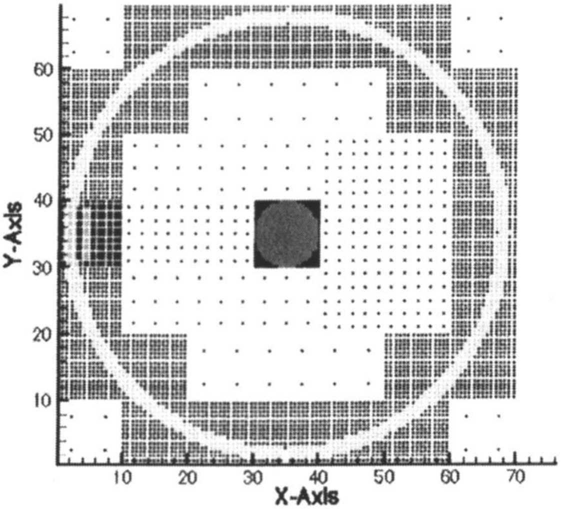
60
50
40
30
20
10
Y-Axis
10
20
30
40
50
60
70
X-Axis

Figure 3. XY Projection of thePENTRAN discretized model.

Downloaded by NORTH CAROLINA STATE UNIV on August 6, 2012 | http://pubs.acs.org
Publication Date: November 16, 2006 | doi: 10.1021/bk-2007-0945.ch012

To overcome this limitation in the number of directions modeled, we first employed the standard equal-weight technique, which does not have any limitations on the number of directions. However, to achieve an accurate solution, we had to use an S50 quadrature set (*i.e.*, 2600 directions/mesh/group) and operate PENTRAN on 20 processors. Figure 5 shows that clearly we eliminate ray effects, but this calculation required significant computational resources.

To reduce the cost of this simulation, we developed new biased quadrature sets that are well suited for medical problems with highly direction sources as in a CT device. One technique is referred to as *ordinate splitting* (OS) (*20,21*), which allows for the splitting of directions in preferred directions of interest.

Figure 6 depicts a comparison of flux distributions obtained via MCNP Monte Carlo and PENTRAN S_N (with different quadrature sets) across the fan beam at a radius of 30 cm from the center of the CT. As shown in Fig. 6, the OS technique in this application can yield accurate solutions with significantly fewer directions than the S50 equal-weight quadrature set. The advantage of the OS technique is more evident in Table III, which compares the computer resources and amount of information generated.

Table III results indicate that compared to the Monte Carlo MCNP calculation, the PENTRAN S_N method, with an appropriate angular quadrature set, *i.e.*, OS, can yield an accurate and detailed solution with minimal computer time. Based on the generated information, the PENTRAN S20 with OS is ~ 2642 times more efficient than the MCNP Monte Carlo calculation.

Table III. Comparison of CPU, Memory for Different CT Simulations

Method	CPU Time	Memory (Mb)	Datapoints/s /processor
MCNP Monte Carlo	3000 s	-	0.0067
PENTRAN S50 Equal Weight (325 dir/octant)	640 s (20 processors) (4/1/5)*	2417	0.98
PENTRAN S20 Equal Weight with Ordinate Splitting (79 dir/octant)	451 s (1 processor, interactive)	204	17.7

*Number of angular, energy, and spatial subdomains, respectively.

Downloaded by NORTH CAROLINA STATE UNIV on August 6, 2012 | http://pubs.acs.org
Publication Date: November 16, 2006 | doi: 10.1021/bk-2007-0945.ch012

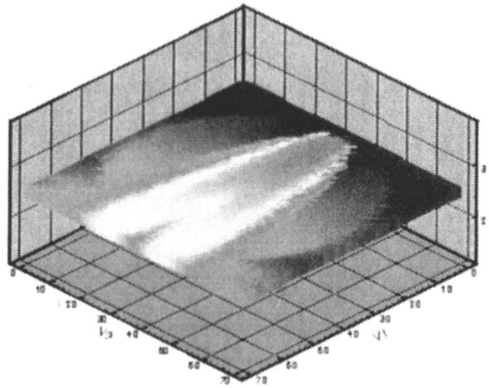

Figure 4. Predicted PENTRAN x-ray distribution in CT device with S20 level-symmetric quadrature set.

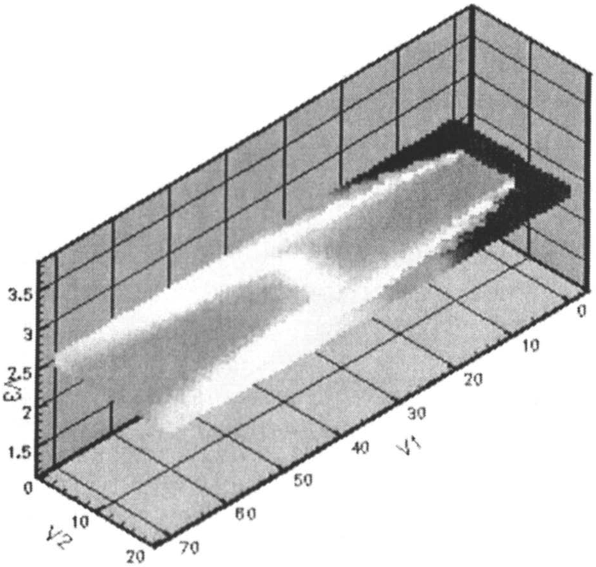

Figure 5. Predicted PENTRAN x-ray distribution in CT device with S50 equal-weight quadrature set.

Downloaded by NORTH CAROLINA STATE UNIV on August 6, 2012 | http://pubs.acs.org
Publication Date: November 16, 2006 | doi: 10.1021/bk-2007-0945.ch012

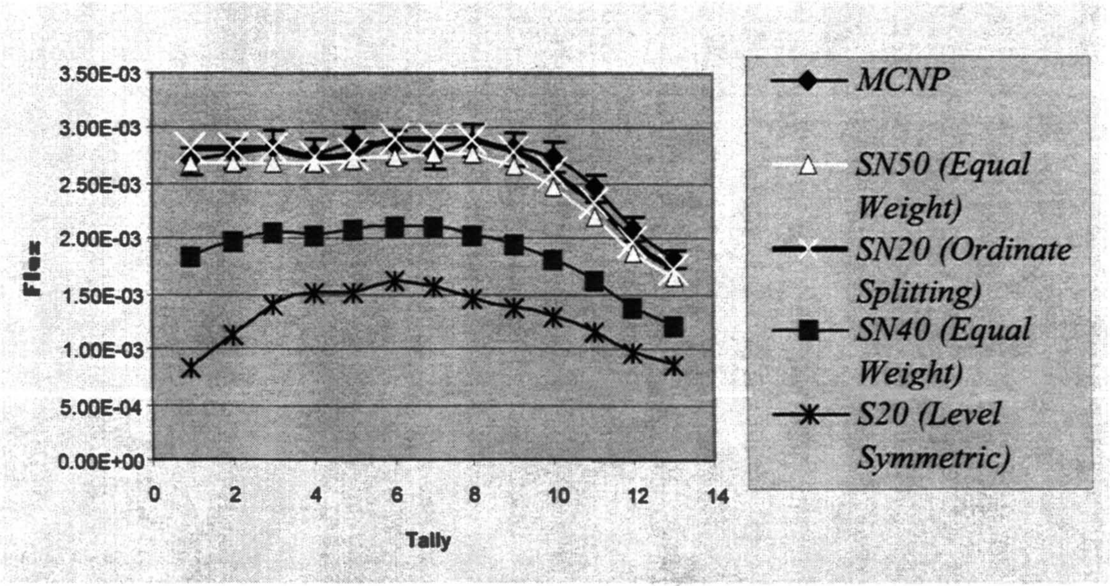

Figure 6. Comparison of flux distributions predicted with different PENTRAN quadrature sets with the Monte Carlo results.

Downloaded by NORTH CAROLINA STATE UNIV on August 6, 2012 | http://pubs.acs.org
Publication Date: November 16, 2006 | doi: 10.1021/bk-2007-0945.ch012

5.3. Simulation of a Fuel Cask

In this section, we will examine the accuracy and performance of S_N, Monte Carlo, and hybrid methods for determination of flux/dose over the surface of an independent spent fuel storage installation (ISFSI) (*23*). For this exercise, we utilize the PENTRAN S_N, MCNP Monte Carlo, and A^3MCNP hybrid code systems. Normally, the MC method is used for this type of simulation.

Typical concrete ISFSIs are approximately 6.10 m high and over 3.30 m in diameter. Their large size and complex material composition presents difficulties for both the S_N and MC methods. A detailed geometric model was developed for both the PENTRAN and MCNP/A^3MCNP code systems. Figure 7 depicts the mesh material distribution for the 3-D PENTRAN model. The ISFSI cask rests on a concrete pad. The source magnitude and spectrum are based on typical spent PWR power reactor fuel assemblies. Flux-to-dose conversion factors and multigroup cross sections were obtained from the CASK-81 cross section library (*24*). CASK is a 40 group, 22 neutron-18 gamma coupled cross section library specifically tailored for shipping casks. The reference PENTRAN model included 195,144 spatial meshes, 22 neutron energy groups, P3 anisotropic scattering, and an S12 quadrature set. This model required ~ 9.2 Gbyte of memory, which was distributed among 8 processors (*i.e.*, ~ 1.15 Gbyte processor) of the UFTTG's *Chadwick* cluster (2Gbyte/node dual Pentium III processors).

Table IV compares the average dose calculated within two axial intervals located in the middle of the cask surface. As expected the continuous-energy MCNP and A^3MCNP calculations yield identical results, while the multigroup MCNP calculation under-predicts the results by ~ 30 %; this partly due to the fact that the CASK library is based on ENDF/B-II continuous-energy cross sections that use old data. Table V compares the calculated multigroup MCNP predictions with the PENTRAN results.

Table IV. Comparison of Calculated Dose Using Continuous Energy A^3MCNP, Continuous and Multigroup MCNP Code Systems

Axial Interval (cm)	*A^3MCNP Cont. Energy [(mrem/hr)/ n/cm^2/s]**	*MCNP Cont. Energy [(mrem/hr)/ n/cm^2/s]**	*MCNP Multigroup [(mrem/hr)/ n/cm^2/s]**
262.9 - 299.5	2.12E–04 (0.83%)	2.13E–04 (1.14%)	1.50E–04 (1.18%)
299.5 - 336.1	1.98E–04 (0.95%)	1.97E–04 (1.19%)	1.39E–04 (1.23%)

*One standard deviation statistical uncertainty is given in %.

Downloaded by NORTH CAROLINA STATE UNIV on August 6, 2012 | http://pubs.acs.org
Publication Date: November 16, 2006 | doi: 10.1021/bk-2007-0945.ch012

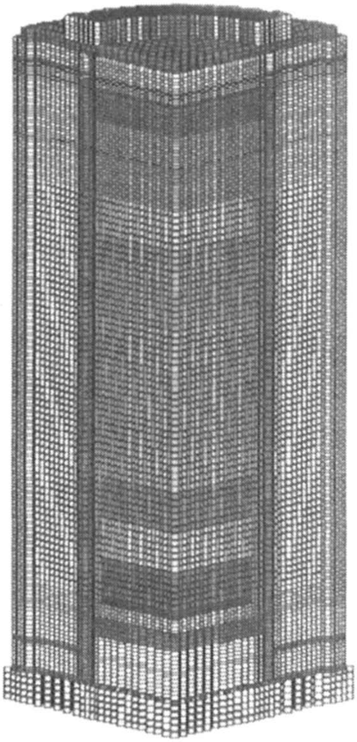

Figure 7. PENTRAN discretized model of fuel cask with material distribution.

Table V. Comparison of Multigroup MCNP and PENTRAN results

Axial Interval (cm)	*MCNP Multigroup [(mrem/hr)/n/cm^2/s]**	*PENTRAN Multigroup [(mrem/hr)/n/cm^2/s]**
262.9 - 299.5	1.50E–04 (1.18%)	1.57E–04
299.5 - 336.1	1.39E–04 (1.23%)	1.47E–04

*One standard deviation statistical uncertainty is given in %.

These results indicate that the PENTRAN results have equivalent accuracy compared to the multigroup MCNP results, *i.e.*, using the same nuclear data library, the PENTRAN predictions are equivalent to the MCNP Monte Carlo predictions.

In addition to the accuracy of these calculations, it is important to examine the computation times and the amount of information obtained. Table VI summarizes comparisons of performance. For consistency, the amount of time required to reach an average one standard deviation statistical uncertainty of 1 % is considered as the basis for the timing comparison among the Monte Carlo calculations.

Table VI data indicate that the A^{3}MCNP computation is highly efficient (by a factor of 140) compared to the unbiased MCNP, and PENTRAN is 1.7 times faster than the unbiased MCNP. Furthermore, if one compares the performance based on the number of data values generated per hour/processor, then PENTRAN is by far the dominant tool, while again A^{3}MCNP is highly effective as compared to the unbiased MCNP.

Table VI. Comparison of Timing for Different Methods

Model	*# CPU*	*Dose Ratio to Reference*	*Run Time (hrs)*	*Speedup*	*Number of data/hr/ processor*
A^{3}MCNP Cont. Energy	1	1.00*	1.5	140	1,856
MCNP Unbiased Cont. Energy	8	0.99	214*	1.0*	3.75
MCNP Unbiased Multigroup	8	0.70	362	0.6	2.37
PENTRAN 'Small' Model	8	0.74	123	1.7	4,375

*MC results at axial mid-plane are converged to one std. dev. uncertainty of 1 %.

Finally, it is interesting to note that the unbiased MCNP calculations lead to no counts tallied in the top or bottom sections of the cask, while the A^{3}MCNP

Downloaded by NORTH CAROLINA STATE UNIV on August 6, 2012 | http://pubs.acs.org
Publication Date: November 16, 2006 | doi: 10.1021/bk-2007-0945.ch012

calculations yield dose values with ~ 20 % uncertainties. To achieve a statistically more reliable result, we ran A^3MCNP for 8 CPU hours to achieve doses with relative errors < ~ 5.1 %. Table VII compares the PENTRAN and A^3MCNP results at top of the cask. It is important to note that PENTRAN yields dose values within 20 % of the continuous energy A^3MCNP predictions. Further, this information is obtained without further effort, obtained in the same calculation.

Table VII. Comparison of PENTRAN & A^3MCNP Results in Top of Cask

Axial Interval (cm)	*A^3MCNP Cont. Energy [(mrem/hr)/n/cm^2/s]**	*Multigroup PENTRAN [(mrem/hr)/ n/cm^2/s]*	*Dose Ratio $\frac{\text{PENTRAN}}{A^3\text{MCNP}}$*
504.8 - 526.6	1.70E–06 (3.36%)	1.843	0.82
526.6 - 548.4	9.97E–07 (5.08%)	0.806	0.79

*One standard deviation statistical uncertainty is given in %.

6. Summary and Conclusions

This chapter reviews both the S_N deterministic and the statistical Monte Carlo methods. It discusses the inherent advantages and disadvantages of each, and briefly reviews work done by the UFTTG to improve the efficiency and accuracy of both methods. Through applications to real-world problems (a contamination interrogation device, a CT scanner, and a fuel storage cask), we demonstrate that depending on the problem and specific user objectives, one method may be superior to the other method. Moreover, in more complex problems, hybrid combinations of the Monte Carlo and S_N techniques can often yield the most efficient simulation approach.

References

1. Bell I. G.; Glasstone, S. *Nuclear Reactor Theory*; Krieger Publishing: Malabar, FL, 1985.
2. Lewis, E. E.; Miller, W. F. *Computational Methods of Neutron Transport*; John Wiley & Sons: New York, NY, 1984.
3. Kalos, M. H.; Whitlock, P. A. *Monte Carlo Methods Volume I: Basics*; John Wiley & Sons: New York, NY, 1986.

Downloaded by NORTH CAROLINA STATE UNIV on August 6, 2012 | http://pubs.acs.org
Publication Date: November 16, 2006 | doi: 10.1021/bk-2007-0945.ch012

4. Morin, L. *Monte Carlo Simulation in the Radiological Sciences*; CRC Press: Boca Raton, 1988.
5. Carlson, B.G. The numerical theory of neutron transport. In Alder, B.; S. Fernbach, S.; Rotenberg, M., Eds.; *Meth. Comp. Phys.* **1963**, *1*, 1-42.
6. Alcouffe, R. E.; O'Dell, R. D. Transport calculations for nuclear reactors. *CRC Handbook of Nuclear Reactor Calculations*, Vol. 1; CRC Press: Boca Raton, 1987.
7. Petrovic, B.; Haghighat, A. Analysis of inherent oscillations in multidimensional S_N solutions of the neutron transport equation. *Nucl. Sci. Eng.* **1996**, *124*, 31-62.
8. Petrovic, B.; Haghighat, A. New directional Θ-weighted S_N differencing scheme and reduction of estimated pressure vessel fluence uncertainty. *Proceedings of the 9th International Symposium on Reactor Dosimetry*; Abderrahim, H.; Nolthenius, H., Eds.; World Scientific: Singapore, 1998.
9. Sjoden, G. E.; Haghighat, A. The exponential directional weighted (EDW) S_N differencing scheme in 3-D Cartesian geometry. *Proceedings of the Joint International Conference on Mathematical Methods and Supercomputing in Nuclear Applications*; Saratoga Springs, NY, 1997, Vol. I, pp. 553-562.
10. Adams, M. L.; Larsen, E. W. Fast iterative methods for discrete-ordinates particle transport calculations. *Prog. Nucl. Energy* **2002**, *40*, 3-159.
11. Longoni, G.; Haghighat, A. A new synthetic acceleration technique based on the simplified even-parity S_N equations. *Transport Theory and Statistical Physics* **2004**, *33*, 347-360.
12. X-5 Monte Carlo Team. *MCNP-A General Monte Carlo N-Particle Transport Code*; Version 5, Volume II: User's Guide. Report LA-CP-03-0245; Los Alamos National Laboratory, Los Alamos, NM, 2003.
13. Haghighat, A.; Wagner, J. C. Monte Carlo variance reduction with deterministic importance functions. *Prog. Nucl. Energy* **2003**, *42*, 25-53.
14. Haghighat, A. Manual of PENMSH version 5 – A Cartesian-based 3-D Mesh Generator; University of Florida: Gainesville, FL, June 2004.
15. Sjoden, G.; Haghighat, A. A new adaptive differencing strategy in the PENTRAN 3-D parallel S_N code. *Trans. Am. Nucl. Soc.* **1996**, *75*.
16. Sjoden, E. G.; Haghighat, A. Taylor projection mesh coupling between 3-D discontinuous grids for S_N. *Trans. Am. Nucl. Soc.* **1996**, *74*, 178-179.
17. Wagner, J. C. Acceleration of Monte Carlo Shielding Calculations with an Automated Variance Reduction Technique and Parallel Processing. Ph.D. Thesis; The Pennsylvania State University: Nuclear Engineering Department, University Park, PA, 1997.
18. Wagner, J. C.; Haghighat, A. Automated variance reduction of Monte Carlo shielding calculations using the discrete ordinates adjoint function. *Nucl. Sci. Eng.* **1998**, *128*, 186-208.

Downloaded by NORTH CAROLINA STATE UNIV on August 6, 2012 | http://pubs.acs.org
Publication Date: November 16, 2006 | doi: 10.1021/bk-2007-0945.ch012

19. Wagner, J. C.; Haghighat, A. A User's Manual for A^3MCNP – Automatic Adjoint Accelerated MCNP. The Pennsylvania State University: Nuclear Engineering Department, University Park, PA, 1997.
20. Brown, J. F.; Haghighat, A. A PENTRAN model for a medical computed tomography (CT) device. *Proceedings of Radiation Protection for our National Priorities*; Spokane, WA, Sep. 17-21, 2000.
21. Longoni, G.; Haghighat, A. Development of new quadrature sets with the ordinate splitting technique. *Proceedings of the 2001 ANS International Meeting on Mathematical Methods for Nuclear Applications (M&C)*; Salt Lake City, UT, Sep. 9-13, 2001.
22. Longoni, G.; Haghighat, A. development and application of the regional angular refinement technique and its application to non-conventional problems; *Proceedings of the International Conference on the New Frontiers of Nuclear Technology: Reactor Physics, Safety and High-Performance Computing (PHYSOR 2002)*; Seoul, Korea, Oct. 7-10, 2002.
23. Sherlock, D.; Haghighat, A. Neutron analysis of spent fuel storage installation using parallel computing and advance discrete ordinates and Monte Carlo techniques. *Rad. Prot. Dosimetry* **2005**, *116*, 662-666.
24. *CASK-81. 22 Neutron, 18 Gamma-Ray Group, P3, Cross Sections for Shipping Cask Analysis*; Report DLC-23; Oak Ridge National Laboratory: Oak Ridge, TN, 1987.

Downloaded by NORTH CAROLINA STATE UNIV on August 6, 2012 | http://pubs.acs.org
Publication Date: November 16, 2006 | doi: 10.1021/bk-2007-0945.ch012

Downloaded by STANFORD UNIV GREEN LIBR on August 9, 2012 | http://pubs.acs.org
Publication Date: November 16, 2006 | doi: 10.1021/bk-2007-0945.ch013

Chapter 13

MCNP-CP: A Correlated Particle Radiation Source Extension of a General Purpose Monte Carlo N-Particle Transport Code

Andrey N. Berlizov

Institute for Nuclear Research, National Academy of Sciences of Ukraine, 47, Prospekt Nauki, MSP 03680, Kyiv, Ukraine

An extended version, MCNP-CP, of the general purpose Monte Carlo N-Particle transport code MCNP4c was created. It allows performing calculations with a source of correlated nuclear particles based on the Evaluated Nuclear Structure Data File ENSDF. Owing to the implemented versatile pulse height tally coincidence/anticoincidence modes, MCNP-CP presents wide possibilities for the calculation and optimization of the performance of single-detector as well as multi-detector systems for measurements with real radiation sources. The chapter gives a brief description of MCNP-CP features and presents a number of examples of its application to modeling responses of typical spectrometry systems.

In Applied Modeling and Computations in Nuclear Science; Semkow, T., et al.;
ACS Symposium Series; American Chemical Society: Washington, DC, 2006.

Downloaded by STANFORD UNIV GREEN LIBR on August 9, 2012 | http://pubs.acs.org
Publication Date: November 16, 2006 | doi: 10.1021/bk-2007-0945.ch013

Decay of radioactive nuclei and isomeric states usually represents a complex multi-stage atomic-nuclear process, in which nuclear transformations are accompanied by cascades of electromagnetic transitions in the nucleus and atomic shell, resulting in emission of space and time correlated particles: photons, β-particles, discrete energy electrons, and X-rays. Correct prediction of a detection system response for measurements of such sources requires application of an adequate source model, which on the basis of the available atomic and nuclear data would accurately reproduce peculiarities of the decay of a particular radionuclide as well as probabilistic characteristics of decay radiations.

Despite the fact that presently MCNP (*1*) is widely utilized for evaluating performance of nuclear radiation detectors, in most cases the capabilities of the code do not allow modeling the response and calculating characteristics of detection systems for measurements with real radiation sources. One of the most essential reasons for this is that the standard version of MCNP considers only one source particle per history and only one particle type per calculation run. Another serious restriction is the absence of standard means for calculating pulse height distributions for the detection systems that use coincidence /anticoincidence measurement techniques.

Believing that overcoming the indicated drawbacks could significantly broaden the scope of MCNP application in the fields of nuclear spectroscopy and applied spectrometry, an extended version of the code, MCNP-CP, was created based on previous developments (*2,3*) by the author. A radionuclide cascade source of correlated particles as well as versatile capabilities for modeling the response of a system of detectors connected in multiple coincidence/anticoincidence modes were implemented in this extended version of the code in a consistent way. The following sections of the chapter present a brief description of MCNP-CP and give a number of examples of its application.

Description of the MCNP-CP Features

As a basic source of information about decay properties of radionuclides MCNP-CP uses the comprehensive Evaluated Nuclear Structure Data File ENSDF. Another option is the use of a problem specific radiation source data file in ENSDF/2 format, which must be prepared by the user according to the established rules (*4*).

The required dataset is specified by means of a ZAM keyword, which was introduced into standard MCNP general source data card

SDEF … ZAM = *zzzaaam* … ,

where *zzz* is nuclear charge, *aaa* is atomic number, and *m* is isomeric index of a radionuclide of interest. This keyword can be used in combination with standard

SDEF keywords, such as CEL, SUR, X, Y, Z, POS, EXT, RAD, AXS, and CCC, which specify radiation source geometry and location.

Where necessary, the ENSDF data are supplemented by calculations with application of known theoretical models and approaches. In particular, spectral distributions of β-particles from β^--decay are calculated for particular energies, forbiddances and uniqueness of the corresponding β-transitions using theoretical formulas. Probabilities of vacancy creation in the atomic K-shell and $L_{1,2,3}$-subshells at electron capture are calculated based on the theoretical calculation data provided in (*5*). In the case of β^+-decay, the probability of emission of a pair of 511-keV annihilation photons is evaluated assuming local deposition of kinetic energy of a positron and neglecting in-the-flight annihilation processes. Energies and directions of the annihilation photons are subject to Doppler shifting in the course of simulation, based on the evaluations in Ref. (*6*). For each electromagnetic transition probability of γ-ray emission as well as probabilities of the K-shell and $L_{1,2,3}$-subshell vacancy creation due to the internal conversion process are evaluated based on the internal conversion coefficient (ICC) data. If experimental ICCs are not provided in the input ENSDF file, the corresponding theoretical values (*7-9*) for particular energy, multipolarity and type of transition are used. Based on the information on momentums of the involved nuclear levels and mixing ratios of the corresponding electromagnetic transitions, angular correlation functions are calculated for each pair of cascade γ-rays on the basis of known theoretical formulas (*10,11*). To ensure correct modeling of intra-atomic transitions resulting in single and double X-ray fluorescence as well as emission of Auger-electrons, data from the evaluation (*12*) of the probabilities of radiative and radiation-less atomic transitions at the K-shell and $L_{1,2,3}$-subshell vacancy filling are used. Energies of the K- and L-shell conversion electrons as well as of the K-LX and K-MX Auger-electrons are calculated for each electromagnetic transition based on the atomic-shell binding energy data reported in (*13*).

The obtained comprehensive data array is used by MCNP-CP for performing a full-scale simulation of the radioactive decay process, which yields random composition (quantity and types) and probabilistic characteristics (energies, times, directional cosines) of a set of emitted correlated nuclear particles. A new card

CPS *RT IGA IAN IKX ILX IBT ICE IAE IGG*

was introduced to specify particular modes of source modeling. The first entry on the card, *RT*, is the basic source mode switch, whose function will be considered further. Next 7 entries provide the possibility to enable or disable simulation of the emission of different types of particles, such as γ-rays (*IGA*), annihilation photons (*IAN*), KX- and LX-rays (*IKX* and *ILX*), β-particles (*IBT*),

Downloaded by STANFORD UNIV GREEN LIBR on August 9, 2012 | http://pubs.acs.org
Publication Date: November 16, 2006 | doi: 10.1021/bk-2007-0945.ch013

conversion and Auger electrons (*ICE* and *IAE*). The last entry, *IGG*, is used for turning on/off modeling of angular correlations of cascade γ-rays.

Depending upon the *RT* value, three different modes of the MCNP-CP source modeling are possible. Any positive number of *RT* is considered as the length of a particle grouping time interval in shakes (one shake equals 10^{-8} s). In this case all emitted particles are grouped within consecutive time intervals according to their emission times, which are sampled based on the lifetimes of nuclear levels involved in the particular realization of a sampled decay. Each of these particle groups is then tracked in different histories (one history per group), thus assuming no correlations between groups. In this source modeling mode *RT* value can be interpreted as the pulse-pair resolving time of the pulse pileup rejection or coincidence/anticoincidence circuits. If *RT* is set to zero then all particles are considered within one group disregarding their emission times. This mode corresponds to the case of a total correlation between all emitted particles, which are tracked within the same history. This is the case of a total (forced) correlation. And if *RT* is set to any negative number then an uncorrelated source mode is turned on. In this mode all particles are sampled independently using per-decay probabilities. Tracking of particles is carried out in separate histories, one history per one particle.

To allow modeling the response of a system of detectors connected in coincidence/anticoincidence modes, a standard MCNP pulse-height tally F8 was upgraded. In particular a new tally bin format was introduced as follows

$$((S_1 \ldots S_I) + (C_{11} \ldots C_{1J_1}) \ldots - (A_{11} \ldots A_{1K_1}) \ldots).$$

The first entry represents a combination of geometry cells, which need to be tallied, while the rest of the bin description specifies a particular condition, under which tallying will be done. In particular, entries preceded with plus/minus signs specify coincidence/anticoincidence channels, whose pulses are appropriately connected to produce a so-called gating signal. As shown on the top of Fig. 1, each coincidence/anticoincidence channel consists of a group of cells, whose pulses are analyzed by single channel analyzers (SCA) and then logically ored to produce an output signal. Lower and upper level thresholds of the SCAs are set for each geometry cell using two specially designed data cards ULD and LLD. The number of coincidence and anticoincidence channels (or in other words coincidence and anticoincidence multiplicities) can be up to 10. Logical schemes of formation of the "*Pulse*" and "*Gate*" signals are shown on the bottom of Figure 1.

As output MCNP-CP produces extensive tables containing detailed decay properties of a radionuclide under consideration and properties of its decay radiations. In addition a γ-γ-coincidence table, sum peak energy table and true coincidence summing-in prediction table are included. Source diagnostics,

Downloaded by STANFORD UNIV GREEN LIBR on August 9, 2012 | http://pubs.acs.org
Publication Date: November 16, 2006 | doi: 10.1021/bk-2007-0945.ch013

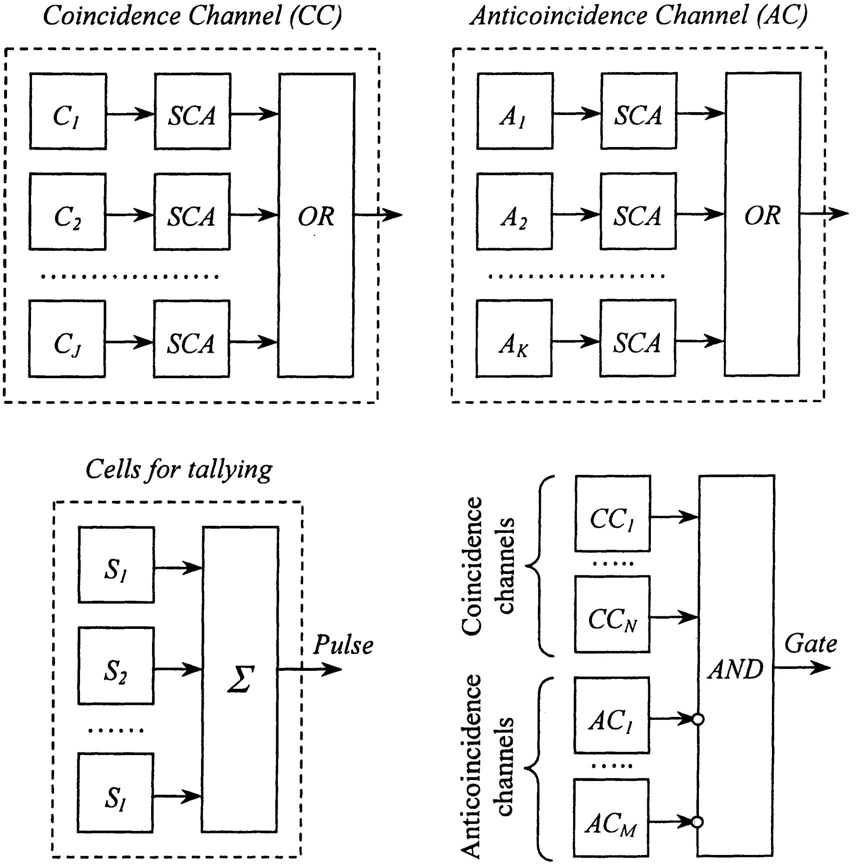
Coincidence Channel (CC)
C1
C2
CJ
SCA
SCA
SCA
OR
Anticoincidence Channel (AC)
A1
A2
AK
SCA
SCA
SCA
OR
Cells for tallying
S1
S2
SI
Σ
Pulse
Coincidence channels
CC1
CCN
Anticoincidence channels
AC1
ACM
AND
Gate

Figure 1. New coincidence/anticoincidence capability of the pulse height tally F8: structure of the cell groups representing coincidence/anticoincidence channels (on the top) and logic of the "Pulse" and "Gate" signal formation (on the bottom).

containing average numbers of sampled particles as well as a matrix of correlations between numbers of different types of particles, are reported also.

MCNP-CP Application Examples

As an example let us consider the case of a γ-spectrum measurement of a ^{94}Nb point source by means of a coaxial HPGe detector having a relative

Downloaded by STANFORD UNIV GREEN LIBR on August 9, 2012 | http://pubs.acs.org
Publication Date: November 16, 2006 | doi: 10.1021/bk-2007-0945.ch013

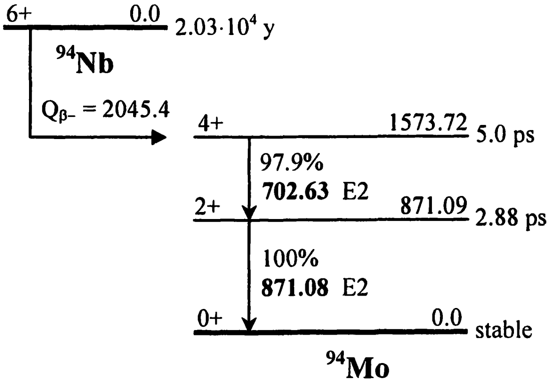

Figure 2. Decay scheme of ^{94}Nb.

efficiency of 60 %. The decay scheme of ^{94}Nb is shown in Fig. 2. The external dimensions of the detector crystal are Ø74 × 53 mm, crystal to end cap distance = 5 mm, rear contact dimensions = Ø10 × 36 mm, input window = 1.5 mm aluminum, inactive germanium from the input window side = 0.7 mm. The detector construction components behind the crystal were imitated with 30 mm thick aluminum disk. The source was placed on the detector axis at 1 mm distance from the detector cap.

Figure 3 shows two simulated responses obtained for $RT = 500$ ns (a typical value for the pulse-pair resolving time of pile-up rejection systems) and $RT = -1$ (source of uncorrelated particles). One can see a significant difference between these two cases all over the energy range, which is explained by the true-coincidence summing of the detector pulses originating from strongly correlated 702.6 keV and 871.1 keV photons. This effect causes transfer of the Compton continuum and full energy peak events into the higher energy region of the spectrum. For this particular case 702.6 keV and 871.1 keV full energy peak areas are decreased by 25 % and 27 % respectively due to the effect, which is essential for quantitative γ-spectrometry measurements.

Figure 4 shows simulated responses for a ^{152}Eu point source and the same detector and measurement geometry. Again, one can notice a significant difference between spectra simulated in correlated and uncorrelated source modes, which is due to the true-coincidence summing effect. As in the previous case the effect causes significant reduction of the full energy peak areas and transferring of low energy continuum counts to the upper energy range of the simulated spectrum.

Downloaded by STANFORD UNIV GREEN LIBR on August 9, 2012 | http://pubs.acs.org
Publication Date: November 16, 2006 | doi: 10.1021/bk-2007-0945.ch013

Downloaded by STANFORD UNIV GREEN LIBR on August 9, 2012 | http://pubs.acs.org
Publication Date: November 16, 2006 | doi: 10.1021/bk-2007-0945.ch013

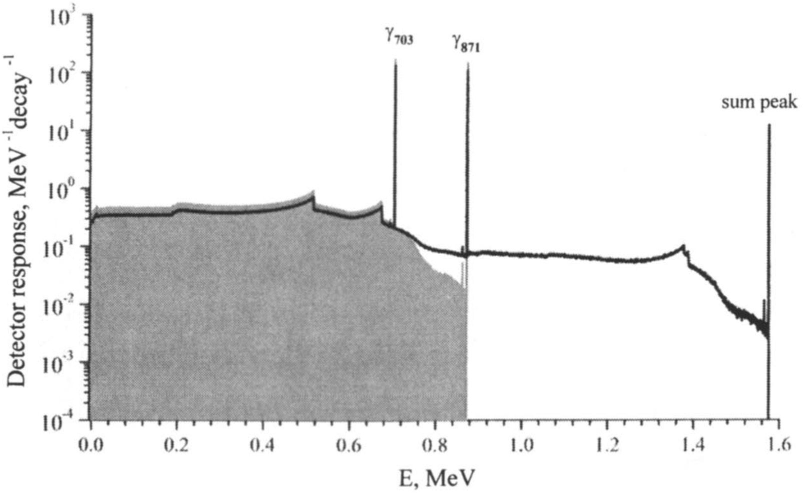

Figure 3. HPGe coaxial detector responses for ^{94}Nb cascade γ-source, simulated in correlated (solid line) and uncorrelated (filled area) source modeling modes.

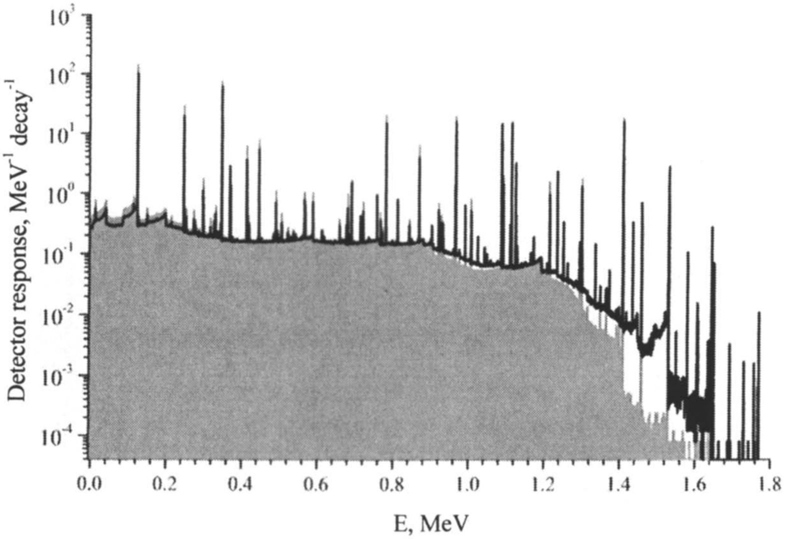

Figure 4. HPGe coaxial detector responses for ^{152}Eu cascade γ-source, simulated in correlated (solid line) and uncorrelated (filled area) source modeling modes.

Next example concerns calculation of the response for a point ^{137}Cs source located at the axis of a planar low-energy HPGe detector with the following geometrical dimensions: crystal = Ø16 × 10 mm, crystal to end cap = 5 mm, thickness beryllium window = 0.13 mm (0.005 in.). Responses were simulated in two different modes of the source modeling - in forced correlation modeling mode ($RT = 0$) and when 500 ns particle grouping time interval was chosen ($RT = 50$).

Simulated responses are shown in Fig. 5, where together with the contribution of 661.7 keV photons one can see a considerable numbers of counts caused by barium X-rays, conversion electrons and β-particles all over the energy range. Note, that the response simulated for 500 ns grouping time gives a much lower intensity of counts in the upper energy range of the spectrum. This reflects the well-known fact that no real correlation actually exists between emitted gammas and beta-particles due to the long half-life of the 661.7 keV isomer ^{137m}Ba ($T_{1/2} = 2.55$ min), which is populated in the considered decay.

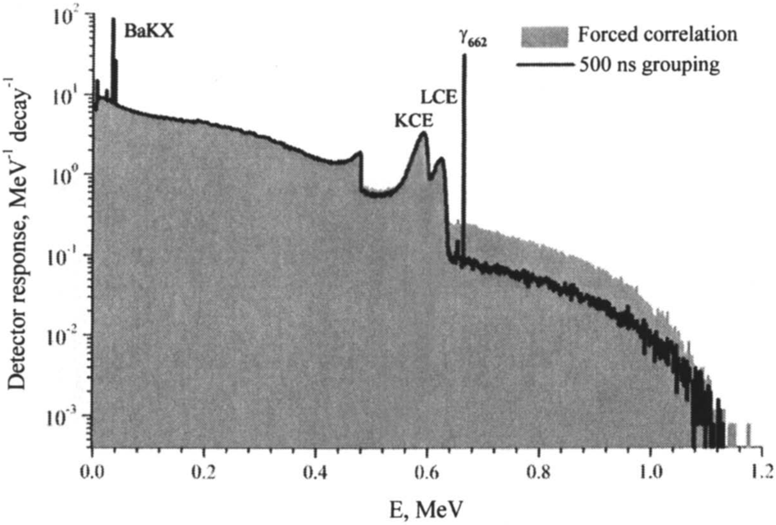

Figure 5. Simulated responses of a planar low-energy HPGe detector with a thin 0.005 in. beryllium window for measurements with ^{137}Cs source.

As the last example, let us consider γ-spectrometry measurements with the use of a hypothetical Compton suppression system, whose model is shown in Figure 6. It consists of the above 60 % HPGe coaxial detector as an analyzing detector, as well as annular and plugs BGO scintillation detectors, which serve

Downloaded by STANFORD UNIV GREEN LIBR on August 9, 2012 | http://pubs.acs.org
Publication Date: November 16, 2006 | doi: 10.1021/bk-2007-0945.ch013

as guard detectors. The thickness of the guard detector crystals was chosen to be 30 mm and 40 mm for annular and plug detectors respectively. Both guard detector crystals were assumed to have 1.5 mm aluminum coating.

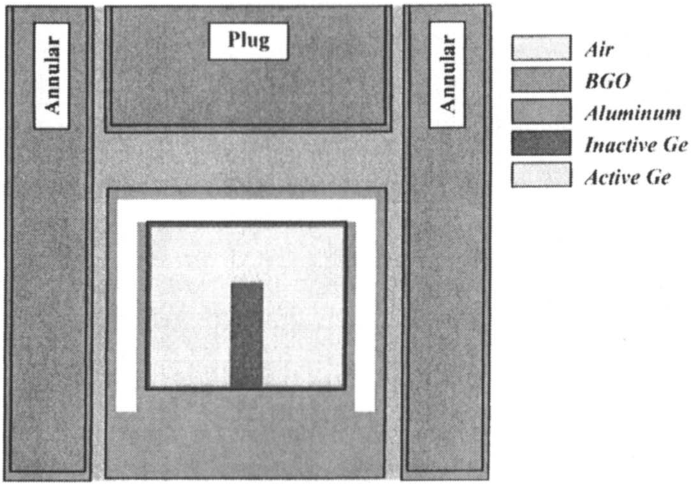

Figure 6. A model of a hypothetical Compton suppression spectrometer with 60 % HPGe analyzing detector and annular and plug guard detectors based on BGO scintillation crystals.

System responses were calculated for a ^{94}Nb point source located in contact with the analyzing detector cap on the detector crystal axis. Results of the calculations for different combinations of guard detectors being connected in anticoincidence mode are shown in Fig. 7. Although the coincidence mode does not correspond to a real operating mode of conventional Compton suppression systems, it was considered also solely with the purpose of demonstration. Results of these calculations are also presented in Fig. 7.

The responses shown demonstrate great potential of MCNP-CP for predicting characteristics as well as for optimizing construction and working modes of spectrometry systems, which use coincidence/anticoincidence measurement techniques. By the way, as it was shown in (*14*), MCNP-CP can adequately address the very actual problem of the true-coincidence summing correction factor calculation, not only for traditional single detector γ-ray spectrometers, but also for the Compton suppression systems, for which the influence of the effect is much more pronounced.

Downloaded by STANFORD UNIV GREEN LIBR on August 9, 2012 | http://pubs.acs.org
Publication Date: November 16, 2006 | doi: 10.1021/bk-2007-0945.ch013

Downloaded by STANFORD UNIV GREEN LIBR on August 9, 2012 | http://pubs.acs.org
Publication Date: November 16, 2006 | doi: 10.1021/bk-2007-0945.ch013

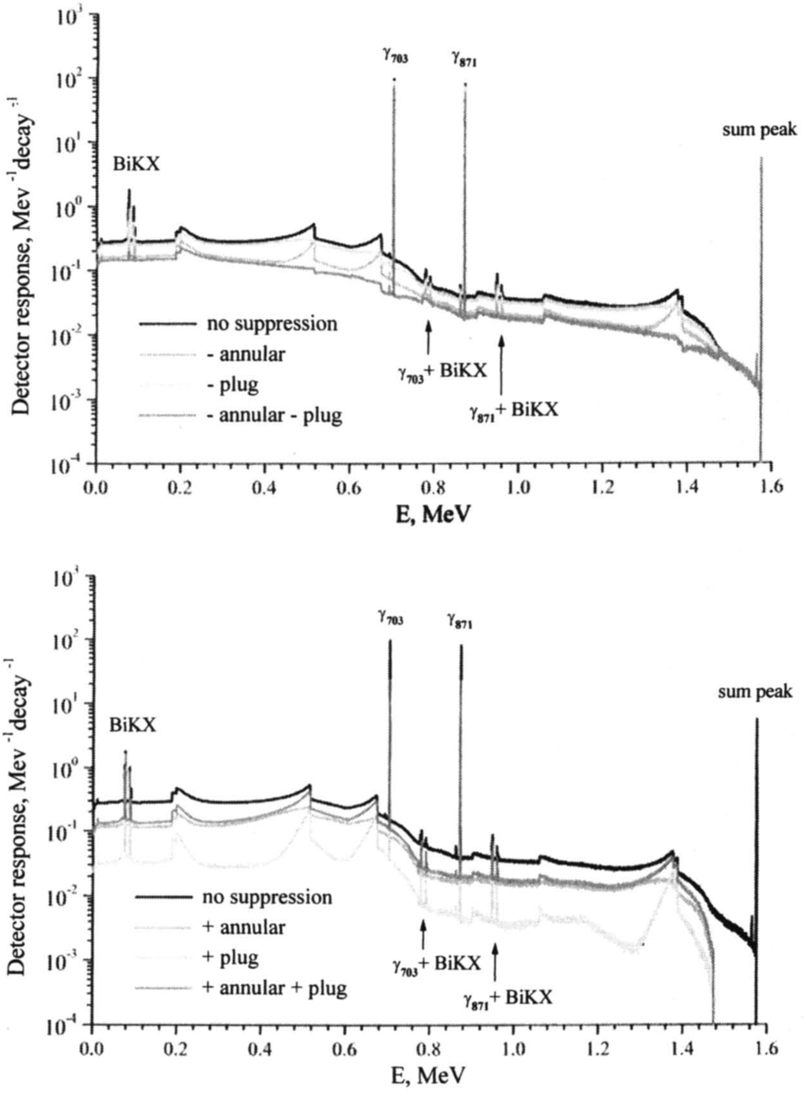

Figure 7. Responses of a hypothetical Compton suppression system for measurements with ^{94}Nb point source and different combinations of guard detectors connected in anticoincidence (on the top) and coincidence (on the bottom) modes.

Summary

A standard MCNP4c code was extended to allow carrying out calculations with a source of correlated nuclear particles. A new version of the code, MCNP-CP, performs statistical simulation of processes accompanying radioactive decay of a specified radionuclide, yielding characteristics of emitted coincident nuclear particles, which are then tracked through the problem geometry within the same history. For modeling radioactive decay, MCNP-CP considers emission of cascade gamma-rays, continuum energy electrons from β^--decay, annihilation photons accompanying β^+-decay, monoenergetic electrons from internal conversion on the atomic K-shell and $L_{1,2,3}$-subshells; K- and LX-rays due to single and double fluorescence occurring with electron capture and internal conversion processes, K-LX and K-MX Auger electrons. Quantity, types, energies and times of emitted particles are sampled according to the properties of the decay scheme of a particular radionuclide, which are taken from the evaluated nuclear structure data file ENSDF. γ-γ angular correlations are taken into account for sampling emission directions of cascade γ-rays.

MCNP-CP presents a powerful tool for predicting performance of γ- and β-spectrometry systems, as well as for optimizing their construction and operational modes for measurements with real radiation sources. A versatile multi-cell coincidence/anticoincidence pulse height tally is another unique feature of MCNP-CP, which gives an opportunity of modeling real source responses and efficiencies of such multi-detector systems as phoswich, cluster, and clover detectors, escape/Compton suppression and pair spectrometers, large detector arrays etc.

Downloaded by STANFORD UNIV GREEN LIBR on August 9, 2012 | http://pubs.acs.org
Publication Date: November 16, 2006 | doi: 10.1021/bk-2007-0945.ch013

Acknowledgements

The author expresses his gratitude to Dr. Volodymyr Tryshyn from the Institute for Nuclear Research of the National Academy of Sciences of Ukraine for useful discussions and his sincere interest in this work.

References

1. Briesmeister, J. F. Report LA-12625-M, 1997.
2. Berlizov, A. N.; Tryshyn, V. V. The ENSDF based radionuclide source for MCNP. Proc. Int. Conf. on Supercomputing in Nucl. Appl., SNA'2003: Paris, France, 22-24 September 2003, CD-edition.

3. Berlizov, A. N. An upgraded multidetector pulse height tally for MCNP. Proc. Monte Carlo 2005 Topical Meeting; Chattanooga, TN, April 17-21, 2005; American Nuclear Society: La Grange Park, IL, 2005, CD-edition.
4. Tuli, J. K. Report BNL-NCS-51655-Rev. 87, 1987.
5. Bambynek, W.; Chen, M. H.; Crasemann, B.; Fitzpatrick, M. L.; Ledingham, L. W. D.; Genz, H.; Mutterer, M.; Intemann, R. L. *Rev. Mod. Phys.* **1977**, *49*, 77-215.
6. Prochazka, I. *Materials Structure* **2001**, *8*, 55-60.
7. Hager, R. S.; Seltzer, E. C. *Nucl. Data* **1968**, *A4*, 1-237.
8. Rosel, F.; Fries, H. M.; Alder, K.; Pauli, H. C. *At. Data Nucl. Data Tables* **1978**, *21*, 91-289.
9. Band, I. M.; Trzhaskovskaya, M. B.; Listengarten, M. A. *At. Data Nucl. Data Tables* **1976**, *18*, 433.
10. Siegbahn, K. *Alpha-, Beta- and Gamma-ray Spectroscopy*; North-Holland: Amsterdam, 1965, Vol. 2, pp. 1029-1195.
11. Ferguson, A. J. *Angular Correlation Methods in Gamma-ray Spectroscopy*; North-Holland: Amsterdam, 1965, pp. 1-256.
12. Krause, M. O. *J. Phys. Chem. Ref. Data* **1979**, *8*, 307-327.
13. Larkins, F. B. *At. Data Nucl. Data Tables* **1977**, *20*, 311-387.
14. Berlizov, A. N.; Tryshyn, V. V. *J. Rad. Nucl. Chem.* **2005**, *263*, 169-174.

Downloaded by STANFORD UNIV GREEN LIBR on August 9, 2012 | http://pubs.acs.org
Publication Date: November 16, 2006 | doi: 10.1021/bk-2007-0945.ch013

Downloaded by COLUMBIA UNIV on August 6, 2012 | http://pubs.acs.org
Publication Date: November 16, 2006 | doi: 10.1021/bk-2007-0945.ch014

Chapter 14

Creation of Realistic Radiation Transport Models of Radiation Portal Monitors for Homeland Security Purposes

S. M. Robinson, R. Kouzes, R. J. McConn Jr., R. Pagh, J. E. Schweppe, and E. R. Siciliano

Pacific Northwest National Laboratory, P.O. Box 999, P8–50, Richland, WA 99352

Much of the data used to analyze and calibrate alarm algorithms for radiation portal monitor (RPM) systems has come from actual measurements of vehicles passing through RPMs. Due to the inherent limitations and expense of taking data with controlled radioactive sources, the majority of these data contain no sources except for naturally occurring radioactive material (NORM) cargo sources in the presence of natural background. Advances in computing capabilities have made it feasible to simulate "in-the-field" detector responses from a wide variety of source/cargo configurations, and to produce data matching that generated in the field. Computational models have been developed by the Radiation Portal Monitor Project (RPMP) for many detectors, vehicles, cargo configurations, and sources. These models are being used to simulate RPM responses to complicated source/cargo configurations for vehicles with and without sources. The simulated data is, and will be used to 1) complement existing field data, 2) help guide the progress of future data taking, 3) improve our ability to calibrate and refine alarm algorithms, 4) verify the causes of effects seen in the field, and 5) look for unknown effects not corresponding to theoretical models. A large set of simulated data that has been validated against field data will allow for in-depth testing of detection alarm

In Applied Modeling and Computations in Nuclear Science; Semkow, T., et al.;
ACS Symposium Series; American Chemical Society: Washington, DC, 2006.

algorithms for a variety of source scenarios. An overview of the PNNL/RPM Modeling System will be presented. Highlights from selected results already obtained and compared to data will be shown, and a set of ongoing cases being simulated will be outlined.

Introduction

Status of Field Data

Although some data from actual Radiation Portal Monitor (RPM) deployments are available to authorized researchers and laboratories, these data are limited in their use to any individual researcher. They are difficult to analyze systematically, mainly because of differences in backgrounds and NORM/TENORM[1] cargo rates at individual installation locations. Furthermore, data involving actual targeted sources (as opposed to only NORM cargo or natural backgrounds) are difficult to obtain, and small in number. This has led researchers to conduct individual tests on desired source scenarios, but these data are not kept in a standard location or format. There is a great need for a large and standardized data set, containing many targeted source scenarios. This would allow for analysis of data characteristics in a well-understood environment. Also, this would facilitate testing of alarm algorithms and source detectability.

Overview of Large-Scale Simulation System

A comprehensive data production system has been created to simulate the results from in-field RPM configurations. This system includes a variety of models of vehicles, cargos and sources. Each vehicle is stepped horizontally through simulated RPM installations, to model drive-throughs at various speeds. To provide a high-degree of realism, the dimensions and composition of all

Downloaded by COLUMBIA UNIV on August 6, 2012 | http://pubs.acs.org
Publication Date: November 16, 2006 | doi: 10.1021/bk-2007-0945.ch014

---

[1] Naturally occurring radioactive material. Road Salt and Granite are two common NORM sources. One subclass of NORM is TENORM (Technologically enhanced NORM). For example, alkaline batteries and some salts are rich in natural ^{40}K due to chemical processing.

components comprising these models are verified for accuracy against actual vehicles and RPM units. As shown in Fig. 1, these models can be used to create simulated data sets which behave like actual field data, giving confidence that they can then be used in evaluating algorithm responses to source scenarios. The ability to test detection algorithms against numerous source scenarios is expected to greatly aid in optimization of future algorithms, including the use of multiple algorithms together in "hybrid" algorithm schemes.

Numerical Modeling

Cargo and Vehicle Models

A set of very specific and detailed models have been constructed for use in the simulation of POV (Personally Owned Vehicle) and Cargo lanes, commonly found at border crossing RPM installations. Of particular interest is the so-called "E-Van Model" (*1*). This model was constructed to simulate the shielding effects an averaged-sized privately-owned vehicle (POV) would have on a small, but finite radioactive source being transported by the vehicle. It was based on the geometry of a Ford Econoline™ van, with the specific component dimensions representing a composite of the Econoline™ models E-150/250/350 for the model year 2000. The E-Van development objective was to include with sufficient detail all the structural features of a realistic van that would provide "intrinsic" shielding.

Also of interest is the "Cargo Truck" lane model (Fig. 2). In this model, a large cargo vehicle is filled with standard cargo boxes, which can be filled with a variety of materials. Materials of disparate densities, hydrogen content and atomic number, such as air, polyethylene and concrete are considered, and modeled in the MCNP input decks. Like the E-van model, the Cargo Truck model also contains specific details of vehicle construction, but is also meant to be a general model for all vehicles carrying standard configurations of commercial cargo. Wooden cargo pallets are present, along with a choice of several cargo box heights and configurations. As in the field, this vehicle model is simulated to pass through a cargo lane, whereas the E-Van model is simulated to pass through a POV lane.

Detector Models

For this work, it is also necessary to simulate the specific detection systems in deployment, and those under consideration for future use. A variety of models for PolyVinyl-Toluene (PVT) and Thallium-doped Sodium-Iodide (NaI(Tl)) based detection systems have been created, verified and validated (see below).

Downloaded by COLUMBIA UNIV on August 6, 2012 | http://pubs.acs.org
Publication Date: November 16, 2006 | doi: 10.1021/bk-2007-0945.ch014

Downloaded by COLUMBIA UNIV on August 6, 2012 | http://pubs.acs.org
Publication Date: November 16, 2006 | doi: 10.1021/bk-2007-0945.ch014

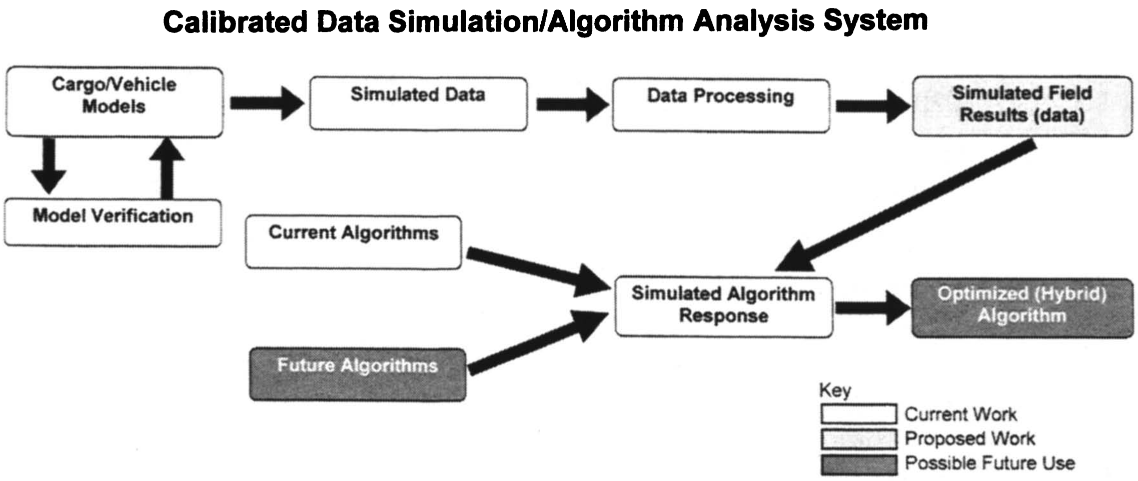
Calibrated Data Simulation/Algorithm Analysis System
Cargo/Vehicle Models
Simulated Data
Data Processing
Simulated Field Results (data)
Model Verification
Current Algorithms
Simulated Algorithm Response
Optimized (Hybrid) Algorithm
Future Algorithms
Key
Current Work
Proposed Work
Possible Future Use

Figure 1. The proposed RPM simulation system.

Downloaded by COLUMBIA UNIV on August 6, 2012 | http://pubs.acs.org
Publication Date: November 16, 2006 | doi: 10.1021/bk-2007-0945.ch014

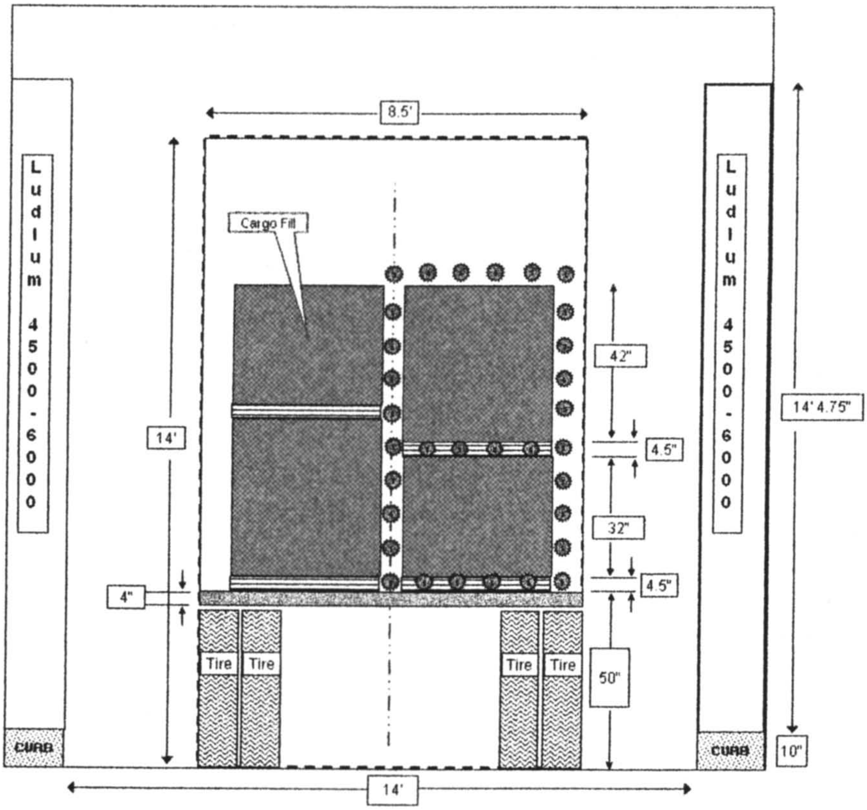
Ludlum 4500-6000
8.5'
Cargo Fill
14'
42"
4.5"
32"
4.5"
4"
Tire
Tire
Tire
Tire
50"
14' 4.75"
Ludlum 4500-6000
CURB
CURB
10"
14'

Figure 2. The "Cargo Truck Model."

In the data sets produced by this research, the responses of each of these systems will be computed.

Verification and Validation of Models

An important step in ensuring the reliability of simulated data is to "verify" the accuracy of all model components, and "validate" the results whenever possible. In generic terms, verification means the encoded instructions solve the model problem correctly, whereas validation indicates the degree to which the model output represents the real world. In the context of the RPMP models, verification is used to mean the dimensions and compositions of the encoded model components represent the corresponding real-world components correctly, and validation means the simulated responses compare well to measured responses. This work is currently in progress, and results have shown that the cargo model exhibits the expected effects on source detectablity, including radiation attenuation by dense cargo, detection asymmetry of a source placed on one side of the vehicle, and "channeling" of gamma rays through less dense cargo areas. As an example, the source is placed either in the middle of the vehicle, or toward the passenger's side, and results are calculated for the detector panels on the top and bottom of either side of the RPM lane (Fig. 3). Once models are verified, the results of the simulations must be validated, meaning that a high level of confidence must be established that the models produce results in keeping with actual quantitative measurements. Measurements have been made on standard sources to validate the simulated detector responses against the actual responses, in the case of PVT and NaI-based portal monitor systems (Fig. 4). Verification and validation of these models are important steps in establishing confidence in the results of the simulations using them.

Downloaded by COLUMBIA UNIV on August 6, 2012 | http://pubs.acs.org
Publication Date: November 16, 2006 | doi: 10.1021/bk-2007-0945.ch014

Computing Environment - MCNP

The calculations use the general-purpose Monte Carlo N-Particle Transport code, MCNP (*2*) with model components constructed to simulate the gamma-ray detection system, a vehicle (in which sources may be located), cargo carried by this vehicle, and the remaining environment (pavement and atmosphere). Simulations must therefore be made to represent all of these parameters, and to estimate the detector response from a vehicle passing through an RPM system. For this purpose, the MCNP environment will be "wrapped" by a set of scripts designed to produce a series of MCNP input files representing the desired scenario. After the vehicle model, cargo, potential sources (NORM and otherwise) and speed of vehicle are specified, an "input script" will take these characteristics and turn them into a time-stepped series of input files, each one representing the vehicle's position at some point in time. These input files are run as a batch, generating the detector's response to the vehicle at every point in time. Then an "output script" will be run on the collection of MCNP outputs, reading the tallied detector responses, and assembling the results into a time-series of data that would be seen by the RPM software in the field. These data are the "Simulated Field Results" of Fig. 1.

Downloaded by COLUMBIA UNIV on August 6, 2012 | http://pubs.acs.org
Publication Date: November 16, 2006 | doi: 10.1021/bk-2007-0945.ch014

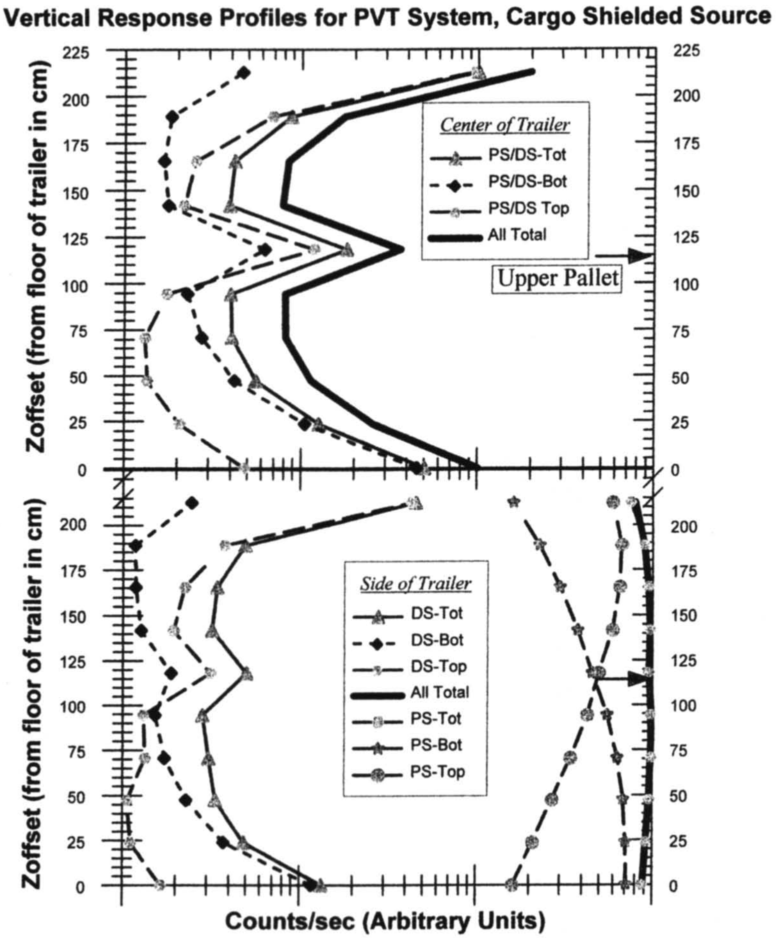

Figure 3. Arbitrary RPM response (Passenger Side, Driver Side and Totals) to source positions in a cargo truck.

Downloaded by COLUMBIA UNIV on August 6, 2012 | http://pubs.acs.org
Publication Date: November 16, 2006 | doi: 10.1021/bk-2007-0945.ch014

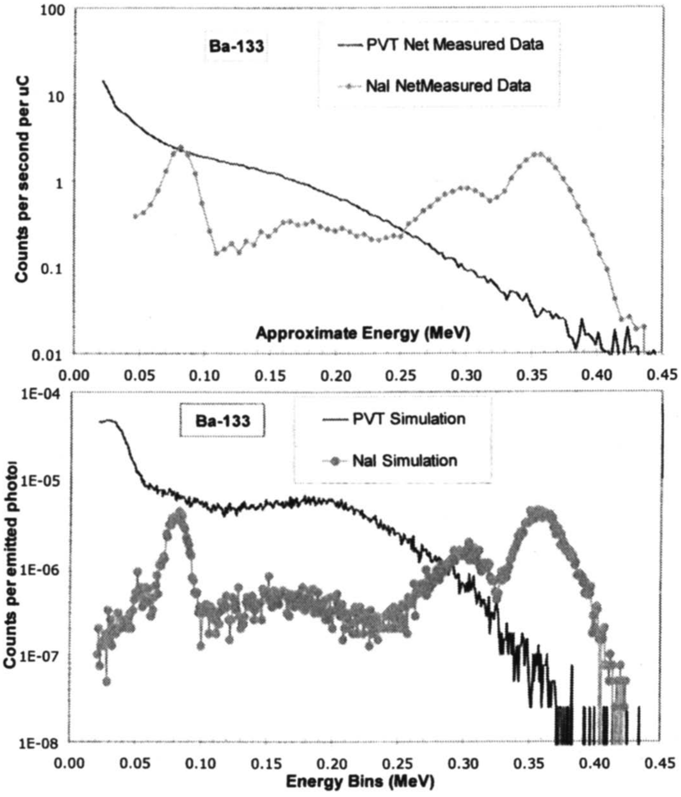

Figure 4. Real and simulated PVT and NaI responses to a ^{133}Ba source.

Computing Environment – Multiprocessing

It is estimated that many tens of thousands of processor hours will be necessary to produce the datasets in this work, and so parallel computational techniques recently evaluated at PNNL will be employed.

Because of the statistical independence of each Monte-Carlo "trajectory," the time required to run MCNP calculations can be reduced significantly by the use of parallel processing, and pre-compiled versions of MCNP that enable such processing are included in its distribution (*3,4*). At PNNL, a prototype system of 10 heterogeneous desktop computers (the "Heterogeneous Windows Cluster") has been constructed for this purpose, and several smaller clusters have been installed and configured for use by individual researchers. These systems afford large speed increases over traditional desktop hardware alone (Fig. 5), and the use of parallel processing solutions makes generation of the proposed data possible in a reasonable time frame.

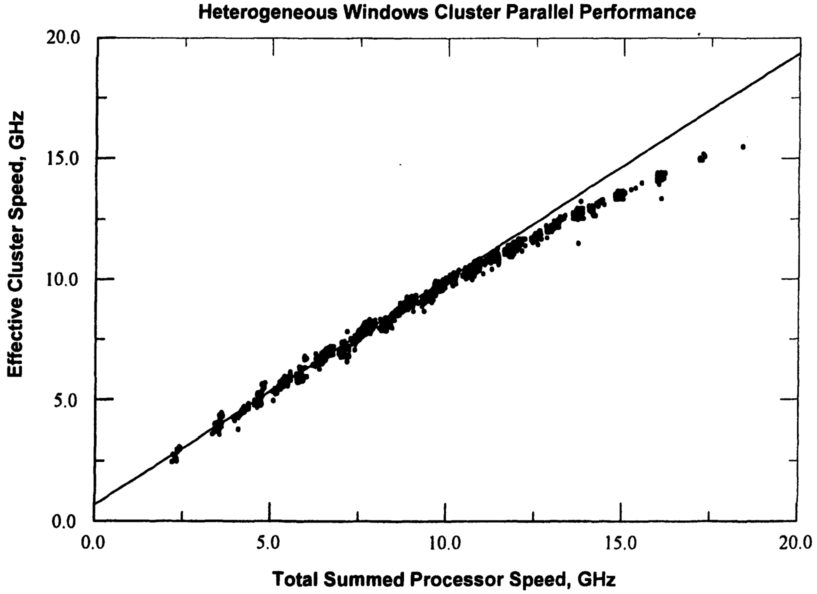

Figure 5. Proportional MCNP speedup of the HWC system in use at PNNL.

A Comprehensive Model

As mentioned earlier, the system for constructing and managing the simulated data is handled by several scripts that "wrap" the MCNP application, providing the desired functionality. A script called Pstudy, written in the Perl language (*5*) has been used in the past for generating this kind of variation in MCNP input decks, for parameter studies. An extension to the Pstudy scripts has been recently written, allowing for entire pieces of code to be inserted or removed automatically. This functionality allows for the iterative replacement of sources and cargos, as well as dynamic time-stepped movement of the vehicle model. In this way, a simple system is established to simulate RPM response from a given vehicle, source(s), velocity and cargo. A further script will be utilized to perform permutations on this parameter space, and automatically provide each set of results. Each scenario will also be repeated several times with a different initial random seed, for greater statistics.

Downloaded by COLUMBIA UNIV on August 6, 2012 | http://pubs.acs.org
Publication Date: November 16, 2006 | doi: 10.1021/bk-2007-0945.ch014

Database of Results

A database will be maintained to hold all of the results from each scenario, and to be accessible and searchable for these results. A "standard set" of scenarios will be kept in database format to provide a standardized set of data for RPM analyses. Each scenario consists of a vehicle driving through the appropriate RPM detector, with some cargo configuration and contained sources. Each scenario also includes many MCNP runs representing different time stepped "snapshots" of the vehicle as it passes through the RPM. In addition to gross counts reported from the RPM system, full spectral information is kept from each run, recorded over a set of narrow energy bins between 0 and 3 MeV. These results will allow for interrogation of energy dependent alarm algorithms. Several repetitions of each such simulation will be made, with a different initial random number, to establish good statistics on the results. With 5 repetitions for each scenario, preliminary results show that the data size of this database will be around 250 Megabytes per scenario.

Downloaded by COLUMBIA UNIV on August 6, 2012 | http://pubs.acs.org
Publication Date: November 16, 2006 | doi: 10.1021/bk-2007-0945.ch014

Alarm Algorithm Testing

An immediate use for these data will be to test the behavior of algorithms deployed in the field. Algorithms will be run directly on simulated field results to test the response to source (as well as non-source) scenarios. In this way, alarm algorithm responses can be further verified, and several pertinent results (such as alarm response to source configuration) can be gained. This will also provide a framework for testing more complex algorithm schemes. Since simulated time series of data from each scenario will be quickly and uniformly accessible, current and future algorithms can be easily tested. It will also be possible to test any "hybrid" alarming scheme, in which the results from multiple algorithms are used together to generate a single alarm decision. A dense collection of source scenario results will make testing and optimization of such complex alarm algorithms possible.

Preliminary Results

Some preliminary work has been completed, with scenarios created and run on the parallel computing infrastructure at PNNL. In one particular case, a ^{133}Ba "check source" is placed at an offset location between the pallets of the cargo truck model in Fig. 2. The truck is then "driven" through the RPM system with the source, at 1 mph. It should be noted that this speed is slower than those observed in the field, and is used here for the sake of reproducing a large number of time steps in the figure. It is expected that more repetitions of each scenario will be needed as vehicle speed increases, and few detections are made per time step. Results from the drive-through simulation show the expected increase of detection rate when the source is near the detector, as well as the asymmetry of detection of a source located to one side of the vehicle (see Figs. 6, 7). Significant expected statistical fluctuations are present, necessitating repetition of these time-histories for good statistical coverage.

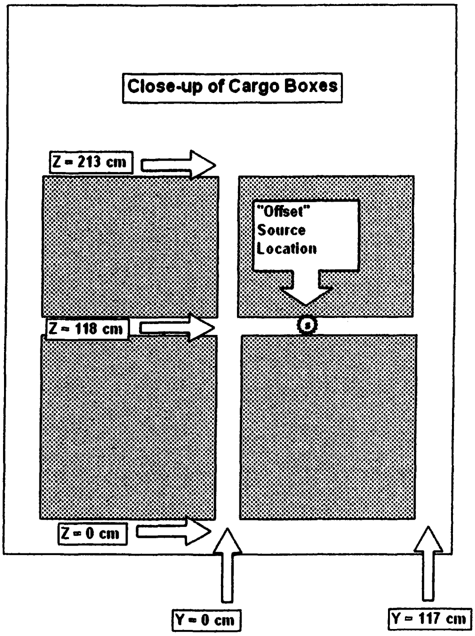

Figure 6. Position of the offset ^{133}Ba source.

Conclusions

The hardware and software infrastructure present at PNNL is capable of being used to produce a wealth of data pertinent to source simulation and algorithm analysis. Insofar as it matches data from actual RPM systems, and provides a dense collection of targeted source scenarios, this data will be useful to evaluate and optimize the algorithms currently used in the field. It will be possible for future algorithms to be characterized with this system, enabling continued improvement of total system performance.

Downloaded by COLUMBIA UNIV on August 6, 2012 | http://pubs.acs.org
Publication Date: November 16, 2006 | doi: 10.1021/bk-2007-0945.ch014

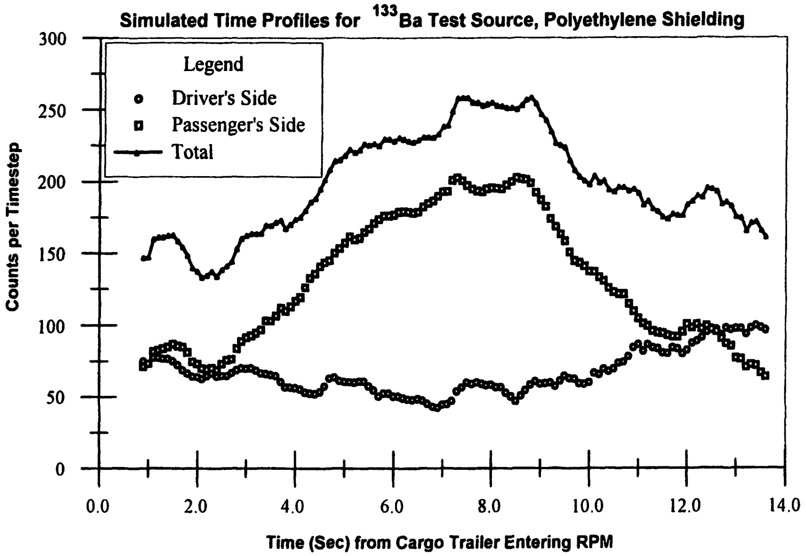

Figure 7. Drive-through data from the offset ^{133}Ba source.

References

1. Siciliano, E. R.; McConn, R. J. Jr.; Schweppe, J. E. The E-Van Vehicle Model for MCNP Simulations. Report PIET-43741-TM-059; Pacific Northwest National Laboratory: Richland, WA, 2005.
2. *MCNP - A General Purpose Monte Carlo N-Particle Transport Code*; Version 5. Report LA-UR-03-1987; Los Alamos National Laboratory: Los Alamos, NM, 2003.
3. Goorley, T.; Brown, F. B; Cox, L. J. MCNP Improvements for Windows PCs. Report LA-UR-02-7162; Los Alamos National Laboratory: Los Alamos, NM, 2002.
4. Brown, F. B.; Martin, W. R. High performance computing and Monte Carlo. *Trans. Am. Nucl. Soc.* **2004**, *91*.
5. Brown F.; Sweezy, J. E.; Hayes, R. B. Monte Carlo Parameter Studies and Uncertainty Analyses with MCNP5; PHYSOR, 2004.

Downloaded by COLUMBIA UNIV on August 6, 2012 | http://pubs.acs.org
Publication Date: November 16, 2006 | doi: 10.1021/bk-2007-0945.ch014

Chapter 15

A Random-Walk Solution to the Heliospheric Transport Equation

Keran O'Brien

Department of Physics and Astronomy, Northern Arizona University, Flagstaff, AZ 86011

Downloaded by UNIV MASSACHUSETTS AMHERST on August 8, 2012 | http://pubs.acs.org
Publication Date: November 16, 2006 | doi: 10.1021/bk-2007-0945.ch015

An adjoint random-walk solution to the problem of heliospheric transport is presented here. The heliosphere is represented by a 140 AU sphere with the sun at 100 AU from the bow shock. The dependence of the solar wind on latitude is included, varying from 400 to 800 km/s. The diffusion coefficient is represented by a simple scalar. Spectra and angular distributions at various locations in the heliosphere are presented. The leakage flux from the heliosphere is also shown.

Introduction

Cosmic rays with energies up to about 10^{16} eV are believed to be produced by shock acceleration as a result of Type II supernovae explosions. Cosmic-rays with higher energies are thought to be accelerated by other mechanisms, perhaps from outside the Milky Way in active galactic nuclei. Scattered by the magnetic fields of our galaxy and altered at low energies by interactions with material in the galaxy, they fall isotropically on our solar system.

Cosmic rays are wholly-ionized nuclei from hydrogen to nickel, with a few higher-mass constituents. Hydrogen nuclei, protons, are, by far, the most numerous of the constituents of cosmic rays.

In Applied Modeling and Computations in Nuclear Science; Semkow, T., et al.;
ACS Symposium Series; American Chemical Society: Washington, DC, 2006.

Downloaded by UNIV MASSACHUSETTS AMHERST on August 8, 2012 | http://pubs.acs.org
Publication Date: November 16, 2006 | doi: 10.1021/bk-2007-0945.ch015

The sun's corona is at some millions of degrees and as a result its material is continually boiling off in the form of wholly ionized plasma. This plasma, known as the solar wind, has a typical speed of 400 km/s in the region of the solar-system ecliptic, rising gradually with latitude to 800 km/s. The incoming cosmic rays, being charged particles, interact with the solar wind, both losing rigidity and intensity.

An understanding of the influence of the solar wind on cosmic-ray intensity in the heliosphere is necessary to determine the radiation dose to air crews, to a space crew on, say, a manned mission to Mars and to the radiation detectors on the space craft.

Theory

The starting points of this investigation are the coupled steady-state adjoint equations (*1*,*2*):

$$\vec{V}D - \overline{\mathrm{K}} \bullet \nabla D = 0, \tag{1a}$$

$$\vec{V} \bullet \nabla D + \nabla \bullet \left(\overline{\mathrm{K}} \bullet \nabla D\right) - \frac{1}{3}\left(\nabla \bullet \vec{V}\right) P \frac{\partial D}{\partial P} = 0. \tag{1b}$$

Cosmic-rays propagating the heliosphere undergo two processes: attenuation and rigidity loss. Eq. 1a describes the former, and Eq. 1b, the latter. In these equations, • is the vector dot product, $\vec{V}$ is the vector solar wind, D is the scalar phase-space density, $\overline{\mathrm{K}}$ is the tensor diffusion coefficient and P is the scalar particle rigidity $\left(= \sqrt{E^2 + 2mE} / q\right)$, in relativistic units, where E is the particle kinetic energy per nucleon, m is the particle mass, and q the nuclear charge. For hydrogen nuclei, $q = 1$, and the rigidity is equal to the momentum $\left(= \sqrt{E^2 + 2mE}\right)$.

In the radial dimension, Eqs. 1a, b become:

$$VD - \kappa \frac{\partial D}{\partial r} = 0, \tag{2a}$$

$$V \frac{\partial D}{\partial r} + \frac{1}{r^2}\left[\frac{\partial}{\partial r}\left(r^2 \kappa \frac{\partial D}{\partial r}\right)\right] - \frac{1}{3r^2}\frac{\partial}{\partial r}\left(r^2 V\right) P \frac{\partial D}{\partial P} = 0. \tag{2b}$$

The tensor diffusion coefficient $\overline{K}$ has now been collapsed to a scalar κ and r is the scalar distance from the "target."

Substituting $\Delta D / \Delta r$ for $\partial D / \partial r$ and $\Delta D / \Delta P$ for $\partial D / \partial P$ yields

$$VD - \kappa \frac{\Delta D}{\Delta r} = 0, \tag{3a}$$

$$V\frac{\Delta D}{\Delta r}+\frac{1}{r^2}\frac{\partial}{\partial r}\left(r^2\kappa\frac{\Delta D}{\Delta r}\right)-\left(\frac{1}{3r^2}\right)\frac{\partial}{\partial r}\left(r^2V\right)P\frac{\Delta D}{\Delta P}=0, \tag{3b}$$

giving us

$$\Delta D = VD\Delta r/\kappa, \tag{4a}$$

$$\Delta P=\frac{2VP(\Delta r)^2}{3\left(Vr\Delta r+2\kappa\Delta r-\kappa r\dfrac{\partial\Delta r}{\partial r}\right)}. \tag{4b}$$

Discarding the second-order term in Eq. 4b yields at last

$$\Delta P=\frac{2VP\Delta r}{3(Vr+2\kappa)}. \tag{4c}$$

The particle-flux is related to the phase-space density by:

$$\varphi_i=\frac{A_i}{Z_i}P^2D \tag{5}$$

where A_i is the atomic weight of particle-species i and Z_i is the corresponding atomic number.

The diffusion coefficient is given by:

$$\kappa=\kappa_0 P\beta, \tag{6}$$

where is $\beta = v/c$, v is the particle velocity, c is the velocity of light, and

$$\kappa_0=\frac{1}{3}\frac{Vr}{U}, \tag{7}$$

where U is the heliocentric potential and r is the distance to the surface of the heliosphere. The mean distance to the sun is essentially the radius of the heliosphere, 140 AU (*3*). 1 AU is the earth-sun distance, equal, approximately, to 1.5×10^{11} m (*4*). A Monte Carlo integration yields 139.95 ± 0.4 %. Since the earth circles the sun at 1 AU, the mean distance to the earth is taken to be the distance to the sun.

While the form of the diffusion coefficient is quite simple, it gives excellent results in the inner heliosphere, where, of course, most of the data are. This is very much a work in progress, and a more elaborate treatment is possible in the future. The reader will also have noted that this is a "shock-free" treatment; the solar-wind transition shock having not been included.

The heliosphere has two distinct boundaries, the solar-wind termination shock and the heliosheath beyond that. This shock-free model cannot distinguish between them.

Downloaded by UNIV MASSACHUSETTS AMHERST on August 8, 2012 | http://pubs.acs.org
Publication Date: November 16, 2006 | doi: 10.1021/bk-2007-0945.ch015

U is determined at one AU from high-latitude neutron monitor counting rates (*2*). In the heliocentric potential approximation, the particle flux is obtained directly from

$$\varphi_i(E, r=1) = \left(\frac{P(E)}{P(T)}\right)^2 \varphi(T, r=r_b), T = E + Z_i U, \qquad (8)$$

where r is the distance from the sun in AU, r_b is the location of the outer boundary, E is, as above, the particle kinetic energy per nucleon at one AU, and T is the particle kinetic energy at r_b.

The sun is located at 100 AU from one surface, 40 AU from the center. This offset is due to the motion of the sun through the local interstellar medium and the surface nearest the sun is in the "bow-shock" direction, toward the constellation Scorpios toward which it moves at about 20 km/s. The solar-wind speed is 400 km/s in the ecliptic region, increasing from 400 to 800 km/s between latitudes of 10° to 30° north and south, zenith and nadir (*1*).

A 3-dimensional Cartesian lattice is erected in the sphere, the nodes separated by a distance Δs. The random walk is started at a "target" with a unit flux equal to D/P^2. The target can be anywhere in the heliosphere. Its location can be represented as (x, y, z) where x and y are parallel to the plane of the ecliptic and z is normal to the ecliptic. Thus the bow-shock boundary is at (100,0,0), in the opposite direction, the termination shock is at (–180,0,0), the zenith, directly above the sun (0,134,0), the nadir, directly below the sun (0,–134,0).

At each node, one of six possible directions is chosen at random. The particle is then moved to the next node in that direction, through a distance Δs resulting in a change in r of Δr. The history proceeds from node to node, gaining or losing rigidity, and increasing or decreasing in phase space density at each step according to Eqs. 4a and 4c.

Each history is terminated when it crosses the surface of the sphere. Histories are run for 120 energies between 10 MeV and 10 TeV. At each energy, histories are run until the coefficient of variation falls below 3 % for both the adjoint energy and the flux at the surface of the sphere.

The coefficient of variation is calculated from the mean average deviation rather than the standard deviation, as the energy scored at the surface of the sphere is strongly skewed and has a high kurtosis. As a result, the quadratic term in the equation for the standard deviation has too high a weight.

A single history is terminated if the particle rigidity falls below zero, or the flux becomes greater than zero. Secondary particle production is not possible by means of the mechanism described by Eq. 1. Negative rigidities, and therefore negative kinetic energies are not physically possible.

Downloaded by UNIV MASSACHUSETTS AMHERST on August 8, 2012 | http://pubs.acs.org
Publication Date: November 16, 2006 | doi: 10.1021/bk-2007-0945.ch015

Calculated Results

Experimental Comparison

To verify the adequacy of this treatment, Eq. 4 was compared with the measurements of Neher of the primary proton spectrum. These measurements were made during a series of balloon flights and the time of each flight was given, allowing a determination of the counting rate of the Deep River neutron monitor corresponding to the measurements (*5*). The measurement was then fit to Eq. 8 by choosing $U = 500$ MV (*cf.* Fig. 1) (*2*). For protons, Z_i is, of course, 1, and the rigidities, P, as noted above, equal the momenta.

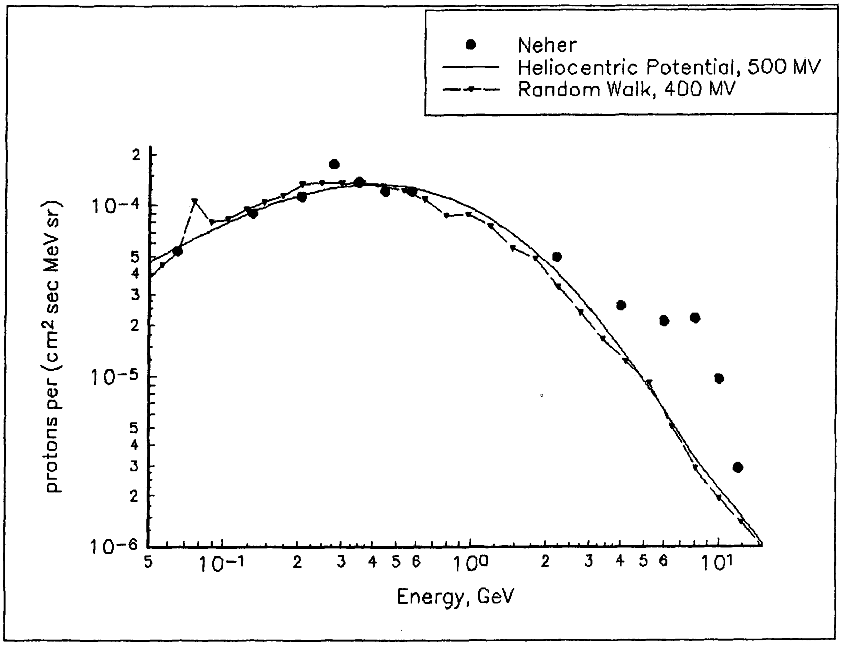

Figure 1. A comparison between the measurements of Neher (5) the heliocentric approximation and the random-walk solution of the primary proton spectrum.

The heliocentric approximation, Eq. 8, is a 1-dimensional approximation to the heliospheric transport equation. Equation 4 is applied here to an entirely different geometry. As noted above, it is applied to a point target that can be located anywhere in a 3-dimensional heliosphere with a latitudinally variable

Downloaded by UNIV MASSACHUSETTS AMHERST on August 8, 2012 | http://pubs.acs.org
Publication Date: November 16, 2006 | doi: 10.1021/bk-2007-0945.ch015

solar wind. One result of that is that the rigidity and energy scale differ from the 1-dimensional case by 25 %. Protons can reach the point target at 1 AU through trajectories that are not possible in the 1-dimensional case, passing, in some cases through a solar wind of higher velocity than in the ecliptic region.

Spectral Calculations in the Plane of the Ecliptic

Cosmic-ray spectra were calculated in the plane of the ecliptic along its center line (x,0,0). The proton spectra are shown in Fig. 2. The complex nuclei that comprise the rest of the cosmic-ray flux, approximately twice as rigid as the proton spectra, are not shown. The spectra are multiplied by arbitrary powers of ten to separate them from one another. The high-energy "tails" would otherwise overlie one another and the spectra would be difficult for the viewer to disentangle.

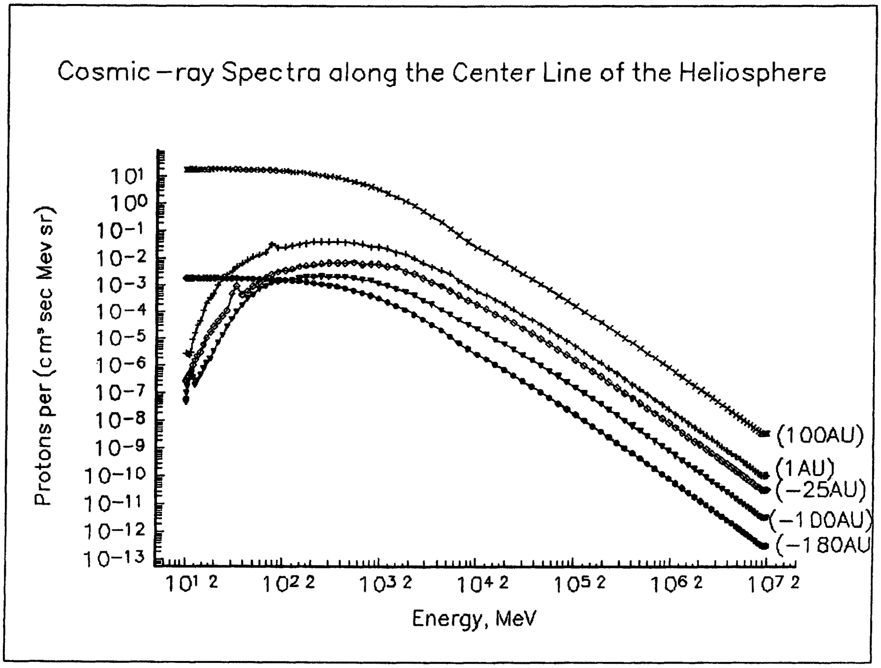

Figure 2. Calculated flux spectra in the plane of the ecliptic from the "bow" to the "stern." The spectra are separated by arbitrary powers of ten to keep them from overlapping.

Downloaded by UNIV MASSACHUSETTS AMHERST on August 8, 2012 | http://pubs.acs.org
Publication Date: November 16, 2006 | doi: 10.1021/bk-2007-0945.ch015

It can be seen that the closer the target point is to the outer surface of the heliosphere, the flatter the spectra become.

Angular Distributions

It is possible by using this method to determine the directions, expressed as coordinates on the surface of the heliosphere, from which particles arrive at a given target. Isotropy would be represented by a uniform distribution of points about the surface of the sphere, anisotropy by a cluster of points in a given direction.

Figure 3 shows the expected isotropy of 1-GeV protons at 1 AU, earth orbit. One thousand particles were scored for this graph.

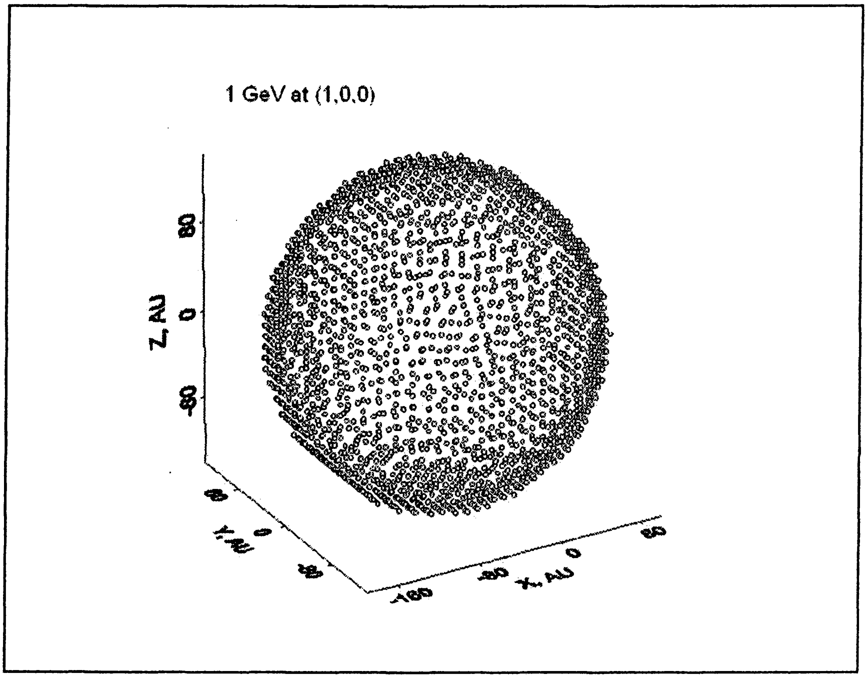

Figure 3. Angular distribution of cosmic-ray protons of 1-GeV energy at 1 AU.

This isotropy exists from the highest energy down to 100 MeV, at least at this resolution. A finer mesh and a greater number of particles might show

Downloaded by UNIV MASSACHUSETTS AMHERST on August 8, 2012 | http://pubs.acs.org
Publication Date: November 16, 2006 | doi: 10.1021/bk-2007-0945.ch015

some structure due to the shape of the heliosphere. No structure due to the structure of the heliospheric magnetic field or to astrophysical sources can be registered at this level of approximation.

At 10 MeV (see Fig. 4), it can be seen that most of the 10 MeV flux arrives from the bow-shock direction. The phase-space target corresponding to 10-MeV is quite small and hard to reach, so particles from the nearest boundary have the greatest chance to reach that target. Again, a thousand particles were scored for the graph.

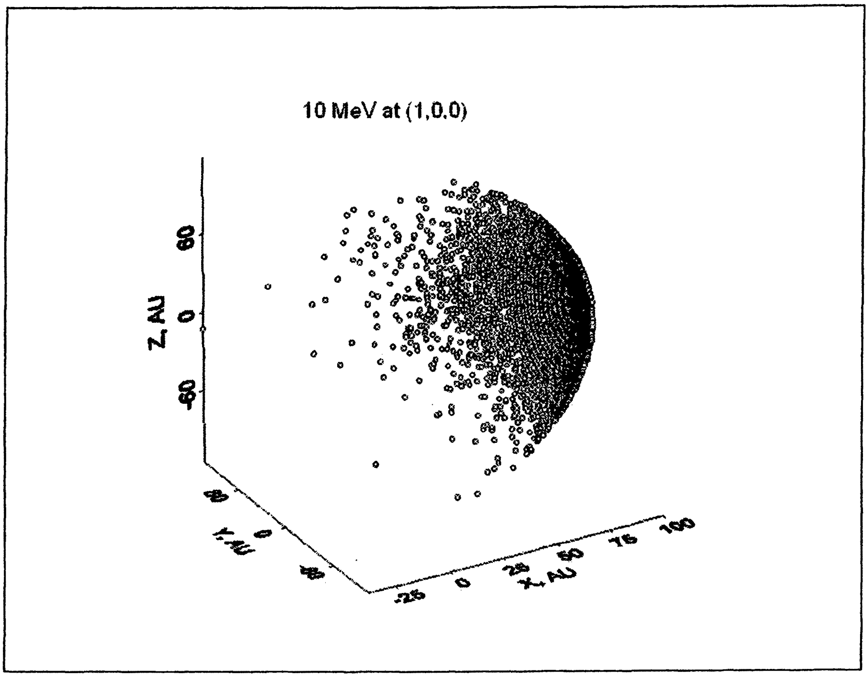

Figure 4. Angular distribution of cosmic-ray protons of 10 MeV energy at 1 AU.

Leakage

The heliosphere is quite transparent to high-energy cosmic rays. However, low-energy cosmic rays can be absorbed as a result of energy or rigidity loss. Cosmic rays produced by the mechanism of shock acceleration will have spectra of the form:

Downloaded by UNIV MASSACHUSETTS AMHERST on August 8, 2012 | http://pubs.acs.org
Publication Date: November 16, 2006 | doi: 10.1021/bk-2007-0945.ch015

$$\varphi(P) = AP^{-\varsigma/h} \approx E^{-\gamma}, \tag{9}$$

where $\varphi(P)$ is the particle flux as a function of rigidity, ς is a proportionality constant, and h is the non-escape probability.

Spectra incident on the heliosphere will have been modified by passage through many "astrospheres." In Fig. 5, the ratio of the proton spectrum that leaks out of the "bottom" of the heliosphere, directly south of the sun, to the local interstellar flux is shown. The leakage flux is somewhat "softer" than the local interstellar spectrum (LIS), and indicates one of the mechanisms by which the original shock-accelerated spectra are modified in passing through the galaxy (*cf.* Fig. 5).

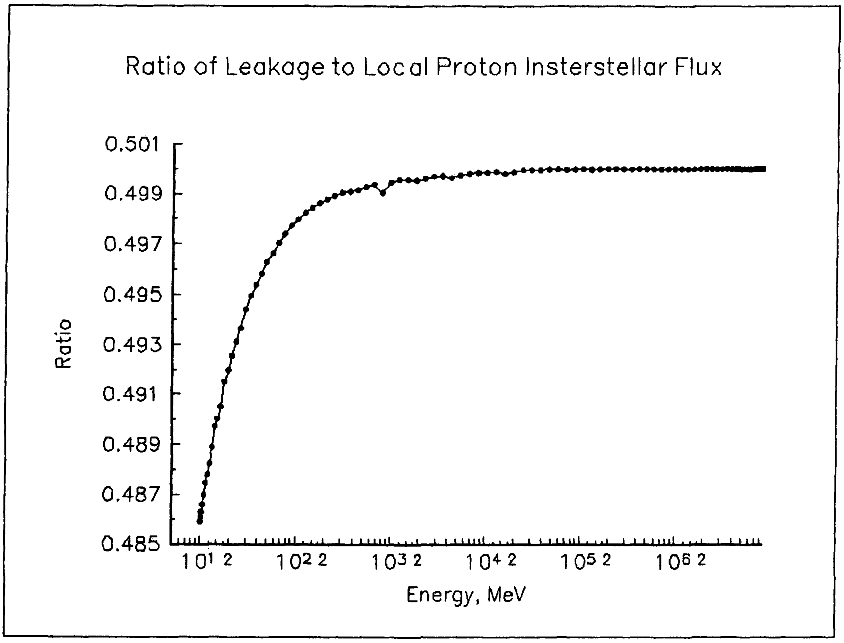

Figure 5. The ratio of the cosmic-ray proton leakage flux, at (0,–134,0), directly below the sun, to the local interstellar flux.

Downloaded by UNIV MASSACHUSETTS AMHERST on August 8, 2012 | http://pubs.acs.org
Publication Date: November 16, 2006 | doi: 10.1021/bk-2007-0945.ch015

Conclusions

An 3-dimensionsional adjoint random-walk calculation of cosmic-ray propagation has been performed which takes into account the non-symmetric position of the sun in the heliosphere and the change in solar-wind velocity with latitude. This method allow a more realistic heliospheric geometry than is possible using standard Runge-Kutta methods (*6*) and are in good agreement with measured proton spectra and angular distributions at earth orbit and can be applied throughout the heliosphere to cases where knowledge of cosmic-ray fluxes and dose rates are desired.

References

1. Caballero-Lopez, R. A; Moraal, H. Limitations of the force field equation to describe cosmic ray modulation. *J. Geophys. Res.* **2004**, *109*, A01101, doi:10.1029/2003JA010098.
2. O'Brien, K. The theory of cosmic-ray and high-energy solar-particle transport in the atmosphere. Proceedings of Seventh International Symposium on the Natural Radiation Environment (NRE-VII); McLaughlin, J. P.; Simopoulos, S. E.; Steinhäusler, F.; Eds.; Elsevier: Amsterdam, 2005, pp. 29-44.
3. *Plasma Physics of the Local Cosmos*; Committee on Solar and Space Physics; Space Studies Board; National Research Council; The National Academies Press: Washington, D.C., 2004, pp. 33-35.
4. Groom, D. E.; Dobbs, M. A. Astrophysical constants and parameters. *Physics Letters B* **2004**, *592*, 92-93.
5. Neher, H. V. Cosmic-ray particles that changed from 1954 to 1958 to 1965. *J. Geophys. Res.* **1967**, *72*, 1527-1539.
6. Caballero-Lopes, R. A.; Moraal, H.; McDonald, F. B. Galactic cosmic ray modulation: Effects of the solar wind termination shock and the heliospheath. *J. Geophys. Res.* **2004**, *109*, A05105, doi:10.1029/2003JA010358.

Downloaded by UNIV MASSACHUSETTS AMHERST on August 8, 2012 | http://pubs.acs.org
Publication Date: November 16, 2006 | doi: 10.1021/bk-2007-0945.ch015

Chapter 16

Dead Time, Pile-Up, and Counting Statistics

S. Pommé

European Commission, Joint Research Centre, Institute for Reference Materials and Measurements, Retieseweg 111, B–2440 Geel, Belgium

Downloaded by UNIV OF ARIZONA on August 6, 2012 | http://pubs.acs.org
Publication Date: November 16, 2006 | doi: 10.1021/bk-2007-0945.ch016

An overview is presented on recent progress in the field of nuclear counting statistics; theoretical expressions are shown to predict deviations from Poisson statistics due to non-random count loss in the spectrometer set-up. Frequently encountered misconceptions in the literature and in daily practice are uncovered: the unconditional belief in the general validity of Poisson statistics, the neglect of the dependency of counting statistics on the considered fraction of the pulse spectrum, the mix-up between pulse pile-up and extending dead time, the unawareness of the influence of pile-up rejection on the counting statistics in fixed live-time measurements, and also with 'loss-free counting'. Insight is provided into the statistical properties of spectra taken with 'loss-free counting' and 'zero dead time' counting, as well as the 'variance spectrum' provided with the latter. Uncertainty formulas are also presented for more conventional nuclear spectrometry measurements, with different types of count loss.

In Applied Modeling and Computations in Nuclear Science; Semkow, T., et al.;
ACS Symposium Series; American Chemical Society: Washington, DC, 2006.

Downloaded by UNIV OF ARIZONA on August 6, 2012 | http://pubs.acs.org
Publication Date: November 16, 2006 | doi: 10.1021/bk-2007-0945.ch016

Radioactivity measurements are usually based on the counting of individual interactions of elementary particles with the sensitive part of a detector. The counting of events is therefore a basic operation, which certainly deserves the scientific attention it has already received in the past (see, *e.g.*, Refs. (*1-22*)). In particular, the problem of count loss is of vital importance in any type of precision work. This is certainly the case with reference measurements, which should be characterised by a great accuracy and precision of the measured value and full statistical control of the experimental uncertainty.

In the field of nuclear counting, reference measurements can reach high levels of accuracy, far below the 1 % level. At low and moderate count rates, the statistical uncertainty is readily available by taking the square root of the number of measured events, as follows conveniently from Poisson statistics. However, when the count rate is very high, pulse loss in the counting set-up does not only lower the observed event rate, but also influences the statistical behaviour of the accepted counts. Therefore, at high count rates, major interventions are required to reproduce the exact incoming event rate and to regain statistical control (see, *e.g.*, (*1*,*14*,*16*,*22*) and references therein).

Throughout recent research efforts to bring nuclear measurements under statistical control, insight was gained into the basics of nuclear counting statistics and, in particular, considerable progress was achieved on the uncertainty associated with the number of counts obtained by spectrometry (*11-22*). New theoretical expressions were developed to predict deviations from the Poisson statistics due to non-random count loss in the spectrometer set-up, as former theoretical models did not rigorously apply to high-rate spectrometry.

Frequently encountered misconceptions in the literature and in daily practice are the unconditional belief in the general validity of the Poisson statistics, the neglect of the dependency of counting statistics on the fraction of the pulse spectrum represented by the considered region of interest, the confusing mix-up between pulse pile-up and extending dead time, unawareness of the influence of pile-up rejection on the counting statistics in fixed live-time measurements and also with loss-free counting. Nevertheless, all these aspects can and have been recently brought under statistical control, as described in the following sections.

Types of Count Loss

In the literature it is often claimed that there are two basic types of dead time, 'extending' and 'non-extending', and that all nuclear counters can be described by one of these two types, or by a combination of them (see, *e.g.*, (*23*,*24*)). However, this does not account for the statistical effects caused by pulse pile-up and pile-up rejection, which is the main loss mechanism in contemporary spectrometry chains (*11*,*13*,*20*).

'Non-extending' means that the dead-time period is not prolonged by a new pulse arriving during the dead-time period. The dead time created by an analog-to-digital converter (ADC) is a typical example. For the so-called 'paralysable' systems, with dead time of the 'extending' type, each incoming event prolongs the system dead time by an amount τ. A clear distinction should be made between count loss of the type '*pile-up*' and '*extending dead time*'. Pulse pile-up occurs when a new pulse from the preamplifier is fed through the shaping amplifier before the ADC has had the chance to properly finish processing the previous pulse. In such cases, an amplifier-ADC combination with pile-up rejection has the ability to inhibit the ADC from processing the composite pulses. Contrary to the case of ordinary dead-time effects, also the 'first' incoming pulse is lost for spectrometric analysis, either by a built-in electronic pile-up rejection system or by the pulse count being assigned to another spectrum channel. Therefore we are facing at least three different types of pulse loss distortions of a Poisson process, each requiring a particular statistical treatment.

Downloaded by UNIV OF ARIZONA on August 6, 2012 | http://pubs.acs.org
Publication Date: November 16, 2006 | doi: 10.1021/bk-2007-0945.ch016

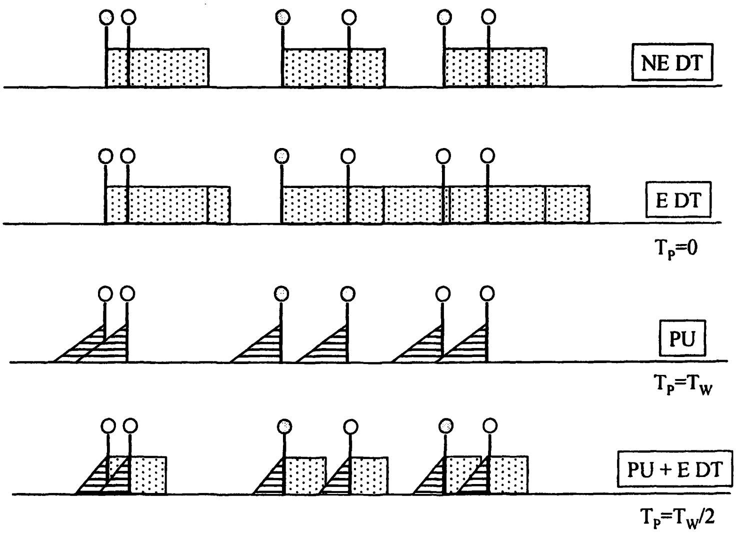

Figure 1. Event train passing through counters having different loss mechanisms; NE DT = non-extending dead time, E DT = extending dead time, and PU = pile-up rejection (14). The case of combined PU and E DT corresponds to a spectrometer with Gaussian pulse shaping and fast ADC with negligible dead time. The empty circles correspond to invalid events. T_P and T_W are leading edge and total pulse width, respectively (see text).

In Fig. 1, an impression is given on how these different loss mechanisms interact with the same pulse train. The circles represent the position of detector pulses, at the point at which the peak is detected. The triangles in front of the peaks represent their leading edge, *i.e.*, the time between pulse arrival and peak detection. The rectangle behind the peak represents dead time; it can correspond to the trailing edge of the pulse, equivalent to extending dead time, or to the non-extending dead time of an analog-to-digital converter. Even though the same effective dead time ($\tau = T_P + T_W$) was considered for all types of count loss, different events are counted as valid or invalid.

Time Interval Distributions

To understand counting statistics, *i.e.*, the probability for observing a given number of events, one should look upon the counting process as a sequence of events developing in time, where loss mechanisms directly affect the statistical distributions of the interval times between successive events. These time intervals are independent, and form a renewal process (*1*). Multiple intervals, *i.e.*, the waiting time for k subsequent events, are obtained from a k-fold convolution of the single time-interval density distributions. The transition from interval densities to counting probabilities can be done via differentiation of the corresponding Laplace transform (see, *e.g.*, Refs. (*5*,*13*,*16*)). Experimental as well as theoretical work for extending or non-extending dead time and their combinations can be found in Refs. (*1*,*5*,*8*,*24*). More recent work (*11*,*13*,*16*) includes the effects of pile-up and limited fractions of spectra. Besides counting statistics, also the throughput factor follows from such analysis, being $e^{-\rho\tau}$ ($\tau = T_P + T_W$ = sum of leading edge and full width of the pulse) in the case of pile-up and/or extending dead time and $(1 + \rho\tau)^{-1}$ in the case of non-extending dead time.

Some insight into the statistics of counting is gained by studying the time-interval distribution between consecutive events. In Fig. 2, the time distortion of a Poisson process is shown for 'non-extending dead time', 'extending dead time' and 'pile-up' at an incoming count rate of $\rho = 1/\tau$. Non-extending dead time preserves the exponential shape of the interval distribution, except that events falling within the dead time τ are eliminated. Extending dead time bends the slope of the interval distribution also after the dead-time period τ, which is most clearly visible in the time interval $[\tau, 2\tau]$. Pile-up has yet another effect on the time-interval distribution and does not preserve the slope of the original Poisson process.

Figure 2 also shows the time-interval distributions for events belonging to an arbitrary 30 % fraction of the total spectrum. Due to the lower probability of occurrence, the time-interval distribution is flatter than for the full spectrum. The time distortions - mainly noticeable at low interval times - are therefore of less influence, which is a sign of convergence towards Poisson statistics. Other points of interest are the altered shape of the distortions, which is most peculiar in the

Downloaded by UNIV OF ARIZONA on August 6, 2012 | http://pubs.acs.org
Publication Date: November 16, 2006 | doi: 10.1021/bk-2007-0945.ch016

Downloaded by UNIV OF ARIZONA on August 6, 2012 | http://pubs.acs.org
Publication Date: November 16, 2006 | doi: 10.1021/bk-2007-0945.ch016

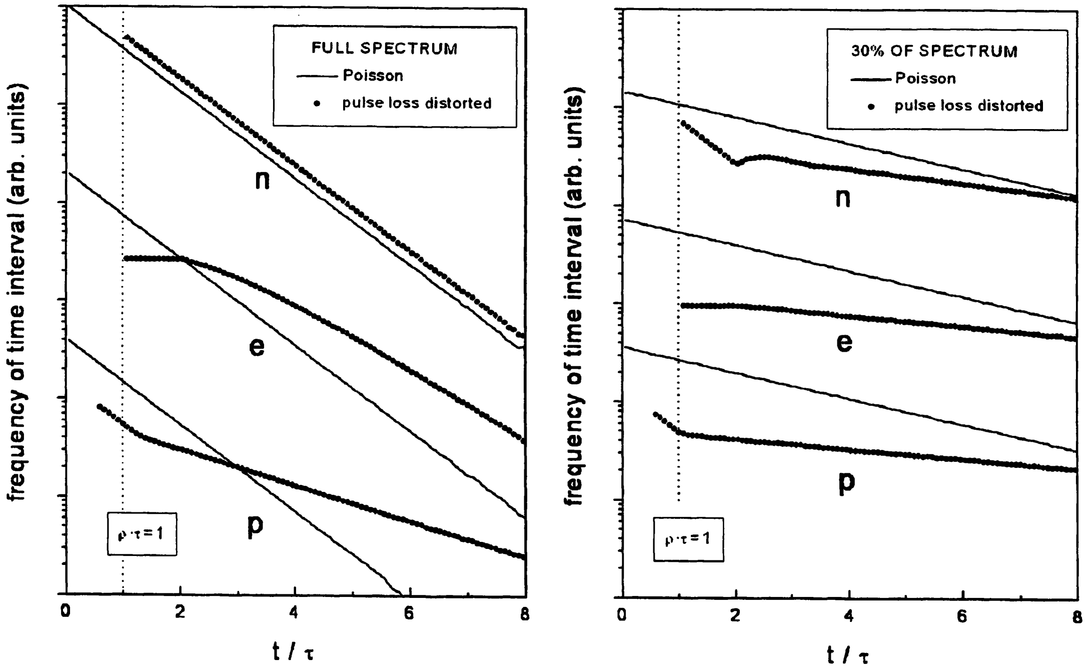

Figure 2. Typical time-interval distribution of consecutive events, when counted at different regimes of event loss; non-extending dead time (n), extending dead time (e) and pile-up (p); (left) for all incoming pulses, (right) for an arbitrary 30 % fraction of the pulses.

case of non-extending dead time (*16*), and the non-conservation of the exponential shape of the interval distribution.

Counting in Live-Time Mode

A live-time clock compensates for dead-time losses by extending the measurement time. It makes the counter behave like a system with zero dead time: dividing the measured counts by the elapsed live-time directly provides an unbiased estimate of the true input rate of a *stationary* counting process and the standard deviation is simply obtained from the square root of the number of counts.

However, contemporary spectrometers applying pile-up rejection are an exception to this rule; they rely on improved live-time clocks that compensate the additional count loss during the leading edge of the pulse, *e.g.*, by backward counting with the Gedcke-Hale method (*23*). One has to realize that the associated extension of the system busy time is artificial and does not prevent valid pulses to be counted meanwhile. Consequently, the count probability distribution for a fixed live time is broadened.

A full probabilistic analysis of count distributions during a fixed live time was published in Ref. (*14*). From that, an approximate correction factor for the statistical uncertainty on the number of counts, N, was derived:

$$\sigma(N) \approx r\sqrt{N}\,, \tag{1}$$

in which

$$r = 1 + \frac{A}{2}\left(\frac{2+A'}{1+A'}\right)f$$
$$A = 1 - e^{-\rho T_P}$$
$$A' = 1 - e^{-f\rho T_P}\,, \tag{2}$$

where ρ is the input rate of the Poisson process, T_P is the characteristic time for pile-up (cf. the leading edge of the pulse), and f is the fraction of the spectrum represented by the considered region of interest (ROI). The validity of Eq. 1 has been confirmed experimentally on an analog (*14*) and a digital (*18*) spectrometer.

For ROIs representing limited fractions of the total count spectrum (f < 100 %), the deviations from Poisson statistics diminish, *e.g.*, for f = 10 % and N = 10,000 a noticeable deviation is achieved only at a count rate of $\rho\tau > 0.7$. Hence, the Poisson statistics is usually a good approximation for high-resolution spectrometry at fixed live time.

Downloaded by UNIV OF ARIZONA on August 6, 2012 | http://pubs.acs.org
Publication Date: November 16, 2006 | doi: 10.1021/bk-2007-0945.ch016

Counting in Real-Time Mode

As a rule, counting with significant non-random count loss (in the time domain) is underdispersed relative to Poisson statistics. However, after proper correction for the count loss, the result is always overdispersed.

The *asymptotic* counting uncertainty (measurement time $t_m \gg$ characteristic dead time τ) for counting with *non-extending dead time* can be calculated from

$$\frac{\sigma(N)}{\sqrt{N}} = \frac{\sqrt{f + (1-f)\,(1+\rho\tau)^2}}{1+\rho\tau}, \tag{3}$$

in which f is the considered fraction of the spectrum. In the limit of extremely small fractions, $f \approx 0$, one readily finds $\sigma(N) = \sqrt{N}$. For the full spectrum, $f = 1$, Eq. 3 reduces to the well-known expression, $(1 + \rho\tau)^{-1}$, from Refs. (*1,5*). An even more general equation can be applied for a part of a count spectrum taken with a Wilkinson ADC (*16,19*):

$$\frac{\sigma(N)}{\sqrt{N}} \approx \frac{\sqrt{f + (1-f)\,(1+\rho<\tau>_{\neq})^2}}{1+\rho<\tau>}, \tag{4}$$

in which $<\tau>_{\neq}$ is the average characteristic dead time for counts outside the considered region of interest. Equation 3 for fixed dead times can be regarded as a special case of Eq. 4, in which $<\tau>=<\tau>_{\neq}$.

The asymptotic counting uncertainty in a counter with *pile-up rejection* (leading pulse edge) and *extending dead time* (trailing pulse edge) equals

$$\frac{\sigma(N)}{\sqrt{N}} = \sqrt{1 + 2f\mathrm{e}^{-\rho T_W}[1-(1+\rho\tau)\mathrm{e}^{-\rho T_P}]}, \tag{5}$$

in which T_W is the full pulse width and T_P that of its leading edge. The equation for *extending dead time* follows as a special case where $T_P = 0$ (and $\tau = T_P + T_W$):

$$\frac{\sigma(N)}{\sqrt{N}} = \sqrt{1 - 2f\rho\tau\mathrm{e}^{-\rho\tau}}\,. \tag{6}$$

In Fig. 3, the standard deviation is shown as a function of the input rate for the three basic types of count loss. The explicit shape for pile-up shows a resemblance with the one for extending dead time, but the deviation from $\sqrt{N}$ is smaller and even becomes positive for $\rho\tau > 2.5$ ($\tau = 2T_P$). Such effect cannot be reproduced by dead time, nor by a generalised dead time as proposed by Albert and Nelson (*25,1,8*). Experimental proof in Fig. 4 shows applicability of Eq. 5 to a digital spectrometer, confirming also the dependence on the spectrum fraction f.

Measurements performed with a real-time clock, for a fixed measurement time t_m, have to be corrected for the non-linearity of the detector throughput to

Downloaded by UNIV OF ARIZONA on August 6, 2012 | http://pubs.acs.org
Publication Date: November 16, 2006 | doi: 10.1021/bk-2007-0945.ch016

obtain the true count rate. The loss correction can either be done by applying the ratio between the measurement real time and the observed system live time, $N_t = N\, T_R/T_L$, or just by relying on the inverse throughput formula, $N_t = X^{-1}(N)$, when the characteristic dead time (= τ) of the counter is known. Both methods yield equally accurate results for non-extending dead time. However, in the case of pulse pile-up and extending dead time, better statistical accuracy can be obtained by using the T_R/T_L -ratio when available.

The variance of the calculated counts, N_t, is obtained by error propagation on the variance of the measured counts, N. In the case of non-extending dead time, the statistical uncertainty on the loss-corrected counting result is represented by (*16,19*)

$$\frac{\sigma(N_t)}{\sqrt{N_t}} = \sqrt{\frac{T_R}{T_L}} = \sqrt{1 + \rho < \tau >} \qquad (7)$$

irrespective of the considered fraction of the count spectrum. Surprisingly, it doesn't only work for fixed-dead-time ADC's, but also for Wilkinson ADC's with a variable characteristic dead time depending on the addressed channel number (*16,19*). The characteristic dead time $<\tau>$ then corresponds to a weighted average for the full spectrum.

To correct for count loss caused by *pulse pile-up* and *extending dead time*, better statistical accuracy can be obtained by using the T_R/T_L-ratio, when available, since this contains additional information on the original count rate compared to the inverse throughput factor. The inversion of the throughput formula, $N = N_t\, e^{-\rho\tau}$, is solved as a special case of Takacs' formula (see Ref. (*8*), applying $\theta = 1$). The uncertainty of the loss-corrected count integral of the full spectrum, $N_t = X^{-1}(N)$, follows then from

$$\sigma^2(N_t) \approx \left(\frac{\partial N}{\partial N_t}\right)^{-2} \sigma^2(N)\,. \qquad (8)$$

Computer simulations show that the relative counting uncertainty gradually diminishes when smaller parts of the spectrum are considered. As a fair approximation, one can apply a linear relationship as a function of the considered fraction ($0 < f < 1$):

$$\frac{\sigma(N_t)}{\sqrt{N_t}} \approx \sqrt{\frac{e^{\rho\tau} + 2[e^{\rho T_P} - (1 + \rho\tau)]}{(1 - \rho\tau)^2}}\, f \;+\; \sqrt{e^{\rho\tau}}\,(1 - f)\,, \qquad (9)$$

in which $\tau = T_P + T_W$, and N_t is calculated from $N_t = X^{-1}(N)$.

Downloaded by UNIV OF ARIZONA on August 6, 2012 | http://pubs.acs.org
Publication Date: November 16, 2006 | doi: 10.1021/bk-2007-0945.ch016

Downloaded by UNIV OF ARIZONA on August 6, 2012 | http://pubs.acs.org
Publication Date: November 16, 2006 | doi: 10.1021/bk-2007-0945.ch016

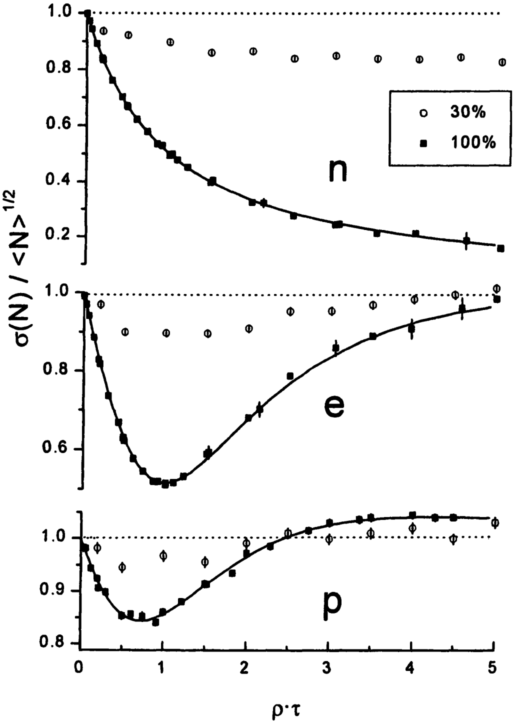

Figure 3. Standard deviation of counting with non-extending dead time (n), extending dead time (e) and pile-up (p). The squares (f=1) and hollow circles (f=0.3) are simulation results and the full lines represent theoretical curves.

Downloaded by UNIV OF ARIZONA on August 6, 2012 | http://pubs.acs.org
Publication Date: November 16, 2006 | doi: 10.1021/bk-2007-0945.ch016

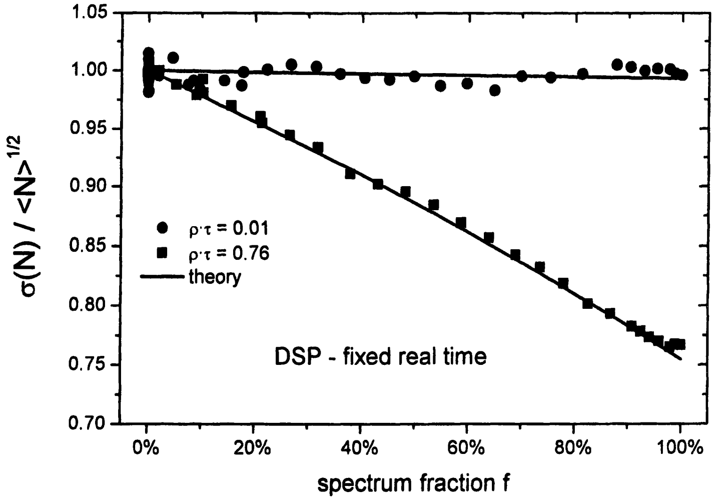

Figure 4. Counting uncertainty as a function of the considered spectrum fraction, for ^{60}*Co γ-ray spectra taken by a digital spectrometer at two different input rates and with a fixed measurement real time (18).*

When applying the T_R/T_L-ratio in the case of extending dead time ($T_P = 0$), one finds that the standard deviation of the loss-corrected number of counts in an arbitrary ROI equals the square root of the inverse throughput factor. However, the variance increases with a factor r (see Eq. 2) when also pile-up comes into play:

$$\frac{\sigma(N_t)}{\sqrt{N_t}} \approx r\sqrt{e^{\rho\tau}} \,. \qquad (10)$$

The uncertainties on the loss-corrected counts, via N_t=X^{-1}(N) and $N_t = N\, T_R/T_L$, are visualised in Fig. 5. The method applying the live-time to real-time ratio is obviously superior, the advantage diminishing for smaller ROIs. The Eqs. 9 and 10 perform adequately for any combination of pile-up followed by extending dead time, as can be observed from a comparison with simulation data in Fig. 5 for T_P varying between 0 and the full pulse width, T_W.

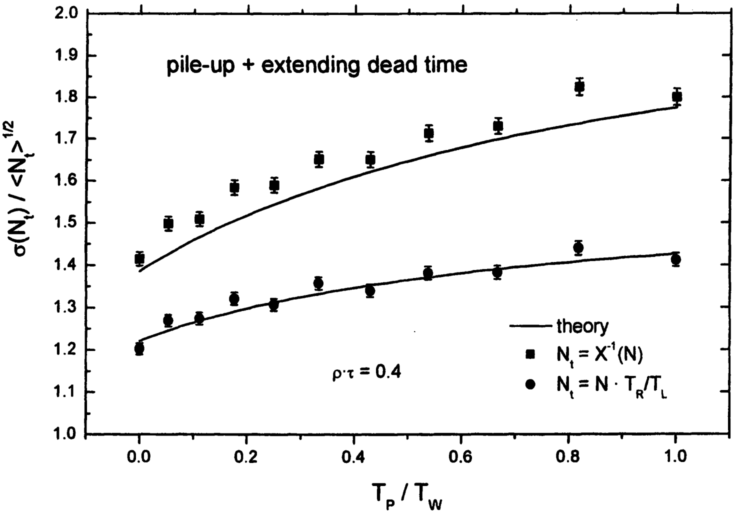

Figure 5. Theoretical (Eqs. 9 and 10) and simulated standard deviation of loss-corrected counts in a spectrometer with a combination of pile-up and extending dead time as a function of the ratio between T_P and T_W, at a fixed normalized input rate of $\rho\tau = 0.4$. (Simulations correspond to $<N_t> = 1000$.) N_t being the count integral of the full spectrum.

'Loss-Free Counting' and 'Zero Dead Time' Counting

'Loss-Free Counting' (LFC) (*26-29,12,22,23*) has found its way to the lab as one of the most powerful tools for correcting rate-related losses in gamma-ray spectrometry. By performing add-n operations to the spectrum instead of add-1, the LFC principle is able to restore the linearity of the spectrometer throughput. 'Zero Dead Time' (ZDT ^{TM}) counting is a comparable technique, also involving the regular addition of virtual counts to the true spectrum, according to a short-term ratio of real time to 'system live time' ($n = T_R/T_L$) (*30,18,20-22*). The LFC method is particularly useful in situations where live-time correction techniques are inadequate, *i.e.*, where count rates vary significantly during the measurement. Typical examples are high-rate counting procedures involving nuclides with half lives that are short compared to the counting time (*e.g.*, in the field of neutron activation analysis) or radioactivity that is physically moving (e.g. real time monitoring of effluents). Moreover, the powerful LFC principle can cope with pile-up (rejection), provided that the duration of the leading edge of the pulse is added to the system busy time.

Downloaded by UNIV OF ARIZONA on August 6, 2012 | http://pubs.acs.org
Publication Date: November 16, 2006 | doi: 10.1021/bk-2007-0945.ch016

The main trade-off is an increase of the count scatter as the clustering of true and artificial events introduce unavoidable deviations from the Poisson conditions. The statistical aspect has been brought under control, by means of the following formula (*14*,*22*):

$$\frac{\sigma(N_{LFC})}{\sqrt{<n>N_{LFC}}}=r\sqrt{1+\left(\frac{\sigma(n)}{<n>}\right)^2}\,, \tag{11}$$

where N_{LFC} is the number of counts in the considered ROI of the LFC (or ZDT) spectrum, corresponding to a fraction f of the total spectrum count integral, $<n>$ is the time-averaged value of the short-term loss-correction factors n pertaining to the ROI; It is a 'weighted' average in the sense that it is taken over every count (true or virtual) in the considered ROI of the ZDT spectrum (*21*,*22*):

$$<n>=\frac{\sum n\cdot n}{\sum n}=\frac{\sum n^2}{N_{LFC}} \tag{12}$$

The variance of the loss-correction factor, $\sigma^2(n)$, can be well predicted from semi-empirical formulas (see also comments in Ref. *22*), in the case of pile-up and extending dead time (*14*):

$$\sigma(n)\approx\sqrt{(n-1)\left(\frac{n+0.45\alpha^{\beta+\Delta}}{1+0.45\alpha^{\beta}}\right)}\,, \tag{13}$$

in which $\Delta=0.6(1-e^{-(n-1)})$, $\beta=-2.6$, $\alpha=\tau/P$, and P is the live-time inspection period in which a new n-value is calculated. In the case of non-extending dead time, a good approximation is (*14*)

$$\sigma(n)\approx\sqrt{\rho\tau-(\rho\tau)^2(1-\alpha)^2} \tag{14}$$

for $\alpha=\tau/P<1$ and $\rho\tau=<n>-1$.

When calculating the statistical counting uncertainty in a certain channel (or ROI) one should refrain from the bad idea of setting $\sigma(n)$ equal to the standard deviation of the 'n'-values within some neighbouring channels, because the time-averaged 'n'-value can (and will) in principle vary from one channel to another due to a different mixture of 'high-rate' and 'low-rate' components.

This uncertainty component, $\sigma(n)$, can be reduced by increasing the time interval, P, in which a new n-value is determined. The correction factor, r, for pile-up (Eq. 2) converges to one, when considering small parts of the spectrum. Consequently, for high resolution spectrometry the variance can be well approximated by

$$\sigma^2(N_{LFC})\approx<n>N_{LFC}=\sum n^2\,. \tag{15}$$

Downloaded by UNIV OF ARIZONA on August 6, 2012 | http://pubs.acs.org
Publication Date: November 16, 2006 | doi: 10.1021/bk-2007-0945.ch016

An important novelty in digital spectrometry is the so-called 'variance' spectrum taken in parallel with the ZDT spectrum (*30*). It consists of the squares of the '*n*'-values registered in the corresponding channels of the ZDT-spectrum. This Σn^2-spectrum was claimed to represent the variance associated with the number of counts, Σn, in the ZDT-corrected spectrum (*30*). From a comparison between Eqs. 11 and 15, it is clear that this is true by approximation, aside from the omission of the two correction factors at the right hand side of Eq. 11.

There is experimental evidence supporting this mathematical interpretation of the Σn^2-spectrum. It has been demonstrated that the variance spectrum taken with a DSPEC^{PLUS}™ digital spectrometer predicts the counting uncertainty well in small parts of γ-ray spectra taken at high, variable as well as fixed, count rates (see Fig. 6) (*20*). This is partly due to the standard deviation $\sigma(n)$ being relatively low, because of the long refreshing period (milliseconds rather than microseconds) for a new correction factor n to be adopted. For larger ROIs, corresponding to a significant fraction of the total spectrum, the Σn^2-spectrum gives an underestimate of the true statistical variation. This can exactly be accounted for by the correction factor *r* (Eq. 2), which corroborates the statement that the Σn^2-spectrum is an approximation of the true variance (*20-22*).

One can conclude that LFC is nearly equally precise as live-time counting techniques at low count rates ($\rho\tau < 0.1$), and compensates for a slightly less favourable statistical accuracy at high count rates (cf. $\sigma(n)$), by the ability to perform measurements and count loss corrections in real time. Hence, it is ideally suited to deal with short-lived isotopes and varying input rates.

Overdispersion in Counting Statistics

The statistics of nuclear counting involves at least a two-step process: radioactive decay and detection. Thus the overall statistics combine that from the original radiation with that of the measurement. From the ample evidence presented in this chapter, it is clear that instrumental dead-time effects introduce violations of the Poisson statistics. The number of counted events is mostly underdispersed, but becomes overdispersed after proper loss-correction.

Overdispersion in counting statistics can also be caused by other instrumental effects, like fluctuation of counting efficiency, measurement time, coincidence timing, etc. When decay of a short-lived radionuclide is followed in equal time intervals, neither the assumptions for binomial nor Poisson distributions are satisfied and the resulting non-standard distribution is overdispersed (*7,10*). Clearly such statistical properties should be taken into account in the estimations of variances, confidence intervals, detection limits, as well as in distinguishing between source and background, since they are traditionally based on the likelihood functions derived from the classical distributions, such as binomial, Poisson, and Gaussian.

Downloaded by UNIV OF ARIZONA on August 6, 2012 | http://pubs.acs.org
Publication Date: November 16, 2006 | doi: 10.1021/bk-2007-0945.ch016

Downloaded by UNIV OF ARIZONA on August 6, 2012 | http://pubs.acs.org
Publication Date: November 16, 2006 | doi: 10.1021/bk-2007-0945.ch016

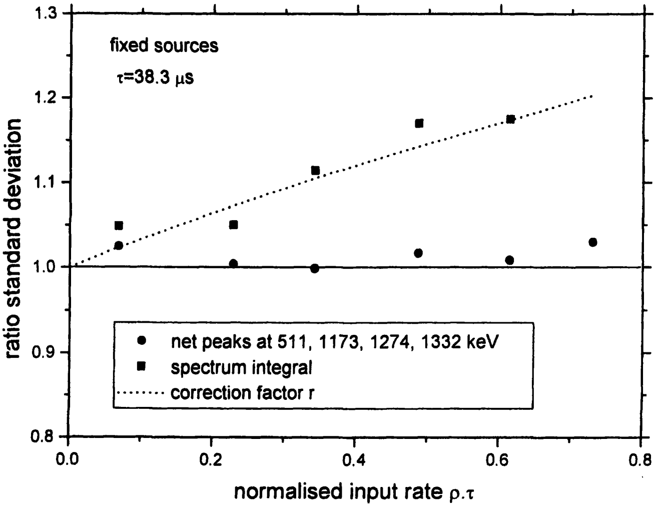

Figure 6. Ratio of the true (measured) statistical counting uncertainty to the value predicted from the variance spectrum of the DSPEC$^{PLUS\ TM}$ as a function of the normalized input rate (20). The circles refer to the standard deviation of the number of counts in a limited part of the ZDT loss-corrected spectrum (the ^{57}Co, ^{22}Na and ^{60}Co γ-ray peaks at 511, 1173, 1274, and 1332 keV) and the squares to the count integral of the entire spectrum. The dashed line shows the correction factor for overdispersion due to pile-up rejection (Eq. 2).

The principle of overdispersion in counting statistics can be treated in a more generalised manner, looking upon counting as a multi-step process, each characterised by its own probability parameter. The central question is then how the combined statistics vary due to fluctuating probability parameters and whether they can be expressed by the common distributions. A formal treatment of this problem, together with many references, can be found in Refs. (*31,32*). The outcome of such fundamental research can contribute to a better understanding and control of sources of uncertainty in nuclear counting.

Conclusions

A theoretical and experimental study of the time-interval distribution of subsequently counted events clearly shows that pile-up (rejection) cannot be treated as equivalent to extending dead time (*11,13*). A formula is presented for the standard deviation of counting with pile-up rejection (*14*). It is also shown that the counting statistics vary as a function of the considered fraction of the spectrum; appropriate adjustments are made to the uncertainty formula for counters with extending dead time (*13*) and non-extending dead time (*16*). In the latter case, also the possibility of a variable characteristic dead time is considered; this yields a practical formula for the statistical uncertainty of counts in spectra obtained with a "slow" Wilkinson ADC (*16,19*).

The counting statistics also depend on whether the measurement is performed in real time or in system live time. In the latter case, Poisson statistics are applicable, except for counters with pile-up rejection; a relative increase of the counting uncertainty is predicted and quantified theoretically (*14*). Such effect is indeed observed experimentally on an analog (*14*) and a digital (*18*) spectrometer. 'Loss-free counting' and 'zero dead time' counting are adequate tools for count loss correction (*12,20*), even at variable rates. Their counting uncertainty is under statistical control (*14,22*) and the 'sum-of-squares' spectrum has been shown to give a good approximation of the associated 'variance' (*20-22*).

References

1. *Particle Counting in Radioactivity Measurements*; ICRU Report 52, International Commission on Radiation Units and Measurements: Bethesda, MD, 1994.
2. Libert, J. *Nucl. Instr. Meth.* **1976**, *136*, 563-568.
3. Libert, J. *Nucl. Instr. Meth.* **1988**, *A265*, 537-540.
4. Libert, J. *Nucl. Instr. Meth.* **1989**, *A274*, 319-323.

Downloaded by UNIV OF ARIZONA on August 6, 2012 | http://pubs.acs.org
Publication Date: November 16, 2006 | doi: 10.1021/bk-2007-0945.ch016

5. Müller, J. W. *Nucl. Instr. Meth.* **1973**, *112*, 47-57.
6. Müller, J. W. *Nucl. Instr. Meth.* **1974**, *117*, 401-404.
7. Müller, J. W. *J. Radioanal. Nucl. Chem.* **1981**, *61*, 345-359.
8. Müller, J. W. *Nucl. Instr. Meth.* **1991**, *A301*, 543-551.
9. Jordan, D. R.; Mcbeth, G. W. *Nucl. Instr. Meth.* **1978**, *155*, 557-562.
10. Salma, I.; Zemplén-Papp, É. *Nucl. Instr. Meth.* **1992**, *A312*, 591-597.
11. Pommé, S. *Appl. Radiat. Isot.* **1998**, *49*, 1213-1218.
12. Pommé, S.; Alzetta, J-P.; Uyttenhove, J.; Denecke, B.; Arana, G.; Robouch, P. *Nucl. Instr. Meth.* **1999**, *A422*, 388-394.
13. Pommé, S.; Denecke, B.; Alzetta, J-P. *Nucl. Instr. Meth.* **1999**, *A426*, 564-582.
14. Pommé, S. *Nucl. Instr. Meth.* **1999**, *A432*, 456-470.
15. Pommé, S. *Biol. Trace Element Res.* **1999**, *71-72*, 415-422.
16. Pommé, S. *Nucl. Instr. Meth.* **1999**, *A437*, 481-489.
17. Pommé, S.; Robouch, P.; Arana, G.; Eguskiza, M.; Maguregui, M. I. *J. Rad. Nucl. Chem.* **2000**, *244*, 501-506.
18. Pommé, S.; Kennedy, G. *Appl. Radiat. Isot.* **2000**, *52*, 377-380.
19. Pommé, S.; Uyttenhove, J. *J. Radioanal. Nucl. Chem.* **2001**, *248*, 263-266.
20. Pommé, S. *Nucl. Instr. Meth.* **2001**, *A474*, 245-252.
21. Pommé, S. *Nucl. Instr. Meth.* **2002**, *A482*, 565-566.
22. Pommé, S. *J. Radioanal. Nucl. Chem.* **2003**, *257*, 463-466.
23. Gilmore, G.; Hemingway, J. *Practical Gamma-Ray Spectrometry*; John Wiley & Sons: Chichester, 1995.
24. Jenkins, R.; Gould, R. W.; Gedcke, D. *Quantitative X-ray Spectrometry*; 2nd Edition; Marcel Dekker, Inc.: New York, NY, 1995.
25. Albert, G. E.; Nelson, L. *Ann. Math. Stat.* **1953**, *24*, 9-22.
26. Harms, J. *Nucl. Instr. Meth.* **1967**, *53*, 192.
27. Westphal, G. P. *Nucl. Instr. Meth.* **1979**, *163*, 189-196.
28. Westphal, G. P. *J. Radioanal. Chem.* **1982**, *70*, 387-410.
29. Westphal, G. P. *Nucl. Instr. Meth.* **1985**, *B10/11*, 1047-1050.
30. Upp, D. L.; Keyser, R. M.; Gedcke, D. A.; Twomey, T. R.; Bingham, R. D. *J. Radioanal. Nucl. Chem.* **2001**, *248*, 377-383.
31. Semkow, T. M. *Appl. Radiat. Isot.* **1999**, *51*, 565-579.
32. Semkow, T. M. *Health Phys.* **2002**, *83*, 485-496.

Downloaded by UNIV OF ARIZONA on August 6, 2012 | http://pubs.acs.org
Publication Date: November 16, 2006 | doi: 10.1021/bk-2007-0945.ch016

Downloaded by CORNELL UNIV on August 8, 2012 | http://pubs.acs.org
Publication Date: November 16, 2006 | doi: 10.1021/bk-2007-0945.ch017

Chapter 17

DCC_SIM: A Simulation Routine for the Validation of 4π β–γ Digital Coincidence Counting Software

J. D. Keightley

European Commission, Joint Research Centre, Institute for Reference Materials and Measurements, Retieseweg 111, B–2440 Geel, Belgium

A 32 bit Dynamic Link Library (DCC_SIM.dll) developed to simulate raw data from a simple radionuclide standardization using 4π β–γ Coincidence Counting with digital data acquisition techniques is introduced. This software is to be used in an ongoing project of the Radionuclide Metrology Techniques Working Group of the International Committee for Radionuclide Metrology (ICRM), and will facilitate the comparison and validation of data analysis routines used in the processing of various digitally acquired data sets pertaining to coincidence counting (and its variants).

1. Digital Coincidence Counting

The concept of Digital Coincidence Counting (DCC) for the standardization of radioisotopes by the 4π β–γ coincidence method was introduced by Buckman and Ius (*1*), and an initial attempt to realize such a system was reported by Buckman *et al.* (*2*). These promising developments resulted in a dedicated PC-based DCC data capture hardware system being developed as a collaboration between NPL (United Kingdom) and ANSTO (Australia), which has been

In Applied Modeling and Computations in Nuclear Science; Semkow, T., et al.;
ACS Symposium Series; American Chemical Society: Washington, DC, 2006.

described elsewhere (*3*,*4*). It incorporates two independent 12-bit flash ADCs, utilising a common 20 MHz sampling clock. Each voltage pulse is stored in list mode in the DCC data binary format (*5*).

Voltage samples above a user defined threshold along with 40-bit time stamps representing the threshold crossing times (with 50 ns resolution) from both channels are interleaved in a single data file, which is streamed to disk in real time. The original pulse trains from each channel may be readily reconstructed from this data format.

The benefits of such a system are obvious: it allows the replacement of a series of expensive dedicated analogue electronic modules required to perform coincidence counting (single channel analyzers, dead time units, linear gates, time-to-amplitude converters, delay units, coincidence mixers and multichannel analysers) by a single digital data acquisition card. The equipment set-up times are minimal and it reduces the need for highly qualified staff to perform the data acquisition. The ability to replay the collected data through the suite of dedicated analysis software routines, whilst altering the counting parameters (number and location of gamma gates, dead times, coincidence resolving times, delays, *etc.*), without the need for data re-collection, is highly desirable.

The DCC data files are analyzed off-line by a suite of software routines which implement the "Computer Discrimination" method of 4π β–γ coincidence counting for radionuclide standardization (*6*,*7*). This approach facilitates the simultaneous determination of a series of beta detector count rates over a range of measured beta detector efficiencies from a single source measurement, and the extrapolation of such data to unit beta efficiency yields an estimate of the source activity. A brief summary of the major calculations performed by the software follows:

- Impose specified non-extendable dead times to all events in the beta and gamma channels.
- Impose specified gamma window(s).
- Construct the corrected total beta spectrum, and (for each gamma window), the corrected coincident beta spectrum and gamma count (N_γ). Corrections are made for dead times, coincidence resolving times, decay and background.
- For a series of specified discrimination levels (z) operating on the beta and coincident beta spectra, calculate the sum of the contents of spectral channels surviving the imposition of this discriminator: $N_\beta(z)$ and $N_c(z)$.
- From each gamma window, form an estimate the beta counter efficiency, $\varepsilon_\beta(z) = N_c(z)/N_\gamma$.

Downloaded by CORNELL UNIV on August 8, 2012 | http://pubs.acs.org
Publication Date: November 16, 2006 | doi: 10.1021/bk-2007-0945.ch017

- Calculate the variance for the data points associated with each discrimination level, as well as the covariances between each pair of levels, generating a full covariance matrix.
- Perform a fit (taking into account the highly correlated nature of the resulting efficiency curves) and extrapolate the efficiency curve to unit beta counter efficiency, (or efficiencies if more than one gamma window is selected) yielding an estimate of the source activity.

In the rest of this report, we consider only the case of a single gamma-window encompassing all available gamma channels. A discussion on the degree of correlation between the data points (*6*) and a suggested data fitting routine is beyond the scope of this report.

The DCC system is unique in its ability to digitise the entire pulse shapes following the operation of both shaping amplifiers. The system itself is "live" at all times, but only those events which exceed the threshold are recorded. At present, other systems used in this field (*8-13*) record only pulse times and pulse heights, and actually impose some dead time in data collection process.

A software package has been developed by the author (under the auspices of the ICRM Radionuclides Techniques Working Group) to convert the DCC data files into a series of data formats used by other National Metrology Institutes using similar systems for radionuclide standardisation purposes. A series of comparisons between the associated analysis software routines is an ongoing project of the Working Group.

All of these digital systems are limited in the count rates that can actually be digitised (typically relating to a source activity of less than 30 kBq), due to the high data throughput rates. In order to test fully the behaviour of each software analysis system, a data simulation model has been developed to mimic the operation of the DCC data collection hardware at higher count rates than are presently achievable.

Downloaded by CORNELL UNIV on August 8, 2012 | http://pubs.acs.org
Publication Date: November 16, 2006 | doi: 10.1021/bk-2007-0945.ch017

2. The Simulation Model

The simulation software was written in Microsoft Visual C++ as a 32-bit dynamic link library ("DCC_SIM.dll") containing the exported function "dcc_sim( )". Full details of the parameter list and calling conventions are given elsewhere (*14*). The simulation is not designed to mimic fully the decay of a radionuclide with a complex decay-scheme, nor the detection processes in each detector; rather it yields a means of validating the digital coincidence counting analysis software routines currently under development by the author. It is useful to define the following subset of the input parameters:

N_0	The total number of decays to simulate.
A_0	The activity of the simulated source (s^{-1}).
T_{ADC}	Interval between ADC samples (or ADC clock ticks).
$[V_{\beta(min)}, V_{\beta(max)}]$	Interval of simulated pulse heights for β detector.
$[V_{\gamma(min)}, V_{\gamma(max)}]$	Interval of simulated pulse heights for γ detector.
$flag_\beta$	0 : rectangular β spectrum. 1 : triangular β spectrum (most at low energy).
$flag_\gamma$	0 : rectangular γ spectrum. 1 : triangular γ spectrum (most at high energy).
P_{ce}	Probability that a conversion electron is emitted.
e_β, $e_{\beta\gamma}$, $e_{\beta ce}$	Beta detector efficiency for beta particles, gamma rays and conversion electrons.
r_1	Defines the range of beta spectral channels for gamma rays detected in the beta counter. They are triangularly distributed (most at high energy) on the interval: $[V_{\beta(min)} + r_1 (V_{\beta(max)} - V_{\beta(min)}), V_{\beta(max)}]$. In this report we only consider the case ($r_1 = 0$).
r_2	Defines the beta spectral channel for monoenergetic conversion electrons detected in the beta counter: $[V_{\beta(min)} + r_2 (V_{\beta(max)} - V_{\beta(min)})]$. In this report we only consider the case ($r_2 = 1$) so that all conversion electrons appear in channel $V_{\beta(max)}$.
e_γ	Gamma detector efficiency for gamma rays.
j_β, j_γ	Random time jitter between decay/registration times.
δ_β, δ_γ	Constant delay between decay/registration times.
W_β, W_γ, τ_p, n	Pulse widths, pulse peak time ratio across these widths and the pulse shaping parameter ($n > 1$).

A constant random decay rate is used to assign the exponentially distributed intervals between successive nuclear disintegrations, and the time of a particular disintegration is constructed from the sum of all previous intervals. The times associated to detected events are modified by the addition of any specified random time-jitter (j_β or j_γ) and/or a constant delay (δ_β or δ_γ). A single beta decay branch is simulated where each nuclear disintegration yields a beta–particle (with unit probability), followed by the prompt emission of either a gamma-ray with probability ($1 - P_{ce}$) or a conversion electron (c.e.) with probability P_{ce}. The fate of these particles in relation to the beta and gamma detectors are determined from the input detector efficiency parameters via the use of a uniform random number generator routine (*15*). Appropriate transformations of uniform random variates are used to determine the pulse

Downloaded by CORNELL UNIV on August 8, 2012 | http://pubs.acs.org
Publication Date: November 16, 2006 | doi: 10.1021/bk-2007-0945.ch017

heights (V_{out}) contributing to the beta and gamma spectral shapes, which are simply represented by rectangular or triangular distributions.

The model assigns zero probability for a single gamma-ray to be recorded in both beta and gamma channels, and subsequently the probability of detecting additional coincidences due to a Compton scattered gamma ray interacting in both detectors is also zero. This may be considered as being akin to only registering gamma pulses that lie within the photopeak. Zero detection probability is assigned for the detection of conversion electrons or beta-particles in the gamma detector, assuming the presence of an inhibitive entrance window. The totals of each type of radiation generating a response in each detector is given in Table I.

Table I. Expected Totals of Radiation Types Interacting in Each Detector

	Type of Radiation Emitted		
	β	γ	*c.e.*
Beta Detector	$N_0 e_\beta$	$N_0\left(1-P_{ce}\right)e_{\beta\gamma}$	$N_0 P_{ce} e_{\beta ce}$
Gamma Detector	0	$N_0\left(1-P_{ce}\right)e_\gamma\left(1-e_{\beta\gamma}\right)$	0

However, if the beta detector registers both a beta particle and its associated gamma-ray or conversion electron, the overall response is a simple summation of the simulated pulse heights, and only one event is recorded. The expected *total* number of counts from the beta, gamma and coincidence channels respectively are then given by:

$$\left.\begin{aligned} \hat{N}_\beta &= N_0\left[e_\beta+\left(1-e_\beta\right)P_{\beta\gamma}\right], \\ \hat{N}_\gamma &= N_0\left[e_\gamma\left(1-P_{ce}\right)\left(1-e_{\beta\gamma}\right)\right], \\ \hat{N}_c &= N_0\left[e_\beta e_\gamma\left(1-P_{ce}\right)\left(1-e_{\beta\gamma}\right)\right], \end{aligned}\right| \qquad (1)$$

where $P_{\beta\gamma} = (1 - P_{ce})\, e_{\beta\gamma} + P_{ce}\, e_{\beta ce}$ is probability of detecting either a gamma ray or a conversion electron in the beta detector.

2.1. Pulse Shapes

To assign somewhat realistic pulse shapes to registered events, the simulated output voltages at a time t (in ADC clock "ticks") after the start time of the registered event are given by:

Downloaded by CORNELL UNIV on August 8, 2012 | http://pubs.acs.org
Publication Date: November 16, 2006 | doi: 10.1021/bk-2007-0945.ch017

$$V_{out}(t) = V_{out}\left(\frac{t}{t_p}e^{\left(1-\frac{t}{t_p}\right)}\right)^n , \qquad (2)$$

where t_p represents the peaking time of the pulse and n represents a shaping parameter ($n \geq 1$). The justification of the use of such pulse shapes based on a simplified model of a nucleonic amplifier system is given elsewhere (*14*) and examples of the simulated pulse shapes for various values of shaping parameter n are given in Fig. 1a.

The fact that the simulated pulses exhibit finite widths and exponentially distributed inter-arrival times leads to the possibility of pulse pile-up occurring between responses due to different parent decays. The model keeps a record of all recorded pulse start times and pulse-shapes from each channel, performs a

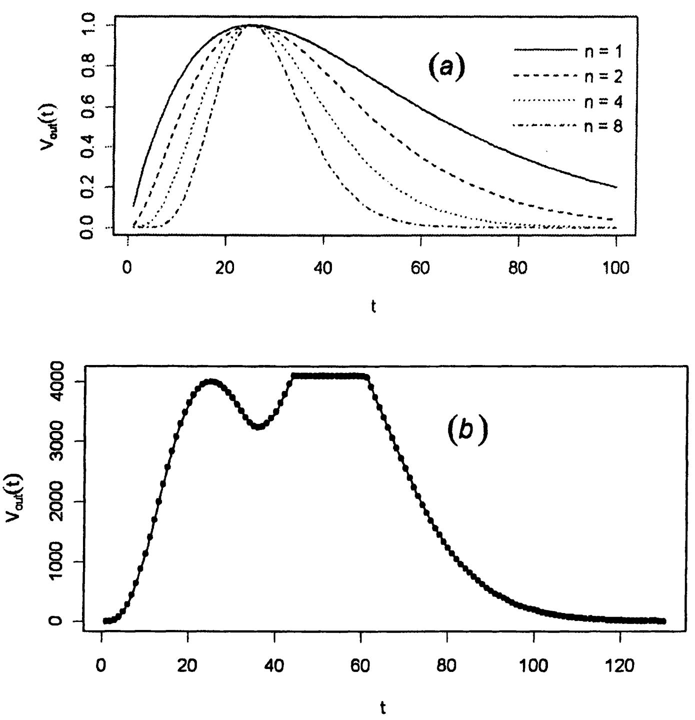

Figure 1. (a) Normalised pulse shapes for various shape parameter n. (W_β = 100 ADC clock ticks; τ_p = 0.25). (b) Simulated pulse pile-up with clipping to 12 bits.

Downloaded by CORNELL UNIV on August 8, 2012 | http://pubs.acs.org
Publication Date: November 16, 2006 | doi: 10.1021/bk-2007-0945.ch017

summation of the responses where appropriate and “extends” the pulses accordingly. In order to mimic the DCC data acquisition hardware, which utilises 12-bit flash ADCs, those voltage data points above ADC channel 4095 are clipped to this maximum value as shown in Fig. 1b.

2.2. Pulse Height Spectra

The model yields a total of four possible combinations of beta and coincident-beta spectral shapes (Fig. 2).

3. Predictions for the Model

Ignoring the obvious distortions to the beta spectral shapes due to pile-up between pulses originating from separate disintegrations, the behaviour of the efficiency-extrapolation curves may be predicted by considering the total-beta and coincident-beta spectra detailed in Fig. 2. The events surviving the impostion of a varying discriminator level at beta channel z, yield a series of values of $N_\beta(z)$ and $N_c(z)$, and thus yields the series of estimates of the beta channel efficiency ($e_\beta(z) = N_c(z)/N_\gamma$) required to generate the efficiency-extrapolation curves. For simplicity, consider the discriminator to operate on a transformed range of channels $[0, N]$, where $z = 0$ corresponds to channel $V_{\beta(min)}$ and $z = N$ to channel $(V_{\beta(max)} - V_{\beta(min)})$.

The proportions of each component surviving the discriminator (referred to as the survival functions $S_\beta(z)$, $S_\gamma(z)$, $S_{ce}(z)$ and $S_{\beta\gamma}(z)$) are listed in Table II. These are readily calculated by assigning to each component the appropriate probability density function (pdf) and calculating the associated cumulative density function (cdf). The survival function is simply the complement to the cdf, *i.e.*, (1 – cdf).

The survival functions $S_\beta(z)$ and $S_\gamma(z)$ are dependent only on the shapes of the simulated beta and gamma spectra, with pdfs $f_\beta(z)$ and $f_\gamma(z)$. For example, consider the case of a triangular beta distribution :

$$S_\beta(z) = 1 - \int_0^z \left(\frac{2(N-z)}{N^2} \right) dz = \frac{(N-z)^2}{N^2}. \qquad (3)$$

$S_{\beta\gamma}(z)$ is dependent on the convolution of the appropriate beta and gamma spectral distributions. These convolutions (denoted by *) are readily calculated by the use of integral transforms, recalling that the convolution of two

Downloaded by CORNELL UNIV on August 8, 2012 | http://pubs.acs.org
Publication Date: November 16, 2006 | doi: 10.1021/bk-2007-0945.ch017

Downloaded by CORNELL UNIV on August 8, 2012 | http://pubs.acs.org
Publication Date: November 16, 2006 | doi: 10.1021/bk-2007-0945.ch017

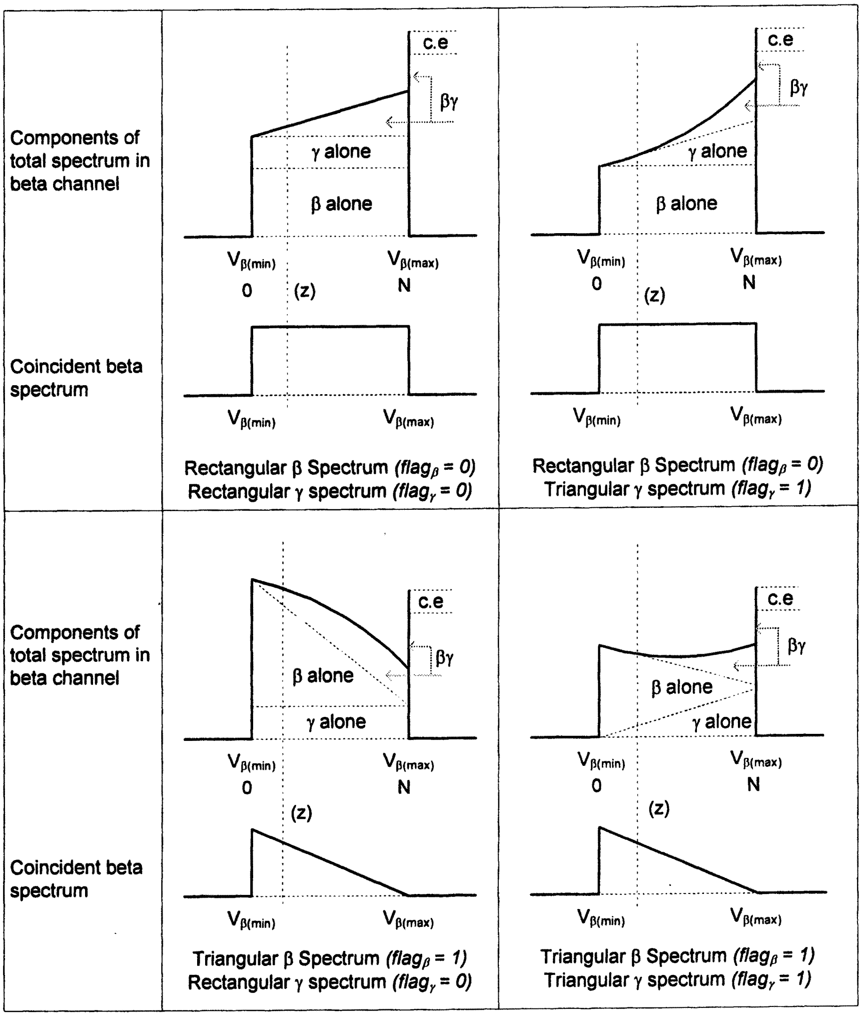
Components of total spectrum in beta channel
Coincident beta spectrum
Components of total spectrum in beta channel
Coincident beta spectrum
c.e
βγ
γ alone
β alone
$V_{\beta(min)}$
$V_{\beta(max)}$
0
(z)
N
Rectangular β Spectrum ($flag_\beta = 0$)
Rectangular γ spectrum ($flag_\gamma = 0$)
Rectangular β Spectrum ($flag_\beta = 0$)
Triangular γ spectrum ($flag_\gamma = 1$)
Triangular β Spectrum ($flag_\beta = 1$)
Rectangular γ spectrum ($flag_\gamma = 0$)
Triangular β Spectrum ($flag_\beta = 1$)
Triangular γ spectrum ($flag_\gamma = 1$)

Figure 2. Components of the total- beta and coincident-beta spectra. The term "βγ" refers to the case where both a β- particle and the γ-ray stemming from the same decay are recorded and "pile-up". All c.e. events are in the maximum channel.

distributions is given by the inverse Laplace transform (L^{-1}) of the product of the Laplace transforms of the component distributions, *i.e.*,

$$f_\beta(z) * f_\gamma(z) = L^{-1}\left(L\left(f_\beta(z)\right).L\left(f_\gamma(z)\right)\right). \tag{4}$$

As a simple example, consider the convolution of the two rectangular spectral distributions, $f_\beta(z) = f_\gamma(z) = 1/N$, both on the interval $[0, N]$:

$$f_\beta(z) * f_\gamma(z) = L^{-1}\left(\left(1/sN\right)^2\right) = z/N^2 . \tag{5}$$

The survival function is then simply:

$$S_{\beta\gamma}(z) \quad = 1 - \int_0^z \left(z/N^2\right)dz = 1 - z^2/\left(2N^2\right). \tag{6}$$

$S_{ce}(z)$ is unity in all cases, as all simulated conversion electrons are situated in the maximum available beta channel.

Table II. Survival Functions for Beta Spectral Components following the Imposition of a Discriminator at Channel *z*

			Gamma Spectral Distribution [0,N]	
			Rectangular (flag$_\gamma$ = 0) $f_\gamma(z) = \frac{1}{N}$	*Triangular (flag$_\gamma$ = 1)* $f_\gamma(z) = \frac{2z}{N^2}$
Beta Spectral Distribution [0,N]	*Rectangular (flag$_\beta$ = 0)* $f_\beta(z) = \frac{1}{N}$	$S_\beta(z)$	$1 - z/N$	$1 - z/N$
		$S_\gamma(z)$	$1 - z/N$	$1 - (z/N)^2$
		$S_{\beta\gamma}(z)$	$1 - z^2/(2N^2)$	$1 - z^3/(3N^3)$
		$S_{ce}(z)$	1	1
	Triangular (flag$_\beta$ = 1) $f_\beta(z) = \frac{2(N-z)}{N^2}$	$S_\beta(z)$	$(N - z)^2/N^2$	$(N - z)^2/N^2$
		$S_\gamma(z)$	$1 - z/N$	$1 - (z/N)^2$
		$S_{\beta\gamma}(z)$	$1 - \frac{z^2(3N - z)}{3N^3}$	$1 - \frac{z^3(4N - z)}{6N^4}$
		$S_{ce}(z)$	1	1

Downloaded by CORNELL UNIV on August 8, 2012 | http://pubs.acs.org
Publication Date: November 16, 2006 | doi: 10.1021/bk-2007-0945.ch017

In Applied Modeling and Computations in Nuclear Science; Semkow, T., et al.;
ACS Symposium Series; American Chemical Society: Washington, DC, 2006.

The expected totals for the relevant channels and the expected beta efficiency in terms of the simulation model's input parameters and the survival functions are then given by:

$$\begin{aligned}
\hat{N}_\beta(z) &= N_0\begin{bmatrix} e_\beta\left(1-P_{\beta\gamma}\right)S_\beta(z)+e_{\beta\gamma}\left(1-P_{ce}\right)\left(1-e_\beta\right)S_\gamma(z) \\ +\, e_\beta e_{\beta\gamma}\left(1-P_{ce}\right)S_{\beta\gamma}(z)+P_{ce}.e_{\beta ce}S_{ce}(z) \end{bmatrix}, \\
\hat{N}_c(z) &= N_0\left[e_\gamma\left(1-P_{ce}\right)\left(1-e_{\beta\gamma}\right)e_\beta S_\beta(z)\right], \\
\hat{N}_\gamma &= N_0\left[e_\gamma\left(1-P_{ce}\right)\left(1-e_{\beta\gamma}\right)\right], \\
\hat{\varepsilon}_\beta(z) &= \frac{\hat{N}_c(z)}{\hat{N}_\gamma} = e_\beta S_\beta(z).
\end{aligned} \tag{7}$$

The predicted shapes of the extrapolation curves may be readily determined by re-expressing Eqs. 7 as MacLaurin series expansions of order M relating the expected beta count rate to the expected beta inefficiency:

$$\hat{N}_\beta(z)=\sum_{j=0}^{M}a_j\left(1-\hat{\varepsilon}_\beta(z)\right)^j, \tag{8}$$

or equivalently:

$$\frac{\hat{N}_\beta(z)}{\hat{\varepsilon}_\beta(z)}=\sum_{j=0}^{M}b_j\left(\frac{1-\hat{\varepsilon}_\beta(z)}{\hat{\varepsilon}_\beta(z)}\right)^j. \tag{9}$$

This approach of finding series approximations, rather than determining exact solutions is undertaken since the DCC analysis software is designed to be used with real radioactive sources of where the exact forms of the efficiency extrapolation curves are generally unknown. It is customary to fit a low-order polynomial and perform the extrapolation to unit beta channel efficiency utilising the calculated fit parameters. This facilitates a robust test of the performance of the entire DCC analysis code, where the fit parameters determined from analysis of the simulated data sets may be directly compared against the appropriate predicted series solutions.

Estimates of the expected extrapolation curves (for all combinations of input beta and gamma spectral shapes) of the types given in Eqs. 8, 9 are given in Tables III and IV respectively. The expansions are taken to third order in the beta channel inefficiency ($M = 3$).

Downloaded by CORNELL UNIV on August 8, 2012 | http://pubs.acs.org
Publication Date: November 16, 2006 | doi: 10.1021/bk-2007-0945.ch017

Table III. Expected Extrapolation Fit Parameters (Eq. 8) to Third Order in the Beta Inefficiency

flag$_\beta = 0$ *flag*$_\gamma = 0$	$a_0 = N_0\left(1+e_{\beta\gamma}(1-P_{ce})(1-e_\beta)^2/(2e_\beta)\right)$ $a_1 = -N_0(1-P_{\beta\gamma})$ $a_2 = -N_0 e_{\beta\gamma}(1-P_{ce})/2e_\beta$ $a_3 = 0$
flag$_\beta = 0$ *flag*$_\gamma = 1$	$a_0 = N_0\left(1-2e_{\beta\gamma}(1-P_{ce})(1-e_\beta)^3/(3e_\beta^{\,2})\right)$ $a_1 = -N_0\left(1-P_{\beta\gamma}+e_{\beta\gamma}(1-P_{ce})\left((1-e_\beta)/e_\beta\right)^2\right)$ $a_2 = 0$ $a_3 = -N_0 e_{\beta\gamma}(1-P_{ce})/(3e_\beta^{\,2})$
flag$_\beta = 1$ *flag*$_\gamma = 0$	$a_0 = N_0\left(1+e_{\beta\gamma}(1-P_{ce})(2+\sqrt{e_\beta})(1-\sqrt{e_\beta})^2/(3\sqrt{e_\beta})\right)$ $a_1 = -N_0(1-P_{\beta\gamma})$ $a_2 = -N_0 e_{\beta\gamma}(1-P_{ce})/(4\sqrt{e_\beta})$ $a_3 = -N_0 e_{\beta\gamma}(1-P_{ce})/(12\sqrt{e_\beta})$
flag$_\beta = 1$ *flag*$_\gamma = 1$	$a_0 = N_0\left(1-e_{\beta\gamma}(1-P_{ce})(3\sqrt{e_\beta}+5)(1-\sqrt{e_\beta})^3/(6e_\beta)\right)$ $a_1 = -N_0\left(1-P_{\beta\gamma}-e_{\beta\gamma}(1-P_{ce})(2+\sqrt{e_\beta})(1-\sqrt{e_\beta})^2/(3e_\beta)\right)$ $a_2 = N_0 e_{\beta\gamma}(1-P_{ce})(2+\sqrt{e_\beta})(1-\sqrt{e_\beta})^2/(12e_\beta)$ $a_3 = N_0 e_{\beta\gamma}(1-P_{ce})(e_\beta-3)/(24\sqrt{e_\beta})$

Determination of the fit parameters a_j yields a simple means of determining the fit parameters b_j, where:

$$\begin{aligned} b_0 &= a_0, \\ b_1 &= a_0 + a_1, \\ b_{j(j\geq 2)} &= \sum_{i=0}^{j-2}\binom{j-2}{i}(-1)^{j-i}\, a_{i+2}. \end{aligned} \qquad (10)$$

Downloaded by CORNELL UNIV on August 8, 2012 | http://pubs.acs.org
Publication Date: November 16, 2006 | doi: 10.1021/bk-2007-0945.ch017

Downloaded by CORNELL UNIV on August 8, 2012 | http://pubs.acs.org
Publication Date: November 16, 2006 | doi: 10.1021/bk-2007-0945.ch017

Table IV. Expected Extrapolation Fit Parameters (Eq. 9) to Third Order in the Beta Inefficiency

flag$_\beta = 0$ *flag*$_\gamma = 0$	$b_0 = N_0\left(1 + e_{\beta\gamma}(1-P_{ce})(1-e_\beta)^2/(2e_\beta)\right)$ $b_1 = N_0\left(P_{\beta\gamma} + e_{\beta\gamma}(1-P_{ce})(1-e_\beta)^2/(2e_\beta)\right)$ $b_2 = -N_0 e_{\beta\gamma}(1-P_{ce})/(2e_\beta)$ $b_3 = N_0 e_{\beta\gamma}(1-P_{ce})/(2e_\beta)$
flag$_\beta = 0$ *flag*$_\gamma = 1$	$b_0 = N_0\left(1 - 2e_{\beta\gamma}(1-P_{ce})(1-e_\beta)^3/(3e_\beta^2)\right)$ $b_1 = N_0\left(P_{\beta\gamma} + e_{\beta\gamma}(1-P_{ce})(1+2e_\beta)(1-e_\beta)^2/(3e_\beta^2)\right)$ $b_2 = 0$ $b_3 = -N_0 e_{\beta\gamma}(1-P_{ce})/(3e_\beta^2)$
flag$_\beta = 1$ *flag*$_\gamma = 0$	$b_0 = N_0\left(1 + e_{\beta\gamma}(1-P_{ce})(2+\sqrt{e_\beta})(1-\sqrt{e_\beta})^2/(3\sqrt{e_\beta})\right)$ $b_1 = N_0\left(P_{\beta\gamma} + e_{\beta\gamma}(1-P_{ce})(2+\sqrt{e_\beta})(1-\sqrt{e_\beta})^2/(3\sqrt{e_\beta})\right)$ $b_2 = -N_0 e_{\beta\gamma}(1-P_{ce})/(4\sqrt{e_\beta})$ $b_3 = N_0 e_{\beta\gamma}(1-P_{ce})/(6\sqrt{e_\beta})$
flag$_\beta = 1$ *flag*$_\gamma = 1$	$b_0 = N_0\left(1 - e_{\beta\gamma}(1-P_{ce})(3\sqrt{e_\beta}+5)(1-\sqrt{e_\beta})^3/(6e_\beta)\right)$ $b_1 = N_0\left(P_{\beta\gamma} + e_{\beta\gamma}(1-P_{ce})(3e_\beta + 4\sqrt{e_\beta} - 1)(1-\sqrt{e_\beta})^2/(6e_\beta)\right)$ $b_2 = N_0 e_{\beta\gamma}(1-P_{ce})(\sqrt{e_\beta}+2)(1-\sqrt{e_\beta})^2/(12e_\beta)$ $b_3 = -N_0 e_{\beta\gamma}(1-P_{ce})\left(e_\beta^{\frac{3}{2}} - 3\sqrt{e_\beta} + 4\right)/(24e_\beta)$

As the input parameter e_β will usually be typically close to unity (> 0.95), and $e_{\beta\gamma}$ will be typically small (< 0.05), a_0 and b_0 are valid estimators of the simulated total number of counts N_0. In all cases, the ratio a_1/a_0 is approximately $(P_{\beta\gamma} - 1)$ and the ratio b_1/b_0 is approximately $P_{\beta\gamma}$. The estimate of the activity A_0 is then given by dividing N_0 by the time of the last disintegration.

4. Testing the DCC Analysis Software

The DCC-SIM simulation software was run using the following input parameters :

• N_0	1000000
• A_0	10000
• T_{ADC}	50 ns (*i.e.*, 20 MHz sampling rate)
• $[V_{\beta(min)}, V_{\beta(max)}]$	[0, 4095]
• $[V_{\gamma(min)}, V_{\gamma(max)}]$	[0, 4095]
• $flag_\beta, flag_\gamma$	1, 1
• P_{ce}	0.1
• $e_\beta, e_{\beta\gamma}, e_{\beta ce}, e_\gamma$	0.95, 0.05, 1.0, 0.6
• r_1, r_2	0, 1
• $j_\beta, j_\gamma, \delta_\beta, \delta_\gamma$	1 μs, 1 μs, 1 μs, 1 μs
• $W_\beta, W_\gamma, \tau_p, n$	2 μs, 2 μs, 0.25, 8.0.

Another data file was created with negligible N_0 to serve as a background file. The files were analysed by the DCC software and the extrapolations performed in order to determine estimates of the simulated source activity, along with the other fit parameters. The coincidence counting parameters used in the DCC analysis software were: imposed beta and gamma channel dead times (10 μs and 12 μs), imposed delay required to ensure coincident beta and gamma pulses arrive at the software coincidence mixer (1 μs to the gamma channel) and coincidence resolving time (1 μs per channel).

The measured maximum beta efficiency was 0.945 compared to the input parameter of ($e_\beta = 0.95$). The fit was performed on data from this maximum beta efficiency down to an apparent beta efficiency of 0.80 (Fig. 3). Both linear extrapolations (Eqs. 8 and 9) yielded the identical activity: (10023 ± 23) Bq compared to the predicted 10016 Bq. The agreement appears to be acceptable, although for this simulation the input activity was rather modest (10 kBq). Indeed, some deviation from the expected values in Tables III and IV is expected due to the finite widths of the simulated pulses leading to the summation of pulses stemming from different simulated disintegrations. This produces distortions of the expected pulse height spectra along with the exponential distribution of inter-arrival times between events. This bias will vanish at low count rates and/or with simulated pulses of minimal width (1 ADC clock "tick").

Downloaded by CORNELL UNIV on August 8, 2012 | http://pubs.acs.org
Publication Date: November 16, 2006 | doi: 10.1021/bk-2007-0945.ch017

Downloaded by CORNELL UNIV on August 8, 2012 | http://pubs.acs.org
Publication Date: November 16, 2006 | doi: 10.1021/bk-2007-0945.ch017

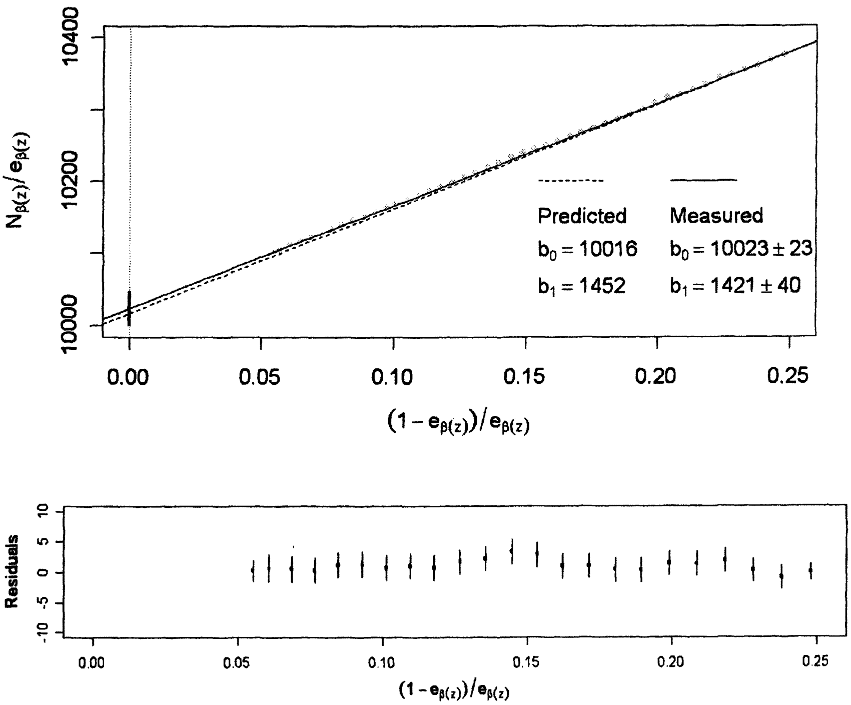

Figure 3. Comparison of measured and predicted extrapolation curves.

5. Future Work

Numerous further tests are currently ongoing to validate fully the DCC analysis software. A project of the ICRM Radionuclide Metrology Techniques Working Group aimed at validating the various DCC analysis routines used worldwide has recently begun. It is proposed to use the DCC data conversion routines mentioned in Section 1 to allow the simulation software described in this report to test other DCC systems at count rates that are much higher than currently achievable. Details of these results will be published on completion of the project.

References

1. Buckman, S. M.; Ius, D. *Nucl. Instr. Meth. Phys. Res. A* **1996**, *369*, 368-374.
2. Buckman, S. M.; Keightley, J. D.; Smith, D.; Woods, M. J. *Appl. Radiat. Isot.* **1998**, *49*, 1135-1140.
3. Butcher, K. S. A.; Watt, G. C.; Alexiev, D.; van der Gaast, H.; Davies, J.; Mo, L.; Wyllie, H. A.; Keightley, J. D.; Smith, D.; Woods, M. J. *Nucl. Instr. Meth. Phys. Res. A* **2000**, *450*, 30-34.
4. Keightley, J. D.; Watt, G. C. *Appl. Radiat. Isot.* **2002**, 56, 205-210.
5. Keightley, J. D. *DCC Data Format*; Report DCC/DCCDataFormat/01, NPL, 2002.
6. Smith, D. *Metrologia*, **1975**, *11*, 73-77.
7. *Particle Counting in Radioactivity Measurements*; ICRU Report 52, International Commission on Radiation Units and Measurements: Bethesda, MD, 1994.
8. Hwang, H. Y.; Park, T. S.; Kim, K. H.; Jeon, W. J.; Oh, P. J.; Lee, M. K.; Han, K. H.; Yun, H. J. *Nucl. Instr. Meth. Phys. Res. A* **1996**, *369*, 363-367.
9. Park, T. S.; Hwang, H. Y.; Lee, J. M. *Appl. Radiat. Isot.* **1998**, *49*, 1147-1151.
10. Havelka, M.; Auerbach, P.; Sochorová, J. *Appl. Radiat. Isot.* **2002**, *56*, 265-268.
11. Havelka, M.; Auerbach, P.; Sochorová, J. *Appl. Radiat. Isot.* **2004**, *60*, 409-413.
12. Chernishev, V. I.; *et al*, *Meas. Techniques* **2004**, *47*, 1204-1210.
13. Chernishev, V. I.; Korostin, S. V. *Equipment and News of Radiation Measurements* **2003**, *4(35)*, 50-56.
14. Keightley, J. D. *Data Simulation for Validation of 4πβ–γ Digital Coincidence Counting Analysis Software*; Report GE/R/IM/11/05, IRMM, 2005.
15. Wichmann, B. A.; Hill, I. D. *Appl. Stat.* **1982**, *31*, 188-190.

Downloaded by CORNELL UNIV on August 8, 2012 | http://pubs.acs.org
Publication Date: November 16, 2006 | doi: 10.1021/bk-2007-0945.ch017

Downloaded by UNIV OF GUELPH LIBRARY on August 6, 2012 | http://pubs.acs.org
Publication Date: November 16, 2006 | doi: 10.1021/bk-2007-0945.ch018

Chapter 18

Corrections for Overdispersion Due to Correlated Counts in Radon Measurements Using Grab Scintillation Cells, Activated Charcoal Devices, and Liquid Scintillation Charcoal Devices

Phillip H. Jenkins[1], James F. Burkhart[2], and Carl J. Kershner[3]

[1]Bowser-Morner, Inc., 4518 Taylorsville Road, Dayton, OH 45424
[2]University of Colorado, 1420 Austin Bluffs Parkway,
Colorado Springs, CO 80918
[3]Mound Laser and Photonics Center, Inc., 720 Mound Road,
Miamisburg, OH 45342

Lucas and Woodward (*1*) published values for a factor, "*J*," for correcting estimates of counting error that were based on Poisson statistics. Their work considered radon measurements using the "Lucas cell." We expanded on their work by considering four different types of scintillation cell currently in use. Also, we investigated the relationships of the individual counting efficiencies for the alpha particles emitted by ^{222}Rn, ^{218}Po and ^{214}Po in these types of scintillation cells and showed that they were not equal as assumed by Lucas and Woodward (*1*) but varied with cell geometry. Further, we measured the proportions among the individual counting efficiencies at two locations of different elevations, Dayton, Ohio and Colorado Springs, Colorado, and showed that the variation of the individual counting efficiencies was affected by air density. Using values of individual counting efficiencies for the three radionuclides, we calculated values of *J* for the four types of scintillation cell at both locations. We calculated values of *J*

In Applied Modeling and Computations in Nuclear Science; Semkow, T., et al.;
ACS Symposium Series; American Chemical Society: Washington, DC, 2006.

for one type of activated charcoal device and showed that these values were much smaller than those for scintillation cells because of smaller counting efficiencies. We also calculated values of J for liquid scintillation charcoal devices and showed that these values were larger than those for scintillation cells because of the potential inclusion of increased correlated counts and because of larger counting efficiencies. An example calculation of how the J might be used to correct the Poisson statistics for measurements from two device types was included.

Downloaded by UNIV OF GUELPH LIBRARY on August 6, 2012 | http://pubs.acs.org
Publication Date: November 16, 2006 | doi: 10.1021/bk-2007-0945.ch018

1. Introduction

It is common for Poisson, or "counting," statistics to be applied to measurements of radioactive materials to determine an estimate of the statistical uncertainty due to the random nature of radioactive decay and measurement of radioactive emissions. Unfortunately, it is also common for limitations of this approach to be ignored. The criteria that must be met in order for Poisson statistics to be valid are: (1) the number of atoms present in the sample must be very much greater than 1, (2) the counting time must be very small compared with the half-life of the radionuclide being detected, and (3) the observed counts must not be correlated. The first criterion is usually not an issue with radon measurements. The effect of violating the second criterion is a true variance that is smaller than the estimate obtained from "counting" statistics (underdispersion), but this criterion is also usually not an issue with radon measurements. The effect of violating the third criterion is a true variance that is larger than the estimate obtained from "counting" statistics (overdispersion). It is the third criterion that often is not met with radon measurements. There are potentially several sources of overdispersion, such as instability of the measurement system, as thoroughly discussed by Semkow (*2*); however, this chapter addresses only overdispersion due to the inclusion of correlated counts in radon measurements. Inkret *et al.* (*3*) also thoroughly discussed sources of overdispersion and underdispersion in radon and radon progeny measurements.

All radon measurement techniques are based on detecting emissions from radon itself and/or emissions from one or more of its short-lived decay products. In cases where emissions from more than one of these radionuclides are observed, correlated counts may result, potentially making Poisson statistics invalid. Simply stated, for Poisson statistics to be valid only one observed count from each atom of radon and its subsequent progeny is allowed.

Lucas and Woodward (*1*) described a factor, "*J*," for correcting Poisson statistics for measurements of radon using the specific type of alpha scintillation cell known as the "Lucas cell." The factor "*J*" is defined as the ratio of the expected variance to the expected mean of the count, or

$$J = \sigma^2/\mu . \tag{1}$$

This factor is frequently called the "coefficient of dispersion." (2) Since μ is the value of the variance predicted by Poisson statistics, J is the ratio of the true variance to the Poisson variance. In this chapter, we expanded on the work of Lucas and Woodward (1) by calculating values of J for four types of grab scintillation cell currently used by the authors, for devices that adsorb radon and are analyzed by gamma-ray spectroscopy and for liquid scintillation charcoal devices. Note that in all three of these techniques the radon is sealed in a container and later analyzed by some type of counting method.

Poisson statistics are commonly, and incorrectly, applied to measurements of radon and radon progeny, leading to unfair comparisons among measurement methods and misleading statements in the advertisement of products. The authors hope that this chapter will help in correcting this situation.

2. Calculation of Values of *J*

Two assumptions are made that simplify the calculations. First, because of the small half-life of ^{214}Po (164 μs (*4*)), it is assumed that the decay of ^{214}Bi can be described as the emission of a beta particle immediately followed by the emission of an alpha particle. Second, because of the long half-life of ^{210}Pb (22.3 y (*4*)) compared with those of the short-lived radon decay products, it is assumed that ^{210}Pb is stable and therefore its decay constant is zero.

H is defined as the maximum number of particles that can be detected by a specific method from the decay of a single radon atom and its subsequent short-lived decay products. Because we expanded on the work of Lucas and Woodward (*1*) to consider radon measurement techniques other than scintillation cells, we used the maximum possible value of *H*, *i.e.*, $H = 5$.

The values of σ^2 and μ can be calculated if the counting efficiencies of all detected radiation emissions are known. The approach is to track a single radon atom and calculate the probabilities of all possible outcomes from the decay of that radon atom until it becomes an atom of ^{210}Pb. These probabilities then also

Downloaded by UNIV OF GUELPH LIBRARY on August 6, 2012 | http://pubs.acs.org
Publication Date: November 16, 2006 | doi: 10.1021/bk-2007-0945.ch018

apply to all the other radon atoms initially present. Consider that the radon nucleus exists in five states as it progresses through the decay series:

State 0 - it is still ^{222}Rn,
State 1 - it has become ^{218}Po,
State 2 - it has become ^{214}Pb,
State 3 - it has become ^{214}Bi/^{214}Po, and
State 4 - it has become ^{210}Pb.

The mean of a count tracking the decay of one radon atom is calculated from the following equation:

$$\mu = \Sigma\, h\, q(h)\,, \qquad (h = 0, 1, \ldots, H) \tag{2}$$

where $q(h)$ is the probability of observing h counts during the counting period. The variance of a count is calculated from the following equation:

$$\sigma^2 = [\Sigma\, h^2\, q(h)] - \mu^2\,. \qquad (h = 0, 1, \ldots, H) \tag{3}$$

Once μ and σ^2 are calculated, J is calculated as the ratio of the two, as shown in Eq. 1. The bulk of the problem is calculating the probabilities $q(h)$.

A. Calculation of p_{ij}

First, the probabilities, p_{ij}, of the nuclide we are tracking going from State i to State j during any time period, t, are calculated. Lucas and Woodward (*1*) used the traditional equations of Bateman (*5*) in their calculations of these factors. However, a much more efficient approach is to use the recurrence formula described by Hamawi (*6*) for linear serial transformations. This formula has been discussed by Scherpelz and DesRosiers (*7*). Jenkins (*8*) presented an example of the use of this formula, comparing it with the use of the Bateman equations, for modeling grab samples of radon decay products in air.

The first step in the process is to define a set of intermediate factors, f_{ij}. First, the "first-tier" factors are calculated, which simply describe the exponential decay of each of the five radionuclides. Note that the exponentials are evaluated only in the first-tier factors.

First-tier factors:

$$f_{00} = \exp(-\lambda_0\, t) \tag{4}$$
$$f_{11} = \exp(-\lambda_1\, t) \tag{5}$$
$$f_{22} = \exp(-\lambda_2\, t) \tag{6}$$
$$f_{33} = \exp(-\lambda_3\, t) \tag{7}$$

Downloaded by UNIV OF GUELPH LIBRARY on August 6, 2012 | http://pubs.acs.org
Publication Date: November 16, 2006 | doi: 10.1021/bk-2007-0945.ch018

$$f_{44} = \exp(-\lambda_4 t). \tag{8}$$

Once the "first-tier" factors are calculated, they are used to calculate the "second-tier" factors.

Second-tier factors:

$$f_{01} = (f_{00} - f_{11}) / (\lambda_1 - \lambda_0) \tag{9}$$
$$f_{12} = (f_{11} - f_{22}) / (\lambda_2 - \lambda_1) \tag{10}$$
$$f_{23} = (f_{22} - f_{33}) / (\lambda_3 - \lambda_2) \tag{11}$$
$$f_{34} = (f_{33} - f_{44}) / (\lambda_4 - \lambda_3). \tag{12}$$

Likewise, the "second-tier" factors are used to calculate the "third-tier" factors.

Third-tier factors:

$$f_{02} = (f_{01} - f_{12}) / (\lambda_2 - \lambda_0) \tag{13}$$
$$f_{13} = (f_{12} - f_{23}) / (\lambda_3 - \lambda_1) \tag{14}$$
$$f_{24} = (f_{23} - f_{34}) / (\lambda_4 - \lambda_2). \tag{15}$$

The pattern of the recurrence formula should be obvious at this point. The "third-tier" factors are used to calculate the "fourth-tier" factors.

Fourth-tier factors:

$$f_{03} = (f_{02} - f_{13}) / (\lambda_3 - \lambda_0) \tag{16}$$
$$f_{14} = (f_{13} - f_{24}) / (\lambda_4 - \lambda_1). \tag{17}$$

And finally, the "fourth-tier" factors are used to calculate the "fifth-tier" factor.

Fifth-tier factor:

$$f_{04} = (f_{03} - f_{14}) / (\lambda_4 - \lambda_0). \tag{18}$$

The values of p_{ij} are calculated from the f_{ij} factors. The first set, p_{0j}, are the probabilities that if the nucleus is in State 0 (^{222}Rn) at the beginning of the time period t, that it will be in State j at the end of the time period:

$$p_{00} = f_{00} \tag{19}$$
$$p_{01} = \lambda_0 f_{01} \tag{20}$$
$$p_{02} = \lambda_0 \lambda_1 f_{02} \tag{21}$$
$$p_{03} = \lambda_0 \lambda_1 \lambda_2 f_{03} \tag{22}$$
$$p_{04} = \lambda_0 \lambda_1 \lambda_2 \lambda_3 f_{04}. \tag{23}$$

The next set, p_{1j}, are the probabilities that if the nucleus is in State 1 (^{218}Po) at the beginning of the time period t, that it will be in State $j > 0$ at the end of the time period:

Downloaded by UNIV OF GUELPH LIBRARY on August 6, 2012 | http://pubs.acs.org
Publication Date: November 16, 2006 | doi: 10.1021/bk-2007-0945.ch018

$$p_{11} = f_{11} \tag{24}$$
$$p_{12} = \lambda_1 f_{12} \tag{25}$$
$$p_{13} = \lambda_1 \lambda_2 f_{13} \tag{26}$$
$$p_{14} = \lambda_1 \lambda_2 \lambda_3 f_{14}. \tag{27}$$

The next set, p_{2j}, are the probabilities that if the nucleus is in State 2 (^{214}Pb) at the beginning of the time period t, that it will be in State $j > 1$ at the end of the time period:

$$p_{22} = f_{22} \tag{28}$$
$$p_{23} = \lambda_2 f_{23} \tag{29}$$
$$p_{24} = \lambda_2 \lambda_3 f_{24}. \tag{30}$$

The next set, p_{3j}, are the probabilities that if the nucleus is in State 3 (^{214}Bi/^{214}Po) at the beginning of the time period t, that it will be in State $j > 2$ at the end of the time period:

$$p_{33} = f_{33} \tag{31}$$
$$p_{34} = \lambda_3 f_{34}. \tag{32}$$

And finally, p_{44} is the probability that if the nucleus is in State 4 (^{210}Pb) at the beginning of the time period t, that it will still be in State 4 at the end of the time period. Because it is assumed that ^{210}Pb is stable, p_{44} always equals 1, but the equation is included here for completeness:

$$p_{44} = f_{44}. \tag{33}$$

B. States at the Ends of Delay Time and Counting Time

There is always a delay time, t_d, between the capture of radon in a sampling device and the counting of the sample in the analysis laboratory. The next step in the calculation process is to determine the state in which the radon nucleus exists at the end of the delay time. Equations 19 through 33 are typically used in a computer subroutine for the calculation of the p_{ij} factors. The time, t, is set equal to the delay time, t_d, and the p_{ij} factors are calculated using that subroutine. The needed probabilities d_{0j} are merely obtained from the p_{0j} factors:

$$d_{00} = p_{00} \tag{34}$$
$$d_{01} = p_{01} \tag{35}$$
$$d_{02} = p_{02} \tag{36}$$
$$d_{03} = p_{03} \tag{37}$$

Downloaded by UNIV OF GUELPH LIBRARY on August 6, 2012 | http://pubs.acs.org
Publication Date: November 16, 2006 | doi: 10.1021/bk-2007-0945.ch018

$$d_{04} = p_{04}. \tag{38}$$

The next step is to calculate the probabilities that the nucleus will go from State i to State j during the counting time. This is done by setting the time, t, equal to the counting time, t_c, and calculating the p_{ij} factors again.

C. Calculation of $q(h)$

Once the d_{0j} and p_{ij} factors are calculated, then it is possible to calculate the values of $q(h)$. ε_0, ε_1 and ε_{3a} are the counting efficiencies in counts per disintegration (c d^{-1}) for the alpha particles emitted from ^{222}Rn, ^{218}Po and ^{214}Po, respectively. ε_2 and ε_{3b} are the counting efficiencies (c d^{-1}) for the beta particles or gamma rays (depending on measurement method) emitted from ^{214}Pb and ^{214}Bi, respectively. The calculation of $q(h)$ is done in steps. First, the probabilities, q_{ik}, of detecting i counts from k emissions are calculated:

$$q_{00} = d_{00}\,p_{00} + d_{01}\,p_{11} + d_{02}\,p_{22} + d_{03}\,p_{33} + d_{04} \tag{39}$$

$$q_{01} = d_{00}\,p_{01}\,(1-\varepsilon_0) + d_{01}\,p_{12}\,(1-\varepsilon_1) + d_{02}\,p_{23}\,(1-\varepsilon_2) \tag{40}$$

$$\begin{aligned} q_{02} = {} & d_{00}\,p_{02}\,(1-\varepsilon_0)(1-\varepsilon_1) + d_{01}\,p_{13}\,(1-\varepsilon_1)(1-\varepsilon_2) \\ & + d_{03}\,p_{34}\,(1-\varepsilon_{3b})(1-\varepsilon_{3a}) \end{aligned} \tag{41}$$

$$q_{03} = d_{00}\,p_{03}\,(1-\varepsilon_0)(1-\varepsilon_1)(1-\varepsilon_2) + d_{02}\,p_{24}\,(1-\varepsilon_2)(1-\varepsilon_{3b})(1-\varepsilon_{3a}) \tag{42}$$

$$q_{04} = d_{01}\,p_{14}\,(1-\varepsilon_1)(1-\varepsilon_2)(1-\varepsilon_{3b})(1-\varepsilon_{3a}) \tag{43}$$

$$q_{05} = d_{00}\,p_{04}\,(1-\varepsilon_0)(1-\varepsilon_1)(1-\varepsilon_2)(1-\varepsilon_{3b})(1-\varepsilon_{3a}) \tag{44}$$

$$q_{11} = d_{00}\,p_{01}\,\varepsilon_0 + d_{01}\,p_{12}\,\varepsilon_1 + d_{02}\,p_{23}\,\varepsilon_2 \tag{45}$$

$$\begin{aligned} q_{12} = {} & d_{00}\,p_{02}\,[\varepsilon_0\,(1-\varepsilon_1) + \varepsilon_1\,(1-\varepsilon_0)] + d_{01}\,p_{13}\,[\varepsilon_1\,(1-\varepsilon_2) + \varepsilon_2\,(1-\varepsilon_1)] \\ & + d_{03}\,p_{34}\,[\varepsilon_{3b}\,(1-\varepsilon_{3a}) + \varepsilon_{3a}\,(1-\varepsilon_{3b})] \end{aligned} \tag{46}$$

$$\begin{aligned} q_{13} = {} & d_{00}\,p_{03}\,[\varepsilon_0\,(1-\varepsilon_1)(1-\varepsilon_2) + \varepsilon_1\,(1-\varepsilon_0)(1-\varepsilon_2) + \varepsilon_2\,(1-\varepsilon_0)(1-\varepsilon_1)] \\ & + d_{02}\,p_{24}\,[\varepsilon_2\,(1-\varepsilon_{3b})(1-\varepsilon_{3a}) \\ & + \varepsilon_{3b}\,(1-\varepsilon_2)(1-\varepsilon_{3a}) + \varepsilon_{3a}\,(1-\varepsilon_2)(1-\varepsilon_{3b})] \end{aligned} \tag{47}$$

$$\begin{aligned} q_{14} = {} & d_{01}\,p_{14}\,[\varepsilon_1\,(1-\varepsilon_2)(1-\varepsilon_{3b})(1-\varepsilon_{3a}) + \varepsilon_2\,(1-\varepsilon_1)(1-\varepsilon_{3b})(1-\varepsilon_{3a}) \\ & + \varepsilon_{3b}\,(1-\varepsilon_1)(1-\varepsilon_2)(1-\varepsilon_{3a}) + \varepsilon_{3a}\,(1-\varepsilon_1)(1-\varepsilon_2)(1-\varepsilon_{3b})] \end{aligned} \tag{48}$$

$$\begin{aligned} q_{15} = {} & d_{01}\,p_{04}\,[\varepsilon_0\,(1-\varepsilon_1)(1-\varepsilon_2)(1-\varepsilon_{3b})(1-\varepsilon_{3a}) \\ & + \varepsilon_1\,(1-\varepsilon_0)(1-\varepsilon_2)(1-\varepsilon_{3b})(1-\varepsilon_{3a}) + \varepsilon_2\,(1-\varepsilon_0)(1-\varepsilon_1)(1-\varepsilon_{3b})(1-\varepsilon_{3a}) \\ & + \varepsilon_{3b}\,(1-\varepsilon_0)(1-\varepsilon_1)(1-\varepsilon_2)(1-\varepsilon_{3a}) \\ & + \varepsilon_{3a}\,(1-\varepsilon_0)(1-\varepsilon_1)(1-\varepsilon_2)(1-\varepsilon_{3b})] \end{aligned} \tag{49}$$

$$q_{22} = d_{00}\,p_{02}\,\varepsilon_0\,\varepsilon_1 + d_{01}\,p_{13}\,\varepsilon_1\,\varepsilon_2 + d_{03}\,p_{34}\,\varepsilon_{3b}\,\varepsilon_{3a} \tag{50}$$

$$\begin{aligned} q_{23} = {} & d_{00}\,p_{03}\,[\varepsilon_0\,\varepsilon_1\,(1-\varepsilon_2) + \varepsilon_0\,\varepsilon_2\,(1-\varepsilon_1) + \varepsilon_1\,\varepsilon_2\,(1-\varepsilon_0)] \\ & + d_{02}\,p_{24}\,[\varepsilon_2\,\varepsilon_{3b}\,(1-\varepsilon_{3a}) + \varepsilon_2\,\varepsilon_{3a}\,(1-\varepsilon_{3b}) + \varepsilon_{3a}\,\varepsilon_{3b}\,(1-\varepsilon_2)] \end{aligned} \tag{51}$$

Downloaded by UNIV OF GUELPH LIBRARY on August 6, 2012 | http://pubs.acs.org
Publication Date: November 16, 2006 | doi: 10.1021/bk-2007-0945.ch018

$$\begin{aligned} q_{24} = d_{01}\, p_{14}\, [&\varepsilon_1\, \varepsilon_2\, (1-\varepsilon_{3b})(1-\varepsilon_{3a}) + \varepsilon_1\, \varepsilon_{3b}\, (1-\varepsilon_2)(1-\varepsilon_{3a}) \\ &+ \varepsilon_1\, \varepsilon_{3a}\, (1-\varepsilon_2)(1-\varepsilon_{3b}) + \varepsilon_2\, \varepsilon_{3b}\, (1-\varepsilon_1)(1-\varepsilon_{3a}) \\ &+ \varepsilon_2\, \varepsilon_{3a}\, (1-\varepsilon_1)(1-\varepsilon_{3b}) + \varepsilon_{3b}\, \varepsilon_{3a}\, (1-\varepsilon_1)(1-\varepsilon_2)] \end{aligned} \tag{52}$$

$$\begin{aligned} q_{25} = d_{00}\, p_{04}\, [&\varepsilon_0\, \varepsilon_1\, (1-\varepsilon_2)(1-\varepsilon_{3b})(1-\varepsilon_{3a}) + \varepsilon_0\, \varepsilon_2\, (1-\varepsilon_1)(1-\varepsilon_{3b})(1-\varepsilon_{3a}) \\ &+ \varepsilon_0\, \varepsilon_{3b}\, (1-\varepsilon_1)(1-\varepsilon_2)(1-\varepsilon_{3a}) + \varepsilon_0\, \varepsilon_{3a}\, (1-\varepsilon_1)(1-\varepsilon_2)(1-\varepsilon_{3b}) \\ &+ \varepsilon_1\, \varepsilon_2\, (1-\varepsilon_0)(1-\varepsilon_{3b})(1-\varepsilon_{3a}) + \varepsilon_1\, \varepsilon_{3b}\, (1-\varepsilon_0)(1-\varepsilon_2)(1-\varepsilon_{3a}) \\ &+ \varepsilon_1\, \varepsilon_{3a}\, (1-\varepsilon_0)(1-\varepsilon_2)(1-\varepsilon_{3b}) + \varepsilon_2\, \varepsilon_{3b}\, (1-\varepsilon_0)(1-\varepsilon_1)(1-\varepsilon_{3a}) \\ &+ \varepsilon_2\, \varepsilon_{3a}\, (1-\varepsilon_0)(1-\varepsilon_1)(1-\varepsilon_{3b}) + \varepsilon_{3b}\, \varepsilon_{3a}\, (1-\varepsilon_0)(1-\varepsilon_1)(1-\varepsilon_2)] \end{aligned} \tag{53}$$

$$q_{33} = d_{00}\, p_{03}\, \varepsilon_0\, \varepsilon_1\, \varepsilon_2 + d_{02}\, p_{24}\, \varepsilon_2\, \varepsilon_{3b}\, \varepsilon_{3a} \tag{54}$$

$$\begin{aligned} q_{34} = d_{01}\, p_{14}\, [&\varepsilon_1\, \varepsilon_2\, \varepsilon_{3b}\, (1-\varepsilon_{3a}) + \varepsilon_1\, \varepsilon_2\, \varepsilon_{3a}\, (1-\varepsilon_{3b}) + \varepsilon_1\, \varepsilon_{3b}\, \varepsilon_{3a}\, (1-\varepsilon_2) \\ &+ \varepsilon_2\, \varepsilon_{3b}\, \varepsilon_{3a}\, (1-\varepsilon_1)] \end{aligned} \tag{55}$$

$$\begin{aligned} q_{35} = d_{00}\, p_{04}\, [&\varepsilon_0\, \varepsilon_1\, \varepsilon_2\, (1-\varepsilon_{3b})(1-\varepsilon_{3a}) + \varepsilon_0\, \varepsilon_1\, \varepsilon_{3b}\, (1-\varepsilon_2)(1-\varepsilon_{3a}) \\ &+ \varepsilon_0\, \varepsilon_2\, \varepsilon_{3b}\, (1-\varepsilon_1)(1-\varepsilon_{3a}) + \varepsilon_1\, \varepsilon_2\, \varepsilon_{3b}\, (1-\varepsilon_0)(1-\varepsilon_{3a}) \\ &+ \varepsilon_0\, \varepsilon_1\, \varepsilon_{3a}\, (1-\varepsilon_2)(1-\varepsilon_{3b}) + \varepsilon_0\, \varepsilon_2\, \varepsilon_{3a}\, (1-\varepsilon_1)(1-\varepsilon_{3b}) \\ &+ \varepsilon_1\, \varepsilon_2\, \varepsilon_{3a}\, (1-\varepsilon_0)(1-\varepsilon_{3b}) + \varepsilon_0\, \varepsilon_{3b}\, \varepsilon_{3a}\, (1-\varepsilon_1)(1-\varepsilon_2) \\ &+ \varepsilon_1\, \varepsilon_{3b}\, \varepsilon_{3a}\, (1-\varepsilon_0)(1-\varepsilon_2) + \varepsilon_2\, \varepsilon_{3b}\, \varepsilon_{3a}\, (1-\varepsilon_0)(1-\varepsilon_1)] \end{aligned} \tag{56}$$

$$q_{44} = d_{01}\, p_{14}\, \varepsilon_1\, \varepsilon_2\, \varepsilon_{3b}\, \varepsilon_{3a} \tag{57}$$

$$\begin{aligned} q_{45} = d_{00}\, p_{04}\, [&\varepsilon_0\, \varepsilon_1\, \varepsilon_2\, \varepsilon_{3b}\, (1-\varepsilon_{3a}) + \varepsilon_0\, \varepsilon_1\, \varepsilon_2\, \varepsilon_{3a}\, (1-\varepsilon_{3b}) + \varepsilon_0\, \varepsilon_1\, \varepsilon_{3b}\, \varepsilon_{3a}\, (1-\varepsilon_2) \\ &+ \varepsilon_0\, \varepsilon_2\, \varepsilon_{3b}\, \varepsilon_{3a}\, (1-\varepsilon_1) + \varepsilon_1\, \varepsilon_2\, \varepsilon_{3b}\, \varepsilon_{3a}\, (1-\varepsilon_0)] \end{aligned} \tag{58}$$

$$q_{55} = d_{00}\, p_{04}\, \varepsilon_0\, \varepsilon_1\, \varepsilon_2\, \varepsilon_{3b}\, \varepsilon_{3a}\, . \tag{59}$$

With all the q_{ik} terms defined, the $q(h)$ terms can be calculated.

$$q(0) = q_{00} + q_{01} + q_{02} + q_{03} + q_{04} + q_{05} \tag{60}$$

$$q(1) = q_{11} + q_{12} + q_{13} + q_{14} + q_{15} \tag{61}$$

$$q(2) = q_{22} + q_{23} + q_{24} + q_{25} \tag{62}$$

$$q(3) = q_{33} + q_{34} + q_{35} \tag{63}$$

$$q(4) = q_{44} + q_{45} \tag{64}$$

$$q(5) = q_{55}\, . \tag{65}$$

Finally, μ, σ^2 and, J are calculated from Eqs. 2, 3, and 1, respectively.

D. Decay Constants

The values of the decay constants used in the calculations are presented in Table I. The two assumptions discussed above make it unnecessary to have correct values of decay constants for ^{214}Po and ^{210}Pb.

Downloaded by UNIV OF GUELPH LIBRARY on August 6, 2012 | http://pubs.acs.org
Publication Date: November 16, 2006 | doi: 10.1021/bk-2007-0945.ch018

Table I. Physical Data for Radionuclides in Radon Decay Series

Radionuclide	*Half-life*	*Decay Constant (h^{-1})*	*Mode of Decay*	*Alpha Particle Energy (Mev)*
^{222}Rn	3.825 d (*4*)	0.007551	Alpha	5.489 (*4*)
^{218}Po	3.05 min (*9*)	13.64	Alpha	6.001 (*4*)
^{214}Pb	26.8 min (*4*)	1.552	Beta	
^{214}Bi/^{214}Po	19.7 min (*9*)	2.111	Beta/Alpha	7.687 (*4*)
^{210}Pb	22.3 y (*4*)	0	Beta	

Downloaded by UNIV OF GUELPH LIBRARY on August 6, 2012 | http://pubs.acs.org
Publication Date: November 16, 2006 | doi: 10.1021/bk-2007-0945.ch018

3. Scintillation Cells

Lucas and Woodward (*1*) published values of *J* for "Lucas cells" assuming (1) a delay time of 4 hours, (2) counting times varying from 0.001 h to 100 h, and (3) counting efficiencies for alpha particles varying from 0.01 to 1.00 c d^{-1}. All alpha particles were assumed to have equal counting efficiencies.

We verified that by setting ε_2 and ε_{3b} equal to zero in our expanded equations, we duplicated the results of Lucas and Woodward (*1*). We extended the counting time to 1000 h, so we could see the effect of very long counting times on the values of *J*. For very short counting times, compared with the half-life of radon, *J* is essentially equal to 1, which is expected as there should be little probability of observing correlated counts. However, even with counting times as small as 0.1 h (6 min) *J* is clearly greater than 1, especially if the counting efficiency is above 0.5 c d^{-1}. The value of *J* maximizes at a counting time near 10 h, and then decreases indicating that there are two phenomena occurring: (1) correlated counts causing overdispersion, and (2) long counting times compared with the half-life of radon causing underdispersion. For counting times greater than about 150 hours, the value of *J* is less than 1.

It is expected that the individual counting efficiencies for alpha particles emitted in a scintillation cell would not be equal for two reasons. First, the geometrical distributions of the radionuclides should be different. Radon being an inert gas should be distributed throughout the volume of the cell. A significant portion of the polonium isotopes would be expected to be deposited on the inside surfaces of the cell and in contact with the coating of the zinc sulfide. Therefore, it would be expected that the counting efficiency for the alpha particles emitted by ^{222}Rn would be less than those for the alpha particles emitted by either of the two polonium isotopes. Second, the energies of the alpha particles emitted by ^{222}Rn, ^{218}Po and ^{214}Po are quite different as shown in Table I. Therefore, for cell sizes that are comparable to, or larger than, the range of the alpha particles in air, it would be expected that the counting efficiencies would differ with the energy of the alpha particle. Consequently, considering the geometrical distribution of the radionuclides and the energies of the emitted alpha particles, it is expected that $\varepsilon_0 < \varepsilon_1 < \varepsilon_{3a}$. Semkow *et al.* (*10*) reported, for a scintillation cell manufactured by Randam Electronics with 4.3 cm diameter and 8.6 cm height, that ε_0, ε_1 and ε_{3a} were 0.76, 0.77 and 0.91 c d^{-1}, respectively. Thus, for this type of cell, the proportions among the counting efficiencies were 0.31 : 0.32 : 0.37. A portion of this study included determining if the types of scintillation cells used by the authors similarly exhibited proportions among the counting efficiencies different from the proportion of ⅓ : ⅓ : ⅓ assumed by Lucas and Woodward (*1*).

Because the range of alpha particles in air was potentially an important factor affecting the individual counting efficiencies, it was felt that the air density or barometric pressure would be an important factor to study. Therefore, cells were studied at two laboratories at different elevations: Dayton, Ohio at 250 m (820 ft) and Colorado Springs, Colorado at 1830 m (6000 ft).

Four types of scintillation cell used by the authors, different in size from the original "Lucas cell," were studied. All cells were in the shape of right circular cylinders. Their dimensions are shown in Table II.

Table II. Physical Dimensions of the Scintillation Cells

Manufacturer	*Diameter*	*Height*	*Volume*
EDA	5 cm (2 in)	10 cm (4 in)	170 ml
Pylon	5 cm (2 in)	15 cm (6 in)	300 ml
Rocky Mountain	7.5 cm (3 in)	10 cm (4 in)	500 ml
Custom	10 cm (4 in)	15 cm (6 in)	1.4 l

An experiment was devised to determine the proportions among the counting efficiencies of the individual alpha-emitting radionuclides. A Tedlar® bag was filled with radon at an elevated concentration (> 50,000 Bq m^{-3}) and scintillation cells were subsequently filled from the bag. Because it was not the intent to determine the calibration factors for the cells, a topic of yet unpublished work by the authors, but only the proportions among the individual counting efficiencies, the exact concentration of radon was not quantified. The background count rate of a cell was determined and the cell was evacuated. The exact pressure to which the cells were evacuated was not critical, because the exact quantity of radon transferred to the cells was not required for the calculations. Because of the short half-lives of the radon decay products, the timing of the filling of the cell with radon and the counting was critical. The cell

Downloaded by UNIV OF GUELPH LIBRARY on August 6, 2012 | http://pubs.acs.org
Publication Date: November 16, 2006 | doi: 10.1021/bk-2007-0945.ch018

was connected through a sampling train to the Tedlar® bag, and at the start of the timing process ($t = 0$) radon was quickly introduced into the cell.

The cell was quickly transferred to an alpha scintillation counting system consisting of a Ludlum Model 218 Radon Flask Counter and a Ludlum Model 4303 Counter. It was critical to use a counting system that is capable of collecting a series of one-minute counts with no delay, or time loss, between counts. At exactly $t = 1$ min (or in two cases $t = 2$ min), a series of one-minute counts was collected and stored in a data file. In order to resolve the counting efficiencies of the three radionuclides, the counting must occur when there are significant differences in concentrations of those radionuclides in the cell, *i.e.*, before a near-equilibrium condition is established. For this reason, the counting time was limited to 120 min, after which the cell was quickly flushed and evacuated to help limit the buildup of the background count rate of the cell.

The data were analyzed using a nonlinear regression technique to fit the one-minute counts to the theoretical model described below. For the purpose of the calculations, a value was assumed for the initial activity of radon in each cell and the resulting individual counting efficiencies were normalized such that their sum totaled 1, thus producing the proportions among the individual counting efficiencies.

Downloaded by UNIV OF GUELPH LIBRARY on August 6, 2012 | http://pubs.acs.org
Publication Date: November 16, 2006 | doi: 10.1021/bk-2007-0945.ch018

A. The Model

The theoretical model for the number of counts observed during any counting interval following the collection of a grab radon sample in a scintillation cell is given by the following equation:

$$C = \varepsilon_0 d_0 + \varepsilon_1 d_1 + \varepsilon_{3a} d_3 , \qquad (66)$$

where C is the number of observed counts, ε_0, ε_1, and ε_{3a} are as defined above, while d_0, d_1, and d_3 are the numbers of disintegrations of ^{222}Rn, ^{218}Po, and ^{214}Po nuclei, respectively, occurring during counting time.

The d_i factors can be calculated from the integrated form of the Bateman (*5*) equations, but a more efficient way of calculating them is by using the integrated form of the recurrence formula of Hamawi (*6*). First a set of "*h* factors" is defined. Note that the exponentials are evaluated only in the "first-tier factors." The times at the beginning and end of the count are t_1 and t_2, respectively. The "first-tier" factors are:

$$h_{00} = [\exp(-\lambda_0 t_1) - \exp(-\lambda_0 t_2)] / \lambda_0 \qquad (67)$$

$$h_{11} = [\exp(-\lambda_1 t_1) - \exp(-\lambda_1 t_2)] / \lambda_1 \qquad (68)$$

$$h_{22} = [\exp(-\lambda_2 t_1) - \exp(-\lambda_2 t_2)] / \lambda_2 \qquad (69)$$

$$h_{33} = [\exp(-\lambda_3 t_1) - \exp(-\lambda_3 t_2)] / \lambda_3 \,. \tag{70}$$

The "second-tier factors" are calculated from the "first-tier factors":

$$h_{01} = (h_{00} - h_{11}) / (\lambda_1 - \lambda_0) \tag{71}$$
$$h_{12} = (h_{11} - h_{22}) / (\lambda_2 - \lambda_1) \tag{72}$$
$$h_{23} = (h_{22} - h_{33}) / (\lambda_3 - \lambda_2) \,. \tag{73}$$

The "third-tier factors" are calculated from the "second-tier factors":

$$h_{02} = (h_{01} - h_{12}) / (\lambda_2 - \lambda_0) \tag{74}$$
$$h_{13} = (h_{12} - h_{23}) / (\lambda_3 - \lambda_1) \,. \tag{75}$$

The "fourth-tier factor" is calculated from the "third-tier factors":

$$h_{03} = (h_{02} - h_{13}) / (\lambda_3 - \lambda_0) \,. \tag{76}$$

The d_i factors are then calculated as follows:

$$d_0 = A_0\, h_{00} \tag{77}$$
$$d_1 = A_0\, \lambda_1\, h_{01} \tag{78}$$
$$d_2 = A_0\, \lambda_1\, \lambda_2\, h_{02} \tag{79}$$
$$d_3 = A_0\, \lambda_1\, \lambda_2\, \lambda_3\, h_{03} \,, \tag{80}$$

where A_0 is the assumed activity (Bq) of radon in the cell at the time of sampling ($t = 0$). The number of counts during the counting interval is determined from Eq. 66.

B. Results of Individual Counting Efficiencies

Each cell was filled and counted a minimum of two and a maximum of five times at the Dayton location. The barometric pressure (local station pressure) was recorded at the time of each filling. In two instances, both with the EDA cell, the fit to the model was inferior due to a radon concentration that was too small, resulting in too few counts during each one-minute counting interval. These two sets of data were discarded and the decision was made to accept only data sets that gave a fit to the model that resulted in a value of R^2 of at least 0.9. It was also recognized that the radon concentration had to be substantial (50,000 Bq m^{-3} or greater) in order to meet this criterion. The measured proportions among the individual counting efficiency from the cells filled and counted in Dayton are presented in Table III.

Downloaded by UNIV OF GUELPH LIBRARY on August 6, 2012 | http://pubs.acs.org
Publication Date: November 16, 2006 | doi: 10.1021/bk-2007-0945.ch018

Table III. Proportions Among Individual Counting Efficiencies - Dayton, OH

Cell Type	^{222}Rn	^{218}Po	^{214}Po	*BP (mbar)*	R^2
EDA	0.31 ± 0.01	0.34 ± 0.02	0.35 ± 0.01	992.3 ± 1.2	0.918 ± 0.008
Pylon	0.26 ± 0.03	0.34 ± 0.05	0.40 ± 0.02	990.0 ± 3.5	0.945 ± 0.015
Rocky Mtn	0.28 ± 0.03	0.34 ± 0.03	0.38 ± 0.00	988.0 ± 3.4	0.947 ± 0.020
Custom	0.22 ± 0.00	0.38 ± 0.00	0.40 ± 0.00	988.0 ± 1.4	0.981 ± 0.000

The cells were each filled and counted twice in Colorado Springs using the same procedure as described for Dayton. The results are shown in Table IV.

Table IV. Proportions Among Individual Counting Efficiencies - Colorado Springs, CO

Cell Type	^{222}Rn	^{218}Po	^{214}Po	*BP (mbar)*	R^2
EDA	0.30 ± 0.01	0.35 ± 0.01	0.35 ± 0.01	818.0 ± 1.4	0.946 ± 0.023
Pylon	0.28 ± 0.01	0.32 ± 0.02	0.40 ± 0.03	818.5 ± 0.7	0.989 ± 0.002
Rocky Mtn	0.30 ± 0.00	0.34 ± 0.01	0.36 ± 0.01	818.0 ± 1.4	0.984 ± 0.008
Custom	0.29 ± 0.02	0.35 ± 0.01	0.36 ± 0.01	818.5 ± 0.7	0.988 ± 0.005

From the data in Tables III and IV, it can be seen that there is little spread among the proportions for the EDA cell and that there is little difference between the two locations for this cell. This was expected because the cell dimensions are smaller than the ranges of the alpha particles, even at the two different barometric pressures. However, as one progresses to the largest, Custom cell, the spread among the proportions becomes greater, especially at the Dayton location. The spread is not quite as great at the Colorado Springs location, due to the lower air density. The data suggest that the theoretical expectations of the relationships among the individual counting efficiencies are true.

Downloaded by UNIV OF GUELPH LIBRARY on August 6, 2012 | http://pubs.acs.org
Publication Date: November 16, 2006 | doi: 10.1021/bk-2007-0945.ch018

The values in Tables III and IV were used to calculate the individual counting efficiencies for the four cells at both locations shown in Table V. We assumed that the total counting efficiency, or calibration factor, for each cell is the same at both the Dayton and the Colorado Springs locations and assumed the following values: 1.8 c d^{-1} for the EDA cell, 1.8 c d^{-1} for the Pylon cell, 1.6 c d^{-1} for the Rocky Mountain cell, and 1.7 c d^{-1} for the Custom cell. These values were based on previous work at both laboratories and are currently undergoing careful assessment in another study to determine how differences in barometric pressure affect the calibration factors for these cells. Therefore, these values may not be entirely correct, as we suspect that there are differences in calibration factors due to differences in air density at the two locations. These values will be refined as more information becomes available. We anticipate, however, that resulting changes to these values will not significantly affect the values of J for the cells.

Downloaded by UNIV OF GUELPH LIBRARY on August 6, 2012 | http://pubs.acs.org
Publication Date: November 16, 2006 | doi: 10.1021/bk-2007-0945.ch018

Table V. Individual Counting Efficiencies (c d^{-1}) for the Cell Types at Both Locations

Cell Type - Location	^{222}Rn	^{218}Po	^{214}Po
EDA - DAY	0.558	0.612	0.630
EDA - COS	0.540	0.630	0.630
Pylon - DAY	0.468	0.612	0.720
Pylon - COS	0.504	0.576	0.720
Rocky Mtn - DAY	0.448	0.544	0.608
Rocky Mtn - COS	0.480	0.544	0.576
Custom - DAY	0.374	0.646	0.680
Custom - COS	0.493	0.595	0.612

C. Values of *J* for Scintillation Cells

The values for individual counting efficiencies shown in Table V were used in the model (Eqs. 1 through 65) and values of J were calculated for the four scintillation cells at both locations. The results for all four cells measured at the Dayton location are shown graphically in Fig. 1. These curves are similar to those published by Lucas and Woodward (*1*) for "Lucas" cells with a counting efficiency of about 0.5 to 0.6 c d^{-1}. The curve from Lucas and Woodward (*1*) for an efficiency of 0.5 c d^{-1} is included in Fig. 1 for comparison purposes. Note that this latter curve has a slightly different shape from the others, likely due to the assumption that the individual counting efficiencies are equal. There is little difference in the curves for the four types of scintillation cells studied here, with the greatest differences being at the maximum which occurs at a counting time of about 10 h. The differences among the cells shown in Fig. 1 may be due to the small differences in the calibration factors that were somewhat approximated, and also assumed to be the same at both locations. When these values are refined further, there may be slight differences in the values of J from those shown in Fig. 1; however, it is expected that the differences will not be significant. For counting times of 10 min and 1 h, the values of J for all of the cells are approximately 1.2 and 1.5, respectively.

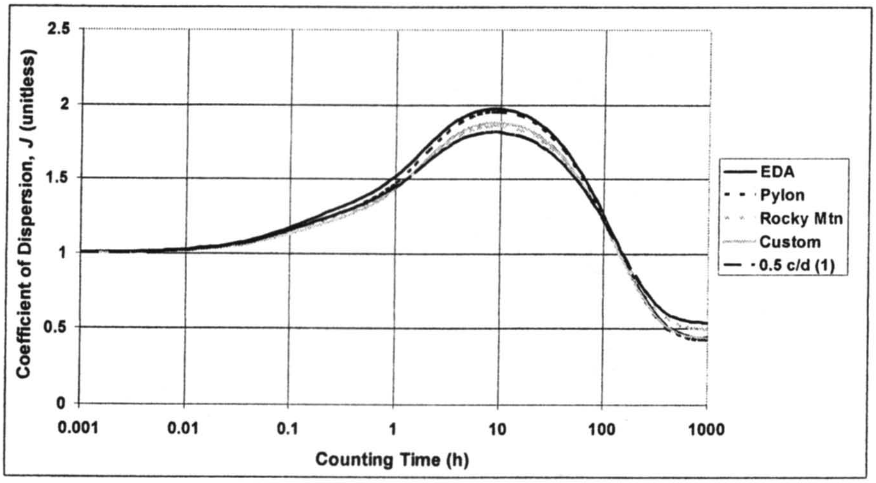

Figure 1. Values of J for the four types of scintillation cells at the Dayton location (one curve from Lucas and Woodward (1) is included for comparison).

We found essentially no differences among the values of J for the EDA, Pylon and Rocky Mountain cells between the Dayton and Colorado Springs locations. In Fig. 2, the curves for the large Custom cell show some differences between the two locations. This demonstrates an effect due to the difference in the air density between Dayton and Colorado Springs, but in terms of J the effect is not large.

Downloaded by UNIV OF GUELPH LIBRARY on August 6, 2012 | http://pubs.acs.org
Publication Date: November 16, 2006 | doi: 10.1021/bk-2007-0945.ch018

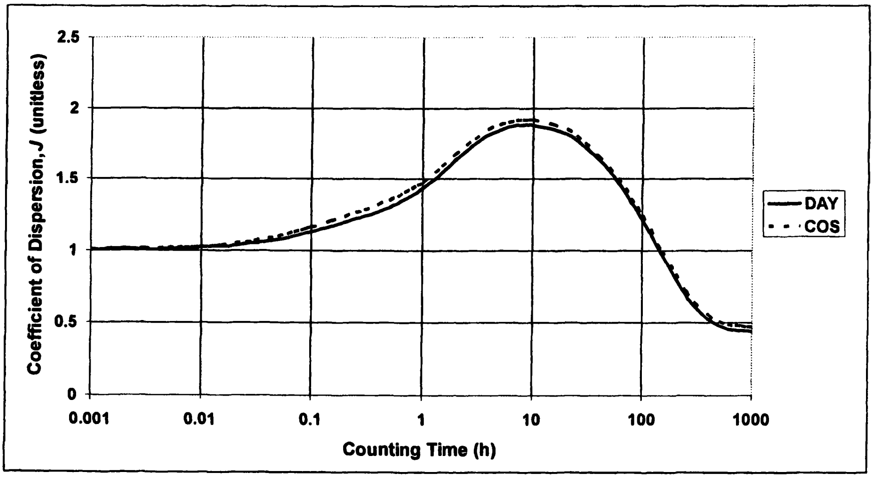

Figure 2. Comparison between locations for values of J for Custom cell.

4. Activated Charcoal Devices

All devices that measure radon concentration in air by adsorbing radon onto activated charcoal, and are analyzed using gamma-ray spectroscopy, are considered here to be activated charcoal devices regardless of the configuration of the container. The analysis is performed by measuring gamma rays emitted by two of the short-lived radon progeny, ^{214}Pb and ^{214}Bi; therefore, the potential exists to have correlated counts. The same general model that was used to calculate values of J for scintillation cells can be used for these devices. Because no alpha particles are detected, the counting efficiencies for the alpha-particle emitters, ε_0, ε_1 and ε_{3a}, are given the value of zero.

The sample is collected usually over a period of from two to seven days; however, for the purpose of calculating J factors, the instant at which the device is sealed can be considered to be the sampling time and the duration from that point until the device is analyzed the delay time. The delay time for charcoal devices is typically a day or longer; we considered delay times of 1, 2, and 3 days.

The specific device we used as an example is the four-inch, open-face charcoal canister counted on a gamma-spectroscopy system using a sodium iodide detector. Two methods are in general use: probably the most commonly used method includes counts from only two of the gamma rays emitted by ^{214}Pb as well as one gamma ray emitted by ^{214}Bi; the other method includes counts from three gamma rays emitted by ^{214}Pb and one gamma ray emitted by ^{214}Bi. The counting efficiencies used for the two radionuclides for the two methods are

Downloaded by UNIV OF GUELPH LIBRARY on August 6, 2012 | http://pubs.acs.org
Publication Date: November 16, 2006 | doi: 10.1021/bk-2007-0945.ch018

shown in Table VI based on experience in the Radon Reference Laboratory at Bowser-Morner, Inc. in Dayton. Persons at other laboratories, using similar or different charcoal devices, may determine different counting efficiencies, but can calculate their own values for *J* from the method presented here.

Table VI. Counting Efficiencies (c d^{-1}) for Charcoal Canisters

Method	*For ^{214}Pb*	*For ^{214}Bi*
Two γs from ^{214}Pb	0.1041	0.03412
Three γs from ^{214}Pb	0.1285	0.03412

The results of the calculations of values of *J* for four-inch, open-face charcoal canisters are shown graphically in Fig. 3. As expected, the values of *J* are much smaller for charcoal canisters than for scintillation cells. For counting times less than 10 h, it does not make a significant difference which of the two methods is used or what the delay time is. *J* maximizes at a value just larger than 1.04 at a counting time of about 10 h, compared to a peak of about 1.8 to 2.0 for scintillation cells. The values of *J* for typical counting times of 5 and 10 minutes are about 1.004 and 1.008, respectively.

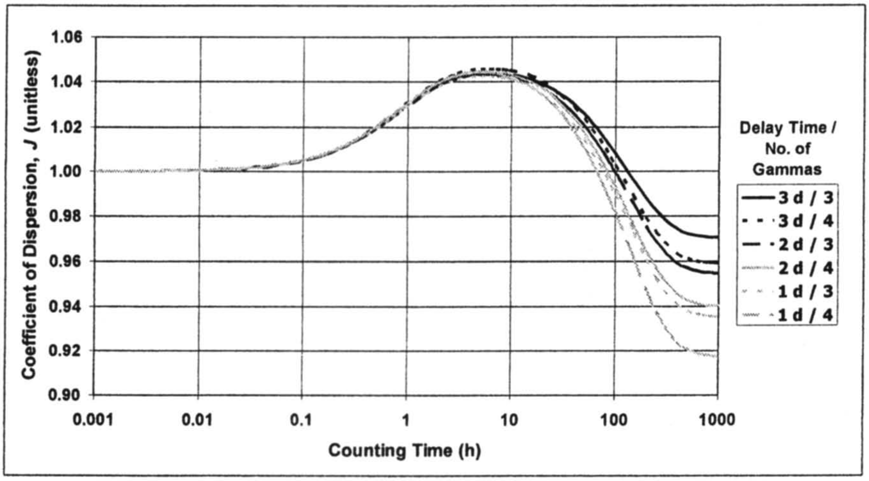

Figure 3. Values of J for four-inch, open-face charcoal canisters.

5. Liquid Scintillation Charcoal Devices

Liquid scintillation charcoal devices are used for measuring radon in air and radon in water. In either case, radon is analyzed by using a liquid scintillation

Downloaded by UNIV OF GUELPH LIBRARY on August 6, 2012 | http://pubs.acs.org
Publication Date: November 16, 2006 | doi: 10.1021/bk-2007-0945.ch018

counter, and potentially counts from the emissions of five different radionuclides could be detected. Therefore, the potential for correlated counts is significant.

For measuring either radon in air or radon in water, it is necessary to add a scintillation cocktail to the liquid scintillation vial and to allow some time for the radon and radon decay products to come into equilibrium. A delay time of four hours was assumed here.

A critical consideration for calculating values of *J* for liquid scintillation charcoal devices is the counting efficiencies for the alpha and beta particles that are, or could be, detected. We spoke to personnel at several laboratories that analyze liquid scintillation charcoal devices and determined that a value of 0.9 c d^{-1} was a reasonable counting efficiency for the alpha particles emitted by ^{222}Rn, ^{218}Po and ^{214}Po. Counting efficiencies for the beta particles emitted by ^{214}Pb and ^{214}Bi, however, was a different issue. Some laboratories discriminated against all beta particles for measurements of radon in air. Some laboratories included counts from beta particles for measurements of radon in air and in water, with counting efficiencies as high as 0.7 c d^{-1}. Therefore, we calculated sets values of *J* assuming a counting efficiency of 0.9 c d^{-1} for the alpha particles, but with the counting efficiency for the beta particles as a parameter ranging from 0 to 0.9 c d^{-1}. The results of the calculations are presented graphically in Fig. 4.

Downloaded by UNIV OF GUELPH LIBRARY on August 6, 2012 | http://pubs.acs.org
Publication Date: November 16, 2006 | doi: 10.1021/bk-2007-0945.ch018

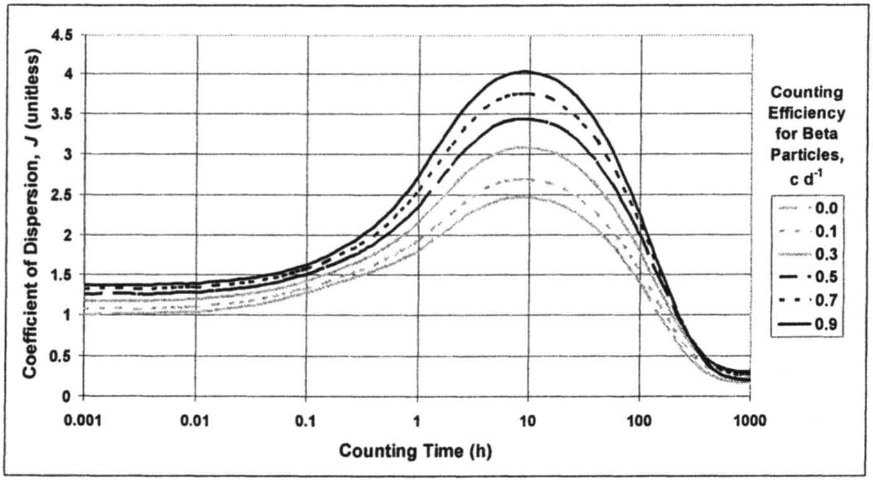

Figure 4. Value of J for liquid scintillation charcoal devices with varying counting efficiency (c d^{-1}) for beta particles.

From Fig. 4 it is easily seen that the potential for a significant correction to Poisson statistics exists for this type of device. The curves peak at a counting time of about 10 h, as do the curves for scintillation cells and activated charcoal devices. However, the peak value of *J* varies from about 2.5 to about 4, depending on the value of the counting efficiency for the beta particles, compared with a peak value of about 1.9 for scintillation cells and about 1.045 for activated charcoal devices. For realistic counting times of 5 and 10 minutes, the value of J varies from about 1.2 to about 1.8 depending on the counting efficiency for the beta particles as well as the exact counting time.

6. Example Calculation

As an example of how the coefficient of dispersion, J, might be applied, we considered the results from the exposures in the Bowser-Morner radon chamber of an activated charcoal device and a liquid scintillation charcoal device. Both devices were exposed for 48 hours under similar conditions of relative humidity, temperature and average radon concentration. Suppose that one were interested in using the coefficient of variation (*CV*) of these measurements as a means of comparing the two methods. The counting data are presented in Table VII. The equations for the sample mean net count rate, standard deviation and *CV* are:

$$X = (SGC - BGC)/t\,, \qquad (81)$$

where X is the sample mean net count rate (c min^{-1}), SGC is the sample gross count, BGC = background gross count, t = counting time (min),

$$s = [(J\,SGC + BGC)\,/\,t^2]^{1/2}, \qquad (82)$$

where s is the standard deviation of the count rate (c min^{-1}), and

$$CV = s/X\,. \qquad (83)$$

If the count is assumed to be Poisson, then $J=1$. Using these equations, the values of *CV* for both devices were calculated, both with and without a correction for overdispersion.

It was assumed that the counting system for the liquid scintillation charcoal device detected beta particles with a counting efficiency of 0.5 c d^{-1} and J was 1.6 (from Fig. 4). If Poisson statistics are assumed then the *CV*'s for the two devices are 0.83% and 1.08%. If J is applied to the sample counts and the corrected standard deviations are calculated, the *CV*'s are 0.86% and 1.36%. Based on Poisson statistics, the liquid scintillation charcoal device had a *CV* that was 30% larger than that of the activated charcoal device. When J was applied, the corrected *CV* for the liquid scintillation charcoal device was 59% greater than that for the activated charcoal device. This demonstrates that the application of J can significantly affect the comparison between two different device types.

Downloaded by UNIV OF GUELPH LIBRARY on August 6, 2012 | http://pubs.acs.org
Publication Date: November 16, 2006 | doi: 10.1021/bk-2007-0945.ch018

Table VII. Count Data, Standard Deviations, and Coefficients of Variation

Variable	*Activated Charcoal Device*	*Liquid Scintillation Charcoal Device*
Gross counts	17587	9229
Bkg counts	1086	229
Counting time (min)	10	10
Uncorrected Std Dev (c min^{-1})	13.665	9.725
CV	0.0083 or 0.83%	0.0108 or 1.08%
Value of *J*	1.008	1.6
Corrected Std Dev (c min^{-1})	14.11	12.25
Corrected *CV*	0.0086 or 0.86%	0.0136 or 1.36%

References

1. Lucas, H. F.; Woodward, D. A. Effect of long decay chains on the counting statistics in the analysis of radium-224 and radon-222. *J. Appl. Phys.* **1964**, *35*, 452-456.
2. Semkow, T. M. Theory of overdispersion in counting statistics caused by fluctuating probabilities. *Appl. Radiat. Isot.* **1999**, *51*, 565-579.
3. Inkret, W. C.; Borak, T. B.; Boes, D. C. Estimating the mean and variance of measurements from serial radioactive decay schemes with emphasis on ^{222}Rn and its short-lived progeny. *Rad. Prot. Dos.* **1990**, *32*, 45-55.
4. *Table of Radioactive Isotopes*; Browne. E., Firestone, R. B., Shirley, V. S., Ed.; J. Wiley & Sons: New York, NY, 1986.
5. Bateman, H. The solution of a system of differential equations occurring in the theory of radioactive transformations. *Proc. Camb. Phil. Soc.* **1910**, *15*, 423-427.
6. Hamawi, J. M. A useful recurrence formula for the equations of radioactive decay. *Nucl. Tech.* **1971**, *11*, 84-88.
7. Scherpelz, R. I.; DesRosiers, A. E. A modification to a recurrence formula for linear first-order equations. *Health Phys.* **1981**, *40*, 904-907.
8. Jenkins, P. H. Equations for modeling of grab samples of radon decay products. *Rad. Safety Journal* **2002**, *83*, Suppl. 1, S48-S51.
9. Friedlander, G.; Kennedy, J. W.; Miller, J. M. *Nuclear and Radiochemistry*; J. Wiley & Sons: New York, NY, 1964.
10. Semkow, T. M.; Parekh, P. P.; Schwendker, C. D.; Dansereau, R.; Webber, J. S. Efficiency of the Lucas scintillation cell. *Nucl. Inst. Meth. Phys. Res. A* **1994**, *353*, 515-518.

Downloaded by UNIV OF GUELPH LIBRARY on August 6, 2012 | http://pubs.acs.org
Publication Date: November 16, 2006 | doi: 10.1021/bk-2007-0945.ch018

Downloaded by NORTH CAROLINA STATE UNIV on August 8, 2012 | http://pubs.acs.org
Publication Date: November 16, 2006 | doi: 10.1021/bk-2007-0945.ch019

Chapter 19

Simulation of Elution Curves for Chromatography Columns with a Low Number of Theoretical Plates

Willy Brüchle

**Gesellschaft für Schwerionenforschung, Planckstrasse 1,
64291 Darmstadt, Germany**

A new description of chromatographic peaks is derived, showing that Poisson curves are good fits to describe the position and the shape of elution peaks as a function of distribution coefficients and the number of theoretical plates.

Introduction

Chromatographic techniques are among the most effective chemical methods to separate and characterize closely related chemical substances or ions. More than half a century ago the main theoretical foundations for these methods were developed; even a Nobel Price was awarded to Martin and Synge (*1*) for their theoretical and practical methodic developments. Meanwhile dozens of journals publish thousands of articles dealing with chromatographic separations, *e.g.*, with gas chromatography, HPLC, countercurrent chromatography, affinity chromatography, to mention only some popular methods. There exist a large number of pioneering theoretical descriptions of the peak position and the width, often based on the molecular dynamic theory of chromatography, originally developed by Giddings and Eyring (*2*). Their model represents the progress of a single molecule through the column as a chain of elementary adsorption-desorption stochastic processes. The majority of these papers have started with partial differential equations leading to Bessel functions. The asymptotic expansion of the Bessel functions weighted by the probability of the initial state of the molecule should yield the distribution curve for the elution. Rather complicated calculations using the characteristic function method are described in Ref. (*3*).

A relatively easy way to describe the chromatographic process is the "theoretical plate" concept, originating from distillation. It is an imaginary section of a column in which a complete equilibrium step takes place. The model was successfully used in Ref. (*1*) for liquid-solid chromatography. Usually textbooks dealing with chromatography present the two following formulae without derivation:

$$K_d = (T_r - T_0)\,F/m = (V_p - V_0)/m\,, \quad \text{or} \quad V_p = K_d m + V_0\,, \tag{1}$$

where
T_r = retention time [min]
T_0 = column hold-up time due to the free column volume [min]
F = flow rate of the mobile phase [mL/min]
m = mass of the stationary phase (ion exchanger, reversed phase material) [g]
K_d = partition coefficient (distribution coefficient)
V_p = volume eluted until the peak maximum [mL]
V_0 = free column volume (dead volume) [mL].

The number of theoretical plates is determined empirically from the chromatogram as:

$$N = (T_r/\sigma)^2 = 16\,(T_r/w)^2\,, \tag{2}$$

where w is the baseline width of the peak, determined graphically by drawing straight lines along the edges of the linear peak diagram. σ is the half width at the inflection point (square root of the variance). T_r is the retention time until the peak maximum is reached. Typically a Gaussian distribution profile is assumed for an ideal elution peak.

To compare the performance of columns of different length, the term height equivalent to a theoretical plate or plate height is used:

$$H = L/N\,, \tag{3}$$

where L is the column length and N is the number of plates.

Downloaded by NORTH CAROLINA STATE UNIV on August 8, 2012 | http://pubs.acs.org
Publication Date: November 16, 2006 | doi: 10.1021/bk-2007-0945.ch019

Downloaded by NORTH CAROLINA STATE UNIV on August 8, 2012 | http://pubs.acs.org
Publication Date: November 16, 2006 | doi: 10.1021/bk-2007-0945.ch019

During a series of fast automated separations on rather small chromatographic columns (1.6 mm i.d., 8 mm long; and 1 mm i.d., 3.5 mm long) with the ARCA and the AIDA systems (*4,5*), it was noticed that the peak shapes differed from a Gaussian; in addition it was often not possible to measure complete elution curves, but only two fractions. Still the distribution coefficient K_d should be determined. The knowledge of the peak shapes is indispensable for the multi-column technique also (*6*). In Ref. (*5*), the Glueckauf equation of chromatography was used (*7*):

$$A(V) = A_{max}\exp(-N(V_p-V)^2/2V_pV)\,, \qquad (4)$$

where A_{max}, N, and V_p are the maximum peak height, the number of theoretical plates, and the peak volume, respectively. There are interesting aspects in Ref. (*7*) about peak broadening when the original band entering the separation column is already broad. But it is nowadays rather simple to put this into a simulation program.

New Results

Is it possible to derive the peak position and the peak shape using simplifying assumptions and not too complicated mathematics? Yes, it is. This chapter will try to show how this can be achieved.

In a real experiment any amount of liquid pumped onto the top of the incompressible chromatography column continuously flows through the column. So, all exchange processes in different layers of the column will proceed simultaneously. In a simulation this behavior has to be modeled stepwise. Instead of using successive infinitesimal volumes of the mobile phase passing the column (*1*), the "theoretical plate" concept (*1,8*) was used in this work. According to it, the volume corresponding to a theoretical plate was used for a discontinuous flow treatment (*8*). As in the treatment of a separating funnel, the partition coefficient

$$K_d = C_s/C_l \qquad (5)$$

describes the ratio of the concentrations of the separated species in the solid and in the liquid phase, for each theoretical plate. The underlying assumption is that the distribution coefficient does not change with the change in concentration of the solute, and the diffusion from one plate to another is negligible. The activity transported from plate i to plate $i + 1$ is:

$$\Delta a(i) = a(i)\,(1 - K_d/(K_d + 1))\ , \tag{6}$$

where $a(i)$ denotes the total (solid plus liquid) activity in plate i.

This is valid for the case of equal volumes of solid and liquid phase. If the volumes are not equal, then Eq. 7 is valid:

$$\Delta a(i) = a(i)\,(1 - K_d/(K_d + r_v))\ . \tag{7}$$

In this formula, r_v is the ratio of the free column volume to the mass of the exchanger material V_0/m. The amount $\Delta a(i)$ corresponds to the activity in the liquid phase of plate i. The small volume of the plate, containing the activity $\Delta a(i)$ is transported to the following plate, where the next equilibrium is established with the activity retained on the solid phase. It is easy to check the validity of these formulae. Dividing the activity of the solid phase, $a(i) - \Delta a(i)$, by $\Delta a(i)$ results in K_d/r_v, consistent with Eq. 5. Mayer and Tompkins (*8*) used this attempt, but their material balance does not fit. In their Eq. 2, they assume that the activity in plate i is composed of the activity eluted from plate $i - 1$ and the activity that was in the plate in the step before; the simultaneous elution to plate $i + 1$ is not considered. The formulae they give would allow some activity to break through the column even with the first small volume of one theoretical plate, especially in the case of small K_d values. The same happened in Ref. (*2*), where it is explicitly mentioned two times, that molecules with no reaction (K_d = 0) will be eluted in exactly the time $t = 0$. This is not correct: even with $K_d = 0$ at least the dead volume of the column must be eluted before the substance will break through the column.

How to solve this problem? Instead of developing the activity distribution from plate 1 to plate N (the last plate of the column), one simply starts the simulation from the last plate, N, and goes back to plate 1. Now it is natural, that in the first step (with the volume of one plate) the substance will only reach plate 2, and one needs at least $N - 1$ steps until some activity will leave the column, when the elution starts with all activity in plate 1. In Fig. 1 and Fig. 2, the wrong treatment, leaving to early break-through for low K_d values is compared to the calculations in reverse order, where a "dead volume" results. Two different K_d values ($K_d = 1$ in Fig. 1, and $K_d = 0.1$ in Fig. 2) are assumed for a simulation with 5 theoretical plates ($N = 5$).

A rather extreme example is shown in Fig. 2. After the first step with the volume of only one plate, the activity would be smeared out over the entire column when the computing is started with the first plate and the eluted activity is transported to plate N. The correct sequence for this simulation is to start with plate N, let the activity from plate $N - 1$ be distributed between both, and go on

Downloaded by NORTH CAROLINA STATE UNIV on August 8, 2012 | http://pubs.acs.org
Publication Date: November 16, 2006 | doi: 10.1021/bk-2007-0945.ch019

Downloaded by NORTH CAROLINA STATE UNIV on August 8, 2012 | http://pubs.acs.org
Publication Date: November 16, 2006 | doi: 10.1021/bk-2007-0945.ch019

in reverse order to plate 1. Now a sharp front is passing through the column, and only after $N - 1$ plate volumes (the dead volume V_0 of the column) the activity will break through. This is in agreement with experimental observations.

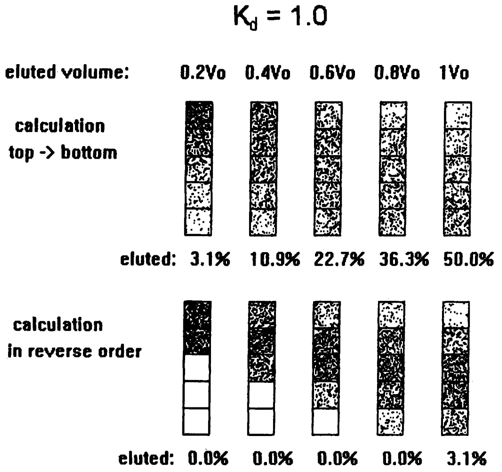
K_d = 1.0
eluted volume:
0.2Vo
0.4Vo
0.6Vo
0.8Vo
1Vo
calculation top -> bottom
eluted: 3.1% 10.9% 22.7% 36.3% 50.0%
calculation in reverse order
eluted: 0.0% 0.0% 0.0% 0.0% 3.1%

Figure 1. Comparison of two different approaches (upper and lower panel) to describe the elution for a column with 5 theoretical plates and $K_d = 1.0$.

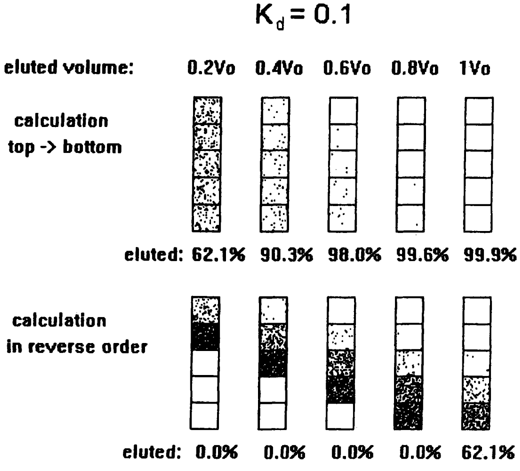
K_d = 0.1
eluted volume:
0.2Vo
0.4Vo
0.6Vo
0.8Vo
1Vo
calculation top -> bottom
eluted: 62.1% 90.3% 98.0% 99.6% 99.9%
calculation in reverse order
eluted: 0.0% 0.0% 0.0% 0.0% 62.1%

Figure 2. Comparison of two different approaches (upper and lower panel) to describe the elution for a column with 5 theoretical plates and $K_d = 0.1$.

The difference between Eqs. 6 and 7 results only in different dead volumes of the column. The shape of the elution curve is not influenced by the coefficient r_V (see Fig. 3). This figure demonstrates, how the dead volume is influenced by the relation of the free column volume to the mass of immobile exchanger.

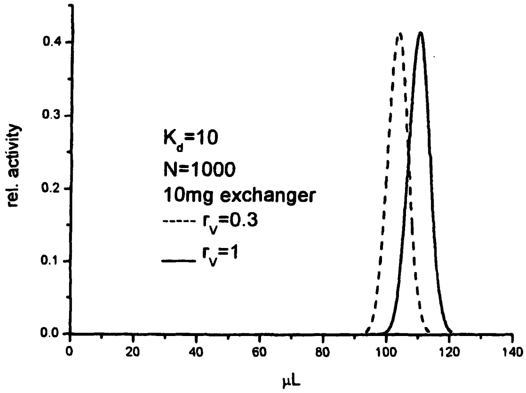

Figure 3. Comparison of different r_V*, resulting only in a shift of the elution curve due to different dead volumes.*

All following pictures were calculated with the mass of exchanger = 10 mg, and a dead volume of the column = 10 μL (corresponding to $r_V = 1$). A small BASIC program, given in the Appendix, is able to describe realistic elution curves. The integral eluted activity is collected in cell $a(N + 1)$. It is easy to display the activity distribution along the column, or the elution curves.

Figures 4 and 5 show some calculated curves for different K_d-values. The difference between Figs. 4 and 5 is the number of theoretical plates. One can see that the maximum of the elution curves is determined by K_d and N, while the shape depends on N only. A similarity with the Poisson curves from Ref. (*9*) is obvious; a numerical comparison shows that the elution curves can very well be described by:

$$A(V) = A_{max}\,\mu^{N-1}\exp(-\mu)\,/\,(N-1)! \quad \text{, with } \mu = (V - V_0)\,N\,/\,(m\,K_d)\,. \qquad (8)$$

Here, V is the eluted volume, m is the mass of the exchanger material, and V_0 is the dead volume of the column. The maximum of the Poisson curve is at $\mu_m = N - 1$; the median (*9*) (50 % of the activity is below, and 50 % above this point) is located at $\mu_m + 0.67$. This is one difference between the symmetric Gaussians, and the skewed Poisson curves. For the Gaussians, the maximum and the median are at the same position.

Downloaded by NORTH CAROLINA STATE UNIV on August 8, 2012 | http://pubs.acs.org
Publication Date: November 16, 2006 | doi: 10.1021/bk-2007-0945.ch019

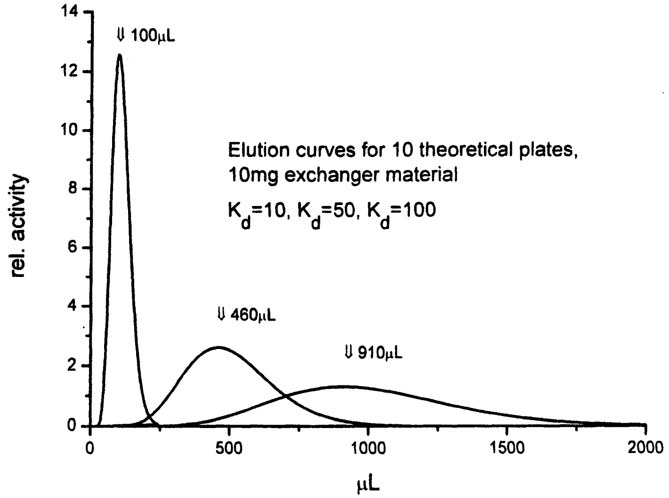

Figure 4. Elution curves for N=10 and different K_d values.

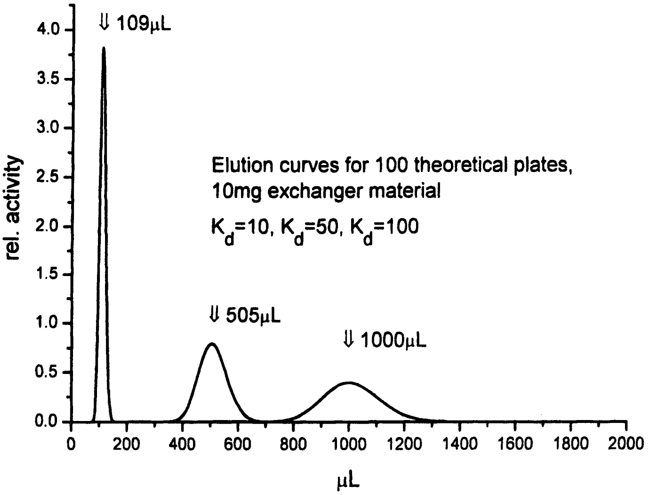

Figure 5. Elution curves for N=100 and different K_d values.

Downloaded by NORTH CAROLINA STATE UNIV on August 8, 2012 | http://pubs.acs.org
Publication Date: November 16, 2006 | doi: 10.1021/bk-2007-0945.ch019

One can determine the K_d value from the peak maximum of the Poisson curve using:

$$K_d = (V - V_0)\, N \,/\, (N-1)\, m\,. \tag{9}$$

The difference from the classical Eq. 1 is the factor $N/(N-1)$. For large N, this factor approximates unity and can be neglected.

In Fig. 6, one can see the influence of the number of theoretical plates N on the shape and position of the elution peaks, when the K_d value and the amount of exchanger material are kept constant. The "classical" peak would be at 110 μL. For $N = 5$, 10, and 100 one gets 90 μL, 100 μL, and 109 μL, respectively. If one has to determine K_d values from the peak position for $N > 100$, the corrections will normally be less than the experimental errors. For a better separation between similar substances, the N in nowadays analytical or gas chromatography columns is usually > 100000. However, this is not the case in fast radiochemical separations taking less than 5 s, using column dimensions of, *e.g.*, 1.6 mm i.d. × 8 mm long.

Downloaded by NORTH CAROLINA STATE UNIV on August 8, 2012 | http://pubs.acs.org
Publication Date: November 16, 2006 | doi: 10.1021/bk-2007-0945.ch019

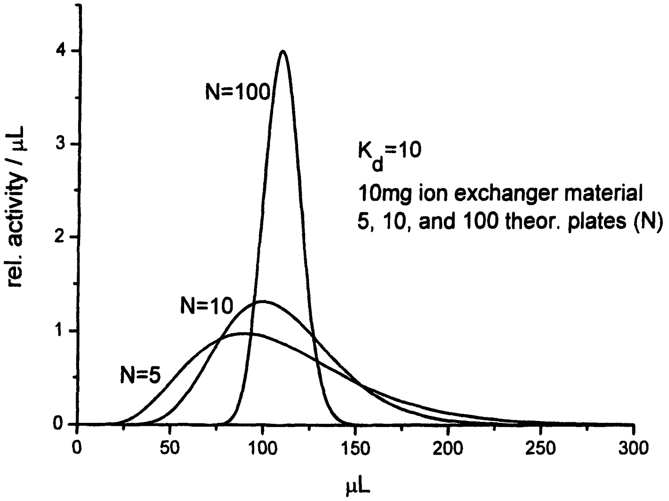

Figure 6. Simulation of different peak shapes with different numbers of theoretical plates N.

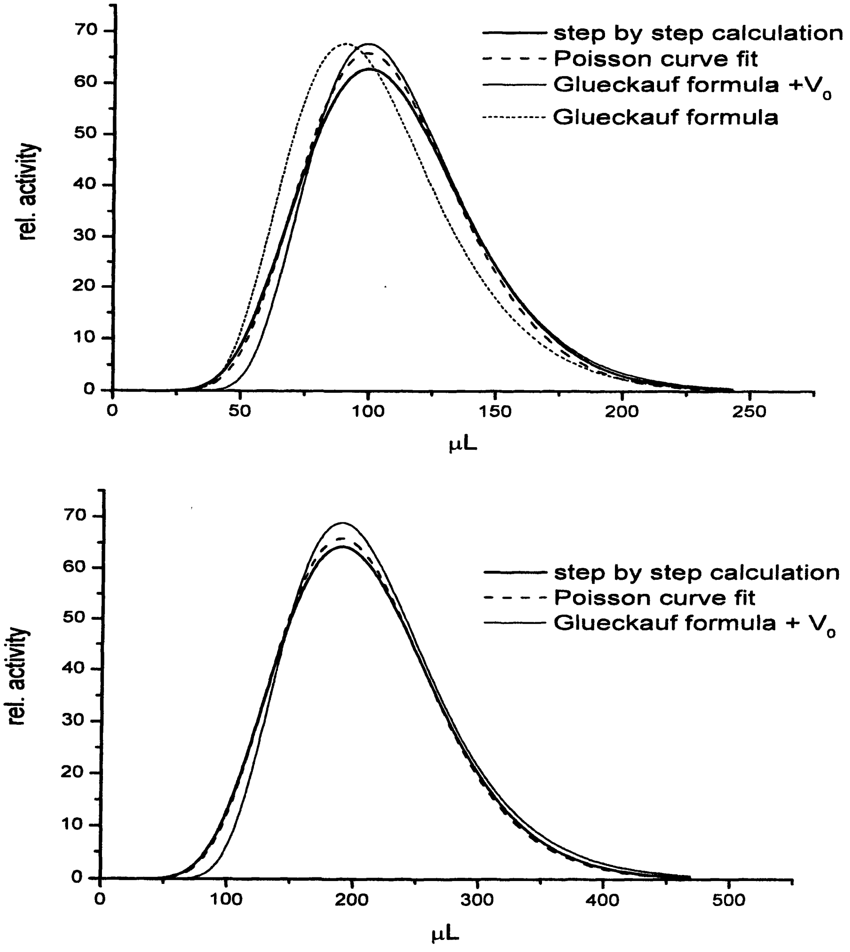

Figure 7. Comparison of different fit curves; Glueckauf's formula is illustrated with and without dead volume. Upper part: $K_d = 10$, $N = 10$, 10 mg ion exchanger material. Lower part: $K_d = 20$, $N = 10$, 10 mg ion exchanger material.

Figure 7 shows a comparison of the stepwise calculation by the program presented in this work, the Poisson-curve fit, and a fit by the Glueckauf equation, shifted by V_0. Glueckauf (*7*) did not use the "free column volume" and he thought it was only a result of the "discontinuous" treatment. To get a reasonable fit, however, one has to consider V_0 in continuous treatments as well

Downloaded by NORTH CAROLINA STATE UNIV on August 8, 2012 | http://pubs.acs.org
Publication Date: November 16, 2006 | doi: 10.1021/bk-2007-0945.ch019

as in discontinuous calculations (see Fig. 3). The higher the K_d values, the better the fits will match the exact calculation. The fits for higher K_d values and larger N are not easy to distinguish from each other.

Summary

It was shown that the chromatographic elution peaks can be well described by the Poisson curves. The position of the maximum as well as the peak width and shape is given by a single formula as a function of K_d value and the number of theoretical plates. In the limit of large numbers of theoretical plates, the formula is identical to the classical one describing elution peaks. The advantage of the new method is that it can also describe the elutions from short ion exchanger columns. For this case, the classical formulae give significant deviations when determining K_d values from the maximum of elution curves.

Acknowledgements

I would like to thank my colleagues: V. Pershina and M. Schädel for their careful reading of the manuscript and for their helpful comments. Last not least, I would like to express my appreciation for the authors of GFA BASIC, a program that has always satisfied my programming needs.

Appendix

Main Part of a BASIC Program to Simulate Elution Peaks

```
DIM a(10000)
INPUT "Kd, number of theor. plates";kd,n
INPUT "mg Exchangermaterial ";mg
INPUT "ratio of phases l/s";rv
a(1) = 1
REM all activity in first plate at start time
on_column = 1
kdiv = 1 - kd / (kd + rv)
v_p = mg * rv / n
REM v_p volume of one plate
DO
  FOR i = n DOWNTO 1
  REM start from last plate, going up
```

Downloaded by NORTH CAROLINA STATE UNIV on August 8, 2012 | http://pubs.acs.org
Publication Date: November 16, 2006 | doi: 10.1021/bk-2007-0945.ch019

```
    dif = a(i) * kdiv
    a(i) -= dif
    a(i + 1) += dif
  NEXT i
  REM one plate volume has passed the column
  INC n_p
  REM nr. of plate volumes
  vol = n_p * v_p
  REM microliters passing the column
  REM PLOT vol,a(n+1)
  REM plot activity leaving the column
  REM PLOT needs some scaling
  on_column -= a(n+1)
  a(n + 1) = 0
LOOP UNTIL on_column < .001
```

References

1. Martin, A. J. P.; Synge, R. L. M.; *Biochem J.* **1941**, *35*, 1358-1368
2. Giddings, J. C.; Eyring, H. *J. Phys. Chem.* **1955**, *59*, 416-421.
3. Cavazzini, A.; Remelli, M.; Dondi, F. *J. Micro Sep.* **1997**, *9*, 295-302.
4. Schädel, M. *Radiochim. Acta* **2001**, *89*, 721-728, and references therein.
5. Haba, H.; *et al. J. Am. Chem. Soc.* **2004**, *126*, 5219-5224.
6. Kronenberg, A.; *et al. Radiochim. Acta* **2004**, *92*, 379-386.
7. Glueckauf, E.; *Trans. Faraday Soc.* **1955**, *51*, 34-44.
8. Mayer, S. W.; Tompkins, E. R. *J. Am. Chem. Soc.* **1947**, *69*, 2866-2874.
9. Brüchle, W. *Radiochim. Acta* **2003**, *91*, 71-80.

Downloaded by NORTH CAROLINA STATE UNIV on August 8, 2012 | http://pubs.acs.org
Publication Date: November 16, 2006 | doi: 10.1021/bk-2007-0945.ch019

Downloaded by PENNSYLVANIA STATE UNIV on August 6, 2012 | http://pubs.acs.org
Publication Date: November 16, 2006 | doi: 10.1021/bk-2007-0945.ch020

Chapter 20

Problems with the Uncertainty Budget of Half-Life Measurements

S. Pommé

European Commission, Joint Research Centre, Institute for Reference Materials and Measurements, Retieseweg 111, B–2440 Geel, Belgium

The apparent tendency to underestimate the uncertainty of experimentally determined half-life values of radionuclides is discussed. It is argued that the uncertainty derived from a least-squares analysis of a decay curve is prone to error, as it does not sufficiently account for systematic deviations and medium frequency instabilities. As it is quite common for a series of activity measurement results to be autocorrelated, the prerequisite of randomness of data for common statistical tests to apply is not fulfilled. In this work, an attempt is made to provide an alternative data analysis method that leads to a complete and realistic uncertainty budget. A procedure is presented in which experimental uncertainties are subdivided into categories according to the rate at which they occur; i.e. at a low, medium or high frequency. All uncertainty components should be reported for traceability and evaluation purposes.

In Applied Modeling and Computations in Nuclear Science; Semkow, T., et al.;
ACS Symposium Series; American Chemical Society: Washington, DC, 2006.

Downloaded by PENNSYLVANIA STATE UNIV on August 6, 2012 | http://pubs.acs.org
Publication Date: November 16, 2006 | doi: 10.1021/bk-2007-0945.ch020

Nuclear data evaluators are frequently confronted with the problem of deriving a recommended value and an associated uncertainty from a discrepant set of data [see references in (*1*)]. This issue is particularly apparent in the case of half-lives of radionuclides. A recent evaluation shows that, for the majority of the radionuclides, the spread of experimentally determined half-life values is larger than expected from the claimed accuracies (*2*). Lack of reliable data leads to recommended values based on a few discrepant data, requiring subjective judgement of the evaluator to identify possible outliers and to adjust unbalanced weighting among the accepted data. The situation is often aggravated by experimenters providing insufficient detail on how the half-life and its uncertainty were determined. The latter is clearly underestimated in many cases. Whereas in recent years more attention is being paid to traceability of results and comprehensiveness of the uncertainty budget, there is no common procedure on how to achieve realistic uncertainties, or on a concise but complete reporting style.

One can identify two major ways to determine a half-life: by an absolute activity measurement of a known amount of radioactive material or by following the decay of a source. In this work we focus on the latter method, which is used for a major part of the radionuclides, excepting extremely long-lived ones. Besides experimental factors, such as the influence of impurities, background signals, detector stability, dead time, statistical fluctuations, etc. also the data analysis is considered as a source of error. In this work it is argued that the uncertainty obtained by least-squares fitting of an exponential to the data gives a false impression of accuracy in most cases. Presumably this is one of the reasons why claimed uncertainties on half-lives are often unrealistic. An attempt is made to demonstrate the mechanism that hides certain types of instability and a method to take them into account in the uncertainty budget.

Basic Uncertainty Equations

Two Activity Measurements

Consider the basic case in which the radioactive decay of a source is measured twice under similar conditions, yielding an activity A_1 and A_2 in the first and second measurement respectively. The duration of the measurements is relatively short and their reference times differ by an amount T. A purely exponential decay curve is assumed, hence the half-life follows from the activity ratio $R = A_1/A_2$ via

$$T_{1/2} = T\frac{\ln 2}{\ln R}. \quad (1)$$

The corresponding relative uncertainty is then

$$\frac{\sigma(T_{1/2})}{T_{1/2}}=\frac{1}{\ln R}\frac{\sigma(R)}{R}=\frac{1}{\lambda T}\frac{\sigma(R)}{R}=\frac{1}{\lambda T}\sqrt{\frac{\sigma^2(A_1)}{A_1^2}+\frac{\sigma^2(A_2)}{A_2^2}}\;, \qquad (2)$$

where the relative uncertainty of R is the (squared) sum of the relative uncertainties of the activities A_1 and A_2. Assuming the latter to be constant, the uncertainty on the half-life is inversely proportional with time (Eq. 2). Consequently, in order to reduce the uncertainty by a factor of two, one needs to double the decay time. This entails a linear relationship on a log-log scale, demonstrating that less and less is gained by continuing this experiment at great length. Eventually, more can be achieved by reducing the random and systematic uncertainties of the activity measurements.

Downloaded by PENNSYLVANIA STATE UNIV on August 6, 2012 | http://pubs.acs.org
Publication Date: November 16, 2006 | doi: 10.1021/bk-2007-0945.ch020

Additional Activity Measurements

In practice, multiple measurements are performed throughout the campaign, spanning a period T between the first and last. Usually, an exponential curve is fitted to the experimental data, yielding a best estimate of two unknown parameters: the activity A_0 at reference time and the half-life $T_{1/2}$. The goodness of the fit is often used as a criterion for the uncertainty. A possible procedure is the following (*3*): 1) calculate the χ^2-value, ensuring that it indeed assumes its expectation value (*i.e.*, the number of degrees of freedom); 2) adjust the half-life so that χ^2 increases by a value of one; 3) adopt as the standard deviation the square root of the amount by which the half-life was varied. Unfortunately, experience has shown that the resulting uncertainty may be unrealistic (*4*).

This procedure is only valid if the assumed exponential shape is rigorously applicable to the data, the deviations being of a stochastic nature and not prone to systematic deviations or patterns. An alternative way of uncertainty assessment will be derived now from some simplifying assumptions, starting from the basic Eq. 2. At this point we make a distinction between the different underlying sources of variation that make a data point deviate from the ideal decay curve. For convenience, they will be subdivided in low, medium and high frequency deviations.

- *High frequency deviations:* these sources of uncertainties occur at a rate that is higher than or comparable to the measurement time of one data point. A typical example would be counting statistics: Poisson processes are characterised by an exponential distribution of the interval times between successive events. By extending the measurement, one improves the statistical uncertainty on the actual count rate. Also ultra-high frequency instabilities, such as electronic noise, are included in this category. They are partly cancelled, though, by the 'integrating' effect of the duration of the measurement. Normal statistical treatments (like LSQ fitting) apply because of the preservation of randomness of the data.

- *Medium frequency deviations:* these instabilities show up (at least partly) as a trend in the residuals. They include the so-called 'seasonal effects' (*e.g.*, on a weekly basis or changing with the seasons of the year). Their effect is greatly underestimated if one simply relies on the goodness of the fit to the data. Moreover, a fit tends to minimise the residuals and partly covers up the true medium frequency effects. Typical examples include the interference by radioactive impurities, the reproducibility of the source-detector geometry and noticeable changes in the detector efficiency (*e.g.*, through temperature, pressure, humidity, electronic flaws).
- *Low frequency deviations:* these sources of uncertainties occur at a rate that is lower than or comparable to the duration of the whole measurement campaign. They remain practically invisible in the residuals, as the fit will compensate for this trend, hence erase it erroneously. Common problems in this range are systematic errors in the background subtraction and counter dead-time correction, long-term drift of the counting efficiency and source degradation (*e.g.*, oxidation of the source, mechanical wear, precipitation of active material in a solution).

Downloaded by PENNSYLVANIA STATE UNIV on August 6, 2012 | http://pubs.acs.org
Publication Date: November 16, 2006 | doi: 10.1021/bk-2007-0945.ch020

Including Instabilities in the Uncertainty Budget

Sensitivity to Instabilities

Figure 1 shows hypothetical residuals of a fitted decay curve to data showing high, medium and low frequency instabilities, respectively. The black dots represent the deviations of the data from the 'true' decay curve, the open circles show the deviations of the data from the fitted decay curve and the solid curve is the difference between the fitted and true decay curve. The experimentalist that performs the LSQ fit perceives only the hollow points. Considering that a slope equal to zero corresponds to the true half-life, one sees that the fitted slope shows in principle no bias with random deviations (high frequency), contrary to the medium and low frequency deviations. Whereas the experimentalist may still observe some 'seasonal' variations (medium frequency), he is unaware whether the LSQ adjustment of the fit has covered up major long-term effects (low frequency), resulting in a wrong half-life value. As the residuals give insufficient indications of these effects, he has to evaluate an exhaustive list of associated uncertainty components in the uncertainty budget.

Downloaded by PENNSYLVANIA STATE UNIV on August 6, 2012 | http://pubs.acs.org
Publication Date: November 16, 2006 | doi: 10.1021/bk-2007-0945.ch020

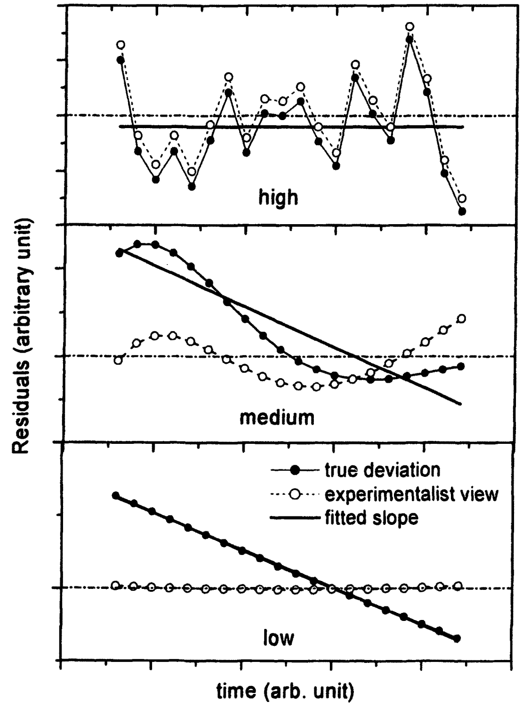

Figure 1. True (black dots) and perceived (hollow circles) residuals from a fit of a decay curve through hypothetical data affected by high (top), medium (middle) and low (bottom) frequency instabilities. Systematic deviations are not fully observed by the experimentalist, as the LSQ fit tends to minimize them.

Simplified Solution for High Frequency Deviations

Some simplifications are assumed for the sake of argument: the activity of a source, A_i ($i = 1,..,n$), is measured n times with an equal relative uncertainty, at regular intervals between time = 0 to T. The residuals of the fitted decay curve show only stochastic deviations due to high frequency deviations (*e.g.*, Poisson counting statistics). These are directly visible, hence can be accounted for without systematic bias.

The half-life of the decay curve, or alternatively the slope of a 'trend line' through the residuals, is primarily determined by the outer data points, respectively at the start and the end of the measurement campaign. If one doubles the number of measurements of A_1 and A_2 in Eq. 2, the uncertainty on

Downloaded by PENNSYLVANIA STATE UNIV on August 6, 2012 | http://pubs.acs.org
Publication Date: November 16, 2006 | doi: 10.1021/bk-2007-0945.ch020

$T_{1/2}$ is reduced by a factor of $\sqrt{2}$. Data points taken half-way through the campaign (*i.e.*, at $t = T/2$), do not influence the slope of the fitted curve. They only make the curve shift as a whole in the vertical direction. By approximation, one can assume that the relative impact of a measurement on the fitted half-life is proportional to the time difference with the middle, *i.e.*, $\sim | t - T/2 | /(T/2)$. Under the aforementioned conditions, and data points being spread somewhat evenly in time over the period T, the uncertainty on $T_{1/2}$ is well approximated by:

$$\frac{\sigma(T_{1/2})}{T_{1/2}} \approx \frac{2}{\lambda T}\left(\sum_{i=1}^{n}\left|\frac{2t_i}{T}-1\right|\right)^{-1/2}\frac{\sigma(A)}{A}. \tag{3}$$

More specifically, if the data are spread equidistantly in time, the reduction factor (for $n > 2$) is approximately equal to

$$\sqrt{\sum_{i=1}^{n}\left|\frac{2t_i}{T}-1\right|} = \sqrt{\sum_{i=0}^{n-1}\left|\frac{2i}{n-1}-1\right|} \approx \sqrt{\frac{n+1}{2}}, \tag{4}$$

resulting in a convenient uncertainty formula for the high-frequency component:

$$\frac{\sigma(T_{1/2})}{T_{1/2}} \approx \left\{\frac{2}{\lambda T}\sqrt{\frac{2}{n+1}}\right\}\frac{\sigma(A)}{A}, \tag{5}$$

in which one should assign a value of 3 to n in the case that $n < 3$.

Using Eq. 5, an evaluator as well as an experimenter can make a realistic estimate of the contribution of counting statistics to the half-life if three variables are available: the number of measurements, the duration of the campaign, and a measure of the uncertainty for a typical activity measurement.

Identification and Treatment of Medium Frequency Deviations

Medium frequency deviations may show up as systematic trends in the residuals of the fitted decay curve. They are partly obscured by data scatter due to high frequency instabilities and by the tendency of the fit to minimize the deviations. Identification and quantification of medium frequency effects require a sufficient amount of observations, at comparably small time intervals and preferably with low short term uncertainties, as *e.g.*, from the counting statistics.

An example is shown in Fig. 2, depicting residuals from a half-life determination of ^{55}Fe (*4*). The uncertainty bars pertain to counting statistics and background correction only. One clearly observes additional uncertainty components attributed to source repositioning and medium-term detection instabilities. Grouped data refer to holiday periods in which the source was not repositioned. Clearly such sources of variation create a non-random spread of data, hence they invalidate the uncertainty on the half-life provided by the LSQ fit. In the present example, the latter underestimates the uncertainty by about a factor of four. In the literature, one finds cases where medium frequency instabilities are clearly present, yet not properly taken into account.

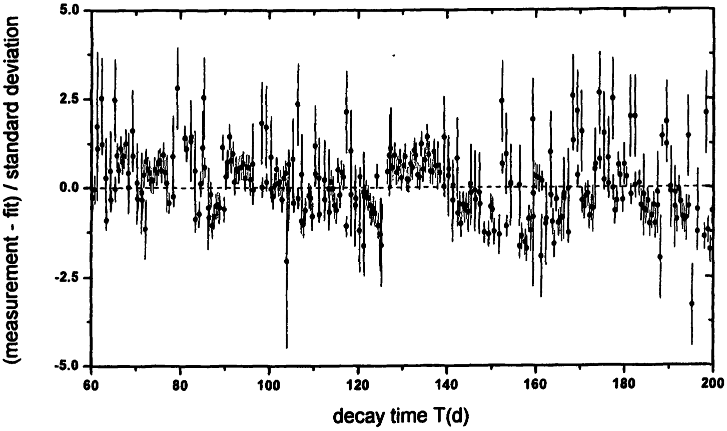

Figure 2. Residuals from the fit of an exponential decay curve to the measured activity of a ^{55}Fe source, relative to the overall standard deviation (4).

If the effects are less obvious than in Fig. 2, one can revert to an autocorrelation plot to check the randomness of the data. Such a plot is presented in Fig. 3 for the ^{55}Fe data (*4*) and also for a set of ^{65}Zn measurement data (*5*). Whereas the ^{65}Zn data show no significant autocorrelation, this is obviously not the case with the ^{55}Fe data.

The impact of medium frequency instabilities on the half-life uncertainty is difficult to quantify. There's the possibility of applying Eqs. 3 or 5, yet this requires the choice of a suitable value *n* for the number of occurrences of the considered effects; *e.g.*, when considering the contribution of the geometrical reproducibility one may set *n* equal to the number of times the source was repositioned. For a conservative approach, $n = 1$ is a safe assumption.

Taking into Account Low Frequency Deviations

Residuals offer practically no help with identifying systematic errors and slowly varying measurement conditions. It is left to the experimenter's expertise to produce an exhaustive list of potential problems, such as systematic errors involved with background subtraction (aside from its random component), changing system dead time conditions, long-term detector instability, source

Downloaded by PENNSYLVANIA STATE UNIV on August 6, 2012 | http://pubs.acs.org
Publication Date: November 16, 2006 | doi: 10.1021/bk-2007-0945.ch020

Downloaded by PENNSYLVANIA STATE UNIV on August 6, 2012 | http://pubs.acs.org
Publication Date: November 16, 2006 | doi: 10.1021/bk-2007-0945.ch020

degradation, structural changes to the set-up, *etc.* Again, one may apply Eqs. 3 and 5 with $n = 1$. The independent contributions are summed quadratically.

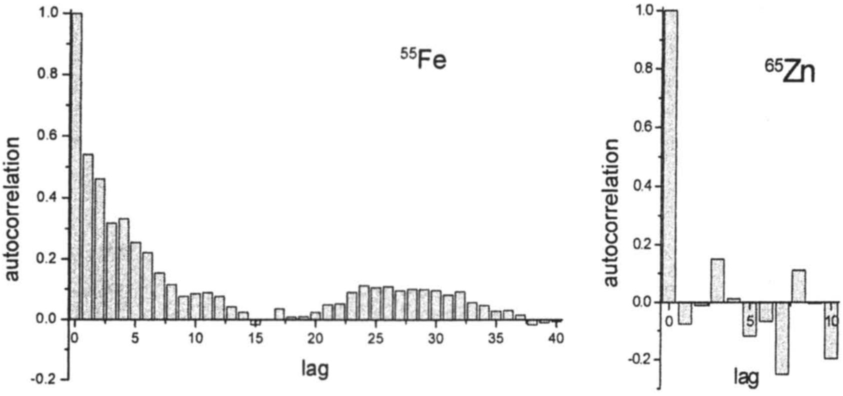

Figure 3. Autocorrelation plot of the residuals of a decay curve fit to ^{55}Fe (4) and ^{65}Zn (5) activity measurement results, respectively.

As an example, consider the error produced by applying a slightly incorrect correction for dead time of the extending type. The ratio R of the activities A_1 and A_2 at a time t_1 and t_2, respectively, is calculated from measured count rates r_1 and r_2 and a correction factor involving the characteristic dead time τ:

$$R = \frac{\rho_1}{\rho_2} = \frac{r_1}{r_2} e^{(\rho_1 - \rho_2)\tau}, \tag{6}$$

where ρ_1 and ρ_2 represent the true count rates (excluding count loss by dead time). Assuming that implicit use is made of an extending dead time $\tau + \Delta$, in which Δ is the absolute uncertainty on τ, one finds a relative uncertainty on the activity ratio of

$$\frac{\sigma(R)}{R} = 1 - e^{-(\rho_1 - \rho_2)\Delta} \approx (\rho_1 - \rho_2)\Delta = \frac{\Delta}{\tau}\left\{ \ln\left[\frac{T_R}{T_L}\right]_1 - \ln\left[\frac{T_R}{T_L}\right]_2 \right\}, \tag{7}$$

in which T_R and T_L represent the system real time and live time, respectively, and the ratio of both corresponds to the dead time correction factor used in the respective measurements. A similar analysis for non-extending dead time yields

$$\frac{\sigma(R)}{R} = 1 - \frac{1 - \rho_1\Delta}{1 - \rho_2\Delta} = \frac{\Delta}{\tau} \frac{\left[\frac{T_R}{T_L}\right]_1 - \left[\frac{T_R}{T_L}\right]_2}{1 - \frac{\Delta}{\tau}\left(\left[\frac{T_R}{T_L}\right]_2 - 1\right)}. \tag{8}$$

The propagation of these uncertainty components follows directly from insertion into Eq. 2.

An Aggregate of Uncertainty Components

A hypothetical uncertainty budget for the activity ratio R is presented in Fig. 4. In the example, the high and medium frequency components were assigned a value of 5 % and 1 % ($n = 1$), respectively, while the low frequency uncertainty was assumed to grow proportionally with time, by an amount of 2 % per decay constant. The graph shows that the main source of uncertainty moves from high to medium and then to low frequency instabilities. The corresponding half-life uncertainty generally decreases with time, because of the propagation factor $(\lambda T)^{-1}$ (Eq. 2). On the other hand, so does usually our grip on its size and origin.

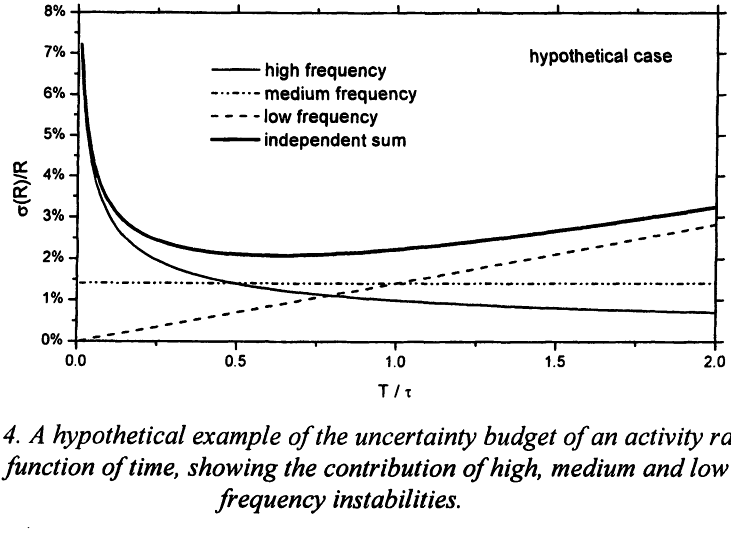

Figure 4. A hypothetical example of the uncertainty budget of an activity ratio as a function of time, showing the contribution of high, medium and low frequency instabilities.

An Alternative to Fitting

If the data points follow a single exponential decay curve, a fit is not required to determine the half-life. An alternative approach is to compare every observation with all previous ones and calculate the corresponding half-life value via Eq. 1. One obtains a distribution, like in Fig. 5, which is a superposition of Cauchy distributions with common maximum but different widths. The top (or

Downloaded by PENNSYLVANIA STATE UNIV on August 6, 2012 | http://pubs.acs.org
Publication Date: November 16, 2006 | doi: 10.1021/bk-2007-0945.ch020

weighted average value) corresponds to the most probable half-life value, in good agreement with the result from the fit.

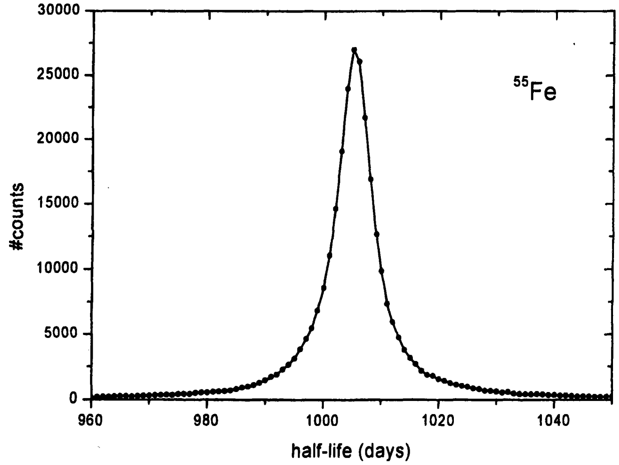

Figure 5. Distribution of half-life values obtained via Eq. 1 using a combination of all activity measurements of a ^{55}Fe source (4).

As data are being collected, one can follow the evolution of the calculated half-life. One should make sure that the deviations between final and intermediate results do not exceed the maximum boundaries allowed by the uncertainty budget. As an additional test, one can *e.g.*, randomize or invert the order of analysis of the data points. Fig. 6 shows the evolution of the intermediate half-life values obtained for ^{55}Fe. It includes one and two standard deviation boundaries (Eq. 5) for the high and medium frequencies combined, assuming the corresponding relative uncertainty on the activity to be 0.02 % (n = number of data analyzed) and 0.018 % ($n = 3$), respectively. Systematic errors and long term effects are not included, as they remain invisible.

Conclusions

Whereas two activity measurements of a radioactive source may in principle suffice to determine the half-life of the decaying radionuclide, it takes considerably more effort to assess the uncertainty on the resulting value. Experience shows that the uncertainty derived merely from a least-squares fit of an exponential decay curve to a sequential series of activity measurements is often suspect. This is partly attributed to observations being correlated over time,

Downloaded by PENNSYLVANIA STATE UNIV on August 6, 2012 | http://pubs.acs.org
Publication Date: November 16, 2006 | doi: 10.1021/bk-2007-0945.ch020

as the stability of the measurement process is to some extent disturbed by effects of various origin and duration. With respect to that, the analyst has to collect a sufficient amount of observations and check for their randomness, the latter being a prerequisite for the validity of statistical tests. Moreover, as long-term effects are mostly obscured by a fit, they have to be identified and scrutinized by other means. In this work, a simplified formula has been suggested to take the various effects and their rate of occurrence into account in the uncertainty budget.

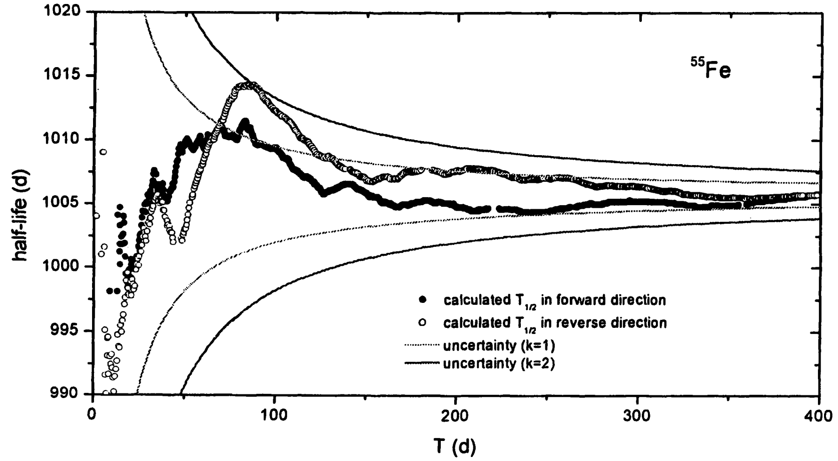

Figure 6. Intermediate results for the half-life of ^{55}Fe with time, analyzed in a forward and in a reverse time order. The uncertainty limits (k = 1 and 2) correspond to the independent sum of a 0.02 % and 0.018 % high and medium frequency component, respectively.

Downloaded by PENNSYLVANIA STATE UNIV on August 6, 2012 | http://pubs.acs.org
Publication Date: November 16, 2006 | doi: 10.1021/bk-2007-0945.ch020

References

1. MacMahon, D.; Pearce, A.; Harris, P. *Appl. Radiat. Isot.* **2004,** *60,* 275-281.
2. Woods, M. J.; Collins, S. M. *Appl. Radiat. Isot.* **2004,** *60,* 257-262.
3. Bevington, P. R. *Data Reduction and Error Analysis for the Physical Sciences*; McGraw-Hill: New York, NY, 1969.
4. Van Ammel, R.; Pommé, S.; Sibbens, G. *Appl. Radiat. Isot.*, in press.
5. Van Ammel, R.; Pommé, S.; Sibbens, G. *Appl. Radiat. Isot.* **2004,** *60,* 337-339.

Chapter 21

Evaluating Detection Limits for Environmental Monitoring Techniques in the Areas of Potential Impact from Nuclear Installations

A. N. Berlizov, M. O. Grygorenko, and V. V. Tryshyn

Institute for Nuclear Research, National Academy of Sciences of Ukraine,
47, Prospekt Nauki, MSP 03680, Kyiv, Ukraine

Downloaded by COLUMBIA UNIV on August 8, 2012 | http://pubs.acs.org
Publication Date: November 16, 2006 | doi: 10.1021/bk-2007-0945.ch021

It is shown that statistical nature of a monitored parameter requires re-formulation of a standard approach to the detection limit evaluation for the radioanalytical techniques used in the environmental monitoring studies, if the efficiency of the applied monitoring methods and techniques is a matter under consideration. Formulas for the detection limit calculations in this case were developed, which take into account log-normality of monitored parameters as well as the variability of the measurement conditions. Practical importance of the proposed approach is demonstrated on the example of the efficiency evaluation of the air-monitoring program in the vicinity of one of the Ukrainian NPPs.

Introduction

Environmental radiation monitoring plays a key role in ensuring *the non-exceeding* of the allowable limits of exposure of the members of public living in the areas affected by the radiation-dangerous objects. Standard monitoring programs apply a set of radioanalytical methods and techniques to analyze

In Applied Modeling and Computations in Nuclear Science; Semkow, T., et al.;
ACS Symposium Series; American Chemical Society: Washington, DC, 2006.

radioactivity content in a variety of environmental objects, being regularly sampled in different points of a monitored area according to the prescribed sampling schedule. This provides a comprehensive control over entry of radionuclides into environment and pathways of potential exposure of population, as shown in Fig. 1.

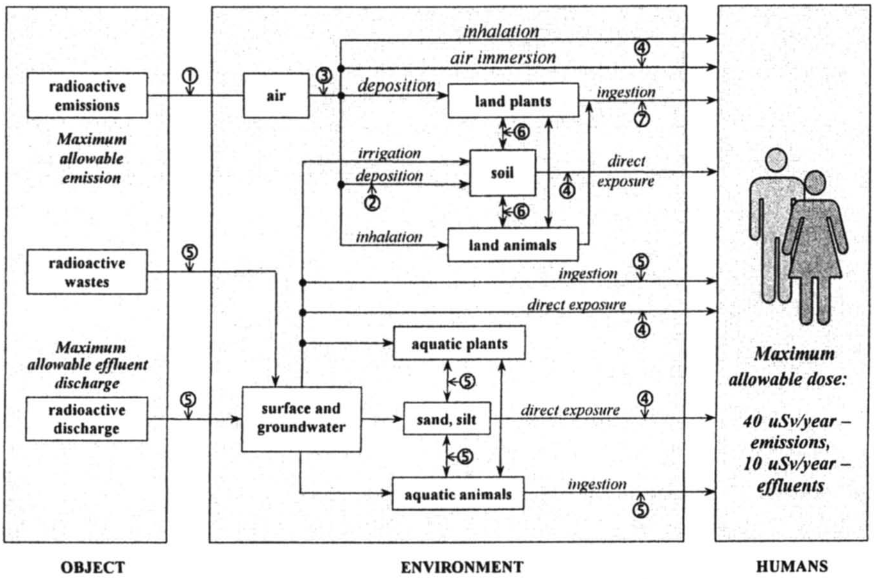
radioactive emissions
Maximum allowable emission
radioactive wastes
Maximum allowable effluent discharge
radioactive discharge
①
⑤
⑤
air
③
inhalation
air immersion
④
deposition
land plants
ingestion
⑦
⑥
irrigation
deposition
②
soil
direct exposure
④
⑥
inhalation
land animals
ingestion
⑤
direct exposure
④
aquatic plants
⑤
surface and groundwater
sand, silt
direct exposure
④
⑤
aquatic animals
ingestion
⑤
Maximum allowable dose:
40 uSv/year – emissions,
10 uSv/year – effluents
OBJECT
ENVIRONMENT
HUMANS

① - stack air-monitoring;
② - control of atmospheric depositions and precipitations;
③ - field air-monitoring;
④ - field dose and dose-rate measurements;
⑤ - control of discharged, natural and portable water, bottom sediments, aquatic plants and animals;
⑥ - radioactivity measurements in soil and land plants;
⑦ - control of local agriculture products.

Figure 1. Environmental monitoring versus potential pathways of the population exposure.

The fundamental question, which might be asked, is how efficient and adequate are the applied analytical tools with respect to the ultimate function of the environmental monitoring? To answer it on a quantitative basis one should use a kind of indicator, which would reflect capabilities of employed methods and techniques for detecting radioactive releases of a monitored object on a given confidence level. One of the most appropriate indicators is the minimum detectable activity *MDA*, which is related to the detection limit L_D by means of Eq. 1:

Downloaded by COLUMBIA UNIV on August 8, 2012 | http://pubs.acs.org
Publication Date: November 16, 2006 | doi: 10.1021/bk-2007-0945.ch021

$$MDA = L_D \mu_X^{-1} . \quad (1)$$

Here μ_X is the expectation value of a calibration coefficient X, which establishes a relation between net-signal S and monitored parameter A (concentration of particular radionuclide in analyzed environmental object)

$$S = XA. \quad (2)$$

Comparing *MDAs* with controlled parameter values, which are to be predicted for the location of a given monitoring station and particular critical level of radioactive emission or effluent discharge, would allow judging about the efficiency of one or another monitoring method.

It must be noted that, owing to statistical nature of radioactive releases and stochasticity of their transport in the environment, monitored parameters should be considered as essentially random quantities ($A \neq$ deterministic). Similarly, variability of the sample treatment and measurement conditions makes the calibration coefficient random ($X \neq$ deterministic) as well. Thus, statistical properties of a measured net signal are subject not only to the counting statistics, but also to the statistical properties of parameters A and X (see Eq. 2).

Calculation of L_D and *MDA* in this situation requires a special consideration, which is presented in the next section of the chapter. Another section demonstrates applicability of the obtained working expressions to the efficiency evaluation of the air-monitoring program in the vicinity of one of the Ukrainian NPPs.

Deriving Working Formulas

To derive working expressions we will follow Currie's approach (*1*), which sets the basis of the present-day methodology (*2,3*) for the estimation of the detection limits and decision thresholds for the ionizing radiation measurements. According to this approach L_D is completely determined by the statistics of a net signal estimate m_S

$$m_S = S + B - m_B, \quad (3)$$

where B and m_B are the background signal and its estimate respectively, and can be obtained by solving the following equation

$$L_D = K_{1-\alpha}(\mu_S = 0)\sqrt{D(m_S;\mu_S = 0)} + \left|K_\beta(\mu_S = L_D)\right|\sqrt{D(m_S;\mu_S = L_D)} . \quad (4)$$

Here $\mu_S = \mu_X \mu_A$ is the expectation value of a net signal, μ_A is the expectation value of a monitored parameter, $D(m_S)$ is the variance of the estimate m_S, $K_{1-\alpha}$ and K_β are the quantiles of the distribution of a normalized random variable

$$\omega = \frac{m_S - \mu_S}{\sqrt{D(m_S)}}, \quad (5)$$

Downloaded by COLUMBIA UNIV on August 8, 2012 | http://pubs.acs.org
Publication Date: November 16, 2006 | doi: 10.1021/bk-2007-0945.ch021

calculated for the confidence probabilities $1 - \alpha$ and β, where α and β are the probabilities of errors of the first and second kind respectively (*4*). The first summand in Eq. 4 is estimated for the situation when the net signal expectation value is zero, while the second - when it equals L_D.

Using standard statistical methods, one can derive the following formula for the variance of a net signal estimate

$$D(m_S) = \sigma^2_{m_S} = \mu_S + 2m_B + \mu_S^2(cv_X^2 + cv_A^2 + cv_X^2 cv_A^2), \qquad (6)$$

where $cv_X = \sigma_X / \mu_X$ and $cv_A = \sigma_A / \mu_A$ are the coefficients of variation of X and A respectively. This formula was developed assuming Poisson statistics for the detected net and background number of counts and using standard formula for the variance of a product of two random quantities. Besides, it was assumed that $D(B) \approx D(m_B) \approx m_B$. If this assumption does not hold then term $2m_B$ in all subsequent formulas should be replaced by an appropriate estimate of the sum $D(B) + D(m_B)$.

Based on the relations between quantities X, A, S, B, and m_B, which are set by Eqs. 2 and 3, one can find the following formula for the probability distribution function of the random variable ω

$$F(\omega) = \int_{-\infty}^{+\infty} \Phi\left(\frac{\omega - \mu(u)}{\sigma(u)}\right) \Psi(u)\, du, \qquad (7)$$

where $\mu(u) = \dfrac{\mu_S(u-1)}{\sigma_{m_S}}$, $\sigma(u) = \dfrac{(u\mu_S + 2m_B)}{\sigma^2_{m_S}}$, $\Phi(x) = \dfrac{1}{\sqrt{2\pi}} \displaystyle\int_{-\infty}^{x} e^{-t^2/2} dt$.

Function $\Psi(u)$ is defined by the following formula

$$\Psi(u) = \int_0^{+\infty} N\left(\frac{u}{v}; 1, cv_X\right) L(v; r, s) \frac{dv}{v}. \qquad (8)$$

Here $N(x;1,cv_X)$ is the normal probability density function with unit mean and standard deviation cv_X, and $L(x;r,s)$ is the log-normal probability density function

$$L(x; r, s) = \frac{1}{xs\sqrt{2\pi}} \exp\left(-\frac{(\log(x) - r)^2}{2s^2}\right), \qquad (9)$$

with $r = -0.5s^2$ and $s^2 = \log(1 + cv_A^2)$. Eqs. 7 and 8 were derived assuming that variables S, B, and m_B are normally-distributed with typical for Poisson distribution relation between their variances and expected values ($\sigma^2 = \mu$). Statistical properties of the calibration coefficient were also assumed to follow the normal law $N(\mu_X, \sigma_X)$, whereas a log-normal probability density function $L(\log(\mu_A) + r, s)$ was used for the monitored parameter. The last choice is supported by the theoretical considerations (*5,6*) as well as by the results of numerous experimental studies of both statistical properties of pollutant

Downloaded by COLUMBIA UNIV on August 8, 2012 | http://pubs.acs.org
Publication Date: November 16, 2006 | doi: 10.1021/bk-2007-0945.ch021

concentrations near the emission sources and statistical properties of the emissions themselves.

Note, that if the monitored parameter and calibration coefficient do not vary (*i.e.*, $\sigma_A = 0$ and $\sigma_X = 0$), then $\Psi(u) = \delta(u - 1)$ and $F(\omega)$ turns to $\Phi(\omega)$. Here $\delta(u - 1)$ is the Dirac delta function. In this case the quantiles in Eq. 4 are the quantiles of a standard normal distribution function $K_{1-\alpha} = k_{1-\alpha} = |k_\alpha|$, $K_\beta = k_\beta$ and, by solving Eq. 4, one can obtain a standard Currie's formula (*1*) for the detection limit:

$$(L_D)_{Currie} = L_C + \frac{k_\beta^2}{2}\left\{1 + \left[1 + \frac{4L_C}{k_\beta^2} + \frac{4L_C^2}{k_\beta^2 k_\alpha^2}\right]^{1/2}\right\}, \qquad (10)$$

where $L_C = k_{1-\alpha}\sqrt{2m_B}$ is a so-called critical level, or decision threshold.

When expectation value of the monitored parameter equals zero ($\mu_A = 0$, $\sigma_A = 0$) or, which is equivalent, the expectation value of the net signal is zero ($\mu_S = 0$), one can easily come to the formula $F(\omega) = \Phi(\omega)$ and, consequently, $K_{1-\alpha}(\mu_S = 0) = k_{1-\alpha} = |k_\alpha|$. Let us denote

$$k'_\beta = K_\beta(\mu_S = L_D) = \left[F^{-1}(\beta)\right]_{\mu_S = L_D}, \qquad (11)$$

where the superscript –1 indicates the inverse function. Then, the solution of Eq. 4 can be written as follows

$$L_D = \frac{L_C}{V} + \frac{k'^2_\beta}{2V}\left\{1 + \left[1 + \frac{4L_C}{k'^2_\beta} + \frac{4L_C^2 W}{k'^2_\beta k_\alpha^2}\right]^{1/2}\right\}, \qquad (12)$$

where $V = 1 - k'^2_\beta t^2$, $W = 1 + (k_\alpha^2 - k'^2_\beta)t^2$, and $t^2 = cv_X^2 + cv_A^2 + cv_X^2 cv_A^2$. If $t = 0$, which means no variation in both the monitored parameter and the calibration coefficient values, the detection limits determined by Eq. 10 and Eq. 12 coincide. At $t \neq 0$ the inequality $L_D > (L_D)_{Currie}$ is always true. It should be noted that Eqs. 11 and 12 represent a system of equations, which should be solved to evaluate L_D and k'_β in the most general case.

In order to derive a ready-to-use formula, numerical calculations were done for a practically important case $cv_A >> cv_X$. Under this condition one can assume $\Psi(u) \approx L(u;r,s)$; this provides significant simplification of the calculations since only a single integration is required for finding $F(\omega)$. Particular calculations were performed for the background signal m_B ranging from 10 to 10^6, the coefficient of variation of the monitored parameter cv_A ranging from 0.1 to 2.5, and for the equal probabilities of the error of the first and second kind $\beta = \alpha$ ranging from 0.005 to 0.05.

Downloaded by COLUMBIA UNIV on August 8, 2012 | http://pubs.acs.org
Publication Date: November 16, 2006 | doi: 10.1021/bk-2007-0945.ch021

Downloaded by COLUMBIA UNIV on August 8, 2012 | http://pubs.acs.org
Publication Date: November 16, 2006 | doi: 10.1021/bk-2007-0945.ch021

The calculation results showed that k'_β practically does not depend upon m_B as its value varied by less than 3 % of magnitude for m_B ranging from 10 to 10^6 at fixed arbitrary values of cv_A and α being chosen within the above indicated intervals. So k'_β is considered to depend only upon the parameters β and cv_A. Based on the carried out calculations, the following parameterization for k'_β when $\beta = \alpha$ can be proposed

$$k'_\beta = k_\beta \left[1+(b_1\, e^{-\beta/t_1} + b_2\, e^{-\beta/t_2})\, cv_A^{t_3}\right]^{-1}. \qquad (13)$$

The coefficient values in this formula are as follows: $b_1 = 1.58904$, $b_2 = 0.61567$, $t_1 = 0.12288$, $t_2 = 0.00753$, and $t_3 = 1.2$. Accuracy of the parameterization is better than 3 %. Eqs. 12 and 13 present a practical approach to calculating the detection limits for a wide range of variation of the monitored parameter values, if variation of the calibration coefficient is negligible and $\beta = \alpha$.

Figure 2a shows the dependence of the ratio k'_β / k_β, upon the coefficient of variation cv_A, calculated using Eq. 13 for different values of probability β. Figure 2b shows the ratio $L_D / (L_D)_{Currie}$ as a function of the background signal value, calculated for different values of the coefficient of variation cv_A. The presented graphs demonstrate importance of taking into account the variation of the monitored parameter for obtaining correct estimates for the detection limits of radioanalytical techniques used in environmental monitoring studies.

Application Example

The derived expressions were applied to the analysis of efficiency of the air-monitoring program in the vicinity of Khmel'nits'kiy NPP (KhNPP), which is located in the northwest part of Ukraine. There are eight permanent air-monitoring stations installed in the monitored area of KhNPP. Location of the stations is schematically shown in Fig. 3. Each station is equipped with a high-volume air-sampler "Typhoon-4" with maximum airflow capacity 1000 cubic meters per hour. Air-samplers are operated continuously with filter changing every ten days. The gross beta activity is measured on every sample by radiometry, while gamma-emitters and Sr-90 are determined on quarterly combined samples using semiconductor gamma-spectrometry and radiometry of the radiochemically pre-treated samples respectively.

The air-monitoring program efficiency analysis consisted of several steps. Firstly, expectation values of the calibration coefficients μ_X were estimated for each controlled parameter based on the characteristics of applied analytical equipment and analysis technique. For instance, the calibration coefficients for gamma-spectrometry measurements were evaluated using formula

$$\mu_X = v_0\, n\, \varepsilon(E)\, p_\gamma\, \tau_1\tau_3 f_1(\lambda\tau_1) f_2(\lambda\tau_2) f_1(\lambda\tau_3), \qquad (14)$$

Downloaded by COLUMBIA UNIV on August 8, 2012 | http://pubs.acs.org
Publication Date: November 16, 2006 | doi: 10.1021/bk-2007-0945.ch021

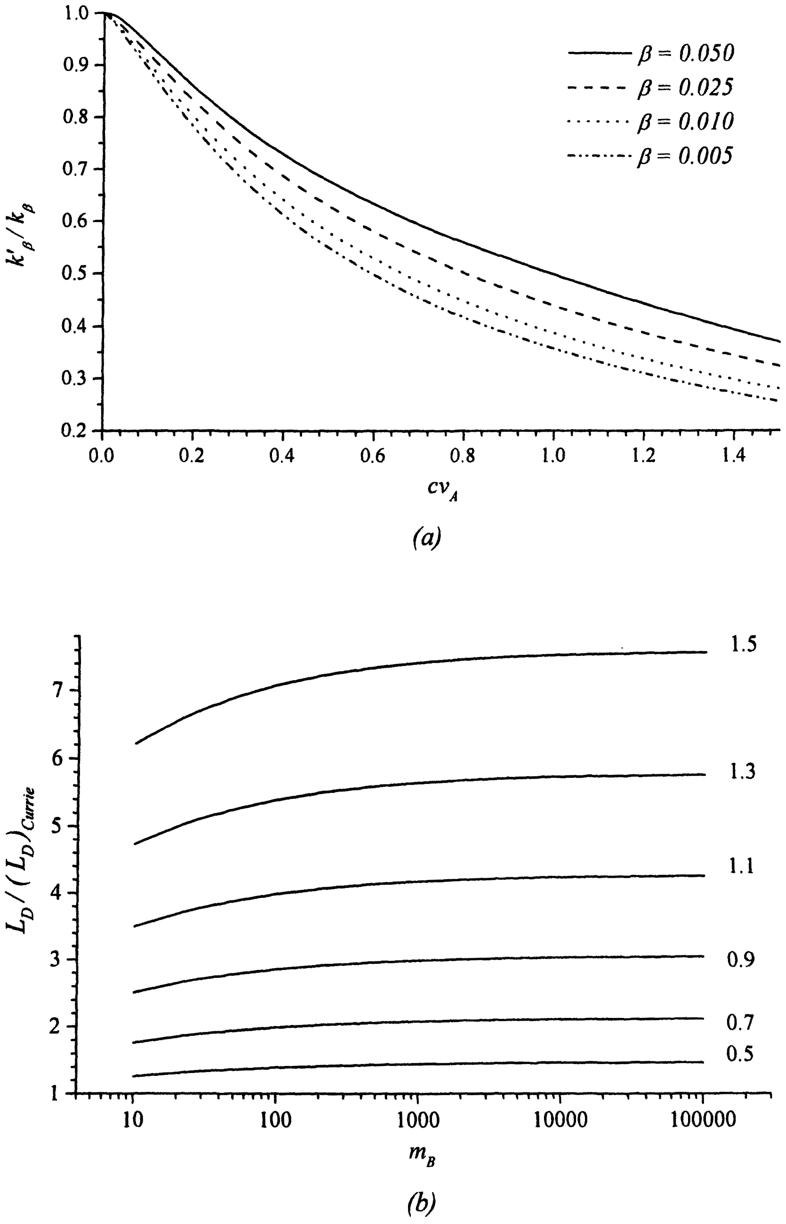

Figure 2. (a) - quantile ratio as a function of the variation of the controlled parameter; (b) - ratio of detection limits as a function of the background signal value (numbers indicate values of cv_A, calculations were done for $\alpha = \beta = 0.025$).

Downloaded by COLUMBIA UNIV on August 8, 2012 | http://pubs.acs.org
Publication Date: November 16, 2006 | doi: 10.1021/bk-2007-0945.ch021

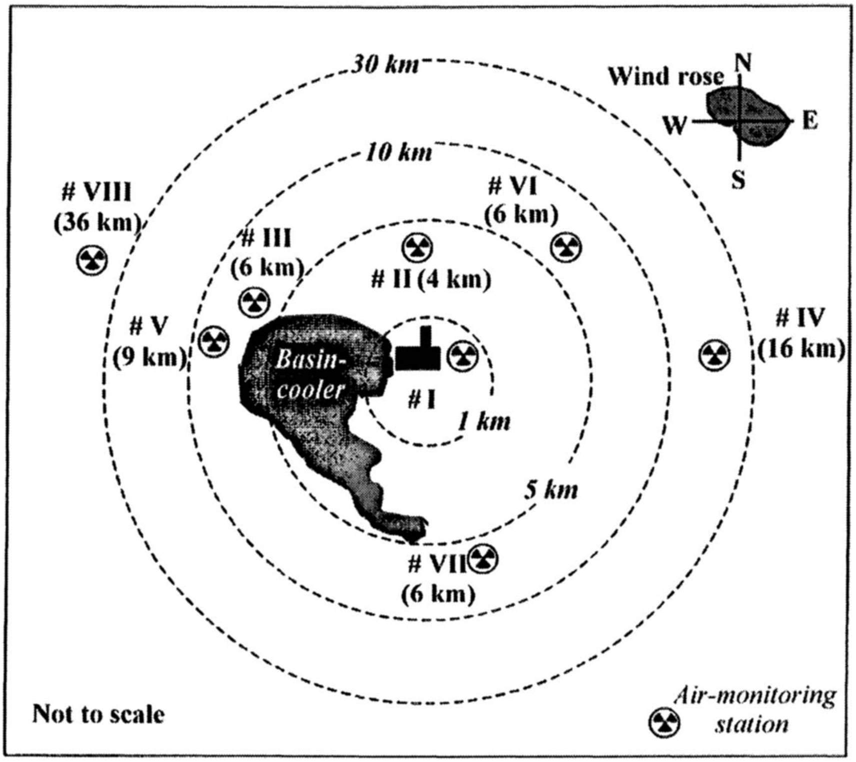

Figure 3. Location of the air-monitoring stations in the vicinity of KhNPP.

where v_0 is the airflow capacity of a sampler, n is the number of combined filters, $\varepsilon(E)$ is the full energy peak efficiency for gamma-rays with energy E, p_γ is the gamma-ray yield per decay of a radionuclide of interest, λ is the decay constant of a radionuclide, τ_1 is a cumulative length of the filter exposure period (a quarter), τ_2 is the time elapsed since the end of the exposure period till the measurement start, τ_3 is the filter measurement time interval. Functions $f_1(x) = (1 - \exp(-x)) / x$ and $f_2(x) = \exp(-x)$ take into account decay of radionuclides during τ_1, τ_2, and τ_3 intervals.

After that, based on the statistical analysis of the long-term emission measurement data, a component cv_{A1} of the coefficient of variation of the monitored parameter related to the emission source statistics was evaluated. Its value was found to be about 0.8 for the emission of long-lived radionuclides in power-generation operating mode of the KhNPP (*7*).

Next, using a developed stochastic atmospheric dispersion model (*8*) the component cv_{A2} of the coefficient of variation was computed for each monitoring station and each monitored parameter. This component is due to the variability of the atmospheric conditions, which are specific to the KhNPP location region. Depending upon the distance to the monitoring station and its azimuth with respect to the emission source, the values of cv_{A2} ranged from 30 % to 70 % and from 70 % to 100 % for quarter and ten-day exposure periods respectively. The cumulative coefficients of variation for the monitored parameters were found as $cv^2_A = cv^2_{A1} + cv^2_{A2}$.

The background signal value m_B was estimated for each monitored parameter taking into account background conditions at the locations of the air-monitoring stations and in the measurement room. The first one was essential for ^{137}Cs and ^{90}Sr radionuclides as the KhNPP location area was subject to radioactive contamination due to the Chernobyl NPP accident. For gamma-spectrometry measurements an additional background component, related to the Compton continuum under analyzed full energy peaks, was evaluated on the basis of real measured spectra, which were provided by KhNPP's external dosimetry service.

The *MDA* values were calculated by means of Eqs. 1, 12, and 13 for two values of the probability $\alpha = 0.01$ and 0.05. The obtained *MDA* values were compared with predicted concentrations of the monitored radionuclides *C* in the near surface atmospheric air, which were computed with the help of CAP-88PC program (*9*) for the specified radionuclide composition and rates of the aerosol emissions. The last ones were chosen to be 5 mCi/day for ^{131}I and 7.5 mCi/day for the sum of the other long-lived radionuclides, which correspond to the authorized control limits of emissions. The control was considered as satisfactory - if $MDA_{0.01} < C$, acceptable - if $MDA_{0.05} < C \leq MDA_{0.01}$, and unacceptable - if $C \leq MDA_{0.05}$.

Results of the performed calculations are presented in Tables I and II. Shaded numbers indicate that the control with the corresponding probabilities of the error of the first and second kind is not possible. The presented data show that gamma-spectrometry of quarterly combined samples provides satisfactory control of the KhNPP emissions for a group of radionuclides, including ^{51}Cr, ^{54}Mn, ^{58}Co, ^{60}Co, ^{134,137}Cs, and ^{131}I, all over 30-km monitored area. Gamma-spectrometry measurements of concentration of such radionuclides as ^{60}Co, ^{134,137}Cs, and ^{131}I provide also satisfactory control in the background monitoring station VIII, which is situated outside the monitored area.

Gross beta activity measurements also provide sufficiently effective monitoring of the radiation situation all over the monitored area. Whereas measurement of ^{90}Sr concentration turned out to be uninformative and can be excluded from the radiation monitoring program without any significant loss in its efficiency, at least for the normal operating conditions of KhNPP's power unit. It should be noted that the main cause for this is that the monitored area is characterized by the elevated levels of ^{90}Sr pollution that resulted from the Chernobyl fallouts.

Downloaded by COLUMBIA UNIV on August 8, 2012 | http://pubs.acs.org
Publication Date: November 16, 2006 | doi: 10.1021/bk-2007-0945.ch021

Downloaded by COLUMBIA UNIV on August 8, 2012 | http://pubs.acs.org
Publication Date: November 16, 2006 | doi: 10.1021/bk-2007-0945.ch021

Table I. Minimal Detectable Activity Values for the Control of KhNPP Emissions by Measuring Gross β-Activity and ^{90}Sr Concentration Levels in the Near Surface Atmospheric Air Versus Predicted Concentrations of Radionuclides in the Vicinity of Different Air-Monitoring Stations

Monitoring Station	*$MDA_{0.05}$, μBq/m^3*	*$MDA_{0.01}$, μBq/m^3*	*C, μBq/m^3*
	Gross β-activity		
I	12	26	96
II	14	30	100
III	16	39	32
IV	14	30	26
V	16	39	21
VI	14	30	54
VII	17	43	44
VIII	16	39	5.4
	^{90}Sr concentration		
I	0.15	0.29	0.14
II	0.18	0.34	0.16
III	0.19	0.41	0.051
IV	0.18	0.37	0.045
V	0.21	0.43	0.035
VI	0.18	0.37	0.085
VII	0.20	0.41	0.069
VIII	0.21	0.44	0.010

Downloaded by COLUMBIA UNIV on August 8, 2012 | http://pubs.acs.org
Publication Date: November 16, 2006 | doi: 10.1021/bk-2007-0945.ch021

Table II. Minimal Detectable Activity Values, μBq/m^3, for the Concentration of Different Radionuclides in the Atmospheric Air, Determined by the Gamma-Spectrometry of Quarterly Combined Samples, Versus Predicted Radionuclide Concentrations, μBq/m^3, in the Vicinity of the Air-Monitoring Stations

Nuclide & Parameter		*Monitoring Station*							
		I	*II*	*III*	*IV*	*V*	*VI*	*VII*	*VIII*
^{51}Cr	MDA$_{0.05}$	1.5	1.7	1.9	1.8	2.1	1.8	1.9	2.1
	MDA$_{0.01}$	2.9	3.5	4.1	3.5	4.1	3.5	4.1	4.4
	C	26	29	9.7	8.2	6.3	16	13	1.9
^{54}Mn	MDA$_{0.05}$	0.18	0.20	0.22	0.20	0.24	0.21	0.23	0.24
	MDA$_{0.01}$	0.33	0.41	0.47	0.41	0.50	0.41	0.47	0.50
	C	4.4	5.1	1.7	1.4	1.1	2.8	2.3	0.34
^{58}Co	MDA$_{0.05}$	0.17	0.19	0.20	0.19	0.22	0.19	0.21	0.22
	MDA$_{0.01}$	0.31	0.38	0.44	0.38	0.47	0.39	0.44	0.47
	C	2.5	2.8	0.90	0.78	0.61	0.15	1.2	0.18
^{59}Fe	MDA$_{0.05}$	0.34	0.39	0.42	0.39	0.45	0.39	0.43	0.45
	MDA$_{0.01}$	0.63	0.78	0.89	0.78	0.95	0.82	0.89	0.96
	C	0.37	0.44	0.14	0.12	0.095	0.23	0.19	0.028
^{60}Co	MDA$_{0.05}$	0.21	0.25	0.26	0.25	0.29	0.25	0.27	0.29
	MDA$_{0.01}$	0.40	0.49	0.56	0.49	0.60	0.52	0.56	0.60
	C	13	14	4.6	4.1	3.1	7.6	6.2	0.93
^{95}Zr	MDA$_{0.05}$	0.17	0.19	0.21	0.20	0.23	0.20	0.22	0.23
	MDA$_{0.01}$	0.32	0.39	0.45	0.39	0.47	0.39	0.45	0.48
	C	0.48	0.54	0.18	0.15	0.12	0.29	0.23	0.035
^{134}Cs	MDA$_{0.05}$	0.25	0.28	0.31	0.28	0.33	0.28	0.31	0.33
	MDA$_{0.01}$	0.46	0.57	0.65	0.57	0.65	0.57	0.65	0.70
	C	17	19	6.1	5.2	3.9	10	8.1	1.2
^{137}Cs	MDA$_{0.05}$	0.50	0.57	0.64	0.60	0.66	0.60	0.64	0.69
	MDA$_{0.01}$	0.96	1.2	1.4	1.2	1.4	1.2	1.4	1.5
	C	27	30	9.9	8.5	6.7	16	13	2.0
^{140}Ba	MDA$_{0.05}$	0.17	0.19	0.21	0.20	0.22	0.20	0.21	0.22
	MDA$_{0.01}$	0.31	0.39	0.44	0.41	0.47	0.41	0.44	0.50
	C	0.44	0.51	0.17	0.14	0.11	0.28	0.22	0.033
^{131}I	MDA$_{0.05}$	0.17	0.19	0.22	0.20	0.23	0.20	0.22	0.24
	MDA$_{0.01}$	0.33	0.40	0.46	0.40	0.46	0.40	0.46	0.50
	C	78	80	21	16	13	38	32	1.9

Conclusions

The formulas were developed for evaluating detection limits and minimum detectable activities of radioanalytical techniques used at the environmental monitoring in the areas affected by the radiation-emitting installations. The essential feature of the obtained formulas is that they take into account the variation of the monitored parameters as well as the variation of the measurement conditions, which can significantly influence the probability of detection of radioactive emissions and effluent discharges on the results of the radionuclide content determination in different environmental objects.

The obtained formulas set the basis for the analysis of the efficiency and adequacy of methods and techniques used in environmental monitoring. As it was shown in the example of the air-monitoring program in the area of the potential impact of one of the Ukrainian NPPs, such analysis provides opportunities for the optimization of radiation monitoring systems with regard to numbers and types of monitored parameters. This approach can be also applied to the optimization of the performance of employed sampling equipment and analytical techniques, choosing optimal locations of the monitoring stations as well as to the development of efficient sampling schedules.

Downloaded by COLUMBIA UNIV on August 8, 2012 | http://pubs.acs.org
Publication Date: November 16, 2006 | doi: 10.1021/bk-2007-0945.ch021

References

1. Currie, L. A. *Anal. Chem.* **1968**, *40*, 586-593.
2. *Limit of Detection and Limit of Decision for Nuclear Radiation Measurements* – Part 5: *Counting Measurements by High-Resolution Gamma Spectrometry, Neglecting the Influence of Sample Treatment*; DIN 25482-5: 1993-06.
3. *Determination of the Detection Limit and Decision Threshold for Ionizing Radiation Measurements* – Part 3: *Fundamentals and Application to Counting Measurements by High Resolution Gamma Spectrometry, without the Influence of Sample Treatment*; ISO/FDIS 11929-3: 1999(E).
4. Bendat, J. S.; Piersol, A. G. *Random Data Analysis and Measurement Procedures*; John Wiley & Sons: New York, NY, 1986, pp. 99-106.
5. Ott, W. R. *J. Air Waste Man. Assoc.* **1990**, *40*, 1378-1383.
6. Limpert, E.; Stahel, W.A.; Abbt, M. *BioScience*, **2001**, *51*, 341-352.
7. Berlizov, A. N.; Grygorenko, M. A.; Tryshyn, V. V. *Atomic Energy* **2005**, in press.
8. Berlizov, A. N.; Grygorenko, M. A.; Tryshyn, V. V. Institute for Nuclear Research, unpublished.
9. B. S. Parks. *User's Guide for CAP88-PC*; EPA 402-B-92-001, March 1992.

Downloaded by CORNELL UNIV on August 6, 2012 | http://pubs.acs.org
Publication Date: November 16, 2006 | doi: 10.1021/bk-2007-0945.ch022

Chapter 22

New Approach for the Decision Level and the Detection Limit in Paired Counting When There Is Uncertainty Concerning the Expected Blank Count

W. E. Potter

1008 Tenth Street, PMB #492, Sacramento, CA 95814

For paired counting, utilizing modified Bessel functions of integer order, Neyman-Pearson confidence intervals, decision levels, detection limits and errors of the first and second kinds are all readily computed when the expected blank count is known. A property of the confidence interval [0, x] is that if the confidence level is X %, then ***at least*** X % of the time the expected value is in the confidence interval. Upon partitioning the possible expected blank count into 21 segments, an approximating probability distribution for the expected blank count is taken from the Neyman-Pearson confidence intervals for the expected blank count. Using the approximating distribution an average decision level with an associated upper bound for the average error of the first kind and an average detection limit with an associated upper bound for the average error of the second kind are computed by a C++ program. Conditions for the validity of the detection limit are discussed.

In Applied Modeling and Computations in Nuclear Science; Semkow, T., et al.;
ACS Symposium Series; American Chemical Society: Washington, DC, 2006.

Introduction

If x and y are Poisson distributed random variables with known expectations a and b, respectively, Skellam (*1*) proved that the probability of observing k net counts is given by the following equation:

$$P(x - y = k) = \exp(-a-b)\ (\sqrt{a/b})^k I_{|k|}(2\sqrt{ab}). \qquad (1)$$

In Eq. 1, x is the gross count, y is the blank count, and I_k is the modified Bessel function of the real variable $(2\sqrt{ab})$ and of integer order k. The function I_k is defined by a power series (*2*) and $|k|$ denotes the absolute value of k. Usually a is the expected value of the gross count and b is taken to be the best estimate for the expected blank count. The double precision function of Potter (*3*), written in C++, is utilized to compute the modified Bessel functions of integer order utilized in this chapter; this function yields values, over the range of interest, with about 14 significant digits. Potter (*4*) discusses exact decision levels, detection limits, and confidence intervals in paired counting; because of the small number of routine operations, the computational methods of this chapter are more than adequate.

The decision level is the value for the net count utilized to make the decision between activity detected and activity not detected; if the measured net count is greater than the decision level, activity is said to have been detected. The probability of concluding there is activity when there is no activity is called the error of the first kind. Exact decision levels are readily computed by summing the right tail of the probability density function given by Eq. 1. For discrete random variables it is generally not possible to determine decision levels yielding errors of the first kind equal to a desired value (*5,6*). Currie (*6*) chose the error of the first kind to be equal to or less than the desired value. In many situations it is possible to arrive at an average error of the first kind equal to the desired error of the first kind by a weighted averaging of an error of the first kind greater than the desired error of the first kind and an error of the first kind less than the desired error of the first kind. A random number would be drawn to arrive at a decision level. Because the probability distribution for the net count, when no activity is present, is symmetric about the origin, increasing the expected blank count will cause the error of the first kind to increase for any given decision level (*7*).

The error of the second kind is the probability of concluding no activity was detected when activity is present. Detection limits can be determined by finding the expected net count such that the sum of the left tail of the probability distribution up to and including the decision level equals the desired error of the second kind. In this chapter the detection limit is that value for the expected net count that yields an actual error of the second kind closest in absolute value to the desired error of the second kind. Because the expected value of the gross

Downloaded by CORNELL UNIV on August 6, 2012 | http://pubs.acs.org
Publication Date: November 16, 2006 | doi: 10.1021/bk-2007-0945.ch022

count is only restricted to be a nonnegative real number, it is possible to have the error of the second kind equal to a desired value. Numerical experimentation shows that for a specified desired error of the second kind not greater than 0.36, increasing the expected blank count will cause the detection limit to increase (*7*). Numerical experimentation also shows that for a specified detection limit with an error of the second kind not greater than 0.36, decreasing the expected blank count will cause the error of the second kind to decrease.

Potter (*3*) gave exact confidence intervals of the form $[0, x]$ for the expected net count in paired counting and called them Neyman-Pearson confidence intervals. The method mimicked that of Pearson and Hartley (*8*) for exact confidence intervals for the expected value of the Poisson distribution; they credited Neyman for the method. Consider the expected blank count to be known and X % to be the desired confidence level for the right limit for the expected net count, x. The right limit of the confidence interval for the expected value of the net count equals that value of the expected net count that gives a probability of $(1 - X/100)$ for getting the observed net count or less net counts (*3*). A property of the confidence interval $[0, x]$ is that if the confidence level is X %, then at least X % of the time the expected value of the net count is contained in the confidence interval (*3*).

When the expected blank count tends to zero, Neyman-Pearson confidence intervals for the expected net count yield confidence intervals for the expected value of the Poisson distribution; both the left and right limits agree with values tabulated by Pearson and Hartley (*8*). Some tables for confidence intervals for the expected value of the Poisson distribution differ in the left limit, most agree about the right limit. For this chapter the use of confidence intervals is limited to describing the existing knowledge of the expected blank count. This chapter uses the fact that the sum of Poisson distributed random variables is Poisson distributed (*9*). Also the expected value of the sum of N random variables is the sum of their expected values (*9*). Take H to be one of N identically distributed Poisson random variables each with expected value h. Then an observation of the sum of these N random yields an X % confidence interval for Nh of the form $[0, x]$. At least X % of the time Nh is in $[0, x]$. It is concluded that at least X % of the time h is in $[0, x/N]$.

Results and Discussion

In this section three methods are discussed that attempt to account for the uncertainty in the expected blank count. The three methods assume that the blank count is Poisson distributed and that the blank has been counted an integral number of times greater than the sample. The first method is only briefly discussed. If there are N observations of the blank count, then the average

Downloaded by CORNELL UNIV on August 6, 2012 | http://pubs.acs.org
Publication Date: November 16, 2006 | doi: 10.1021/bk-2007-0945.ch022

observed blank count is used to estimate the expected blank count. If there are a reasonable number of total blank counts observed, then the results may be acceptable. A possible criterion is to compare the average expected blank count with the upper limit of a confidence interval for the expected blank count; furthermore a comparison can be made between the decision levels calculated for these two values of the expected blank count.

An example will be worked. Assume there is one observed blank count in one repetition. The results from a computer code using 1.0 as the expected blank count and 0.05 as the error of both kinds are as follows:

- decision level for average expected blank count = 2,
- associated error of first kind = 0.03723752,
- detection limit for average expected blank count = 7.2338,
- associated error of second kind = 0.05000031.

From a computer code the 99 % confidence interval for the expected blank count is [0, 6.6384]. So it is clear that the uncertainty in the expected blank count is important.

Downloaded by CORNELL UNIV on August 6, 2012 | http://pubs.acs.org
Publication Date: November 16, 2006 | doi: 10.1021/bk-2007-0945.ch022

Upper Bounds for Errors

This method assumes that there are N observations of the expected blank count in the sample count time that can be used to characterize the expected blank count. The total blank count is used to determine a X % confidence interval of the form $[0, x]$. The quantity x can be determined by a computer code or a table. It is concluded that at least X % of the time the expected value of the blank count lies in the interval $[0, x/N]$. Define $BUCL = x/N$. Substituting $BUCL$ in a code for the decision level will guarantee that at least X % of the time the error of the first kind is not greater than the desired error of the first kind for all expected blank counts.

If the desired error of the second kind is not larger than 0.36, then increasing the expected blank count will cause the detection limit to increase. That is a larger value of the expected blank count will have a larger detection limit; also there exists a unique detection limit corresponding to each value for the expected blank count. Again substituting $BUCL$ in the appropriate code for the detection limit will guarantee that at least X % of the time the error of the second kind is not greater than the desired error of the second kind. This approach of bounding the errors of both types guarantees that, regardless of the underlying expected blank count, errors of both kinds can be controlled at least 99 % of the time.

Continuing with the example and using the upper limit of a 99 % confidence interval to determine $BUCL$ gives the following results:

- $BUCL = 6.6384$,
- decision level = 6,
- associated error of first kind = 0.03688636,
- detection limit = 15.0893,
- associated error of second kind = 0.04999922.

Average Upper Bounds for Errors of Both Types

The results above suggest that there exist values for the decision level and detection limit that sometimes have errors of the first and second kinds greater than 0.05 and sometimes less than 0.05 with average errors equal to 0.05. Consider the expected blank count, *B*, to be partitioned into nineteen segments from 0.0 to its 95 % right confidence limit with a difference between upper and lower limits of 5 % in confidence for *B*. The twentieth segment goes from the upper limit of the 95 % confidence interval to the right limit of a selected confidence interval that is not less than 95 % and not greater than 99.9 %. The twenty-first segment goes from the upper limit of the twentieth segment to three times this same limit. All reasonable values for the expected blank count are assumed to lie in these twenty-one segments. Figure 1 below shows the above described partition. Figure 1 is an example where the right limit of the twentieth segment is taken to be the right limit of a 99 % confidence interval; it could have been from the right limit of a 95 % confidence interval to the right limit of a 99.9 % confidence interval.

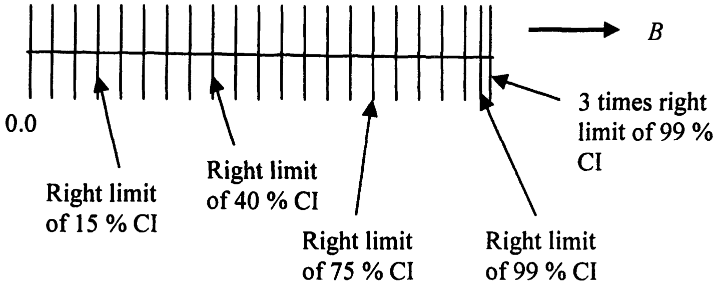

Figure 1. Partition of expected blank count, B.

Downloaded by CORNELL UNIV on August 6, 2012 | http://pubs.acs.org
Publication Date: November 16, 2006 | doi: 10.1021/bk-2007-0945.ch022

For the example the twenty-one right confidence limits, with the right limit of the twentieth segment taken to be the right limit of a 99 % confidence for the expected blank count, are as follows: 0.3554, 0.5318, 0.6832, 0.8244, 0.9613, 1.0973, 1.235, 1.3764, 1.5235, 1.6783, 1.8436, 2.0223, 2.2188, 2.4392, 2.6926, 2.9943, 3.3724, 3.8897, 4.7439, 6.6384, 19.9152.

It is realized that there is insufficient information about the probability distribution for the expected blank count to exactly compute the average (expected) value of the error of either kind; however approximate upper bounds for the average errors of both kinds can be computed. Starting from the left and continuing through the nineteenth segment 5 % of the time the expected value for *B* is taken to be in each segment. The percentage occupancy of the twentieth segment is taken to be (confidence level for right limit of the twentieth segment - confidence level for the right limit of the nineteenth segment). The percentage occupancy of the twenty-first segment is taken to be (100 - confidence level for the right limit of the twentieth segment). That is the occupancy of the twenty-one segments are taken so that the property of Neyman-Pearson confidence intervals is not violated and also so that larger expected blank counts, *B,* will have their larger errors weighted more heavily.

Downloaded by CORNELL UNIV on August 6, 2012 | http://pubs.acs.org
Publication Date: November 16, 2006 | doi: 10.1021/bk-2007-0945.ch022

Average Decision Levels

Next pick a trial average decision level. The expected blank count associated with each segment is taken to be the value at the right limit of each segment; this is the maximum value of *B* in each individual segment and this yields the maximum error of the first kind for each segment. Then an approximate upper bound for the average error of the first kind can be computed by summing the product of the occupancy of each segment and the maximum error of the first kind of each segment. Trial values for the average decision level are increased by 1 until the average decision level yields an upper bound for the average error of the first kind equal to or less than the desired error of the first kind. Select this value and the average decision level that is 1 less than the previous selection. If possible, blend the two average decision levels using a ***random number*** to yield an overall average decision level with an actual approximate upper bound for the average error of the first kind equal to the desired error of the first kind. If the approximate upper bound for the error of the first kind, when the average decision level is equal to zero, is less than the desired error of the first kind, blending is not possible; in this case take the average decision level to be zero and its corresponding approximate upper bound for the average error of the first kind to be the approximate upper bound for the average error of the first kind.

Table I lists partial results from a computer code for the example that is being worked. If the desired error of the first kind is 0.05 then two contenders for the average decision level are 2 and 3. By taking a combination of 2 and 3 to be the overall average decision level the actual approximate upper bound on the average error of the first kind can be made equal to 0.05. From the code 7.314 percent of the time use 2 for the average decision level and 92.686 per cent of the time use 3 for the average decision level. The overall average decision level is 2.927. If the partition had more segments, then the approximate upper bounds would be smaller. Two different effects are as follows:

1. Averaging of the two contenders to get an overall average decision level decreases the decision level from the value that would otherwise be utilized.

2. In this example the overall average decision level is greater than that decision level computed by substituting the average blank count for the expected blank count.

Table I. Average Decision Level and Approximate Upper Bound for Average Error of First Kind

Average decision level	*Bound on error rate*
0	0.3743
1	0.1958
2	0.09646
3	0.04633
4	0.02219

Average Detection Limits

For each decision level an average detection limit is determined such that the approximate upper bound for the average error of the second kind equals the desired error of the second kind. That is for the above example an average detection limit would be determined for decision levels of 2 and 3. The same partition of the expected blank count and the percentage occupancies of the twenty-one segments, as described above, are utilized. For a specified average detection limit an approximate upper bound for the average error of the second kind can be computed by summing the product of the occupancy of each segment and the maximum error of the second kind for each segment. Coupling a code for detection limits together with one for confidence intervals allows the

Downloaded by CORNELL UNIV on August 6, 2012 | http://pubs.acs.org
Publication Date: November 16, 2006 | doi: 10.1021/bk-2007-0945.ch022

computation of the average detection limit and the corresponding approximate upper bound for the average error of the second kind. It is assumed that the maximum error of the second kind occurs at the right limit of all twenty-one segments. Above it was noted that numerical experimentation shows for a specified detection limit with an error of the second kind not greater than 0.36, decreasing the expected blank count will cause the error of the second kind to decrease.

After the computations for the two average detection limits, an overall average detection limit can be computed. Also the errors of the second kind at the left limit of the first segment and right limit of each of the twenty-one segments are included in the output of the code. This enables the verification for the above statement. In particular if the error of the second kind is not greater than 0.36 at the right limit of the twenty-first segment, then the maximum error of the second kind for each of the twenty-one segments occurs at its right limit.

The output of the computer code for the example that has been worked previously is as follows:

- For average decision level = 2: approximate upper bound for average error of 2nd kind = 0.05000113 and average detection limit = 8.0562.
- For average decision level = 3: approximate upper bound for average error of 2nd kind = 0.05000082 and average detection limit = 9.3488.
- The overall average detection limit = 9.2543.
- The errors of the second kind, when the average decision level = 2, for the left limit of the first segment and the 21 right limits of the 21 segments are as follows, respectively: 0.013163221, 0.019376757, 0.022479548, 0.025142495, 0.027621403, 0.030017313, 0.032387553, 0.034775112, 0.037211911, 0.039729009, 0.042356294, 0.04513556, 0.04810784, 0.051335599, 0.054903434, 0.058934863, 0.063634251, 0.069367972, 0.076932978, 0.0887361, 0.11210725, 0.21075447.
- The errors of the second kind, when the average decision level = 3, for the left limit of the first segment and the 21 right limits of the 21 segments are as follows, respectively: 0.016563278, 0.02221558, 0.025023295, 0.027428207, 0.029664221, 0.031823773, 0.033959316, 0.036110148, 0.03830551, 0.040573854, 0.042942626, 0.045450113, 0.048134104, 0.051052029, 0.054281822, 0.057937485, 0.062207887, 0.067432365, 0.074350835, 0.085206056, 0.10692865, 0.20187149.
- The range of expected blank counts from 0.0 to the right limit of the twenty-first segment is uniformly divided into 20000 equal segments. The computer code performs a check that outputs to the monitor when while increasing the expected bank count the error of the second kind decreases.

Downloaded by CORNELL UNIV on August 6, 2012 | http://pubs.acs.org
Publication Date: November 16, 2006 | doi: 10.1021/bk-2007-0945.ch022

The last item above can be viewed as an option if there is concern that the error of the second kind has a maximum somewhere in the interior of a segment. Generally if the error of the second kind at the right hand limit of the twenty-first segment is not greater than 0.36 an error of the second kind greater than that value at the right hand limit is not expected elsewhere. Without running the option the code executes within about five seconds on a newer home computer; running the option adds about three minutes to the execution time.

Conclusion

Three methods have been discussed for decision levels and detection limits when there is uncertainty concerning the expected blank count. The first method is commonly used and utilizes the average blank count as an estimate for the expected blank count. Confidence intervals for the expected blank count assist in deciding the validity of this method.

In the second method the expected blank count is taken to be the upper limit of, for example, a 99 % confidence interval. This value is used to determine a decision level and a detection limit. If the associated decision level is exceeded then it is likely activity is present in the sample or there is an error in understanding concerning the measurement process.

The third method computes two average decision levels, if possible, and two associated approximate upper bounds for the average error of the first kind. Then by blending the two average decision levels and their associated approximate upper bounds for the average errors of the first kind utilizing a random number it is possible to have this average of the two approximate upper bounds for the average error of the first kind equal to the desired error of the first kind. Also an overall average decision level can be given. A method has been presented that yields decision levels dependent on the knowledge available for the expected blank count. If there is very limited knowledge concerning the expected blank count the results for the decision levels will be consistent with that fact and will tend to be larger than the decision levels of Currie (*6*) and Brodsky (*5*); that this is correct is discussed by Strom and MacLellan (*10*). If there is data from many repetitions of the blank count, then the results for the decision levels will be consistent with this fact and will tend to be close to those of Currie (*6*) and Brodsky (*5*). Associated with each average decision level are an average detection limit and an associated approximate upper bound for the average error of the second kind that is equal to the desired error of the second kind. Better knowledge of the expected blank count leads to smaller average detection limits. The two average detection limits are combined in the same ratio as their associated average decision levels to yield an overall average detection limit. Running the computer code for the previous example, when there are ten

Downloaded by CORNELL UNIV on August 6, 2012 | http://pubs.acs.org
Publication Date: November 16, 2006 | doi: 10.1021/bk-2007-0945.ch022

observed blank counts in ten repetitions, yields an overall average decision level of 1.976 and an overall average detection limit of 7.3286.

It is possible that one may find it preferable to *not* combine the two average decision levels. For a measurement on highly radiotoxic materials, it may be preferable to take a conservative approach and use the decision level having an upper bound for the average error of the first kind greater than the desired error of the first kind.

Increasing the number of segments will decrease the upper bounds for the average errors of the first kind, the overall average decision levels, and the overall average detection limits. If each of the first nineteen segments is divided into two separate segments, a limited study reveals very minimal changes. Specifically, the overall average decision level of 2.927 decreases to 2.892, and the overall average detection limit of 9.2543 decreases to 9.1485. The decision to increase the number of segments could be decided by the speed of the computer to be utilized.

Downloaded by CORNELL UNIV on August 6, 2012 | http://pubs.acs.org
Publication Date: November 16, 2006 | doi: 10.1021/bk-2007-0945.ch022

Acknowledgments

Discussions with many individuals in different forums concerning the materials of this chapter are appreciated. In particular, interactions with Joe Alvarez concerning the use of modified Bessel functions of integer order to arrive at the exact results for paired counting and with Tom Semkow concerning the application of the results of this chapter are appreciated. The author also gives thanks to the reviewers of this manuscript.

References

1. Skellam, J. G. The frequency distribution of the difference between two Poisson variates belonging to different populations. *Royal Statistical Society* **1946**, *109*, 296.
2. Abramowitz, M.; Stegun, I. A. *Handbook of Mathematical Functions with Formulas, Graphs, and Mathematical Tables*; NBS Applied Mathematics Series 55, Tenth printing; U. S. Government Printing Office: Washington, DC, 1972; p. 374.
3. Potter, W. E. Neyman-Pearson confidence intervals for extreme low-level, paired counting. *Health Phys.* **1999**, *76*, 186-190.
4. Potter, W. E. Exact results for paired counting. *Radiat. Protect. Manag.* **2000**, *17*, 22-25.
5. Brodsky, A. Exact calculation of probabilities of false positives and false negatives for low background counting. *Health Phys.* **1992**, *63*, 198-204.

6. Currie, L. A. *Lower Limit of Detection: Definition and Elaboration of a Proposed Position for Radiological Effluent and Environmental Measurements*; Report NUREG/CR-4007; Nuclear Regulatory Commission: Washington, DC, 1984.
7. Potter, W. E. Comparison of approximate formulas for decision levels and detection limits for paired counting with the exact results. *J. Radioanal. Nucl. Chem.* **2005**, *263*, 321-325.
8. Pearson, E. S.; Hartley, H. O. *Biometrika Tables for Statisticians*; University Press: Cambridge, 1966; Vol. 1.
9. Meyer, S. L. *Data Analysis for Scientists and Engineers*; J. Wiley & Sons: New York, NY, 1975.
10. Strom, D. J.; MacLellan, J. A. Evaluation of eight decision rules for low-level radioactive counting. *Health Phys.* **2001,** *81*, 27-34.

Downloaded by CORNELL UNIV on August 6, 2012 | http://pubs.acs.org
Publication Date: November 16, 2006 | doi: 10.1021/bk-2007-0945.ch022

Downloaded by UNIV OF GUELPH LIBRARY on August 8, 2012 | http://pubs.acs.org
Publication Date: November 16, 2006 | doi: 10.1021/bk-2007-0945.ch023

Chapter 23

Count Rate Estimation of a Poisson Process: Unbiased Fit versus Central Moment Analysis of Time Interval Spectra

S. Pommé and J. Keightley

European Commission, Joint Research Centre, Institute for Reference Materials and Measurements, Retieseweg 111, B–2440 Geel, Belgium

Least squares fitting procedures and weighted averages imply the assignment of proper weighting factors to the stochastically distributed data involved. In the case of a Poisson distribution, the obvious choice of setting the weighting factor equal to the inverse of the measured value is prone to bias towards low values. Alternatively, using the inverse of the fitted value may turn out to be biased towards higher values, depending on the procedure followed. Additional problems arise when also the possibility of zero counts has to be taken into account. In this work, several least squares statistics are considered and their performance compared with maximum likelihood estimation. The particular case of an exponential time interval distribution of a stationary Poisson process is investigated. Formulas are presented to determine the event rate of the Poisson process from the central moments of the time interval distribution. These count rates are compared to estimated values from the fit procedures.

In Applied Modeling and Computations in Nuclear Science; Semkow, T., et al.;
ACS Symposium Series; American Chemical Society: Washington, DC, 2006.

Introduction

Radioactivity measurements at the highest level of accuracy require a reduction of all sources of uncertainty. This is achieved by a good definition of the detector response to the radioactivity in the measured source, and the collection of a sufficient number of events. The activity of the sources is often chosen in the kBq range, which is a compromise to achieve good statistical accuracy in reasonably short measuring times, and yet not to paralyze the detection chain too much. The pulse pair resolution of each detector set-up is limited (typically of the order of microseconds) by the limited processing speed of its components, giving rise to system 'dead time' of different types, like extending dead time, non-extending dead time, pileup or combinations of them (*1*,*2*).

An alternative to particle counting and subsequent correction for dead time is a time interval distribution (TID) analysis of the counted events. In the particular case of a Poisson process, the time interval distribution of subsequent events has an exponential shape. This feature is well preserved after processing through a counter with non-extending dead time, allowing a determination of the incoming count rate from the slope of the TID when plotted in a log scale. The count rate results directly from parameter estimation, using the least squares (LSQ) or maximum likelihood estimation (MLE) methods. In spite of the apparent simplicity of such procedure, the result may significantly deviate from the true value. This is exemplified by publications on radionuclide half-life estimation, revealing problems with least squares fitting of an exponential fit function to data from counting experiments (*3*-*6*). In fact, least squares methods are generally known to deliver biased parameter estimates to Poisson distributed data (*7*-*16*). An excellent review on the matter can be found in Ref. (*7*).

The problem resides with the assignment of proper statistical weights to the stochastically distributed data. Weighting is commonly accepted as a means to improve estimations, such as averaging and fitting, as one can take into account an appreciated difference in accuracy between data values pertaining to the same variable. The expectation value is independent of the weights, provided that they are uncorrelated with the data (*12*). The most efficient choice for the weights is the inverse of the variance (if known!), as advocated by the least squares method (*17*). At first sight, Poisson distributed data seem to be extremely well suited for weighting. Indeed, the observations are usually independent and the variance equals the expectation value of the variable. Moreover, the observed number of counts is a good estimate of the variance, considering that the difference between its square root value and the standard deviation usually differs by less than one count. Nevertheless, several authors (*3*-*6*) have warned for the direct use of the inverse of the number of counts as a weighting factor, as this tends to overweight the low end of the distribution. Alternatively, if one uses the fitted value as

Downloaded by UNIV OF GUELPH LIBRARY on August 8, 2012 | http://pubs.acs.org
Publication Date: November 16, 2006 | doi: 10.1021/bk-2007-0945.ch023

weighting factor, one is also not free of bias, as this favors a fit that is slightly high [see, *e.g.*, references in (*7*)]. On the other hand, there is a subtle way out of this problem, by adding an additional step to the estimation process, in which the variance is put equal to the estimated values obtained in the previous iteration (*3*,*5*,*6*), and kept constant during the new iteration.

In this work, we explore some least squares methods and compare with maximum likelihood estimation. Additionally, a statistical analysis of the central moments of the time interval distribution is presented as an alternative means to estimate the count rate of the Poisson process.

Downloaded by UNIV OF GUELPH LIBRARY on August 8, 2012 | http://pubs.acs.org
Publication Date: November 16, 2006 | doi: 10.1021/bk-2007-0945.ch023

Weighted Average

First we consider repeated observations of a Poisson process, using the following nomenclature:

- n = the number of observations
- y_i = the result of the i^{th} observation of the Poisson distributed variable y
- $<y>$ = the unweighted mean of the observed data
- ε_i = $y_i/<y> - 1$ = a measure for the deviation of the observation from the average
- μ = the expectation value of $<y>$, $E(<y>)$
- Y = the result of the estimation (averaging, fitting) on the observed data.

As the observations in this case are supposed to be of equal quality, a constant weighting factor is recommendable and averaging should lead to the unweighted mean $<y>$. Nonetheless, it is instructive to try weighting by the inverse variance, approximated by the number of observed counts y_i (> 0):

$$Y = \frac{\sum_{i=1}^{n} \frac{y_i}{y_i}}{\sum_{i=1}^{n} \frac{1}{y_i}} = \left\langle y^{-1} \right\rangle^{-1} \neq < y > \tag{1}$$

Obviously this weighting procedure yields a value that slightly differs from the preferred value $<y>$, as also concluded by others (*6*,*9*,*13*). One can quantify the expected bias:

$$Y = < y > \left\langle \frac{1}{1+\varepsilon} \right\rangle^{-1} \approx \frac{< y >}{1 + < \varepsilon^2 >} \approx \frac{< y >}{1 + < y >^{-1}} \approx < y > -1, \text{ for } \mu >> 1, \tag{2}$$

in which $E(<\varepsilon^2>) = E(<y>^{-1})$ follows directly from the variance formula for a Poisson distribution. It turns out that the weighted average will be typically one unit value lower than the expectation value. This simple mathematical result agrees with the limit value obtained from a more elaborate mathematical analysis (*13*):

$$Y \approx \frac{e^{\mu}-1}{1+\left[\mathrm{Ei}(\mu)-\gamma-\ln(\mu)\right]} \approx \left(\frac{\mathrm{e}^{\mu}-1}{\mathrm{e}^{\mu}}\right)\left(\mu-1-\frac{1}{\mu}\right) \xrightarrow[\mu>>1]{} \mu-1\,, \tag{3}$$

in which μ is the expectation value of y, $\mathrm{Ei}(x)$ is the exponential integral of x, and γ is the Euler-Mascheroni constant. Even though the average value is affected, it was shown that the variance is not (*13*), *i.e.*, the expectation value of the variance is still equal to μ (for $\mu >> 1$).

An additional problem arises as to the assignment of an appropriate weight for observations with zero counts. Some of the classical solutions are the omission of such data points, applying a weight equal to one or systematically adding one count to all weights. All these approximations carry along certain biases:

- omission of the zeros in the weighted average leads to:

$$Y = \frac{\sum\limits_{y_i \neq 0} \frac{y_i}{y_i}}{\sum\limits_{y_i \neq 0} \frac{1}{y_i}} = \left\langle y^{-1} \right\rangle_{y \neq 0}^{-1}\quad , \tag{4}$$

- using a weight of 1 for $y_i = 0$, one can expect (see also Ref. (*6*))

$$Y = \frac{\sum\limits_{i} \frac{y_i}{\max(y_i,1)}}{\sum\limits_{i} \frac{1}{\max(y_i,1)}} \rightarrow \left(\frac{e^{-\mu}}{1-e^{-\mu}} + \left\langle y^{-1} \right\rangle_{y \neq 0}\right)^{-1}\quad , \tag{5}$$

- and applying a slightly modified weight = $(y_i + 1)^{-1}$, one gets (*13*)

$$Y = \frac{\sum\limits_{i} \frac{y_i}{y_i+1}}{\sum\limits_{i} \frac{1}{y_i+1}} \rightarrow \frac{\mu}{1-e^{-\mu}} - 1\,, \tag{6}$$

which is close to $\mu - 1$ for $\mu >> 1$. Again the variance is almost unaffected (*13*).

Mighell (*9*) investigated also other approaches, such as:

$$Y = \frac{\sum\limits_{i} \frac{y_i+1}{y_i+1}}{\sum\limits_{i} \frac{1}{y_i+1}} \rightarrow \frac{\mu}{1-e^{-\mu}}\quad , \tag{7}$$

Downloaded by UNIV OF GUELPH LIBRARY on August 8, 2012 | http://pubs.acs.org
Publication Date: November 16, 2006 | doi: 10.1021/bk-2007-0945.ch023

and a particular one which converges to μ in the limit of a high number of observations:

$$Y = \frac{\sum_i \frac{y_i + \min(1, y_i)}{y_i + 1}}{\sum_i \frac{1}{y_i + 1}} \xrightarrow[n \to \infty]{} \mu . \qquad (8)$$

One can conclude that most of the considered weighted averages tend to yield a slightly biased estimate of the expectation value. The difference, being typically less than one, is of minor importance if $\mu >> 1$. Nevertheless, only an unweighted average is unbiased, in particular for a limited number of observations and a low expectation value.

Parameter Estimation of a Constant Function

The problem of a weighted average can also be looked upon as a constant function (= *Y*) to be fitted to the observed data by the least squares method. The 'least squares' solution for *Y* is reached when

$$\chi^2 = \sum_{i=1}^{n} \left(\frac{y_i - Y}{\sigma_i} \right)^2 \qquad (9)$$

is at a minimum, or its partial derivative for *Y* is zero. Constant weights yield the average value, $Y = <y>$. The true variance being unknown, one often uses Neyman's chi square (*7*,*11*,*15*,*18*):

$$\chi_N^2 = \sum_{i=1}^{n} \frac{(y_i - Y)^2}{y_i} , \qquad (10)$$

in which the variance is replaced by y_i. One can easily prove that this yields the same result as does a weighted average (see Eq. 1), *i.e.*,

$$Y = < y^{-1} >^{-1} . \qquad (11)$$

Alternatively, one can consider the minimisation of another statistic, Pearson's chi-square (*7*,*11*,*15*):

$$\chi_P^2 = \sum_{i=1}^{n} \frac{(y_i - Y)^2}{Y} . \qquad (12)$$

It turns out that also this procedure is not fully unbiased. Indeed, its solution is found by setting the derivative of $\chi_P{}^2$ for *Y* equal to zero:

$$\sum_{i=1}^{n} \left\{ \frac{-2(y_i - Y)}{Y} + \frac{-(y_i - Y)^2}{Y^2} \right\} = 0$$

Downloaded by UNIV OF GUELPH LIBRARY on August 8, 2012 | http://pubs.acs.org
Publication Date: November 16, 2006 | doi: 10.1021/bk-2007-0945.ch023

$$\text{or} \sum_{i=1}^{n} \left\{1 - \frac{y_i - Y}{Y}\right\}^2 = n, \tag{13}$$

which readily leads to the result

$$Y = \sqrt{<y^2>} = <y> \sqrt{1 + <\varepsilon^2>} \approx <y> \sqrt{1 + 1/<y>} \approx <y> + 0.5, \tag{14}$$

for $\mu >> 1$.The fitted value leads to $<y>$ increased by typically half a count (see also (*11*)). Some modest overestimation of Y is not that unexpected, as this reduces χ_P^2 through the denominator. Hence, the fit evolves from $<y> - 1$ (Eq. 11) to $<y> + 0.5$ (Eq. 14) after introducing Y as the variance.

Yet there is a way to overcome this bias. Cabell *et al.* (*3*) and others (*5,6*) recommend an iterative procedure in which, at a certain point, the fitted function value Y is used as an estimate of the variance rather than the observed values y_i. Now, to avoid a feedback loop by which one would end up in the same situation as with χ_P^2 (Eq. 12), it is essential that the variance is kept constant during the LSQ fit. The fitted value Y may then be introduced as the new inverse weight for a next iteration.

Another good approach (*7,8,15*) is to apply the MLE statistic for the Poisson distribution (*19*):

$$\chi_\lambda^2 = 2\sum_{i=1}^{n} \left[Y - y_i - y_i \ln\left(\frac{Y}{y_i}\right)\right], \tag{15}$$

in which the last term is set equal to zero for $y_i = 0$. The optimum is reached at:

$$\sum_{i=1}^{n} \left[1 - y_i \frac{1}{Y}\right] = 0, \tag{16}$$

which exactly corresponds to $Y = <y>$ for any value of μ. It should be noted that the MLE statistic in Eq. 15 is not generally applicable for goodness-of-fit estimation, even in the case of many data points (*7*). For $Y = <y>$, Eq. 15 can be made more explicit:

$$\begin{aligned} \chi_\lambda^2 &= 2\sum_{i=1}^{n} y_i \left[\ln(y_i) - \ln(<y>)\right] = 2 <y> \sum_{i=1}^{n} (1+\varepsilon_i)\ln(1+\varepsilon_i) \\ &\approx 2 <y> \sum_{i=1}^{n} (\varepsilon_i + \frac{\varepsilon_i^2}{2}) \qquad (\mu >> 1) \\ &\approx 2\mu(0 + \frac{1}{2\mu}) = 1 \qquad (\mu >> 1, n >> 1). \end{aligned} \tag{17}$$

Downloaded by UNIV OF GUELPH LIBRARY on August 8, 2012 | http://pubs.acs.org
Publication Date: November 16, 2006 | doi: 10.1021/bk-2007-0945.ch023

As a chi-square should be distributed around one, Eq. 17 can only satisfy these conditions for large numbers ($\mu >> 1$). In fact, other statistics also fail, like Neyman's chi-square (Eq. 10), except for Pearson's chi-square (Eq. 12) (*7*).

Whereas the MLE method is normally regarded as a safe method for parameter estimation, it was recently claimed to yield biased results, unless the theoretical function is very 'simple' (*20*).

One can also apply the maximum likelihood ratio method to the Gaussian distributed data. This is equivalent to minimising Neyman's chi-square (Eq. 10), if the variance is replaced by the observed counts. However, if the fitted value is used instead, the MLE does not correspond exactly with Pearson's chi-square (*7,8*). This is because the implicitly made assumption that the σ is independent of the fitted Y does not hold, so an extra term comes into play in the log-likelihood. As a result of that, the best estimate of the counts y are no longer the counts themselves, but (*8*)

$$y_i' = \sqrt{1/4 + y_i^2} - 1/2 . \qquad (18)$$

The Gauss MLE corresponds only asymptotically to Pearson's chi-square:

$$\chi^2_{\lambda,G} = \chi^2_P + \sum_{i=1}^{n} \left[\ln\frac{Y}{y_i'} - \frac{(y_i - y_i')^2}{y_i'} \right] \qquad (y_i > 0). \qquad (19)$$

Equation 19 is only to be used if all measured values are non-zero. Otherwise, one can minimise

$$\chi^2_{\lambda,G} = \chi^2_P + \sum_{i=1}^{n} \ln Y , \qquad (20)$$

taking into account that the latter statistic is not suited for goodness-of-fit testing.

Now, it is challenging to look for alternative statistics producing (nearly) unbiased fits. In analogy with Eq. 8 for the weighted average, Mighell (*9*) suggested the following:

$$\chi^2_\gamma = \sum_{i=1}^{n} \frac{\left(y_i + \min(y_i, 1) - Y\right)^2}{y_i + 1} . \qquad (21)$$

Some other candidate statistics are investigated in this work:

$$P^2 = \sum_{i=1}^{n} \frac{(y_i - Y)^2}{Y^2 y_i} , \qquad (22)$$

$$Q^2 = \sum_{i=1}^{n} \frac{(y_i - Y)^2}{\sqrt[3]{Y^2 y_i}} , \qquad (23)$$

Downloaded by UNIV OF GUELPH LIBRARY on August 8, 2012 | http://pubs.acs.org
Publication Date: November 16, 2006 | doi: 10.1021/bk-2007-0945.ch023

$$R^2 = \sum_{i=1}^{n} \frac{(y_i - Y + 1)^2}{y_i}, \tag{24}$$

$$S^2 = \sum_{i=1}^{n} \frac{(y_i - Y/(1 + 1/Y))^2}{y_i}, \tag{25}$$

$$T^2 = \sum_{i=1}^{n} \frac{(y_i - Y - 0.5)^2}{Y}, \tag{26}$$

$$U^2 = \sum_{i=1}^{n} \frac{(y_i - Y\sqrt{1 + 1/Y})^2}{Y}, \tag{27}$$

$$V^2 = \sum_{i=1}^{n} \frac{\left[y_i + 1 - Y(1 + e^{-Y})\right]^2}{y_i + 1}. \tag{28}$$

The choice of a weight $= y_i Y^2$ in P^2 (Eq. 22) was inspired by the fact that the deviations in Eqs. 11 and 14 are quite similar and of the opposite sign. The solution for Y is the value that makes the first derivative of P^2 for Y equal to zero:

$$\frac{d}{dY} P^2 \propto \sum_{i=1}^{n} \frac{1}{Y^2} \left\{ \frac{y_i}{Y} - 1 \right\} = 0, \tag{29}$$

which leads directly to $Y = <y>$, an unbiased fit.

The weight $\sqrt[3]{y_i Y^2}$ in Q^2 (Eq. 23) is a variation on previous choice, in which the root is included to compensate for the third power dependency. Its solution is close to the average value $<y>$, since the first derivative to Y of the reduced statistic, Q^2/n, is small for $Y = <y>$:

$$\frac{1}{n} \frac{d}{dY} Q^2 \bigg|_{Y=<y>} = \left(\frac{-2}{n}\right) \sum_{i=1}^{n} \left\{ \frac{(y_i - <y>) + \frac{1}{3<y>}(y_i - <y>)^2}{\sqrt[3]{<y>^2\, y_i}} \right\}$$

$$= \left(\frac{-2}{n}\right) \sum_{i=1}^{n} \left\{ (1 + \varepsilon_i)^{-1/3} \left(\varepsilon_i + \frac{\varepsilon_i^2}{3}\right) \right\}$$

$$\approx \left(\frac{-2}{n}\right) \sum_{i=1}^{n} \left\{ \varepsilon_i + \frac{1}{9}\varepsilon_i^3 - \frac{8}{81}\varepsilon_i^4 + \frac{7}{81}\varepsilon_i^5 - \ldots \right\}$$

$$\xrightarrow[n \to \infty]{} (-2) \left\{ 0 + \frac{1}{9\mu^2} - \frac{8}{81} \left(\frac{1}{\mu^3} + \frac{3}{\mu^2} \right) \right\} \approx 0 \text{ for } \mu >> 1. \tag{30}$$

Downloaded by UNIV OF GUELPH LIBRARY on August 8, 2012 | http://pubs.acs.org
Publication Date: November 16, 2006 | doi: 10.1021/bk-2007-0945.ch023

In Eq. 24, a constant value 1 is subtracted from Y in the numerator, to anticipate the systematic shift towards $<y> - 1$ in Eq. 10. This will indeed move the fit into the right direction, as (for $\mu >> 1$):

$$\frac{d}{dY} R^2 = 0 \Rightarrow Y = \left\langle y^{-1} \right\rangle^{-1} + 1 \quad \approx < y > . \tag{31}$$

Equation 25 has a similar solution (for $\mu >> 1$), as $Y/(1 + 1/Y)^{-1}$ is in the first order approximation equal to $Y - 1$. Still, the use of y_i^{-1} as a weighting factor remains problematic for observations with zero counts, $y_i = 0$. In Eqs. 26 and 27, the estimated value Y is used instead, now corrected by half a count in the numerator. Eq. 26 reaches a minimum for:

$$Y = \sqrt{< (y - 0.5)^2 >} \approx \sqrt{< y >^2 + 1/4n} \rightarrow < y > , \tag{32}$$

in which $< y^2 > \approx < y >^2 + < y >$ in the case of a Poisson process (see also Eq. 14). The expression in Eq. 27 is similar to Eq. 26, as $Y(1 + 1/Y)^{0.5}$ is equal to $Y + 0.5$ in the first order approximation.

Eq. 28 is based on Eq. 7, applying $y_i + 1$ as the weight, and also compensating for the expected bias. The solution reaches the expected value for a sufficiently large set of data ($n >> 1$). Yet, the situation is still not ideal for small expectation values (say $\mu < 5$).

Parameter Estimation for an Arbitrary Function

The least squares method is commonly used to fit any kind of function to a set of data, the case of a constant function being an untypical example. Several questions are of importance: the systematic biases encountered up to this point are relatively small, but is this also the case for a least squares fit to an arbitrary function? Are any of the suggested 'unbiased' minimisation procedures applicable to non-constant functions? The nomenclature is extended as follows:

- $g(x;a)$ = theoretical function that describes the observed data y as a function of x, containing parameters a, the value of which has to be estimated by a fit
- Y_i = the result of the fit at point x_i, being an estimate for the observed number y_i.

Revisiting the case of a weighting by the inverse of the measured value, weight = $1/y_i$, one finds a more general expression for the corresponding least squares solution:

$$\sum_{i=1}^{n} \frac{Y_i}{y_i} = n , \tag{33}$$

and a similar expression for weighting by the fitted value, weight = $1/Y_i$:

Downloaded by UNIV OF GUELPH LIBRARY on August 8, 2012 | http://pubs.acs.org
Publication Date: November 16, 2006 | doi: 10.1021/bk-2007-0945.ch023

$$\sum_{i=1}^{n}\left(\frac{y_i}{Y_i}\right)^2 = n\,. \tag{34}$$

In order to assess the impact of bias on the estimation of a significantly varying function, we consider the hypothetical case of an exponential decay in which the expectation value changes by a factor c for every subsequent point, *i.e.*, $E(y_i) = cE(y_{i+1})$. This decay is known *a priori* and taken into account in the fit, $Y_i = cY_{i+1}$, and the aim of the fit is an unbiased value of Y_0. Then, Eq. 33 can be made more explicit:

$$\sum_{i=1}^{n}\frac{Y_0/c^i}{<y_i>(1+\varepsilon_i)} = n \tag{35}$$

and, considering the increase of the relative uncertainty following, $\varepsilon_i = \sqrt{c}\,\varepsilon_{i-1}$, one gets:

$$Y_0 = <y_0>\frac{n}{\sum_{i=1}^{n}(1+\varepsilon_0\sqrt{c}^{\,i})} \approx <y_0>(1-<\varepsilon_0^2 c^i>)$$

$$\approx <y_0> - <c^i> = <y_0> - \frac{c(c^n-1)}{n(c-1)}\,, \tag{36}$$

showing a bias that can be much higher than with a constant function, certainly if the fit is performed over a broad range in which the function varies significantly ($c^n >> 1$). A similar result is found in the case of Eq. 34, for weight = Y_i:

$$Y_0^2 \approx <y_0>^2 (1+<\varepsilon_0^2 c^i>) \;\Rightarrow Y_0 \approx <y_0> + <c^i>/2\,. \tag{37}$$

Whereas the biases in Eqs. 11 and 14 could still be regarded as an insignificant artefact, the general problem of least squares fitting of an arbitrary function to Poisson distributed data turns out to be more than just philosophical. Fits to data ranging over one or more orders of magnitude may prove to deliver results that deviate significantly from the attainable 'best' value. Possibly the importance of choosing a proper statistical weight is insufficiently recognised by the scientific community. Therefore, its relevance will be demonstrated below in the case of fitting to an exponential time interval distribution.

Moment Analysis of an Exponential Time Interval Distribution

Particular to a Poisson process, is the exponential shape of the time interval distribution (TID) of subsequent events. A common example is the counting process of the decaying nuclei in a radioactive source, and in particular the subset of decays being measured by a detector (assuming a simple decay scheme).

Downloaded by UNIV OF GUELPH LIBRARY on August 8, 2012 | http://pubs.acs.org
Publication Date: November 16, 2006 | doi: 10.1021/bk-2007-0945.ch023

However, the pulse pair resolution of the detector set-up is limited (typically of the order of microseconds) by the processing speed of its components, giving rise to system 'dead time' of different types, like extending dead time, non-extending dead time, pileup or combinations of them. This affects TIDs mainly in the short interval region; yet, the exponential shape is rather well preserved after processing through a counter with non-extending dead time only. An example TID is shown in Fig. 1, produced by a time-interval digitizer (*21*) processing pulses from a detector to which a long artificial non-extending dead time was added, in order to control both the type as well as the duration of the predominant dead time component.

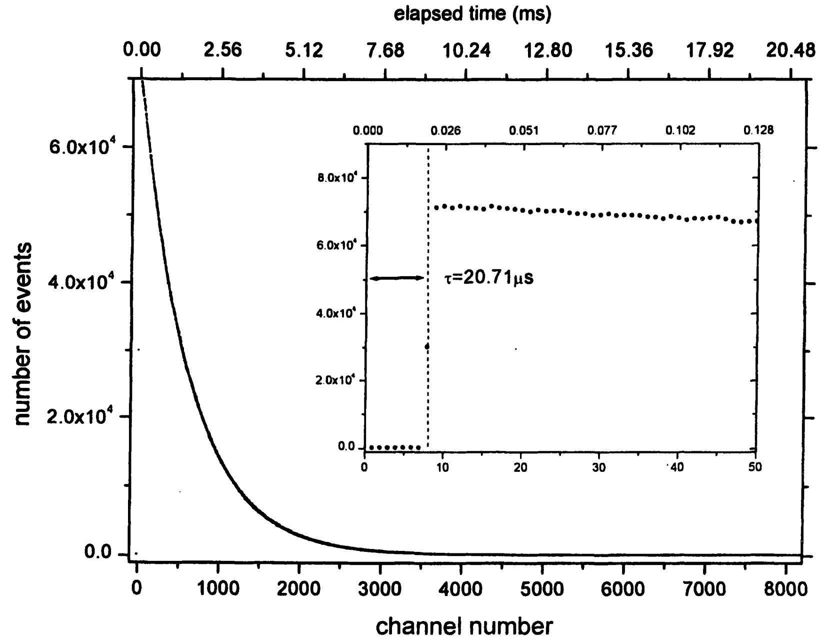

Figure 1. Time interval spectrum of pulses induced by β-decaying ^{39}Ar atoms in a proportional counter. An artificial, non-extending system dead time of 20.71 μs was imposed after each pulse. The spectrum was taken with a time interval digitizer (21), using a (selectable) resolution of 2560 ns.

Downloaded by UNIV OF GUELPH LIBRARY on August 8, 2012 | http://pubs.acs.org
Publication Date: November 16, 2006 | doi: 10.1021/bk-2007-0945.ch023

In Applied Modeling and Computations in Nuclear Science; Semkow, T., et al.;
ACS Symposium Series; American Chemical Society: Washington, DC, 2006.

Non-Extending Dead Time, the Ideal Case

For a stationary Poisson process, the time-interval distribution of subsequently counted events with a "non-paralyzable" counter having a fixed non-extending dead time τ is represented by a shifted exponential (*1*)

$$f(t) = \mathrm{U}(t-\tau)\rho \mathrm{e}^{-\rho(t-\tau)}, \qquad (38)$$

in which $\mathrm{U}(t) = \begin{cases} 0 & for \quad t < 0 \\ 1 & for \quad t > 0 \end{cases}$ is the unit step function whereas the 'normalization factor' ρ corresponds to the input rate of the considered Poisson process.

There is a direct relationship between the input rate, the dead time and the average time interval between subsequently counted events. Indeed, for the *complete* time interval spectrum in the case of *non-extending* dead time, one easily finds

$$M = E(<t>) = \int_{0}^{+\infty} \mathrm{U}(t-\tau)\rho t\, \mathrm{e}^{-\rho(t-\tau)}\, dt = \rho^{-1} + \tau, \qquad (39)$$

which is equivalent to the well-known throughput formula for non-paralyzable counters.

Moreover, the relationships between the input rate and the higher central moments of the time interval distribution are amazingly simple. For instance, the second central moment equals the inverse square of ρ:

$$\mu_2 = \rho^{-2}. \qquad (40)$$

Similar expressions are found for all central moments:

$$\mu_k = \rho^{-k} \sum_{j=0}^{k} \frac{k!}{(k-j)!}(-1)^{(k-j)}. \qquad (41)$$

Consequently, the central moments of the dead time distorted interval distributions turn out to be identical to those of the undisturbed exponential probability distribution, hence independent of the imposed dead time. They are linearly proportional to a power of the count rate.

The count rate (assuming it is constant during measurement) can simply be obtained from the observed variance of the time intervals, since its expectation value is closely related to the second central moment (*22*):

$$V = E\left(\frac{1}{n}\Sigma[t-<t>]^2\right) = \frac{n-1}{n}\mu_2 \approx \rho^{-2}, \quad \text{for } n >> 1. \qquad (42)$$

The variance of the estimated mean M and variance V are calculated from the following generally applicable equations (*22*):

$$\mathrm{VAR}(M) = \frac{\mu_2}{n} = \frac{1}{n\rho^2}, \qquad (43)$$

Downloaded by UNIV OF GUELPH LIBRARY on August 8, 2012 | http://pubs.acs.org
Publication Date: November 16, 2006 | doi: 10.1021/bk-2007-0945.ch023

Downloaded by UNIV OF GUELPH LIBRARY on August 8, 2012 | http://pubs.acs.org
Publication Date: November 16, 2006 | doi: 10.1021/bk-2007-0945.ch023

$$\mathrm{VAR}(V) = \left(\frac{n-1}{n}\right)^2 \left\{ \frac{\mu_4 - \mu_2^2}{n} - \frac{2\mu_2^2}{n(n-1)} \right\}$$

$$\approx \frac{\mu_4 - \mu_2^2}{n} = \frac{8}{n\rho^4} \qquad (n >> 1), \qquad (44)$$

and their covariance is

$$\mathrm{COVAR}(V,M) = \frac{1}{n}\left(\mu_3 - 2\mu_2\mu_1\right) = \frac{\mu_3}{n} = \frac{2}{n\rho^3}. \qquad (45)$$

Hence, the variance of the count rate derived from the inverse square root of V is

$$\mathrm{VAR}(\rho) = \mathrm{VAR}(V^{-1/2}) = \frac{1}{4V^3}\mathrm{VAR}(V) \approx \frac{2\rho^2}{n} \qquad (n >> 1), \qquad (46)$$

corresponding to a relative uncertainty of

$$\frac{\sigma(\rho)}{\rho} = \sqrt{\frac{2}{n}}. \qquad (47)$$

Besides the input rate, in principle, also the second 'unknown', τ, can be derived from the time interval distribution via the mean M and the variance V, since

$$\tau = M - \sqrt{V}, \qquad (48)$$

with a theoretical variance of

$$\mathrm{VAR}(\tau) = \mathrm{VAR}(M) + \frac{1}{4V}\mathrm{VAR}(V) - \frac{1}{\sqrt{V}}\mathrm{COVAR}(V,M) \approx \frac{1}{n\rho^2}. \qquad (49)$$

Non-Extending Dead Time, a Selected Region of Interest

Physical measurements of the TID are limited with respect to resolving power and range. If the TID is subdivided into coarse spectrum channels, Sheppard's corrections can be used to remedy possible grid effects. In the case of the variance for instance, one adds a term $h^2/12$ to the calculated variance (h being the channel width).

More importantly, various practical reasons can prevent one from performing the integration of the TID from zero up to infinity; such as physical limitations to the maximum time interval range, disturbing 'noise' or dead time effects in certain parts of the TID, *etc.*

Alternative statistical equations can be used pertaining to a limited "region-of-interest" (ROI) of the TID, comprised between two time interval values T_1 and T_2 ($T_1 < T_2$). The normalization factor is then equal to

$$\left[\int_{T_1}^{T_2} U(t-\tau)\rho\, e^{-\rho(t-\tau)}\, dt\right]^{-1} = \frac{\rho}{1-e^{-\rho(T_2-T)}}\,, \tag{50}$$

in which $T = \max(\tau, T_1)$.

One can show that there is still a rather simple mathematical relationship between the input rate and the expectation value of the mean time interval in the ROI:

$$M = E(<t>)_{\mathrm{ROI}} = \rho^{-1} + T - \frac{(T_2 - T)e^{-\rho(T_2-T)}}{1-e^{-\rho(T_2-T)}}\,. \tag{51}$$

The correction term converges to zero in the limit of T_2 going to infinity. It converges to $-\rho^{-1}$ in the limit of T_2 going to $T = \max(\tau, T_1)$. A similar correction term is found in the corresponding equation for the variance:

$$(\mu_2)_{\mathrm{ROI}} = \rho^{-2} - \frac{(T_2 - T)^2 e^{-\rho(T_2-T)}}{\left(1-e^{-\rho(T_2-T)}\right)^2}\,. \tag{52}$$

In fact, the correction terms C_k for the central moments of order k can simply be obtained as the k^{th} order derivatives of the same term:

$$C_k = (-1)^k \frac{d^k}{d\rho^k} \ln(1 - e^{-\rho(T_2-T)})\,. \tag{53}$$

The relative contribution of the correction factor increases for higher moments. One can easily verify that Eqs. 51-53 converge to the ideal case in Eq. 41 in the limit of T_2 going to infinity, with the additional constraint that $0 \le T_1 \le \tau$ in the specific case of Eq. 51.

Now, one can choose the time interval (T_1, T_2) such that $\tau \le T_1 << T_2 = \infty$, so that

$$\rho = (M - T_1)^{-1}\,, \tag{54}$$

and the uncertainty on T_1 can be neglected (compared to the less precise value of τ):

$$\mathrm{VAR}(\rho) = (M - T_1)^{-4}\, \mathrm{VAR}(M) = \frac{\rho^2}{n_{\mathrm{ROI}}}\,, \tag{55}$$

which corresponds to a relative uncertainty of

$$\frac{\sigma(\rho)}{\rho} = \sqrt{\frac{1}{n_{\mathrm{ROI}}}}\,. \tag{56}$$

Downloaded by UNIV OF GUELPH LIBRARY on August 8, 2012 | http://pubs.acs.org
Publication Date: November 16, 2006 | doi: 10.1021/bk-2007-0945.ch023

For large regions of interest $(T_1 \approx \tau, n_{\mathrm{ROI}} \approx n)$, this is nearly a factor of $\sqrt{2}$ lower than Eq. 47, in which ρ was derived from the variance V. A more general expression of the uncertainty for any given value of T_1 and T_2 $(T_1 < T_2)$ is obtained from

$$\begin{aligned} \mathrm{VAR}(\rho^{-1}) &= \mathrm{VAR}(M) + \mathrm{VAR}(C_1) - 2\mathrm{COVAR}(M, C_1) \\ &= \mathrm{VAR}(M) + (-C_2)^2 \mathrm{VAR}(\rho) - 2C_2(\rho^{-2} + C_2)\mathrm{COVAR}(\rho, \rho)\,, \end{aligned} \tag{57}$$

which leads to

$$\mathrm{VAR}(\rho) = \frac{\left[\rho^{-2} + C_2\right]^{-1}}{n_{\mathrm{ROI}}}\,, \tag{58}$$

and a relative uncertainty of

$$\frac{\sigma(\rho)}{\rho} = \sqrt{\frac{1}{n_{\mathrm{ROI}}(1 + \rho^2 C_2)}}\,. \tag{59}$$

Discussion

The incoming count rate ρ of a counting experiment (see Fig. 1) has been determined by several methods: (1) particle counting over a certain time period and subsequent correction for the system dead time, (2) a statistical analysis of the central moments of the TID, (3) weighted least squares fits of an exponential to the TID, and (4) maximum likelihood estimation for Poisson distributed data.

Particle Counting with Dead Time Correction

First the incoming count rate was determined by particle counting over a certain time period and subsequent correction for the system dead time. The discriminator output pulses pass to a non-extending retriggerable dead-time generator of zero recovery time and a live time clock gate checking the system availability at a rate of 100 kHz. System live time and real time are established by counting pulses that are generated after one thousand successful checks. The count rate follows from the ratio of counted events to the live time, $\rho = N/T_L$, and the Poisson uncertainty follows from $\sigma(\rho)/\rho = 1/\sqrt{N}$. In the considered example, we get $\rho = 636.38 \pm 0.10\ \mathrm{s}^{-1}$ (with a characteristic non-extending dead time of $\tau = 20.71\ \mu\mathrm{s}$).

Downloaded by UNIV OF GUELPH LIBRARY on August 8, 2012 | http://pubs.acs.org
Publication Date: November 16, 2006 | doi: 10.1021/bk-2007-0945.ch023

Central Moments of TID

From the first and second central moment of the TID (Fig. 1), applying Eqs. 39 and 48, one obtains a similar count rate and characteristic dead time: $\rho =$ 636.43 s^{-1} and $\tau =$ 20.91 μs. Considering that the measured TID does not rigorously match the theoretical shape, one gets more precise results by setting an artificial limit T_1 slightly larger than τ, which yields (via Eqs. 51, 54) $\rho =$ 636.35 ± 0.10 s^{-1}. This is confirmed with almost the same precision by the second central moment (Eq. 52), $\rho =$ 636.35 ± 0.13 s^{-1}, demonstrating the validity of the assumed exponential shape of the TID. Also the analysis of more limited intervals of the TID reproduces the same result, with random deviations in a range that can be expected from the uncertainty.

Downloaded by UNIV OF GUELPH LIBRARY on August 8, 2012 | http://pubs.acs.org
Publication Date: November 16, 2006 | doi: 10.1021/bk-2007-0945.ch023

Least Squares Fitting

Least squares fits of an exponential function to the TID, involves the estimation of two free parameters: the amplitude and the slope, the latter being related to the count rate ρ. Minimising Neyman's (Eq. 10) and Pearson's chi square (Eq. 12), one finds $\rho =$ 636.85 s^{-1} and $\rho =$ 636.02 s^{-1}, respectively. These values are clearly biased by a multiple of the expected uncertainty of 0.10 s^{-1}. The absolute value of the error can be quite large when fitting to small numbers. An example is presented in Fig. 2, showing a fit to the data points in a restricted ROI (between channel 5000 and 6500, with typically 2-10 counts per channel). The corresponding results are $\rho =$ 750 s^{-1} (Neyman) and $\rho =$ 604 s^{-1} (Pearson), whereas the central moment analysis still gives a realistic value of $\rho =$ 643 ± 10 s^{-1}.

Maximum Likelihood and 'Unbiased' Least Squares Methods

In Table I, a sample is shown of fits to specific ROIs of the TID, using the various statistics discussed above (Eqs. 10, 12, 15, 21-28). The first ROI concerns nearly the full spectrum, the second ROI is somewhere in the middle and the third and fourth are at the end, where the number of counts is low. The uncertainty from the central moment analysis, Eq. 56, is used as a criterion for the quality of the results. The fits based on Neyman's and Pearson's chi squares are significantly biased, whereas the central moment analysis, maximum likelihood estimation, Mighell's least square and the iterative procedure on Pearson chi square lead to unbiased results. The unbiasedness of MLE is compatible with the prerequisite of 'simplicity' of the exponential function (*20*). Also the other statistics (Eqs. 23-28) are well suited for fitting to Poisson distributed data, except for P^2 (Eq. 22), which is inefficient. Nevertheless, they suffer from bias when the counts are very close to zero.

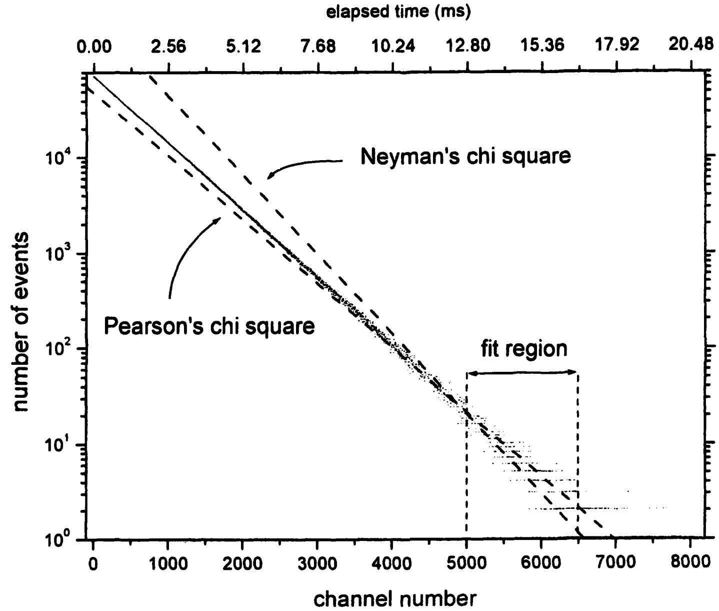

Figure 2. Same time interval spectrum as in Fig. 1. The dashed lines represent biased least squares fits to the experimental data from channel 5000 to 6500, minimizing Pearson's and Neyman chi squares, respectively.

Conclusions

The rate of a Poisson process observed by a counter with non-extending dead time can be derived from the slope of the time interval distribution of subsequently observed events. Unbiased results were obtained with a central moment analysis (Eqs. 51, 52), maximum likelihood estimation (Eq. 15) and Mighell's least square procedure (Eq. 21). Least squares fits based on Neyman's (Eq. 10) and Pearson's (Eq. 12) chi squares are significantly biased. Nevertheless, the latter can be used correctly in an iterative way, by keeping the uncertainties constant during each fit procedure, and then iteratively adapt them according to the newly obtained fitted values. Alternative statistics suggested in this work (Eqs. 23-28) are well suited for fitting to Poisson distributed data, unless the counts are very close to zero.

Downloaded by UNIV OF GUELPH LIBRARY on August 8, 2012 | http://pubs.acs.org
Publication Date: November 16, 2006 | doi: 10.1021/bk-2007-0945.ch023

Table I. Count Rate of the Poisson Process (see Figs. 1 and 2) as Derived from Different Analysis Methods in Four Fit Regions (Begin and End Channels Are Indicated on Top of the Column, as Well as the Corresponding Number of Events n_{ROI}). Biased Results Are in *Italic*.

		ROI (channels, n_{ROI})			
Statistic	*Eq.*	10–8000 #43887431	3000–6000 #333861	5000–6500 #11806	6000–8192 #2505
$M\text{-}T_1\text{-}C_1$	51 59	636.35 ± 0.10	635.9 ± 1.2	643 ± 10	624 ± 16
$V\text{-}C_2$	52	636.34	636.1	633	650
χ_N^2	10	*636.85*	*649.0*	*750*	*555*
χ_P^2 (free)	12	*636.12*	*630.8*	*604*	*601*
χ_P^2 (iterate)	12’	636.36	637.8	645	623
MLE χ_λ^2	15	636.35	637.8	645	623
χ_γ^2	21	636.35	637.8	641	595
P^2	22	*582*	*633.0*	*592*	*235*
Q^2	23	636.33	637.8	643	*491*
R^2	24	636.28	637.9	630	*234*
S^2	25	636.34	638.0	*665*	*402*
T^2	26	636.27	637.7	641	*418*
U^2	27	636.27	637.7	638	*499*
V^2	28	636.33	637.8	642	*347*

References

1. *Particle Counting in Radioactivity Measurements*; ICRU Report 52, International Commission on Radiation Units and Measurements: Bethesda, MD, 1994.
2. Pommé, S.; Denecke, B.; Alzetta, J.-P. *Nucl. Instr. Meth.* **1999**, *A426*, 564-582.
3. Cabell, M. J.; Wilkins, M. *J. Inorg. Nucl. Chem.* **1970**, *32*, 1409-1412.

Downloaded by UNIV OF GUELPH LIBRARY on August 8, 2012 | http://pubs.acs.org
Publication Date: November 16, 2006 | doi: 10.1021/bk-2007-0945.ch023

4. Müller, J. W. Some mathematical problems in counting statistics; International Workshop on Advanced Mathematical Tools in Metrology, Torino, October, 1993.
5. Tagesen, S.; Winkler, G. In *Proc. Int. Symp. on Nuclear Data Evaluation Methodology*; Brookhaven National Laboratory: Upton, NY, 12-16 Oct. 1992; Dunford, Ch. L., Ed.; World Scientific: Singapore, 1993, pp. 267-272.
6. Blaauw, M.; Fleming, R. Possible biases due to weighted averaging or fitting of Poisson-distributed data; *Unpublished.*
7. Hauschild, T.; Jentschel, M. *Nucl. Instr. Meth.* **2001**, *A457*, 384-401.
8. Hannam, M. D.; Thompson, W. J. *Nucl. Instr. Meth.* **1999**, *A431*, 239-251.
9. Mighell, K. J. *Astrophys. J.* **1999**, *518*, 380-393.
10. Muravsky, V. A.; Tolstov, S. A.; Kholmetskii, A. L. *Nucl. Instr. Meth.* **1998**, *B145*, 573-577.
11. Jading, Y.; Riisager, K. *Nucl. Instr. Meth.* **1996**, *A372*, 289-292.
12. Wheaton, W. A. ; Kunklee, A. L.; Jacobson, A. S.; Ling, J. C.; Mahoney, W. A.; Radocinski, R. G. *Astrophys. J.* **1995**, *438*, 322-340.
13. Müller, J. W. A propos d'un abus de poids statistiques. Report BIPM-84/7, Bureau International des Poids et Mesures : Sèvres, 1984.
14. Gregorich, K. E. *Nucl. Instr. Meth.* **1991**, *A302*, 135-142.
15. Baker, S.; Cousins, R. D. *Nucl. Instr. Meth.* **1984**, *221*, 437-442.
16. Awaya, T. *Nucl. Instr. Meth.* **1979**, *165*, 317-323.
17. Bevington, P. R. *Data Reduction and Error Analysis for the Physical Sciences*; McGraw-Hill: New York, NY, 1969.
18. Neyman, J.; Pearson, E. S. *Biometrika* **1928**, *20A*, 175-240.
19. Cash, W. *Astrophys. J.* **1979**, *228*, 939-947.
20. Bergmann, U. C.; Riisager, K. *Nucl. Instr. Meth.* **2002**, *A489*, 444-447.
21. Denecke, B.; De Jonge, S. *Appl. Rad. Isot.* **1998**, *49*, 1099-1105.
22. Kendall, M. G.; Stuart, A. *The Advanced Theory of Statistics*; 5th edition; Griffin: London, 1952; Vol. 1.

Downloaded by UNIV OF GUELPH LIBRARY on August 8, 2012 | http://pubs.acs.org
Publication Date: November 16, 2006 | doi: 10.1021/bk-2007-0945.ch023

Chapter 24

Bayesian Inference from the Binomial and Poisson Processes for Multiple Sampling

Thomas M. Semkow

Wadsworth Center, New York State Department of Health and State University of New York, P.O. Box 509, Albany, NY 12201

Downloaded by COLUMBIA UNIV on August 6, 2012 | http://pubs.acs.org
Publication Date: November 16, 2006 | doi: 10.1021/bk-2007-0945.ch024

The binomial and Poisson distributions are fundamental to the statistics of radioactive decay and measurement, and are widely used in the interpretation of counting data. This chapter reviews the subject of Bayesian inference from these distributions and provides some new derivations and approaches for the point estimators. Two groups of prior distributions are considered: conjugate - including beta, gamma, and negative binomial, as well as noninformative - including uniform, Jeffreys, Jaynes, and convergent. The relationship between Bayes priors and overdispersion is discussed. Multiple sampling from the distributions is emphasized. The numerical examples are given.

1. Introduction

The first published application of the Bayes inference to radioactivity counting was that by Rainwater and Wu (*1*). The Bayes methodology has been described in many editions of the Friedlander *et al.* textbook (*2*). Since then, the Bayes inference has become a widely used technique in nuclear science, such as in radioactivity counting (*3*-*7*), nuclear physics (*8*-*10*), half-life studies (*11*), health physics (*12*-*14*), and spectra deconvolutions (*15*,*16*). A review of the Bayes methods in health-physics applications has been done by Martz (*17*).

In Applied Modeling and Computations in Nuclear Science; Semkow, T., et al.;
ACS Symposium Series; American Chemical Society: Washington, DC, 2006.

The goal of this chapter is to review the principles of the Bayesian inference for the two fundamental distributions used in nuclear science: binomial and Poisson. An advanced statistical approach is followed. In this chapter we do not cover specific topics of applications such as distinguishing between the source and background counts, detection limits, or health physics applications. Instead, we show how the population parameters can be inferred from the above distributions using the Bayes method. This is illustrated with several numerical examples in nuclear science and from the literature.

The binomial distribution describes dispersion of the number of decayed atoms x, given the original number of atoms N and the probability of decay p (*2,18*),

$$P(x\,|\,N,p)=\binom{N}{x}p^{x}q^{N-x}, \qquad 0<p<1,\ q=1-p,\ 0\le x\le N. \tag{1}$$

The probability of decay of a single atom in time t is equal to $1 - e^{-\lambda t}$, where $\lambda = \ln 2/T_{½}$ is the decay constant (rate constant), and $T_{½}$ is a half-life. If the process is statistically sequential and conditional (but not branched), for instance, if the decay is followed by the detection with a probability ε, then $p = (1 - e^{-\lambda t})\,\varepsilon$, and x describes the statistics of counts (*19*). In general, p can be a product of such sequential event probabilities. We will not be distinguishing the contributors to p in the equations, however. The binomial distribution has the following properties (*20*): mean $\mu(x) = Np$, variance $\mu_2(x) = Npq$, and a dispersion coefficient $\delta_x = \mu_2(x)/\mu(x) = q$.

When the population $N \gg 1$, and $p \ll 1$, the binomial distribution transforms into the Poisson distribution (*2,18*). In this case, a low value for p is usually caused by a slow decay, $\lambda t \ll 1$. Then, we have $p = \lambda t$ for the statistics of decays or $p = \lambda t\varepsilon$ for the statistics of counts. However, the Poisson distribution depends on one parameter only, $\theta = Np$,

$$P(x\,|\,\theta)=\frac{\theta^{x}e^{-\theta}}{x!}, \qquad \theta>0,\ x\ge 0. \tag{2}$$

The Poisson distribution has the following properties: $\mu(x) = \mu_2(x) = \theta$, $\delta_x = 1$. One can also factor $\theta = \rho t$, where ρ is the rate.

Since we are ultimately interested in the Bayesian inference for multiple sampling, we outline the likelihood functions for such sampling in Section 2. It is important to note that the Bayesian inference is related to the subject of overdispersion in nuclear statistics, described in Section 3. Section 4 summarizes the Bayes theorem and discusses the various prior distributions of interest. In Section 5, we apply the Bayes inference to the binomial parameters N and p, under various scenarios of known N/unknown p, unknown N/known p, as well as unknown N/unknown p. The posterior distributions are derived, as well as their point and interval estimators. The Bayesian inference of the Poisson parameter θ,

Downloaded by COLUMBIA UNIV on August 6, 2012 | http://pubs.acs.org
Publication Date: November 16, 2006 | doi: 10.1021/bk-2007-0945.ch024

as well as that for p, is performed in Section 6. The summary and conclusions are contained in Section 7. Although this chapter is a review, we provide some generalized derivations as well as new proposed approaches, particularly in the case of the binomial distribution. We also compare different priors in detail.

2. Likelihood Functions

Let us assume that n independent samplings (measurements) were made with an outcome $x = \{x_1 ,\dots, x_n\}$. The sample mean can be defined as $\bar{x} = \frac{1}{n}\sum_{i=1}^{n} x_i$. Then, the likelihood function for the binomial distribution is obtained from Eq. 1:

$$P(x \mid N, p) = \left[\prod_{i=1}^{n} \binom{N}{x_i}\right] p^{n\bar{x}} q^{nN-n\bar{x}}. \qquad (3a)$$

Equation 3a is normalized with respect to each x_i, since n consecutive sums over x_i will result in unity. To calculate the moments of counts, however, we are not interested in the moment of each x_i individually, but in the moment of $n\bar{x}$. This will be shown in Section 3. We are also interested in normalizable and tractable posteriors of the parameters in Section 5. For the above two reasons, Eq. 3a is renormalized to the statistics of $n\bar{x}$:

$$P(n\bar{x} \mid nN, p) = \binom{nN}{n\bar{x}} p^{n\bar{x}} q^{nN-n\bar{x}}. \qquad (3b)$$

As an example, we provide the relationship between the maximum-likelihood estimators (MLE), $\hat{N}$ and $\hat{p}$, which is obtained by differentiating Eq. 3b with respect to p and equating to zero (*20*), yielding $\bar{x} = \hat{N}\hat{p}$. The second MLE equation, obtained by differentiating with respect to N, is given in Ref. (*20*). It can be shown that $\bar{x}$ is an unbiased estimator of the product Np (*21*).

In the case of the Poisson distribution, the likelihood function is obtained from Eq. 2, and is given by Eq. 4a. This likelihood is renormalized to the statistics of $n\bar{x}$, resulting in Eq. 4b, which will be used in Sections 3 and 6.

$$P(x \mid \theta) = \left[\prod_{i=1}^{n} \left(\frac{1}{x_i!}\right)\right] \theta^{n\bar{x}} e^{-n\theta}, \qquad (4a)$$

$$P(n\bar{x} \mid n\theta) = \frac{(n\theta)^{n\bar{x}} e^{-n\theta}}{(n\bar{x})!}. \qquad (4b)$$

The MLE in this case is equal to $\bar{x} = \hat{\theta}$ (*20*) and it is unbiased (*21*).

Downloaded by COLUMBIA UNIV on August 6, 2012 | http://pubs.acs.org
Publication Date: November 16, 2006 | doi: 10.1021/bk-2007-0945.ch024

3. Overdispersion

It has been experimentally recognized that the counting statistics are often overdispersed with respect to the basic distributions, Eqs. 1 and 2, (*7*,*22*). The theory of overdispersion has been developed (*19*,*22*-*24*). The reason for the overdispersion is that the parameters φ such as p, θ, or N are not constant, but rather fluctuate during the measurements. We can define a statistical event as a single decay or a count, and a statistical trial as a measurement consisting of several events. If the parameters fluctuate from event to event, in such a way that the mean values of φ remain constant from trial to trial, the statistics are not overdispersed. However, when the mean values of φ change from the trial to trial, the statistics become overdispersed.

The physics of parameter fluctuations fits well within the existing statistical distributions theory. We discuss the binomial probability parameter first. It has been proved (*19*), that the fluctuations of p can be described by a beta distribution (*25*),

$$P(p\,|\,a,b)=\frac{\Gamma(a+b)}{\Gamma(a)\Gamma(\mathrm{b})}\,p^{a-1}q^{b-1}, \qquad 0<p<1, \qquad (5)$$

where $a > 0$ and $b > 0$ are parameters, and $\Gamma(a)=\int_0^\infty u^{a-1}\,\mathrm{e}^{-u}du$ is the gamma function. This distribution has a mean $\mu(p) = a/(a+b)$, and a variance $\mu_2(p) = ab/(a+b)^2(a+b+1)$ (*25*).

The overdispersed statistics of counts are obtained by mixing the beta distribution, Eq. 5, with the binomial likelihood, Eq. 3b,

$$\begin{aligned}P(n\bar{x}\,|\,nN,a,b) &= \int_0^1 P(n\bar{x}\,|\,nN,p)\,P(p\,|\,a,b)\,dp\\ &= \binom{nN}{n\bar{x}}\frac{\Gamma(a+b)\,\Gamma(n\bar{x}+a)\,\Gamma(nN-n\bar{x}+b)}{\Gamma(a)\,\Gamma(b)\,\Gamma(nN+a+b)}.\end{aligned} \qquad (6)$$

Equation 6 is called a beta-binomial (negative hypergeometric) distribution (*20*). The moments of this distribution can be calculated (*20*) as:

$$\mu(n\bar{x}) = nN\mu(p), \qquad (7a)$$

$$\mu_2(n\bar{x}) = \mu(n\bar{x})\,[1-\mu(p)+\mu(n\bar{x})\,v_p^2(1-1/nN)], \qquad (7b)$$

where the square of the variation coefficient for the fluctuating probability is defined as $v^2_p = \mu_2(p)/\mu^2(p)$. The factor within the brackets in Eq. 7b is the dispersion coefficient. The last term within the brackets is the excess dispersion over the binomial dispersion of $1-\mu(p)$, and it is equal to zero if there are no p fluctuations, $v_p = 0$.

It has been shown by Dennis and Patil (*26*) that the gamma distribution (*25*) is a general model for a non-negative random variable fluctuating around the steady state:

Downloaded by COLUMBIA UNIV on August 6, 2012 | http://pubs.acs.org
Publication Date: November 16, 2006 | doi: 10.1021/bk-2007-0945.ch024

$$P(\theta \mid a,b) = \frac{b^a}{\Gamma(a)} \theta^{a-1} \mathrm{e}^{-b\theta}, \qquad \theta \geq 0, \tag{8}$$

where $a > 0$ and $b > 0$ are parameters. The gamma distribution has a mean $\mu(\theta) = a/b$, and a variance $\mu_2(\theta) = a/b^2$ (*25*).

To obtain the overdispersed statistics of counts, we mix the gamma distribution, Eq. 8, with the Poisson likelihood, Eq. 4b,

$$P(n\bar{x} \mid a,b) = \int_0^\infty P(n\bar{x} \mid n\theta)\, P(\theta \mid a,b)\, d\theta$$

$$= \binom{n\bar{x}+a-1}{a-1} \left(\frac{n}{b+n}\right)^{n\bar{x}} \left(1-\frac{n}{b+n}\right)^{a}, \tag{9}$$

which is one of the forms of the negative binomial distribution (*20*). The moments can be calculated (*20*) as:

$$\mu(n\bar{x}) = n\mu(\theta), \tag{10a}$$

$$\mu_2(n\bar{x}) = \mu(n\bar{x})[1 + \mu(n\bar{x})\, v_\theta^2], \tag{10b}$$

where $v^2_\theta = \mu_2(\theta)/\mu^2(\theta)$ is a square of the variation coefficient for the fluctuating θ. The factor within the brackets is the dispersion coefficient. The last term of it is the excess dispersion over the Poisson distribution, and it is equal to zero if there are no θ fluctuations, $v_\theta = 0$. Equation 10b reveals also the transition from the binomial to the Poisson case, since it represents a limit of Eq. 7b for $\mu(p) \rightarrow 0$ and $N \rightarrow \infty$.

Finally, we discuss the overdispersion of the binomial parameter N, which may not be constant in the course of samplings. The fluctuations of N can be assumed according to the Poisson distribution. It has a good physical justification, since the generation of the number of radioactive atoms in nuclear-science experiments is often governed by the Poisson process. However, because in this case the binomial processes (such decay and counting) follow the Poisson process of N fluctuations, the combined statistics is that of the Poisson. If even further overdispersion of N over the Poisson is desired, a negative binomial distribution can be assumed. This is the most general case which we discuss below:

$$P(nN \mid c,nd) = \binom{nd+nN-1}{nd-1} c^{nN} (1-c)^{nd}, \qquad N \geq 0, \tag{11}$$

where $0 < c < 1$ and $d > 0$ are parameters. The distribution above has a mean $\mu(nN) = ncd/(1-c)$ and a variance $\mu_2(nN) = ncd/(1-c)^2$ (*20*).

The overdispersed statistics of counts is obtained by mixing the negative binomial distribution, Eq. 11, with the binomial likelihood, Eq. 3b,

$$P(n\bar{x} \mid p,c,nd) = \sum_{nN=n\bar{x}}^{\infty} P(n\bar{x} \mid nN,p)\, P(nN \mid c,nd)$$

Downloaded by COLUMBIA UNIV on August 6, 2012 | http://pubs.acs.org
Publication Date: November 16, 2006 | doi: 10.1021/bk-2007-0945.ch024

$$= \binom{nd+n\bar{x}-1}{nd-1}\left(\frac{pc}{1-qc}\right)^{n\bar{x}}\left(1-\frac{pc}{1-qc}\right)^{nd}. \tag{12}$$

Equation 12 is, amazingly, still another negative binomial distribution, whose moments give the overdispersed statistics of counts

$$\mu(n\bar{x}) = \mu(nN)p, \tag{13a}$$

$$\mu_2(n\bar{x}) = \mu(n\bar{x})[1+\mu(n\bar{x})/nd]. \tag{13b}$$

The factor within the brackets is the dispersion coefficient. The last term of it is the excess dispersion over the Poisson process for N, and it is equal to zero when $c \to 0$ and $d \to \infty$ in such a way that cd = const. Then Eq. 11 transforms to the Poisson distribution for nN.

Downloaded by COLUMBIA UNIV on August 6, 2012 | http://pubs.acs.org
Publication Date: November 16, 2006 | doi: 10.1021/bk-2007-0945.ch024

4. The Bayes Theorem and Prior Distributions

The likelihoods in Eqs. 3 and 4 can be abbreviated as $P(x|\varphi)$, which expresses the probability of obtaining a set of experimental observations x, given a set of parameters φ. However, we are interested in the inverse problem of estimating φ, given the set of observations x. This inversion can be obtained with the Bayes theorem (*27,28*):

$$P(\varphi\,|\,x) = \frac{P(x\,|\,\varphi)\,P(\varphi)}{\int P(x\,|\,\varphi)\,P(\varphi)\,d\varphi}. \tag{14}$$

In Eq. 14, $P(\varphi|x)$ is called a posterior distribution, whereas $P(\varphi)$ is a prior. The integral over the parameter space in the denominator (or the sum for discrete parameters) is called a normalization factor.

The choice of the prior distribution is an important part of Bayesian inference (*28-31*). We describe two classes of priors: conjugate and noninformative. The conjugate priors are those that cause the posteriors to belong to the same class of distributions as the priors: examples are the beta prior, Eq. 5, the gamma prior, Eq. 8, for the binomial and Poisson distributions, respectively. These priors are convenient to use owing to their mathematical properties. Gamma priors have been applied in nuclear science (*3,7,11*).

The second important class of priors is the noninformative priors, which attempt to model no prior knowledge about the parameters sought. The uniform prior belongs to this class, $P(\varphi) \sim$ const, where all values of φ are equally likely. It is also called a Laplace prior (*32*). Jeffreys proposed that the noninformative prior should satisfy information-theory invariance (*28,33*). This invariance leads to the priors $P(p) \sim p^{-1/2}q^{-1/2}$ and $P(\theta) \sim \theta^{-1/2}$ for the binomial and Poisson distributions, respectively. Furthermore, Jaynes proposed that the prior should be invariant under rescaling of the parameter, which results in $P(\theta) \sim \theta^{-1}$ for the Poisson distribution (*34,35*). Another special transformation was proposed by

Jaynes, resulting in $P(p) \sim p^{-1}q^{-1}$ for the binomial distribution (*34*). The noninformative priors for p and θ are also the limiting cases of the beta and gamma priors for the specific values of parameters a and b, as illustrated in Table I.

The noninformative priors are improper, meaning that their integrals over the parameter space can be divergent. For instance, the abovementioned Jaynes priors will have singularities at $p = 0, 1$, and $\theta = 0$; a uniform prior for θ will lead to a diverging integral at infinity. This can lead to a divergent normalization integral in the denominator of Eq. 14, and an example of this will be given in Section 5. However, often the normalization integral converges, since the integrand (the product of likelihood and prior) may nevertheless converge to zero at the integration limits. If the normalization integral diverges, one cannot normalize the posterior, which then ceases to be a probability distribution. Only its mode can be calculated; other point estimators or credibility intervals cannot. Some numerical remedies are possible, for instance truncation of the integration limits based on the knowledge of the range of parameters. For a uniform prior, the mode of the posterior is equal to the one from MLE.

Downloaded by COLUMBIA UNIV on August 6, 2012 | http://pubs.acs.org
Publication Date: November 16, 2006 | doi: 10.1021/bk-2007-0945.ch024

Table I. Priors for p and θ Parameters

Parameter	*Prior class*	*Prior*	*a*	*b*	*Formula*
p	conjugate	beta	a	b	$p^{a-1}q^{b-1}$
	noninformative	uniform	1	1	const
		Jeffreys	½	½	$p^{-1/2}q^{-1/2}$
		Jaynes	0	0	$p^{-1}q^{-1}$
θ	conjugate	gamma	a	b	$\theta^{a-1}e^{-b\theta}$
	noninformative	uniform	1	0	const
		Jeffreys	½	0	$\theta^{-1/2}$
		Jaynes	0	0	θ^{-1}

The negative binomial prior, Eq. 11, is a conjugate prior for parameter N of the binomial distribution (*36,37*). A Poisson prior has also been used as a conjugate prior (*36-39*). Among noninformative priors, a $1/N$ prior (*38,40,41*) and a uniform prior (*39,42,43*) were used. In some cases, the prior was truncated, based on the knowledge that N cannot be greater than a prescribed value (*39,42*). This is equivalent to a rectangular prior (*29*). The priors for N parameter do not conform to such a compact presentation as for the parameters p and θ in Table I.

Bayesian methods are typically used in two situations (*28,30,31*). The first is when the parameters vary from sample to sample, leading to overdispersed statistics. The prior distribution models this variation, which is actual physical variability, and the prior probability of some parameter value is the long-term frequency of obtaining that value when sampling repeatedly. This interpretation of probability is the *frequentist* approach. This kind of prior is used in the empirical Bayes or hierarchical Bayes model. Conjugate priors are useful in these approaches, and we showed in Section 3 that the conjugate priors describe the statistical physics of overdispersion very well. Non-conjugate priors have been used in empirical and hierarchical Bayes models as well.

The second situation defines probability as a measure of degree of belief. This is the *subjectivist* approach. For the last few decades many practitioners have used the term *Bayesian* as synonymous with *subjectivist*. In the subjectivist viewpoint, any unknown parameter can have a prior distribution, even if the parameter is inherently constant. The prior distribution is a distillation of any information or belief that may be present before the current data are observed. The posterior distribution updates the belief to reflect both the prior information and the observed data. Both noninformative and conjugate priors can be used in this approach. The idea of noninformative priors only makes sense in the subjectivist framework.

In the following Sections 5 and 6, we describe the Bayesian inference from the binomial and Poisson distributions, respectively. All point and interval estimators are discussed. However, the emphasis is given to the mean and the variance. The posterior mean is admissible under a quadratic loss function and is, therefore, more appropriate than the mode (*28,39*).

Downloaded by COLUMBIA UNIV on August 6, 2012 | http://pubs.acs.org
Publication Date: November 16, 2006 | doi: 10.1021/bk-2007-0945.ch024

5. Bayesian Inference from the Binomial Distribution

The Bayesian inference from the binomial distribution has been described for case A - known N and an unknown p (*29,44*). This is the easiest and best established case. Cases B - when N is unknown and p is known (*36,37,39-41*), and especially C - when both N and p are unknown (*38,39,42,43,45,46*) are much more involved and have been the subjects of recent research. Yet, it is the number of atoms N that we may wish to infer in nuclear science, for instance, in experiments involving a few or rare events.

Case A uses essentially a $n\bar{x}$ statistic, since p has an exponent $n\bar{x}$ in Eqs. 3a, b. Most authors have been using individual x_i statistic for cases B and C, since N is combined with x_i in Eq. 3a. One exception was Rukhin (*40*), who used the $n\bar{x}$ statistic for case B. Applying the $n\bar{x}$ statistic to cases B and C is an approximation. We have decided to do the latter, despite some loss of generality, offset by the benefit of more tractable formulas. This approach can be further justified by often large uncertainties of the estimators. In fact, Kahn (*45*), and

DasGupta and Rubin (*46*) have shown that there are no unbiased estimators for case C.

Any estimator of N must have the property $N \geq x_m$, where $x_m = \max(x_i)$. Cases A, B, and C are described below separately.

Case A: *N* Known, *p* Unknown

Since N is known, we neglect the prefactor in Eq. 3b. We also neglect the prefactor in Eq. 5, since it is not a function of p. Then, according to the Bayes theorem, Eq. 14, the posterior is proportional to $p^{n\bar{x}+a-1}q^{nN-n\bar{x}+b-1}$. This case can be generalized further by assuming that each measurement started from a different number of atoms N_i, *i.e.*, $N = \{N_1,\ldots,N_n\}$. The known mean of N_i can be defined as $\bar{N} = \frac{1}{n}\sum_{i=1}^{n} N_i$. The posterior is finally proportional to $p^{n\bar{x}+a-1}q^{n\bar{N}-n\bar{x}+b-1}$. Therefore, the posterior is the beta distribution:

$$P(p \mid n\bar{x}) \equiv P(p \mid n\bar{x}, a, b) = \frac{\Gamma(n\bar{N}+a+b)}{\Gamma(n\bar{x}+a)\,\Gamma(n\bar{N}-n\bar{x}+b)}\, p^{n\bar{x}+a-1} q^{n\bar{N}-n\bar{x}+b-1}. \tag{15}$$

The point estimators of the posterior are calculated (*25*) from the uncorrected rth moments μ'_r,

$$\mu'_r(p \mid n\bar{x}) = \int_0^1 p^r P(p \mid n\bar{x})\, dp = \frac{(n\bar{x}+a)_r}{(n\bar{N}+a+b)_r}, \tag{16}$$

where $(u)_r = u(u+1)\cdots(u+r-1)$ is an ascending factorial, $(u)_0 = 1$ (*20*). The mean μ and the variance μ_2 are then calculated from Eq. 16:

$$\mu(p \mid n\bar{x}) = \mu'_1(p \mid n\bar{x}) = \frac{\bar{x}+a/n}{\bar{N}+(a+b)/n}, \tag{17a}$$

$$\mu_2(p \mid n\bar{x}) = \mu'_2(p \mid n\bar{x}) - \mu^2(p \mid n\bar{x}) = \frac{\mu(p|n\bar{x})\left[1-\mu(p|n\bar{x})\right]}{n\bar{N}+a+b+1}. \tag{17b}$$

It is seen from Eqs. 17a, b and Table I, that the Jaynes prior ($a = b = 0$) yields the posterior mean equal to the MLE estimator, whereas other noninformative priors produce shifted estimates. The estimates become less dependent on the choice of prior for large n, and large number of decays or counts.

The mode of the posterior is determined by differentiating Eq. 15 with respect to p and equating to zero:

$$Mo(p \mid n\bar{x}) = \frac{\bar{x}+(a-1)/n}{\bar{N}+(a+b-2)/n}. \tag{17c}$$

Special cases are: when $n\bar{x}+a<1$ and $n\bar{N}-n\bar{x}+b>1$, then the half-mode (at end-point) (*47*) is equal to zero, and in the opposite case, it is equal to one. It is

Downloaded by COLUMBIA UNIV on August 6, 2012 | http://pubs.acs.org
Publication Date: November 16, 2006 | doi: 10.1021/bk-2007-0945.ch024

seen that the mode is equal to MLE of the parameter for the uniform prior ($a = b = 1$).

There are several ways to determine the interval estimators (*29*). Let the lower and higher Bayesian credibility intervals on p be abbreviated as l and h, respectively. We follow the convention of the highest posterior density, according to which $P(l\,|\,n\bar{x}) = P(h\,|\,n\bar{x})$ from Eq. 15. If we assign a $1 - \alpha$ credibility level that $l \le p \le h$, the credibility intervals can be obtained by a numerical solution of Eqs. 18a, b:

$$\int_l^h P(p\,|\,n\bar{x})\,dp = 1-\alpha\,, \tag{18a}$$

$$\left(\frac{h}{l}\right)^{n\bar{x}+a-1} = \left(\frac{1-l}{1-h}\right)^{n\bar{N}-n\bar{x}+b-1} \tag{18b}$$

As an example, let us consider an experiment, where 3 and 5 rare nuclear atoms were created in each of the two separate runs. The decay of those atoms was followed for 2 min, resulting in 2 and 3 observed decays in each experiment, respectively. What was the half-life of the rare species and its uncertainty? We have $n = 2$, $\bar{N} = 4$, $\bar{x} = 2.5$, and we assume $a = b = 1$, since we do not know anything about the half-life. Then we obtain $p = 0.60 \pm 0.15$ from Eqs. 17a, b. Using the information from Section 1, we obtain $T_{½} = 1.5 \pm 0.2$ min. This is just an illustrative example and no comparison with other noninformative priors is provided.

Case B: *N* Unknown, *p* Known

Negative-binomial and Poisson N Priors

We use a normalized likelihood for multiple sampling from Eq. 3b and the negative-binomial prior for N from Eq. 11. The posterior for N is obtained from Eq. 14:

$$P(nN\,|\,n\bar{x}) \equiv P(nN\,|\,n\bar{x}, p, c, nd) = \frac{P(n\bar{x}\,|\,nN, p)\,P(nN\,|\,c, nd)}{\sum_{nN=n\bar{x}}^{\infty} P(n\bar{x}\,|\,nN, p)\,P(nN\,|\,c, nd)}.$$

The marginal distribution in the denominator can be evaluated by substituting the variables $s = qc$, $y = nN - n\bar{x}$, $e = nd + n\bar{x}$, and subsequently summing a variant of the binomial series (*48*): $(1-s)^{-e} = \sum_{k=0}^{\infty} \binom{e+k-1}{k} s^k$. Finally, we obtain the posterior distribution, which is (as it should be) another negative binomial distribution:

Downloaded by COLUMBIA UNIV on August 6, 2012 | http://pubs.acs.org
Publication Date: November 16, 2006 | doi: 10.1021/bk-2007-0945.ch024

$$P(y \mid s,e) = \binom{e+y-1}{e-1} s^y (1-s)^e. \tag{19}$$

The uncorrected factorial moments $\mu'_{[r]}$ of Eq. 19 are given (*20*) by $\mu'_{[r]} = (e)_r \left(\frac{s}{1\text{-}s}\right)^r$, from which the central moments can be calculated: $\mu = \mu'_{[r]}$ and $\mu_2 = \mu'_{[2]} + \mu - \mu^2$. For practical applications below, it is convenient to take the Poisson limit of Eq. 19 at this point. This is accomplished by taking the limits $c \longrightarrow 0$ and $d \longrightarrow \infty$ in such a way that cd = const = μ (*39*). Then, the mean and variance of N are calculated as:

$$\mu(N \mid \bar{x}) = \bar{x}/p, \tag{20a}$$

$$\mu_2(N \mid \bar{x}) = \mu(N \mid \bar{x})(1-p^2)/n. \tag{20b}$$

To test our method, we consider two numerical examples by Draper and Guttman (*42*), for one and two samplings of x at a fixed value of p = 0.8. They are listed Table II. Our estimates for N and 1σ uncertainties are listed in Table II for conjugate Poisson prior, which means that Eqs. 20a, b were used (after rounding off to integers). Our estimates of the same examples for noninformative priors will be discussed in the next subsection. By comparison, Draper and Guttman obtained N = 12 and 13 for n = 1 and 2, respectively, using their method, whereas Hamedani and Walter (*39*) obtained 13 in both cases. None of the above authors provided any estimates of the uncertainties.

Table II. Bayesian Estimates of *N* for *p* = 0.8

Draper and Guttman examples (*42*)		*n*	1	2
		x	10	10, 12
N *prior*	conjugate	Poisson	12 + 3 − 2	14 + 1 − 2
	noninformative	uniform	13 ± 2	14 ± 1
		Jaynes	12 + 2 − 1	14 + 1 − 2

To complete this case, we can calculate the mode of posterior by a numerical solving of Eq. 20c for N,

$$\psi(nN + nd) - \psi(nN - n\bar{x} + 1) = N \ln(1/qc), \tag{20c}$$

where $\psi(u) = d \ln \Gamma(u)/du$ (*48*). The credibility intervals for nN, l and h, at 1 – α credibility level can be obtained by a numerical solution of Eqs. 21a, b

Downloaded by COLUMBIA UNIV on August 6, 2012 | http://pubs.acs.org
Publication Date: November 16, 2006 | doi: 10.1021/bk-2007-0945.ch024

$$\sum_{nN=l}^{h} P(nN \mid n\bar{x}) = 1-\alpha, \tag{21a}$$

$$\frac{\Gamma(nl+nd)\,\Gamma(nh-n\bar{x}+1)}{\Gamma(nh+nd)\,\Gamma(nl-n\bar{x}+1)} = (qc)^{n(h-l)}. \tag{21b}$$

Since N is an integer, such solution may not exist for a given α. Then, one can either adjust α to get the integer N, or solve for a noninteger N and truncate.

Noninformative N Priors

In order to study noninformative N priors for multiple sampling, it is convenient to start with the likelihood proportional only to the terms dependent on N in Eq. 3b:

$$P(n\bar{x} \mid nN, p) \propto \frac{\Gamma(nN+1)}{\Gamma(nN-n\bar{x}+1)} q^{nN}, \tag{22}$$

where $\Gamma(u+1) = u!$ for an integer argument. In order to have the posterior of N normalizable, we study an asymptotic behavior of Eq. 22 by taking limits of the gamma functions as well as the limit of $1-p$ at large N (*48*). We obtain $P \propto N^{n\bar{x}}\,\mathrm{e}^{-nNp}$. The Jeffreys prior for N is proportional to $|E[\partial^2 \ln P / \partial N^2]|^{1/2} \propto 1/N^{1/2}$ (*30,33*). We thus take the prior

$$P(N \mid c) \propto N^{c-1}, \tag{23}$$

where $c = 0$, ½, 1 for Jaynes, Jeffreys, and uniform priors, respectively. In the following, we shall only consider $c = 0$, 1, since it leads to tractable formulas.

The posterior is given by Eq. 14 with Eqs. 22, 23:

$$P(nN \mid n\bar{x}) \equiv P(nN \mid n\bar{x}, p, c) = \frac{\dfrac{\Gamma(nN+1)}{\Gamma(nN-n\bar{x}+1)} q^{nN} (nN)^{c-1}}{\sum_{nN=n\bar{x}}^{\infty} \dfrac{\Gamma(nN+1)}{\Gamma(nN-n\bar{x}+1)} q^{nN} (nN)^{c-1}}$$

$$= \binom{nN-1}{n\bar{x}-1} p^{n\bar{x}} q^{nN-n\bar{x}} \left(\frac{pN}{\bar{x}}\right)^{c}, \tag{24}$$

where the binomial series was summed up similarly to that in the previous section.

The point estimators can be evaluated from Eq. 24:

$$\mu(N \mid \bar{x}) = \frac{\bar{x}}{p} + \frac{cq}{np}, \tag{25a}$$

$$\mu_2(N \mid \bar{x}) = \left[\mu(N \mid \bar{x}) + \frac{c}{n}\right] \frac{q}{np}. \tag{25b}$$

Using Eqs. 25a, b, we calculate the estimated means and uncertainties for the examples in Table II. It is seen that for $n = 2$, the three priors: conjugate Poisson, uniform, and Jaynes, yield the same estimated mean of 14, while the

Downloaded by COLUMBIA UNIV on August 6, 2012 | http://pubs.acs.org
Publication Date: November 16, 2006 | doi: 10.1021/bk-2007-0945.ch024

uncertainties are comparable. For $n = 1$, the estimated mean of 13 from the uniform prior differs by one unit from the other two (12).

One could apply Eqs. 25 to estimate the number of products from a nuclear reaction. Let us suppose that the products from an in-beam reaction were mass separated, collected on the detector, and their decay measured. The life-time of the products was not known precisely, however, the measurement time was sufficiently long to allow for a complete decay. Then, $p \approx \varepsilon$ (Section 1). In 3 experiments, 2, 1, and 4 decays were observed. Taking $\varepsilon = 0.30 \pm 0.02$, and assuming Jaynes ($c = 0$) prior for an illustration only, one obtains from Eqs. 25a, b $N = 7.8 \pm 2.7$, where the error in ε was propagated. The result is not rounded off to an integer, since such N can be used for a calculation of cross-section of the nuclear reaction, given integrated beam.

The posterior mode can be calculated by a numerical solution of Eq. 26 for N,

$$\psi(nN+1) - \psi(nN - n\bar{x} + 1) = \frac{1-c}{nN} + \ln(1/q). \qquad (25c)$$

The credibility intervals for nN, l and h, at $1 - \alpha$ credibility level can be obtained by a numerical solution of Eqs. 26a, b

$$\sum\nolimits_{nN=l}^{h} P(nN \mid n\bar{x}) = 1 - \alpha, \qquad (26a)$$

$$\frac{\Gamma(nl)\,\Gamma(nh-n\bar{x}+1)}{\Gamma(nh)\,\Gamma(nl-n\bar{x}+1)} = q^{n(h-l)}(h/l)^{c}. \qquad (26b)$$

The limitations regarding integer N are the same as listed below Eqs. 21.

Case C: *N*, *p* Unknown

In this case, we have two unknown parameters. The procedure employed below follows the original literature (*42*,*43*), where one parameter is marginalized over. Subsequently, the second parameter is estimated from the Bayes posterior. The first parameter can then be calculated from the unbiased estimator $\bar{x} = Np$ (Section 2). It is more convenient mathematically to marginalize over p.

We assume a beta prior for the p parameter (Eq. 5) and marginalize over p which results in Eq. 6. The likelihood function for N is then proportional to the factors dependent on N in Eq. 6:

$$P(n\bar{x} \mid nN, a, b) \propto \frac{\Gamma(nN+1)\,\Gamma(nN-n\bar{x}+b)}{\Gamma(nN-n\bar{x}+1)\,\Gamma(nN+a+b)}. \qquad (27)$$

One can use any prior for N with Eq. 27, calculate the posterior according to Eq. 14, as well as the estimators, which is a numerical problem.

To investigate the possible noninformative priors for N, we study the asymptotic behavior of Eq. 27 similarly to case B. For large N,

Downloaded by COLUMBIA UNIV on August 6, 2012 | http://pubs.acs.org
Publication Date: November 16, 2006 | doi: 10.1021/bk-2007-0945.ch024

$P(n\bar{x} \mid nN, a, b) \propto N^{-a}$, so it is dependent solely on the choice of p prior and not on the data (*45*). Therefore, such prior for p has to be considered noninformative. We apply the Jeffreys procedure (see previous section) to the above equation, and obtain N^{-1} for the N prior. We generalize this prior further to a power function of the type N^{-c} where c is a parameter to be determined later. The posterior for N becomes

$$P(nN \mid n\bar{x}) \equiv P(nN \mid n\bar{x}, a, b, c) = \frac{P(n\bar{x} \mid nN, a, b)(nN)^{-c}}{\sum_{nN=n\bar{x}}^{\infty} P(n\bar{x} \mid nN, a, b)(nN)^{-c}}. \qquad (28)$$

The uncorrected moment of the rth order can be calculated from Eq. 29

$$\mu_r'(nN \mid n\bar{x}) = \sum_{nN=n\bar{x}}^{\infty} (nN)^r P(nN \mid n\bar{x}). \qquad (29)$$

The convergence of the sum in Eq. 29 requires $c > r - a + 1$. Therefore, we call the power-function prior for N a convergent prior.

Proposition 1. The posterior in Eq. 28 does not have a mode for a noninformative prior of p.

Proof. By taking a logarithm of the numerator in Eq. (28), differentiating it with respect to nN, and using the definition of ψ function, one obtains

$$\psi(nN+1) - \psi(nN+a+b) + \psi(nN - n\bar{x} + b) - \psi(nN - n\bar{x} + 1) - c/nN.$$

By subtracting the ψ functions, one obtains (*49*)

$$\sum_{k=0}^{\infty} \left\{ \frac{1-a-b}{(nN+a+b+k)(nN+1+k)} + \frac{b-1}{(nN-n\bar{x}+b+k)(nN-n\bar{x}+1+k)} \right\} - c/nN.$$

It is seen that the above expression is negative for a and b both equal to 0, ½, 1, and $c > 0$. Therefore, the posterior is a decreasing function of N and has a half-mode at $n\bar{x}$. □

This lack of mode is apparent in the tables in Ref. (*42*).

The credibility intervals for nN, l and h, with $1 - \alpha$ credibility level can be calculated from the equations below

$$\sum_{nN=l}^{\mu(nN)} P(nN \mid n\bar{x}) = \sum_{nN=\mu(nN)}^{h} P(nN \mid n\bar{x}) = (1-\alpha)/2. \qquad (30)$$

The limitations regarding integer N are the same as listed below Eqs. 21.

Equations 28, 29 are valid for any beta prior for p and its limits. As examples, we evaluate below two cases for uniform and Jaynes p priors, respectively. In doing so, we replace the sums by the integrals. While an approximation, this can be justified by the large uncertainties in the estimators, as well as by the fact that most of the systematically introduced error is expected to cancel out by taking the ratio of integrals leading to the moments in Eq. 29.

Downloaded by COLUMBIA UNIV on August 6, 2012 | http://pubs.acs.org
Publication Date: November 16, 2006 | doi: 10.1021/bk-2007-0945.ch024

Uniform p Prior, a = b = 1

In this case, the likelihood for N from Eq. 27 is proportional to $1/(nN + 1)$. By plugging it to Eq. 29, the uncorrected moments can be calculated using tabulated integrals (*49*)

$$\mu'_r(nN \mid n\bar{x}) = \frac{\displaystyle\int_{n\bar{x}}^{\infty} \frac{d(nN)}{(nN+1)(nN)^{c-r}}}{\displaystyle\int_{n\bar{x}}^{\infty} \frac{d(nN)}{(nN+1)(nN)^{c}}} = (-1)^r \frac{\ln(1+1/n\bar{x}) + \sum_{k=1}^{c-r-1}(-n\bar{x})^{-k}/k}{\ln(1+1/n\bar{x}) + \sum_{k=1}^{c-1}(-n\bar{x})^{-k}/k}. \tag{31}$$

The corrected moments can be calculated from Eq. 31: mean with $r = 1$, $c = 2$, and variance with $r = 2$, $c = 3$, the minimum values to achieve convergence of the integrals. Working formulas for the moment estimators are given below:

$$\mu(N \mid \bar{x}) = \frac{\bar{x}\ln(1+1/n\bar{x})}{1 - n\bar{x}\ln(1+1/n\bar{x})} \tag{32a}$$

$$\mu_2(N \mid \bar{x}) = \frac{2\bar{x}^2\left[(2n\bar{x}+1)\ln(1+1/n\bar{x}) - 2\right]}{\left[2(n\bar{x})^2\ln(1+1/n\bar{x}) - 2n\bar{x} + 1\right]^2}. \tag{32b}$$

This method was used to calculate the Bayesian estimate of N and its uncertainty for another Draper and Guttman (*42*) example: $n = 1$, $x = 10$, unknown N and p. The results calculated using Eqs. 32a, b are given for the third case in Table III. It is seen that this method estimated N twice as large as x, implying $p = 0.5$. This is not surprising, since the uniform prior for p was assumed. The method is compared with other literature estimates of this case. Draper and Guttman severely underestimated N (case 1), a problem that has been discussed in general by DasGupta and Rubin (*46*). None of the authors (*39*,*42*) provided estimates of the uncertainty.

Table III. Bayesian Estimates of N for $n = 1, x = 10$

No	*Prior*		*Estimate*		*Ref.*
	p	*N*	*N*	1σ	
1	uniform	rectangular	10		(*42*)
2	$a = 5, b = 2$	uniform	17		(*39*)
3	uniform	convergent	20	± 9	
4	Jaynes	convergent	16	± 6	

Downloaded by COLUMBIA UNIV on August 6, 2012 | http://pubs.acs.org
Publication Date: November 16, 2006 | doi: 10.1021/bk-2007-0945.ch024

Another interesting example has been provided by Carroll and Lombard (*43*). It consists of counting the waterbucks in Kruger Park, South Africa. The results of counts ($n = 5$) were $x_i = 53, 57, 66, 67, 72$. The aim was to estimate the number of waterbucks N without knowledge of p. Several authors attempted solving this example by various methods, which are listed in Table IV. It is seen that the Monte Carlo simulation (case 10) yielded N in the range 80 - 598 for the 80 % highest posterior density coverage. However, this distribution is skewed towards the lower values. Both MME and MLE resulted in unstable estimates. Most Bayesian estimates yielded similar results, including ours (case 11), except case 8. None of the authors (*38,43*) provided estimates of the uncertainty. Our case 12 will be discussed below.

Downloaded by COLUMBIA UNIV on August 6, 2012 | http://pubs.acs.org
Publication Date: November 16, 2006 | doi: 10.1021/bk-2007-0945.ch024

Table IV. Bayesian Estimates of *N* for Carroll and Lombard (*40*) Example

No	*Method*	*Type*	*Prior*		*Estimate*		*Ref.*
			p	*N*	*N*	1σ	
1	MME[a]				272		(*43*)
2	MME[a]	stabilized			199		(*43*)
3	MLE[b]				265		(*43*)
4	MLE[b]	stabilized			72		(*43*)
5	Bayes	mode	uniform	uniform	146		(*43*)
6	Bayes	mode	$a = b = 2$	uniform	140		(*43*)
7	Bayes	mode	uniform	N^{-1}	122		(*38*)
8	Bayes	median	uniform	N^{-1}	223		(*38*)
9	Bayes	mean	uniform	N^{-1}	131		(*38*)
10	Monte Carlo	simulation			80 – 598	80 % coverage	(*38*)
11	Bayes	mean	uniform	convergent	126	$-54+56$	
12	Bayes	mean	Jaynes	convergent	109	$-37+41$	

[a]Method of moments estimator, [b]Maximum likelihood estimator

Jaynes p Prior, $a = b = 0$

In this case, the likelihood for N from Eq. 27 is proportional to $nN/(nN - n\bar{x})$. There are two difficulties with this likelihood. One is a singularity at $n\bar{x}$ and another is biasing towards low N. To alleviate these problems, the lower integration limit was set at $nx_m + 1$, where one was added to bypass the singularity which still exists for $n = 1$. By plugging the likelihood to Eq. 29, the uncorrected moments can be calculated using tabulated integrals (*49*)

$$\mu_r'(nN \mid n\bar{x}) = \frac{\displaystyle\int_{nx_m+1}^{\infty} \frac{d(nN)}{(nN - n\bar{x})(nN)^{c-r-1}}}{\displaystyle\int_{nx_m+1}^{\infty} \frac{d(nN)}{(nN - n\bar{x})(nN)^{c-1}}}$$

$$= (n\bar{x})^r \frac{\ln\dfrac{nx_m+1}{nx_m - n\bar{x}+1} - \sum_{k=1}^{c-r-2} \dfrac{1}{k}\left(\dfrac{n\bar{x}}{nx_m+1}\right)^k}{\ln\dfrac{nx_m+1}{nx_m - n\bar{x}+1} - \sum_{k=1}^{c-2} \dfrac{1}{k}\left(\dfrac{n\bar{x}}{nx_m+1}\right)^k}. \tag{33}$$

The corrected moments can be calculated from Eq. 33: mean with $r = 1$, $c = 3$, and variance with $r = 2$, $c = 4$, the minimum values to achieve convergence of the integrals. Working formulas for the moment estimators are given below:

$$\mu(N \mid \bar{x}) = \frac{\bar{x}\ln\dfrac{nx_m+1}{nx_m - n\bar{x}+1}}{\ln\dfrac{nx_m+1}{nx_m - n\bar{x}+1} - \dfrac{n\bar{x}}{nx_m+1}} \tag{34a}$$

$$\mu_2(N \mid \bar{x}) = \frac{\bar{x}^2 \dfrac{n\bar{x}}{nx_m+1}\left[\left(1 - \dfrac{1}{2}\dfrac{n\bar{x}}{nx_m+1}\right)\ln\dfrac{nx_m+1}{nx_m - n\bar{x}+1} - \dfrac{n\bar{x}}{nx_m+1}\right]}{\left[\ln\dfrac{nx_m+1}{nx_m - n\bar{x}+1} - \dfrac{n\bar{x}}{nx_m+1}\left(1 + \dfrac{1}{2}\dfrac{n\bar{x}}{nx_m+1}\right)\right]^2}. \tag{34b}$$

The Bayesian estimates of N and its uncertainty for the Draper and Guttman (*42*) example using Eqs. 34a, b are given in Table III (case 4). The estimate of 16 is lower than the one for the uniform p prior, and comparable with the one in Ref. (*39*). The estimate of N for the Carroll and Lombard (*43*) example is given as case 12 in Table IV. It is slightly lower than other Bayesian estimates, however, it overlaps with them within given uncertainty (with the exception of case 8).

6. Bayesian Inference from the Poisson Distribution

The Bayesian inference from the Poisson distribution for multiple sampling has been described (*29*,*44*). Since the prefactors in Eqs. 4a and 8 do not depend on θ, we neglect them. Then, according to the Bayes theorem, Eq. 14, the posterior is proportional to $\theta^{n\bar{x}+a-1}\,e^{-(n+b)\theta}$. The normalization integral is then calculated (*20*) as: $\int_0^{\infty} \theta^{n\bar{x}+a-1}\,e^{-(n+b)\theta} d\theta = \frac{\Gamma(n\bar{x}+a)}{(n+b)^{n\bar{x}+a}}$. The posterior turns out to be the gamma distribution:

Downloaded by COLUMBIA UNIV on August 6, 2012 | http://pubs.acs.org
Publication Date: November 16, 2006 | doi: 10.1021/bk-2007-0945.ch024

$$P(\theta \mid n\bar{x}) \equiv P(\theta \mid n\bar{x}, a, b) = \frac{(n+b)^{n\bar{x}+a}}{\Gamma(n\bar{x}+a)} \theta^{n\bar{x}+a-1} \, \mathrm{e}^{-(n+b)\theta} . \tag{35}$$

The point estimators of the posterior are calculated from the uncorrected *r*th moments (*25*) of Eq. 35, μ_r',

$$\mu_r'(\theta \mid n\bar{x}) = \int_0^\infty \theta^r P(\theta \mid n\bar{x}) \, d\theta = \frac{(n\bar{x}+a)_r}{(n+b)^r} , \tag{36}$$

The mean μ and the variance μ_2 are then calculated from Eq. 36:

$$\mu(\theta \mid n\bar{x}) = \mu_1'(\theta \mid n\bar{x}) = \frac{\bar{x}+a/n}{1+b/n}, \tag{37a}$$

$$\mu_2(\theta \mid n\bar{x}) = \mu_2'(\theta \mid n\bar{x}) - \mu^2(\theta \mid n\bar{x}) = \frac{\bar{x}+a/n}{n(1+b/n)^2} . \tag{37b}$$

It is seen from Eq. 37a and Table I, that the Jaynes prior ($a = b = 0$) yields the estimate of the mean equal to the MLE, whereas other noninformative estimators are shifted. The estimates become less dependent on the choice of a prior for large n and $\bar{x}$.

The mode of the posterior is determined by differentiating Eq. 35 with respect to θ and equating to zero:

$$Mo(\theta \mid n\bar{x}) = \frac{\bar{x}+(a-1)/n}{1+b/n} . \tag{37c}$$

In a special case, when $n\bar{x} + a < 1$, the half-mode is equal to zero.

The credibility intervals l and h on θ can be obtained similarly to the binomial case in Section 5A, by a numerical solution of Eqs. 38a, b:

$$\int_l^h P(\theta \mid n\bar{x}) \, d\theta = 1 - \alpha , \tag{38a}$$

$$\left(\frac{h}{l}\right)^{n\bar{x}+a-1} = \mathrm{e}^{(n+b)(h-l)} . \tag{38b}$$

As a nuclear-science example of using the Bayesian inference, let us consider counting radiations from decay of a long-lived radionuclide, governed by the Poisson process (compare Section 1). In the course of n measurements (sampling) x_i counts were measured. The Poisson parameter of counts is $\theta = \rho t$, where $\rho = N\lambda\varepsilon$. We are interested in the determination of counting rate ρ in counts per unit time, given that each measurement lasted time t. Assuming a gamma prior for ρ, the posterior is proportional to $\rho^{n\bar{x}+a-1} \, \mathrm{e}^{-(nt+b)\rho}$. By repeating the derivations as for Eqs. 35-37, we obtain the formulas for the mean rate and its variance

$$\mu(\rho) = \frac{\sum x_i + a}{nt+b}, \tag{39a}$$

$$\mu_2(\rho) = \frac{\sum x_i + a}{(nt+b)^2} . \tag{39b}$$

It is seen from Eqs. 39a, b that for the Jaynes prior ($a = b = 0$) the estimates are

Downloaded by COLUMBIA UNIV on August 6, 2012 | http://pubs.acs.org
Publication Date: November 16, 2006 | doi: 10.1021/bk-2007-0945.ch024

equal to the MLE treatment. However, conjugate as well as other noninformative priors produces shifts in the estimates. It is also seen that there is no statistical difference in making, say, one 10-min measurement or ten 1-min measurements ($\sum x_i$ as well as the product nt are constant in both cases), which is a property of the Poisson distribution.

7. Summary and Conclusions

We have provided a review of the Bayesian approaches to the two statistical distributions that model stochasticity of nuclear processes: binomial and Poisson. Inferences of the parameter θ of the Poisson distribution and associated rate ρ, as well as parameters N and p of the binomial distribution were described. We provided formulas for the posteriors, point estimators - mean, variance, and mode; as well as interval estimators. The posteriors and point estimators for the N parameter have been derived under simplified assumptions of $n\bar{x}$ statistic and, for the unknown N/unknown p case, by approximating infinite sums with the integrals. Several posteriors and point estimators for the N parameter were derived for the first time. The formulas are given generally for multiple sampling, from which a single sampling case can be easily deduced. The binomial case when both p and N are unknown continues to be a challenge justifying further research.

Several prior distributions of the parameters in question were discussed: conjugate beta for p, conjugate gamma for θ and ρ, conjugate negative binomial and Poisson for N, as well as noninformative - uniform, Jeffreys, Jaynes, and convergent. It was shown that the priors introduce shifts in the mean estimators as well as overdispersion in the sampling outcome variable x. The Jaynes prior results in the estimators of mean equal to the maximum-likelihood estimators, and it causes the smallest modification of the variance. The effect of priors on the posteriors diminishes as the number of samplings increases.

We provided numerical examples of the Bayesian inference using several illustrative cases from nuclear science. We also analyzed several well known cases from the literature, unrelated to nuclear science: three numerical cases by Draper and Guttman (*42*), as well as one case by Carroll and Lombard (*43*). Our inferred means were in agreement with the literature, whereas our inferred uncertainties were calculated for the first time.

Acknowledgments

Thanks are due to C. Atwood and A. Forbes for critical reviewing the manuscript and their valuable comments.

Downloaded by COLUMBIA UNIV on August 6, 2012 | http://pubs.acs.org
Publication Date: November 16, 2006 | doi: 10.1021/bk-2007-0945.ch024

References

1. Rainwater, L. J.; Wu, C.S. Applications of probability theory to nuclear particle detection. *Nucleonics* **1947**, 1(2), 60-69.
2. Friedlander G.; Kennedy, J. W.; Macias, E. S.; Miller, J. M. *Nuclear and Radiochemistry*; J. Wiley & Sons: New York, NY, 1981.
3. Little, R. J. A. The statistical analysis of low-level radioactivity in the presence of background counts. *Health Phys.* **1982**, 43, 693-703.
4. Moreno, A.; Navarro, E.; Senent, F. A Bayesian interpretation of a decision level in radioactivity counting data. *Anal. Fis. B* **1988**, 84, 297-312.
5. Michel, R. Quality assurance of nuclear analytical techniques based on Bayesian characteristic limits. *J. Radioanal. Nucl. Chem.* **2000**, 245, 137-144.
6. Groer, P.G. Exact and approximate Bayesian estimation of net counting rates. *Rad. Prot. Dosimetry* **2002**, 102, 265-268.
7. Miller, G.; Martz, H. F.; Little, T. T.; Guilmette, R. Using exact Poisson likelihood function in Bayesian interpretation of counting measurements. *Health Phys.* **2002**, 83, 512-518.
8. Aurela, A. M. Counting a small number of radioactive atoms. *Comp. Phys. Comm.* **1977**, 13, 281-287.
9. Prosper, H. B. A Bayesian analysis of experiments with small number of events. *Nucl. Instr. Meth. Phys. Res. A* **1985**, 241, 236-240.
10. Escoubes, B.; De Unamuno, S.; Helene, O. Experimental signs pointing to a Bayesian instead of classical approach for experiments with a small number of events. *Nucl. Instr. Meth. Phys. Res. A* **1987**, 257, 346-360.
11. Heřmanská, J; Kárný, M. Effective half-life estimation: Bayesian solution. *Rad. Prot. Dosimetry* **1995**, 62, 223-232.
12. Miller, G.; Inkret, W. C.; Martz, H. F. Bayesian detection analysis for radiation exposure. *Rad. Prot. Dosimetry* **1993**, 48, 251-256.
13. Price, P. N.; Nero, A. V.; Gelman, A. Bayesian prediction of mean indoor radon concentrations for Minnesota counties. *Health Phys.* **1996**, 71, 922-936.
14. Miller, G.; Inkret, W. C.; Schillaci, M. E.; Martz, H. F.; Little, T. T. Analyzing bioassay data using Bayesian methods – a primer. *Health Phys.* **2000**, 78, 598-613.
15. D'Agostini, G. A multidimensional unfolding method based on Bayes' theorem. *Nucl. Instr. Meth. Phys. Res. A* **1995**, 362, 487-498.
16. Dou, L.; Hodgson, R. J. W.; Rancourt, D. G. Bayesian inference theory applied to hyperfine parameter distribution extraction in Mössbauer spectroscopy. *Nucl. Instr. Meth. Phys. Res. B* **1995**, 100, 511-518.
17. Martz, H. F. An introduction to Bayes, hierarchical Bayes, and empirical Bayes statistical methods in health physics. *Applications of Probability and*

Downloaded by COLUMBIA UNIV on August 6, 2012 | http://pubs.acs.org
Publication Date: November 16, 2006 | doi: 10.1021/bk-2007-0945.ch024

Statistics in Health Physics; Borak, T. B., Ed.; Medical Physics Publishing: Madison, WI, 2000; 55-84.

18. Semkow, T. M. Exponential decay law and nuclear statistics. This book.
19. Semkow, T. M. Theory of overdispersion in counting statistics caused by fluctuating probabilities. *Appl. Rad. Isot.* **1999**, 51, 565-579.
20. Johnson, N. L.; Kotz, S.; Kemp, A. W. *Univariate Discrete Distributions*; J. Wiley & Sons: New York, NY, 1993.
21. Stuart, A.; Ord, J. K.; Arnold, S. *Kendall's Advanced Theory of Statistics*, Vol. 2A, *Classical Inference and the Linear Model*; Arnold: London, 1999.
22. Semkow, T. M. Experimental verification of overdispersion in radioassay data. *Health Phys.* **2002**, 83, 485-496.
23. Pazdur, M. F. Counting statistics in low level radioactivity measurements with fluctuating counting efficiency. *Int. J. Appl. Radiat. Isot.* **1976**, 27, 179-184.
24. Müller, J. W. A test for judging the presence of additional scatter in a Poisson process. Report BIPM-78/2; Bureau International des Poids et Mesures: Sèvres, 1978.
25. Johnson, N. L.; Kotz, S.; Balakrishnan, N. *Continuous Univariate Distributions*; Vols. 1, 2, J. Wiley & Sons: New York, NY, 1994/5.
26. Dennis, B.; Patil, G. P. The gamma distribution and weighted multimodal gamma distributions as models of population abundance. *Math. Biosci.* **1984**, 68, 187-212.
27. Bayes, T. An essay towards solving a problem in the doctrine of chances. *Phil. Trans. Roy. Soc.* (London) **1763**, 53, 370-418. Reprinted with an introduction by Barnard, G.A. *Biometrika* **1958**, 45, 293-315.
28. Box, G. E. P.; Tiao, G. C. *Bayesian Inference in Statistical Analysis*; J. Wiley & Sons: New York, NY, 1994.
29. Irony, T. Z. Bayesian estimation for discrete distributions. *J. Appl. Stat.* **1992**, 19, 533-549.
30. O'Hagan, A.; Forster, J. *Kendall's Advanced Theory of Statistics*, Vol. 2B, *Bayesian Inference*; Arnold: London, 2004.
31. Atwood, C. L.; LaChance, J. L.; Martz, H. F.; Anderson, D. J.; Englehardt, M.; Whitehead, D.; Wheeler, T. *Handbook of Parameter Estimation for Probabilistic Risk Assessment*; Report NUREG/CR-6823, U.S. Nuclear Regulatory Commission: Washington, DC, 2003.
32. Laplace, P. S. Mémoire sur la probabilité des causes par les évènemens. *Mémoires de mathématique et de physique presentés à l'Académie royale des sciences, par divers savans, & lús dans ses assemblées* **1774**, 6, 621-656. Reprinted with an introduction and English translation by Stigler, S.M. *Stat. Sci.* **1986**, 1, 359-378.
33. Jeffreys, H. *Theory of Probability*; Clarendon Press: Oxford, 2003.

Downloaded by COLUMBIA UNIV on August 6, 2012 | http://pubs.acs.org
Publication Date: November 16, 2006 | doi: 10.1021/bk-2007-0945.ch024

34. Jaynes, E. T. Prior probabilities. *IEEE Trans. Sys. Sci. Cyb.* **1968**, SSC-4, 227-241.
35. Jaynes, E. T. *Probability Theory, the Logic of Science*; Cambridge: Cambridge, 2003.
36. Sadooghi-Alvandi, S. M.; Parsian, A. Estimation of the binomial parameter *n* using a linex loss function. *Commun. Statist. - Theory Meth.* **1992**, 21, 1427-1439.
37. Iliopoulus, G. Some new estimators of the binomial parameter *n*. *Commun. Statist. - Theory Meth.* **2003**, 32, 1361-1372.
38. Raftery, A. E. Inference for the binomial *N* parameter: a hierarchical Bayes approach. *Biometrika* **1988**, 75, 223-228.
39. Hamedani, G. G.; Walter, G. G. Bayes estimation of the binomial parameter *n*. *Commun. Statist. - Theory Meth.* **1988**, 17, 1829-1843.
40. Rukhin, A. L. Statistical decision about the total number of observable objects. *Sankhya A* **1975**, 37, 514-522.
41. Sadooghi-Alvandi, S. M. Admissible estimation of the binomial parameter *n*. *Ann. Statist.* **1986**, 14, 1634-1641.
42. Draper, N.; Guttman, I. Bayesian estimation of the binomial parameter. *Technometrics* **1971**, 13, 667-673.
43. Carroll, R.J.; Lombard, F. A note on N estimators for the binomial distribution. *J. Am. Stat. Assoc.* **1985**, 80, 423-426.
44. Müller, J. W. Un nouveau regard sur les probabilitiés a priori. Report BIPM-80/6; Bureau International des Poids et Mesures: Sèvres, 1980.
45. Kahn, W. D. A cautionary note for Bayesian estimation of the binomial parameter *n*. *Am. Statist.* **1987**, 41, 38-40.
46. DasGupta, A.; Rubin, H. Estimation of binomial parameters when both *n*, *p* are unknown. *J. Statist. Plann. Inference* **2005**, 130, 391-404.
47. Stuart, A.; Ord, K. *Kendall's Advanced Theory of Statistics*, Vol. 1, *Distribution Theory*; Arnold: London, 2003.
48. *Handbook of Mathematical Functions*. Abramowitz, M.; Stegun, I. A., Eds.; Dover: New York, NY, 1977.
49. Gradshteyn, I.S.; Ryzhik, I.M. *Table of Integrals, Series and Products*; Jeffrey, A., Ed.; Academic Press: San Diego, CA, 1980.

Downloaded by COLUMBIA UNIV on August 6, 2012 | http://pubs.acs.org
Publication Date: November 16, 2006 | doi: 10.1021/bk-2007-0945.ch024

Downloaded by 89.163.34.136 on August 6, 2012 | http://pubs.acs.org
Publication Date: November 16, 2006 | doi: 10.1021/bk-2007-0945.ap001

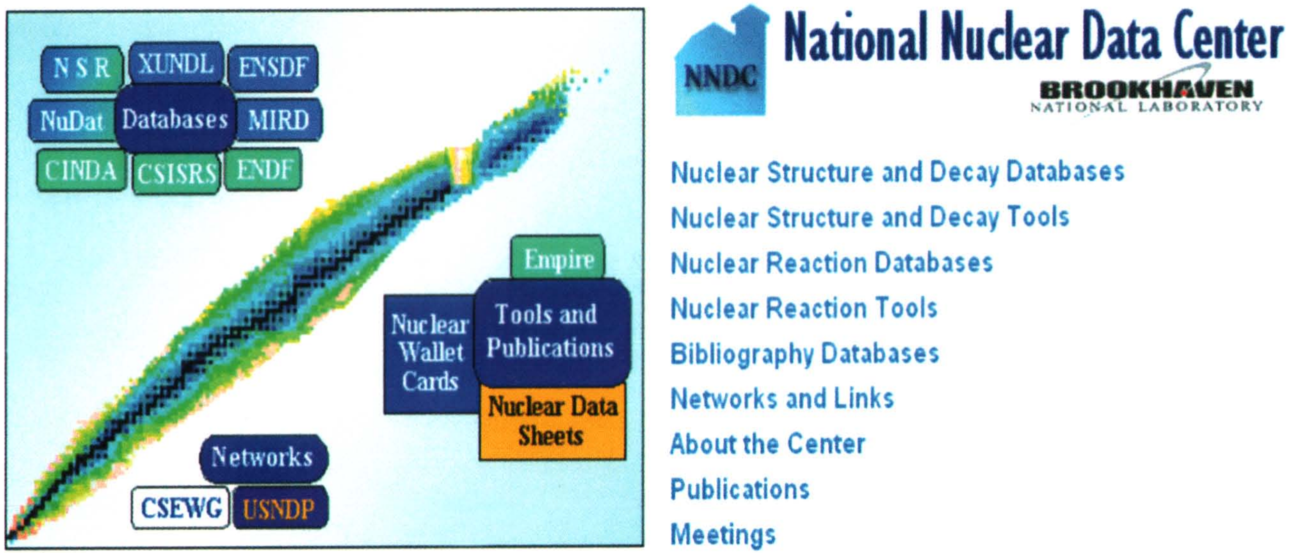
N S R
XUNDL
ENSDF
NuDat
Databases
MIRD
CINDA
CSISRS
ENDF
Empire
Nuclear Wallet Cards
Tools and Publications
Nuclear Data Sheets
Networks
CSEWG
USNDP
NNDC
National Nuclear Data Center
BROOKHAVEN NATIONAL LABORATORY
Nuclear Structure and Decay Databases
Nuclear Structure and Decay Tools
Nuclear Reaction Databases
Nuclear Reaction Tools
Bibliography Databases
Networks and Links
About the Center
Publications
Meetings

Figure 2.1. Front page of the web service of the National Nuclear Data Center (NNDC), www.nndc.bnl.gov, offers nuclear databases at top left.

Downloaded by 89.163.34.136 on August 6, 2012 | http://pubs.acs.org
Publication Date: November 16, 2006 | doi: 10.1021/bk-2007-0945.ap001

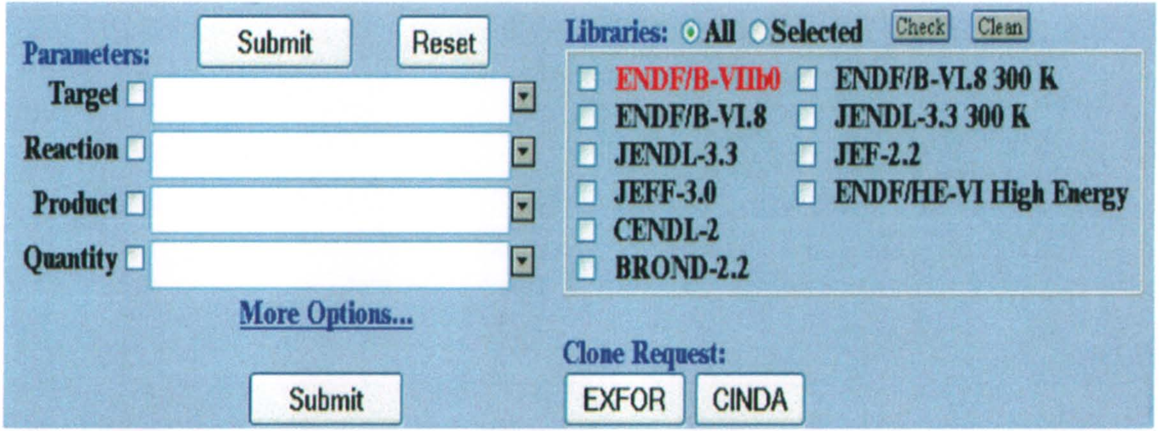
Parameters:
Submit
Reset
Target ☐
Reaction ☐
Product ☐
Quantity ☐
More Options...
Submit
Libraries: ● All ○ Selected
Check
Clean
☐ ENDF/B-VIIb0
☐ ENDF/B-VI.8
☐ JENDL-3.3
☐ JEFF-3.0
☐ CENDL-2
☐ BROND-2.2
☐ ENDF/B-VI.8 300 K
☐ JENDL-3.3 300 K
☐ JEF-2.2
☐ ENDF/HE-VI High Energy
Clone Request:
EXFOR
CINDA

Figure 2.2. Web interface for the Evaluated Nuclear Data File operated by the NNDC, www.nndc.bnl.gov/endf. The latest ENDF/B-VI.8 along with preliminary ENDF/B-VII and databases from Japan, EU, China and Russia are available.

Downloaded by 89.163.34.136 on August 6, 2012 | http://pubs.acs.org
Publication Date: November 16, 2006 | doi: 10.1021/bk-2007-0945.ap001

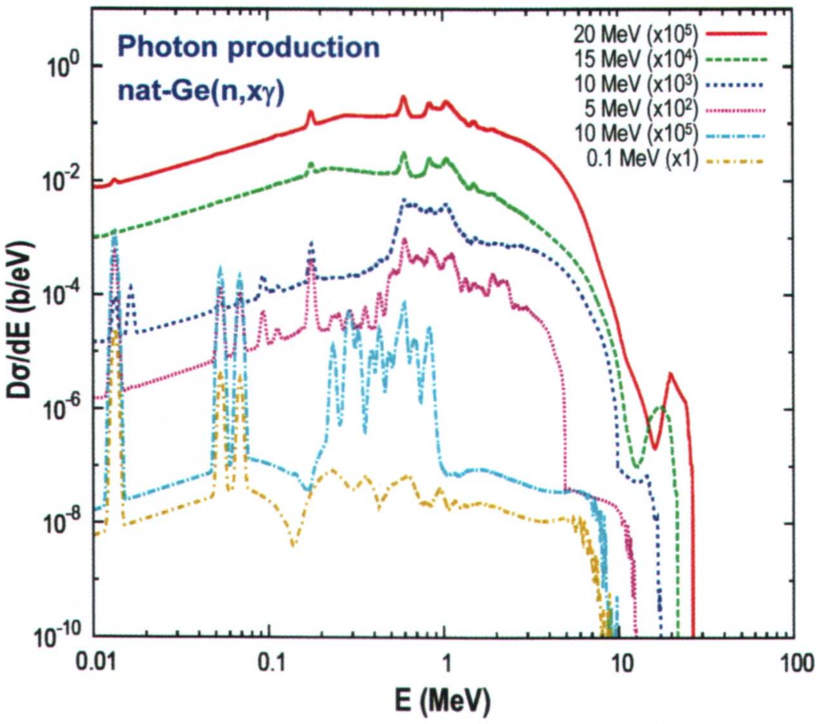

Figure 2.3. Photon production spectra from Ge(n,xγ) reactions for neutrons of several incident energies in the range of 0.1- 20 MeV.

In Applied Modeling and Computations in Nuclear Science; Semkow, T., et al.;
ACS Symposium Series; American Chemical Society: Washington, DC, 2006.

Downloaded by 89.163.34.136 on August 6, 2012 | http://pubs.acs.org
Publication Date: November 16, 2006 | doi: 10.1021/bk-2007-0945.ap001

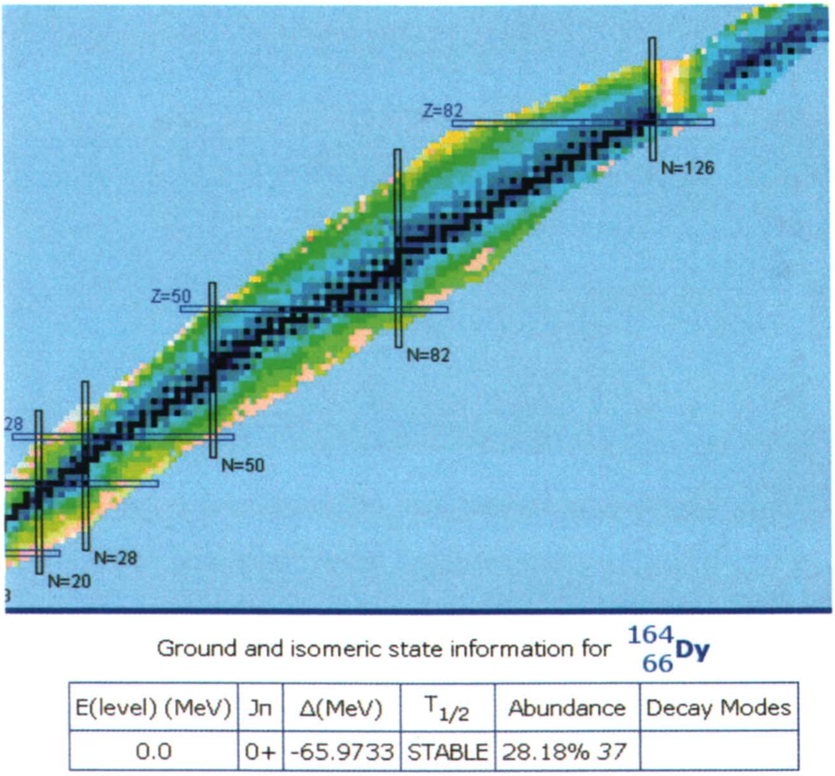

Ground and isomeric state information for $^{164}_{66}$**Dy**

E(level) (MeV)	Jπ	Δ(MeV)	$T_{1/2}$	Abundance	Decay Modes
0.0	0+	-65.9733	STABLE	28.18% *37*	

Figure 2.4. NuDat web interface operated by the National Nuclear Data Center, www.nndc.bnl.gov/nudat. Shown is the front page with the chart of nuclei (20, 28,…, 128 are magic numbers) and basic information retrieved for Dy-164.

Downloaded by 89.163.34.136 on August 6, 2012 | http://pubs.acs.org
Publication Date: November 16, 2006 | doi: 10.1021/bk-2007-0945.ap001

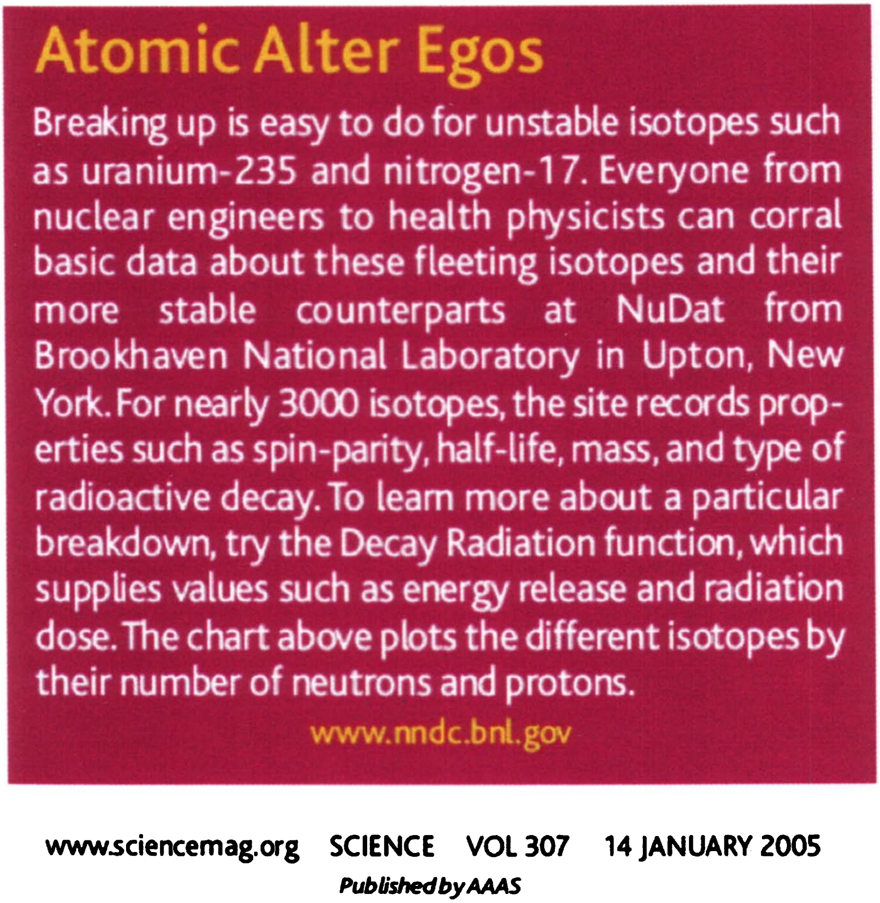

Atomic Alter Egos

Breaking up is easy to do for unstable isotopes such as uranium-235 and nitrogen-17. Everyone from nuclear engineers to health physicists can corral basic data about these fleeting isotopes and their more stable counterparts at NuDat from Brookhaven National Laboratory in Upton, New York. For nearly 3000 isotopes, the site records properties such as spin-parity, half-life, mass, and type of radioactive decay. To learn more about a particular breakdown, try the Decay Radiation function, which supplies values such as energy release and radiation dose. The chart above plots the different isotopes by their number of neutrons and protons.

www.nndc.bnl.gov

www.sciencemag.org SCIENCE VOL 307 14 JANUARY 2005
Published by AAAS

Figure 2.5. Recognition to NuDat interface published in Science, Vol. 307, 2005, 187.

Author Index

Aanenson, Jill W., 71
Berlizov, Andrey N., 183, 293
Bertelli, L., 93
Brüchle, Willy, 269
Burkhart, James F., 249
Culbreth, William G., 131
Currie, L. A., 19
Grogan, Helen A., 2, 71
Grygorenko, M. O., 293
Guilmette, R., 93
Haghighat, Alireza, 162
Haines, Douglas K., 142
Jenkins, Phillip H., 249
Jerome, Simon M., xi
Keightley, J. D., 234, 316
Kershner, Carl J., 249
Kouzes, R., 195
Little, T., 93
McConn, R. J., Jr., 195
McGavran, Patricia D., 71
Meyer, Kathleen R., 71
Miller, G., 93
Mohler, H. Justin, 71
Mohler, S. Shawn, 71
O'Brien, Keran, 207
Obložinský, P., 10
Pagh, R., 195
Parekh, Pravin P., 142
Pommé, S., 218, 282, 316
Potter, W. E., 305
Robinson, S. M., 195
Rocco, James R., 71
Rood, Arthur S., 71
Schweppe, J. E., 195
Semkow, Thomas M., 42, 142, 335
Siciliano, E. R., 195
Sjoden, Glenn E., 162
Strom, Daniel J., xi
Till, John E., 2, 71
Tryshyn, V. V., 293
Viggato, Jason C., 131
Vojtyla, P., 104
Wilson, Lesley H., 71
Xu, X. George, 115
Yu, Charley, 58

Downloaded by 89.163.34.136 on August 6, 2012 | http://pubs.acs.org
Publication Date: November 16, 2006 | doi: 10.1021/bk-2007-0945.ix001

In Applied Modeling and Computations in Nuclear Science; Semkow, T., et al.;
ACS Symposium Series; American Chemical Society: Washington, DC, 2006.

Subject Index

A

A^{3}MCNP code system, description, 168–170
Accelerator facilities, airborne releases, radioactive substances, effective dose to public, 104–114
Activated charcoal devices, count data, 264–265*f*, 268*t*
Adaptive differencing strategy in PENTRAN code system, 168
Adult male whole-body model. *See* VIP-Man
Africa. *See* Gabon
Afterpulse probability in NIST system, 37–38
Air density effect on coefficients of dispersion, 263–264*f*
Air monitoring program efficiency analysis at Khmel'nits'kiy nuclear power plant, 298, 300–304
Air pathway risks, radionuclides and chemicals released during Cerro Grande Fire, 84–85
Air transport pathway, radionuclides and chemicals released during Cerro Grande Fire, 76*f*, 77–79
Alarm algorithm testing for radiation portal monitor systems, 204
Alpha particles in scintillation cells, counting efficiencies, 257–264*f*
American Society for Testing and Materials (ASTM) interlaboratory standards, 20
Angular distribution, cosmic-ray protons, 213–214*f*
Applications
  air monitoring efficiency, Khmel'nits'kiy nuclear power plant, 298, 300–304
  computed tomography, 172–174*t*
  decay from long-lived radionuclide, counting using Bayesian inference, 352–353
  homeland security, models of radiation portal monitors, 195–206
  radiation dose to space crews, solar wind influence on cosmic-ray intensity, 208
  spent fuel cask for spent nuclear fuel storage, flux/dose determination, 177–180
  waste assay, prompt gamma neutron activation analysis, 170–172*t*
Applications, Monte Carlo N-particle transport code extension, 187–192
Arbitrary function, parameter estimation, 324–325
Argonne National Laboratory, RESRAD codes, 59
Assessing risk and modeling radionuclide transport, RESRAD family of codes, 58–70
ASTM. *See* American Society for Testing and Materials
Asymptote, background, Poisson detection decisions and detection limits, 29–30
Asymptote, extreme low-level Poisson detection decisions and limits for paired counting, 30–33
Asymptotic counting uncertainties, counting in real-time mode, 224
Automated Adjoint Accelerated MCNP. *See* A^{3}MCNP code system, description
Average blank count, method to compensate for uncertainty in blank count, 307–308

Downloaded by 89.163.34.136 on August 6, 2012 | http://pubs.acs.org
Publication Date: November 16, 2006 | doi: 10.1021/bk-2007-0945.ix002

Average decision levels in average upper bounds for errors of both types, 310–311*t*
Average detection limits in average upper bounds for errors of both types, 311–313
Average upper bounds for errors of both types, compensation for uncertainty in blank count, 309–313

B

^{133}Ba check source testing, 204–205*f*, 206*f*
Background
  asymptote, Poisson detection decisions and detection limits, 29–30
  counts, Poisson hypothesis validity, 21*f*, 33–38
  radiation, importance in future nuclear science research, 7–8
  signal value, estimates, 301
  See also Blank
Barometric pressure, source, non-Poisson, non-random C-background variance, 36
Baseline. *See* Background; Blank
Bayes theorem and prior distributions, 340–342
Bayesian approach to internal dosimetry, 94–96
Bayesian inference for binomial and Poisson distributions, 335–356
Bayesian inference from binomial distribution, cases
  N known, *p* unknown, 343–344
  N unknown, *p* known, 344–347
  N, *p* unknown, 347–351
Bayesian inference from Poisson distributions, 351–353
Beta-binomial (negative hypergeometric) distribution, 338
Beta-decay for mass numbers 90 and 137, 152–153
Binomial distribution, Bayesian inference, cases
  N known, *p* unknown, 343–344
  N unknown, *p* known, 344–347
  N, *p* unknown, 347–351
Binomial distribution, likelihood function, 337
Binomial distribution, principles, 336
Binomial probability parameter, 338
Biota Dosimetry Working Group, 66
Blank
  nuclear detection, 19–41
  uncertainty, decision levels and detection limits in paired counting, 305–315
  See also Background
Boltzmann equation. *See* Linear Boltzmann equation

C

Calibration coefficients, γ-spectrometry measurements, evaluation, 298, 300
CALPUFF, three-dimensional complex terrain model system, 77
Cargo and vehicle models, numerical modeling, radiation portal monitor systems, 197, 199
Cargo Truck lane model, numerical modeling, radiation portal monitor systems, 197, 199*f*, 200–201*f*
Carroll and Lombard, example, Bayesian estimates, 350, 351
CEDE (Committed Effective Dose Equivalent) calculations at Los Alamos, method comparisons, 93–103
Cell type influence on counting efficiencies, alpha particles in scintillation cell, 257–264*f*

Downloaded by 89.163.34.136 on August 6, 2012 | http://pubs.acs.org
Publication Date: November 16, 2006 | doi: 10.1021/bk-2007-0945.ix002

Central moment analysis, time interval spectra, versus unbiased fit, 316–334
Cerro Grande fire at Los Alamos, modeling exposure, health risk and communication with public, 71–92
Chemicals and radionuclides, releases into air and surface water from Cerro Grande fire, geographic area, 72–73*f*
Chernobyl, Ukraine, 26 April 1986 event, 24, 301
Chromatography columns, elution curve simulation, 269–279
Chromatography theories, 269–271
CINDA (Computer Index to Nuclear Reaction Data), description, 11
Coefficient of dispersion. *See* J factor
Coefficient of variation components, evaluation, 300–301
Coincidence/anticoincidence capability, 186–187
Colorado Springs, Colorado, radon decay measurements in scintillation cells, 258–259, 260–264*f*
Committed Effective Dose Equivalent. *See* CEDE
Comparative detection capabilities in extreme low-level Poisson detection decisions, 33
Complete decay probabilities, radionuclides, 53–54
Compton suppression spectrometer, model, 190–192*f*
Computational models, human body for radiation protection dosimetry, 115–130
Computed tomography, application, 172–174*t*
Computer cluster, Lambda, at Los Alamos, for internal dosimetry calculations, 96
Computer Index to Nuclear Reaction Data. See CINDA
Conjugate prior distributions, description, 340, 341–342
Consistent Adjoint Driven Importance Sampling methodology, 168–169
Consortium of Computational Human Phantoms, 124
Constant function parameter estimation, 320–324
Constant rate coefficient, necessary condition in exponential decay, 46
Convergence conditions for Monte Carlo integral, 110
Conversion coefficients for external exposure, 108
Correlated counts in radon measurements, overdispersion corrections, 249–268
Correlation coefficient between workstation and supercomputer internal dosimetry, 97
Correlation coefficient for internal dosimetry and unfolding codes at Los Alamos, 101–102
Cosmic ray propagation, 3-dimensional adjoint random-walk calculation, 207–216
Cosmic-ray proton leakage flux, 214–215*f*
Cosmic-ray protons, angular distribution, 213–214*f*
Cosmic-ray spectra, calculations in ecliptic plane, 212
Cosmic rays, definition, 208
Count loss, types, 219–221
Count rate estimation, Poisson process, 316–334
Count scatter in loss-free counting, 229
Counting efficiencies, alpha particles in scintillation cell, 257–262
Counting in live-time mode, 223
Counting in real-time mode, 224–228*f*
Counting statistics
  dead time and pile-up, 218–233
  overdispersion, 230–232, 338–340

Downloaded by 89.163.34.136 on August 6, 2012 | http://pubs.acs.org
Publication Date: November 16, 2006 | doi: 10.1021/bk-2007-0945.ix002

stretching the Poisson-normal approximation, 24–29
Critical level. *See* Decision threshold
Critical region in extreme low-level Poisson detection decisions, 31
Critical Value. *See* Detection Decision
Currie's approach, 26, 295–297, 306

D

Dayton, Ohio, radon decay measurements in scintillation cells, 258–259, 260–264*f*
DCCs. *See* Dose conversion coefficients
DCFs. *See* Dose conversion factors
Dead time correction in particle counting, 330
Decay constants for radionuclides in radon decay series, 256–257*f*
Decaying state, quantum theory, 47–48
Decision level, definition, 306
Decision threshold, algebraic expression, 297
Deposition exponent, radionuclides in Trinitite, 153–154*f*
Detection capabilities, concepts and international standards, 20–22
Detection decision, algebraic expression, 20–22
Detection limit
  algebraic expression, 20–22
  Currie's, 297
  determination, 306–307
  evaluation for environmental monitoring techniques, 293–304
  extreme low-level Poisson detection decisions, 32
Detection limit ratio, background signal function, 298, 299*f*
Detection system response, coincidence/anticoincidence modes, 186–187
Detector models, radiation portal monitor systems, 197
Deterministic methods compared to statistical Monte Carlo methods, applications, 170–180
  See also Discrete ordinate method
Diffusion coefficient, 208–209
Digital coincidence counting for radioisotope standardization, 234–236
Discrete ordinates method (S_N) applied to Boltzmann particle transport, 164–165, 167
  See also Deterministic methods
Distribution coefficient. *See* Partition coefficient
Dose assessment for flora and fauna, 65–69
Dose assessment for humans, 63–65
Dose build-up factors, 107
Dose conversion coefficients (DCCs), 66, 67, 68*f*
Dose conversion factors (DCFs), 64, 111–113*f*
Draper and Guttman examples, Bayesian estimates, 345, 347, 349
Ducks, dose conversion coefficients, 67, 68*f*
Dynamic link library, raw data simulation routine, radionuclide standardization, 234–248

E

E-Van model, realistic radiation transport models, 197
Effective dose equivalent. *See* Effective dose
Effective dose radionuclides, 63–64, 112–113
Elution curve peaks, shape dependence on number of theoretical plates, 274–276*f*

Downloaded by 89.163.34.136 on August 6, 2012 | http://pubs.acs.org
Publication Date: November 16, 2006 | doi: 10.1021/bk-2007-0945.ix002

Elution curve simulation for chromatography columns, 269–279
Emissions Production Model, 78
EMPIRE (Nuclear Reaction Model Code), description, 13, 15*f*
Empirical distributions and tests, Poisson background hypothesis, 35–38
ENDF (Evaluated Nuclear Data File) database, description, 11, 13, 14*f*
ENSDF (Evaluated Nuclear Structure Data File), 13, 16–17*f*, 184–185
Environmental monitoring techniques, detection limit evaluation, 293–304
Environmental risk analysis. *See* Risk assessment
Environmental risk assessment. *See* Risk assessment
Euler-Mascheroni constant, 319
Evaluated Nuclear Data File. *See* ENDF
Evaluated Nuclear Structure Data File. *See* ENSDF
Explosive yield, Gadget, 150–154, 156*f*
Explosives, estimated risk associated with air release during Cerro Grande Fire, 84–85
Exponential decay law
  discovery, 42–44
  experimental verification, 49–50
  first theory, 44–46
Exponential decay theory, 44–49
Exponential directional weighted scheme, 165
Exponential time interval distribution, moment analysis, 325–330
Exposure scenarios, radionuclides and chemicals released during Cerro Grande Fire, 82–83
External effective dose calculation by Monte Carlo dose kernel integration, 104–114
External exposure, humans
  radioactive plume, dose kernel integration, 105–109
  radionuclides present in the environment, 65
Extrapolation fit parameters for beta and gamma input, digital coincidence counting software, 243–245

F

Fauna and flora, dose assessment, 65–67, 68*f*
Federal Guidance Reports (US), 64
Fermi, Enrico, 145
Fermi Golden Rule No. 2, 48
Field data, radiation portal monitor deployments, 196
Fire at Los Alamos, modeling exposure, health risk and communication with public, 71–92
Fitting alternative, radionuclide half-life determinations, 290–291
Flora and fauna, dose assessment, 65–67, 68*f*
Flux/dose determination, spent fuel cask for spent nuclear fuel storage, 177–180
Ford Econoline van. *See* E-Van model
Forest fires, combustion product behavior, 77
Freeze-out time, Trinitite, 147–148, 156*t*
Frequentist approach to probability interpretation, 342

G

Gabon, Africa, natural reactors, thermohydraulic and nuclear modeling, 131–141

Downloaded by 89.163.34.136 on August 6, 2012 | http://pubs.acs.org
Publication Date: November 16, 2006 | doi: 10.1021/bk-2007-0945.ix002

Downloaded by 89.163.34.136 on August 6, 2012 | http://pubs.acs.org
Publication Date: November 16, 2006 | doi: 10.1021/bk-2007-0945.ix002

Gadget
  explosive yield, 150–154, 156*t*
  first nuclear explosive device, 143–144
Gamma distribution, general model, 338–339
Gauss-Seidel iterative techniques, 134, 165
Gedcke-Hale method, backward counting, 223
Glueckauf equation of chromatography, 271, 277–278
Ground zero, desert sand meltdown from Trinity Test, 145
  See also Trinitite

H

Half-life measurements (radionuclides), uncertainties, 282–292
Hanford reactors, 146
Hazard quotient, definition, 75
Hazard quotients, estimated air pathway risks from radionuclides and chemicals released during Cerro Grande Fire, 84–85
Health risk calculations from radionuclides and chemicals release during Cerro Grande Fire, recommendations, 89–90
Health risk communication on radionuclides and chemicals release during Cerro Grande Fire, recommendations, 90–91
Heliospheric transport equation, random-walk solution, 207–216
Heterogeneous Windows Cluster, increased speed by parallel processing, 202–203
Hexahydro-1,3,5-trinitro-1,3,5-triazine. *See* RDX
High frequency deviations, uncertainties source, 284–285, 286–287
Homeland security application, models of radiation portal monitors, 195–206
Human anatomy modeling for radiation dosimetry, 115–130
Human dose assessment, RESRAD codes, 63–65
Hypothesis testing for detection decisions and capabilities, basic concepts, 20–22

I

ICRM. *See* International Committee for Radionuclide Metrology
ICRP. *See* International Commission on Radiological Protection
Implosion compression factor in Trinity Test, calculations, 155, 156*t*
Ingestion and inhalation, radiation dose, 64–65
Ingestion pathways, radiation exposure, 62–63
Inhalation pathways, radiation exposure, 60, 62
Instabilities in uncertainty budget, sensitivity, 285
Inter-arrival time distributions, background in NIST system, 36–38
Interdisciplinary nature, risk assessment, overview, 4–5
Internal biota dose calculations 66, 67
Internal dosimetry calculations using Markov chain Monte Carlo, 93–103
International Commission on Radiological Protection (ICRP)
  bikinetic methods, 94
  biota dose evaluation, 65–66
  publications on effective dose, 63–64

International Committee for Radionuclide Metrology (ICRM)
  Conference on Low-level Radioactivity Measurement Techniques, 20
  Radionuclides Techniques Working Group, 236
International Organization for Standardization (ISO), recommendations for detection and quantification, 20
International Union of Pure and Applied Chemistry (IUPAC), recommendations for detection and quantification, 20
ISO. *See* International Organization for Standardization
IUPAC. *See* International Union of Pure and Applied Chemistry

J

J factor (coefficient of dispersion)
  activated charcoal devices, 265, 268*t*
  calculations, 251–257
  liquid scintillation charcoal devices, 265–268*t*
  scintillation cells, 262–264*f*
Jaynes, prior distributions, 340–341, 350–351
Jeffreys, prior distributions, 340, 341, 346, 348

K

K_d. *See* Partition coefficient
Khmel'nits'kiy nuclear power plant, Ukraine, air monitoring program, 298–304
^{85}Kr case study, blank as environmental baseline, 21*f*, 22–24

L

Lambda computer cluster, Los Alamos, internal dosimetry calculations, 96
Laplace prior distribution, 340
Large-scale simulation system, radiation portal monitor configurations, 196–197, 198*f*
Leakage flux, cosmic-ray proton, 214–215*f*
Least-squares fit, exponential decay curve, uncertainty problems, 282–292
Least squares fitting
  exponential function to time interval distribution, 331
  'unbiased' method, 331–332, 333*t*
Likelihood functions for multiple sampling, 337
Linear Boltzmann equation, 163–164
Linear diamond-differencing scheme, 165
Liquid scintillation charcoal devices, count data, 265–267, 268*t*
Live-time mode counting, 223
Los Alamos National Laboratory, New Mexico, Cerro Grande fire, modeling exposure, health risk and communication with public, 71–92
Loss correction factor variance in loss-free counting, 229
Loss corrections, counting in real-time mode, 224–227
Loss-free counting, 228–230
Low frequency deviations
  accounting for, 288–290
  uncertainties source, 285
Lucas cell (alpha scintillation cell), J factor, 251, 257
  See also Scintillation cells

Downloaded by 89.163.34.136 on August 6, 2012 | http://pubs.acs.org
Publication Date: November 16, 2006 | doi: 10.1021/bk-2007-0945.ix002

Downloaded by 89.163.34.136 on August 6, 2012 | http://pubs.acs.org
Publication Date: November 16, 2006 | doi: 10.1021/bk-2007-0945.ix002

M

MacLaurin series expansion, 243
Markov chain, definition, 95
Markov chain Monte Carlo method for internal dosimetry calculations, 93–103
  See also Stochastic Markov approach
MARLAP. *See* Multi-Agency Radiological Laboratory Analytical Protocols Manual
Maximum likelihood estimation method, 331–332, 333*t*
Maximum likelihood estimation statistic, 321–322
Maximum likelihood estimators, binomial and Poisson distributions, 337
MDA. *See* Minimum detectable activity
Medical imaging diagnosis, computed tomography application, 172–174*t*
Medium frequency deviations, identification and treatment, 287–288
Medium frequency deviations, uncertainties source, examples, 285
Mercury determination in waste, prompt gamma neutron activation analysis, 170–172*t*
Mighell's least square, 331
Minimum detectable activity (MDA), definition, 294–295
Minimum detectable activity (MDA) for nuclear power plant emission control, 301–303*t*
Minimum Detectable Value. *See* Detection Limit
Minimum Quantifiable Value. *See* Quantification Limit
MIRD Phantom, heterogeneous anthropomorphic model, 116–118*f*
Modeling radionuclide transport and assessing risk, RESRAD family of codes, 58–70
Molecular dynamic theory of chromatography, 269–270
Moment analysis, exponential time interval distribution, 325–330
Monte Carlo dose kernel integration, external effective dose, calculation, 104–114
Monte Carlo methods compared to deterministic methods, real-world applications, 170–180
Monte Carlo methods computational models in radiation dosimetry, 119–120
Monte Carlo methods for particle transport simulation, 166, 167
Monte Carlo N-particle transport code extension, 183–194
Multi-Agency Radiological Laboratory Analytical Protocols Manual (MARLAP), 20, 26

N

National Incident Management System implementation, 90–91
National Institute for Science and Technology study on background counts, 21*f*, 35–39
National Library of Medicine, Visible Human Project, images, 120–122
National Nuclear Data Center (NNDC), 10–18
  See also entity names; US EPA
Natural fission reactors, thermohydraulic and nuclear modeling, 131–141
Negative-binomial and Poisson *N* prior distributions for multiple sampling, 344–346
Neutron fluences in Trinity Test, 148–150

New Mexico. *See* Los Alamos National Laboratory; Trinity Test
Neyman-Pearson confidence intervals, 307
Neyman's chi square, 320, 322, 331
NNDC. *See* National Nuclear Data Center
Non-counting variance, 24
Non-extending dead-time
  count loss, definition, 219–220
  exponential time interval
    distribution, moment analysis, 327–330
Noninformative *N* prior distributions for multiple sampling, 346–347
Noninformative prior distributions, description, 340–341
NSR (Nuclear Science References) database, description, 11
Nuclear counting statistics, overview of progress, 218–233
Nuclear eyeball size in Trinity Test, 155, 156*t*
Nuclear installation areas, detection limit evaluations, environmental monitoring techniques, 293–304
Nuclear Reaction Model Code. *See* EMPIRE
Nuclear science and risk assessment, connection, 3–7
Nuclear science example using Bayesian inference, 352–353
Nuclear Science References database. *See* NSR database
Nuclear science research, risk assessment guide, 7–8
Nuclear statistics, exponential decay law, 42–56
Nuclear Structure References database. *See* NSR database
Nuclear Wallet Cards, 17–18
NuDat database, 16–17*f*

O

Ohio. *See* Dayton, Ohio
Oklo natural reactors, thermohydraulic and nuclear modeling, 131–141
Oklo two-dimensional numerical reactor model development, 135–138
Operating Characteristic, detection significance test, 22
Operational periodicity in Oklo code predictions, 139–140
Overdispersion corrections due to correlated counts in radon measurements, 249–268
Overdispersion in counting statistics, 230–232, 338–340

P

4π β-γ coincidence method. *See* Digital coincidence counting
Paired counting
  decision levels and detection limits, 305–315
  limits, and extreme low-level Poisson detection decisions, 30–33
Parallel Environment Neutral-particle Transport. *See* PENTRAN code system
Parameter estimation for arbitrary function, 324–325
Parameter estimation for constant function, 320–324
Particle counting with dead time correction, 330
Particle-flux relationship to phase-space density, 209
Particle transport methods, three-dimensional, 162–182
Particulate matter less than 10 micrometers. See PM_{10}

Downloaded by 89.163.34.136 on August 6, 2012 | http://pubs.acs.org
Publication Date: November 16, 2006 | doi: 10.1021/bk-2007-0945.ix002

Partition coefficient (K_d), chromatography column simulations, 270–278
Pathway analysis, for RESRAD (onsite) code, 59–63
Pathways to population exposure, environmental monitoring for radionuclides, 293–294
Pearson's chi-square, 320–321, 322, 331
PENTRAN code system, description, 168
Performance prediction, γ- and β-spectrometry systems, Monte Carlo N-particle transport code extension, 187–192
Phantom. *See* MIRD phantom
Photon radiation from radioactive gases in airborne plume, 105
Plutonium composition in Trinity Test, 155, 156*t*
Plutonium production for Gadget fuel, 146–147
PM_{10} (particulate matter less than 10 micrometers) model calibration, 78, 80*f*–81*f*
Poisson curve fit, chromatography elution peaks, 274–278
Poisson detection decisions
  detection limits for background asymptote, 29–30
  extreme low-level, 30–33
Poisson distribution
  Bayesian inference, 351–353
  likelihood function, 337
  principles, 336
  properties, 336
Poisson hypothesis for background counts, validity, 21*f*, 33–38
Poisson *N* and negative-binomial prior distributions for multiple sampling, 344–346
Poisson-normal approximation in counting statistics, 24–29
Poisson process, count rate estimation, 316–334
Poisson statistics
  predicted deviations, 218–233
  validity criteria, 250
Poisson treatment, exact, history, 29–33
Polyvinyl-toluene detection systems, models, 197, 200–202*f*
Primary proton spectrum, random-walk solution, 211–212
Prior distributions and Bayes theorem, 340–342
Probabilistic approach, exponential decay theory, 44–47
Prompt gamma neutron activation analysis, waste assay, 170–172*t*
Prompt neutrons in Trinity Test, 154–155, 156*t*
Pulse and gate signal formation logic, 186–187
Pulse height spectra, simulation model in Visual C^{++}, 32-bit dynamic link library, 240–241*f*
Pulse pile-up, count loss, definition, 220
Pulse shapes, simulation model in Visual C^{++}, 32-bit dynamic link library, 238–240

Q

Quantification Limit, algebraic expression, 20–22
Quantum mechanics treatment, radioactive decay, 47–48
Quantum Zeno effect, 48, 50

R

Radiation dosimetry, human anatomy modeling, 115–130

Downloaded by 89.163.34.136 on August 6, 2012 | http://pubs.acs.org
Publication Date: November 16, 2006 | doi: 10.1021/bk-2007-0945.ix002

Radiation portal monitors, models for homeland security applications, 195–206
Radioactive decay, specific nuclides, statistical simulation, Monte Carlo N-particle transport code extension, application, 187–192
Radioactive plume-caused external exposure, dose kernel integration, 105–109
Radioactive plume external effective dose, calculation by Monte Carlo dose kernel integration, 104–114
Radionuclide standardization, raw data simulation by dynamic link library, 234–248
Radionuclides, complete decay probabilities, 53–54
Radionuclides with chemicals, releases into air and surface water from Cerro Grande fire, geographic area, 72–73*f*
Radon decay series, physical data for radionuclides, 256–257*t*
Radon measurements, overdispersion corrections due to correlated counts, 249–268
Random-walk solution, heliospheric transport equation, 207–216
RDX (hexahydro-1,3,5-trinitro-1,3,5-triazine), risk from air release, Cerro Grande Fire, 84–85
Real-time mode, counting, 224–228*f*
RESRAD code family, modeling radionuclide transport and assessing risk, 58–70
  availability, 69
  RESRAD-BIOTA code, 60
  RESRAD-BUILD code, 60
  RESRAD-OFFSITE code, 60
  RESRAD (onsite) code, pathway analysis, 59–63
  RESRAD-RECYCLE code, 60
Risk assessment application to nuclear science, overview, 3–9
Risk assessment codes, RESRAD family, 58–70
Risk communication on radionuclides and chemicals release during Cerro Grande Fire, 87, 89–91
Risk equation with components, 4–7
Rutherford and Soddy, exponential decay law discovery, 42–44

S

Schweidler, first exponential decay theory, 44–46
Scintillation cells, 257–263*f*
  See also Lucas cell
Simplification, risk estimation methods, importance to nuclear science research, 8
Simulation model, Visual C^{++}, 32-bit dynamic link library, 236–240, 241*f*
  predictions, 240, 242–245
  testing, 246–247
Single workstation calculations on internal dosimetry at Los Alamos, 96–97
S_N method. *See* Discrete ordinates method; Deterministic methods
Solar wind, influence on cosmic-ray intensity, radiation dose determination to space crew, 208
Source modeling in extended Monte Carlo N-particle transport code, 184–186
Space crews, radiation dose determination, solar wind influence on cosmic-ray intensity, 208
Standard deviations, counting in real-time mode, 224, 226*f*, 227–28*f*
Stochastic Markov approach to radioactive decay, 50–53
  See also Markov chain
Stylized models, human body for radiation protection dosimetry, 116–118*f*

Downloaded by 89.163.34.136 on August 6, 2012 | http://pubs.acs.org
Publication Date: November 16, 2006 | doi: 10.1021/bk-2007-0945.ix002

Subjectivist approach to probability interpretation, 342
Surface pathway risks, estimated risk associated with air release during Cerro Grande Fire, 85–86, 88*t*
Surface water transport, radionuclides and chemicals released during Cerro Grande Fire, 79, 82
Survival functions, digital coincidence counting software, 240, 242
Swiss directive HSK-R-41, dose conversion factors, 112, 113*f*

T

Temperature profiles, uranium concentrations in Oklo two-dimensional numerical reactor model, 136–139
Thallium-doped sodium-iodide-based detection systems, models, 197, 200–202*f*
Theoretical plates, chromatography elusion curve simulations, 269–279
Three-dimensional particle transport methods, 162–182
Throughput factors, definition, 221
Time interval distribution analysis, 317
Time interval distribution central moments, 326*f*, 331
Time interval distributions between consecutive events, 221–223
Time interval spectra, central moment analysis, versus unbiased fit, 316–334
Tomographic model development, human body for radiation protection dosimetry, 117, 119, 120–125
Transient computer model development for Oklo natural reactor, 133–135
Trinitite, radioactivity and freeze-out time, 146–148, 154, 156*t*
  See also Ground zero
Trinity Test, modeling the effects, 142–159

U

Ukraine. *See* Chernobyl; Khmel'nits'kiy nuclear power plant
Unbiased fit versus central moment analysis of time interval spectra, 316–334
Uncertainties in modeling radionuclide and chemical releases from Cerro Grande Fire, 87
Uncertainties in radionuclide half-life measurements, 282–292
Uncertainty component in loss-free counting, 229
Uncertainty components, aggregate, 290
Uncertainty equations, 283–285
Uncertainty estimate improvement, importance to nuclear science research, 8
Uncertainty in blank count, method to compensate, 307–313
Unfolding code calculations for internal dosimetry at Los Alamos, 98–102
Upper bounds for errors, method to compensate for uncertainty in blank count, 308–309
Uranium concentrations with temperature profiles in Oklo two-dimensional numerical reactor model, 136–139
US EPA Report 402-R-93-081, dose conversion factors, 111–112, 113*f*
  See also entity names; National entries

Downloaded by 89.163.34.136 on August 6, 2012 | http://pubs.acs.org
Publication Date: November 16, 2006 | doi: 10.1021/bk-2007-0945.ix002

V

Validation and verification, radiation portal monitor systems, 200–203
Validation importance to nuclear science research, 8
Validity criteria for Poisson statistics, 250
Validity for Poisson hypothesis for background counts, 21*f*, 33–38
Variance reduction techniques, Monte Carlo calculations, 166–167
Verification and validation, radiation portal monitor systems, 200–203
VIP-man model
  construction, 120–124
  human anatomy modeling for radiation dosimetry, 115–130
Visible Human Project, National Library of Medicine, images, 120–122
Visible Photographic Man. *See* VIP-Man

W

Washington State. *See* Hanford reactors
Waste assay, prompt gamma neutron activation analysis, 170–172*t*
Waste determination, flux/dose determination, spent fuel cask for spent nuclear fuel storage, 177–180
Weighted average, Poisson process, 318–320

Z

Zero dead time counting, 228–230

Downloaded by 89.163.34.136 on August 6, 2012 | http://pubs.acs.org
Publication Date: November 16, 2006 | doi: 10.1021/bk-2007-0945.ix002